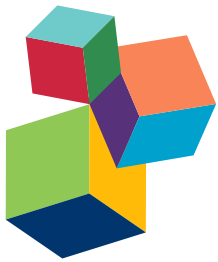


# QUANTITATIVE BIOLOGY: DYNAMICS OF LIVING SYSTEMS

**EDITED BY:** Noriko Hiroi, Viji M. Draviam, Tetsuya J. Kobayashi, Akira Funahashi,  
Chun-Biu Li, Douglas B. Murray, Hiroaki Takagi, Ziya Kalay, Rinshi S. Kasai,  
Jason Edward Shoemaker, Akatsuki Kimura and Naoki A. Irie

**PUBLISHED IN:** Frontiers in Physiology, Frontiers in Neuroscience and  
Frontiers in Cell and Developmental Biology



# frontiers

## **Frontiers Copyright Statement**

© Copyright 2007-2017 Frontiers Media SA. All rights reserved.

All content included on this site, such as text, graphics, logos, button icons, images, video/audio clips, downloads, data compilations and software, is the property of or is licensed to Frontiers Media SA ("Frontiers") or its licensees and/or subcontractors. The copyright in the text of individual articles is the property of their respective authors, subject to a license granted to Frontiers.

The compilation of articles constituting this e-book, wherever published, as well as the compilation of all other content on this site, is the exclusive property of Frontiers. For the conditions for downloading and copying of e-books from Frontiers' website, please see the Terms for Website Use. If purchasing Frontiers e-books from other websites or sources, the conditions of the website concerned apply.

Images and graphics not forming part of user-contributed materials may not be downloaded or copied without permission.

Individual articles may be downloaded and reproduced in accordance with the principles of the CC-BY licence subject to any copyright or other notices. They may not be re-sold as an e-book.

As author or other contributor you grant a CC-BY licence to others to reproduce your articles, including any graphics and third-party materials supplied by you, in accordance with the Conditions for Website Use and subject to any copyright notices which you include in connection with your articles and materials.

All copyright, and all rights therein, are protected by national and international copyright laws.

The above represents a summary only. For the full conditions see the Conditions for Authors and the Conditions for Website Use.

**ISSN 1664-8714**

**ISBN 978-2-88945-213-2**

**DOI 10.3389/978-2-88945-213-2**

## **About Frontiers**

Frontiers is more than just an open-access publisher of scholarly articles: it is a pioneering approach to the world of academia, radically improving the way scholarly research is managed. The grand vision of Frontiers is a world where all people have an equal opportunity to seek, share and generate knowledge. Frontiers provides immediate and permanent online open access to all its publications, but this alone is not enough to realize our grand goals.

## **Frontiers Journal Series**

The Frontiers Journal Series is a multi-tier and interdisciplinary set of open-access, online journals, promising a paradigm shift from the current review, selection and dissemination processes in academic publishing. All Frontiers journals are driven by researchers for researchers; therefore, they constitute a service to the scholarly community. At the same time, the Frontiers Journal Series operates on a revolutionary invention, the tiered publishing system, initially addressing specific communities of scholars, and gradually climbing up to broader public understanding, thus serving the interests of the lay society, too.

## **Dedication to Quality**

Each Frontiers article is a landmark of the highest quality, thanks to genuinely collaborative interactions between authors and review editors, who include some of the world's best academicians. Research must be certified by peers before entering a stream of knowledge that may eventually reach the public - and shape society; therefore, Frontiers only applies the most rigorous and unbiased reviews.

Frontiers revolutionizes research publishing by freely delivering the most outstanding research, evaluated with no bias from both the academic and social point of view.

By applying the most advanced information technologies, Frontiers is catapulting scholarly publishing into a new generation.

## **What are Frontiers Research Topics?**

Frontiers Research Topics are very popular trademarks of the Frontiers Journals Series: they are collections of at least ten articles, all centered on a particular subject. With their unique mix of varied contributions from Original Research to Review Articles, Frontiers Research Topics unify the most influential researchers, the latest key findings and historical advances in a hot research area! Find out more on how to host your own Frontiers Research Topic or contribute to one as an author by contacting the Frontiers Editorial Office: [researchtopics@frontiersin.org](mailto:researchtopics@frontiersin.org)

# QUANTITATIVE BIOLOGY: DYNAMICS OF LIVING SYSTEMS

Topic Editors:

**Noriko Hiroi**, Keio University, Japan

**Viji M. Draviam**, Queen Mary University of London, United Kingdom

**Tetsuya J. Kobayashi**, University of Tokyo, Japan

**Akira Funahashi**, Keio University, Japan

**Chun-Biu Li**, Hokkaido University, Japan

**Douglas B. Murray**, Keio University, Japan

**Hiroaki Takagi**, Nara Medical University, Japan

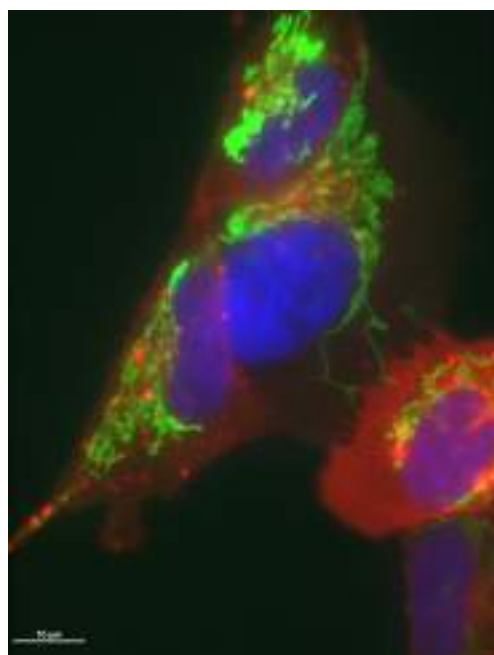
**Ziya Kalay**, Kyoto University, Japan

**Rinshi S. Kasai**, Kyoto University, Japan

**Jason Edward Shoemaker**, University of Pittsburgh, United States

**Akatsuki Kimura**, National Institute of Genetics, Japan

**Naoki A. Irie**, University of Tokyo, Japan



These cells are human derived neuroblastoma SH-SY5Y cell line (ECACC Cell Bank, No. 94030304), incorporated Qdots 655 (Invitrogen, red spots), cultured with normal growth medium (DMEM/F-12; Wako, 15% FBS). Nuclei were stained with Hoechst 33342 (Lonza, blue), mitochondria were stained with MitoTracker Green FM (Invitrogen, green).

The image was provided by Ryuichi Tanimoto (Keio University), captured with FV1000 inverted confocal microscope (Olympus) equipped with a 100X objective (NA = 1.4)

With the emergence of Systems Biology, there is a greater realization that the whole behavior of a living system may not be simply described as the sum of its elements. To represent a living system using mathematical principles, practical quantities with units are required. Quantities are not only the bridge between mathematical description and biological observations; they often stand as essential elements similar to genome information in genetics. This important realization has greatly rejuvenated research in the area of Quantitative Biology.

Because of the increased need for precise quantification, a new era of technological development has opened. For example, spatio-temporal high-resolution imaging enables us to track single molecule behavior *in vivo*. Clever artificial control of experimental conditions and molecular structures has expanded the variety of quantities that can be directly measured. In addition, improved computational power and novel algorithms for analyzing theoretical models have made it possible to investigate complex biological phenomena.

This research topic is organized on two aspects of technological advances which are the backbone of Quantitative Biology: (i) visualization of biomolecules, their dynamics and function, and (ii) generic technologies of model optimization and numeric integration. We have also included articles highlighting the need for new quantitative approaches to solve some of the long-standing cell biology questions.

In the first section on visualizing biomolecules, four cutting-edge techniques are presented. Ichimura et al. provide a review of quantum dots including their basic characteristics and their applications (for example, single particle tracking). Horisawa discusses a quick and stable labeling technique using click chemistry with distinct advantages compared to fluorescent protein tags. The relatively small physical size, stability of covalent bond and simple metabolic labeling procedures in living cells provides this type of technology a potential to allow long-term imaging with least interference to protein function. Obien et al. review strategies to control microelectrodes for detecting neuronal activity and discuss techniques for higher resolution and quality of recordings using monolithic integration with on-chip circuitry. Finally, the original research article by Amariei et al. describes the oscillatory behavior of metabolites in bacteria. They describe a new method to visualize the periodic dynamics of metabolites in large scale cultures populations. These four articles contribute to the development of quantitative methods visualizing diverse targets: proteins, electrical signals and metabolites.

In the second section of the topic, we have included articles on the development of computational tools to fully harness the potential of quantitative measurements through either calculation based on specific model or validation of the model itself. Kimura et al. introduce optimization procedures to search for parameters in a quantitative model that can reproduce experimental data. They present four examples: transcriptional regulation, bacterial chemotaxis, morphogenesis of tissues and organs, and cell cycle regulation. The original research article by Sumiyoshi et al. presents a general methodology to accelerate stochastic simulation efforts. They introduce a method to achieve 130 times faster computation of stochastic models by applying GPGPU. The strength of such accelerated numerical calculation are sometimes underestimated in biology; faster simulation enables multiple runs and in turn improved accuracy of numerical calculation which may change the final conclusion of modeling study. This also highlights the need to carefully assess simulation results and estimations using computational tools.

The final section of our research topic illustrates open questions in our understanding of dynamic cellular events—molecular crowding and cell division—that could benefit using quantitative biology approaches. The review by Aon and Cortassa focuses on macromolecular crowding in a cell. The authors discuss that the self-organizing capability of the cytoskeleton can orchestrate metabolic flux, while the fractal organization can frame the scaling activity. The review aims to shed light on ways to integrate the structural and functional linkage via crowding. Molecular crowding of each organelle may be affected by the flow into and out of the compartment. Vincent et al. focus on proteins in endoplasmic reticulum which have to enter through membrane-embedded translocons. They present concrete estimates on the flow of proteins entering the ER

lumen. Berry and Soula present original findings on the importance of transient subdiffusion for protein distribution in space, when transient subdiffusion is restricted to a subregion of the space. Their simulations reveal a strong accumulation at equilibrium in the subdiffusion region that is controlled by the long-time asymptotic Brownian regime rather than the initial short-time subdiffusion.

Cell division is a fundamental process that goes awry in cancers yet there has been a puzzling absence of prominent oncogenic mutations in key cell division regulators. By measuring cell size and duration of cell cycle in early embryonic development of *C. elegans*, Arata et al., reveal a power law relationship between cell cycle duration and cell volume. They propose that geometric constraints between intracellular structures may coordinate cell cycle with the size of the original cell. In the opinion article Chin et al., highlight the need to build multiscale models for understanding pathways that jointly control the plane of cell division. Using structural knowledge of multi-protein complexes, Lee and Bolanos-Gracia review the dynamics of checkpoint signal amplification during cell division which ensures the accurate segregation of chromosomes. Mathematical models of dynamic cytoskeletal processes may be required to understand and intervene with tumor cell behavior.

In summary, our topic gives a flavor of new candidate probes for rigorous quantification, which needs to be perpetually emphasized in Quantitative Biology. Non-linear dynamic behavior of living systems is likely to be a leading challenge that needs to be described quantitatively. We hope the articles in this Research Topic will help you find your own, attractive perspective of biology via quantitative analyses.

**Citation:** Hiroi, N., Draviam, V. M., Kobayashi, T. J., Funahashi, A., Li, C.-B., Murray, D. B., Takagi, H., Kalay, Z., Kasai, R. S., Shoemaker, J. E., Kimura, A., Irie, N. A., eds. (2017). Quantitative Biology: Dynamics of Living Systems. Lausanne: Frontiers Media. doi: 10.3389/978-2-88945-213-2

# Table of Contents

- 07 Editorial: Quantitative Biology: Dynamics of Living Systems**  
Noriko Hiroi, Viji M. Draviam and Akira Funahashi

## **Section 1. Visualization technologies of biomolecules, their dynamics and function**

- 09 Nano-scale measurement of biomolecules by optical microscopy and semiconductor nanoparticles**  
Taro Ichimura, Takashi Jin, Hideaki Fujita, Hideo Higuchi and Tomonobu M. Watanabe
- 22 Specific and quantitative labeling of biomolecules using click chemistry**  
Kenichi Horisawa
- 28 Revealing neuronal function through microelectrode array recordings**  
Marie Engelene J. Obien, Kosmas Deligkaris, Torsten Bullmann, Douglas J. Bakkum and Urs Frey
- 58 Quantifying periodicity in omics data**  
Cornelia Amariei, Masaru Tomita and Douglas B. Murray

## **Section 2. Generic technologies of model optimization and numeric integration**

- 67 Estimating cellular parameters through optimization procedures: elementary principles and applications**  
Akatsuki Kimura, Antonio Celani, Hiromichi Nagao, Timothy Stasevich and Kazuyuki Nakamura
- 76 Acceleration of discrete stochastic biochemical simulation using GPGPU**  
Kei Sumiyoshi, Kazuki Hirata, Noriko Hiroi and Akira Funahashi

## **Section 3. Open questions in our understanding of dynamic cellular events**

### **Subsection 3-1. Intracellular Molecular Crowding**

- 86 Function of metabolic and organelle networks in crowded and organized media**  
Miguel A. Aon and Sonia Cortassa
- 96 Surveying the floodgates: estimating protein flux into the endoplasmic reticulum lumen in *Saccharomyces cerevisiae***  
Michael Vincent, Mark Whidden and Santiago Schnell
- 102 Spatial distributions at equilibrium under heterogeneous transient subdiffusion**  
Hugues Berry and Hédi A. Soula

### **Subsection 3-2. Cell Division**

- 110 Power law relationship between cell cycle duration and cell volume in the early embryonic development of *Caenorhabditis elegans***  
Yukinobu Arata, Hiroaki Takagi, Yasushi Sako and Hitoshi Sawa

- 121 Need for multi-scale systems to identify spindle orientation regulators relevant to tissue disorganization in solid cancers**  
Hui Men Selina Chin, Karandeep Nandra, Joanna Clark and Viji M. Draviam
- 126 The dynamics of signal amplification by macromolecular assemblies for the control of chromosome segregation**  
Semin Lee and Victor M. Bolanos-Garcia



# Editorial: Quantitative Biology: Dynamics of Living Systems

Noriko Hiroi<sup>1\*</sup>, Viji M. Draviam<sup>2</sup> and Akira Funahashi<sup>1</sup>

<sup>1</sup> Systems Biology Laboratory, Department of Biosciences and Informatics, Keio University, Yokohama, Japan, <sup>2</sup> Cell and Molecular Biology, School of Biological and Chemical Sciences, Queen Mary University of London, London, UK

**Keywords:** quantitative biology, bioimaging, parameter optimization, generic technologies, cell division

## The Editorial on the Research Topic

### Quantitative Biology: Dynamics of Living Systems

With the emergence of Systems Biology, there is a greater realization that the whole behavior of a living system may not be simply described as the sum of its elements. To represent a living system using mathematical principles, practical quantities with units are required. Quantities are not only the bridge between mathematical description and biological observations; they often stand as essential elements similar to genome information in genetics. This important realization has greatly rejuvenated research in the area of Quantitative Biology.

Because of the increased need for precise quantification, a new era of technological development has opened. For example, spatio-temporal high-resolution imaging enables us to track single molecule behavior *in vivo*. Clever artificial control of experimental conditions and molecular structures has expanded the variety of quantities that can be directly measured. In addition, improved computational power and novel algorithms for analyzing theoretical models have made it possible to investigate complex biological phenomena.

This research topic is organized on two aspects of technological advances which are the backbone of Quantitative Biology: (i) visualization of biomolecules, their dynamics and function, and (ii) generic technologies of model optimization and numeric integration. We have also included articles highlighting the need for new quantitative approaches to solve some of the long-standing cell biology questions.

In the first section on visualizing biomolecules, four cutting-edge techniques are presented. Ichimura et al. provide a review of quantum dots including their basic characteristics and their applications (for example, single particle tracking). Horisawa discusses a quick and stable labeling technique using click chemistry with distinct advantages compared to fluorescent protein tags. The relatively small physical size, stability of covalent bond and simple metabolic labeling procedures in living cells provides this type of technology a potential to allow long-term imaging with least interference to protein function. Obien et al. review strategies to control microelectrodes for detecting neuronal activity and discuss techniques for higher resolution and quality of recordings using monolithic integration with on-chip circuitry. Finally, the original research article by Amariei et al. describes the oscillatory behavior of metabolites in bacteria. They describe a new method to visualize the periodic dynamics of metabolites in large scale cultures populations. These four articles contribute to the development of quantitative methods visualizing diverse targets: proteins, electrical signals and metabolites.

In the second section of the topic, we have included articles on the development of computational tools to fully harness the potential of quantitative measurements through either calculation based on specific model or validation of the model itself. Kimura et al. introduce optimization procedures to search for parameters in a quantitative model that can reproduce experimental data. They present four examples: transcriptional regulation, bacterial chemotaxis,

## OPEN ACCESS

### Edited by:

Raina Robeva,  
Randolph-Macon College and Sweet Briar College, USA

### Reviewed by:

Adrienne H. K. Roeder,  
Cornell University, USA

### \*Correspondence:

Noriko Hiroi  
hiroi@bio.keio.ac.jp

### Specialty section:

This article was submitted to  
Systems Biology,  
a section of the journal  
*Frontiers in Physiology*

Received: 25 April 2016

Accepted: 17 May 2016

Published: 02 June 2016

### Citation:

Hiroi N, Draviam VM and Funahashi A (2016) Editorial: Quantitative Biology: Dynamics of Living Systems. *Front. Physiol.* 7:196.  
doi: 10.3389/fphys.2016.00196

morphogenesis of tissues and organs, and cell cycle regulation. The original research article by Sumiyoshi et al. presents a general methodology to accelerate stochastic simulation efforts. They introduce a method to achieve 130 times faster computation of stochastic models by applying GPGPU. The strength of such accelerated numerical calculation are sometimes underestimated in biology; faster simulation enables multiple runs and in turn improved accuracy of numerical calculation which may change the final conclusion of modeling study. This also highlights the need to carefully assess simulation results and estimations using computational tools.

The final section of our research topic illustrates open questions in our understanding of dynamic cellular events—molecular crowding and cell division—that could benefit using quantitative biology approaches. The review by Aon and Cortassa focuses on macromolecular crowding in a cell. The authors discuss that the self-organizing capability of the cytoskeleton can orchestrate metabolic flux, while the fractal organization can frame the scaling activity. The review aims to shed light on ways to integrate the structural and functional linkage *via* crowding. Molecular crowding of each organelle may be affected by the flow into and out of the compartment. Vincent et al. focus on proteins in endoplasmic reticulum which have to enter through membrane-embedded translocons. They present concrete estimates on the flow of proteins entering the ER lumen. Berry and Soula present original findings on the importance of transient subdiffusion for protein distribution in space, when transient subdiffusion is restricted to a subregion of the space. Their simulations reveal a strong accumulation at equilibrium in the subdiffusion region that is controlled by the long-time asymptotic Brownian regime rather than the initial short-time subdiffusion.

Cell division is a fundamental process that goes awry in cancers yet there has been a puzzling absence of prominent oncogenic mutations in key cell division regulators. By measuring cell size and duration of cell cycle in early embryonic development of *C. elegans*, Arata et al., reveal a power law relationship between cell cycle duration and cell volume. They propose that geometric constraints between intracellular structures may coordinate cell cycle with the size of the original cell. In the opinion article Chin et al., highlight the need to build multiscale models for understanding pathways that jointly control the plane of cell division. Using structural knowledge of multi-protein complexes, Lee and Bolanos-Gracia review

the dynamics of checkpoint signal amplification during cell division which ensures the accurate segregation of chromosomes. Mathematical models of dynamic cytoskeletal processes may be required to understand and intervene with tumor cell behavior.

In summary, our topic gives a flavor of new candidate probes for rigorous quantification, which needs to be perpetually emphasized in Quantitative Biology. Non-linear dynamic behavior of living systems is likely to be a leading challenge that needs to be described quantitatively. We hope the articles in this Research Topic will help you find your own, attractive perspective of biology via quantitative analyses.

## AUTHOR CONTRIBUTIONS

NH prepared the first draft, and VD and AF made critical revision of the manuscript.

## FUNDING

The International workshop on Quantitative Biology 2012 to 2014 were supported by The Royal society, UK, Industrial Institute of the University of Tokyo, Japan, Keio University, Japan, Transdisciplinary Research Integration Center of Research Organization of Information and Systems, RIKEN CDB, Japan, VLSCI Life Science Computation, Australia, and DaiNippon Sumitomo Pharma, Japan.

## ACKNOWLEDGMENTS

We are grateful to all the authors who contributed to this research topic. We also thank the editors and reviewers of the articles. We express our gratitude to all the organizers and attendees of International Workshop of Quantitative Biology 2012 to 2014, especially Prof. Akatsuki Kimura and Prof. Hugues Berry who added revisions to our manuscript.

**Conflict of Interest Statement:** The authors declare that the research was conducted in the absence of any commercial or financial relationships that could be construed as a potential conflict of interest.

Copyright © 2016 Hiroi, Draviam and Funahashi. This is an open-access article distributed under the terms of the Creative Commons Attribution License (CC BY). The use, distribution or reproduction in other forums is permitted, provided the original author(s) or licensor are credited and that the original publication in this journal is cited, in accordance with accepted academic practice. No use, distribution or reproduction is permitted which does not comply with these terms.



# Nano-scale measurement of biomolecules by optical microscopy and semiconductor nanoparticles

Taro Ichimura<sup>1</sup>, Takashi Jin<sup>2,3,4</sup>, Hideaki Fujita<sup>1,4</sup>, Hideo Higuchi<sup>5</sup> and Tomonobu M. Watanabe<sup>1,3,4\*</sup>

<sup>1</sup> Laboratory for Comprehensive Bioimaging, RIKEN Quantitative Biology Center, Saita, Osaka, Japan

<sup>2</sup> Laboratory for Nano-Bio Probes, RIKEN Quantitative Biology Center, Saita, Osaka, Japan

<sup>3</sup> Graduate School of Frontier Biosciences, Osaka University, Saita, Osaka, Japan

<sup>4</sup> WPI, Immunology Frontier Research Center, Osaka University, Saita, Osaka, Japan

<sup>5</sup> Department of Physics, School of Science, The University of Tokyo, Bunkyo, Tokyo, Japan

**Edited by:**

Rinshi S. Kasai, Institute for Frontier Medical Sciences, Japan

**Reviewed by:**

Takahiro Fujiwara, Kyoto University, Japan

Yajima Junichiro, Tokyo, Japan

**\*Correspondence:**

Tomonobu M. Watanabe,  
Laboratory for Comprehensive Bioimaging, RIKEN Quantitative Biology Center, 6-2-3, Furuie-dai,  
Saita, Osaka 565-0874, Japan  
e-mail: tomowatanabe@riken.jp

Over the past decade, great developments in optical microscopy have made this technology increasingly compatible with biological studies. Fluorescence microscopy has especially contributed to investigating the dynamic behaviors of live specimens and can now resolve objects with nanometer precision and resolution due to super-resolution imaging. Additionally, single particle tracking provides information on the dynamics of individual proteins at the nanometer scale both *in vitro* and in cells. Complementing advances in microscopy technologies has been the development of fluorescent probes. The quantum dot, a semi-conductor fluorescent nanoparticle, is particularly suitable for single particle tracking and super-resolution imaging. This article overviews the principles of single particle tracking and super resolution along with describing their application to the nanometer measurement/observation of biological systems when combined with quantum dot technologies.

**Keywords:** single particle tracking, super-resolution, fluorescent microscopy, quantum dot, nanoparticle

## INTRODUCTION

Fluorescence microscopy has become standard for studying the dynamic behavior of biological phenomena such as the expression, movement, and localization of proteins and other molecules (Ellinger, 1940; Lichtman and Conchello, 2005; Drummel, 2012; Miyawaki, 2013; Peter et al., 2014). Optical diffraction, however, limits the spatial resolution to several 100 nanometers, denying information on many details about these phenomena (Abbe, 1873). Two technologies have since overcome this limitation and permit the observation of even smaller nano-scale dynamics: single particle tracking (Ritchie and Kusumi, 2003; Saxton, 2009; Chenouard et al., 2014) and super-resolution microscopy (Schermelleh et al., 2010; Galbraith and Galbraith, 2011; Leung and Chou, 2011). Single particle tracking pursues the position of single fluorescent probes conjugated to separate target proteins over a two-dimensional (2D) plane. Super-resolution microscopy, on the other hand, provides highly resolved optical images beyond the aforementioned spatial resolution.

To conduct the above imaging techniques, it is often required to label the target protein with a fluorescent probe. Fluorescent proteins are most popular for this purpose because of their simple and easy labeling procedure in live cells (Shimomura and Johnson, 1962; Tsien, 1998; Nifosi et al., 2007). Organic dyes are also common because of their wide application (Wombacher and Cornish, 2011; Wysocki and Lavis, 2011; Terai and Nagano, 2013). Another group of probes gaining attention is inorganic nanoparticles made of semiconductors, metals, silicon, etc. (Ruedas-Rama et al., 2012; Chinnathambi et al., 2014; Cupaioli et al., 2014).

Although usually larger than fluorescent proteins and organic dyes, inorganic nanoparticles have generally stronger and more stable fluorescence profiles, which makes them applicable not only to basic research, but also to clinical studies (Byers and Hitchman, 2010; Choi and Frangioni, 2010; Saadeh et al., 2014; Wang and Wang, 2014). Furthermore, these same properties make them well suited for single particle tracking methods (Chang et al., 2008; Saxton, 2008; Barroso, 2011; Bruchez, 2011; Clausen and Lagerholm, 2011; Ruthardt et al., 2011; Pierobon and Cappello, 2012; Kairdolf et al., 2013; Petryayeva et al., 2013).

This review article focuses on advanced microscopy using quantum dots (Qdots), perhaps the most studied of inorganic nanoparticles for biological application (Pilla et al., 2012). Single particle tracking using Qdots has reached three dimensions (X, Y, Z) (Genovesio et al., 2006; Holtzer et al., 2007; Watanabe and Higuchi, 2007; Watanabe et al., 2007; Ram et al., 2008, 2012; Wells et al., 2008, 2010; Yajima et al., 2008), and more recently has even reached four dimensions (X, Y, Z,  $\theta$  or X, Y,  $\theta$ ,  $\phi$ ) (Ohmachi et al., 2012; Watanabe et al., 2013). For all their benefits, Qdots do have drawbacks, however, including high blinking (Nirmal et al., 1996; van Sark et al., 2001; Schlegel et al., 2002; Hohng and Ha, 2004; Ko et al., 2011) and a spectral blue-shift during observation (Nirmal et al., 1996; van Sark et al., 2002; Hoyer et al., 2011), which complicate the continuous tracking of the single particle and emerge due to photo-oxidation while under high-power illumination. These limitations have stimulated research into new super-resolution microscopy methods (Lidke et al., 2005; Dertinger et al., 2009; Watanabe et al., 2010; Chien et al., 2011; Hoyer et al., 2011; Deng et al., 2014).

## Qdots AS FLUORESCENT LABELING PROBES

A Qdot is a semiconductor nanocrystal with electronic characteristics that depend on its size and shape (Rossetti et al., 1980; Ekimov and Onushchenko, 1981). Because of its unique characteristics and ease of synthesis, Qdots have been applied not only to biomedical research, but also to engineering- and industrial-related fields such as transistors, solar cells, LEDs, and diode lasers (Pilla et al., 2012). Qdots used in biological studies have a core-shell structure (**Figure 1A**); the most famous being the cadmium selenide (CdSe) core and zinc sulfide (ZnS) shell (Dabbousi et al., 1997; Bruchez et al., 1998; Chan and Nie, 1998; Pilla et al., 2012). This structure results in Qdots having narrow emission spectra but wide absorption spectra (**Figure 1B**). There are

two important criteria when applying Qdots to biological studies: solubility and conjugating capability (Li et al., 2010). Highly fluorescent Qdots are usually synthesized in organic solvents in coordination with compounds such as tri-n-octylphosphine oxide (TOPO) or alkylamine. These compounds coat the Qdot, making it too hydrophobic to be dissolved in water. Therefore, further surface coating or exchange with hydrophilic compounds is needed for use in biological assay. Furthermore, upon becoming water soluble, the surface of the Qdot must have reactive groups such as amino and carboxyl chains in order for the Qdot to conjugate with the target biological sample. The surface coating contributes not only to the water-solubilization but also to the stabilization of the fluorescence of Qdot in water because the

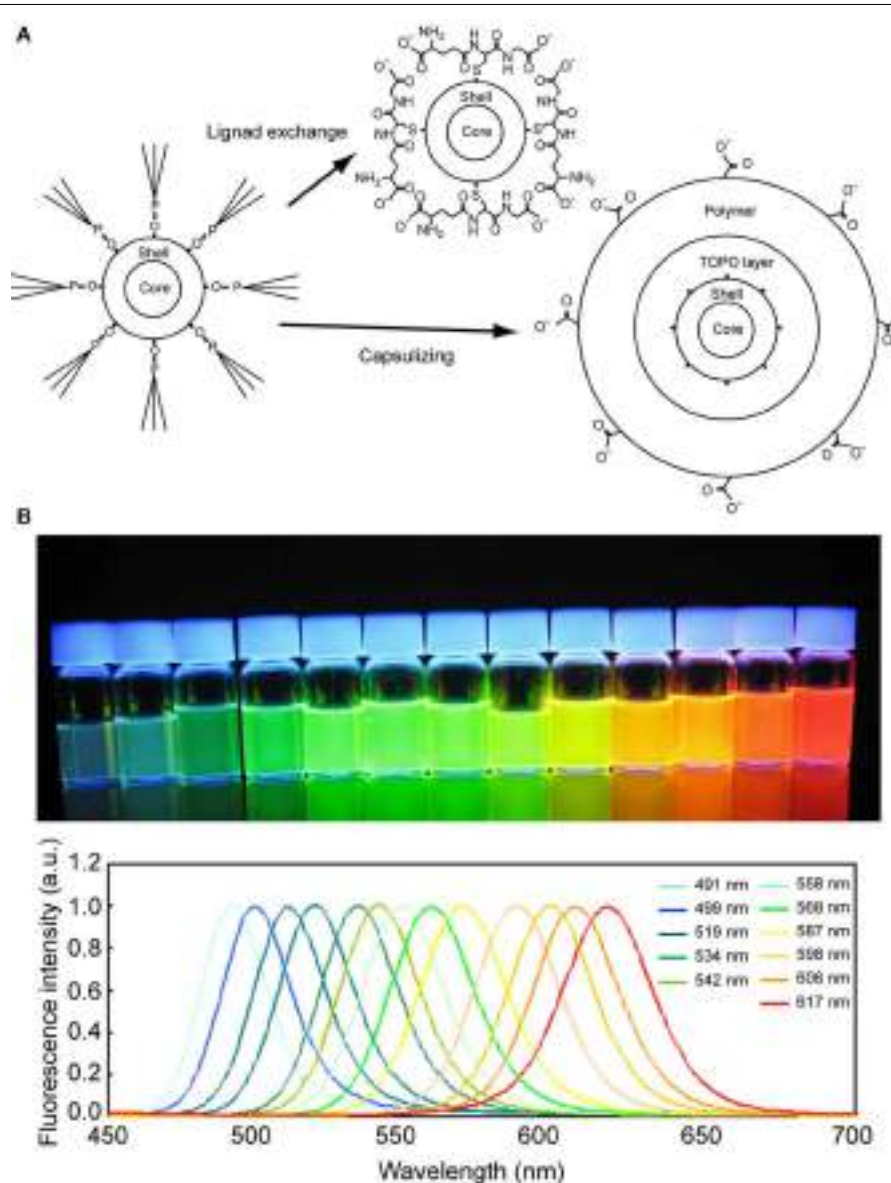


**FIGURE 1 | Quantum dot.** (A) Schematic drawing of the surface modification of a Qdot. (B) Fluorescence photograph (upper) and spectra (lower) of Qdots of various diameters. The Qdots were excited by a UV light of 365 nm wavelength.

photophysical properties are well affected by the surface coating (Kuno et al., 1997; Kloepfer et al., 2005). Some surface coating methods suppress the blinking that is a drawback of Qdot (Hohng and Ha, 2004; Fomenko and Nesbitt, 2008; Mandal and Tamai, 2011; Zhang et al., 2013).

There are mainly two ways to prepare water-soluble Qdots (**Figure 1A**) (Erathodiyil and Ying, 2011; Zhang and Clapp, 2011). The first is to encapsulate a hydrophobic Qdot with an amphiphilic polymer or phospholipid (Dubertret et al., 2002; Gao et al., 2005; Li et al., 2010; Tomczak et al., 2013). The second is a ligand-exchange method in which the capping hydrophobic ligands are exchanged with hydrophilic ones (Gerion et al., 2001; Guo et al., 2003; Pinaud et al., 2004; Kim et al., 2005; Nann, 2005; Jiang et al., 2006; Dubois et al., 2007). While the water-solubilized Qdot obtained by the first method is more stable and suitable for commercialization, its size increases to about 20~40 nm, which risks steric hindrance against the function of the target protein (Li et al., 2010). The ligand-exchange method is inferior in stability, but is a simpler synthesis process and produces a smaller Qdot. The thin coating layer is another advantage of this method, as it reduces the risk of steric effects that could compromise the function of the protein upon conjugation with the Qdot.

Many coating agents exist for the ligand-exchange method. These include mercaptocarboxylic acid (Jiang et al., 2006), carbon disulfide (Dubois et al., 2007), thiosilanol (Gerion et al., 2001), dendrimer (Guo et al., 2003), peptide (Pinaud et al., 2004), phosphine oxide (Kim et al., 2005), and polyethylenimine (Nann, 2005). Coating agents can also sometimes functionalize Qdots for specific purposes. Examples include  $\beta$ -cyclodextrin for ion-sensing (Palaniappan et al., 2004), cyclodextrin for redox-active substrates (Palaniappan et al., 2006), and cyclodextrin thiol for pH-sensing (Cao et al., 2006). We usually use glutathione as the coating compound because of its easier preparation, which requires only the mixing of hydrophobic Qdots with an aqueous glutathione solution (Jin et al., 2008; Tiwari et al., 2009). Glutathione-coated Qdots have two reactive groups (amino and carboxyl) that enable easy conjugation with the target protein and show no cytotoxicity (Tiwari et al., 2009). They can also be kept mono-dispersed in solution for 3 months after solubilization.

## FLUORESCENCE MICROSCOPY FOR NANO-SCALE MEASUREMENTS/OBSERVATIONS

The microscopy introduced in this review requires a regular wide-field fluorescence microscope and no complicated optical principles nor devices (**Figure 2A**). However, because nano-scale measurements require a high signal-to-noise ratio, a highly photon-sensitive camera, such as an electron multiplying charge coupled device (EMCCD) camera, is recommended. More recently, complementary metal-oxide-semiconductor (sCMOS) cameras have become available as alternatives (Huang et al., 2011; Long et al., 2012; Ma et al., 2013). The vibration and/or stage drift of the microscope should also be considered, as these can cause artifacts in the measurement by obscuring the behavior and structure of the target. Consequently, the microscope should be set on a vibration-isolation table and built with as minimal height and maximal rigidity as possible to decrease any vibration. Because thermal expansion of the metals composing the

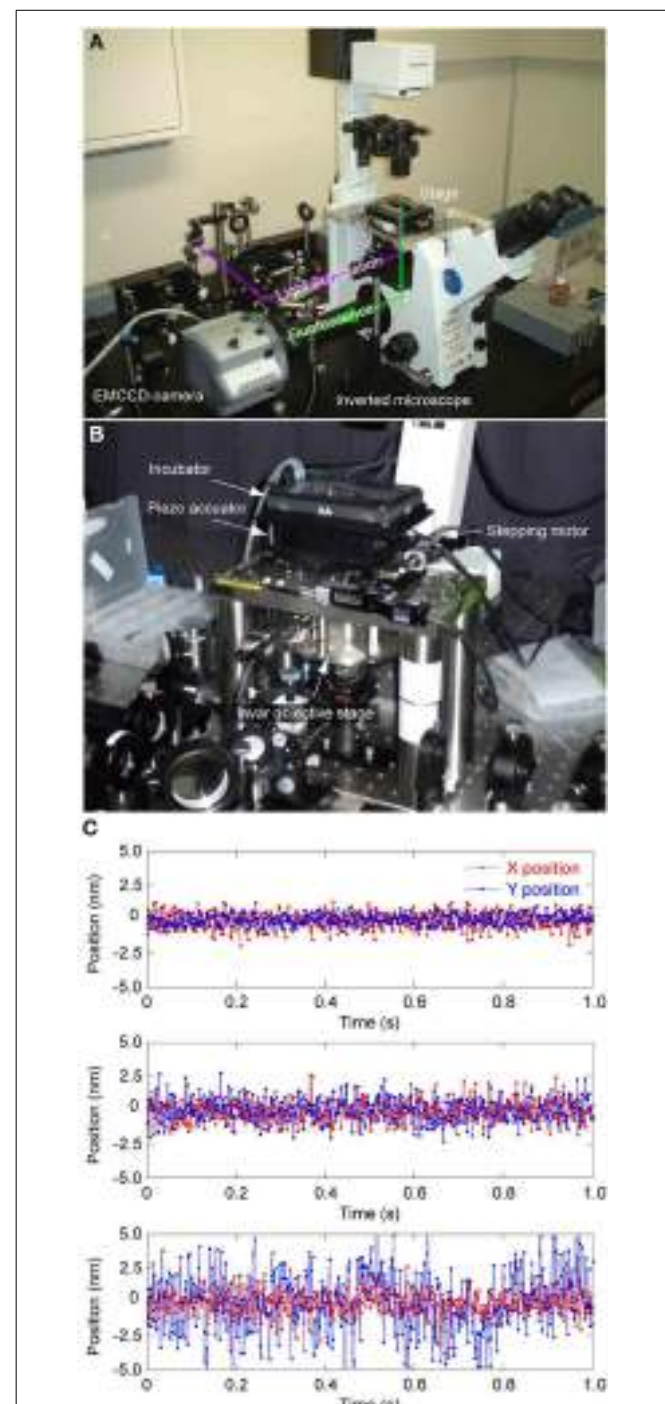


**FIGURE 2 | Microscopic system for nanometry. (A)** Photograph of a typical microscopy setup. The system is mainly composed of an inverted fluorescent microscope (Olympus IX71), an objective lens (Olympus 60 $\times$  PlanApo, 1.45 NA, oil immersion) and EMCCD camera (Andor iXon887 or 867). **(B)** The stage and objective revolver are made of duralumin and custom built. **(C)** Vibrations caused by different components of the microscope: all components rigidly fixed (upper), all components except the camera rigidly fixed (middle), and substitution of the mono-objective revolver with a 6-position revolver (lower). Red, X-position. Blue, Y-position. The stage position was determined by measuring the position of a glass bead absorbed on the sample surface.

microscope causes drifts in the stage and focus position, microscopes made of metals with lower thermal expansion such as invar are generally preferred (**Figure 2B**). The drifts can be further suppressed by setting the microscopic system in a room with constant temperature and humidity.

Here we show one strategy for reducing vibrations. The transition images of a silica bead with 1  $\mu\text{m}$  diameter absorbed on a coverslip surface were acquired with excess illumination so that the camera gain could be set to zero. The frame rate was 2.0 ms, the images were acquired for 1.0 s, and the precise position (X, Y) of the bead was calculated by image analysis. In our usual setup, the position of the bead was kept stable within 0.7 nm in the X-axis and 0.4 nm in the Y-axis (**Figure 2C**, upper). When a screw to fix the CCD camera was loosened, the vibration increased to 0.8 nm in both axes (**Figure 2C**, middle). Normally, we use a mono-objective revolver, but when instead a commercially-available 6-position revolver was used, we found the vibration enhanced in the Y-axis to 2 nm (**Figure 2C**, bottom). Thus, rigid construction of the microscope is paramount for nano-scale measurements and observations.

## SINGLE PARTICLE TRACKING WITH NANOMETER PRECISION USING Qdots

Single particle tracking is well applied for studies of motor proteins and membrane proteins, because resolving nano-scale movements is necessary for understanding the protein function (Ritchie and Kusumi, 2003; Park et al., 2007; Toprak and Selvin, 2007; Saxton, 2009). Although the resolution of conventional fluorescence microscopes is constrained by the diffraction limit, the 2D position of a single particle can be determined by calculating the weight center of the image of the fluorescent spot (**Figure 3A**). The fluorescence emitted from a fluorescent probe forms a point spread function (PSF) that can be fitted with a Gaussian distribution as

$$f(x, y) = I_0 \cdot \exp \left\{ -\frac{(x - x_0)^2 + (y - y_0)^2}{2 \cdot \sigma^2} \right\} + C,$$

where  $I_0$  and  $(x_0, y_0)$  are the fluorescence intensity and the position of the fluorescing center, respectively,  $\sigma$  is the radial standard deviation of the Gaussian function, and  $C$  is the background fluorescence. This analysis can be used to measure the center position of the image (Kubitscheck et al., 2000; Cheezum et al., 2001; Thompson et al., 2002; Small and Stahlheber, 2014). Though there are other common methods for determining the center, including cross-correlation, sum-absolute difference, and simple centroid, Gaussian fitting has the highest robustness at low signal-to-noise ratios, which is common in biological studies (Thompson et al., 2002). In our case, the actual fitting computation is done by the Levenberg-Marquardt method (Levenberg, 1944). A practical example of our fitting is described below (**Figure 3B**). Because the background baseline is not always uniform in live-cell observations, we added additional parameters into the  $C$  term to fit the local background fluorescence with a tilted plane,

$$f(x, y) = I_0 \cdot \exp \left\{ -\frac{(x - x_0)^2 + (y - y_0)^2}{2 \cdot \sigma^2} \right\} + C_0 + C_1x + C_2y.$$

This equation assumes the small area inside the region of interest (ROI) can be approximated by the plane. The initial parameters of the fitting are calculated by the linear least-square method for  $C_0$ ,  $C_1$ , and  $C_2$  using only the outer boundary of the ROI. Because the logarithm of the subtraction between  $f(x_0, y_0)$  and  $C_0 + C_1x + C_2y$  is a simple quadratic function, the other initial parameters are obtained by the linear least-square method, too. Setting the initial values close to the true values by these simple pre-calculations allows us to effectively reduce the number of the loop iterations in the Levenberg-Marquardt method.

The calculation precision by Gaussian fitting strongly depends on the photon number that the detection device receives from the emission of the fluorescent probe and can be as small as a few nanometers (**Figure 3C**) (Deschout et al., 2014; Small and Stahlheber, 2014). The method described above is called fluorescence imaging with one-nanometer accuracy (FIONA) and has quickly become a standard in the field (Yildiz et al., 2003; Yildiz and Selvin, 2005; Park et al., 2007; Hoffman et al., 2011). However, the number of photons emitted by single organic dyes and fluorescent protein molecules before photobleaching, about 110,000 (Kubitscheck et al., 2000), is too low for the observation of protein movement over a long time. Since the cause of photobleaching is thought to be oxygen collisions with the dye molecule in its excited state, it can be mitigated by the addition of oxygen scavengers (Sambongi et al., 1999; Adachi et al., 2000). Thus, the photon number from a single dye molecule can be increased to 1.4 million photons before photobleaching (Yildiz and Selvin, 2005). Meanwhile, Qdots show slight photobleaching and strong fluorescence even in the absence of scavengers (Bruchez et al., 1998). Though non-fluorescent nano-particles such as gold nano-particles are becoming increasingly popular for precise and long-term tracking using absorption (Kusumi et al., 2005; Lasne et al., 2006) or scattering (Nishikawa et al., 2010), the Qdot is still preferred in biological studies because of its wider color spectrum.

We investigated the relationship between the tracking precision and the average number of photons emitted from a Qdot (**Figure 3C**). The tracking precision was defined as the standard deviation of 100 data obtained with a Qdot immobilized on a glass surface in our case. While the experimental accuracy was a little lower than the theoretical expectation because of high blinking, it was still 2 nm when the photon number from a Qdot was 15,000 per exposure. To demonstrate the potential of single particle tracking as a biological tool, we measured the movement of kinesin, a microtubule-mediated motor protein (**Figure 3D**). The motor domain of the kinesin was fused with biotin carrier protein (BCCP) and conjugated with a Qdot via biotin-avidin affinity. The Qdot-labeled kinesin were then bound to microtubules adsorbed onto a cover slip. Upon adding 1 mM ATP, the Qdot was seen to move unidirectionally along the microtubule without detaching, which is consistent with kinesin using ATP to move (**Figure 3D**, left). The unidirectional movement of kinesin

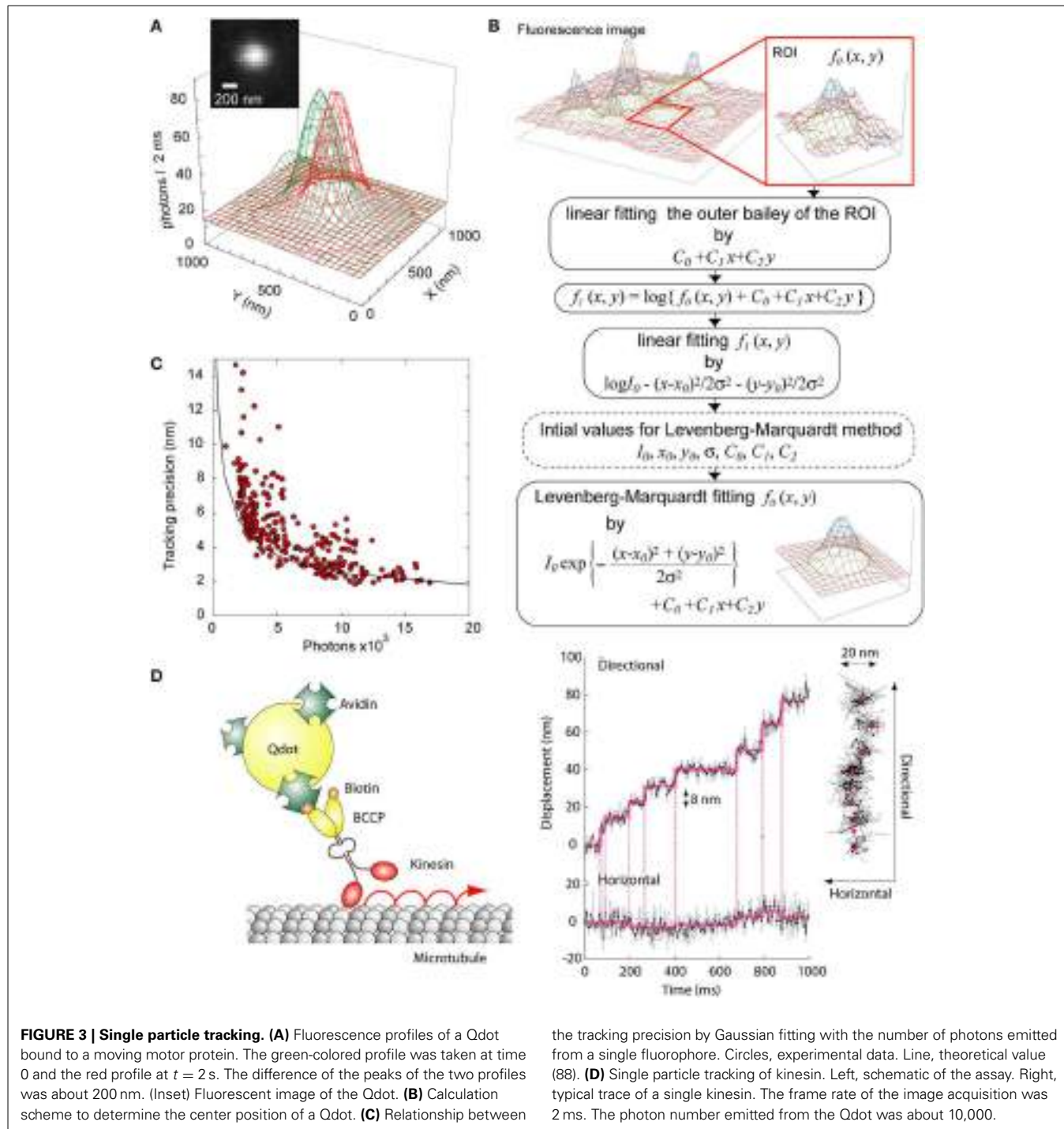


**FIGURE 3 | Single particle tracking.** **(A)** Fluorescence profiles of a Qdot bound to a moving motor protein. The green-colored profile was taken at time 0 and the red profile at  $t = 2$  s. The difference of the peaks of the two profiles was about 200 nm. (Inset) Fluorescent image of the Qdot. **(B)** Calculation scheme to determine the center position of a Qdot. **(C)** Relationship between

the tracking precision by Gaussian fitting with the number of photons emitted from a single fluorophore. Circles, experimental data. Line, theoretical value (88). **(D)** Single particle tracking of kinesin. Left, schematic of the assay. Right, typical trace of a single kinesin. The frame rate of the image acquisition was 2 ms. The photon number emitted from the Qdot was about 10,000.

was composed of successive 8 nm steps (Figure 3D, right). Thus, FIONA using Qdots provides a simple quantitative measurement for nano-scale tracking of proteins at the single molecular level.

### THREE-DIMENSIONAL SINGLE PARTICLE TRACKING WITH NANOMETER PRECISION USING Qdots

The original FIONA only measured movement on a spatial plane, but has since been expanded to three spatial dimensions. For this purpose, a three-dimensional (3D) image under

a microscope is obtained by scanning the objective lens along the focal axis with an actuator (Watanabe and Higuchi, 2007; Wells et al., 2008). This scanning, however, decreases the temporal resolution of the tracking. To solve this problem, 3D tracking methods without the objective scanning have been developed (Genovesio et al., 2006; Holtzer et al., 2007; Watanabe et al., 2007; Ram et al., 2008, 2012; Wells et al., 2010; Jia et al., 2014). Multifocal planes microscopy uses the difference of distinct optical pathways to estimate the Z-position by obtaining

simultaneously the fluorescence intensities of several focal images (Toprak et al., 2007; Watanabe et al., 2007; Dalgarno et al., 2010; Juette and Bewersdorf, 2010; Ram et al., 2012). Similarly, 3D tracking using a photon-limited double-helix response system with a spatial light modulator, which has two twisting lobes along the optical axis of the image, results in a single fluorescent probe appearing as two fluorescent spots from which the Z-position can be determined (Pavani et al., 2009; Lew et al., 2010).

One of the simplest 3D tracking methods intentionally generates astigmatism (Kao and Verkman, 1994; Holtzer et al., 2007; Izeddin et al., 2012). Here, a pair of convex and concave cylindrical lenses is inserted into the optical pathway before the detection device (**Figure 4A**) (Watanabe et al., 2013). These lenses generate different optical path lengths along the X- and Y-axes, resulting in a measurable relationship between the Z-position of the particle and the ellipticity of the PSF (**Figure 4B**). To calculate the ellipticity in addition to the 2D position, the below approximation formula is used

$$f(x, y) = I_0 \cdot \exp \left\{ -\frac{(x - x_0)^2}{2 \cdot \sigma_x^2} \right\} \cdot \exp \left\{ -\frac{(y - y_0)^2}{2 \cdot \sigma_y^2} \right\} + C_0 + C_1 x + C_2 y,$$

where  $\sigma_x$  and  $\sigma_y$  are the radial standard deviations of the Gaussian function along the X- and Y-axes respectively. The ellipticity is defined as the ratio of the full width at half maximum (FWHM) of the 2D Gaussian in the X- and Y- axes due to the different focal lengths (**Figure 4C**). Changing the distance between the convex and concave cylindrical lenses permits astigmatism for optimal tracking resolution (**Figure 4D**). When the detection device received 15,000 photons from a fluorescent probe, we achieved 3D tracking with precisions of 2 nm in the X and Y-axes and 5 nm along the Z-axis (**Figure 4E**). However, a reliable range was limited between a field view of  $-800$  and  $800$  nm (**Figure 4D**, lower and **Figure 4E**). This drawback is common in many 3D tracking methods. A new 3D tracking method based on Airy beams, however, overcomes this problem. Here, a diffraction free self-bending PSF is applied to a two-channeled detection system (Jia et al., 2014), and the Z-position is translated to the distance difference of the two X-positions of the two channels. This method elongates the dynamic range of 3D tracking to  $3 \mu\text{m}$ . Regardless of the 3D tracking method, the key is to extract Z information from the XY projection.

#### FOUR-DIMENSIONAL SINGLE PARTICLE USING POLARIZED Qdots

As significant as acquiring the third spatial dimension is, 3D single particle tracking ignores any rotational movement made by the protein. To acquire the orientation, fluorescence anisotropy can be used, because the fluorescence emissions are of unequal intensities along the P and S polar axes (P- and S-polarization), which are defined by the polarizing beam-splitter, as described below (Werver, 1953; Albrecht, 1961; Harms et al., 1999). Anisotropy is defined as  $(I_p - I_s)/(I_p + I_s)$ , where  $I_p$  and  $I_s$  are the intensities in P- and S-polarization, respectively (Harms et al., 1999). Anisotropy measurements have successfully tracked the rotatory dynamics of single protein molecules *in vitro* (Sase et al.,

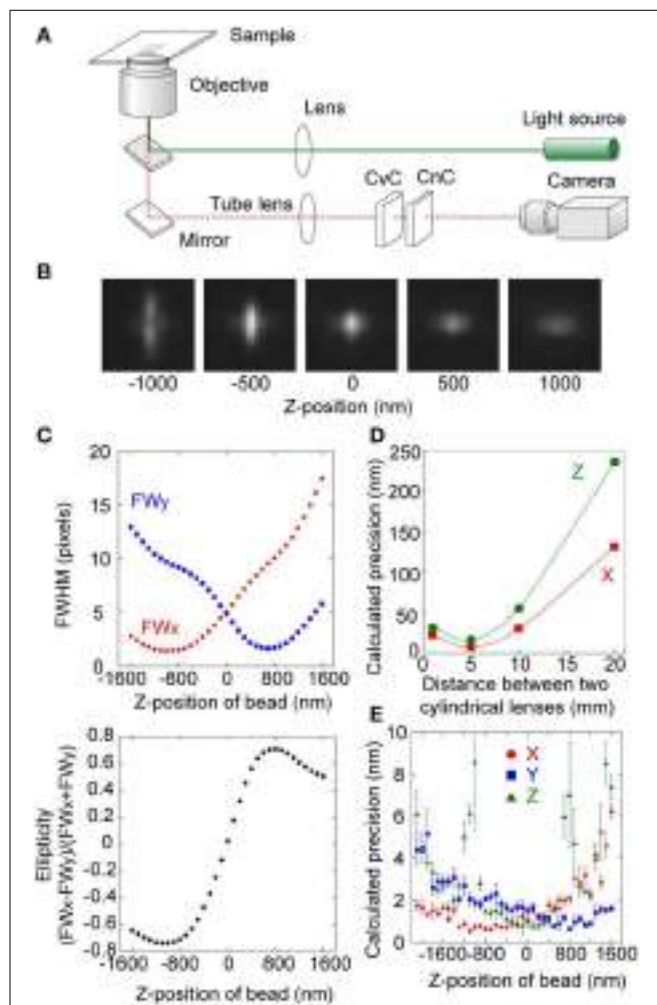
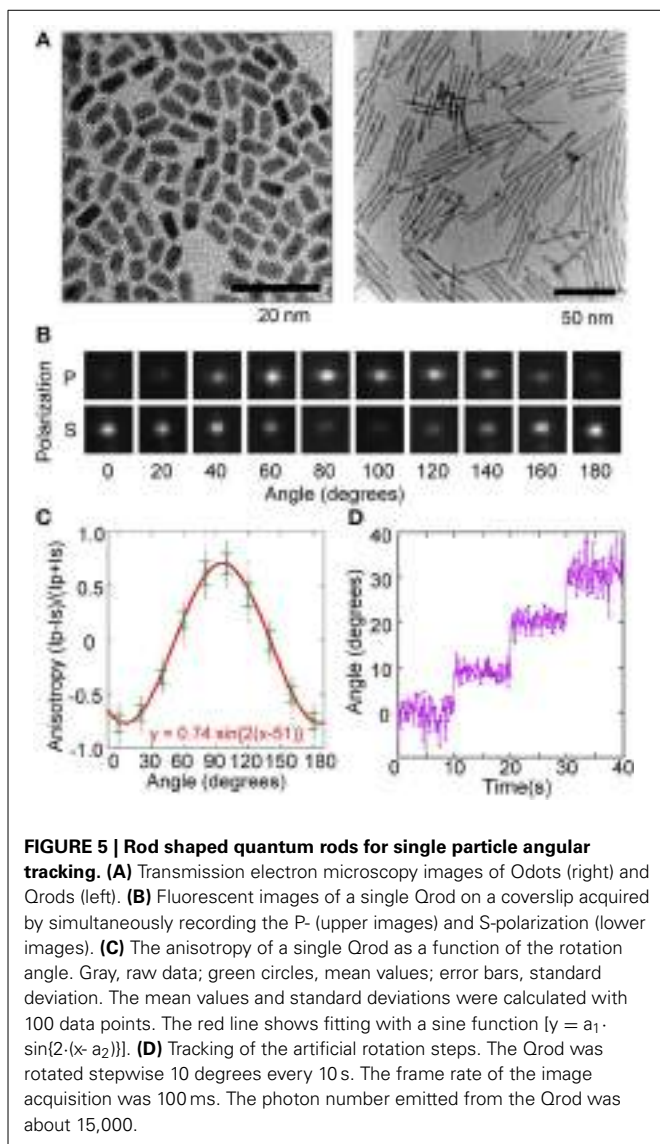


**FIGURE 4 |** 3D single particle tracking using a pair of convex and concave cylindrical lens. **(A)** Schematic drawing of the optical setup for 3D single particle tracking. CvC, convex cylindrical lens; CnC, concave cylindrical lens. **(B)** Fluorescent images of a single fluorescent bead with a diameter of 100 nm at various Z-positions ( $-1000$  to  $1000$  nm). **(C)** Radial variances in the X-axis (FWx, red in upper panel) and Y-axis (FWy, blue in upper panel) of the Gaussian function, and ellipticity (lower panel) of a single fluorescent bead as a function of the Z-position ( $-1600$  to  $1600$  nm). **(D)** Calculated precision in the X- (red) and Z-directions (green) as a function of distance between CvC and CnC. **(E)** Calculated precision in the X-, Y-, and Z-directions (red, blue, and green, respectively) as a function of Z-position when the camera received 15,000 photons from a fluorophore. The 3D tracking precisions was 2 nm in the X- and Y-axes and 5 nm along the Z-axis. Error bars represent standard deviations of 20 data.

1997; Forkey et al., 2003) and in cells (Mizuno et al., 2011). The fluorescence anisotropy of a Qdot depends on the aspect ratio of its shape (Peng et al., 2000; Hu et al., 2001; Deka et al., 2009). Taking advantage of this property, a highly polarized rod-shaped Qdot (Qrod) can be synthesized by elongating the CdS shell along one-axis of the CdSe core (**Figure 5A**) (Peng et al., 2000; Hu et al., 2001). The anisotropy changes in Qrod fluorescence can be described as a sine function (**Figures 5B,C**) and the angular position by the arcsine function. The tracking precision of the



orientation was about  $1\text{--}2^\circ$  when the photon number from a Qrod was 15,000 (Figure 8D). By utilizing this anisotropy technique, a fourth dimension, the angular ( $\theta$ ) component, could be added to the orthogonal 3 coordinate axes described by single particle tracking.

In our 4D tracking system, a polarizing beam splitter is set before the cylindrical lens pair in the 3D tracking optics to divide the fluorescent image into S- and P- polar channels (Figure 6A) (Watanabe et al., 2013). For 3D tracking, the P- and S-polarized images are summed before calculating the 3D position. A small gap is generated if the two channels are not completely overlapped, leading to an asymmetrical relationship between the respective FWHM values of the X- and Y-axes (Figure 6B). The 3D position can be determined by fitting the merged PSF with a 2D Gaussian function, as mentioned above, and the orientation can be determined by the ratio of the intensities of the S- and P- polarized images. Thus, X, Y, Z, and  $\theta$  are simultaneously obtained with an acquired image. In our case, when the

number of photons from a single Qrod was about 10,000 and the Z-position was near zero, the calculated precisions for the X, Y, Z, and  $\theta$ -positions were at maximum 5, 7, 9 nm and  $1^\circ$ , respectively (Figure 6C).

We used 4D tracking to observe the movement of a membrane protein conjugated with a Qrod via antibody affinity (Figures 6D–F) (Watanabe et al., 2013). Isolated Qrods moving on the membrane were identified under a fluorescence microscope (Figure 6E). The different intensities in the P- and S-polarized images indicated that the Qrod was inclined against the optical axis (Figure 6F, upper panels). One circular and one elliptical spot indicated that the two Qrods were at distinct Z-positions (Figure 6F, lower panels). One Qrod showed a half-moon like motion in the X- and Y-axes, which was accompanied by highly fluctuating movements along the Z-axis and fast rotational motion before endocytosis (Figure 6G). This observation suggests that this protein's lateral diffusion was constrained by the membrane undercoat, but that it could rotate freely along the plasma membrane. In the cytoplasm, a membrane protein seemed to be moving along tracks, most likely microtubules, in three-dimensions and slowly rotated helically (Figure 6H).

Another 4D tracking method was developed to obtain X, Y,  $\theta$ , and  $\varphi$  coordinates, the last of which provides information on the out-of-plane tilt angle (Ohmachi et al., 2012). In this method, single Qrods are imaged as four crowded fluorescent spots by dividing the beam path using a beam splitter and two Wollaston prisms. Otherwise, the orientation of the individual fluorescent probe can be directly estimated using the dipole emission patterns of a defocused image (Bartko and Dickson, 1999a,b; Fourkas, 2001; Böhmer and Enderlein, 2003; Lieb et al., 2004), an approach that was successfully applied to the 4D tracking of a motor protein (Toprak et al., 2006). The combination of the Wollaston prism method with defocusing could achieve comprehensive tracking of all rotatory and translational movements of a biomolecule in a living cell.

## SUPER-RESOLUTION USING BLINKING OF Qdots

Super-resolution microscopy describes the resolution of two objects closer than the diffraction limit of light (Schermelleh et al., 2010; Galbraith and Galbraith, 2011; Leung and Chou, 2011). It can be classified into two main categories. The first is based on the photo-transition of a fluorescent probe between its radiative and non-radiative states in order to confine the fluorescence emission into a sub-diffraction-limit sized volume. This approach is known as RESOLFT (REversible Saturable OpticaL Fluorescence Transitions) and was first proposed and demonstrated by STED (STimulated Emission Depletion), which exploits the stimulated emission phenomenon of a fluorescent dye (Hell and Wichmann, 1994; Klar and Hell, 1999). RESOLFT can also be realized by other photoreactions, including those from a ground-state transition phenomenon (GSD: Ground State Depletion) (Hell and Kroug, 1995; Bretschneider et al., 2007), the saturation of fluorescence excitation (SAX: SAturated eXcitation) (Fujita et al., 2007), or from reversibly photoswitchable fluorescent proteins (Hofmann et al., 2005). RESOLFT can also be combined with structured illumination microscopy (SIM) (Heintzmann and Cremer, 1999;

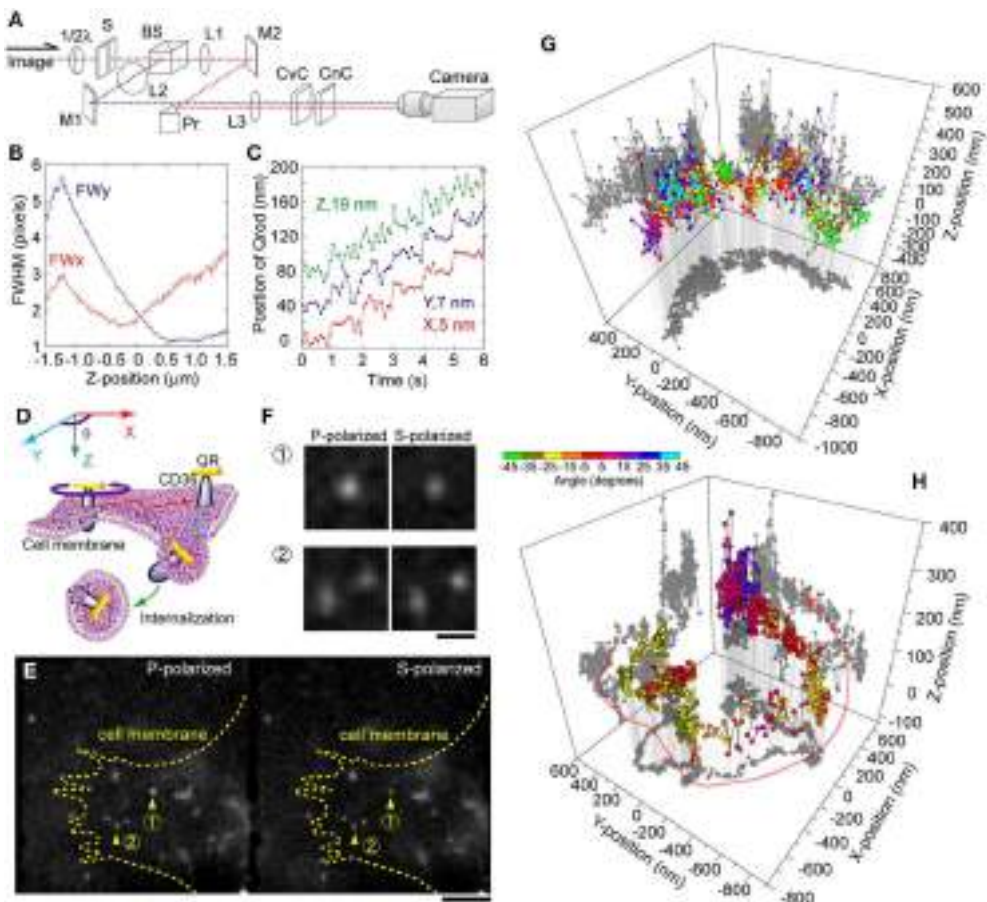


**FIGURE 6 |** 4D single particle tracking using Qrod anisotropy. **(A)** Schematic drawing of the optical setup for simultaneous 3D and angular single particle tracking.  $1/2\lambda$ ,  $1/2$ -wave plate; S, slit; BS, beam splitter; L, lens; M, mirror; Pr, prism; CvC, convex cylindrical lens; and CnC, concave cylindrical lens. **(B)** FWHM values of the merged images of S- and P-polarized images as a function of the Z-position along the X- (red line) and Y-axes (blue line). **(C)** Tracking 20 nm steps when the Z-position of the Qrod was near zero. A Qrod fixed on a coverslip was moved at discrete 20 nm steps once every 1 s simultaneously along the X- (red), Y- (blue), and Z- axes (green). The frame rate of the image acquisition was 100 ms. Standard deviations of the tracking

for 10 s (excluding the stepping moments) were 5, 7, and 19 nm along the three respective axes. The photon number emitted from the Qrot was about 1500. **(D)** Schematic depiction of the internalization of Qrod-labeled CD36, a membrane protein, from the cell membrane to the cytoplasm. **(E)** Fluorescent images of Qrods bound to membrane proteins in a living cell and simultaneously recorded in P- (left panel) and S-polarization (right panel). Arrowheads indicate two typical views that are enlarged in **(F)**. Scale bar is 5  $\mu$ m. **(F)** Enlarged images of the spots marked by arrowheads in **(E)**. Scale bar, 1  $\mu$ m. **(G,H)** Typical 4D traces of a single Qrod on the membrane **(G)** and near the nucleus **(H)**. The angle of the Qrod is indicated by the color bar.

Gustafsson, 2000) to provide wide field imaging capability with superresolution (Heintzmann, 2003; Gustafsson, 2005).

The second category is based on the separate detection of individual single fluorescent probes in the time domain or spectra domain, and can be further decomposed into different concepts. One, known as SPDM (Spectral Precision Distance Microscopy), precisely localizes individual probes over the many frames of sequentially obtained images (Bornfleth et al., 1998; Lemmer et al., 2008). Stochastic optical reconstruction microscopy (STORM) (Rust et al., 2006) and fluorescence photoactivation localization microscopy (FPALM) (Betzig et al., 2006) are both SPDM-based techniques that utilize repeated activation-deactivation cycles of photoswitchable fluorophores such that the fluorescence spots on an obtained image are completely discrete.

Another method from the second category is blinking based superresolution (BBS). BBS relies on the randomness and non-Gaussian property of blinking, which means stochastic processing can be used to localize individual fluorescent probes. The first report of BBS used independent component analysis, which is a computational method that decomposes a multivariate signal into independent non-Gaussian signals (Lidke et al., 2005). Other BBS-based techniques use the temporal high-order cumulant (super-resolution optical fluctuation imaging: SOFI) (Dertinger et al., 2009), the temporal high-order variance (Variance Imaging for Superresolution: VISion) (Watanabe et al., 2010), spatial covariance (spatial covariance reconstructive: SCORE) (Deng et al., 2014), or Bayesian statistics (Cox et al., 2011). A great advantage of SPDM and BBS is that they need only a relatively simple fluorescent microscope and no complicated optics.

Qdots are the most compatible with BBS owing to their strong blinking phenomenon. Supposing that there are two adjoining Qdots independently and randomly fluctuating, the moment that one Qdot emits and the other does not is a stochastic event (**Figure 7A**). As an example, a solution to identifying the Qdot for SOFI and ViSION is shown below (Dertinger et al., 2009). A fluorescent image of Qdots,  $F(\mathbf{r},t)$ , is expressed by the convolution of a PSF,  $U(\mathbf{r})$ , of the optical system and the brightness,  $\varepsilon_k s_k(t)$ , where  $\mathbf{r}_k$ ,  $\varepsilon_k$ , and  $s_k(t)$  are the position and the time-invariant and -variant components of brightness of the  $k$ -th Qdot, respectively.

$$F(\mathbf{r}, t) = \sum_k U(\mathbf{r} - \mathbf{r}_k) \cdot \varepsilon_k \cdot s_k(t)$$

The second-order autocorrelation function,  $G_2(\mathbf{r},\tau)$ , is then given by  $F(\mathbf{r},t)$  as follows,

$$\begin{aligned} G_2(\mathbf{r}, \tau) &= \langle \delta F(\mathbf{r}, t + \tau) \cdot t F(\mathbf{r}, t) \rangle_t \\ &= \sum_{j,k} U(r - r_j) \cdot U(r - r_k) \cdot \varepsilon_j \cdot \varepsilon_k \cdot \\ &\quad \langle \delta s_j(r, t + \tau) \cdot t s_k(r, t) \rangle_t \\ &= \sum_k U^2(r - r_k) \cdot \varepsilon_k^2 \cdot \langle \delta s_k(r, t + \tau) \cdot t s_k(r, t) \rangle_t \end{aligned}$$

where  $\langle \dots \rangle_t$  and  $\delta(\cdot)$  denote a time-averaging operation and deviation from the time-average, respectively. Because of the independency of the fluorescence fluctuation of the two distinct Qdots ( $k \neq j$ ), the time average of their product is zero. For simple comparison of the raw image,  $F(\mathbf{r},t)$ , and the auto-correlation image  $G_2(\mathbf{r},\tau)$ , we here substitute 0 for the delay time,  $\tau$ , to reduce  $G_2(\mathbf{r},\tau)$  to  $G_2(\mathbf{r},0)$ .

$$G_2(\mathbf{r}, 0) = \sum_k U^2(r - r_k) \cdot \varepsilon_k^2 \cdot \langle \delta s_k^2(r) \rangle_t$$

This equation indicates that  $G_2(\mathbf{r},\tau)$  is given by the convolution of  $U^2(r)$  and the square of  $\varepsilon_k s_k(t)$ . Assuming that  $U(r)$  is approximated by a Gaussian distribution, the spatial resolution of  $G_2(\mathbf{r},0)$  is improved  $\sqrt{2}$  times from  $F(\mathbf{r},t)$ , but at the expense of temporal information, since the spatial resolution of the optical microscopic image is limited by the sharpness of the PSF (**Figures 7B,C**). The higher-order autocorrelation contains high-spatial frequency information. However, because this is a moment value that contains cross-terms from the lower-order correlation contributions, the accrual spatial resolution for distinguishing two Qdots cannot be improved more than  $\sqrt{2}$  times. It is therefore necessary to transform the  $n$ th-order correlation into an  $n$ th-order cumulant that consists only of terms containing the  $n$ th power of the PSF. While the higher order cumulant gives higher spatial resolution (**Figure 7D**), a huge number of images are still needed.

To decrease the required number of images, we developed a highly fluctuating Qdot in which the switching frequency between the on- and off-state was greatly increased by optimizing the shell thickness to promote more interaction between the CdSe-core and oxygen atoms in water (**Figures 8A,B**). Though the quantum

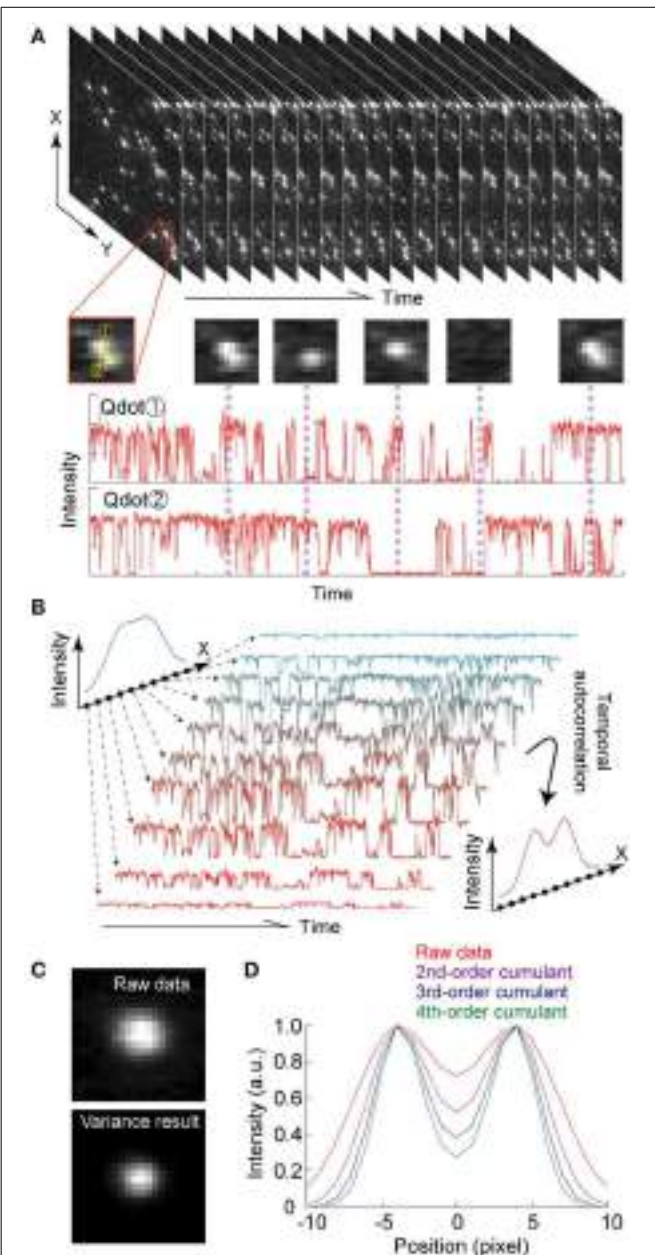
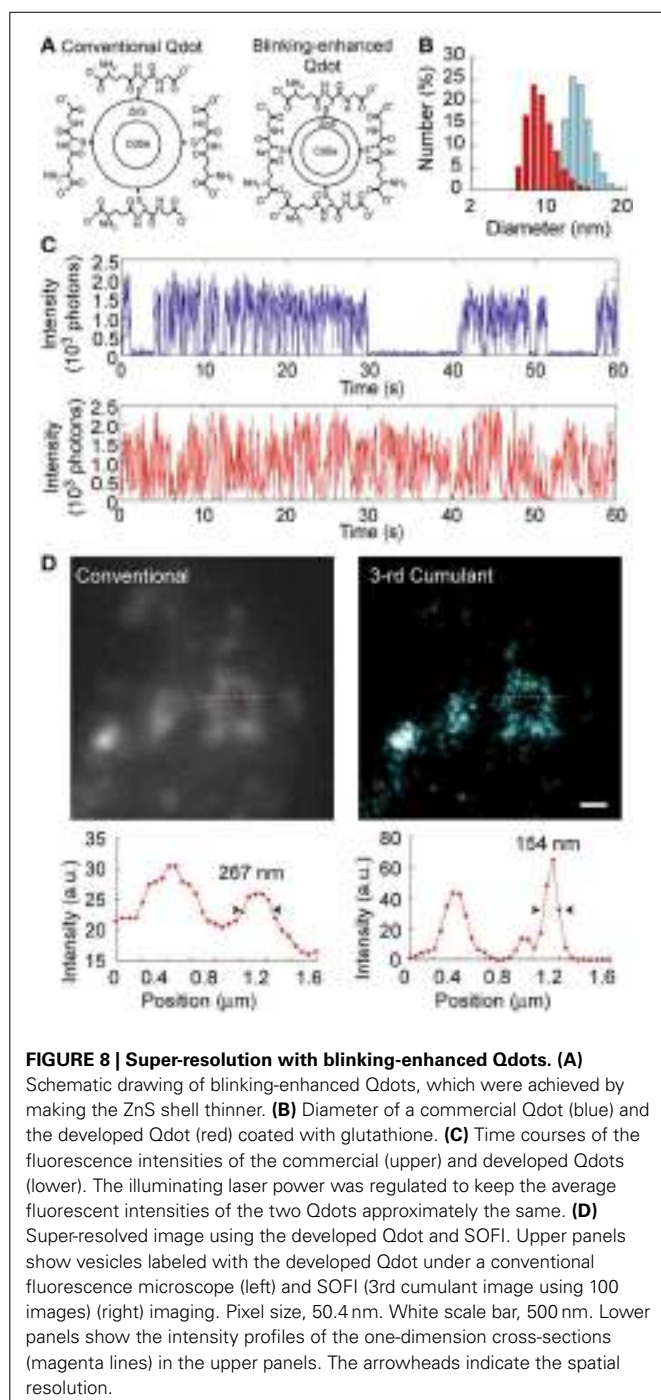


**FIGURE 7 | Super-resolution using fluorescence fluctuations of a Qdot.** **(A)** Conceptual drawing super-resolution microscopy using fluorescence fluctuations of a Qdot. For details, see text. **(B)** Principle of SOFI. Each pixel contains a time trace, which is composed of the sum of the fluorescence from individual Qdots. Calculating the temporal autocorrelation of each pixel gives a new image whose spatial resolution is improved. **(C)** Fluorescent image (upper) and 2nd autocorrelation (equal to variance; lower) image of a single Qdot. Pixel size, 50.4 nm. **(D)** Point spread functions in one-dimension of the SOFI simulation results. In the simulation, the two Qdots were set at distance of 4 pixels apart. The FWHM of each Qdot was also 4 pixels. 2500 images were used.

yield of this Qdot was less than that of standard Qdots, it still had sufficient intensity and stability when exposed to high power illumination, and no long off-state was observed (**Figure 8C**). Hence, we could easily obtain a super-resolved image by only



labeling the target protein and calculating the fluctuation of the blinking-enhanced Qdots (**Figure 8D**). In our case, the spatial resolution was improved from 267 to 154 nm using SOFI and only 100 images (Watanabe et al., 2010).

## CONCLUSION

Conventional optical microscopy can quantitatively acquire 3D position and orientation information at the nano-scale from the shape of the PSF and the polarization characteristics of Qdots and Qrods. The amount of spatial information can be increased by

analyzing the stochastic fluctuations of the fluorescence. Thus, the fluorescence of a probe attached to a molecule can reveal information about the molecular phenomena and/or state. Increasing the intensity, stability, and blinking of Qdots and its derivatives will make the acquisition of such information even more feasible.

Super-resolution microscopy and single particle tracking have made it possible to resolve and follow two objects closer than the diffraction limit of light. The result is quantitative information of the dynamics of biological phenomena at the nano-scale. Even more details of the dynamics can be acquired with the above technologies by using Qdots and their derivatives as probes for labeling the molecules of interest. The PSF and the polarization characteristics of the Qdots can be used to provide comprehensive information on both the position and orientation of the molecule of interest. Because this information can be extracted from the stochastic properties of the fluorescence, increasing the intensity, stability, and blinking of Qdots should provide even more quantitative details about the dynamics.

## ACKNOWLEDGMENT

We gratefully acknowledge to Peter Karagiannis (Riken QBiC) for critical reading of this manuscript.

## REFERENCES

- Abbe, E. (1873). Contributions to the theory of the microscope and the microscopic perception. *Arch. Mikr. Anat.* 9, 413–468. doi: 10.1007/BF02956173
- Adachi, K., Yasuda, R., Noji, H., Itoh, H., Harada, Y., Yoshida, M., et al. (2000). Stepping rotation of F1-ATPase visualized through angle-resolved single-fluorophore imaging. *Proc. Natl. Acad. Sci. U.S.A.* 97, 7243–7237. doi: 10.1073/pnas.120174297
- Albrecht, A. (1961). Polarizations and assignments of transitions: the method of photoselection. *J. Mol. Spectrosc.* 6, 84–108. doi: 10.1016/0022-2852(61)90234-X
- Barroso, M. M. (2011). Quantum dots in cell biology. *J. Histochem. Cytochem.* 59, 237–251. doi: 10.1369/0022155411398487
- Bartko, A. P., and Dickson, R. M. (1999a). Imaging three-dimensional single molecule orientations. *J. Phys. Chem. B*, 103, 11237–11241. doi: 10.1021/jp993364q
- Bartko, A. P., and Dickson, R. M. (1999b). Three-dimensional orientations of polymer-bound single molecules. *J. Phys. Chem. B* 103, 3053–3056. doi: 10.1021/jp9846330
- Betzig, E., Patterson, G. H., Sougrat, R., Lindwasser, O. W., Olenych, S., Bonifacino, J. S., et al. (2006). Imaging intracellular fluorescent proteins at nanometer resolution. *Science* 313, 1642–1645 doi: 10.1126/science.1127344
- Böhmer, M., and Enderlein, J. (2003). Orientation imaging of single molecules by wide-field epifluorescence microscopy. *J. Opt. Soc. Am. B* 20, 554–559. doi: 10.1364/JOSAB.20.000554
- Bornfleth, H., Satzler, K., Elis, R., and Cremer, C. (1998). High-precision distance measurements and volume-conserving segmentation of objects near and below the resolution limit in three-dimensional confocal fluorescence microscopy. *J. Microsc.* 189, 118–136. doi: 10.1046/j.1365-2818.1998.00276.x
- Bretschneider, S., Eggeling, S., and Hell, S. W. (2007). Breaking the diffraction barrier in fluorescence microscopy by optical shelving. *Phys. Rev. Lett.* 98, 218103. doi: 10.1103/PhysRevLett.98.218103
- Bruchez, M. Jr., Moronne, M., Gin, P., Weiss, S., and Alivisatos, A. P. (1998). Semiconductor nanocrystals as fluorescent biological labels. *Science* 281, 2013–2016. doi: 10.1126/science.281.5385.2016
- Bruchez, M. P. (2011). Quantum dots find their stride in single molecule tracking. *Curr. Opin. Chem. Biol.* 15, 775–780. doi: 10.1016/j.cbpa.2011.10.011
- Byers, R. J., and Hitchman, E. R. (2010). Quantum dots brighten biological imaging. *Prog. Histochem. Cytochem.* 45, 201–237. doi: 10.1016/j.proghi.2010.11.001
- Cao, H., Chen, B., Squier, T. C., and Mayer, M. U. (2006). CrAsH: a biarsenical multi-use affinity probe with low non-specific fluorescence. *Chem. Commun.* 24, 2601–2603. doi: 10.1039/B602699K

- Chan, W. C. W., and Nie, S. (1998). Quantum dot bioconjugates for ultrasensitive nonisotopic detection. *Science* 281, 2016–2018. doi: 10.1126/science.281.5385.2016
- Chang, Y. P., Pinaud, F., Antelman, J., and Weiss, S. (2008). Tracking bio-molecules in live cells using quantum dots. *J. Biophotonics* 1, 287–298. doi: 10.1002/jbio.200810029
- Cheezum, M. K., Walker, W. F., and Guilford, W. H. (2001). Quantitative comparison of algorithms for tracking single fluorescent particles. *Biophys. J.* 281, 2378–2388. doi: 10.1016/S0006-3495(01)75884-5
- Chenouard, N., Smal, I., de Chaumont, F., Maška, M., Sbalzarini, I. F., Gong, Y., et al. (2014). Objective comparison of particle tracking methods. *Nat. Methods* 11, 281–289. doi: 10.1038/nmeth.2808
- Chien, F. C., Kuo, C. W., and Chen, P. (2011). Localization imaging using blinking quantum dots. *Analyst* 136, 1608–1613. doi: 10.1039/c0an00859a
- Chinnathambi, S., Chen, S., Ganesan, S., and Hanagata, N. (2014). Silicon quantum dots for biological applications. *Adv. Healthc. Mater.* 3, 10–29. doi: 10.1002/adhm.201300157
- Choi, H. S., and Frangioni, J. V. (2010). Nanoparticles for biomedical imaging: fundamentals of clinical translation. *Mol. Imaging* 9, 291–310. doi: 10.2310/7290.2010.00031
- Clausen, M. P., and Lagerholm, B. C. (2011). The probe rules in single particle tracking. *Curr. Protein Pept. Sci.* 12, 699–713. doi: 10.2174/138920311798841672
- Cox, S., Rosten, E., Monypenny, J., Jovanovic-Talisman, T., Burnette, D. T., Lippincott-Schwartz, J., et al. (2011). Bayesian localization microscopy reveals nanoscale podosome dynamics. *Nat. Methods* 9, 195–200. doi: 10.1038/nmeth.1812
- Cupaioli, F. A., Zucca, F. A., Boraschi, D., and Zecca, L. (2014). Engineered nanoparticles. How brain friendly is this new guest? *Prog Neurobiol.* pii: S0301-0082(14)00051-3. doi: 10.1016/j.pneurobio.2014.05.002
- Dabbousi, B. O., Rodriguez-Viejo, O. J., and Bawendi, M. G. (1997). (CdSe)ZnS core-shell Qdots: synthesis and characterization of a size series of highly luminescent nanocrystallites. *J. Phys. Chem. B* 101, 9463–9475. doi: 10.1021/jp971091y
- Dalgarno, P. A., Dalgarno, H. I., Putoud, A., Lambert, R., Paterson, L., Logan, D. C., et al. (2010). Multiplane imaging and three dimensional nanoscale particle tracking in biological microscopy. *Opt. Express.* 18, 877–884. doi: 10.1364/OE.18.000877
- Deka, S., Quarta, A., Lupo, M. G., Falqui, A., Boninelli, S., Giannini, C., et al. (2009). CdSe/CdS/ZnS double shell nanorods with high photoluminescence efficiency and their exploitation as biolabeling probes. *J. Am. Chem. Soc.* 131, 2948–2958. doi: 10.1021/ja808369e
- Deng, Y., Sun, M., Lin, P. H., Ma, J., and Shaevitz, J. W. (2014). Spatial covariance reconstructive (SCORE) super-resolution fluorescence microscopy. *PLoS ONE* 9:e94807. doi: 10.1371/journal.pone.0094807
- Derstinger, T., Colyer, R., Iyer, G., Weiss, S., and Enderlein, J. (2009). Fast, background-free, 3D super-resolution optical fluctuation imaging (SOFI). *Proc. Natl. Acad. Sci. U.S.A.* 106, 22287–22292. doi: 10.1073/pnas.0907866106
- Deschout, H., Cella Zanacchi, F., Mlodzianoski, M., Diaspro, A., and Bewersdorf, J. (2014). Precisely and accurately localizing single emitters in fluorescence microscopy. *Nat. Methods* 11, 253–266. doi: 10.1038/nmeth.2843
- Drummen, G. P. (2012). Fluorescent probes and fluorescence (microscopy) techniques-illuminating biological and biomedical research. *Molecules* 17, 14067–14140. doi: 10.3390/molecules171214067
- Dubertret, B., Skourides, P., Norris, D. J., Noireaux, V., Brivanlou, A. H., and Libchaber, A. (2002). *In vivo* imaging of quantum dots encapsulated in phospholipid micelles. *Science* 98, 1759–1762. doi: 10.1126/science.1077194
- Dubois, F., Mahler, B., Dubertret, B., Doris, E., and Mioskowski, C. (2007). A versatile strategy for quantum dot ligand exchange. *J. Am. Chem. Soc.* 129, 482–483. doi: 10.1021/ja067742y
- Ekimov, A. I., and Onushchenko, A. A. (1981). Quantum size effect in three-dimensional microscopic semiconductor crystals. *JETP Lett.* 34, 345–349.
- Ellinger, P. (1940). Fluorescence microscopy in biology. *Biol. Rev.* 15, 323–347. doi: 10.1111/j.1469-185X.1940.tb00761.x
- Erathodiyl, N., and Ying, J. Y. (2011). Functionalization of inorganic nanoparticles for bioimaging applications. *Acc. Chem. Res.* 44, 925–935. doi: 10.1021/ar2000327
- Fomenko, V., and Nesbitt, D. J. (2008). Solution control of radiative and nonradiative lifetimes: a novel contribution to quantum dot blinking suppression. *Nano Lett.* 8, 287–293. doi: 10.1021/nl0726609
- Forkey, J. N., Quinlan, M. E., Shaw, M. A., Corrie, J. E., and Goldman, Y. E. (2003). Three-dimensional structural dynamics of myosin V by single-molecule fluorescence polarization. *Nature* 422, 399–404. doi: 10.1038/nature01529
- Fourkas, J. T. (2001). Rapid determination of the three-dimensional orientation of single molecules. *Opt. Lett.* 26, 211–213. doi: 10.1364/OL.26.000211
- Fujita, K., Kobayashi, M., Kawano, S., Yamanaka, M., and Kawata, S. (2007). High-resolution confocal microscopy by saturated excitation of fluorescence. *Phys. Rev. Lett.* 99:228105. doi: 10.1103/PhysRevLett.99.228105
- Galbraith, C. G., and Galbraith, J. A. (2011). Super-resolution microscopy at a glance. *J. Cell Sci.* 124(Pt 10), 1607–1611. doi: 10.1242/jcs.080085
- Gao, X., Yang, L., Petros, J. A., Marshall, F. F., Simons, J. W., and Nie, S. (2005). *In vivo* molecular and cellular imaging with quantum dots. *Curr. Opin. Biotechnol.* 16, 63–72. doi: 10.1016/j.copbio.2004.11.003
- Genovesio, A., Liedl, T., Emiliani, V., Parak, W. J., Coppey-Moisan, M., and Olivio-Marin, J. C. (2006). Multiple particle tracking in 3-D+ time microscopy: method and application to the tracking of endocytosed quantum dots. *IEEE Trans. Image Process.* 15, 1062–1070. doi: 10.1109/TIP.2006.872323
- Gerion, D., Pinaud, F., Williams, S., Parak, W., Zanchet, D., Weiss, S., et al. (2001). Synthesis and properties of biocompatible water-soluble silica-coated CdSe/ZnS semiconductor quantum dots. *J. Phys. Chem. B* 105, 8861–8871 doi: 10.1021/jp0105488
- Guo, W., Li, J. J., Wang, Y. A., Peng, X. (2003). Conjugation chemistry and bioapplications of semiconductor box nanocrystals prepared via dendrimer bridging. *Chem. Mater.* 15, 3125–3133. doi: 10.1021/cm034341y
- Gustafsson, M. G. L. (2000). Surpassing the lateral resolution limit by a factor of two using structured illumination microscopy. *J. Microsc.* 198, 82–87 doi: 10.1046/j.1365-2818.2000.00710.x
- Gustafsson, M. G. L. (2005). Nonlinear structured-illumination microscopy: Wide-field fluorescence imaging with theoretically unlimited resolution. *Proc. Natl. Acad. Sci. U.S.A.* 102, 13081–13086. doi: 10.1073/pnas.0406877102
- Harms, G. S., Sonnleitner, M., Schütz, G. J., Gruber, H. J., and Schmidt, T. (1999). Single-molecule anisotropy imaging. *Biophys. J.* 77, 2864–2870. doi: 10.1016/S0006-3495(99)77118-3
- Heintzmann, R. (2003). Saturated patterned excitation microscopy with two-dimensional excitation patterns. *Micron* 34, 283–291. doi: 10.1016/S0968-4328(03)00053-2
- Heintzmann, R., and Cremer, C. (1999). “Laterally modulated excitation microscopy: improvement of resolution by using a diffraction grating,” in *Proceedings for the SPIE Vol. 3568, Optical Biopsies and Microscopic Techniques III*, (Stockholm), 185. doi: 10.1117/12.336833
- Hell, S. W., and Kroug, M. (1995). Ground-state-depletion fluorescence microscopy: A concept for breaking the diffraction resolution limit. *Appl. Phys. B* 60, 495–497. doi: 10.1007/BF01081333
- Hell, S. W., and Wichmann, J. (1994). Breaking the diffraction resolution limit by stimulated emission: stimulated-emission-depletion fluorescence microscopy. *Opt. Lett.* 19, 780–782. doi: 10.1364/OL.19.000780
- Hoffman, M. T., Sheung, J., and Selvin, P. R. (2011). Fluorescence imaging with one nanometer accuracy: *in vitro* and *in vivo* studies of molecular motors. *Methods Mol. Biol.* 778, 33–56. doi: 10.1007/978-1-61779-261-8\_4
- Hofmann, M., Eggeling, C., Jakobs, S., and Hell, S. W. (2005). Breaking the diffraction barrier in fluorescence microscopy at low light intensities by using reversibly photoswitchable proteins. *Proc. Natl. Acad. Sci. U.S.A.* 102, 17565–17569. doi: 10.1073/pnas.0506010102
- Hohng, S., and Ha, T. (2004). Near-complete suppression of quantum dot blinking in ambient conditions. *J. Am. Chem. Soc.* 126, 1324–1325. doi: 10.1021/ja039686w
- Holtzer, L., Meckel, T., and Schmidt, T. (2007). Nanometric three-dimensional tracking of individual quantum dots in cells. *Appl. Phys. Lett.* 90, 053902 doi: 10.1063/1.2437066
- Hoyer, P., Staudt, T., Engelhardt, J., and Hell, S. W. (2011). Quantum dot bleaching and blinking enables fluorescence nanoscopy. *Nano Lett.* 11, 245–250. doi: 10.1021/nl103639f
- Hu, J., Li, L. S., Yang, W., Manna, L., Wang, L. W., and Alivisatos, A. P. (2001). Linearly polarized emission from colloidal semiconductor quantum rods. *Science* 292, 2060–2063. doi: 10.1126/science.1060810
- Huang, Z. L., Zhu, H., Long, F., Ma, H., Qin, L., Liu, Y., et al. (2011). Localization-based super-resolution microscopy with an sCMOS camera. *Opt. Express.* 19, 19156–19168. doi: 10.1364/OE.19.019156
- Izeddin, I., El Beheiry, M., Andilla, J., Ciepielewski, D., Darzacq, X., and Dahan, M. (2012). PSF shaping using adaptive optics for three-dimensional

- single-molecule super-resolution imaging and tracking. *Opt. Express.* 20, 4957–4967. doi: 10.1364/OE.20.004957
- Jia, S., Vaughan, V. C., and Zhuang, Z. (2014). Isotropic three-dimensional super-resolution imaging with a self-bending point spread function. *Nat. Photonics* 8, 302–306. doi: 10.1038/nphoton.2014.13
- Jiang, W., Mardyani, S., Fischer, H., and Chan, W. C. W. (2006). Design and characterization of lysine cross-linked mercapto-acid biocompatible quantum dots. *Chem. Mater.* 18, 872–878. doi: 10.1021/cm051393+
- Jin, T., Fujii, F., Komai, Y., Seki, J., Seiyama, A., and Yoshioka, Y. (2008). Preparation and characterization of highly fluorescent, glutathione-coated near infrared quantum dots for *in vivo* fluorescence imaging. *Int. J. Mol. Sci.* 9, 2044–2061. doi: 10.3390/ijms9102044
- Juette, M. F., and Bewersdorf, J. (2010). Three-dimensional tracking of single fluorescent particles with submillisecond temporal resolution. *Nano Lett.* 10, 4657–4663. doi: 10.1021/nl1028792
- Kairdolf, B. A., Smith, A. M., Stokes, T. H., Wang, M. D., Young, A. N., and Nie, S. (2013). Semiconductor quantum dots for bioimaging and biodiagnostic applications. *Annu. Rev. Anal. Chem.* 6, 143–162. doi: 10.1146/annurev-anchem-060908-155136
- Kao, H. P., and Verkman, A. S. (1994). Tracking of single fluorescent particles in three dimensions: use of cylindrical optics to encode particle position. *Biophys. J.* 67, 1291–1300. doi: 10.1016/S0006-3495(94)80601-0
- Kim, S. W., Kim, S., Tracy, J. B., Jasanoft, A., and Bawendi, M. G. (2005). Phosphine oxide polymer for water-soluble nanoparticles. *J. Am. Chem. Soc.* 127, 4556–4557. doi: 10.1021/ja043577f
- Klar, T. A., and Hell, S. W. (1999). Subdiffraction resolution in far-field fluorescence microscopy. *Opt. Lett.* 24, 954–956. doi: 10.1364/OL.24.000954
- Kloepfer, J. A., Bradforth, S. E., and Nadeau, J. L. (2005). Photophysical properties of biologically compatible CdSe quantum dot structures. *J. Phys. Chem. B* 109, 9996–10003. doi: 10.1021/jp044581g
- Ko, H. C., Yuan, C. T., and Tang, J. (2011). Probing and controlling fluorescence blinking of single semiconductor nanoparticles. *Nano Rev.* 2:5895. doi: 10.3402/nano.v2i0.5895
- Kubitscheck, U., Kückmann, O., Kues, T., and Peters, R. (2000). Imaging and tracking of single GFP molecules in solution. *Biophys. J.* 78, 2170–2179. doi: 10.1016/S0006-3495(00)76764-6
- Kuno, M., Lee, J. K., Dabbousi, B. O., Mikulec, F. V., and Bawendi, M. G. (1997). The band edge luminescence of surface modified CdSe nanocrystallites: probing the luminescing state. *J. Chem. Phys.* 106, 9869. doi: 10.1063/1.473875
- Kusumi, A., Nakada, C., Ritchie, K., Murase, K., Suzuki, K., Murakoshi, H., et al. (2005). Paradigm shift of the plasma membrane concept from the two-dimensional continuum fluid to the partitioned fluid: high-speed single-molecule tracking of membrane molecules. *Annu. Rev. Biophys. Biomol. Struct.* 34, 351–378. doi: 10.1146/annurev.biophys.34.040204.144637
- Lasne, D., Blab, G. A., Berciaud, S., Heine, M., Groc, L., Choquet, D., et al. (2006). Single nanoparticle photothermal tracking (SNaPT) of 5-nm gold beads in live cells. *Biophys. J.* 91, 4598–4604. doi: 10.1529/biophysj.106.089771
- Lemmer, P., Gunkel, M., Baddeley, D., Kaufmann, R., Urich, A., Weiland, Y., et al. (2008). SPDM: light microscopy with single-molecule resolution at the nanoscale. *Appl. Phys. B* 93, 1–12. doi: 10.1007/s00340-008-3152-x
- Leung, B. O., and Chou, K. C. (2011). Review of super-resolution fluorescence microscopy for biology. *Appl. Spectrosc.* 65, 967–980. doi: 10.1366/11-06398
- Levenberg, K. (1944). A method for the solution of certain non-linear problems in least squares. *Q. Appl. Math.* 2, 164–168.
- Lew, M. D., Thompson, M. A., Badieirostami, M., and Moerner, W. E. (2010). *In vivo* three-dimensional superresolution fluorescence tracking using a double-helix point spread function. *Proc. Soc. Photo Opt. Instrum. Eng.* 7571, 75710Z. doi: 10.1117/12.842608
- Li, J., Wu, D., Miao, Z., and Zhang, Y. (2010). Preparation of quantum dot bioconjugates and their applications in bio-imaging. *Curr. Pharm. Biotechnol.* 11, 662–671. doi: 10.2174/138920110792246582
- Lichtman, J. W., and Conchello, J. A. (2005). Fluorescence microscopy. *Nat. Methods* 2, 910–919. doi: 10.1038/nmeth817
- Lidke, K., Rieger, B., Jovin, T., and Heintzmann, R. (2005). Superresolution by localization of quantum dots using blinking statistics. *Opt. Express.* 13, 7052–7062. doi: 10.1364/OPEX.13.007052
- Lieb, M. A., Zavislan, J. M., and Novotny, L. (2004). Single-molecule orientations determined by direct emission pattern imaging. *J. Opt. Soc. Am. B* 21, 1210–1215. doi: 10.1364/JOSAB.21.001210
- Long, F., Zeng, S., and Huang, Z. L. (2012). Localization-based super-resolution microscopy with an sCMOS camera part II: experimental methodology for comparing sCMOS with EMCCD cameras. *Opt. Express.* 20, 17741–17759. doi: 10.1364/OE.20.017741
- Ma, H., Kawai, H., Toda, E., Zeng, S., and Huang, Z. L. (2013). Localization-based super-resolution microscopy with an sCMOS camera part III: camera embedded data processing significantly reduces the challenges of massive data handling. *Opt. Lett.* 38, 1769–1771. doi: 10.1364/OL.38.001769
- Mandal, A., and Tamai, N. (2011). Suppressed blinking behavior of thioglycolic acid capped CdTe quantum dot by amine functionalization. *Appl. Phys. Lett.* 99, 263111. doi: 10.1063/1.3671075
- Miyawaki, A. (2013). Fluorescence imaging in the last two decades. *Microscopy (Oxf.)* 62, 63–68. doi: 10.1093/jmicro/dfs130
- Mizuno, H., Higashida, C., Yuan, Y., Ishizaki, T., Narumiya, S., and Watanabe, N. (2011). Rotational movement of the formin mDia1 along the double helical strand of an actin filament. *Science* 331, 80–83. doi: 10.1126/science.1197692
- Nann, T. (2005). Phase-transfer of CdSe@ZnS quantum dots using amphiphilic hyperbranched polyethylenimine. *Chem. Commun.* 7, 1735–1736. doi: 10.1039/b414807j
- Nifosi, R., Amat, P., and Tozzini, V. (2007). Variation of spectral, structural, and vibrational properties within the intrinsically fluorescent proteins family: a density functional study. *J. Comput. Chem.* 28, 2366–2377. doi: 10.1002/jcc.20764
- Nirmal, M., Dabbousi, B. O., and Brus, L. E. (1996). Fluorescence intermittency in single cadmium selenide nanocrystals. *Nature* 383, 802–804. doi: 10.1038/383802a0
- Nishikawa, S., Arimoto, I., Ikezaki, K., Sugawa, M., Ueno, H., Komori, T., et al. (2010). Switch between large hand-over-hand and small inchworm-like steps in myosin VI. *Cell* 42, 879–888. doi: 10.1016/j.cell.2010.08.033
- Ohmachi, M., Komori, Y., Iwane, A. H., Fujii, F., Jin, T., and Yanagida, T. (2012). Fluorescence microscopy for simultaneous observation of 3D orientation and movement and its application to quantum rod-tagged myosin V. *Proc. Natl. Acad. Sci. U.S.A.* 109, 5294–5298. doi: 10.1073/pnas.1118472109
- Palaniappan, K., Hackney, S. A., and Liu, J. (2004). Supramolecular control of complexation-induced fluorescence change of water-soluble, beta-cyclodextrin-modified CdS quantum dots. *Chem. Commun.*, 23, 2704–2705. doi: 10.1039/B409075F
- Palaniappan, K., Xue, C., Arumugam, G., Hackney, S. A., and Liu, J. (2006). Water-soluble, cyclodextrin-modified CdSe-CdS core-shell structured quantum dots. *Chem. Mater.* 18, 1275–1280. doi: 10.1021/cm051602q
- Park, H., Toprak, E., and Selvin, P. R. (2007). Single-molecule fluorescence to study molecular motors. *Q. Rev. Biophys.* 40, 87–111. doi: 10.1017/S0033583507004611
- Pavani, S. R., Thompson, M. A., Biteen, J. S., Lord, S. J., Liu, N., Twieg, R. J., et al. (2009). Three-dimensional, single-molecule fluorescence imaging beyond the diffraction limit by using a double-helix point spread function. *Proc. Natl. Acad. Sci. U.S.A.* 106, 2995–2999. doi: 10.1073/pnas.0900245106
- Peng, X., Manna, L., Yang, W., Wickham, J., Scher, E., Kadavanich, A., et al. (2000). Shape control of CdSe nanocrystals. *Nature* 404, 59–61. doi: 10.1038/35003535
- Peter, S., Harter, K., and Schleifenbaum, F. (2014). Fluorescence microscopy. *Methods Mol. Biol.* 1062, 429–452. doi: 10.1007/978-1-62703-580-4\_23
- Petryayeva, E., Algar, W. R., and Medintz, I. L. (2013). Quantum dots in bioanalysis: a review of applications across various platforms for fluorescence spectroscopy and imaging. *Appl. Spectrosc.* 67, 215–252. doi: 10.1366/12-06948
- Pierobon, P., and Cappello, G. (2012). Quantum dots to tail single biomolecules inside living cells. *Adv. Drug Deliv. Rev.* 64, 167–178. doi: 10.1016/j.addr.2011.06.004
- Pilla, V., Munin, E., Dantas, N. O., Silva, A. C. A., and Andrade, A. A. (2012). “Photothermal spectroscopic characterization in CdSe/ZnS and CdSe/CdS quantum dots: a review and new applications,” in *Quantum Dots - A Variety of New Applications*, ed A. Al-Ahmadi (InTech), 3–22. doi: 10.5772/2645
- Pinaud, F., King, D., Moore, H. P., and Weiss, S. (2004). Bioactivation and cell targeting of semiconductor CdSe/ZnS nanocrystals with phytochelatin-related peptides. *J. Am. Chem. Soc.* 126, 6115–6123. doi: 10.1021/ja031691c
- Ram, S., Kim, D., Ober, R. J., and Ward, E. S. (2012). 3D single molecule tracking with multifocal plane microscopy reveals rapid intercellular transferrin transport at epithelial cell barriers. *Biophys. J.* 103, 1594–1603. doi: 10.1016/j.bpj.2012.08.054
- Ram, S., Prabhat, P., Chao, J., Ward, E. S., and Ober, R. J. (2008). High accuracy 3D quantum dot tracking with multifocal plane microscopy for the study

- of fast intracellular dynamics in live cells. *Biophys. J.* 95, 6025–6043. doi: 10.1529/biophysj.108.140392
- Ritchie, K., and Kusumi, A. (2003). Single-particle tracking image microscopy. *Meth. Enzymol.* 360, 618–634. doi: 10.1016/S0076-6879(03)60131-X
- Rossetti, R., Nakahara, S., and Brus, L. E. (1980). Quantum size effects in the redox potentials, resonance Raman spectra, and electronic spectra of CdS crystallites in aqueous solution. *J. Chem. Phys.* 79, 1086–1088 doi: 10.1063/1.445834
- Ruedas-Rama, M. J., Walters, J. D., Orte, A., and Hall, E. A. (2012). Fluorescent nanoparticles for intracellular sensing: a review. *Anal. Chim. Acta* 751, 1–23. doi: 10.1016/j.aca.2012.09.025
- Rust, M. J., Bate, M., and Zhuang, X. (2006). Sub-diffraction-limit imaging by stochastic optical reconstruction microscopy (STORM). *Nat. Methods* 3, 793–796 doi: 10.1038/nmeth929
- Rutherford, N., Lamb, D. C., and Bräuchle, C. (2011). Single-particle tracking as a quantitative microscopy-based approach to unravel cell entry mechanisms of viruses and pharmaceutical nanoparticles. *Mol. Ther.* 19, 1199–1211. doi: 10.1038/mt.2011.102
- Saadeh, Y., Leung, T., Vyas, A., Chaturvedi, L. S., Perumal, O., and Vyas, D. (2014). Applications of nanomedicine in breast cancer detection, imaging, and therapy. *J. Nanosci. Nanotechnol.* 14, 913–923. doi: 10.1166/jnn.2014.8755
- Sambongi, Y., Iko, Y., Tanabe, M., Omote, H., Iwamoto-Kihara, A., Ueda, I., et al. (1999). Mechanical rotation of the c subunit oligomer in ATP synthase (FOF1): direct observation. *Science* 286, 1722–1724. doi: 10.1126/science.286.5445.1722
- Sase, I., Miyata, H., Ishiwata, S., and Kinoshita, K. Jr. (1997). Axial rotation of sliding actin filaments revealed by single-fluorophore imaging. *Proc. Natl. Acad. Sci. U.S.A.* 94, 5646–5650. doi: 10.1073/pnas.94.11.5646
- Saxton, M. J. (2008). Single-particle tracking: connecting the dots. *Nat. Methods* 5, 671–672. doi: 10.1038/nmeth0808-671
- Saxton, M. J. (2009). “Single particle tracking,” in *Fundamental Concepts of Biophysics*, ed T. Jue (New York, NY: Humana Press), 147–169. doi: 10.1007/978-1-59745-397-4\_6
- Schermelleh, L., Heintzmann, R., and Leonhardt, H. (2010). A guide to super-resolution fluorescence microscopy. *J. Cell Biol.* 190, 165–175. doi: 10.1083/jcb.201002018
- Schlegel, G., Bohnenberger, J., Potapova, I., and Mews, A. (2002). Fluorescence decay time of single semiconductor nanocrystals. *Phys. Rev. Lett.* 88, 137401. doi: 10.1103/PhysRevLett.112.068103
- Shimomura, O., and Johnson, F. H. (1962). Extraction, purification and properties of aequorin, a bioluminescent protein from the luminous hydromedusan. *Aequorea. J. Cell. Comp. Physiol.* 59, 223–239. doi: 10.1002/jcp.1030590302
- Small, A., and Stahlheber, S. (2014). Fluorophore localization algorithms for super-resolution microscopy. *Nat. Methods*. 11, 267–279. doi: 10.1038/nmeth.2844
- Terai, T., and Nagano, T. (2013). Small-molecule fluorophores and fluorescent probes for bioimaging. *Pflugers Arch.* 465, 347–359. doi: 10.1007/s00424-013-1234-z
- Thompson, R. E., Larson, D. R., and Webb, W. W. (2002). Precise nanometer localization analysis for individual fluorescent probes. *Biophys. J.* 82, 2775–2783. doi: 10.1016/S0006-3495(02)75618-X
- Tiwari, D. K., Tanaka, S., Inouye, Y., Yoshizawa, K., Watanabe, T. M., and Jin, T. (2009). Synthesis and characterization of anti-HER2 antibody conjugated CdSe/CdZnS quantum dots for fluorescence imaging of breast cancer cells. *Sensors* 9, 9332–9364. doi: 10.3390/s91109332
- Tomczak, N., Liu, R., and Vancso, J. G. (2013). Polymer-coated quantum dots. *Nanoscale* 5, 12018–12032. doi: 10.1039/c3nr03949h
- Toprak, E., Balci, H., Blehm, B. H., and Selvin, P. R. (2007). Three-dimensional particle tracking via bifocal imaging. *Nano Lett.* 7, 2043–2045. doi: 10.1021/nl0709120
- Toprak, E., Enderlein, J., Syed, S., McKinney, S. A., Petschek, R. G., Ha, T., et al. (2006). Defocused orientation and position imaging (DOPI) of myosin V. *Proc. Natl. Acad. Sci. U.S.A.* 103, 6495–6499. doi: 10.1073/pnas.0507134103
- Toprak, E., and Selvin, P. R. (2007). New fluorescent tools for watching nanometer-scale conformational changes of single molecules. *Annu. Rev. Biophys. Biomol. Struct.* 36, 349–369. doi: 10.1146/annurev.biophys.36.040306.132700
- Tsien, R. Y. (1998). The green fluorescent protein. *Annu. Rev. Biochem.* 67, 509–544. doi: 10.1146/annurev.biochem.67.1.509
- van Sark, W. G. J. H.M., Frederix, P. L. T. M., Bol, A. A., Gerritsen, H. C., and Meijerink, A. (2002). Blueing, Bleaching, and Blinking of Single CdSe/ZnS Quantum Dots. *ChemPhysChem* 3, 871–879. doi: 10.1002/1439-7641(20021018)3:10<871::AID-CPHC871>3.0.CO;2-T
- van Sark, W. G. J. H.M., Frederix, P. L. T. M., den Heuvel, D. J. V., Gerritsen, H. C. J., Bol, A. A., van Lingen, J. N. J., et al. (2001). Letter photooxidation and photobleaching of single CdSe/ZnS Quantum dots probed by room-temperature time-resolved spectroscopy. *Phys. Chem. B* 105, 8281–8284. doi: 10.1021/jp012018h
- Wang, E. C., and Wang, A. Z. (2014). Nanoparticles and their applications in cell and molecular biology. *Integr. Biol.* 6, 9–26. doi: 10.1039/c3ib40165k
- Watanabe, T. M., Fujii, F., Jin, T., Umemoto, E., Miyasaka, M., Fujita, H., et al. (2013). Four-dimensional spatial nanometry of single particles in living cells using polarized quantum rods. *Biophys. J.* 105, 555–564. doi: 10.1016/j.bpj.2013.07.001
- Watanabe, T. M., Fukui, S., Jin, T., Fujii, F., and Yanagida, T. (2010). Real-time nanoscopy by using blinking enhanced quantum dots. *Biophys. J.* 99, L50–L52. doi: 10.1016/j.bpj.2010.07.036
- Watanabe, T. M., and Higuchi, H. (2007). Stepwise movements in vesicle transport of HER2 by motor proteins in living cells. *Biophys. J.* 92, 4109–4120. doi: 10.1529/biophysj.106.094649
- Watanabe, T. M., Sato, T., Gonda, K., and Higuchi, H. (2007). Three-dimensional nanometry of vesicle transport in living cells using dual-focus imaging optics. *Biochem. Biophys. Res. Commun.* 359, 1–7. doi: 10.1016/j.bbrc.2007.04.168
- Wells, N. P., Lessard, G. A., Goodwin, P. M., Phipps, M. E., Cutler, P. J., Lidke, D. S., et al. (2010). Time-resolved three-dimensional molecular tracking in live cells. *Nano Lett.* 10, 4732–4737. doi: 10.1021/nl103247v
- Wells, N. P., Lessard, G. A., and Werner, J. H. (2008). Confocal, three-dimensional tracking of individual quantum dots in high-background environments. *Anal. Chem.* 80, 9830–9834. doi: 10.1021/ac8021899
- Werner, G. (1953). Rotational Brownian motion and polarization of the fluorescence of solutions. *Adv. Protein Chem.* 8, 415–459. doi: 10.1016/s0065-3233(08)60096-0
- Wombacher, R., and Cornish, V. W. (2011). Chemical tags: applications in live cell fluorescence imaging. *J. Biophotonics* 4, 391–402. doi: 10.1002/jbio.201100018
- Wysocki, L. M., and Lavis, L. D. (2011). Advances in the chemistry of small molecule fluorescent probes. *Curr. Opin. Chem. Biol.* 15, 752–759. doi: 10.1016/j.cbpa.2011.10.013
- Yajima, J., Mizutani, K., and Nishizaka, T. (2008). A torque component present in mitotic kinesin Eg5 revealed by three-dimensional tracking. *Nat. Struct. Mol. Biol.* 15, 1119–1121. doi: 10.1038/nsmb.1491
- Yildiz, A., Forkey, J. N., McKinney, S. A., Ha, T., Goldman, Y. E., and Selvin, P. R. (2003). Myosin V walks hand-over-hand: single fluorophore imaging with 1.5-nm localization. *Science* 300, 2061–2065. doi: 10.1126/science.1084398
- Yildiz, A., and Selvin, P. R. (2005). Fluorescence imaging with one nanometer accuracy: application to molecular motors. *Acc. Chem. Res.* 38, 574–582. doi: 10.1021/ar040136s
- Zhang, A., Dong, C., Liu, H., and Ren, J. (2013). Blinking behavior of CdSe/CdS quantum dots controlled by alkylthiols as surface trap modifiers. *J. Phys. Chem. C*, 117, 24592–24600. doi: 10.1021/jp408544x
- Zhang, Y., and Clapp, A. (2011). Overview of stabilizing ligands for biocompatible quantum dot nanocrystals. *Sensors* 11, 11036–11055. doi: 10.3390/s111211036
- Conflict of Interest Statement:** The authors declare that the research was conducted in the absence of any commercial or financial relationships that could be construed as a potential conflict of interest.
- Received:** 05 June 2014; **paper pending published:** 18 June 2014; **accepted:** 05 July 2014; **published online:** 29 July 2014.
- Citation:** Ichimura T, Jin T, Fujita H, Higuchi H and Watanabe TM (2014) Nano-scale measurement of biomolecules by optical microscopy and semiconductor nanoparticles. *Front. Physiol.* 5:273. doi: 10.3389/fphys.2014.00273
- This article was submitted to Systems Biology, a section of the journal *Frontiers in Physiology*.
- Copyright © 2014 Ichimura, Jin, Fujita, Higuchi and Watanabe. This is an open-access article distributed under the terms of the Creative Commons Attribution License (CC BY). The use, distribution or reproduction in other forums is permitted, provided the original author(s) or licensor are credited and that the original publication in this journal is cited, in accordance with accepted academic practice. No use, distribution or reproduction is permitted which does not comply with these terms.



# Specific and quantitative labeling of biomolecules using click chemistry

Kenichi Horisawa \*

Division of Organogenesis and Regeneration, Department of Molecular and Cellular Biology, Medical Institute of Bioregulation, Kyushu University, Fukuoka, Japan

**Edited by:**

Noriko Hiroi, Keio University, Japan

**Reviewed by:**

Noriko Hiroi, Keio University, Japan

Remigiusz Adam Serwa, Imperial College London, UK

**\*Correspondence:**

Kenichi Horisawa, Division of Organogenesis and Regeneration, Department of Molecular and Cellular Biology, Medical Institute of Bioregulation, Kyushu University, 3-1-1 Maidashi, Higashi-ku, Fukuoka 812-8582, Japan

e-mail: horisawa@bioreg.kyushu-u.ac.jp

Specific and highly efficient fluorescent labeling techniques for biomolecules, especially for proteins, are required for the quantitative analyses of bio-phenomena and for subsequent systems biology. Although expression of exogenous proteins fused with fluorescent tags, such as green fluorescent protein, is the most widely used method for quantitative bio-analysis, the following problems need to be considered carefully: (1) precise stoichiometric control in living cells is difficult, and (2) the bulkiness of the fluorescent tags restricts analysis of the inherent physical and biological properties of the proteins. Therefore, novel techniques to specifically and stoichiometrically label intrinsic proteins or other biomolecules in living cells should be developed. Click chemistry reactions (e.g., Huisgen cycloaddition and Staudinger ligation) are the most promising approaches for this purpose, because these chemical reactions have following advantages: (1) bioorthogonal reactions; (2) mild reaction conditions suitable for fragile biomolecules, cells, and tissues; (3) extremely high reaction ratio; (4) small size of the functional groups for the cross-coupling reactions; (5) stable covalent bonding; and (6) simple metabolic labeling procedures in living cells, using various biomolecular analogs. Diverse quantitative biological studies have been carried out using this technology (e.g., quantification of novel synthesized proteins and observation of post-translational modifications). In this review, I explain the basics of chemical probing with click chemistry, and discuss its recent applications in the field of quantitative biology. Furthermore, I discuss the capability, significance, and future of the chemical probing of proteins, with an emphasis on the use of click chemistry in the field of the quantitative biology.

**Keywords:** click chemistry, fluorescent labeling, metabolic labeling, bioorthogonal reaction

## QUANTITATIVE FLUORESCENCE IMAGING OF BIOMOLECULES IN LIVING CELLS

Fluorescent imaging tools such as fluorescent microscopy are one of the most efficient and widely used modern techniques in the life sciences for analyzing the quantitative behavior of biomolecules in living cells, tissues, and organisms (Stephens and Allan, 2003). Although a lot of alternative imaging technologies exist, such as electron microscopy, autoradiography, and immunochemistry, the fluorescent labeling of biomolecules and their subsequent observation with various optical instruments shows greater advantages, especially in the area of high temporal resolution, as this is one of the most important factors that needs to be analyzed for understanding biomolecular dynamics. Around the end of the last century and at the beginning of this century, the application of green fluorescent protein (Shimomura et al., 1962; Xue et al., 1993; Chalfie et al., 1994; Heim and Tsien, 1996) and its derivatives (Shaner et al., 2005) drastically improved the available fluorescence imaging methods for live samples. The huge impact of genetic fluorescent labeling in living cells can be seen from the wide variety of available fluorescent proteins. Indeed, the Nobel prize was awarded to Drs. Shimomura, Chalfie, and Tsien, in 2008 for the discovery and application of green fluorescent protein.

An alternative to fluorescent protein tagging is the use of fluorescent chemical compounds. These chemicals have long been employed in the field of bioscience. **Table 1** shows the difference in the properties of fluorescent proteins and chemicals. As live imaging tools, fluorescent proteins are more predominantly used as compared to their chemical counterparts, because the genetic labeling procedure is very easy and reliable. However, fluorescent proteins also show certain disadvantages, especially during quantitative analysis (**Table 1**). The biggest issue of the protein-tagging method is the difficulty in controlling the stoichiometry of the target proteins inside the cell. Basically, the number of the proteins is controlled at the transcriptional level in living cells. Although the transcriptional activity can be roughly regulated through an appropriate choice of promoters or other artificial molecular systems, strict stoichiometric control is beyond the capability of the current molecular biological technology. The second problem pertains to the adverse effects of the tagged fluorescent proteins. The molecular size of the fluorescent proteins is larger than that of the fluorescent chemicals and other widely used conventional protein tags (e.g., FLAG, HA, V5, T7, and Myc tags). The bulkiness of the fluorescent protein tag is likely to affect the behavior, stability, and function of the target proteins.

For the reasons stated above, caution must be exercised when using fluorescent proteins for quantitative analyses. On the other hand, some fluorescent chemicals exhibit properties appropriate for the quantitative fluorescent observation of biomolecules, including small molecule size, various labeling positions, nonessentiality of transgene expression, and wide variation of their optical spectrum (Jung et al., 2013). However, the efficient and specific conjugation of fluorescent chemicals to the target proteins poses a major problem. For example, the NHS ester and isothiocyanate coupling reactions are the most general methods for the fluorescent labeling of proteins, although their target functional (amino) group is present not only in the target protein but also in other biomolecules such as DNA and RNA. Therefore, this makes it impossible to label target molecules specifically if presented with a mixture of biomolecules.

Click chemistry reactions have been recently developed for chemical coupling. This chemical method has the potential to be a breakthrough in the field of live fluorescence imaging. In the following sections, I introduce some of the applications of click chemistry for cell and tissue imaging, and discuss the various applications of this technology in the field of quantitative biology.

## CLICK CHEMISTRY IN BIOLOGICAL STUDIES

Click chemistry does not correspond to one particular chemical reaction. This concept is related to the use of novel chemical reactions, as proposed by Prof. K. Barry Sharpless of the Scripps Research Institute (Kolb et al., 2001). A click chemistry reaction shows the following properties: (1) it uses a solvent that is benign or easily removable, such as water; (2) it only generates inoffensive byproducts; (3) it gives very high chemical yields; (4) it does not need extremely high temperature or pressure; and (5) the products from the reactions are physiologically stable. All of the characteristics above are regarded to be suitable for the chemical labeling of biomolecules, because almost all biomolecules, especially biopolymers, are fragile in the extreme conditions necessary for carrying out the standard chemical reactions. Thus, the number of applications focusing on the use of click chemistry in the life sciences is increasing every year (Best, 2009; Lang and Chin, 2014a).

Among the various click chemistry reactions, the azide-alkyne Huisgen cycloaddition is the most widely employed reaction in biological studies. This is a coupling reaction between the azide and alkyne groups, which form a very stable triazole ring as a

linker (**Figure 1A**) (Huisgen, 1963). For the progression of this reaction, no additional factors are needed, such as heating and high pressure; the only requirement is the use of a monovalent copper ion as a catalyst (Rostovtsev et al., 2002; Tornøe et al., 2002). This reaction is termed the copper-catalyzed azide-alkyne cycloaddition (CuAAC). The most important characteristic of the CuAAC is that the azide and the alkyne do not react with any other molecules inside the cells and tissues. This property enables highly bioorthogonal fluorescent labeling in living and complex samples (Best, 2009; Lang and Chin, 2014a).

Although the fluorescent labeling of various biomolecules such as proteins, peptides, sugar chains, DNAs, RNAs, and lipids via CuAAC has proven to be successful (Lahann, 2009; Lang and Chin, 2014a), several problems still remain to be solved. The most serious issue for CuAAC is the cytotoxicity of the copper ion (Boyce and Bertozzi, 2011). High concentrations of this metal ion catalyst make it impossible to fluorescently label living cells and organisms. As a solution to the problem, copper-free click reactions have been developed in recent years. In these reactions, cyclic derivatives of the alkynyl group [e.g., cyclooctyne (Agard et al., 2004), difluorinated cyclooctyne (Baskin et al., 2007), and dibenzocyclooctyne (Sletten et al., 2010)] are employed as reactive partners for the azide group (**Figure 1B**). These kinds of

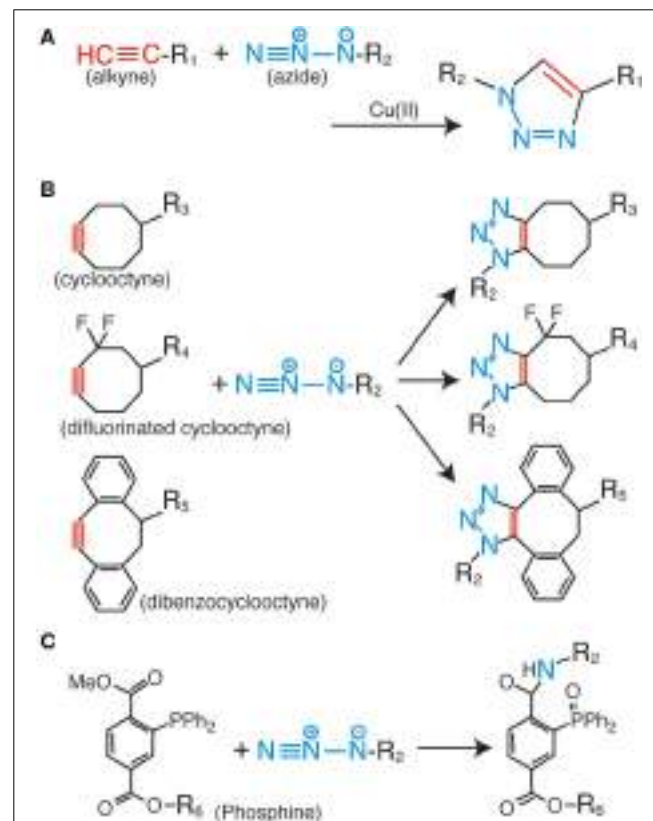


**FIGURE 1 | Huisgen cycloaddition and Staudinger ligation.** **(A)** Copper-catalyzed azide-alkyne cycloaddition (CuAAC). **(B)** Copper-free azide-alkyne cycloaddition reactions using cyclic alkynes. **(C)** Staudinger-Bertozzi ligation.

**Table 1 | Comparison of fluorescent proteins and chemicals.**

Property	Fluorescent proteins	Fluorescent chemicals
Molecule size	Large	Small
Timing for labeling	During translation	Anytime
Transgene expression	Essential	Nonessential
Labeling position	Basically C/N-terminus	Reactive side-chains or C/N-terminus
Variation	Relatively narrow	Wide
Labeling efficiency	High	Case by case

\*Gray-shaded columns highlight the disadvantages for live cell imaging.

cyclic alkyne derivatives harness the intrinsic energy from their distorted structures; therefore, no additional energy or catalysis is needed. Some of these derivatives are already commercially available as fluorescence labeling reagents for living cells, and have been successfully employed in live cell analyses. However, the relatively bulky size of the cyclic alkyl groups affects the membrane permeability of the labeling reagents; therefore, almost all of the previous examples are limited to extracellular labeling studies.

The Staudinger-Bertozzi ligation is regarded as an effective alternative to CuAAC. This chemical reaction also involves a coupling reaction between an azide and a phosphine (**Figure 1C**) (Saxon and Bertozzi, 2000). Similar to the azide and the alkyne, the phosphine group also does not react with any of the functional groups on the biomolecules. However, the Staudinger-Bertozzi ligation has some useful characteristics for the fluorescent labeling of biomolecules in living cells. Unlike CuAAC, no catalyst is necessary for the coupling reaction between the azide and the phosphine groups. Indeed, several studies showed successful live cell fluorescent imaging with this technology (Chang et al., 2007; Hangauer and Bertozzi, 2008). Although this technology has a potential to be a universal tool for the live cell imaging, the membrane permeability of phosphine-dyes is a remaining issue to be solved.

More recently, novel bioorthogonal uses of “click” reactions have been published (Kodama et al., 2007; Song et al., 2008; Tong et al., 2009; Nguyen et al., 2011). Among them, the most promising reaction for live cell imaging study is the inverse-electron-demand Diels-Alder cycloaddition, which is a coupling reaction between strained alkenes and tetrazines (Blackman et al., 2008). A lot of studies for the live cell imaging by using the reaction have been published in recent years (Selvaraj et al., 2011; Lang et al., 2012; Plass et al., 2012; Liu et al., 2012a). This technology might become a primary tool for live cell imaging studies, because this reaction has not only harmlessness for living cells but also a very fast rate constant as compared with other reactions (Lang and Chin, 2014b), which is an important parameter for the quantitative labeling.

## INDUCTION METHODS FOR THE ANCHOR GROUPS OF BIOMOLECULES IN LIVING SAMPLES

The application of click chemistry in bioscience is increasing every year. To date, a wide variety of “clickable” reagents for the fluorescent labeling of biomolecules have been identified, many of which are also commercially available. However, the more important and challenging issue pertaining to the fluorescent labeling of living samples with click chemistry is the induction of the anchor groups (i.e., the azide, alkyne, and phosphine groups) into the biomolecules inside living samples. The most widely used induction method for the anchor groups in living cells is through metabolic incorporation, which uses monomer analogs for biopolymers, such as nucleotides, sugars, and amino acids (**Figure 2A**). These molecular anchors are of a relatively smaller size, thereby making it easier to enzymatically incorporate the derivatives into the biopolymers.

Among the metabolic labeling targets identified for click labeling, the sugar chains on the membrane proteins hold the biggest promise. Although the sugar chains on the membrane

proteins have important roles in various physiological phenomena, including cell-cell adhesion, signal transduction, and immunologic response, their specific characteristics such as localization, amount, half-life, function, and the difference between cell types continue to remain elusive. In order to visualize the sugar chains containing particular types of sugars, different types of unnatural monosaccharide residues containing an azide group (azide sugars), i.e., N-azidoacetylmannosamine (Saxon and Bertozzi, 2000), N-azidoacetylglucosamine (Vocadlo et al., 2003), N-azidoacetylgalactosamine (Hang et al., 2003), and 6-azidofucose (Sawa et al., 2006), were produced and used for metabolic labeling studies. These derivatives were successfully incorporated into the sugar chains on the cell membrane through the intrinsic metabolic machinery, and were clearly visualized by following the click ligation with fluorescent dyes. The live imaging of the sugar chains uses this technique, and such experiments have already been done, not only in cultured cells but also in the tissues of living organisms. The copper-free click reagents such as difluorinated cyclooctyne (**Figure 1B**) have made this possible (Baskin et al., 2007). Therefore, the sugar chains could be regarded as a relatively easier target as compared to the other intracellular biopolymers.

Proteins have also been a primary target for analyses during metabolic labeling and click ligation. Several labeling reagents for newly synthesized proteins have been developed in recent years. Methionine derivatives bearing azido or alkyne groups, termed L-azidehomoolanine and L-homopropagylglycine, respectively (Wang et al., 2008), are the most widely used and commercially available reagents for the metabolic labeling of nascent proteins in living cells (**Figure 2A**). These are counterparts of the <sup>35</sup>S-labeled methionine used in radiographic analyses, and are able to label the nascent proteins synthesized during a particular period or under specific signals. Although these methionine analogs are useful and reliable, pretreatment of cells with a methionine-free medium is necessary (Soundrarajan et al., 2012), and this can affect the cells physiologically. Hence, alternatives with different labeling machineries were developed. The derivatives of puromycin, which is an inhibitor of protein biosynthesis, are one of the most promising reagents for the labeling of nascent proteins. The labeling method using these reagents needs no culture condition change, unlike the methionine analogs. Liu et al. reported an alkyne-conjugated puromycin derivative for nascent protein labeling in cultured cells and tissues (Liu et al., 2012b). Beatty and colleagues attempted the live cell imaging of nascent proteins in live fibroblast cells by using the L-azidehomoolanine- and a BODIPY®-conjugated cyclooctyne (Beatty et al., 2011). The fluorescent signals inside the cells were confirmed using confocal microscopy and protein fractionation. However, these data also revealed the preferential click labeling of membrane proteins, which might have resulted from the low cell penetrability of BODIPY®-conjugated cyclooctyne. In order to develop a reliable protein-labeling method for quantitative analyses, the development of membrane-penetrable click reagents seems essential. Genetic code reprogramming technologies, which change the usage of codons, are also powerful method to introduce unnatural amino acids into proteins. Several teams have reported a lot of successful result of protein labeling by using

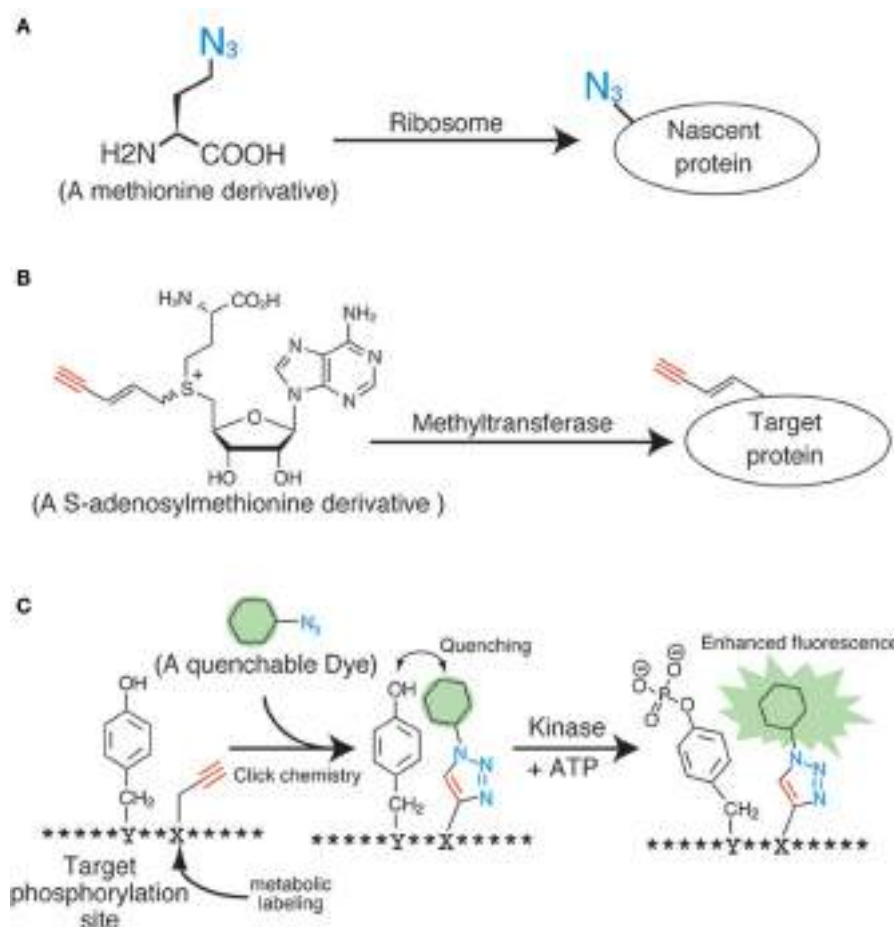


**FIGURE 2 | Applications of click chemistry for biomolecular labeling.** **(A)** An example of the metabolic labeling methods. **(B)** An example of the enzymatic labeling methods. **(C)** A fluorescent chemosensor for detecting phosphorylation.

the genetic code reprogramming (Zhang et al., 2002; Chin et al., 2003).

The biosynthesis of RNA and DNA has also been analyzed in living cells using metabolic labeling followed by click ligation. The data collected from these kinds of analyses can be used to understand DNA replication, DNA repair, and transcriptional control. For example, the use of 5-ethynyl-2'-deoxyuridine as a DNA precursor or the use of 5-ethynyluridine as an RNA precursor during microscopic or flow cytometric analyses enables quantitative analyses of DNA replication and whole transcription (Figure 2A) (Darzynkiewicz et al., 2011).

Metabolic labeling coupled with click labeling is a highly effective tool to analyze biomolecular transitions during the cell cycle, cell differentiation, signal responses, and apoptosis. However, the metabolic labeling methods for the anchor groups are not suitable for the analyses of particular species of biomolecules. Therefore, more specific labeling methods will be needed in the future.

### NOVEL LABELING METHODS AND THE USE OF CLICK CHEMISTRY IN QUANTITATIVE BIOLOGY

Several technologies are currently under development for the molecular species-specific labeling of the anchor chemical groups

present in biomolecules. The enzymatic labeling method for substrates is one such successful example. Many kinds of biomolecules such as proteins and nucleic acids are modified by methyl groups following neogenesis. These serve as important intrinsic functional markers, and are controlled by various methyltransferases. Prof. E. Weinhold and his colleagues developed analogs of S-adenosylmethionine, a methyl-group donor for almost all of the methyltransferases (Figure 2B) (Klimasauskas and Weinhold, 2007). These analogs work well *in vitro* and *in vivo*, and can modify the substrates with the anchor groups instead of the methyl groups in an enzyme-specific manner. By using this technology, DNAs (Schmidt et al., 2008), RNAs (Motorin et al., 2010), and proteins (Peters et al., 2010) have been successfully labeled with an alkyne or an azide. Similar enzymatic labeling methods for protein substrates have also been studied for other post-translational modifications, including phosphorylation (Lee et al., 2009) and acetylation (Yang et al., 2010). Although these technologies could potentially be used for substrate-specific labeling in living cells, an improvement of the molecular architecture of the methyl-donor analogs is necessary, because the degree of specificity and efficiency is still not up to the mark.

Other novel ideas using click chemistry for biological quantification have also been proposed. For example, Kamaruddin et al. devised a fluorescent chemosensor for detecting tyrosine phosphorylation, by metabolically labeling the residues near the phosphorylation sites with a quenchable dye (**Figure 2C**) (Kamaruddin et al., 2011). The strategy might enable quantitative phosphorylation analysis in an enzyme-specific manner in living cells.

Novel fluorescent labeling techniques have been continually devised in the past decade. Many more innovative fluorescence labeling methods that use click chemistry are expected to be developed in the near future to enhance research in the field of quantitative biology.

## ACKNOWLEDGMENT

This work was supported by JSPS and MEXT KAKENHI Grant Numbers 24500447, 24116523.

## REFERENCES

- Agard, N. J., Prescher, J. A., and Bertozzi, C. R. (2004). A strain-promoted [3 + 2] azide-alkyne cycloaddition for covalent modification of biomolecules in living systems. *J. Am. Chem. Soc.* 126, 15046–15047. doi: 10.1021/ja044996f
- Baskin, J. M., Prescher, J. A., Laughlin, S. T., Agard, N. J., Chang, P. V., Miller, I. A., et al. (2007). Copper-free click chemistry for dynamic *in vivo* imaging. *Proc. Natl. Acad. Sci. U.S.A.* 104, 16793–16797. doi: 10.1073/pnas.0707090104
- Beatty, K. E., Szychowski, J., Fisk, J. D., and Tirrell, D. A. (2011). A BODIPY-cyclooctyne for protein imaging in live cells. *Chembiochem* 12, 2137–2139. doi: 10.1002/cbic.201100277
- Best, M. D. (2009). Click chemistry and bioorthogonal reactions: unprecedented selectivity in the labeling of biological molecules. *Biochemistry* 48, 6571–6584. doi: 10.1021/bi9007726
- Blackman, M. L., Royzen, M., and Fox, J. M. (2008). Tetrazine ligation: fast bioconjugation based on inverse-electron-demand Diels-Alder reactivity. *J. Am. Chem. Soc.* 130, 13518–13519. doi: 10.1021/ja8053805
- Boyce, M., and Bertozzi, C. R. (2011). Bringing chemistry to life. *Nat. Methods* 8, 638–642. doi: 10.1038/nmeth.1657
- Chalfie, M., Tu, Y., Euskirchen, G., Ward, W. W., and Prasher, D. C. (1994). Green fluorescent protein as a marker for gene expression. *Science* 263, 802–805.
- Chang, P. V., Prescher, J. A., Hangauer, M. J., and Bertozzi, C. R. (2007). Imaging cell surface glycans with bioorthogonal chemical reporters. *J. Am. Chem. Soc.* 129, 8400–8401. doi: 10.1021/ja0702380
- Chin, J. W., Cropp, T. A., Anderson, J. C., Mukherji, M., Zhang, Z., and Schultz, P. G. (2003). An expanded eukaryotic genetic code. *Science* 301, 964–967. doi: 10.1126/science.1084772
- Darzynkiewicz, Z., Traganos, F., Zhao, H., Halicka, H. D., and Li, J. (2011). Cytometry of DNA replication and RNA synthesis: historical perspective and recent advances based on “click chemistry.” *Cytometry A* 79, 328–337. doi: 10.1002/cyto.a.21048
- Hang, H. C., Yu, C., Kato, D. L., and Bertozzi, C. R. (2003). A metabolic labeling approach toward proteomic analysis of mucin-type O-linked glycosylation. *Proc. Natl. Acad. Sci. U.S.A.* 100, 14846–14851. doi: 10.1073/pnas.2335201100
- Hangauer, M. J., and Bertozzi, C. R. (2008). A FRET-based fluorogenic phosphine for live-cell imaging with the Staudinger ligation. *Angew. Chem. Int. Ed. Engl.* 47, 2394–2397. doi: 10.1002/anie.200704847
- Heim, R., and Tsien, R. Y. (1996). Engineering green fluorescent protein for improved brightness, longer wavelengths and fluorescence resonance energy transfer. *Curr. Biol.* 6, 178–182.
- Huisgen, R. (1963). 1,3-Dipolar cycloadditions. Past and future. *Angew. Chem. Int. Ed. Engl.* 2, 565–598. doi: 10.1002/anie.196305651
- Jung, D., Min, K., Jung, J., Jang, W., and Kwon, Y. (2013). Chemical biology-based approaches on fluorescent labeling of proteins in live cells. *Mol. Biosyst.* 9, 862–872. doi: 10.1039/c2mb25422k
- Kamaruddin, M. A., Ung, P., Hossain, M. I., Jarasrassamee, B., O’Malley, W., Thompson, P., et al. (2011). A facile, click chemistry-based approach to assembling fluorescent chemosensors for protein tyrosine kinases. *Bioorg. Med. Chem. Lett.* 21, 329–331. doi: 10.1016/j.bmcl.2010.11.005
- Klimasauskas, S., and Weinhold, E. (2007). A new tool for biotechnology: AdoMet-dependent methyltransferases. *Trends Biotechnol.* 25, 99–104. doi: 10.1016/j.tibtech.2007.01.006
- Kodama, K., Fukuzawa, S., Nakayama, H., Sakamoto, K., Kigawa, T., Yabuki, T., et al. (2007). Site-specific functionalization of proteins by organopalladium reactions. *Chembiochem* 8, 232–238. doi: 10.1002/cbic.200600432
- Kolb, H. C., Finn, M. G., and Sharpless, K. B. (2001). Click chemistry: diverse chemical function from a few good reactions. *Angew. Chem. Int. Ed. Engl.* 40, 2004–2021. doi: 10.1002/1521-3773(20010601)40:11<2004::AID-ANIE2004>3.0.CO;2-5
- Lahann, J. (ed.). (2009). *Click Chemistry for Biotechnology and Materials Science*. Chichester: John Wiley & Sons, Ltd.
- Lang, K., and Chin, J. W. (2014a). Cellular incorporation of unnatural amino acids and bioorthogonal labeling of proteins. *Chem. Rev.* 114, 4764–4806. doi: 10.1021/cr400355w
- Lang, K., and Chin, J. W. (2014b). Bioorthogonal reactions for labeling proteins. *ACS Chem. Biol.* 9, 16–20. doi: 10.1021/cb4009292
- Lang, K., Davis, L., Wallace, S., Mahesh, M., Cox, D. J., Blackman, M. L., et al. (2012). Genetic Encoding of bicyclononynes and trans-cyclooctenes for site-specific protein labeling *in vitro* and in live mammalian cells via rapid fluorogenic Diels-Alder reactions. *J. Am. Chem. Soc.* 134, 10317–10320. doi: 10.1021/ja302832g
- Lee, S. E., Elphick, L. M., Anderson, A. A., Bonnac, L., Child, E. S., Mann, D. J., et al. (2009). Synthesis and reactivity of novel gamma-phosphate modified ATP analogues. *Bioorg. Med. Chem. Lett.* 19, 3804–3807. doi: 10.1016/j.bmcl.2009.04.028
- Liu, D. S., Tangpeerachaikul, A., Selvaraj, R., Taylor, M. T., Fox, J. M., and Ting, A. Y. (2012a). Diels-Alder cycloaddition for fluorophore targeting to specific proteins inside living cells. *J. Am. Chem. Soc.* 134, 792–795. doi: 10.1021/ja209325n
- Liu, J., Xu, Y., Stoleru, D., and Salic, A. (2012b). Imaging protein synthesis in cells and tissues with an alkyne analog of puromycin. *Proc. Natl. Acad. Sci. U.S.A.* 109, 413–418. doi: 10.1073/pnas.1111561108
- Motorin, Y., Teimer, R., Koynov, K., Willnow, S., Weinhold, E., and Helm, M. (2010). Expanding the chemical scope of RNA: methyltransferases to site-specific alkynylation of RNA for click labeling. *Nucleic Acids. Res.* 39, 1943–1952. doi: 10.1093/nar/gkq825
- Nguyen, D. P., Elliott, T., Holt, M., Muir, T. W., and Chin, J. W. (2011). Genetically encoded 1,2-aminothiols facilitate rapid and site-specific protein labeling via a bio-orthogonal cyanobenzothiazole condensation. *J. Am. Chem. Soc.* 133, 11418–11421. doi: 10.1021/ja203111c
- Peters, W., Willnow, S., Duisken, M., Kleine, H., Macherey, T., Duncan, K. E., et al. (2010). Enzymatic site-specific functionalization of protein methyltransferase substrates with alkynes for click labeling. *Angew. Chem. Int. Ed. Engl.* 49, 5170–5173. doi: 10.1002/anie.201001240
- Plass, T., Milles, S., Koehler, C., Szymbański, J., Mueller, R., Wiessler, M., et al. (2012). Amino acids for Diels-Alder reactions in living cells. *Angew. Chem. Int. Ed. Engl.* 51, 4166–4170. doi: 10.1002/anie.201108231
- Rostovtsev, V. V., Green, L. G., Fokin, V. V., and Sharpless, K. B. (2002). A stepwise huisgen cycloaddition process: copper(I)-catalyzed regioselective “ligation” of azides and terminal alkynes. *Angew. Chem. Int. Ed. Engl.* 41, 2596–2599. doi: 10.1002/1521-3773(20020715)41:14<2596::AID-ANIE2596>3.0.CO;2-4
- Sawa, M., Hsu, T. L., Itoh, T., Sugiyama, M., Hanson, S. R., Vogt, P. K., et al. (2006). Glycoproteomic probes for fluorescent imaging of fucosylated glycans *in vivo*. *Proc. Natl. Acad. Sci. U.S.A.* 103, 12371–12376. doi: 10.1073/pnas.0605418103
- Saxon, E., and Bertozzi, C. R. (2000). Cell surface engineering by a modified Staudinger reaction. *Science* 287, 2007–2010. doi: 10.1126/science.287.5460.2007
- Schmidt, F. H. G., Hüben, M., Gider, B., Renault, F., Teulade-Fichou, M. P., and Weinhold, E. (2008). Sequence-specific Methyltransferase-Induced Labelling (SMILING) of plasmid DNA for studying cell transfection. *Bioorg. Med. Chem.* 16, 40–48. doi: 10.1016/j.bmc.2007.04.054
- Selvaraj, R., Liu, S., Hassink, M., Huang, C. W., Yap, L. P., Park, R., et al. (2011). Tetrazine-trans-cyclooctene ligation for the rapid construction of integrin  $\alpha\beta_3$  targeted PET tracer based on a cyclic RGD peptide. *Bioorg. Med. Chem. Lett.* 21, 5011–5014. doi: 10.1016/j.bmcl.2011.04.116
- Shaner, N. C., Steinbach, P. A., and Tsien, R. Y. (2005). A guide to choosing fluorescent proteins. *Nat. Methods* 2, 905–909. doi: 10.1038/nmeth819

- Shimomura, O., Johnson, F. H., and Saiga, Y. (1962). Extraction, purification and properties of aequorin, a bioluminescent protein from the luminous hydromedusan, Aequorea. *J. Cell. Comp. Physiol.* 59, 223–239.
- Sletten, E. M., Nakamura, H., Jewett, J. C., and Bertozzi, C. R. (2010). Difluorobenzocyclooctyne: synthesis, reactivity, and stabilization by beta-cyclodextrin. *J. Am. Chem. Soc.* 132, 11799–11805. doi: 10.1021/ja105005t
- Song, W., Wang, Y., Qu, J., and Lin, Q. (2008). Selective functionalization of a genetically encoded alkene-containing protein via “photoclick chemistry” in bacterial cells. *J. Am. Chem. Soc.* 130, 9654–9655. doi: 10.1021/ja803598e
- Soundrarajan, N., Sokalingam, S., Raghunathan, G., Budisa, N., Paik, H. J., Yoo, T. H., et al. (2012). Conjugation of proteins by installing BIO-orthogonally reactive groups at their N-termini. *PLoS ONE* 7:e46741. doi: 10.1371/journal.pone.0046741
- Stephens, D. J., and Allan, V. J. (2003). Light microscopy techniques for live cell imaging. *Science* 300, 82–86. doi: 10.1126/science.1082160
- Tong, G. J., Hsiao, S. C., Carrico, Z. M., and Francis, M. B. (2009). Viral capsid DNA aptamer conjugates as multivalent cell-targeting vehicles. *J. Am. Chem. Soc.* 131, 11174–11178. doi: 10.1021/ja903857f
- Tornøe, C. W., Christensen, C., and Meldal, M. (2002). Peptidotriazoles on solid phase: [1,2,3]-triazoles by regiospecific copper(I)-catalyzed 1,3-dipolar cycloadditions of terminal alkynes to azides. *J. Org. Chem.* 67, 3057–3064. doi: 10.1021/jo011148j
- Vocadlo, D. J., Hang, H. C., Kim, E. J., Hanover, J. A., and Bertozzi, C. R. (2003). A chemical approach for identifying O-GlcNAc-modified proteins in cells. *Proc. Natl. Acad. Sci. U.S.A.* 100, 9116–9121. doi: 10.1073/pnas.1632821100
- Wang, A., Winblad-Nairn, N., Johnson, R. S., Tirrell, D. A., and Grabstein, K. (2008). Processing of N-terminal unnatural amino acids in recombinant human interferon-beta in *Escherichia coli*. *Chembiochem* 9, 324–330. doi: 10.1002/cbic.200700379
- Xue, D., Tu, Y., and Chalfie, M. (1993). Cooperative interactions between the *Caenorhabditis elegans* homeoproteins UNC-86 and MEC-3. *Science* 261, 1324–1328.
- Yang, Y.-Y., Ascano, J. M., and Hang, H. C. (2010). Bioorthogonal chemical reporters for monitoring protein acetylation. *J. Am. Chem. Soc.* 132, 3640–3641. doi: 10.1021/ja908871t
- Zhang, Z., Wang, L., Brock, A., and Schultz, P. G. (2002). The selective incorporation of alkenes into proteins in *Escherichia coli*. *Angew. Chem. Int. Ed. Engl.* 41, 2840–2842. doi: 10.1002/1521-3773(20020802)41:15<2840::AID-ANIE2840>3.0.CO;2-#

**Conflict of Interest Statement:** The author declares that the research was conducted in the absence of any commercial or financial relationships that could be construed as a potential conflict of interest.

Received: 29 September 2014; paper pending published: 21 October 2014; accepted: 06 November 2014; published online: 24 November 2014.

Citation: Horisawa K (2014) Specific and quantitative labeling of biomolecules using click chemistry. *Front. Physiol.* 5:457. doi: 10.3389/fphys.2014.00457

This article was submitted to Systems Biology, a section of the journal *Frontiers in Physiology*.

Copyright © 2014 Horisawa. This is an open-access article distributed under the terms of the Creative Commons Attribution License (CC BY). The use, distribution or reproduction in other forums is permitted, provided the original author(s) or licensor are credited and that the original publication in this journal is cited, in accordance with accepted academic practice. No use, distribution or reproduction is permitted which does not comply with these terms.



# Revealing neuronal function through microelectrode array recordings

**Marie Engelene J. Obien<sup>1\*</sup>, Kosmas Deligkaris<sup>1,2</sup>, Torsten Bullmann<sup>1</sup>, Douglas J. Bakkum<sup>3</sup> and Urs Frey<sup>1,2,3</sup>**

<sup>1</sup> RIKEN Quantitative Biology Center, RIKEN, Kobe, Japan

<sup>2</sup> Graduate School of Frontier Biosciences, Osaka University, Osaka, Japan

<sup>3</sup> Department of Biosystems Science and Engineering, ETH Zurich, Basel, Switzerland

**Edited by:**

Noriko Hiroi, Keio University, Japan

**Reviewed by:**

Ahmed El Hady, Princeton University/HHMI, USA  
Yoonkey Nam, Korea Advanced Institute of Science and Technology, Korea (South)

**\*Correspondence:**

Marie Engelene J. Obien, Frey Initiative Research Unit, RIKEN Quantitative Biology Center, RIKEN, Minatojima-minamimachi 2-2-3 Chuo-ku, Kobe, Hyogo 650-0047 Japan  
e-mail: meobien@riken.jp

Microelectrode arrays and microprobes have been widely utilized to measure neuronal activity, both *in vitro* and *in vivo*. The key advantage is the capability to record and stimulate neurons at multiple sites simultaneously. However, unlike the single-cell or single-channel resolution of intracellular recording, microelectrodes detect signals from all possible sources around every sensor. Here, we review the current understanding of microelectrode signals and the techniques for analyzing them. We introduce the ongoing advancements in microelectrode technology, with focus on achieving higher resolution and quality of recordings by means of monolithic integration with on-chip circuitry. We show how recent advanced microelectrode array measurement methods facilitate the understanding of single neurons as well as network function.

**Keywords:** **microelectrode array, neuronal function, extracellular recording, stimulation, CMOS, multielectrode array, neuron-electrode interface, multi-scale modeling**

## INTRODUCTION

Studying the function and connectivity of neurons in the brain involves coordinated, interdisciplinary efforts among scientists from various fields. Through the years, advancements in genetic markers, immunostaining, optical and electro-optical methods, electrophysiology, and computational tools have been made to identify neuronal types, explain their molecular machinery, untangle their wiring, decipher principles of neural coding, and to attribute functional roles to specific regions of the brain. The brain is a complex system and its activity spans over multiple temporal and spatial scales that require a comprehensive set of technologies to address these scales. Innovations in experimental methods to observe and perturb brain activity and in computational tools to analyze recorded data are needed to master the brain's complexity and advance our understanding of its function. Systems biology has allowed to bridge between molecular dynamics and whole cell simulations using multi-scale modeling. Applying similar approaches to brain activity will allow us to gain a more encompassing understanding of it. However, quantitative data at all these spatial and temporal scales are a prerequisite.

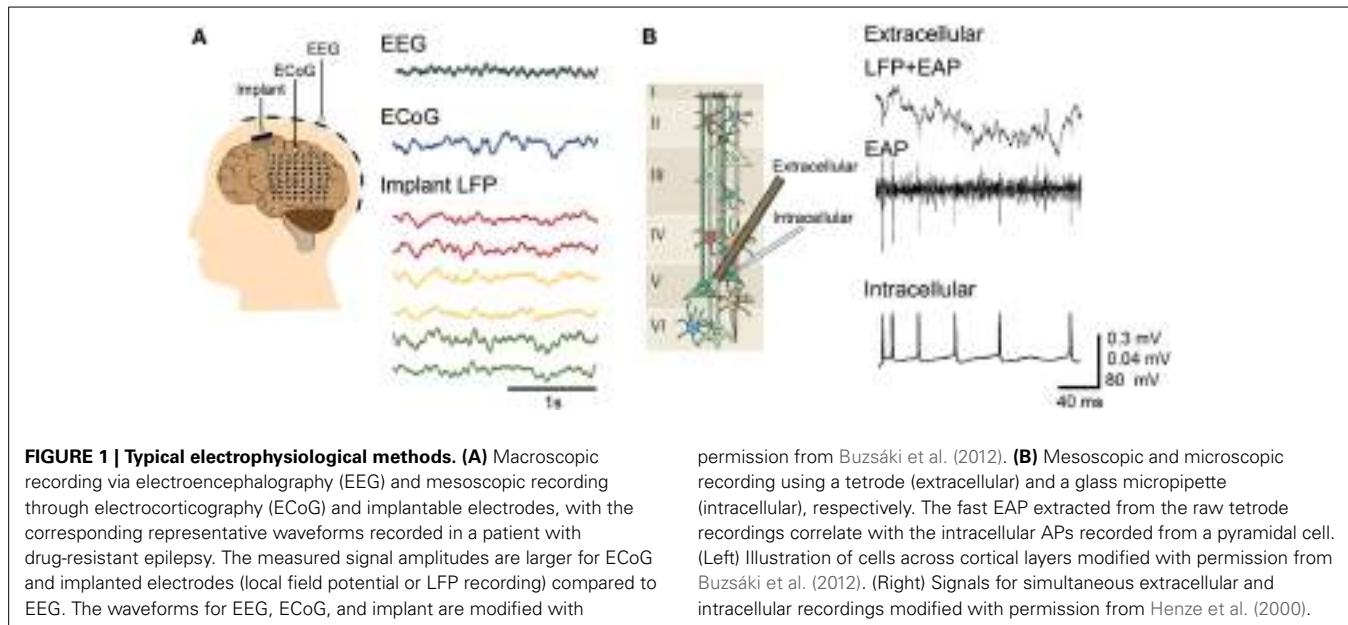
Electrophysiology has been the preferred means of analyzing brain activity due to the ability to capture a wide range of neural phenomena, from the spiking activity of individual neurons to the slower network oscillations of small populations (Llinás, 1988; Contreras, 2004; Assad et al., 2014). The electrical nature of neuronal activity makes it possible to detect signals on electrodes at a distance from the source, but not without caveats. It is necessary to determine the recording capabilities and limits of the device used and to understand how the neuronal signal is transduced

into a recorded digital form. Typical electrophysiological methods are shown in **Figure 1** and further described below.

At the microscale, patch-clamp can be used to measure currents of single ion channels. The function of single neurons is often explored by direct measurements of the intracellular voltage, using patch-clamp or a sharp microelectrode. It is a powerful but tedious method and often its use is limited to a few neurons per experiment (Wood et al., 2004). Planar patch-clamp systems allow rapid *in vitro* patch-clamping, mostly used for high-throughput ion channel screening of dissociated cells (Dunlop et al., 2008). Automated patch-clamp allows for fast *in vivo* intracellular recording and it is feasible to extend the method to measure several neurons simultaneously (Kodandaramaiah et al., 2012). The bulkiness of current micromanipulators and patch-clamp systems together with the necessity for accurate and precise control have limited simultaneous patch-clamp recordings to a few—maximum of four and twelve for *in vivo* (Kodandaramaiah et al., 2014) and *in vitro* (Perin et al., 2011), respectively.

At the macroscale, indirect measurement of large areas of the brain's activity is achieved via functional magnetic resonance imaging (fMRI), positron emission tomography (PET), and electroencephalography (EEG). These methods can be used to resolve functional connectivity among brain regions. For example, EEG detects spontaneous or evoked electrical activity from the scalp with low spatial resolution (cm range).

In this review, we focus on electrophysiology at the mesoscale—extracellular recordings via metal electrodes, open-gate field-effect transistors (OGFETs) or oxide-semiconductor FET (OSFET) integrated into large arrays, so-called microelectrode arrays (MEAs). This method enables simultaneous and



long-term recordings of local field potentials (LFPs) and extracellular action potentials (EAPs) from a population of neurons at millisecond time scale. It also allows perturbing neuronal activity using electrical stimulation. As data obtained from *in vivo* and *in vitro* experiments are often very similar, the MEA technology, concepts, and applications we include here apply to both and will be helpful for scientists and engineers from either field. In particular, we explain the interface between the neuron and the electrode in order to understand how to interpret the recordings. We highlight trends in the development of complementary metal-oxide-semiconductor (CMOS) based high-density MEAs (HDMEAs). The advantages of HDMEAs include the capability to map neuronal activity at sub-cellular resolution, localize single cells, and to constrain full-compartmental neuron models.

The outline is as follows. Chapter 2 gives an overview of the MEA technologies, including the comparison between *in vivo* and *in vitro* MEA devices from a technical aspect. Chapter 3 describes the current understanding on microelectrode recordings and introduces the different factors that shape the recorded signals. Chapter 4 discusses how to process MEA signals and reviews recent works on using MEAs for neuroscience studies. We then conclude in Chapter 5 with perspectives on advanced measurements and applications of MEAs for studying neuronal function.

## MEA TECHNOLOGY

This chapter reviews the technology involved in MEA development.

### DEVICE TYPES AND TERMINOLOGY

Over the years, a wide repertoire of terms has been used to refer to and distinguish between all the different forms of MEAs, e.g., emphasizing the type of transducers used (multi-transistor array, microelectrode array, multielectrode array, micro-nail array, capacitive-coupled array, 3D MEA), the type of substrate (active array, passive array, silicon array, CMOS array), the shape of the

device (needle-type probe, polytrode, neuro dish), the channel count (multichannel array), the electrode density (HDMEA) or the application (implantable array, *in vivo* MEA, *in vitro* MEA) and more. We would therefore like to briefly explain the terminology used in the context of this review. We generalize the term microelectrodes and MEA to cover both substrate-integrated planar MEAs and implantable neural probes. We also include capacitive-coupled devices, such as multi-transistor arrays in the definition of MEAs. We then distinguish between implantable, *in vivo* MEAs, such as polytrodes and neural probes, and *in vitro* MEAs that generally include a cell culture dish or some other sort of medium chamber. Further, we classify the different array architectures, as will be explained in Section Advances in MEA and Probe Devices (Figure 3). Briefly, we distinguish between “fixed wiring” arrays, meaning that each transducer in the array has a *direct wire* to the outside of the array and “multiplexed arrays,” in which some sort of switching mechanism is employed *within* the array. We use the term “array” to refer to the actual area that encompasses the transducer elements only and we use device or MEA to refer to the entire device. With system, we refer to the MEA and all required components to operate it, such as the data acquisition hardware and software. We use the terms “active” and “passive” to distinguish between devices with active circuit elements, such as transistors, and devices without such elements.

### ELECTRODES AND TRANSDUCERS

There are various techniques for fabricating microelectrodes, which are reviewed by Li et al. (2003), Park and Shuler (2003), Huang et al. (2009). Choosing the materials for the insulator, conductor, microelectrode, and substrate is crucial, in particular with respect to biocompatibility. All materials in the MEA that will be near to or in contact with cells and tissue need to be tested for toxicity in prolonged periods of time (Hassler et al., 2011). It is also important to consider the biological experiments for which the microelectrodes will be used, whether *in vivo* or *in vitro*, culture or acute preparation. Moreover, deciding the type of MEA to use is

highly dependent on the type of recorded signals needed, whether EAPs and/or LFPs or intracellular action potentials (IAPs), single cell resolution or not. If the MEA is to be used for stimulation, the charge capacity of electrodes is an important aspect. The electrode needs to be able to mediate reactions at the electrode-electrolyte interface to allow electron flow in the electrode to transition into ion flow in the electrolyte toward stimulating nearby cells (Cogan, 2008).

Generally, an important goal of electrode fabrication is to achieve low impedance. Low electrode impedance results in higher signal-to-noise ratio (SNR), with the usual target SNR of 5:1 or higher. Uniformity of the electrode impedance across an array of electrodes may also be important to obtain consistent data.

Typically, electrodes are made with metallic conductors such as gold (Au), titanium nitride (TiN), platinum (Pt), stainless steel, aluminum (Al), and alloys like iridium oxide (IrOx). Since the electrodes used in MEAs are on the micrometer scale, it is a challenge to achieve low electrode impedance with plain conductors only. Increasing the effective surface area of electrodes can be achieved by modification with porous conductive materials such as Pt-black, Au nanostructures, carbon nanotubes (CNTs), and conductive polymers like poly(3,4-ethylenedioxythiophene) (PEDOT). Emerging materials aside from PEDOT and CNTs include doped diamond and graphene. By modifying the surface, the electrode impedance can be decreased drastically and neuronal recording can be improved (Cui et al., 2001; Franks et al., 2005; Ludwig et al., 2006; Keefer et al., 2008; Viswam et al., 2014). Nam and Wheeler (2011), Kim et al. (2014) for a review of electrode materials and surface modification.

Non-metallic electrodes have been mostly used in conjunction with field-effect transistor (FET) based transducers (Bergveld, 1970; Fromherz et al., 1991). An OGFET can, e.g., be obtained if the fabrication process of a FET is stopped before depositing the gate material (Jenker et al., 2004). Easier to fabricate is the so-called extended-gate FET (EGFET), in which the FET is fabricated without modification from a standard CMOS process. Metal and via interconnections are used to extend the gate to the surface of the chip, where an insulated electrode implements the “extended gate.” Such insulation ensures that no faradaic currents occur. However, as Hierlemann et al., pointed out, devices with metal electrodes also usually connect to a FET directly (Imfeld et al., 2008) or through a filter capacitor (Heer et al., 2006), resulting in a largely capacitive recording situation (Hierlemann et al., 2011). OGFET, EGFET, and devices that directly connect the electrode to the first FET usually need to include some measures to properly bias the gate or some calibration mechanism, which may cause transient currents to flow at the electrode. Whereas for devices with a capacitively coupled front-end stage, controlling the electrode input node is generally not needed. Devices with a FET-based transducer, but using a metalized gate exposed to the liquid, have also been developed (Jobling et al., 1981).

Recently, ultra-small electrodes are being developed to record intracellular activity, including subthreshold signals, as reviewed in Spira and Hai (2013). This is achieved by 3D structured electrodes such as silicon nanowires (Robinson et al., 2013) and Au mushrooms (Hai et al., 2009) penetrating the cell membrane.

Electroporation was shown to facilitate measurement of intracellular activity (Koester et al., 2010; Hai and Spira, 2012).

## ADVANCES IN MEA AND PROBE DEVICES

Since the single extracellular microelectrodes used in the middle of the last century (Weale, 1951; Gesteland et al., 1959), development quickly proceeded to MEAs with multiple transducers for the purpose of increasing the number of neurons observed (Thomas et al., 1972; Gross et al., 1977; Pine, 1980; Csicsvari et al., 2003) to increase reliability of spike sorting (Gray et al., 1995; Harris et al., 2000) and to allow for source localization (Blanche et al., 2005; Chelaru and Jog, 2005; Frey et al., 2009b; Somogyvári et al., 2012; Delgado Ruz and Schultz, 2014). The advances in lithographic techniques, fueled by the semiconductor industry, allowed a gradual increase in performance and reliability of such multichannel devices. Passive transducer devices based on electrodes embedded in glass or silicon substrates with fixed wiring to amplifiers for *in vitro* and also *in vivo* applications became commercially available in the late 90s and early years of this century. Already early on, silicon-based biosensors for interfacing cells with microelectronics were developed (Bergveld, 1970; Parce et al., 1989). Active devices, employing FETs were fabricated and 2D arrays demonstrated (Besl and Fromherz, 2002). Devices using CMOS technology were fabricated in academic facilities (DeBusschere and Kovacs, 2001) and industrial foundries, usually in conjunction with additional processing steps for biocompatibility reasons (Berdondini et al., 2002; Eversmann et al., 2003b; Franks et al., 2003).

The key advantage of integrating active electronic components on the same substrate as the actual electrodes is the possibility of a much higher electrode number and density. Due to the possibility of using active switches to time multiplex signals, integrated circuits make it feasible to transfer data from such high channel counts off chip and to overcome the connectivity limitation of passive devices. Additionally, such co-integration allows amplifying the signals with optimal quality, due to minimal parasitic capacitances and resistances (Hierlemann et al., 2011). The monolithic co-integration also allows including additional functionality, e.g., on-chip spike detection, closed-loop capabilities, electrical stimulation, electronic chip identification, device calibration, and other type of sensing modalities, such as temperature, pH or optical sensing (Baumann et al., 1999; Tokuda et al., 2006; Johnson et al., 2013b).

**Figure 2A** compares a variety of historical and current devices, to illustrate the evolution of MEAs with respect to overall sensing area and electrode densities. The electrode count is shown with solid lines. The devices are categorized into fixed wiring (Type A&B in **Figure 3**) and multiplexed arrays (Types C–E in **Figure 3**). Fixed-wiring arrays include devices without any on-chip circuitry (Alpha MED Science Co., Ltd.<sup>1</sup>; Multi Channel Systems GmbH<sup>2</sup>; Thomas et al., 1972; Gross et al., 1977; Pine, 1980;

<sup>1</sup> Alpha MED Science Co., Ltd. MED64: A low-noise and user-friendly multi-electrode array system for *in-vitro* electrophysiology. Available at: <http://www.med64.com> [Accessed December 1, 2014].

<sup>2</sup> Multi Channel Systems GmbH. MCS: Innovations in Electrophysiology. Available at: <http://www.multichannelsystems.com> [Accessed December 1, 2014].

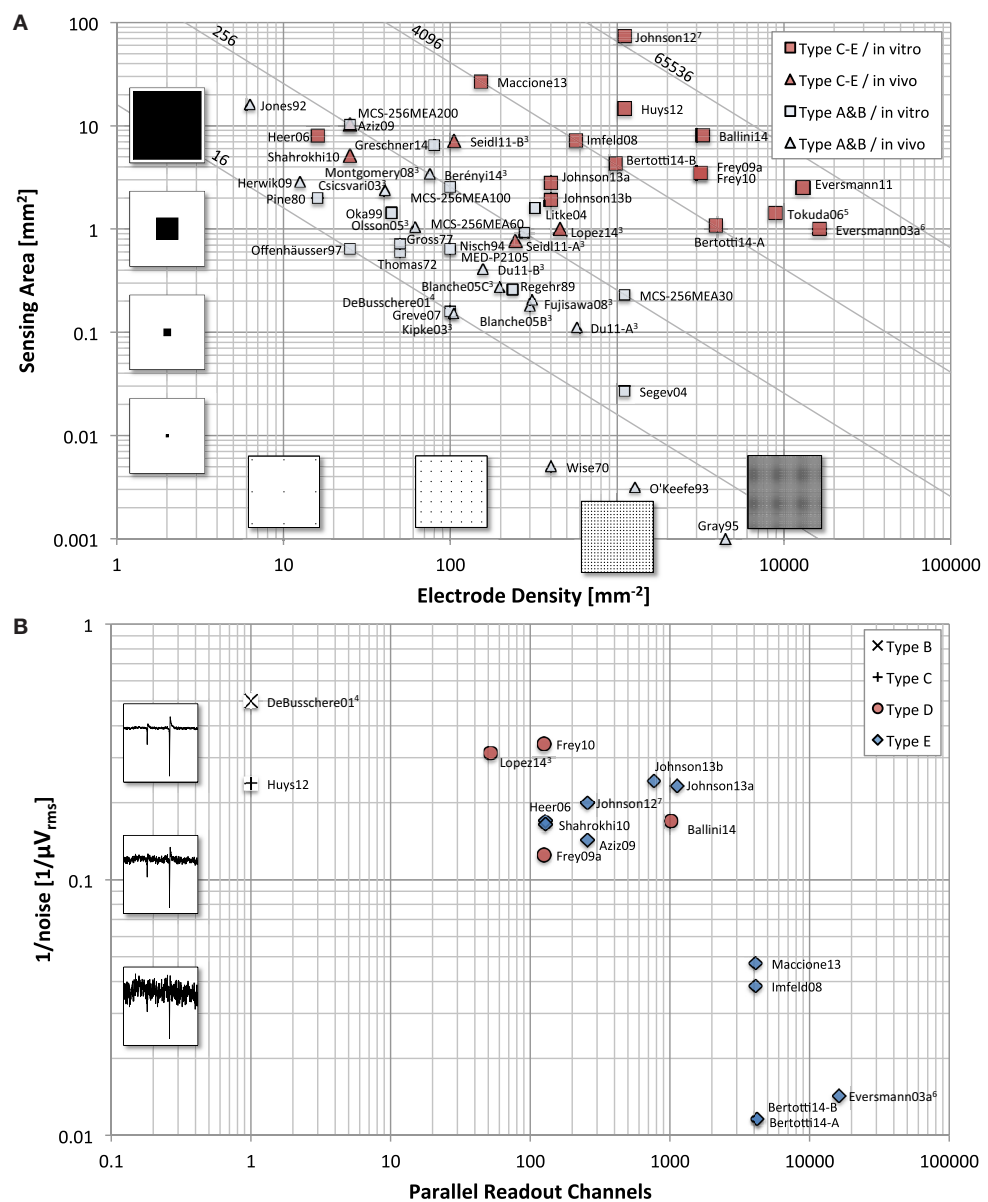


**FIGURE 2 | Device comparison.** MEA comparison with respect to (A) electrode density and total sensing area, and (B) parallel recording channel count and noise level. (A) For devices with a regular sensor pitch, such as most *in vitro* MEA devices, the total area is calculated as number of electrodes times the pixel area. For all devices, the number of electrode times the inverse of the electrode density matches the total area. The light gray lines illustrate the number of electrodes. (B) The noise values shown are approximated RMS values stated in the respective citations. The conditions

under which these measurements were taken usually differ significantly (such as noise bandwidth, in- or exclusion of electrode noise, inclusion of ADC quantization noise, etc.). Therefore, this graph only serves as a rough comparison. The waveforms to illustrate the noise levels are simulated and have a spectrum typical for MEA recordings. The simulated spikes are typical spikes for acute brain slice measurements recorded with microelectrodes. The recorded amplitudes may vary significantly depending on preparation and sensor characteristics. See Footnotes.<sup>3,4,5,6,7</sup>

Regehr et al., 1989; Nisch et al., 1994; Oka et al., 1999; Litke et al., 2004; Segev et al., 2004; Greschner et al., 2014), but also MEAs with on-chip circuitry limited to the surrounding of the array (Greve et al., 2007) and arrays that include FETs (Offenbässer et al., 1997) and source follower devices directly wired to circuitry outside the array (DeBusschere and Kovacs, 2001). Multiplexed arrays employ some sort of multiplexing within the actual array

<sup>3</sup>The area is calculated as the rectangle of the maximum vertical extend times the maximum horizontal extend, whereas for probes, the horizontal extend is taken as the shaft width.

<sup>4</sup>Only a single sub array of 16 electrodes is considered.

<sup>5</sup>Features a frame rate significantly lower as compared to the other devices.

<sup>6</sup>Noise values are taken from Lambacher et al. (2010).

<sup>7</sup>The authors state that with a new acquisition board, the parallel channel count could be increased to 1024 at 9300 fps.

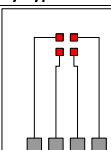
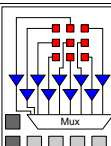
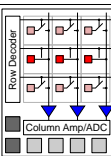
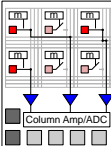
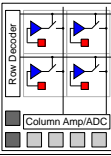
(Eversmann et al., 2003a, 2011; Heer et al., 2006; Tokuda et al., 2006; Aziz et al., 2009; Berdondini et al., 2005, 2009; Frey et al., 2010; Huys et al., 2012; Johnson et al., 2012, 2013a,b; Maccione et al., 2013; Ballini et al., 2014; Bertotti et al., 2014).

For *in vivo* MEAs, the connectivity limitation is even more severe, as connections cannot be wired out on all four sides of the array, but only on one of the narrow sides. **Figure 2A** includes some examples of such devices using fixed wiring (Wise et al., 1970; Najafi and Wise, 1986; Jones et al., 1992; O'Keefe and Recce, 1993; Gray et al., 1995; Bai and Wise, 2001; Csicsvari et al., 2003; Kipke et al., 2003; Blanche et al., 2005; Olsson and Wise, 2005; Fujisawa et al., 2008; Montgomery et al., 2008; Herwik et al., 2009; Du et al., 2011; Berényi et al., 2014) and three recent *in vivo* MEAs with multiplexing on the shaft itself (Shahrokhi et al., 2010; Seidl et al., 2011; Lopez et al., 2014). For detailed reviews of *in vivo* MEAs (see Wise et al., 2008, 2004; Ruther et al., 2010).

**Figure 2B**, on the other hand, focuses only on CMOS-based devices and illustrates the tradeoff between the number of parallel (or quasi parallel) readout channels and the input referred noise of the amplification chain. It illustrates the fundamental fact that a low-noise front-end amplifier requires both area and power. Limiting either will inherently increase the noise levels.

The power budget for the entire device, including all circuitry within the array and surrounding it, is limited by the amount of produced heat that one can tolerate. For the area constraints, one has to separately consider the area within the array and surrounding it. Within the array, the electrode density dictates the available area per pixel. Outside the array, the area is limited mostly by the fabrication cost. As a trivial approach to decouple the area requirement from the noise specifications, one can simply place the amplifiers outside the array and directly wire one electrode to one amplifier (**Figure 3B**). However, this approach still does not allow achieving both a high density and a large electrode count at the same time. **Figure 3** lists these fixed-wiring approaches and typical array architectures using multiplexing within the array to overcome this limitation.

Active switching can be integrated into the array, allowing to time multiplex the signals from many electrodes to a few wires that carry the signals out of the array. We now consider two types of time multiplexing, static (**Figures 3C,D**) and dynamic (**Figure 3E**) operation (Imfeld et al., 2008). In dynamic mode, each pixel (or electrode) is sampled once within each frame, with typical frame-rates of 2–10 kHz for CMOS-based MEAs (Eversmann et al., 2003a; Johnson et al., 2013b) and some devices

Array Type	Advantages	Disadvantages	Selected References
<b>A</b> 	<b>Fixed wiring with no active circuitry</b> <ul style="list-style-type: none"> <li>• Direct access of all electrodes</li> <li>• Simple fabrication</li> <li>• Free choice of substrate and electrode material</li> <li>• No power supply needed</li> </ul>	<ul style="list-style-type: none"> <li>• Electrode number limited by the number of pads</li> <li>• Increased parasitic capacitance</li> </ul>	(Regehr et al., 1989; Segev et al., 2004; Thomas et al., 1972; Litke et al., 2004; Greschner et al., 2014; Oka et al., 1999; Nisch et al., 1994; Jones et al., 1992; Du et al., 2011; Blanche et al., 2005; Berényi et al., 2014; O'Keefe and Recce, 1993)
<b>B</b> 	<b>Fixed wiring with on-chip active circuitry</b> <ul style="list-style-type: none"> <li>• Not limited by the number of pads</li> <li>• On-chip signal conditioning</li> <li>• Possibility to include additional functionality</li> <li>• Dynamic mode if amplifier and filter before the multiplexer</li> </ul>	<ul style="list-style-type: none"> <li>• Electrode density limited by interconnection limitation within the array</li> <li>• Area used inefficiently</li> <li>• Only static mode if amplifier and filter are placed after the multiplexer</li> </ul>	(Greve et al., 2007; DeBusschere and Kovacs, 2001; Olsson and Wise, 2005; Najafi and Wise, 1986; Bai and Wise, 2001)
<b>C</b> 	<b>Multiplexed array with column, row addressing in static mode</b> <ul style="list-style-type: none"> <li>• On-chip signal conditioning</li> <li>• High sensor count</li> <li>• High spatial resolution</li> </ul>	<ul style="list-style-type: none"> <li>• Restricted parallel readout</li> </ul>	(Huys et al., 2012) Note: This device splits the amplifier into two parts, one inside and one outside of the array.
<b>D</b> 	<b>Multiplexed array with switch-matrix concept</b> <ul style="list-style-type: none"> <li>• On-chip signal conditioning</li> <li>• Number of electrodes decoupled from number of channels</li> <li>• High spatial resolution</li> <li>• Large area for front-end amplifier</li> </ul>	<ul style="list-style-type: none"> <li>• No full-frame readout</li> <li>• Limited number of readout channels</li> </ul>	(Frey et al., 2010; Ballini et al., 2014; Lopez et al., 2014; Seidl et al., 2011)
<b>E</b> 	<b>Multiplexed array with full-frame readout (APS)</b> <ul style="list-style-type: none"> <li>• On-chip signal conditioning</li> <li>• Minimal parasitic capacitance</li> <li>• Full-frame readout</li> </ul>	<ul style="list-style-type: none"> <li>• Limited area for front-end amplifier</li> </ul>	(Eversmann et al., 2003a; Berdondini et al., 2009; Heer et al., 2006; Maccione et al., 2013; Eversmann et al., 2011; Bertotti et al., 2014; Johnson et al., 2013a, 2013b; Aziz et al., 2009)

▶ Front-end Amplifier ■ Selected Electrode □ Inactive Electrode □ Signal Pad ■ Power Supply Pad ▾ Switch □ Local Memory

**FIGURE 3 | Array architectures.** This table summarizes and classifies the different architectures that are typically used for MEAs. Advantages, disadvantages are stated and representative selected references given. **(A,B)** Fixed wiring. **(A)** Electrodes are directly connected to signal pads with no active circuitry. **(B)** Electrodes are directly connected to on-chip active

circuitry for signal conditioning. **(C–E)** Multiplexed arrays. **(C)** Signals are multiplexed to the signal pads via column, row addressing in static mode. **(D)** More flexible addressing is achieved by adding more routing resources within the array in the switch-matrix mode. **(E)** All electrodes can be sampled at fast speeds in full-frame readout implemented in active pixel sensor (APS) MEAs.

allowing as high as 77 kHz (Bertotti et al., 2014). This mode is similar to image sensors used in cameras. Typically, rectangular sub-arrays can be chosen as regions of interest and sampled at faster rates. From a circuit perspective, the challenge in designing full-frame readout MEAs lies in the fact that the multiplexing within the array requires the front-end amplifier to be located within the pixel itself, as the electrode alone exhibits a high impedance and therefore cannot drive the multiplexed readout lines at sufficient speed. Inherently, the available area within the pixels is limited in high-density arrays, making it difficult to build very low noise amplifiers. In addition, the electrodes themselves and the activity within the culture medium show wide band noise (see Section Noise and SNR), thus requiring a low-pass filter within the pixel to prevent noise from being aliased into the signal band due to the sampling. Generally full-frame readout arrays have a high channel count, and therefore the power budget per channel is very limited.

Alternative approaches to circumvent this issue and to allow for devices in which the circuit itself is not the limiting factor with respect to noise performance have been demonstrated. Arrays operating in static mode (**Figures 3C,D**) have only switches and no amplifiers as active devices within the array. The switches are used to wire electrodes to front-end amplifiers placed outside of the array, where sufficient area for the implementation of low-noise amplifiers is available. This also decouples the number of electrodes from the number of readout channels, which allows budgeting of the available power in more flexible ways. Devices that employ a simple column and row based static addressing are limited in the flexibility of choosing electrodes for parallel readout. A switch-matrix implementation, which consists of a large set of routing wires, routing switches, and local memory, such as SRAM cells within the array, allows the use of complex routing paths to rewire a subset of electrodes to the available readout and stimulation channels in a flexible manner. Often, such an approach is sufficient to observe biological phenomena of interest, as typically not all electrodes exhibit activity. However, experimental protocols tend to get more complex, as one needs to select the “right” electrodes during the experiment. One of the protocols commonly used for such devices is to first scan the entire array in static mode, i.e., record from each rectangular sub-block for, e.g., a few minutes, run some online or quasi online data processing on the recorded data, and select a more refined subset based on the recorded activity and the scientific objective of the experiment.

Apart from the array, CMOS devices also require the design of neuronal amplifiers and some sort of data transmitter, either of the amplified analog signals or, more typically, of the already digitized data. Generally, a neural amplifier needs to have high input impedance, which is significantly higher than the electrode impedance, to ensure signal integrity. The amplifier should be of low power to prevent substrate heating that could damage cells or tissue. For *in vitro* MEA devices, a variety of target applications have to be considered. Therefore, gain and dynamic range requirements can be quite demanding and should be adjustable, such as to cover applications with maximal amplitudes of a few hundred microvolts in acute slice preparations and, on the other hand, up to 10 mV in measurements from cardiomyocytes. The

same also holds true for the flexibility in the recording bandwidth. Some applications may require lower frequency signals only, some only spikes in the EAP band, some both bands with different gain requirements at the same time. The circuits need to implement some sort of high-pass filter to block the large  $1/f$  noise of the electrode-liquid interface typically observed. MEA systems can also include stimulation circuitry, covered in the next section, and analog-to-digital conversion (ADC). They need to include an interface to transmit the data and receive commands for controlling the system’s operation. The requirements are different for implantable devices, where usually the target application is much more defined, but also the power, reliability, and safety requirements are more stringent. These systems often implement spike detection or classification and wireless transmission in the system, either as a monolithic implementation or hybrid approach using multiple ICs. They may also be powered wirelessly. On the other hand, *in vitro* MEA systems do not require wireless power or data transmission, as they can generally be directly wired to the data-receiving device. In this case, often common interface standards are employed, such as USB (Multi Channel Systems GmbH<sup>2</sup>), Ethernet (Frey et al., 2010), National Instrument’s DAQ card (Alpha MED Science Co., Ltd.<sup>1</sup>), CameraLink (Imfeld et al., 2008), or others. Most of these systems support online storage of the full raw data to hard disks, sometimes including some form of lossless data compression (Sedivy et al., 2007).

Many of the circuit requirements can be traded against each other, e.g., one can easily lower the noise by increasing the area or power consumption. The key challenge therefore is to set the target specifications for the given application accurately and optimize the systems for it, without overdesigning specific requirements. Further considerations with respect to noise are given in Section Noise and SNR. Reviews focusing on circuit related issues can be found here: (Wise et al., 2004, 2008; Harrison, 2008; Jochum et al., 2009; Gosselin, 2011).

## STIMULATION

MEAs allow passive observation, and also active influence and control of neuronal activity. Metal electrodes can deliver electrical stimuli directly using the microelectrodes, whereas for OGFET-based devices, typically an extra capacitive stimulation spot is used to deliver stimuli (Stett et al., 1997). In addition, monolithic CMOS integration of MEAs opens up the possibility to include electrical stimulation circuitry directly on-chip, in turn allowing a high degree of flexibility in generating spatiotemporal patterns of stimulation, higher spatial resolution for stimulation and direct on-chip stimulation artifact blanking or suppression.

Already the very first electrophysiological experiments with frogs by Galvani (1791) involved electrical stimulations using metal wires connected to various sources, e.g., Leyden jars, Franklin’s magic squares, and even atmospheric electricity during lightning. *In vivo*, electrical stimulation is commonly used to stimulate nerves for transmitting sensory information to the brain, such as for cochlear implants (Wilson and Dorman, 2008) and retinal implants (Ahuja et al., 2011; Zrenner et al., 2011); to control, e.g., limbs for neurorehabilitation after nervous system injury; and to treat disorders, e.g., Parkinson’s disease by deep

brain stimulation using brain pacemakers (Montgomery and Gale, 2008). In such applications, the physical distance between the stimulation electrode and target nerves can be rather large, requiring the delivery of high amplitude stimuli.

Lilly et al. (1955) established charged balanced methods using biphasic brief pulses to limit the damage to the tissue and the degradation of the electrodes themselves. Merrill et al. reviewed electrical stimulation using electrodes, listing various materials (Merrill et al., 2005). For *in vitro* MEAs, effective stimulation protocols were characterized by Wagenaar et al. (2004). The authors studied different stimulation parameters (pulse width, amplitude, pulse shape) that evoke neuronal activity.

One application of electrical stimulation is the use of it as a “trigger,” so-called stimulus-triggered averaging (Cheney and Fetz, 1985). Electrical stimulation allows delivering trigger pulses of high temporal resolution in the order of a few microseconds, depending on the stimulation buffer used and the capacitive load of the electrode. Stimulation can evoke responses with small temporal jitter, e.g., Bakkum et al. observed a jitter of 160  $\mu$ s using passive MEAs (Bakkum et al., 2008). Bakkum et al. used trigger signals to study the velocity of action potential (AP) propagation in axons of cultured neurons (Bakkum et al., 2013). **Figure 4A** shows how such stimulus-triggered averages revealed small axonal spikes of different shapes, such as bi- and tri-phasic types. **Figure 4B** illustrates the reduction in uncorrelated noise with increasing number of averaged repetitions. One potential issue with delivering electrical stimulation to neuronal cells and tissue is the occurrence of artifacts in recording channels, due to the fact that stimulation pulses are typically three to four orders of magnitude larger than the recorded signals. This coupling between stimulation and recording is difficult to prevent, and artifacts are picked up both within the wiring of the array and circuits, but also through the medium of the cell culture or tissue. However, as long as the coupling is purely capacitive, artifacts usually only prevent recording during the stimulation period itself. If the amplitude of an artifact is large, which can occur when a recording electrode is near the stimulation electrode, the artifact may saturate the amplification circuits of the recording electrode. This saturation will prevent recording for an extended period of time after the stimulation ended. **Figure 4C** shows an example of such a saturated signal from an electrode located 18  $\mu$ m (center-center) away from the stimulation electrode and a signal without saturation from an electrode located about a 1 mm away. **Figure 4D** shows the relationship between the distance from stimulation to recording electrode and the duration of saturation for a 11,011-electrode MEA (Frey et al., 2010), without employing any artifact suppression measures. As long as the amplifiers do not fully saturate, it is possible to suppress such artifacts in software by subtracting the estimated artifact (based on templates, filters or local curve fitting) from the data (Hashimoto et al., 2002; Wagenaar and Potter, 2002). To also allow recording from electrodes on which saturation would occur, counter measures in hardware have to be employed. One solution is to use a “reset” switch that can bring back the saturated amplifier into normal operation quickly, by resetting the high-pass filter of the front-end amplifier (Heer et al., 2006; Frey et al., 2010). To suppress artifacts even on the stimulation electrode itself, more sophisticated

methods are used. Jimbo et al. proposed a method to decouple the recording amplifiers during stimulation, sample the electrode potential during recording and add the stimulation pulse to the stored electrode potential (Jimbo et al., 2003). This scheme has also been implemented on dedicated ASICs to be used in conjunction with MEA devices (Brown et al., 2008; Hottowy et al., 2012; Tateno and Nishikawa, 2014). **Figures 4E,F** show stimuli activated neuronal responses with high spatiotemporal precision. In a study to track axonal APs (Bakkum et al., 2013) several ten thousands of stimuli were required, which was possible without damaging the electrodes or cells. In this case, voltage-mode stimulation was used, although the stimulation hardware supported both current- and voltage-mode (Livi et al., 2010).

Closed-loop experiments, in which neural activity triggers electrical stimulation, employing on-chip stimulation circuitry have been presented by Hafizovic et al. (2007) and Müller et al. (2013). In both cases, the spike detection is performed off-chip on dedicated FPGA hardware. The actual decision to stimulate and the selection of the stimulation waveform patterns is performed on a personal computer in Hafizovic et al. (2007), whereas in Müller et al. (2013) an event engine performing this task is implemented directly on the FPGA platform, making the latency until stimulation shorter and, importantly, reducing its temporal jitter.

CMOS-based devices exclusively devoted to stimulation at high spatio-temporal resolution of close to 7000 electrode per square millimeter and with variable voltage mode pulses have been developed as well (Lei et al., 2008, 2011). Circuit considerations for CMOS-based devices for clinical *in vivo* application are reviewed (e.g., Ortmanns et al., 2008; Ohta et al., 2009).

## APPLICATIONS OF IN VITRO CMOS-BASED MEAs

*In vitro* CMOS MEAs have already been used in a wide variety of applications, for recording, for electrical stimulation or for both. **Figure 5** lists *in vitro* CMOS MEAs, their key specifications and preparations for which they have been used so far. Some additional *in vitro* CMOS-based MEAs that are not listed in **Figure 5** can be found here: (Tokuda et al., 2006; Greve et al., 2007; Meyburg et al., 2007; Yegin et al., 2009; Johnson et al., 2012). In addition, the functionality of some *in vivo* CMOS MEAs has also been demonstrated using *in vitro* applications (Aziz et al., 2009).

The two most prominent preparations investigated with *in vitro* CMOS MEAs so far are acute retina preparations from mice (Menzler and Zeck, 2011; Fiscella et al., 2012; Maccione et al., 2014), rats (Eickenscheidt et al., 2012; Lloyd et al., 2014; Stutzki et al., 2014), rabbits (Zeck et al., 2011; Ballini et al., 2014; Fiscella et al., 2014), guinea pig (Velychko et al., 2014) and humans (Reinhardt and Blickhan, 2014); and cultured neuronal cells from snails (Eversmann et al., 2003a), rats (Hafizovic et al., 2007; Heer et al., 2007; Gandolfo et al., 2010; Lambacher et al., 2010; Bakkum et al., 2013; Ballini et al., 2014) and chicken (Hafizovic et al., 2007). Additionally, data from acute slices of the cerebellum (Frey et al., 2009a; Obien et al., 2014), cortex (Ferreia et al., 2012; Medrihan et al., 2014) and olfactory bulb (Johnson et al., 2013a) have been shown. Also cultured cardiomyocytes were studied (DeBusschere and Kovacs, 2001; Heer et al., 2004; Imfeld et al., 2008; Sanchez-Bustamante et al., 2008; Huys

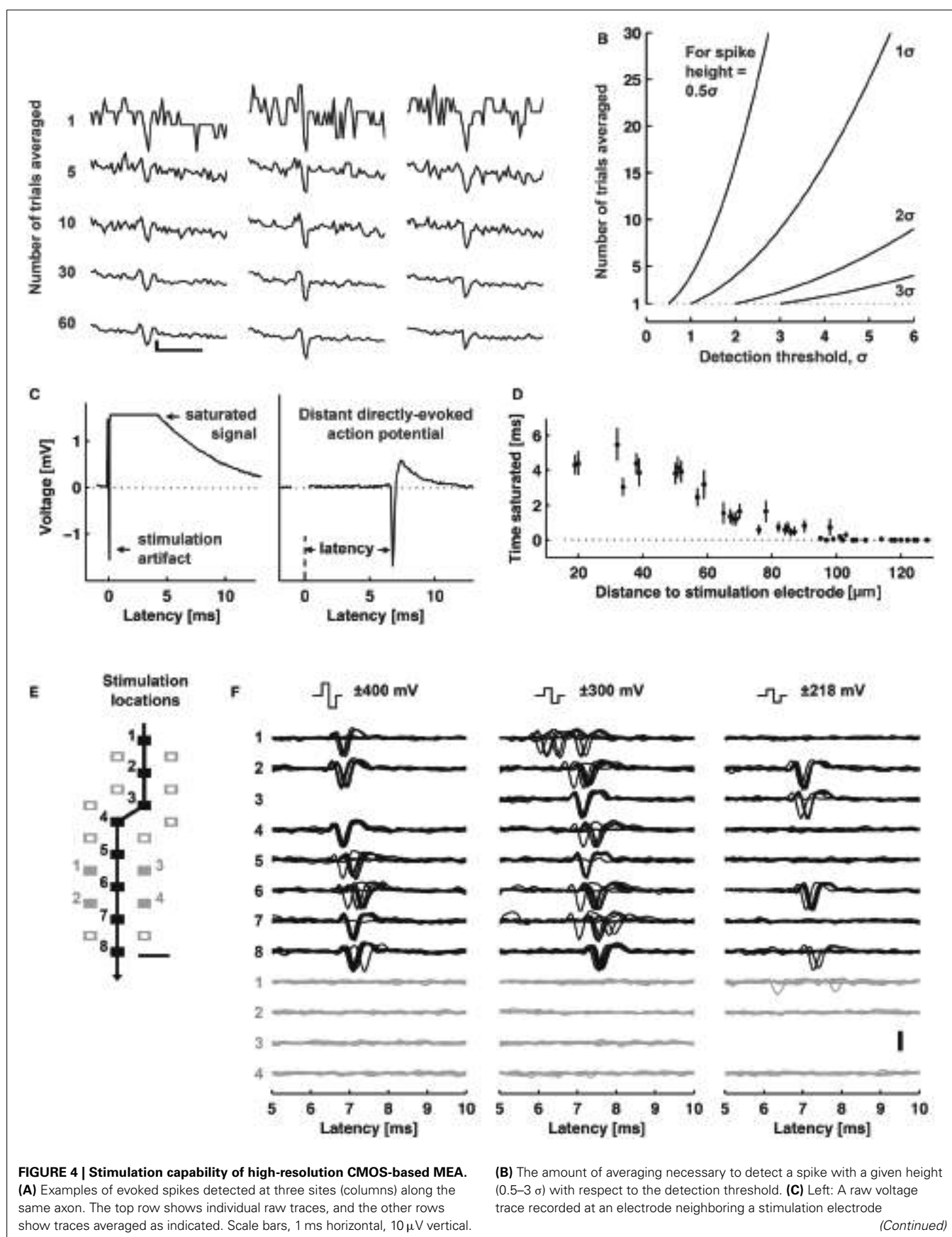


**FIGURE 4 | Continued**

saturated for about 4 ms (flat line). Right: A raw voltage trace recorded at an electrode located 1.46 mm away from a stimulation electrode did not saturate. **(D)** The duration of a saturated signal occurring after stimuli is plotted vs. distance from the stimulation electrode (mean  $\pm$  s.e.m.;  $N = 18$  stimulation electrodes from five CMOS-based MEAs). Stimuli consisted of biphasic voltage pulses between 100 and 200 ms duration per phase and between  $\pm$  400 and 800 mV amplitude. **(E)** Locations of stimulation electrodes that directly evoked (black boxes) or did not evoke

(empty or filled gray boxes) APs detected at a soma located  $\sim$ 890  $\mu$ m away. The line arrow indicates the orthodromic propagation direction. Scale bar, 20  $\mu$ m. **(F)** Voltage traces of somatic APs elicited by biphasic voltage stimuli. Traces in response to eight stimuli are overlaid for each of three stimulation magnitudes (indicated at the top), plotted for all effective (black) and four ineffective stimulation sites (gray at the bottom). Stimulation electrode locations are represented as numbered boxes in **(E)**. Scale bar, 200  $\mu$ V. All panels and description adapted with permission from Bakkum et al. (2013).

et al., 2012) and first results from mice organotypic slices were presented (Gong et al., 2014).

Certainly, *in vitro* CMOS-based MEAs, being still an emerging technology with commercial availability only starting recently, have a high potential for future biomedical research and diagnostics (Jones et al., 2011).

## UNDERSTANDING MEA SIGNALS

Here, we describe the parameters that contribute to neuronal signal transduction from the source into digital form.

### WHAT DO MICROELECTRODES DETECT?

A microelectrode can detect the changes in the extracellular field caused by the current flows from all ionic processes across the morphology of the closest neuron and from other nearby cells, not only neurons (Buzsáki et al., 2012; Anastassiou et al., 2013). The effect of the transmembrane currents on the electric field and the detected potential on a microelectrode depend on the magnitude, sign, and the distance from the recording site (Nunez and Srinivasan, 2006), see Section The extracellular space.

An AP is a biophysical event that occurs once the neuron's transmembrane potential reaches a threshold due to stimuli or other inputs (e.g., synapses, gap junctions). On the other hand, we consider a "spike" to be the signal from a putative AP. For extracellular recordings, spikes are commonly identified as voltage signals that exceed a threshold. During an AP, the initial rapid  $\text{Na}^+$  ion influx creates a sink and results in a large negative spike in the EAP. Thereafter, the slow  $\text{K}^+$  efflux produces a source resulting in a small positive spike. In contrast, IAP first shows a positive spike and later a negative volley. EAPs are usually around tens to hundreds of microvolts in amplitude and <2 ms in duration while IAPs are at tens of millivolts and around the same duration as EAPs (Buzsáki et al., 2012). If IAPs can only be detected by direct access inside the neuron, e.g., patch-clamp, EAPs can be identified when electrodes are placed at the vicinity ( $\sim$ 100  $\mu$ m) of the spike origin (Henze et al., 2000; Egert et al., 2002), usually at the perisomatic area, i.e., around the soma or near the axon initial segment.

Aside from measuring single- and multi-unit spiking activity, electrodes also sample LFPs. The LFP is assessed by the signal content in the low-frequency band of the recorded signal (<300 Hz) (Belitski et al., 2008; Buzsáki et al., 2012), while EAPs are analyzed after filtering the LFP out (300–3000 Hz) (Quijan Quiroga, 2009). Although the contribution of EAPs to LFP is still unclear, a synchrony of APs from many neurons can participate in the generation of LFPs (Buzsáki et al., 2012). The current opinion is that synchronized synaptic currents in cortical neurons produce LFPs,

through the formation of dipoles (Niedermeyer and da Silva, 2005; Nunez and Srinivasan, 2006). We refer the reader to Einevoll et al.'s extensive review on the modeling and analysis of LFPs for further details (Einevoll et al., 2013). The relationship between LFPs and spikes has also been discussed and studied in several works (Khazipov et al., 2004; Belitski et al., 2008; Montemurro et al., 2008; Minlebaev et al., 2011; Kayser et al., 2012; Cingolani, 2014).

### MEA SIGNAL FLOW

We consider the components of the MEA recording and stimulation system diagram as shown in **Figure 6**: (A) the conductive extracellular volume where the electric field caused by neural signal sources forms; (B) the substrate with the embedded microelectrodes; and (C) the hardware connected to the electrodes, including amplifiers, filters, digitizer, data transmission, and stimulator (Stett et al., 2003; Fejtl et al., 2006).

### Noise and SNR

One crucial aspect of the MEA signal flow is how noise is fed into the amplification chain and how it affects the SNR of the recorded data. SNR is the key specification for the amplifier design, regardless of the actual amplification (Jochum et al., 2009). It is important to consider where the noise, or interference, is injected in the signal chain, as the implications on SNR will differ.

- (a) *Biological noise.* This is a major source of noise stems from the electrical activity of other cells around the recording electrode, e.g., APs of distant cells, but also ionic activity, e.g., subthreshold events in neurites of nearby cells, and synaptic noise due to the stochastic nature of synaptic transmission. Several models of biological noise, or sometimes also called background noise, have been developed by simulating uncorrelated single-unit spiking activities or examining multi-compartmental neuron models located at distances far enough away from the electrodes such that the spikes cannot be resolved (Eaton and Henriquez, 2005; Martinez et al., 2009; Lempka et al., 2011; Jäckel et al., 2012; Camuñas-Mesa and Quijan Quiroga, 2013). Although such models replicate the average biological noise in experiments, it is possible that the cell type, size, and morphology, along with the firing rates and correlated activity, can affect the shape of the background signal. For spike analysis, the LFP is also considered biological noise and filtered out.

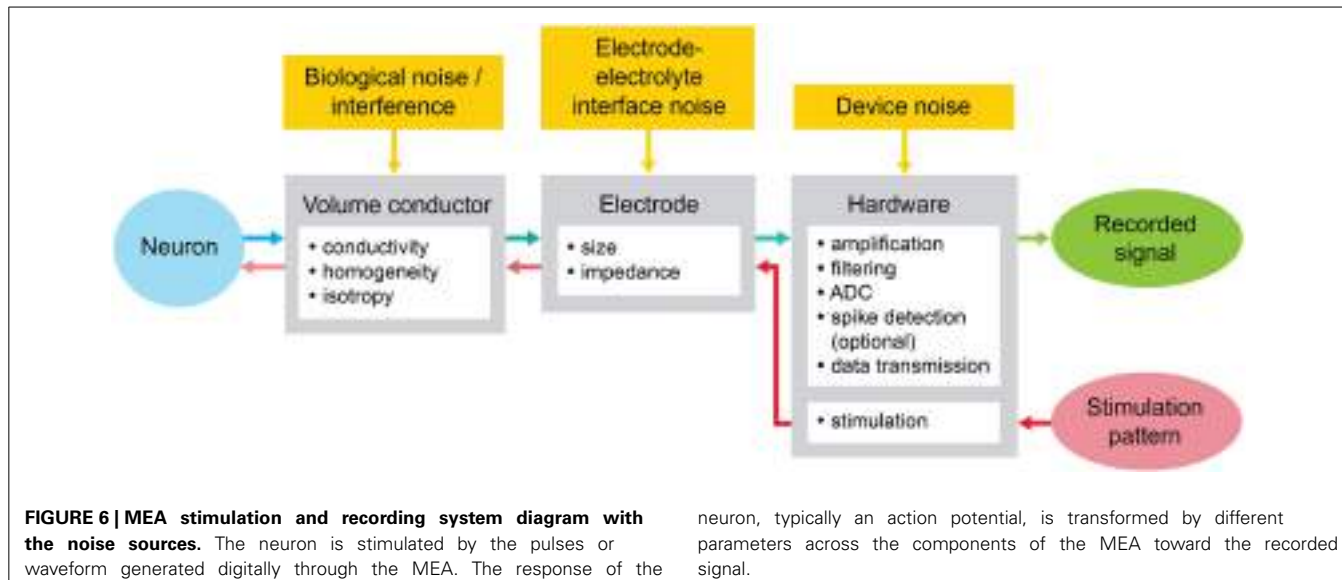
- (b) *Electrode-electrolyte interface noise.* On top of the biological noise, the liquid-metal interface also adds to noise. At low

Ref	Micrograph	Key Specs	Published Recordings	Published Stimulation
Type B (DeBusschere and Kovacs, 2001)		<ul style="list-style-type: none"> <li>Technology: 3µm</li> <li>Chip area: 54mm<sup>2</sup></li> <li>Array area: 1.3mm<sup>2</sup> (2.4%)</li> <li>Rec. sites: 128 (Al/Au)</li> <li>Stim. sites: 0</li> <li>Channels: 8</li> <li>Trans. density: 100mm<sup>-2</sup></li> <li>Power: 7mW</li> </ul>	<ul style="list-style-type: none"> <li>Cultures (Mh): (DeBusschere and Kovacs, 2001)</li> </ul>	
Type E (Eversmann et al., 2003a; Other versions: (Eversmann et al., 2011))		<ul style="list-style-type: none"> <li>Technology: 0.5µm</li> <li>Chip area: 35mm<sup>2</sup></li> <li>Array area: 1.0mm<sup>2</sup> (2.9%)</li> <li>Rec. sites: 16384 (OSFET)</li> <li>Stim. sites: 0</li> <li>Channels: 16384</li> <li>Trans. density: 16384mm<sup>-2</sup></li> <li>Power: 656mW</li> </ul>	<ul style="list-style-type: none"> <li>Acute (Rr, Mr, Lr): (Stutzki et al., 2014; Menzler and Zeck, 2011; Zeck et al., 2011)</li> <li>Cultures (S, Rc): (Eversmann et al., 2003a; Lambacher et al., 2010)</li> </ul>	<ul style="list-style-type: none"> <li>Acute (Lr): (Eickenscheidt et al., 2012)</li> </ul>
Type E (Heer et al., 2006; Other versions: (Heer et al., 2004))		<ul style="list-style-type: none"> <li>Technology: 0.6µm</li> <li>Chip area: 42mm<sup>2</sup></li> <li>Array area: 8.0mm<sup>2</sup> (19%)</li> <li>Rec. sites: 128 (Pt)</li> <li>Stim. sites: 128 (Pt)</li> <li>Channels: 128</li> <li>Trans. density: 16mm<sup>-2</sup></li> <li>Power: 120mW</li> </ul>	<ul style="list-style-type: none"> <li>Cultures (Cch, Rc): (Heer et al., 2004; Hafizovic et al., 2007; Heer et al., 2007)</li> </ul>	<ul style="list-style-type: none"> <li>Cultures (Rc): (Hafizovic et al., 2007)</li> </ul>
Type E (Imfeld et al., 2008; Other versions: (Maccione et al., 2013; Berdondini et al., 2005))		<ul style="list-style-type: none"> <li>Technology: 0.35µm</li> <li>Chip area: 29mm<sup>2</sup></li> <li>Array area: 7.2mm<sup>2</sup> (25%)</li> <li>Rec. sites: 4096</li> <li>Stim. sites: 16 (newer versions)</li> <li>Channels: 4096</li> <li>Trans. density: 567mm<sup>-2</sup></li> <li>Power: 132mW</li> </ul>	<ul style="list-style-type: none"> <li>Acute (Mcr): (Maccione et al., 2014; Medrihan et al., 2014; Ferrea et al., 2012)</li> <li>Cultures (Rch): (Imfeld et al., 2008; Gandolfo et al., 2010)</li> </ul>	<ul style="list-style-type: none"> <li>Cultures (Rc): (Maccione et al., 2013)</li> </ul>
Type D (Frey et al., 2009a)		<ul style="list-style-type: none"> <li>Technology: 0.6µm</li> <li>Chip area: 46mm<sup>2</sup></li> <li>Array area: 3.5mm<sup>2</sup> (7.6%)</li> <li>Rec. sites: 11011 (Pt)</li> <li>Stim. sites: 11011 (Pt)</li> <li>Channels: 126</li> <li>Trans. density: 3150mm<sup>-2</sup></li> <li>Power: 135mW</li> </ul>	<ul style="list-style-type: none"> <li>Acute (Rpr, Lr, Hr, Mpr): (Frey et al., 2009a; Fiscella et al., 2014; Reinhard et al., 2014; Fiscella et al., 2012; Lloyd et al., 2014; Obien et al., 2014)</li> <li>Cultures (Rh, Rc): (Sanchez-Bustamante et al., 2008; Bakkum et al., 2013)</li> <li>Organotypic (Mc): (Gong et al., 2014)</li> </ul>	<ul style="list-style-type: none"> <li>Acute (Rr): (Lloyd et al., 2014)</li> <li>Cultures (Rc): (Bakkum et al., 2013)</li> </ul>
Type C (Huys et al., 2012)		<ul style="list-style-type: none"> <li>Technology: 0.18µm</li> <li>Chip area: 64mm<sup>2</sup></li> <li>Array area: 14.7mm<sup>2</sup> (23%)</li> <li>Rec. sites: 16384 (W)</li> <li>Stim. sites: 16384 (W)</li> <li>Channels: 1</li> <li>Trans. density: 1111mm<sup>-2</sup></li> <li>Power: 35mW</li> </ul>	<ul style="list-style-type: none"> <li>Cultures (Rh): (Huys et al., 2012)</li> </ul>	<ul style="list-style-type: none"> <li>Cultures (Rh): (Huys et al., 2012)</li> </ul>
Type E (Johnson et al., 2013a; Other versions: (Johnson et al., 2013b))		<ul style="list-style-type: none"> <li>Technology: 0.18µm</li> <li>Chip area: 4mm<sup>2</sup></li> <li>Array area: 2.8mm<sup>2</sup> (70%)</li> <li>Rec. sites: 1120 (Al/Pt)</li> <li>Stim. sites: 0</li> <li>Channels: 1120</li> <li>Trans. density: 400mm<sup>-2</sup></li> <li>Power: 14.1mW</li> </ul>	<ul style="list-style-type: none"> <li>Acute (Mo): (Johnson et al., 2013a)</li> </ul>	
Type D (Ballini et al., 2014)		<ul style="list-style-type: none"> <li>Technology: 0.35µm</li> <li>Chip area: 77mm<sup>2</sup></li> <li>Array area: 8.1mm<sup>2</sup> (11%)</li> <li>Rec. sites: 26400 (Pt)</li> <li>Stim. sites: 26400 (Pt)</li> <li>Channels: 1024</li> <li>Trans. density: 3265mm<sup>-2</sup></li> <li>Power: 75mW</li> </ul>	<ul style="list-style-type: none"> <li>Acute (Lr): (Ballini et al., 2014)</li> <li>Cultures (Rc): (Ballini et al., 2014)</li> </ul>	<ul style="list-style-type: none"> <li>Cultures (Rc): (Ballini et al., 2014)</li> </ul>
Type E (Berotti et al., 2014)		<ul style="list-style-type: none"> <li>Technology: 0.18µm</li> <li>Array area: 4.3,1.1mm<sup>2</sup></li> <li>Rec. sites: 4225 (OSFET)</li> <li>Stim. sites: 1024 (CAP)</li> <li>Channels: 4225</li> <li>Trans. density: 977, 3906mm<sup>-2</sup></li> </ul>	<ul style="list-style-type: none"> <li>Acute (Gr): (Velychko et al., 2014)</li> </ul>	<ul style="list-style-type: none"> <li>Acute (Gr): (Velychko et al., 2014)</li> </ul>

M: Mouse, R: Rat, H: Human, L: Rabbit, C: Chicken, G: Guinea pig, S: Snail  
r: Retina, p: Cerebellum, o: Olfactory bulb, c: Cerebral cortex/hippocampus, h: Cardiomyocytes

**FIGURE 5 | CMOS-based *in vitro* MEAs.** CMOS-based *in vitro* MEAs, their key specifications and references to biological applications for recording and stimulation are listed in this table. The application list includes only one

representative citation for each type of preparation. The specification for each device are taken from the reference listed on top and may differ for other versions of the device.



frequencies, such as below 10 Hz, processes at the electrode generate noise with a steep roll-off of  $1/f$  or even  $1/f^2$  (Hassibi et al., 2004; Heer, 2005). More relevant for electrophysiology are the frequencies above that, where thermal noise is the main contributor (Gesteland et al., 1959; Liu et al., 2007). The equivalent thermal noise can be calculated as follows:

$$v_n = \sqrt{4 \cdot k \cdot T \cdot \text{Re}(Z'_e) \cdot \Delta f},$$

where  $k$  is the Boltzmann constant,  $T$  is the absolute temperature,  $\text{Re}(Z'_e)$  is the real part of the effective electrode impedance (see Section Neuron-electrode interface), and  $\Delta f$  is the noise bandwidth. Another source of noise is the 50–60 Hz hum from power lines. This noise is largely picked up between the microelectrode and the connection to the input of the preamplifier, due to its high impedance at that frequency. Hence, minimizing the distance between the electrode and the amplifier is a major design requirement for MEA circuits (Harrison, 2008). Proper grounding and shielding of the MEA setup can minimize interference.

(c) *Device noise.* Finally, the device or the system that amplifies and digitizes the signals further adds to noise. Usually, the front-end amplifier is the most important factor to consider. A general design objective for such amplifiers is to ensure that the signal acquisition system does not limit the system performance with regard to noise. As discussed above, this is a design tradeoff in which also power and circuit area may play a role. For example, if the maximal allowed contribution to noise from the circuitry is set to 10%, the amplifier noise needs to be 45% or less as compared to the noise of the electrode. A commonly used figure of merit that captures the tradeoff between noise and amplifiers' supply current is the noise efficiency factor (NEF) proposed in Steyaert and Sansen (1987). This figure has also been adapted to capture the different supply voltages used to allow a better comparison with respect to power consumption, coined the power

neuron, typically an action potential, is transformed by different parameters across the components of the MEA toward the recorded signal.

efficiency factor or PEF (Muller et al., 2012). For *in vitro* MEAs, area is also of critical importance, as it usually impacts electrode density and total channel count. The efficient use of the overall area is reflected in the ratio of the actual array area divided by the overall chip area (see Figure 5). Quantization noise is another noise contributor of the hardware. It originates from the discretization error made at the ADC part of the MEA system. As an approximation for the quantization noise, typically a value of  $\frac{1}{\sqrt{12}}$  times the magnitude of the least significant bit (LSB) is used. Typical ADCs applied for MEA systems have a minimum of 8-bit resolution, with systems that employ off-chip ADCs often using 16-bit or higher resolution. The transmission of data may also affect the quality of the recorded signal, e.g., if a lossy compression has to be used due to bandwidth constraints.

#### The extracellular space

The analysis of EAPs and LFPs usually assume a homogeneous, resistive extracellular space based on the volume conductor theory, i.e., Kirchhoff's current law or charge conservation and Ohm's law (Nunez and Srinivasan, 2006). The difference in waveforms of a signal recorded at different locations in the tissue is mainly due to how each neuronal source linearly sums up, with source contributions weighted inversely proportional to their distance (Nunez and Srinivasan, 2006). Under the assumption of a purely homogeneous, isotropic, and ohmic extracellular medium, Maxwell's equations of electromagnetism can be rewritten with appropriate Laplace boundary conditions, such that for a single point current source the following equation holds true for the potential at an electrode,  $V_e$  (Klee and Rall, 1977; Nunez and Srinivasan, 2006; Anastassiou et al., 2013):

$$V_e = \frac{I}{4\pi\sigma r},$$

where  $I$  is the point current,  $\sigma$  is the conductivity of the medium, and  $r$  is the distance between the point source and the recording

electrode. Since the membrane currents are distributed over the cable-like morphology of a neuron, a line source approximation (LSA) of current sources was also proposed (Holt, 1997; Gold et al., 2006; Einevoll et al., 2007).

The presence of numerous cell bodies, dendritic structures, axonal bundles, blood vessels, and white matter in brain tissue raises questions as to whether the brain can really be considered as purely ohmic. Moreover, the frequency spectra observed in LFP and EEG (Pritchard, 1992; Freeman et al., 2003; Bédard et al., 2006a; Buzsaki, 2006; Bédard and Destexhe, 2009; Miller et al., 2009; Milstein et al., 2009) led to uncertainties regarding the role of extracellular space in frequency dependent filtering. Pettersen and Einevoll (2008) clarified that in a purely resistive and homogeneous extracellular medium, amplitude variability and low-pass filtering of EAPs occur due to the spatial separation of correlated current sources and sinks during a spike. Similarly, Lindén et al. (2010) found that an intrinsic dendritic low-pass filtering affects the LFP, not the extracellular space. Other interesting studies described how low-pass filtering effects can be achieved in a medium of radially decaying conductivity (exponential) around the source (Bédard et al., 2004, 2006b).

Already in 1968, Robinson (1968) suggested that inhomogeneities, such as the presence of glial cells in brain tissue, can considerably impact the extracellular recording of spiking activity. He also argued that since the resistance of the paths around the glial cells are lower (for signals at 1 kHz) than the paths through them (due to the membranes), the extracellular signals would flow between the cells, not through them. Thus, the structures in the tissue can cause directional differences in the conduction of signals (Rice et al., 1993; Okada et al., 1994). Similar results were achieved by Nelson et al. (2013) across fiber and cell obstructions. Various studies explored different properties of brain tissue conduction, such as anisotropy (Nicholson and Freeman, 1975; Logothetis et al., 2007); anisotropy and inhomogeneity (Ranck, 1963a,b; Hoeltzell and Dykes, 1979; Goto et al., 2010); and capacitive property (Gabriel et al., 1996a,b; Bédard et al., 2004; Bédard and Destexhe, 2009). Whole brain analysis of the electrical tissue properties at the microscale may be useful for modeling and analyzing EAPs and LFPs from different groups of neurons in different brain areas. Using the four-point probes method (Kelvin sensing, with separate pairs of current-carrying and voltage-sensing electrodes) is advisable for measuring the electrical impedance of brain tissue, since it minimizes the influence of the impedance of the current carrying electrodes.

### Neuron-electrode interface

Using an equivalent circuit model, the interface between neurons and microelectrodes *in vivo* has been described and characterized by Robinson (1968). Later, this concept has been adapted for substrate integrated MEA devices, e.g., to compare metal microelectrodes with OGFET devices in simulations (Grattarola and Martinoia, 1993). This representation of the neuron-electrode interface was then coined the *point-contact model* (Weis and Fromherz, 1997) and is shown in Figure 7A. It is a standard model of the electrical characteristics of the interface, which has also been extended to an *area-contact model* (Buitenhewg et al., 2003; Fromherz, 2003) to consider the spatial distributions that

can accurately describe the interface at subcellular resolution. Detailed characterizations of the electrode model for various materials have been carried out, see Section Electrodes and Transducers. Other studies on similar neuron-electrode equivalent circuits were conducted by Ingebrandt et al. (2005), Joye et al. (2008), Thakore et al. (2012). These models assume that a tight seal between the neuron and electrode is needed to measure EAPs from isolated neurons. In the *in vivo* situation, such close contacts usually do not exist and models usually focus less on the electrode properties themselves, but more on the electric field generated by current sources in a conductive volume (Lind et al., 1991; Moffitt and McIntyre, 2005; Gold et al., 2006). For HDMEAs, such volume conductor models match measurements for, e.g., the idealized case of point source in saline (Obien et al., 2013), but also for complex neuronal morphologies in acute brain slices (Frey et al., 2009a). In cell cultures, it has been observed that EAPs are also detected by electrodes that do not have a tight seal with the isolated neuron, even by electrodes that are relatively distant from the neuronal source (Bakkum et al., 2013). Thus, we generalize the neuron-electrode model in Figure 7B, which applies to tissue slices and dissociated cell cultures.

One important assumption for this generalization is that we can treat the MEA surface as an insulator allowing us to separate the neuron-electrode interface problem into two parts: (i) “fluid”-side and (ii) “metal”-side. We are able to do this separation because the high input impedance of MEA amplifiers largely prevents any effect of the metal electrode on the potential at the “fluid”-side of the interface. This is valid, as long as the impedance on the “metal”-side seen by the electrode is much larger as compared to the tissue or fluid impedance at all frequencies of interest. The generalized interface model can then be interpreted such that an electrode detects the average voltage present at the recording site, as claimed by Robinson (1968), Nunez and Srinivasan (2006), Nelson et al. (2008). The detected voltage is then shaped by the electrical characteristics of the interface. It should be noted that the model, as shown here, is adapted for the recording situation, focusing on the understanding of the neuronal signals as recorded by MEAs. Similar models have also been developed and used for the application of electrical stimulation using microelectrodes or capacitive stimulation spots, as discussed in Section Stimulation.

**“Fluid”-side: voltage at the electrode by volume conduction.** For simple geometries of the “fluid”-side, assuming that the MEA surface is an insulating infinite plane and the fluid a homogenous, isotropic medium, we can apply the method of images to the point-source equation given in Section The extracellular space, such that the potential  $V_e$  at any given electrode  $e$  can be solved using the following equation (Obien et al., 2013):

$$V_e = \frac{1}{2\pi\sigma} \sum I_n / r_n$$

$I_n$  represents the  $n^{th}$  point current source and  $r_n$  represents the distance between the point source and the recording electrode, with  $n = 1 \dots N$ , where  $N$  is the number of individual point sources. For electrodes larger than an ideal point electrode,  $V_e$  can be solved at multiple locations of the surface area of

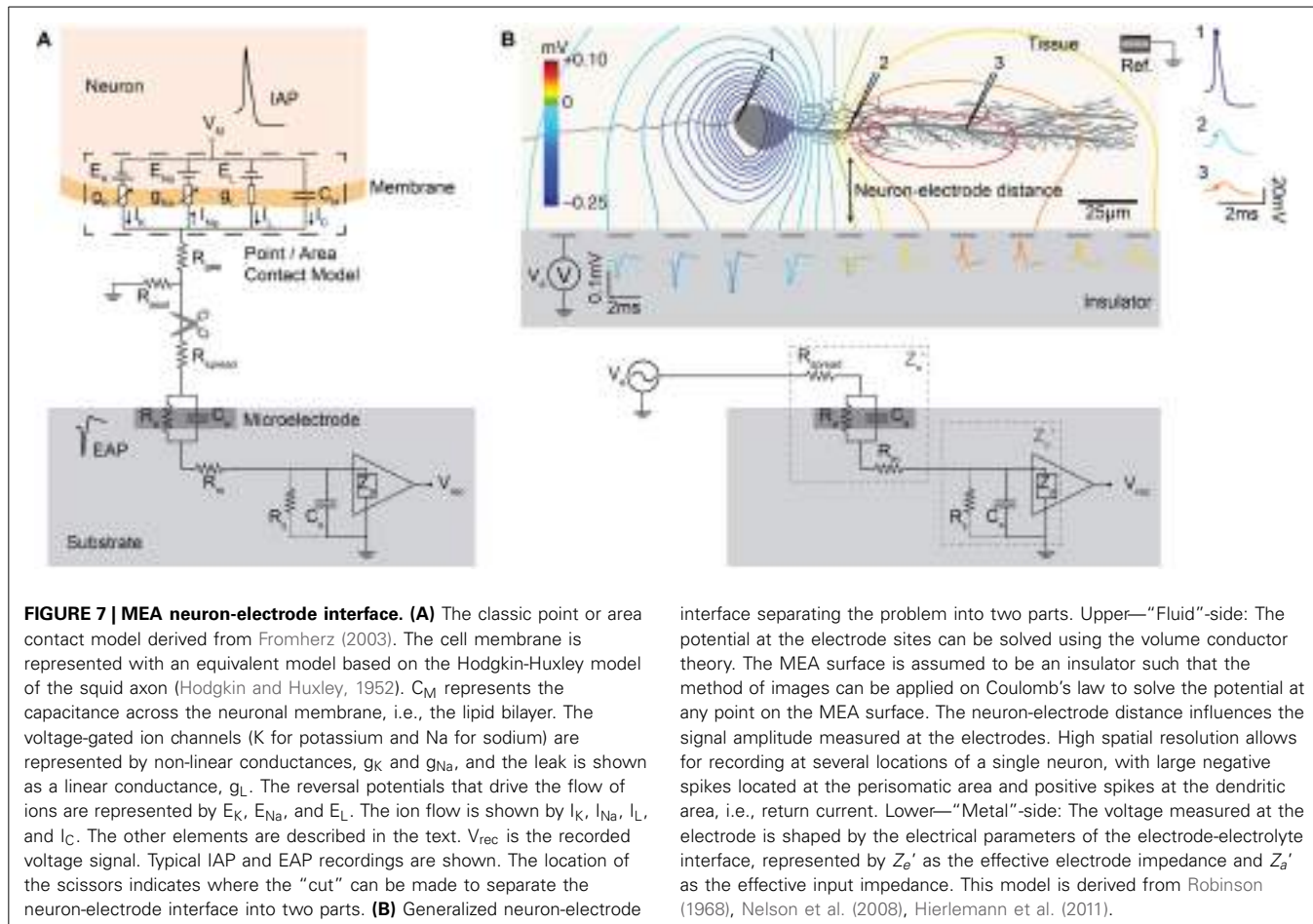


**FIGURE 7 | MEA neuron-electrode interface.** **(A)** The classic point or area contact model derived from Fromherz (2003). The cell membrane is represented with an equivalent model based on the Hodgkin-Huxley model of the squid axon (Hodgkin and Huxley, 1952).  $C_M$  represents the capacitance across the neuronal membrane, i.e., the lipid bilayer. The voltage-gated ion channels ( $K$  for potassium and  $Na$  for sodium) are represented by non-linear conductances,  $g_K$  and  $g_{Na}$ , and the leak is shown as a linear conductance,  $g_L$ . The reversal potentials that drive the flow of ions are represented by  $E_K$ ,  $E_{Na}$ , and  $E_L$ . The ion flow is shown by  $I_K$ ,  $I_{Na}$ ,  $I_L$ , and  $I_C$ . The other elements are described in the text.  $V_{rec}$  is the recorded voltage signal. Typical IAP and EAP recordings are shown. The location of the scissors indicates where the “cut” can be made to separate the neuron-electrode interface into two parts. **(B)** Generalized neuron-electrode

interface separating the problem into two parts. Upper—“Fluid”-side: The potential at the electrode sites can be solved using the volume conductor theory. The MEA surface is assumed to be an insulator such that the method of images can be applied on Coulomb’s law to solve the potential at any point on the MEA surface. The neuron-electrode distance influences the signal amplitude measured at the electrodes. High spatial resolution allows for recording at several locations of a single neuron, with large negative spikes located at the perisomatic area and positive spikes at the dendritic area, i.e., return current. Lower—“Metal”-side: The voltage measured at the electrode is shaped by the electrical parameters of the electrode-electrolyte interface, represented by  $Z'_e$  as the effective electrode impedance and  $Z'_a$  as the effective input impedance. This model is derived from Robinson (1968), Nelson et al. (2008), Hierlemann et al. (2011).

the microelectrode and then averaged. The larger the electrode area, the larger the averaging effect (Grimnes and Martinsen, 2008). Anisotropy can also be incorporated in this model easily (Nicholson and Freeman, 1975). However, more complex geometries of, e.g., the MEA device (such as *in vivo* neural probes) or an inhomogeneous medium generally require a finite element method to solve for the electric field and the potential at the electrode.

The orientation and distance between the neuronal source and the measuring electrode affect the amplitude and shape of the signals detected, as discussed in Section The extracellular space. The spread and decay of the signal over the MEA surface plane is highly correlated with the distance of the signal source from the surface. This makes it possible to estimate the distance between a current source and the MEA electrodes by measuring the voltages at high spatial resolution using an HDMEA (Obien et al., 2013). The same concept can be applied to estimate the neuron-electrode distance given a good model of the membrane currents of the neuron being recorded (Somogyvári et al., 2005, 2012; Frey et al., 2009b; Delgado Ruz and Schultz, 2014).

**“Metal”-side: signal transformation by the electrode-electrolyte interface.** The “metal”-part of the model is an equivalent circuit of the microelectrode modified from Robinson (1968), Franks et al. (2005), Nelson et al. (2008), Hierlemann et al. (2011). In this

model, the input to the circuit is a low impedance voltage source with the value corresponding to the potential resulting from the currents in the volume conductor discussed above. This voltage ( $V_e$ ) is connected to the effective electrode impedance  $Z'_e$ , consisting of  $R_{spread}$ ,  $R_m$ ,  $R_e$ ,  $C_e$ .  $R_{spread}$  is the spreading resistance, which is the resistance a current sees, that spreads from the microelectrode into the electrolyte. Its value is mostly dependent on the electrode geometry and the electrolyte conductivity.  $R_e$  and  $C_e$  are the resistance and capacitance, respectively, of a simplified model of the electric double layer that forms at the electrode-electrolyte interface. This is a reduction of the more complex model, consisting of a constant-phase-angle impedance, a charge-transfer resistance, and a Warburg impedance.  $R_m$  is an additional resistance representing the metallic part of the microelectrode.

The effective amplifier input impedance,  $Z'_a$ , is connected in series to  $Z'_e$ , which includes the actual input impedance of the amplifier  $Z_a$  and the shunting paths to ground outside the amplifier ( $R_s$  and  $C_s$ ). Input amplifiers are designed to have a high  $Z_a$  (above  $10\text{ M}\Omega$  at  $1\text{ kHz}$ ) to limit the influence of  $Z_a$  on the measured voltage (Robinson, 1968). The shunt resistance ( $R_s$ ) is usually negligible, but the shunt capacitance ( $C_s$ ) reduces  $Z'_a$ , especially at higher frequencies (Robinson, 1968; Nelson et al., 2008).  $C_s$  is the combination of all capacitances from connectors and wires from the bath to the amplifier, and the capacitance from metal of the electrode (through the insulation) to the bath

(Robinson, 1968). The ratio of  $Z'_e$  (mostly  $C_e$ ) and  $Z'_a$  is of importance, so if the electrode impedance is low enough, the influence of shunt capacitance to the signal is small (Robinson, 1968; Nelson et al., 2008). HDMEAs require small electrodes to achieve a high resolution, and therefore also the  $C_e$  is usually small. However, monolithic integration allows keeping  $C_s$  small too. For example,  $C_s$  is estimated to be below 0.5 pF for the HDMEA presented in Frey et al. (2010), whereas passive MEA can have a significantly larger parasitic capacitance, depending on the thickness of the insulation and the track width [e.g., James et al. measured values of 60–100 pF (James et al., 2004) and Nisch et al. estimated it to be below 15 pF (Nisch et al., 1994)]. For measurements requiring a high accuracy despite having a device with a large  $C_s$ , capacitance compensation circuits can be used, as those commonly used in patch-clamp amplifiers and, e.g., also used for highly accurate tissue impedance measurements (Logothetis et al., 2007).

### **Effect of electrode size and density**

Sizes of published microelectrodes range from 5 to 50  $\mu\text{m}$  in diameter (Kim et al., 2014). Larger electrodes have a higher possibility of getting physically near the neurons and of picking up higher amplitude spikes (Camuñas-Mesa and Quian Quiroga, 2013), e.g., studies by Moxon (1999), Paik et al. (2003), Ward et al. (2009), Andersen et al. (2010) claim that larger recording electrodes can record from more neurons simultaneously. However, large electrodes ( $>50 \mu\text{m}$  diameter) can average out a neuron's spatially localized peak signal amplitude with nearby smaller amplitude signals. This reduces the peak signals, which can result in a lower SNR. Electrode size also affects the electrode impedance  $Z'_e$ , which in turn determines electrode noise (see Section Noise and SNR). With that, there are three effects for which SNR improves with larger electrodes (reduced electrode noise, reduced attenuation due to large  $Z_e/Z_a$  ratio, and increased chance to “being at the right spot”), and one effect for which SNR gets worse with larger electrodes (increased signal averaging).

As discussed above, for EAP recording in the 300–3000 Hz frequency band, electrode noise is mostly thermal and comparably small, especially if some sort of electrode coating is used and the electrode size is  $>5 \mu\text{m}$  in diameter. Without considering electrode noise, Camuñas-Mesa et al. studied via simulation the optimal electrode size for an *in vivo* situation, considering neuronal background activity. For their simulation parameters, they found 40  $\mu\text{m}$  to be the optimum (Camuñas-Mesa and Quian Quiroga, 2013). For HDMEAs, the situation is a bit different. Most importantly, there is no need to enlarge the electrode to be close to the location with the largest signal, as there will always be another electrode “at the right spot”. Secondly, the effective input capacitance can be significantly smaller as compared to passive devices, due to a small  $C_s$ , which in turn allows for a smaller  $C_e$ . As a result, small electrodes are much more preferable in this situation, with only electrode noise being the limiting factor.

LFP and EAP recordings from neurons located distant to the electrodes feature lower spatial frequencies and therefore allow for larger electrodes without signal degradation than recordings from neurons within close proximity. Especially for LFPs, Nelson and Pouget (2010) discussed that the electrode impedance and

recording site geometry are not crucial. This is because LFPs only vary in a spatial scale much larger than the size of electrodes used for extracellular recordings, e.g., by a few hundred micrometers (Katzner et al., 2009) or even by 1 mm (Destexhe et al., 1999). In addition, LFPs are of lower temporal frequency, making electrode noise a more important factor as in that range, it is dominated by  $1/f^2$  noise, which makes larger electrodes more favorable.

It is therefore important to choose optimal electrode sizes depending on the targeted application. In addition, a high density of electrodes will inherently limit the electrode size.

## **PRACTICAL APPLICATION OF MICROELECTRODE RECORDINGS**

Here, we provide a brief overview on how to extract relevant information from distorted, convoluted, and noisy recorded signals. We then review relevant applications of MEAs for the study of single neurons and networks using various techniques and preparations.

### **MEA SIGNAL PROCESSING AND SPIKE SORTING**

MEA signal processing usually includes (1) filtering the raw data traces, (2) spike detection, and (3) spike sorting.

First, the raw signal is processed to separate the fast APs from LFP and noise by applying a band-pass filter (Quian Quiroga, 2007), with a typical narrow band of 300–3000 Hz. Filtering methods aim to attain higher SNR and lower false positive rates. The filtering process can add phase distortions and therefore alter the shape of the detected EAP. One can avoid such phase distortions by using non-causal filters when future inputs are also used for computation. In hardware implementations and online filters, causal filters are typically used though, as non-causal filters would require the usage of a data buffer (Quian Quiroga, 2009). Depending on the scientific goal, good practice is to record data with wide-band filters (e.g., 1–7000 Hz) and negligible phase distortion, then apply the narrower band filters only for the purpose of the extraction of spike timing information, for which undistorted spike shapes are not needed. One can then still use the spike timing information generated by the spike sorter to re-extract the undistorted spike shapes from the original data.

Once the signal is filtered, the spikes are detected. Amplitude thresholding is commonly used, although other spike detection methods have been implemented, e.g., two-point procedure (Borghi et al., 2007; Maccione et al., 2009) and template-matching (Kim and McNames, 2007). The threshold is usually set as a multiple (5 times) of the baseline noise level, calculated as the root mean square (RMS) of the signals with a mean value of zero. In the presence of many spikes, the threshold can be estimated using a measure based on the median, which is less sensitive to outliers and therefore more robust with regard to spike frequency (Quian Quiroga et al., 2004).

After spike detection, spike shapes are grouped according to their spike shape, which is referred to as spike sorting. Several feature extraction techniques have been used, e.g., principal component analysis or PCA (Quian Quiroga, 2007) and wavelet transform (Mallat, 1989). In the ideal case, distinct neurons will have spikes whose features belong to well-separated clusters, and each neuron will only be part of one cluster. In

practice, spike sorting often requires user supervision in order to manually evaluate the performance of the procedure and correct for errors, e.g., to merge nearby clusters or remove outliers. For a detailed explanation of the spike sorting steps, the reader is referred to other review articles (Lewicki, 1998; Einevoll et al., 2012a). Available spike sorting packages and frameworks include Wave\_Clus (Quian Quiroga et al., 2004), NeuroQuest (Kwon et al., 2012), SigMate (Mahmud et al., 2012), UltraMegaSort (Hill et al., 2011), EToS (Takekawa et al., 2010, 2012), and QSpikes tools (Mahmud et al., 2014), among others. HDMEAs can improve spike sorting performance since with high-resolution spatial information, one can more efficiently separate individual neurons (Gray et al., 1995; Jäckel et al., 2011; Franke et al., 2012).

A number of concerns have been raised regarding the effectiveness of spike sorting. In fact, it is difficult to validate spike sorting algorithms and it is important to test them based on realistic simulated data (Einevoll et al., 2012b). For *in vivo* experiments, or in acute recordings where the electrodes can move with respect to the neurons, drift may occur and alter the recorded signal. Another issue is the amplitude variability of APs from a single neuron that can lead to clustering errors, either intrinsically or due to bursts (McCormick et al., 1985; Henze et al., 2000; Delescluse and Pouzat, 2006; Stratton et al., 2012), such that one cluster may contain the large amplitude spikes and the second one the smaller amplitude ones (Van Dijck et al., 2012).

## USING MEAs FOR NEUROSCIENCE STUDIES

MEA recordings have been employed to understand neuronal communication, information encoding, propagation, and processing in neuronal cultures as well as in brain slices and retina explants (Taketani and Baudry, 2006). Recent works start to take full advantage of the unique abilities of HDMEAs.

### Bursts

Bursts and burst rates of APs in a neuron or across a network of neurons is a common feature extracted from data in MEA applications. Bursts have several meanings and functions in neuroscience, e.g., synchronization, information carrier, and motor pattern generation. Single neurons can exhibit *bursting*, or burst firing, when APs fire at a high frequency for a period of time, followed by a quiet period. Bursts can be triggered by the network activity (environment) or can be intrinsic to the neuron (phenotype of the cell). There are many algorithms to detect the presence of bursts from single neurons (see Samengo et al., 2013; Bakkum et al., 2014 for some methods).

Besides single neuron bursting, population-wide synchronous activities are also of interest. For example, repetition of activation patterns (Abeles and Gerstein, 1988; Sun et al., 2010) can be considered as memory traces, replayed by the appearance of a similar stimulus or due to internal processes that occur, e.g., during sleep (O'Neill et al., 2008; Abel et al., 2013). Bakkum et al. (2014) investigated parameters for and compared the performance of various burst detectors on population-wide bursts. An inter-spike interval (ISI) based network burst detector was able to identify small and large bursts better than other techniques in cultured networks. Rate-based detectors detected larger bursts only, while prematurely identifying the end of bursts. See

Kreuz (2013) for further details and methods on quantifying synchronization.

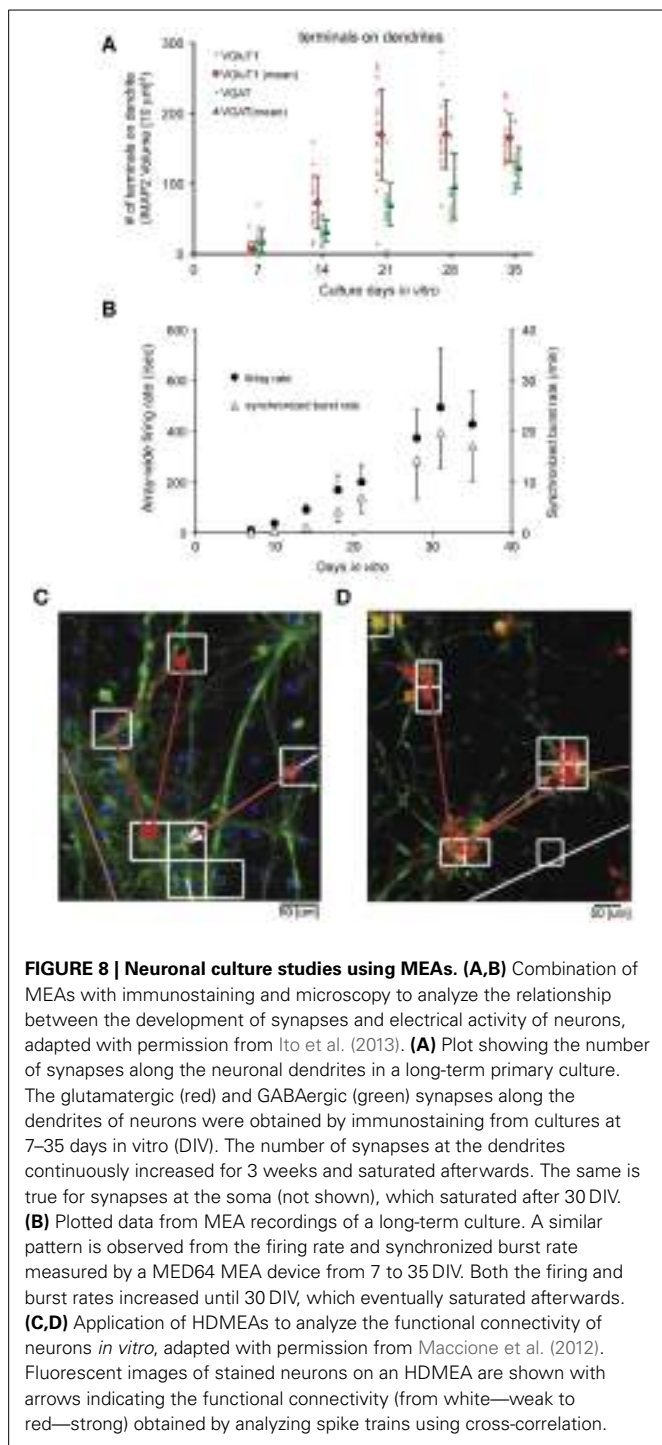
### MEAs and neuronal cultures

Since Pine reported the first MEA recordings from dissociated neuronal cultures in 1980 (Pine, 1980), the method has been expanded for pharmacological tests, diagnostics, and investigation of neuronal growth and connectivity. Combination of immunostaining, fluorescence microscopy, and MEA recording allows the identification of neuronal types and synapses, e.g., GABAergic and glutamatergic, and the analysis of neuronal electrical activity in long-term cultures. Using this technique, Ito et al. (2013) observed a correlation between synapse densities and electrical activity of cultured rat cortical networks (Figures 8A,B). The initial increase in glutamatergic and also GABAergic synapses was accompanied with increasing electric activity, which reached a plateau after 28 days in culture when the synapses reached their final density.

More complex neuronal culture analyses can be done using HDMEAs such as burst pattern tracking (Gandolfo et al., 2010) and functional connectivity estimation (Maccione et al., 2012). By plating low-density cultures, it is feasible to not only optically visualize the network of stained neurons, but also to estimate the functional connections and to obtain detailed functional maps at cellular resolution (Maccione et al., 2012), see Figures 8C,D. Maccione et al. processed and analyzed the HDMEA signals by ad hoc developed spatio-temporal filtering and by applying a cross-correlation based method.

### MEAs and brain slices

A brain slice is a 3D environment of neurons that can be placed on MEAs to monitor electrical activity. Cutting the brain into very thin slices has allowed access to neurons deep in the brain for imaging, i.e., mapping the anatomy. The same method can be used for recording the activity of neurons that are otherwise difficult to reach and identify *in vivo*. This requires a setup to keep the neurons viable, i.e., by perfusion with artificial cerebrospinal fluid (ACSF) with continuous carbogen (95% oxygen and 5% carbon dioxide) gassing. The neurons and network structure in slices are physiologically and biochemically more similar to the *in vivo* situation. It is possible to observe LFPs and oscillations inherent in different states of the brain. Such recordings have been done for different brain areas, e.g., hippocampus, suprachiasmatic nucleus, etc. For instance, MEAs have been employed to investigate the disruption of normal network waves and oscillations in the brain caused by the absence of certain ion channels in neurons. In one particular case, Simeone et al. studied the effect of the delayed rectifier potassium channel  $\alpha$ -subunit Kv1.1 to the oscillations in the hippocampus shown in Figures 9A–C (Simeone et al., 2013). By reducing or eliminating the expression of Kv1.1 in the axons of the hippocampal tri-synaptic pathway, the authors were able to observe an increase in occurrence of fast ripples (80–200 Hz bandwidth, 50% longer duration) and high frequency oscillations associated with epilepsy, as shown in Figure 9C. Similar applications have been done using HDMEAs. Medrihan et al. (2014) showed that the absence of synapsin II (Syn II), a protein related to epilepsy,



decreases tonic inhibition in mouse hippocampal slices, thus increasing synchronized bursts (see Figures 9D,E). THIP (4,5,6,7-tetrahydroisoxazolo[5,4-c]pyridin-3-ol; gaboxadol), a selective agonist of  $\delta$  subunit-containing GABA $A$  receptors, restores tonic inhibition.

Depth recording of EAPs from neurons up to 100  $\mu\text{m}$  distance from the MEA surface was also shown (Egert et al., 2002; Frey et al., 2009b). Subcellular resolution recording from single

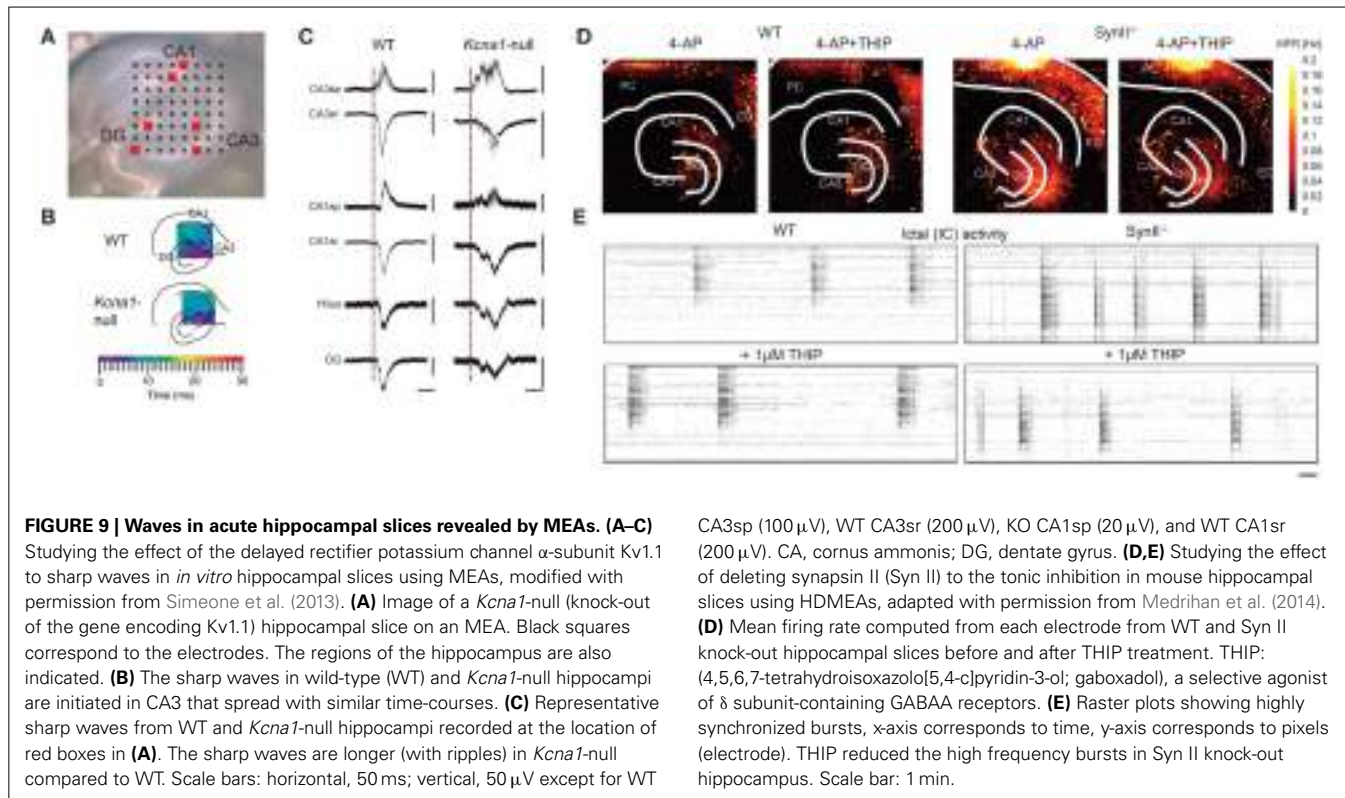
Purkinje cells (PCs) in acute cerebellar slices was demonstrated using HDMEAs (Frey et al., 2009a). One important factor is to ensure tissue adhesion on the MEA surface. Adhesion can be achieved by cellulose nitrate coating (Egert et al., 2002), but also by a slice anchor typically used for patch-clamp recordings. EAPs were observed along the PC layer and, after spike sorting, the EAP footprint of a single PC was analyzed. The negative spikes were recorded around the perisomatic area of the neuron, while positive spikes were obtained along the molecular layer corresponding to the dendrites of the PC. A comparison of the high spatiotemporal resolution recording with simulations of a full-compartmental model based on the stereotypical morphology of a PC was done. **Figure 10** shows both measured and simulated EAP data from PCs at high resolution. Although the planar geometry of PC is advantageous, similar results might be obtained from neurons in other brain areas.

Aside from acute preparations, MEAs have been used to analyze the brain function using organotypic slice cultures. For example, Ito et al. studied the functional connectivity in hippocampal and cortical organotypic cultures (Ito et al., 2014). They analyzed the network activity at different frequency ranges using the wavelet transform of the cross-correlogram.

#### MEAs and retina

The planar arrangement of retinal ganglion cell (RGC) bodies and axons is highly compatible with MEA recordings from retina explants. Responses of RGCs can be recorded using different types of light stimulations (Segev et al., 2004; Wässle, 2004; Jones et al., 2011). This allowed the identification of cell types of populations of RGCs and the mapping of their receptive fields (Meister et al., 1994; Chichilnisky, 2001), in different regions of the retina. Fiscella et al. (2012) established a methodology applied to mice retina that uses light stimulation and HDMEAs to identify, select, and record from defined populations of RGCs. After spike sorting the HDMEA recordings, the EAP footprints of detected RGCs were obtained, as shown in **Figures 11A,B**. Each detected RGC is assigned to one of the four types of ON-OFF direction-selective RGCs, depending on the occurrence of the response to different light stimulation patterns (see **Figures 11C–E**).

Another study on retina (macaque) using HDMEAs revealed the identification of the type, location, and strength of the functional input of each cone photoreceptor to each RGC (Field et al., 2010). Populations of midget, parasol, and small bistratified RGCs were recorded simultaneously in the presence of white noise “visual” stimulation. The spatial receptive field and response time of RGCs were detected by computing the spike-triggered average of the stimuli. Afterwards, the detected clusters of cells obtained by PCA were further stimulated with 10-fold smaller pixels ( $5 \times 5 \mu\text{m}^2$ ) to reveal finer details of the receptive fields. The method was able to map putative cones accumulated across the receptive field of RGCs, which were verified by overlaying a microscopy image of cones labeled with peanut agglutinin (see **Figure 11F**). The authors were able to quantify the strength of connectivity between different RGC types and different types of cones (sensitive to red, green, or blue). These exhibit the capability of HDMEAs, combined with advanced stimulation and analysis techniques, to resolve the functional connectivity of neurons



in the retina at single-cell resolution. There are also other recent works on population coding in the retina using MEA recordings (Marre et al., 2012; Tkačik et al., 2014).

#### MEAs and axonal signal tracking

Taking advantage of the spatiotemporal resolution and high signal quality of HDMEAs, tracking the propagation of APs between cells can be performed. Bakkum et al. (2013) achieved this in dissociated neuronal cultures (see Figures 12A–C). Axonal signals are difficult to identify using conventional methods: thin axons are difficult to patch and extracellular signal amplitudes are rather low compared to those from the soma. A major accomplishment of this work is the capability to electrically image the propagation of APs along axons, across the topology of the whole neuronal network. By using HDMEAs that can record and dynamically stimulate at defined locations, with little artifact to the signals, it was possible to quantify the direction, velocity, and extent of axonal AP propagation. The stimulation and recording techniques are shown in Figures 12B,C. This is a suitable platform to study the role of axons in neuronal computation in the future.

Axonal conduction was also measured by Zeck et al. (2011) from rabbit retina using HDMEAs. The authors were able to measure the velocity of axonal AP caused by stimuli and discovered that similar RGC types respond with the same latency and conduct with similar velocity (see Figure 12D). Except for the area where axons are myelinated, axonal signals were detected from all stimulated RGCs. This work also shows that when axons are very near or flat on the electrode array surface, it is possible

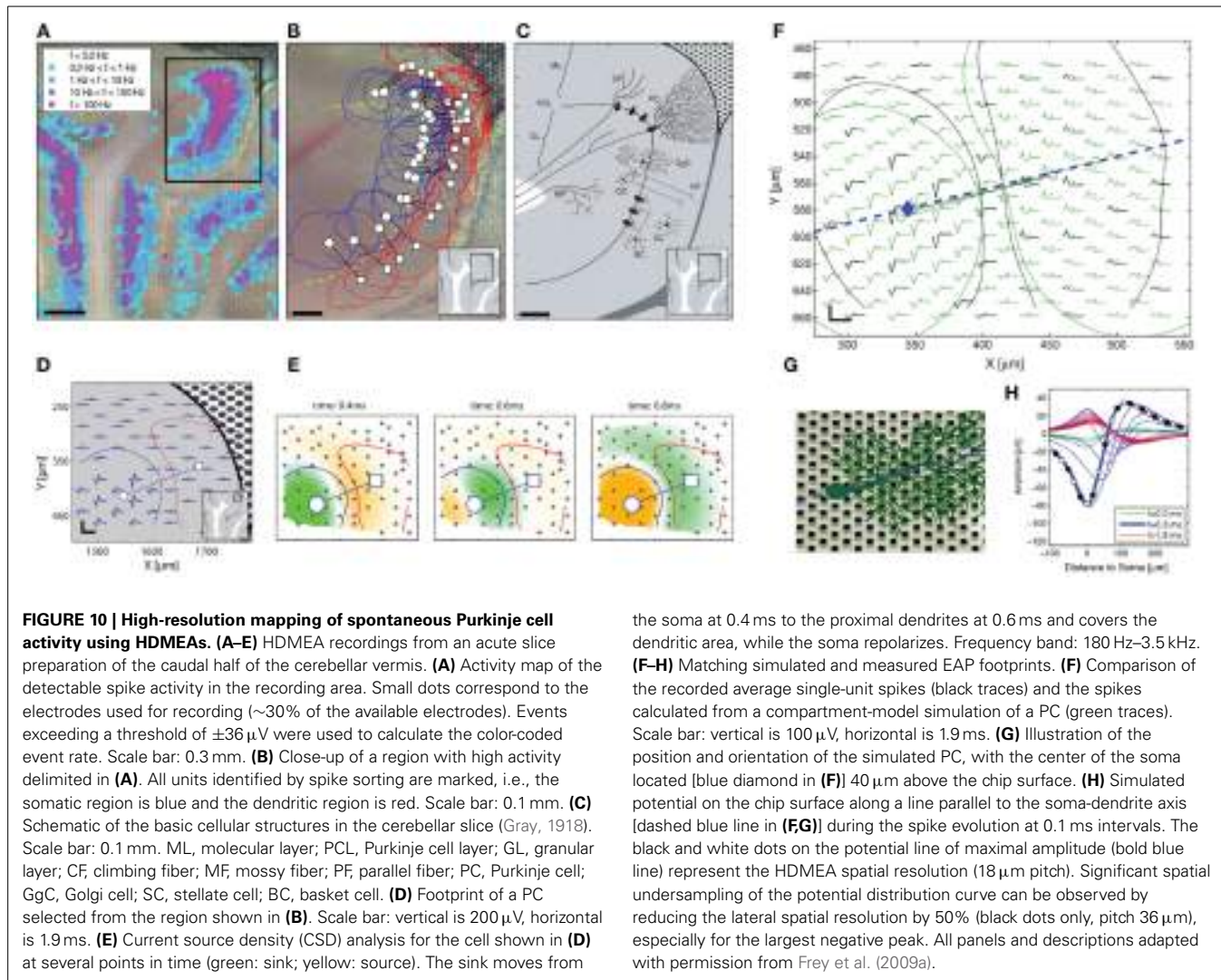
to map the flow of APs. The axons do not necessarily need a tight contact on the electrodes, since the potential due to the APs was also detected from other surrounding electrodes, with lower amplitude compared to the electrode nearest the axon.

#### NEURONAL MODELING AND HDMEA RECORDINGS

Computational modeling is useful to interpret the dynamics and processing of neurons and networks. MEA recordings are commonly analyzed to model neuronal networks (Taketani and Baudry, 2006; Kreuz, 2013; Samengo et al., 2013). Here, we focus on the use of HDMEA data to analyze and model single neurons.

#### Localization of neurons

Neuronal circuits are arranged with high spatial precision and specificity and therefore, spatial information is an important factor in deciphering neuronal activity. Microscopy, fluorescent markers, and transgenic animals have enabled researchers to localize and classify neurons in a high-throughput manner. Together with dynamic multineuron Ca-imaging using spinning-disk confocal microscopy with two-photon excitation, spatial and functional information can be obtained simultaneously. However, the temporal resolution of MEA recordings can capture neuronal responses better than these imaging technologies (Delgado Ruz and Schultz, 2014) and the optical tools described above may not be applicable to all experiments, e.g., due to the unavailability of the transgenic animals, the duration of the experiment, optical access such as in *in vivo* experiments with freely moving animals, etc. Therefore, localization of neurons in



MEA recordings has been of interest for *in vivo* and acute slice *in vitro* experiments too.

Based on the volume conductor theory several current source density (CSD) methods have been proposed to solve for the current sources and sinks from LFP and EAP data (Nicholson and Freeman, 1975; Mitzdorf, 1985; Plenz and Aertsen, 1993; Okada et al., 1994; Pettersen et al., 2010; Łęski et al., 2011). A volume CSD approach for measurements using a 3D MEA has also been done (Riera et al., 2014). These methods approximate the location of the sources prior to solving the CSD and may not be suitable for localizing single neurons. Different methods to localize single neurons depend on the source models used, e.g., monopole source type models such as exponential decay and inverse power law models (Blanche et al., 2005; Chelaru and Jog, 2005; Kubo et al., 2008), dipole models (Blanche et al., 2005; Mechler and Victor, 2012), line source models (Somogyvári et al., 2005, 2012), and simplified line model fitted to the perisomatic area of a full-compartmental neuron model (Delgado Ruz and Schultz, 2014).

Somogyvári et al. (2012) proposed spike CSD (sCSD) to estimate the CSD after optimizing for the best locations of the sources from the recording electrodes that recreates the spike data (see Figure 13A). The method has been used to analyze recordings from a 16-electrode probe *in vivo*. Although sCSD has been used to solve for the CSD at the optimized locations of the sources, it assumes that the number of electrodes is equal to the number of sources to solve for. The over-simplification of the number of current sources in sCSD results in errors, especially when the orientation of the neuron being analyzed is at an angle with respect to the measuring electrodes.

On the other hand, Delgado Ruz and Schultz (2014) introduced a neuronal-based model for localization, utilizing known current distributions and morphological traits. The method was tested in simulations and *in vivo* recordings using high-density probes. The authors showed that different morphologies and ion channel distributions of neurons elicit different localization accuracies (see Figures 13B–D). This method, however, assumes that the experimenter knows the type (morphology and

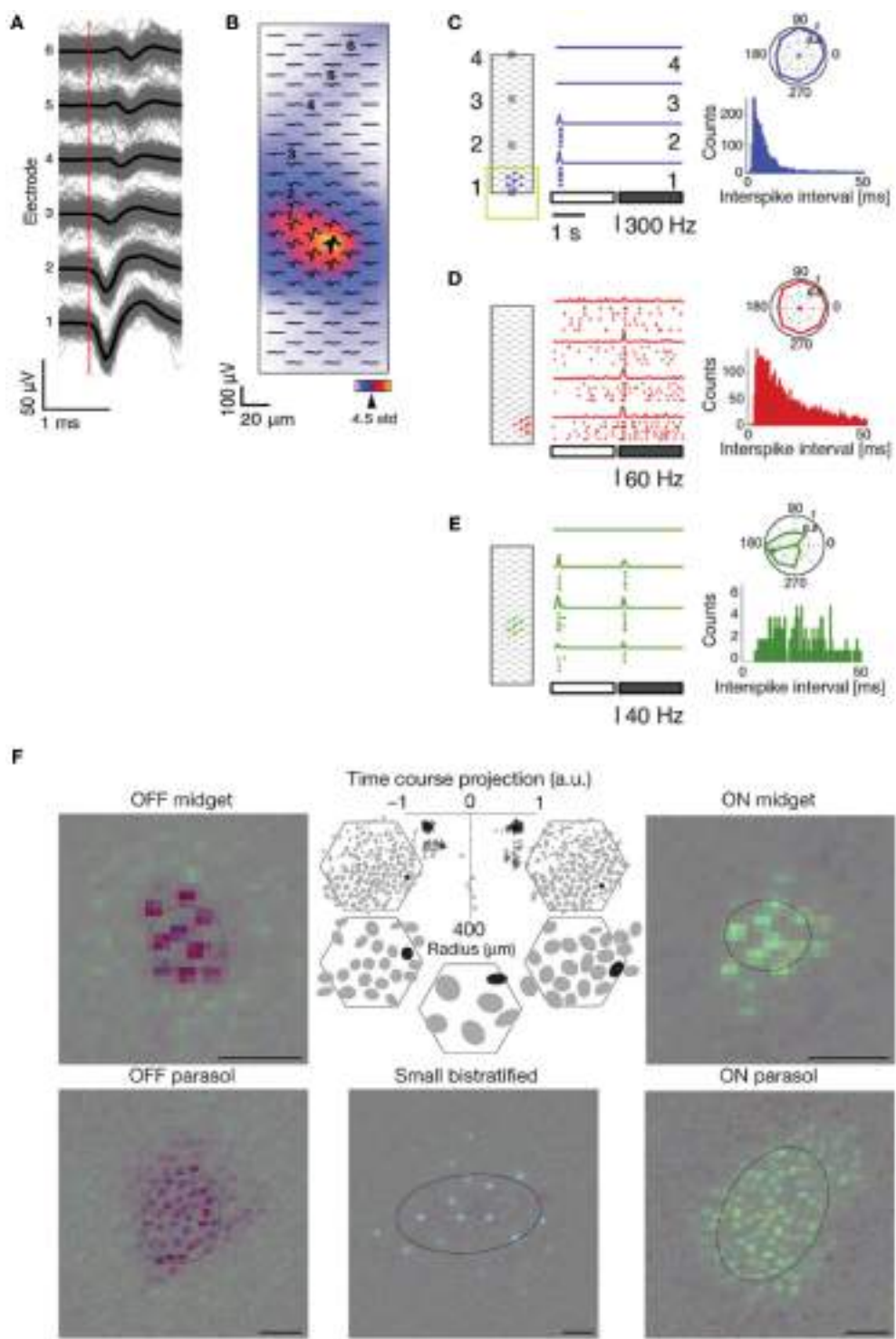


**FIGURE 11 | Identification of retinal ganglion cell receptive fields using HDMEAs.** **(A–E)** Characterization and analysis of HDMEA recordings from defined populations of mouse retinal ganglion cells (RGCs), adapted with permission from Fisicella et al. (2012). **(A)** Each trace shows the average (thick black lines) of the 959 superimposed EAPs (gray lines). The electrode locations are indicated in **(B)**. The propagation speed of the spike was calculated to be 0.7 m/s. **(B)** Footprint of an RGC over an area of 0.025 mm<sup>2</sup>. The highest peak-to-peak amplitude is shown by the thick dark waveform. **(C–E)** Physiological response of RGCs. Left panel: RGC footprint on a

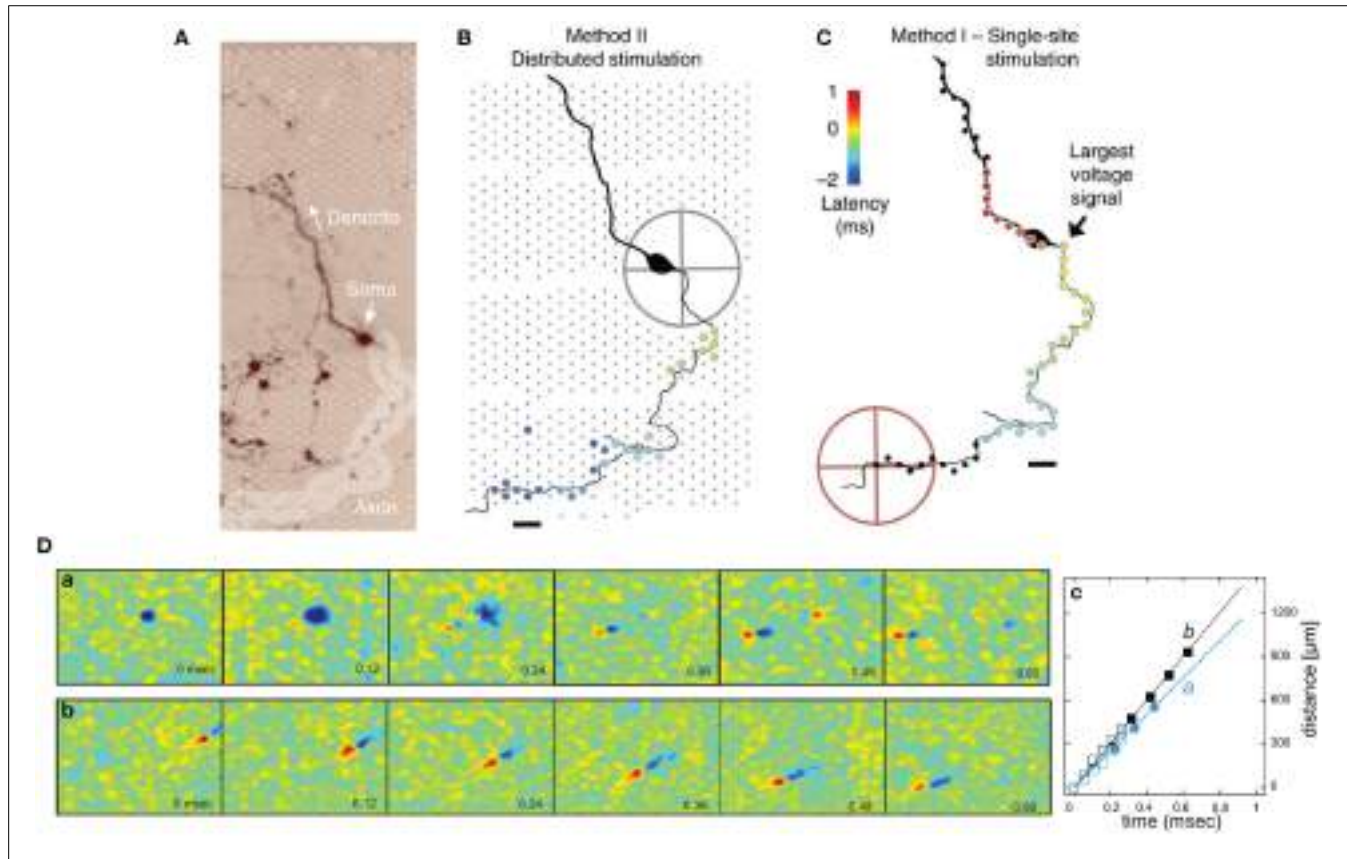
recording block of the HDMEA. The yellow square indicates the location of the light stimulus, with the gray squares indicating the center of the stimulus at four positions. Middle panel: Raster plots corresponding to four stimulation locations indicated in the left panel. Each dot corresponds to a single EAP. Each raster plot shows the response to five repetitions of the same stimulus. The firing rate of the RGC (averaged from five responses) is indicated below. Right panel top: Polar plot showing the responses of the RGC to motion of a bar in 8 directions at 45° radial intervals. Right panel bottom: Inter-spike

(Continued)

**FIGURE 11 | Continued**

interval distribution showing the time intervals between consecutive spikes. (C) Blue = ON RGC. (D) Red = OFF RGC. (E) Green = ON-OFF RGC. (F) Classification of RGC types and receptive fields at single cone resolution, adapted with permission from Field et al. (2010). The RGCs were recorded simultaneously and classified using the

responses to white noise stimuli. Top middle panel: Receptive field radius vs. the first principal component of the response time course. The clusters reveal different RGC types. Surrounding panels: Identified RGC types highlighted at the top middle panel. The RGCs are stimulated with fine-grained white noise to reveal single cone receptive fields. Scale bars: 50  $\mu$ m.

**FIGURE 12 | Imaging axonal signal propagation using HDMEAs. (A–C)**

Axonal propagation of a cultured neuron on an HDMEA, adapted with permission from Bakkum et al. (2013). (A) Live image of a neuron at 21 DIV transfected with red fluorescent protein (RFP). The axon is highlighted. (B) Illustration of the distributed stimulation method. The crosshair represents the location of the “somatic” AP observed while stimulating different electrodes represented by colored dots (color represent the median latency until AP detection, where light gray corresponds to electrodes that did not evoke an AP). The small dots represent the location of the HDMEA electrodes. Scale bar, 40  $\mu$ m. (C) Illustration of the single-site stimulation

method. The red crosshair represents the stimulated electrode. The colored dots represent the latencies of detected APs with respect to the largest voltage signal indicated by the arrow. Scale bar, 40  $\mu$ m. (D) Axonal propagation of an RGC from rabbit retina, adapted with permission from Zeck et al. (2011). Consecutive electrical images of the EAP propagation allow for the calculation of axonal conduction velocity. (a) Image of a somatic AP (blue spot in the first window) propagating along the proximal axon. (b) Image of a biphasic spike recorded from an axon. (c) Plot indicating the distance traveled of the AP in time. Open symbols represent data calculated from recordings at 16.4 kHz; closed symbols are recordings at 8.2 kHz.

current distributions) of neurons being measured for localization and that the dynamics of neurons of the same type are stereotypical.

### Constraining compartmental models

Aside from localization of neurons, it has also been demonstrated that with known morphology, it is possible to estimate the ion channel density from extracellular recordings. Gold et al. (2006, 2007) simulated realistic extracellular signals based on adjusting the ion channel distributions in full-compartmental models (see Figure 14). With such a method, the EAP waveforms

across the neuron’s morphology, measured by multielectrodes, can then be used to constrain compartmental models (Gold et al., 2007). Frey et al. (2009a) used this approach to model a full-compartmental Purkinje neuron using HDMEA recordings, see Figure 10. This shows that using high-density EAP recordings, it is possible to model the ion channel dynamics during neuronal function.

### OUTLOOK

We have shown the current status of MEA research in terms of technology, the understanding of signal transduction, and the

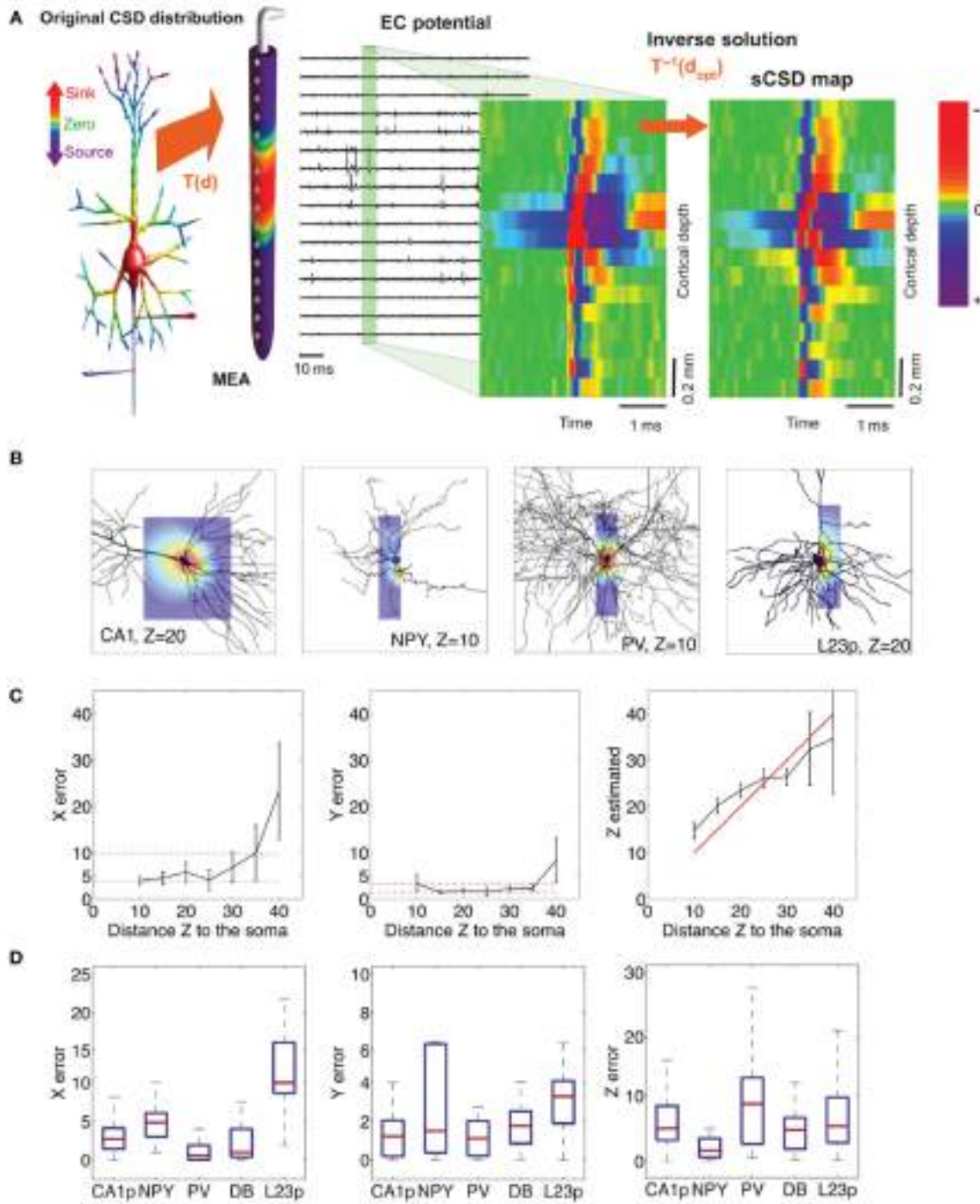


**FIGURE 13 | Localization of single neurons.** (A) Spike current source density (sCSD) method by Somogyvári et al. (2012), figure modified with permission. The experimental setup is shown on the left, where the neuron is oriented at a distance  $d$  parallel to the *in vivo* MEA. The highest amplitude comes from the current sources at the soma of the neuron (sink) and is detected by multiple electrodes. The forward solution at  $d$  is given by the  $T(d)$  matrix, which transforms the CSD on the neuron to the EAP detected by the MEA. The EAPs are shown in the voltage traces per electrode, where one spike is plotted as a color map, indicating the spatial EAP pattern in time. The sCSD obtained from the EAP signals by inverse solution  $T^{-1}(d_{opt})$  is shown on the right. The EAP spatio-temporal map is transformed into a series of

normalized CSD distributions  $||/d||$  with different  $d$ -values. Localization is done by solving for  $d_{opt}$ . The optimum  $d$  ( $d_{opt}$ ) is chosen as the value where  $||/d||$  is the most spike-like, i.e., similar to the normalized amplitude of the EAP during the whole duration of the spike. Thus, the EAP and sCSD color maps are similar. (B–D) Localization of simulated neurons using simplified line model by Delgado Ruz and Schultz (2014), figures adapted with permission. (B) The simulated neurons are CA1 pyramidal, L2/3 pyramidal, double bouquet or DB (not shown), NPY interneurons, and PV interneuron. Localization depends on the location of the sodium trough, which corresponds to the moment when currents are concentrated near the soma.

(Continued)

**FIGURE 13 | Continued**

As shown by the color map embedded on the neuron morphologies, the sodium trough (red) is displaced from the soma for NPY due to the contribution of the dendritic arbor and axon, leading to higher localization error along the Y axis shown in **(D)**. **(C)** Localization results for CA1, where the errors along X-Z axes remained low for

neuron-electrode distances under  $35\text{ }\mu\text{m}$  and increased thereafter, especially along the Z axis. (**D**) The localization errors were not similar for all simulated neurons. The differences in morphology and electrophysiology cause the errors, although the maximum EAP (location of sodium trough) is more or less confined to the perisomatic area.

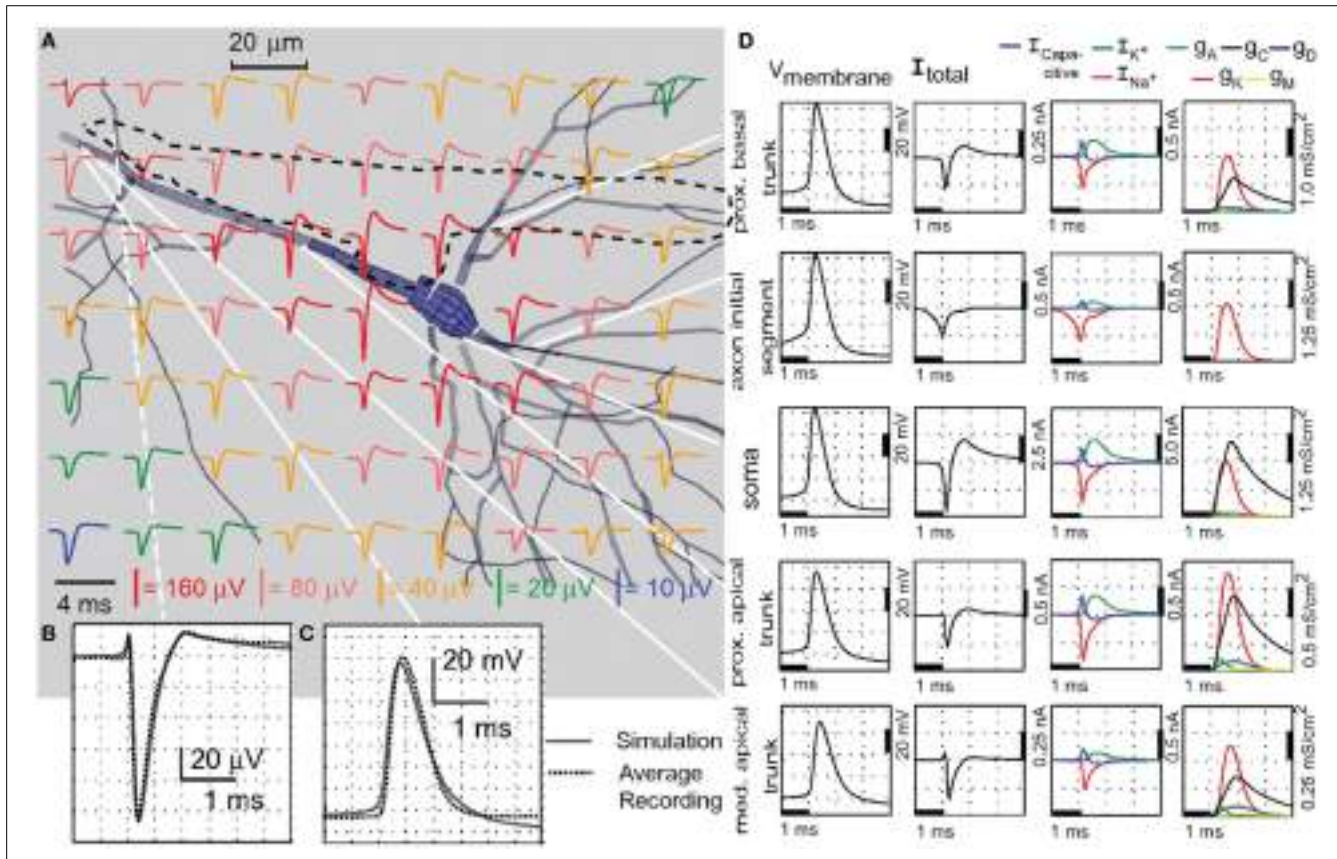


**FIGURE 14 | Ion channel density estimation.** Adapted from Gold et al. (2006). **(A)** The extracellular action potentials (EAPs) solved in a grid from the multicompartmental model of a CA1 pyramidal neuron. The dotted black line indicates the tip of the electrode used to measure the EAPs. **(B)** Enlarged image of the EAP at the electrode tip. Location is indicated by the white dotted line in **(A)**. Solid line in the plot corresponds to the simulated EAP, which is superimposed with the recorded EAP shown as dotted line. **(C)** Comparison of the simulated intracellular signal (solid line) at the proximal apical trunk to the

intracellular recording (dotted line). **(D)** First column: The details of the intracellular signal simulation for each compartment. White solid lines in **(A)** indicate the locations of the compartments. Second column: The simulated membrane currents in the same compartments as the first column. The net membrane current across the soma and proximal dendrites best estimates the EAP waveform. Third column: Membrane current components in terms of  $\text{Na}^+$ ,  $\text{K}^+$ , and mixed-ion capacitive current. Last column: Conductivity densities of the A, C, D, K, and M type  $\text{K}^+$  currents. For further details, see Gold et al. (2006).

application to neuroscience studies. After years of MEA development, what is next? One path is to continuously improve the devices, i.e., better SNR, higher spatial resolution, more parallel readouts, scalability, portability, and increased ease-of-use. Additionally, device flexibility and biocompatibility are targets for long-term *in vivo* recording and stimulation. Another approach is to enhance MEA signal pre-processing for experimenters to easily extract meaningful information from recordings in real time. This is crucial for applications where fast, online analysis is required, e.g., closed-loop experiments and brain machine interfaces (BMIs) combined with stimulation therapies.

A promising route is the combination of MEAs with other modalities. Aside from electrical recording and stimulation, brain activity mapping and manipulation at cellular resolution have also been done using optical methods, e.g., fluorescent calcium indicators, genetic markers, optogenetics, two-photon microscopy, etc. Similar to extracellular recordings, the presence of many molecules and compartments in the brain with different optical properties render optical recording and analysis challenging. It is of interest to pinpoint the advantages and constraints of both electrophysiological and optical methods to determine how they can complement each other. Another example is the use of optogenetics to manipulate the activity of

specific cellular subpopulations. By using MEAs to measure the response of the cortical circuit at multiple locations during optogenetic manipulation, it is possible to study the functional roles of different classes of neurons (El Hady et al., 2013). Simultaneous multi-scale recording of neuronal electrical activity is also of interest, e.g., concurrent ECoG, *in vivo* MEA, and multiple patch-clamp recordings allow for investigating the relationship between oscillations, LFPs, EAPs, IAPs, and subthreshold activity during different brain states. Additionally, other technologies that can enhance MEA experiments are microfluidics for controlled delivery of drugs, chemical sensing to study the biochemistry involved in neuronal function, and measurement of metabolic processes.

The complexity of the data obtained from all the above mentioned advanced measurement schemes necessitates the application of systems biology techniques for analysis (Ghosh et al., 2011). Computational methods such as multi-scale modeling can combine recordings from different modalities at different time and/or spatial scales into a topological model of a system, e.g., cortical circuit. Through multi-scale modeling, the overall neuronal network activity can be understood, while also having the ability to zoom in to single neurons and even in a specific part of a neuron to study the details of the biochemical and electrical reactions involved. Some works have already started in this direction (Mattioni and Le Novère, 2013). There are already available platforms and packages to develop full compartment models of neurons and neuronal networks based on electrical activity, e.g., NEURON (Hines and Carnevale, 1997) and GENESIS (Bower and Beeman, 1998). There are also tools for modeling biochemical processes, e.g., E-CELL3 (Takahashi et al., 2004), STEPS (Wils and De Schutter, 2009; Hepburn et al., 2012), COPASI (Hoops et al., 2006), SBMLOdeSolver (Machné et al., 2006). The main challenge is to efficiently combine the modules by synchronizing the events properly at different time scales, by matching the spatial information into a topology or morphology, and by using optimization methods to computationally handle such massive amounts of data.

## ACKNOWLEDGMENTS

This work was supported by the Japan Society for Promotion of Science (JSPS) under Grants-in-Aid for Young Scientists (B) (No. 25730183) and Swiss National Science Foundation Ambizione Grant PZ00P3\_132245.

## REFERENCES

- Abel, T., Havekes, R., Saletin, J. M., and Walker, M. P. (2013). Sleep, plasticity and memory from molecules to whole-brain networks. *Curr. Biol.* 23, R774–R788. doi: 10.1016/j.cub.2013.07.025
- Abeles, M., and Gerstein, G. L. (1988). Detecting spatiotemporal firing patterns among simultaneously recorded single neurons. *J. Neurophysiol.* 60, 909–24.
- Ahuja, A. K., Dorn, J. D., Caspi, A., McMahon, M. J., Dagnelie, G., Dacruz, L., et al. (2011). Blind subjects implanted with the Argus II retinal prosthesis are able to improve performance in a spatial-motor task. *Br. J. Ophthalmol.* 95, 539–543. doi: 10.1136/bjo.2010.179622
- Anastassiou, C. A., Buzsáki, G., and Koch, C. (2013). “Biophysics of extracellular spikes,” in *Principles of Neural Coding*, eds. R. Quiroga and S. Panzeri (Boca Raton, FL: CRC Press), 15–36. doi: 10.1201/b14756-4
- Andersen, R. A., Hwang, E. J., and Mulliken, G. H. (2010). Cognitive neural prosthetics. *Annu. Rev. Psychol.* 61, 169–90, C1–C3. doi: 10.1146/annurev.psych.093008.100503
- Assad, J. A., Berdondini, L., Cancedda, L., De Angelis, F., Diaspro, A., Dipalo, M., et al. (2014). “Brain function: novel technologies driving novel understanding,” in *Bioinspired Approaches for Human-Centric Technologies*, ed R. Cingolani (Cham: Springer International Publishing), 299–334. doi: 10.1007/978-3-319-04924-3\_10
- Aziz, J. N. Y., Abdelhalim, K., Shulyzki, R., Genov, R., Bardakjian, B. L., Derchansky, M., et al. (2009). 256-Channel neural recording and delta compression microsystem with 3D electrodes. *IEEE J. Solid-State Circuits* 44, 995–1005. doi: 10.1109/JSSC.2008.2010997
- Bai, Q., and Wise, K. D. (2001). Single-unit neural recording with active micro-electrode arrays. *IEEE Trans. Biomed. Eng.* 48, 911–920. doi: 10.1109/10.936367
- Bakkum, D. J., Chao, Z. C., and Potter, S. M. (2008). Long-term activity-dependent plasticity of action potential propagation delay and amplitude in cortical networks. *PLoS ONE* 3:e2088. doi: 10.1371/journal.pone.0002088
- Bakkum, D. J., Frey, U., Radivojevic, M., Russell, T. L., Müller, J., Fiscella, M., et al. (2013). Tracking axonal action potential propagation on a high-density microelectrode array across hundreds of sites. *Nat. Commun.* 4, 2181. doi: 10.1038/ncomms3181
- Bakkum, D. J., Radivojevic, M., Frey, U., Franke, F., Hierlemann, A., and Takahashi, H. (2014). Parameters for burst detection. *Front. Comput. Neurosci.* 7:193. doi: 10.3389/fncom.2013.00193
- Ballini, M., Müller, J., Livi, P., Chen, Y., Frey, U., Stettler, A., et al. (2014). A 1024-Channel CMOS microelectrode array with 26,400 electrodes for recording and stimulation of electrogenic cells *in vitro*. *IEEE J. Solid-State Circuits* 49, 2705–2719. doi: 10.1109/JSSC.2014.2359219
- Baumann, W., Lehmann, M., Schwinde, A., Ehret, R., Brischwein, M., and Wolf, B. (1999). Microelectronic sensor system for microphysiological application on living cells. *Sen. Actuators B. Chem.* 55, 77–89. doi: 10.1016/S0925-4005(99)00116-1
- Bédard, C., and Destexhe, A. (2009). Macroscopic models of local field potentials and the apparent 1/f noise in brain activity. *Biophys. J.* 96, 2589–2603. doi: 10.1016/j.bpj.2008.12.3951
- Bédard, C., Kröger, H., and Destexhe, A. (2004). Modeling extracellular field potentials and the frequency-filtering properties of extracellular space. *Biophys. J.* 86, 1829–1842. doi: 10.1016/S0006-3495(04)74250-2
- Bédard, C., Kröger, H., and Destexhe, A. (2006a). Does the 1/f frequency scaling of brain signals reflect self-organized critical states? *Phys. Rev. Lett.* 97:118102. doi: 10.1103/PhysRevLett.97.118102
- Bédard, C., Kröger, H., and Destexhe, A. (2006b). Model of low-pass filtering of local field potentials in brain tissue. *Phys. Rev. E Stat. Nonlin. Soft Matter Phys.* 73, 51911. doi: 10.1103/PhysRevE.73.051911
- Belitski, A., Gretton, A., Magri, C., Murayama, Y., Montemurro, M. A., Logothetis, N. K., et al. (2008). Low-frequency local field potentials and spikes in primary visual cortex convey independent visual information. *J. Neurosci.* 28, 5696–5709. doi: 10.1523/JNEUROSCI.0009-08.2008
- Berdondini, L., van der Wal, P. D., Guenat, O., de Rooij, N. F., Koudelka-Hep, M., Seitz, P., et al. (2005). High-density electrode array for imaging *in vitro* electrophysiological activity. *Biosens. Bioelectron.* 21, 167–174. doi: 10.1016/j.bios.2004.08.011
- Berdondini, L., Imfeld, K., Maccione, A., Tedesco, M., Neukom, S., Koudelka-Hep, M., et al. (2009). Active pixel sensor array for high spatio-temporal resolution electrophysiological recordings from single cell to large scale neuronal networks. *Lab. Chip.* 9, 2644–2651. doi: 10.1039/b907394a
- Berdondini, L., Overstolz, T., De Rooij, N., Koudelka-Hep, M., Wanly, M., and Seitz, P. (2002). “High-density microelectrode arrays for electrophysiological activity imaging of neuronal networks,” in *Electronics, Circuits and Systems, 2001. ICECS 2001. The 8th IEEE International Conference on* (IEEE), 1239–1242. doi: 10.1109/ICECS.2001.957439
- Berényi, A., Somogyvári, Z., Nagy, A. J., Roux, L., Long, J. D., Fujisawa, S., et al. (2014). Large-scale, high-density (up to 512 channels) recording of local circuits in behaving animals. *J. Neurophysiol.* 111, 1132–1149. doi: 10.1152/jn.00785.2013
- Bergveld, P. (1970). Development of an ion-sensitive solid-state device for electrophysiological measurements. *IEEE Trans. Biomed. Eng.* BME-17, 70–71. doi: 10.1109/TBME.1970.4502688
- Bertotti, G., Velychko, D., Dodel, N., Keil, S., Wolansky, D., Tillak, B., et al. (2014). “A CMOS-based sensor array for *in-vitro* neural tissue interfacing with 4225

- recording sites and 1024 stimulation sites," in *Biomedical Circuits and Systems Conference (BioCAS)* (Lausanne), 1199.
- Besl, B., and Fromherz, P. (2002). Transistor array with an organotypic brain slice: field potential records and synaptic currents. *Eur. J. Neurosci.* 15, 999–1005. doi: 10.1046/j.1460-9568.2002.01943.x
- Blanche, T. J., Spacek, M. A., Hetke, J. F., and Swindale, N. V. (2005). Polytrodes: high-density silicon electrode arrays for large-scale multiunit recording. *J. Neurophysiol.* 93, 2987–3000. doi: 10.1152/jn.01023.2004
- Borghici, T., Gusmeroli, R., Spinelli, A. S., and Baranauskas, G. (2007). A simple method for efficient spike detection in multiunit recordings. *J. Neurosci. Methods* 163, 176–180. doi: 10.1016/j.jneumeth.2007.02.014
- Bower, J. M., and Beeman, D. (1998). *The Book of GENESIS: Exploring Realistic Neural Models with the General Neural Simulation System*. Electronic Library of Science. 2nd edn (New York, NY: Springer-Verlag).
- Brown, E. A., Ross, J. D., Blum, R. A., Nam, Y., Wheeler, B. C., and DeWeerth, S. P. (2008). Stimulus-artifact elimination in a multi-electrode system. *IEEE Trans. Biomed. Circuits Syst.* 2, 10–21. doi: 10.1109/TBCAS.2008.918285
- Buitenhuis, J. R., Rutten, W. L. C., and Marani, E. (2003). Geometry-based finite-element modeling of the electrical contact between a cultured neuron and a microelectrode. *IEEE Trans. Biomed. Eng.* 50, 501–509. doi: 10.1109/TBME.2003.809486
- Buzsáki, G. (2006). *Rhythms of the Brain*. (New York, NY: Oxford University Press). doi: 10.1093/acprof:oso/9780195301069.001.0001
- Buzsáki, G., Anastassiou, C. A., and Koch, C. (2012). The origin of extracellular fields and currents—EEG, ECoG, LFP and spikes. *Nat. Rev. Neurosci.* 13, 407–420. doi: 10.1038/nrn3241
- Camuñas-Mesa, L. A., and Quiroga, R. (2013). A detailed and fast model of extracellular recordings. *Neural Comput.* 25, 1191–1212. doi: 10.1162/NECO\_a\_00433
- Chelaru, M. I., and Jog, M. S. (2005). Spike source localization with tetrodes. *J. Neurosci. Methods* 142, 305–315. doi: 10.1016/j.jneumeth.2004.09.004
- Cheney, P. D., and Fetz, E. E. (1985). Comparable patterns of muscle facilitation evoked by individual corticomotoneuronal (CM) cells and by single intracortical microstimuli in primates: evidence for functional groups of CM cells. *J. Neurophysiol.* 53, 786–804.
- Chichilnisky, E. J. (2001). A simple white noise analysis of neuronal light responses. *Netw. Comput. Neural Syst.* 12, 199–213. doi: 10.1080/713663221
- Cingolani, R. (2014). *Bioinspired Approaches for Human-Centric Technologies* (Cham: Springer International Publishing). doi: 10.1007/978-3-319-04924-3
- Cogan, S. F. (2008). Neural stimulation and recording electrodes. *Annu. Rev. Biomed. Eng.* 10, 275–309. doi: 10.1146/annurev.bioeng.10.061807.160518
- Contreras, D. (2004). Electrophysiological classes of neocortical neurons. *Neural Netw.* 17, 633–646. doi: 10.1016/j.neunet.2004.04.003
- Csicsvari, J., Henze, D. A., Jamieson, B., Harris, K. D., Sirota, A., Barthó, P., et al. (2003). Massively parallel recording of unit and local field potentials with silicon-based electrodes. *J. Neurophysiol.* 90, 1314–1323. doi: 10.1152/jn.00116.2003
- Cui, X., Lee, V. A., Raphael, Y., Wiler, J. A., Hetke, J. F., Anderson, D. J., et al. (2001). Surface modification of neural recording electrodes with conducting polymer/biomolecule blends. *J. Biomed. Mater. Res.* 56, 261–72.
- DeBusschere, B. D., and Kovacs, G. T. (2001). Portable cell-based biosensor system using integrated CMOS cell-cartridges. *Biosens. Bioelectron.* 16, 543–56. doi: 10.1016/S0956-5663(01)00168-3
- Delescluse, M., and Pouzat, C. (2006). Efficient spike-sorting of multi-state neurons using inter-spike intervals information. *J. Neurosci. Methods* 150, 16–29. doi: 10.1016/j.jneumeth.2005.05.023
- Delgado Ruz, I., and Schultz, S. R. (2014). Localising and classifying neurons from high density MEA recordings. *J. Neurosci. Methods* 233C, 115–128. doi: 10.1016/j.jneumeth.2014.05.037
- Destexhe, A., Contreras, D., and Steriade, M. (1999). Spatiotemporal analysis of local field potentials and unit discharges in cat cerebral cortex during natural wake and sleep states. *J. Neurosci.* 19, 4595–608.
- Du, J., Blanche, T. J., Harrison, R. R., Lester, H. A., and Masmanidis, S. C. (2011). Multiplexed, high density electrophysiology with nanofabricated neural probes. *PLoS ONE* 6:e26204. doi: 10.1371/journal.pone.0026204
- Dunlop, J., Bowlby, M., Peri, R., Vasilev, D., and Arias, R. (2008). High-throughput electrophysiology: an emerging paradigm for ion-channel screening and physiology. *Nat. Rev. Drug Discov.* 7, 358–368. doi: 10.1038/nrd2552
- Eaton, K. P., and Henriquez, C. S. (2005). Confounded spikes generated by synchrony within neural tissue models. *Neurocomputing* 65–66, 851–857. doi: 10.1016/j.neucom.2004.10.082
- Egert, U., Heck, D., and Aertsen, A. (2002). Two-dimensional monitoring of spiking networks in acute brain slices. *Exp. Brain Res.* 142, 268–274. doi: 10.1007/s00221-001-0932-5
- Eickenscheidt, M., Jenkner, M., Thewes, R., Fromherz, P., and Zeck, G. (2012). Electrical stimulation of retinal neurons in epiretinal and subretinal configuration using a multicapacitor array. *J. Neurophysiol.* 107, 2742–2755. doi: 10.1152/jn.00909.2011
- Einevoll, G. T., Franke, F., Hagen, E., Pouzat, C., and Harris, K. D. (2012a). Towards reliable spike-train recordings from thousands of neurons with multielectrodes. *Curr. Opin. Neurobiol.* 22, 11–17. doi: 10.1016/j.conb.2011.10.001
- Einevoll, G. T., Franke, F., Hagen, E., Pouzat, C., and Harris, K. D. (2012b). Towards reliable spike-train recordings from thousands of neurons with multielectrodes. *Curr. Opin. Neurobiol.* 22, 11–17. doi: 10.1016/j.conb.2011.10.001
- Einevoll, G. T., Kayser, C., Logothetis, N. K., and Panzeri, S. (2013). Modelling and analysis of local field potentials for studying the function of cortical circuits. *Nat. Rev. Neurosci.* 14, 770–785. doi: 10.1038/nrn3599
- Einevoll, G. T., Pettersen, K. H., Devor, A., Ulbert, I., Halgren, E., and Dale, A. M. (2007). Laminar population analysis: estimating firing rates and evoked synaptic activity from multielectrode recordings in rat barrel cortex. *J. Neurophysiol.* 97, 2174–2190. doi: 10.1152/jn.00845.2006
- El Hadj, A., Afshar, G., Bröking, K., Schlüter, O. M., Geisel, T., Stühmer, W., et al. (2013). Optogenetic stimulation effectively enhances intrinsically generated network synchrony. *Front. Neural Circuits* 7:167. doi: 10.3389/fncir.2013.00167
- Eversmann, B., Jenkner, M., Hofmann, F., Paulus, C., Brederlow, R., Holzapfl, B., et al. (2003a). A 128 × 128 cmos biosensor array for extracellular recording of neural activity. *IEEE J. Solid-State Circuits* 38, 2306–2317. doi: 10.1109/JSSC.2003.819174
- Eversmann, B., Jenkner, M., Paulus, C., Hofmann, F., Brederlow, R., Holzapfl, B., et al. (2003b). "A 128 × 128 CMOS bio-sensor array for extracellular recording of neural activity," in *2003 IEEE International Solid-State Circuits Conference, 2003. Digest of Technical Papers. ISSCC* (San Francisco, CA: IEEE), 222–489.
- Eversmann, B., Lambacher, A., Gerling, T., Kunze, A., Fromherz, P., and Thewes, R. (2011). A neural tissue interfacing chip for *in-vitro* applications with 32k recording/stimulation channels on an active area of 2.6 mm<sup>2</sup>. *2011 Proceedings ESSCIRC* (Helsinki), 211–214.
- Fejtí, M., Stett, A., Nisch, W., Boven, K., and Möller, A. (2006). "On micro-electrode array revival: its development, sophistication of recording, and stimulation," in *Advances in Network*, eds M. Taketani and M. Baudry (New York, NY: Springer), 24–37. doi: 10.1007/0-387-25858-2\_2
- Ferreira, E., Maccione, A., Medrihan, L., Nieus, T., Ghezzi, D., Baldelli, P., et al. (2012). Large-scale, high-resolution electrophysiological imaging of field potentials in brain slices with microelectronic multielectrode arrays. *Front. Neural Circuits* 6:80. doi: 10.3389/fncir.2012.00080
- Field, G. D., Gauthier, J. L., Sher, A., Greschner, M., Machado, T. A., Jepson, L. H., et al. (2010). Functional connectivity in the retina at the resolution of photoreceptors. *Nature* 467, 673–677. doi: 10.1038/nature09424
- Fiscella, M., Farrow, K., Jones, I. L., Jäckel, D., Müller, J., Frey, U., et al. (2012). Recording from defined populations of retinal ganglion cells using a high-density CMOS-integrated microelectrode array with real-time switchable electrode selection. *J. Neurosci. Methods* 211, 103–113. doi: 10.1016/j.jneumeth.2012.08.017
- Fiscella, M., Franke, F., Müller, J., Jones, I. L., and Hierlemann, A. (2014). "Decoding of motion directions by direction-selective retina cells," in *Proceedings of the 9th International Meeting on Substrate-Integrated Microelectrode Arrays* (Reutlingen), 98–99.
- Franke, F., Jäckel, D., Dragas, J., Müller, J., Radivojevic, M., Bakum, D., et al. (2012). High-density microelectrode array recordings and real-time spike sorting for closed-loop experiments: an emerging technology to study neural plasticity. *Front. Neural Circuits* 6:105. doi: 10.3389/fncir.2012.00105
- Franks, W., Heer, F., McKay, I., Taschini, S., Sunier, R., Hagleitner, C., et al. (2003). "CMOS monolithic microelectrode array for stimulation and recording of natural neural networks" in *TRANSDUCERS'03. 12th International Conference on Solid-State Sensors, Actuators and Microsystems. Digest of Technical Papers* (Cat. No.03TH8664) (Boston, MA: IEEE), 963–966. doi: 10.1109/SENSOR.2003.1216927

- Franks, W., Schenker, I., Schmutz, P., and Hierlemann, A. (2005). Impedance characterization and modeling of electrodes for biomedical applications. *Biomed. Eng. IEEE Trans.* 52, 1295–1302. doi: 10.1109/TBME.2005.847523
- Freeman, W. J., Holmes, M. D., Burke, B. C., and Vanhatalo, S. (2003). Spatial spectra of scalp EEG and EMG from awake humans. *Clin. Neurophysiol.* 114, 1053–1068. doi: 10.1016/S1388-2457(03)00045-2
- Frey, U., Egert, U., Heer, F., Hafizovic, S., and Hierlemann, A. (2009a). Microelectronic system for high-resolution mapping of extracellular electric fields applied to brain slices. *Biosens. Bioelectron.* 24, 2191–2198. doi: 10.1016/j.bios.2008.11.028
- Frey, U., Egert, U., Jackel, D., Sedivy, J., Ballini, M., Livi, P., et al. (2009b). “Depth recording capabilities of planar high-density microelectrode arrays,” in 2009 4th International IEEE/EMBS Conference on Neural Engineering (Antalya: IEEE), 207–210.
- Frey, U., Sedivy, J., Heer, F., Pedron, R., Ballini, M., Mueller, J., et al. (2010). Switch-matrix-based high-density microelectrode array in CMOS technology. *Solid-State Circuits IEEE J.* 45, 467–482. doi: 10.1109/JSSC.2009.2035196
- Fromherz, P. (2003). “Neuroelectronic interfacing: semiconductor chips with ion channels, nerve cells, and brain,” *Nanoelectronics and Information Technology*, ed R. Waser (Weinheim: Wiley-VCH Verlag), 783–810.
- Fromherz, P., Offenhausser, A., Vetter, T., and Weis, J. (1991). A neuron-silicon junction: a Retzius cell of the leech on an insulated-gate field-effect transistor. *Science* 252, 1290–1293. doi: 10.1126/science.1925540
- Fujisawa, S., Amarasingham, A., Harrison, M. T., and Buzsáki, G. (2008). Behavior-dependent short-term assembly dynamics in the medial prefrontal cortex. *Nat. Neurosci.* 11, 823–833. doi: 10.1038/nn.2134
- Gabriel, S., Lau, R. W., and Gabriel, C. (1996a). The dielectric properties of biological tissues: II. Measurements in the frequency range 10 Hz to 20 GHz. *Phys. Med. Biol.* 41, 2251–2269. doi: 10.1088/0031-9155/41/11/002
- Gabriel, S., Lau, R. W., and Gabriel, C. (1996b). The dielectric properties of biological tissues: III. Parametric models for the dielectric spectrum of tissues. *Phys. Med. Biol.* 41, 2271–2293. doi: 10.1088/0031-9155/41/11/003
- Galvani, L. (1791). *Commentary on the Effects of Electricity on Muscular Motion* (transl. by MG Foley). Norwalk, CT: Burndy Library, 1954. *Viribus Electr. Motu Musculari Comment.*
- Gandolfo, M., Maccione, A., Tedesco, M., Martinioia, S., and Berdoncini, L. (2010). Tracking burst patterns in hippocampal cultures with high-density CMOS-MEAs. *J. Neural Eng.* 7, 056001. doi: 10.1088/1741-2560/7/5/056001
- Gesteland, R., Howland, B., Lettvin, J., and Pitts, W. (1959). Comments on microelectrodes. *Proc. IRE* 47, 1856–1862. doi: 10.1109/JRPROC.1959.287156
- Ghosh, S., Matsuoaka, Y., Asai, Y., Hsin, K.-Y., and Kitano, H. (2011). Software for systems biology: from tools to integrated platforms. *Nat. Rev. Genet.* 12, 821–832. doi: 10.1038/nrg3096
- Gold, C., Henze, D. A., and Koch, C. (2007). Using extracellular action potential recordings to constrain compartmental models. *J. Comput. Neurosci.* 23, 39–58. doi: 10.1007/s10827-006-0018-2
- Gold, C., Henze, D. A., Koch, C., Buzsáki, G., Carl, G., Darrell, A. H., et al. (2006). On the origin of the extracellular action potential waveform: a modeling study. *J. Neurophysiol.* 95, 3113–3128. doi: 10.1152/jn.00979.2005
- Gong, W., Jäckel, D., Müller, J., Fiscella, M., Radivojevic, M., Franke, F., et al. (2014). “Long-term cultivation and recording from organo-typic brain slices on high-density micro-electrode arrays,” in *Proceedings of the 9th International Meeting on Substrate-Integrated Microelectrode Arrays* (Reutlingen), 335–336.
- Gosselin, B. (2011). Recent advances in neural recording microsystems. *Sensors* 11, 4572–4597. doi: 10.3390/s110504572
- Goto, T., Hatanaka, R., Ogawa, T., Sumiyoshi, A., Riera, J., and Kawashima, R. (2010). An evaluation of the conductivity profile in the somatosensory barrel cortex of Wistar rats. *J. Neurophysiol.* 104, 3388–3412. doi: 10.1152/jn.00122.2010
- Grattarola, M., and Martinioia, S. (1993). Modeling the neuron-microtransducer junction: from extracellular to patch recording. *IEEE Trans. Biomed. Eng.* 40, 35–41. doi: 10.1109/10.204769
- Gray, H. (1918). *Anatomy of the Human Body*, ed W. H. Lewis (New York, NY: Lea & Febiger).
- Gray, C. M., Maldonado, P. E., Wilson, M., and McNaughton, B. (1995). Tetrodes markedly improve the reliability and yield of multiple single-unit isolation from multi-unit recordings in cat striate cortex. *J. Neurosci. Methods* 63, 43–54. doi: 10.1016/0165-0270(95)00085-2
- Greschner, M., Field, G. D., Li, P. H., Schiff, M. L., Gauthier, J. L., Ahn, D., et al. (2014). A polyaxonal amacrine cell population in the primate retina. *J. Neurosci.* 34, 3597–3606. doi: 10.1523/JNEUROSCI.3359-13.2014
- Greve, F., Lichtenberg, J., Kirstein, K.-U. U., Frey, U., Perriard, J.-C., and Hierlemann, A. (2007). A perforated CMOS microchip for immobilization and activity monitoring of electrogenic cells. *J. Micromech. Microeng.* 17, 462–471. doi: 10.1088/0960-1317/17/3/007
- Grimnes, S., and Martinsen, Ø. G. (2008). “Geometrical analysis,” in *Bioimpedance and Bioelectricity Basics* (Oxford, UK: Academic Press), 161–204. doi: 10.1016/B978-0-12-374004-5.00006-4
- Gross, G., Rieske, E., Kreutzberg, G., and Meyer, A. (1977). A new fixed-array multi-microelectrode system designed for long-term monitoring of extracellular single unit neuronal activity *in vitro*. *Neurosci. Lett.* 6, 101–105. doi: 10.1016/0304-3991(77)90003-9
- Hafizovic, S., Heer, F., Ugnivenko, T., Frey, U., Blau, A., Ziegler, C., et al. (2007). A CMOS-based microelectrode array for interaction with neuronal cultures. *J. Neurosci. Methods* 164, 93–106. doi: 10.1016/j.jneumeth.2007.04.006
- Hai, A., Dormann, A., Shappir, J., Yitzchaik, S., Bartic, C., Borghs, G., et al. (2009). Spine-shaped gold protrusions improve the adherence and electrical coupling of neurons with the surface of micro-electronic devices. *J. R. Soc. Interface* 6, 1153–1165. doi: 10.1098/rsif.2009.0087
- Hai, A., and Spira, M. E. (2012). On-chip electroporation, membrane repair dynamics and transient in-cell recordings by arrays of gold mushroom-shaped microelectrodes. *Lab. Chip.* 12, 2865–2873. doi: 10.1039/c2lc40091j
- Harris, K. D., Henze, D. A., Csicsvari, J., Hirase, H., and Buzsaki, G. (2000). Accuracy of tetrode spike separation as determined by simultaneous intracellular and extracellular measurements. *J. Neurophysiol.* 84, 401–414. Available online at: <http://www.ncbi.nlm.nih.gov/pubmed/10899214> [Accessed December 1, 2014].
- Harrison, R. R. (2008). The design of integrated circuits to observe brain activity. *Proc. IEEE* 96, 1203–1216. doi: 10.1109/JPROC.2008.922581
- Hashimoto, T., Elder, C. M., and Vitek, J. L. (2002). A template subtraction method for stimulus artifact removal in high-frequency deep brain stimulation. *J. Neurosci. Methods* 113, 181–186. doi: 10.1016/S0165-0270(01)00491-5
- Hassibi, A., Navid, R., Dutton, R. W., and Lee, T. H. (2004). Comprehensive study of noise processes in electrode electrolyte interfaces. *J. Appl. Phys.* 96, 1074. doi: 10.1063/1.1755429
- Hassler, C., Boretius, T., and Stieglitz, T. (2011). Polymers for neural implants. *J. Polym. Sci. Part B Polym. Phys.* 49, 18–33. doi: 10.1002/polb.22169
- Heer, F. (2005). *CMOS-Based Microelectrode Array for Communication with Electrogenic Cells*. Ph.D. thesis, No. 16330, Zurich: ETH Zurich Available online at: <http://e-collection.ethbib.ethz.ch/view/eth:28441>
- Heer, F., Franks, W., Blau, A., Taschini, S., Ziegler, C., Hierlemann, A., et al. (2004). CMOS microelectrode array for the monitoring of electrogenic cells. *Biosens. Bioelectron.* 20, 358–366. doi: 10.1016/j.bios.2004.02.006
- Heer, F., Hafizovic, S., Franks, W., Blau, A., Ziegler, C., and Hierlemann, A. (2006). CMOS microelectrode array for bidirectional interaction with neuronal networks. *IEEE J. Solid-State Circuits* 41, 1620–1629. doi: 10.1109/JSSC.2006.873677
- Heer, F., Hafizovic, S., Ugnivenko, T., Frey, U., Franks, W., Perriard, E., et al. (2007). Single-chip microelectronic system to interface with living cells. *Biosens. Bioelectron.* 22, 2546–2553. doi: 10.1016/j.bios.2006.10.003
- Henze, D. A., Borhegyi, Z., Csicsvari, J., Mamiya, A., Harris, K. D., and Buzsaki, G. (2000). Intracellular features predicted by extracellular recordings in the hippocampus *in vivo*. *J. Neurophysiol.* 84, 390–400. Available online at: <http://jn.physiology.org/cgi/content/abstract/84/1/390> [Accessed December 11, 2014].
- Hepburn, I., Chen, W., Wils, S., and De Schutter, E. (2012). STEPS: efficient simulation of stochastic reaction-diffusion models in realistic morphologies. *BMC Syst. Biol.* 6:36. doi: 10.1186/1752-0509-6-36
- Herwig, S., Kisban, S., Aarts, A. A. A., Seidl, K., Girardeau, G., Benchenane, K., et al. (2009). Fabrication technology for silicon-based micropore arrays used in acute and sub-chronic neural recording. *J. Micromech. Microeng.* 19, 074008. doi: 10.1088/0960-1317/19/7/074008
- Hierlemann, A., Frey, U., Hafizovic, S., and Heer, F. (2011). Growing cells atop microelectronic chips: interfacing electrogenic cells *in vitro* with cmos-based microelectrode arrays. *Proc. IEEE* 99, 252–284. doi: 10.1109/JPROC.2010.2066532

- Hill, D. N., Mehta, S. B., and Kleinfeld, D. (2011). Quality metrics to accompany spike sorting of extracellular signals. *J. Neurosci.* 31, 8699–8705. doi: 10.1523/JNEUROSCI.0971-11.2011
- Hines, M. L., and Carnevale, N. T. (1997). The NEURON simulation environment. *Neural Comput.* 9, 1179–1209. doi: 10.1162/neco.1997.9.6.1179
- Hodgkin, A. L., and Huxley, A. F. (1952). A quantitative description of membrane current and its application to conduction and excitation in nerve. *J. Physiol.* 117, 500–544. Available online at: <http://www.ncbi.nlm.nih.gov/pmc/articles/PMC1392413/>
- Hoeltzell, P. B., and Dykes, R. W. (1979). Conductivity in the somatosensory cortex of the cat—evidence for cortical anisotropy. *Brain Res.* 177, 61–82. doi: 10.1016/0006-8993(79)90918-1
- Holt, G. R. (1997). *A Critical Reexamination of Some Assumptions and Implications of Cable Theory in Neurobiology*. California I. of T.
- Hoops, S., Sahle, S., Gauges, R., Lee, C., Pahle, J., Simus, N., et al. (2006). COPASI—A Complex pathway simulator. *Bioinformatics* 22, 3067–3074. doi: 10.1093/bioinformatics/btl485
- Hottowy, P., Skoczeń, A., Gunning, D. E., Kachigine, S., Mathieson, K., Sher, A., et al. (2012). Properties and application of a multichannel integrated circuit for low-artifact, patterned electrical stimulation of neural tissue. *J. Neural Eng.* 9, 066005. doi: 10.1088/1741-2560/9/6/066005
- Huang, X.-J., O'Mahony, A. M., and Compton, R. G. (2009). Microelectrode arrays for electrochemistry: approaches to fabrication. *Small* 5, 776–788. doi: 10.1002/smll.200801593
- Huys, R., Braeken, D., Jans, D., Stassen, A., Collaert, N., Wouters, J., et al. (2012). Single-cell recording and stimulation with a 16k micro-nail electrode array integrated on a 0.18 μm CMOS chip. *Lab. Chip.* 12, 1274–1280. doi: 10.1039/c2lc21037a
- Imfeld, K., Neukom, S., Maccione, A., Bornat, Y., Martinoia, S., Farine, P.-A., et al. (2008). Large-scale, high-resolution data acquisition system for extracellular recording of electrophysiological activity. *Biomed. Eng. IEEE Trans.* 55, 2064–2073. doi: 10.1109/TBME.2008.919139
- Ingebrandt, S., Yeung, C.-K., Krause, M., and Offenbässer, A. (2005). Neuron-transistor coupling: interpretation of individual extracellular recorded signals. *Eur. Biophys. J.* 34, 144–154. doi: 10.1007/s00249-004-0437-9
- Ito, D., Komatsu, T., and Gohara, K. (2013). Measurement of saturation processes in glutamatergic and GABAergic synapse densities during long-term development of cultured rat cortical networks. *Brain Res.* 1534, 22–32. doi: 10.1016/j.brainres.2013.08.004
- Ito, S., Yeh, F., Hiolski, E., Rydygier, P., Gunning, D. E., Hottowy, P., et al. (2014). Large-scale, high-resolution multielectrode-array recording depicts functional network differences of cortical and hippocampal cultures. *PLoS ONE* 9:e105324. doi: 10.1371/journal.pone.0105324
- Jäckel, D., Frey, U., Fiscella, M., Franke, F., and Hierlemann, A. (2012). Applicability of independent component analysis on high-density microelectrode array recordings. *J. Neurophysiol.* 108, 334–348. doi: 10.1152/jn.01111.2011
- Jäckel, D., Frey, U., Fiscella, M., and Hierlemann, A. (2011). “Blind source separation for spike sorting of high density microelectrode array recordings,” in *Proceedings of the 5th International IEEE EMBS Conference on Neural Engineering (Cancun)*, Paper ThA1.2.
- James, C. D., Spence, A. J. H., Dowell-Mesfin, N. M., Hussain, R. J., Smith, K. L., Craighead, H. G., et al. (2004). Extracellular recordings from patterned neuronal networks using planar microelectrode arrays. *Biomed. Eng. IEEE Trans.* 51, 1640–1648. doi: 10.1109/TBME.2004.827252
- Jenkner, M., Tartagni, M., Hierlemann, A., and Thewes, R. (2004). Cell-based CMOS sensor and actuator arrays. *Solid-State Circuits IEEE J.* 39, 2431–2437. doi: 10.1109/JSSC.2004.837082
- Jimbo, Y., Kasai, N., Torimitsu, K., Tateno, T., and Robinson, H. P. C. (2003). A system for MEA-based multisite stimulation. *Biomed. Eng. IEEE Trans.* 50, 241–248. doi: 10.1109/TBME.2002.805470
- Jobling, D. T., Smith, J. G., and Wheal, H. V. (1981). Active microelectrode array to record from the mammalian central nervous system *in vitro*. *Med. Biol. Eng. Comput.* 19, 553–60. doi: 10.1007/BF02442768
- Jochum, T., Denison, T., and Wolf, P. (2009). Integrated circuit amplifiers for multi-electrode intracortical recording. *J. Neural Eng.* 6, 26. doi: 10.1088/1741-2560/6/1/012001
- Johnson, B., Peace, S. T., Cleland, T. A., and Molnar, A. (2013a). “A 50 μm pitch, 1120-channel, 20kHz frame rate microelectrode array for slice recording,” in *2013 IEEE Biomed. Circuits Syst. Conf. (BioCAS)* (Rotterdam), 109–112. doi: 10.1109/BioCAS.2013.6679651
- Johnson, B., Peace, S. T., Wang, A., Cleland, T. A., and Molnar, A. (2013b). A 768-channel CMOS microelectrode array with angle sensitive pixels for neuronal recording. *IEEE Sens. J.* 13, 3211–3218. doi: 10.1109/JSEN.2013.2266894
- Johnson, L. J., Cohen, E., Ilg, D., Klein, R., Skeath, P., and Scribner, D. A. (2012). A novel high electrode count spike recording array using an 81,920 pixel transimpedance amplifier-based imaging chip. *J. Neurosci. Methods* 205, 223–232. doi: 10.1016/j.jneumeth.2012.01.003
- Jones, I. L., Livi, P., Lewandowska, M. K., Fiscella, M., Roscic, B., and Hierlemann, A. (2011). The potential of microelectrode arrays and microelectronics for biomedical research and diagnostics. *Anal. Bioanal. Chem.* 399, 2313–2329. doi: 10.1007/s00216-010-3968-1
- Jones, K. E., Campbell, P. K., and Normann, R. A. (1992). A glass/silicon composite intracortical electrode array. *Ann. Biomed. Eng.* 20, 423–37. doi: 10.1007/BF02368134
- Joye, N., Schmid, A., and Leblebici, Y. (2008). An electrical model of the cell-electrode interface for high-density microelectrode arrays. *Conf. Proc. IEEE Eng. Med. Biol. Soc.* 2008, 559–562.
- Katzner, S., Nauhaus, I., Benucci, A., Bonin, V., Ringach, D. L., and Carandini, M. (2009). Local origin of field potentials in visual cortex. *Neuron* 61, 35–41. doi: 10.1016/j.neuron.2008.11.016
- Kayser, C., Ince, R. A. A., and Panzeri, S. (2012). Analysis of slow (theta) oscillations as a potential temporal reference frame for information coding in sensory cortices. *PLoS Comput. Biol.* 8:e1002717. doi: 10.1371/journal.pcbi.1002717
- Keefer, E. W., Botterman, B. R., Romero, M. I., Rossi, A. F., and Gross, G. W. (2008). Carbon nanotube coating improves neuronal recordings. *Nat. Nanotechnol.* 3, 434–439. doi: 10.1038/nnano.2008.174
- Khazipov, R., Sirota, A., and Leinekugel, X. (2004). Early motor activity drives spindle bursts in the developing somatosensory cortex. *Nature* 432, 9–12. doi: 10.1038/nature03132
- Kim, R., Joo, S., Jung, H., Hong, N., and Nam, Y. (2014). Recent trends in microelectrode array technology for *in vitro* neural interface platform. *Biomed. Eng. Lett.* 4, 129–141. doi: 10.1007/s13534-014-0130-6
- Kim, S., and McNames, J. (2007). Automatic spike detection based on adaptive template matching for extracellular neural recordings. *J. Neurosci. Methods* 165, 165–174. doi: 10.1016/j.jneumeth.2007.05.033
- Kipke, D. R., Vetter, R. J., Williams, J. C., and Hetke, J. F. (2003). Silicon-substrate intracortical microelectrode arrays for long-term recording of neuronal spike activity in cerebral cortex. *IEEE Trans. Neural Syst. Rehabil. Eng.* 11, 151–155. doi: 10.1109/TNSRE.2003.814443
- Klee, M., and Rall, W. (1977). Computed potentials of cortically arranged populations of neurons. *J. Neurophysiol.* 40, 647–666.
- Kodandaramaiah, S. B., Flores, F., Holst, G., Wickersham, I., Brown, E., Forest, C. R., et al. (2014). “The multipatcher: a robot for high density measurement of intracellular recordings *in vivo*,” in *Proceedings of the Biomedical Engineering Society (BMES)* (San Antonio, TX).
- Kodandaramaiah, S. B., Franzesi, G. T., Chow, B. Y., Boyden, E. S., and Forest, C. R. (2012). Automated whole-cell patch-clamp electrophysiology of neurons *in vivo*. *Nat. Methods* 9, 585–587. doi: 10.1038/nmeth.1993
- Koester, P. J., Tautrat, C., Beikirch, H., Gimsa, J., and Baumann, W. (2010). Recording electric potentials from single adherent cells with 3D microelectrode arrays after local electroporation. *Biosens. Bioelectron.* 26, 1731–1735. doi: 10.1016/j.bios.2010.08.003
- Kreuz, T. (2013). “Synchronization measures,” in *Principles of Neural Coding*, eds R. Q. Quiroga and S. Panzeri (Boca Raton, FL: CRC Press), 97–120. doi: 10.1201/b14756-8
- Kubo, T., Katayama, N., Karashima, A., and Nakao, M. (2008). The 3D position estimation of neurons in the hippocampus based on the multi-site multi-unit recordings with silicon tetrodes. *Conf. Proc. Annu. Int. Conf. IEEE Eng. Med. Biol. Soc. IEEE Eng. Med. Biol. Soc. Annu. Conf.* 2008, 5021–5024.
- Kwon, K., Eldawlatly, S., and Oweiss, K. (2012). NeuroQuest: a comprehensive analysis tool for extracellular neural ensemble recordings. *J. Neurosci. Methods* 204, 189–201. doi: 10.1016/j.jneumeth.2011.10.027
- Lambacher, A., Vitzthum, V., Zeitler, R., Eickenscheidt, M., Eversmann, B., Thewes, R., et al. (2010). Identifying firing mammalian neurons in networks with high-resolution multi-transistor array (MTA). *Appl. Phys. A* 102, 1–11. doi: 10.1007/s00339-010-6046-9

- Lei, N., Ramakrishnan, S., Shi, P., Orcutt, J. S., Yuste, R., Kam, L. C., et al. (2011). High-resolution extracellular stimulation of dispersed hippocampal culture with high-density CMOS multielectrode array based on non-faradaic electrodes. *J. Neural Eng.* 8, 044003. doi: 10.1088/1741-2560/8/4/044003
- Lei, N., Watson, B. O., MacLean, J. N., Yuste, R., and Shepard, K. L. (2008). "A 256×256 CMOS microelectrode array for extracellular neural stimulation of acute brain slices," in *2008 IEEE International Solid-State Circuits Conference—Digest of Technical Papers* (San Francisco, CA: IEEE), 148–603.
- Lempka, S. F., Johnson, M. D., Moffitt, M. A., Otto, K. J., Kipke, D. R., and McIntyre, C. C. (2011). Theoretical analysis of intracortical microelectrode recordings. *J. Neural Eng.* 8, 045006. doi: 10.1088/1741-2560/8/4/045006
- Łęski, S., Pettersen, K. H., Tunstall, B., Einevoll, G. T., Gigg, J., and Wójcik, D. K. (2011). Inverse current source density method in two dimensions: inferring neural activation from multielectrode recordings. *Neuroinformatics* 9, 401–425. doi: 10.1007/s12021-011-9111-4
- Lewicki, M. S. (1998). A review of methods for spike sorting: the detection and classification of neural action potentials. *Network* 9, R53–R78. doi: 10.1088/0954-898X/9/4/001
- Li, N., Tourovskaia, A., and Folch, A. (2003). Biology on a chip: microfabrication for studying the behavior of cultured cells. *Crit. Rev. Biomed.* 31, 423–488. doi: 10.1615/CritRevBiomedEng.v31.i56.20
- Lilly, J. C., Hughes, J. R., Alvord, E. C., and Galkin, T. W. (1955). Brief, noninjurious electric waveform for stimulation of the brain. *Science* 121, 468–469. doi: 10.1126/science.121.3144.468
- Lind, R., Connolly, P., Wilkinson, C. D. W., and Thomson, R. D. (1991). Finite-element analysis applied to extracellular microelectrode design. *Sens. Actuators B. Chem.* 3, 23–30. doi: 10.1016/0925-4005(91)85004-3
- Lindén, H., Pettersen, K. H., and Einevoll, G. T. (2010). Intrinsic dendritic filtering gives low-pass power spectra of local field potentials. *J. Comput. Neurosci.* 29, 423–444. doi: 10.1007/s10827-010-0245-4
- Litke, A. M., Bezayiff, N., Chichilnisky, E. J., Cunningham, W., Dabrowski, W., Grillo, A. A., et al. (2004). What does the eye tell the brain?: development of a system for the large-scale recording of retinal output activity. *IEEE Trans. Nucl. Sci.* 51, 1434–1440. doi: 10.1109/TNS.2004.832706
- Liu, X., Demosthenous, A., and Donaldson, N. (2007). "On the noise performance of pt electrodes," in *Conference Proceedings. Annual International Conference of the IEEE Engineering in Medicine and Biology Society. IEEE Engineering in Medicine and Biology Society* (Lyon: Annual Conference), 434–436.
- Livi, P., Heer, F., Frey, U., Bakkum, D. J., and Hierlemann, A. (2010). Compact voltage and current stimulation buffer for high-density microelectrode arrays. *Biomed. Circuits Syst. IEEE Trans.* 4, 372–378. doi: 10.1109/TBCAS.2010.2080676
- Llinás, R. (1988). The intrinsic electrophysiological properties of mammalian neurons: insights into central nervous system function. *Science* 242, 1654–1664. doi: 10.1126/science.3059497
- Lloyd, J. I., Thomas, R., Michele, F., Felix, F., Jan, M., Milos, R., et al. (2014). "Characterization of mammalian retinal ganglion cell response to voltage stimulus," in *Proceedings of the 9th International Meeting on Substrate-Integrated Microelectrode Arrays (Reutlingen)*, 74–75.
- Logothetis, N. K., Kayser, C., and Oeltermann, A. (2007). *In vivo* measurement of cortical impedance spectrum in monkeys: implications for signal propagation. *Neuron* 55, 809–823. doi: 10.1016/j.neuron.2007.07.027
- Lopez, C. M., Andrei, A., Mitra, S., Welkenhuysen, M., Eberle, W., Bartic, C., et al. (2014). An implantable 455-active-electrode 52-channel CMOS neural probe. *IEEE J. Solid-State Circuits* 49, 248–261. doi: 10.1109/JSSC.2013.2284347
- Ludwig, K. A., Uram, J. D., Yang, J., Martin, D. C., and Kipke, D. R. (2006). Chronic neural recordings using silicon microelectrode arrays electrochemically deposited with a poly(3,4-ethylenedioxythiophene) (PEDOT) film. *J. Neural Eng.* 3, 59–70. doi: 10.1088/1741-2560/3/1/007
- Maccione, A., Gandolfo, M., Massobrio, P., Novellino, A., Martinioia, S., and Chiappalone, M. (2009). A novel algorithm for precise identification of spikes in extracellularly recorded neuronal signals. *J. Neurosci. Methods* 177, 241–249. doi: 10.1016/j.jneumeth.2008.09.026
- Maccione, A., Garofalo, M., Nieuw, T., Tedesco, M., Berdondini, L., and Martinioia, S. (2012). Multiscale functional connectivity estimation on low-density neuronal cultures recorded by high-density CMOS micro electrode arrays. *J. Neurosci. Methods* 207, 161–171. doi: 10.1016/j.jneumeth.2012.04.002
- Maccione, A., Hennig, M. H., Gandolfo, M., Muthmann, O., van Coppenhagen, J., Eglen, S. J., et al. (2014). Following the ontogeny of retinal waves: pan-retinal recordings of population dynamics in the neonatal mouse. *J. Physiol.* 592, 1545–1563. doi: 10.1113/jphysiol.2013.262840
- Maccione, A., Simi, A., Nieuw, T., Gandolfo, M., Imfeld, K., Ferrea, E., et al. (2013). "Sensing and actuating electrophysiological activity on brain tissue and neuronal cultures with a high-density CMOS-MEA," in *2013 Transducers & Eurosensors XXVII: The 17th International Conference on Solid-State Sensors, Actuators and Microsystems (TRANSDUCERS & EUROSENSORS XXVII)* (Barcelona: IEEE), 752–755.
- Machné, R., Finney, A., Müller, S., Lu, J., Widder, S., and Flamm, C. (2006). The SBML ODE Solver Library: a native API for symbolic and fast numerical analysis of reaction networks. *Bioinformatics* 22, 1406–1407. doi: 10.1093/bioinformatics/btl086
- Mahmud, M., Bertoldo, A., Girardi, S., Maschietto, M., and Vassanelli, S. (2012). SigMate: a Matlab-based automated tool for extracellular neuronal signal processing and analysis. *J. Neurosci. Methods* 207, 97–112. doi: 10.1016/j.jneumeth.2012.03.009
- Mahmud, M., Pulizzi, R., Vasilaki, E., and Giugliano, M. (2014). QSpikes tools: a generic framework for parallel batch preprocessing of extracellular neuronal signals recorded by substrate microelectrode arrays. *Front. Neuroinform.* 8:26. doi: 10.3389/fninf.2014.00026
- Mallat, S. (1989). A theory for multiresolution signal decomposition: the wavelet representation. *IEEE Trans. Pattern Anal. Mach. Intell.* 11, 674–693. doi: 10.1109/34.192463
- Marre, O., Amodei, D., Deshmukh, N., Sadeghi, K., Soo, F., Holy, T. E., et al. (2012). Mapping a complete neural population in the retina. *J. Neurosci.* 32, 14859–14873. doi: 10.1523/JNEUROSCI.0723-12.2012
- Martinez, J., Pedreira, C., Ison, M. J., and Quijan Quiroga, R. (2009). Realistic simulation of extracellular recordings. *J. Neurosci. Methods* 184, 285–293. doi: 10.1016/j.jneumeth.2009.08.017
- Mattioni, M., and Le Novère, N. (2013). Integration of biochemical and electrical signaling-multiscale model of the medium spiny neuron of the striatum. *PLoS ONE* 8:e66811. doi: 10.1371/journal.pone.0066811
- McCormick, D. A., Connors, B. W., Lighthill, J. W., and Prince, D. A. (1985). Comparative electrophysiology of pyramidal and sparsely spiny stellate neurons of the neocortex. *J. Neurophysiol.* 54, 782–806.
- Mechler, F., and Victor, J. D. (2012). Dipole characterization of single neurons from their extracellular action potentials. *J. Comput. Neurosci.* 32, 73–100. doi: 10.1007/s10827-011-0341-0
- Medrihan, L., Ferrea, E., Greco, B., Baldelli, P., and Benfenati, F. (2014). Asynchronous GABA release is a key determinant of tonic inhibition and controls neuronal excitability: a study in the synapsin II-/- mouse. *Cereb. Cortex*. doi: 10.1093/cercor/bhu141. [Epub ahead of print].
- Meister, M., Pine, J., and Baylor, D. A. (1994). Multi-neuronal signals from the retina: acquisition and analysis. *J. Neurosci. Methods* 51, 95–106. doi: 10.1016/0165-0270(94)90030-2
- Menzler, J., and Zeck, G. (2011). Network oscillations in rod-degenerated mouse retinas. *J. Neurosci.* 31, 2280–2291. doi: 10.1523/JNEUROSCI.4238-10.2011
- Merrill, D. R., Bikson, M., and Jefferys, J. G. R. (2005). Electrical stimulation of excitable tissue: design of efficacious and safe protocols. *J. Neurosci. Methods* 141, 171–198. doi: 10.1016/j.jneumeth.2004.10.020
- Meyburg, S., Stockmann, R., Moers, J., Offenhäusser, A., and Ingebrandt, S. (2007). Advanced CMOS process for floating gate field-effect transistors in bioelectronic applications. *Sens. Actuators B. Chem.* 128, 208–217. doi: 10.1016/j.snb.2007.06.003
- Miller, K. J., Sorensen, L. B., Ojemann, J. G., and den Nijs, M. (2009). Power-law scaling in the brain surface electric potential. *PLoS Comput. Biol.* 5:e1000609. doi: 10.1371/journal.pcbi.1000609
- Milstein, J., Mormann, F., Fried, I., and Koch, C. (2009). Neuronal shot noise and Brownian 1/f<sub>2</sub> behavior in the local field potential. *PLoS ONE* 4:e4338. doi: 10.1371/journal.pone.0004338
- Minlebaev, M., Colonnese, M., Tsintsadze, T., Sirota, A., and Khazipov, R. (2011). Early γ oscillations synchronize developing thalamus and cortex. *Science* 334, 226–229. doi: 10.1126/science.1210574
- Mitzdorf, U. (1985). Current source-density method and application in cat cerebral cortex: investigation of evoked potentials and EEG phenomena. *Physiol. Rev.* 65, 37–100.

- Moffitt, M. A., and McIntyre, C. C. (2005). Model-based analysis of cortical recording with silicon microelectrodes. *Clin. Neurophysiol.* 116, 2240–2250. doi: 10.1016/j.clinph.2005.05.018
- Montemurro, M. A., Rasch, M. J., Murayama, Y., Logothetis, N. K., and Panzeri, S. (2008). Phase-of-firing coding of natural visual stimuli in primary visual cortex. *Curr. Biol.* 18, 375–380. doi: 10.1016/j.cub.2008.02.023
- Montgomery, E. B., and Gale, J. T. (2008). Mechanisms of action of deep brain stimulation(DBS). *Neurosci. Biobehav. Rev.* 32, 388–407. doi: 10.1016/j.neubiorev.2007.06.003
- Montgomery, S. M., Sirota, A., and Buzsáki, G. (2008). Theta and gamma coordination of hippocampal networks during waking and rapid eye movement sleep. *J. Neurosci.* 28, 6731–6741. doi: 10.1523/JNEUROSCI.1227-08.2008
- Moxon, K. A. (1999). “Multichannel electrode design: considerations for different applications,” in *Methods for Neural Ensemble Recordings*, ed M. A. L. Nicolelis (Boca Raton, FL: CRC Press), 25–45. doi: 10.1201/9781420048254.ch2
- Müller, J., Bakum, D. J., and Hierlemann, A. (2013). Sub-millisecond closed-loop feedback stimulation between arbitrary sets of individual neurons. *Front. Neural Circuits* 6:121. doi: 10.3389/fncir.2012.00121
- Muller, R., Gambini, S., and Rabaey, J. M. (2012). A 0.013 mm<sup>2</sup>, 5uW, DC-coupled neural signal acquisition IC with 0.5 V supply. *IEEE J. Solid-State Circuits* 47, 232–243. doi: 10.1109/JSSC.2011.2163552
- Najafi, K., and Wise, K. D. (1986). An implantable multielectrode array with on-chip signal processing. *IEEE J. Solid-State Circuits* 21, 1035–1044. doi: 10.1109/JSSC.1986.1052646
- Nam, Y., and Wheeler, B. C. (2011). *In vitro* microelectrode array technology and neural recordings. *Crit. Rev. Biomed. Eng.* 39, 45–61. doi: 10.1615/CritRevBiomedEng.v39.i1.40
- Nelson, M. J., Bosch, C., Venance, L., and Pouget, P. (2013). Microscale inhomogeneity of brain tissue distorts electrical signal propagation. *J. Neurosci.* 33, 2821–2827. doi: 10.1523/JNEUROSCI.3502-12.2013
- Nelson, M. J., and Pouget, P. (2010). Do electrode properties create a problem in interpreting local field potential recordings? *J. Neurophysiol.* 103, 2315–2317. doi: 10.1152/jn.00157.2010
- Nelson, M. J., Pouget, P., Nilsen, E. A., Patten, C. D., and Schall, J. D. (2008). Review of signal distortion through metal microelectrode recording circuits and filters. *J. Neurosci. Methods* 169, 141–157. doi: 10.1016/j.jneumeth.2007.12.010
- Nicholson, C., and Freeman, J. A. (1975). Theory of current source-density analysis and determination of conductivity tensor for anuran cerebellum. *J. Neurophysiol.* 38, 356.
- Niedermeyer, E., and da Silva, F. H. L. (2005). *Electroencephalography: Basic Principles, Clinical Applications, and Related Fields*. Lippincott Williams & Wilkins Available online at: <http://books.google.co.jp/books?id=tndqYGPHQdEC>
- Nisch, W., Böck, J., Egert, U., Hämerle, H., and Mohr, A. (1994). A thin film microelectrode array for monitoring extracellular neuronal activity *in vitro*. *Biosens. Bioelectron.* 9, 737–41. doi: 10.1016/0956-5663(94)80072-3
- Nunez, P. L., and Srinivasan, R. (2006). *Electric Fields of the Brain: The Neurophysics of EEG*. Oxford University Press Available online at: [http://books.google.co.jp/books?id=fUV54as56\\_8C](http://books.google.co.jp/books?id=fUV54as56_8C)
- Obien, M. E. J., Hierlemann, A., and Frey, U. (2013). “Factors affecting blind localization of a glass micropipette using a high-density microelectrode array,” in *Proceedings of IEEE Sensors, 2013* (Baltimore, Maryland), 932–935.
- Obien, M. E. J., Hierlemann, A., and Frey, U. (2014). “Technique for analysis of purkinje cell sub-cellular functional dynamics in acute cerebellar slices using a high-density microelectrode array,” in *Proceedings of the 9th International Meeting on Substrate-Integrated Microelectrode Arrays* (Reutlingen), 88–90.
- Offenhäusser, A., Sprössler, C., Matsuzawa, M., and Knoll, W. (1997). Field-effect transistor array for monitoring electrical activity from mammalian neurons in culture. *Biosens. Bioelectron.* 12, 819–826. doi: 10.1016/S0956-5663(97)00047-X
- Ohta, J., Tokuda, T., Sasagawa, K., and Noda, T. (2009). Implantable CMOS biomedical devices. *Sensors (Basel)* 9, 9073–9093. doi: 10.3390/s91109073
- Okada, Y., Shimojo, K., Ogawa, R., Sugihara, H., and Taketani, M. (1999). A new planar multielectrode array for extracellular recording: application to hippocampal acute slice. *J. Neurosci. Methods* 93, 61–67. doi: 10.1016/S0165-0270(99)00113-2
- Okada, Y. C., Huang, J. C., Rice, M. E., Tranchina, D., and Nicholson, C. (1994). Origin of the apparent tissue conductivity in the molecular and granular layers of the *in vitro* turtle cerebellum and the interpretation of current source-density analysis. *J. Neurophysiol.* 72, 742–753.
- O’Keefe, J., and Recce, M. L. (1993). Phase relationship between hippocampal place units and the EEG theta rhythm. *Hippocampus* 3, 317–330.
- Olsson, R. H. IIrd, and Wise, D. K. (2005). A three-dimensional neural recording microsystem with implantable data compression circuitry. *Solid-State Circuits IEEE J.* 40, 2796–2804. doi: 10.1109/JSSC.2005.858479
- O’Neill, J., Senior, T. J., Allen, K., Huxter, J. R., and Csicsvari, J. (2008). Reactivation of experience-dependent cell assembly patterns in the hippocampus. *Nat. Neurosci.* 11, 209–215. doi: 10.1038/nn2037
- Ortmanns, M., Buhmann, A., and Manoli, Y. (2008). “Interface circuits,” in *Comprehensive Microsystems*, eds Y. Gianchandani, O. Tabata, and H. Zappe (Amsterdam: Elsevier), 465–493. doi: 10.1016/B978-044452190-3.00063-X
- Paik, S.-J., Park, Y., and Cho, D. (2003). Roughened polysilicon for low impedance microelectrodes in neural probes. *J. Micromech. Microeng.* 13, 373–379. doi: 10.1088/0960-1317/13/3/304
- Parce, J. W., Owicki, J. C., Kercso, K. M., Sigal, G. B., Wada, H. G., Muir, V. C., et al. (1989). Detection of cell-affecting agents with a silicon biosensor. *Science* 246, 243–7. doi: 10.1126/science.2799384
- Park, T. H., and Shuler, M. L. (2003). Integration of cell culture and microfabrication technology. *Biotechnol. Prog.* 19, 243–253. doi: 10.1021/bp020143k
- Perin, R., Berger, T. K., and Markram, H. (2011). A synaptic organizing principle for cortical neuronal groups. *Proc. Natl. Acad. Sci. U.S.A.* 108, 5419–5424. doi: 10.1073/pnas.1016051108
- Petersen, K. H., and Einevoll, G. T. (2008). Amplitude variability and extracellular low-pass filtering of neuronal spikes. *Biophys. J.* 94, 784–802. doi: 10.1529.biophysj.107.111179
- Petersen, K. H., Lindén, H., Dale, A. M., and Einevoll, G. T. (2010). “Extracellular spikes and current-source density,” in *Handbook of Neural Activity Measurement*, eds R. Brette and A. Destexhe (Cambridge: Cambridge University Press), 92–129.
- Pine, J. (1980). Recording action potentials from cultured neurons with extracellular microcircuit electrodes. *J. Neurosci. Methods* 2, 19–31. doi: 10.1016/0165-0270(80)90042-4
- Plenz, D., and Aertsen, A. (1993). Current source density profiles of optical recording maps: a new approach to the analysis of spatio-temporal neural activity patterns. *Eur. J. Neurosci.* 5, 437–448. doi: 10.1111/j.1460-9568.1993.tb00510.x
- Pritchard, W. S. (1992). The brain in fractal time: 1/f-like power spectrum scaling of the human electroencephalogram. *Int. J. Neurosci.* 66, 119–129. doi: 10.3109/0020745920899976
- Quian Quiroga, R. (2009). What is the real shape of extracellular spikes? *J. Neurosci. Methods* 177, 194–198. doi: 10.1016/j.jneumeth.2008.09.033
- Quian Quiroga, R. (2007). Spike sorting. *Scholarpedia* 2, 3583. doi: 10.4249/scholarpedia.3583
- Quian Quiroga, R., Nadasy, Z., and Ben-Shaul, Y. (2004). Unsupervised spike detection and sorting with wavelets and superparamagnetic clustering. *Neural Comput.* 16, 1661–1687. doi: 10.1162/089976604774201631
- Ranck, J. B. (1963a). Analysis of specific impedance of rabbit cerebral cortex. *Exp. Neurol.* 7, 153–174. doi: 10.1016/S0014-4886(63)80006-0
- Ranck, J. B. (1963b). Specific impedance of rabbit cerebral cortex. *Exp. Neurol.* 7, 144–152. doi: 10.1016/S0014-4886(63)80005-9
- Regehr, W. G., Pine, J., Cohan, C. S., Mischke, M. D., and Tank, D. W. (1989). Sealing cultured invertebrate neurons to embedded dish electrodes facilitates long-term stimulation and recording. *J. Neurosci. Methods* 30, 91–106. doi: 10.1016/0165-0270(89)90055-1
- Reinhardt, L., and Blickhan, R. (2014). Ultra-miniature force plate for measuring triaxial forces in the micronewton range. *J. Exp. Biol.* 217, 704–710. doi: 10.1242/jeb.094177
- Rice, M. E., Okada, Y. C., and Nicholson, C. (1993). Anisotropic and heterogeneous diffusion in the turtle cerebellum: implications for volume transmission. *J. Neurophysiol.* 70, 2035–2044.
- Riera, J. J., Goto, T., and Kawashima, R. (2014). A methodology for fast assessments to the electrical activity of barrel fields *in vivo*: from population inputs to single unit outputs. *Front. Neural Circuits* 8:4. doi: 10.3389/fncir.2014.00004
- Robinson, D. A. (1968). The electrical properties of metal microelectrodes. *Proc. IEEE* 56, 1065–1071. doi: 10.1109/PROC.1968.6458

- Robinson, J. T., Jorgolli, M., and Park, H. (2013). Nanowire electrodes for high-density stimulation and measurement of neural circuits. *Front. Neural Circuits* 7:38. doi: 10.3389/fncir.2013.00038
- Ruther, P., Herwik, S., Kisban, S., Seidl, K., and Paul, O. (2010). Recent progress in neural probes using silicon MEMS technology. *IEEE Trans. Electr. Electron. Eng.* 5, 505–515. doi: 10.1002/tee.20566
- Samengo, I., Elijah, D., and Montemurro, M. (2013). “Spike-Train Analysis,” in *Principles of Neural Coding*, eds R. Q. Quiroga and S. Panzeri (Boca Raton, FL: CRC Press), 75–96. doi: 10.1201/b14756-7
- Sanchez-Bustamante, C. D., Frey, U., Kelm, J. M., Hierlemann, A., and Fussenegger, M. (2008). Modulation of cardiomyocyte electrical properties using regulated bone morphogenetic protein-2 expression. *Tissue Eng. Part A* 14, 1969–1988. doi: 10.1089/ten.tea.2007.0302
- Sedivy, J., Frey, U., Heer, F., Hafizovic, S., and Hierlemann, A. (2007). “Multi-Chip high-density microelectrode system for electrogenic-cell recording and stimulation,” in *Proceedings of 2007 IEEE Sensors* (Atlanta: IEEE), 716–719.
- Segev, R., Goodhouse, J., Puchalla, J., and Berry, M. J. (2004). Recording spikes from a large fraction of the ganglion cells in a retinal patch. *Nat. Neurosci.* 7, 1154–1161. doi: 10.1038/nn1323
- Seidl, K., Herwik, S., Torfs, T., Neves, H. P., Paul, O., and Ruther, P. (2011). CMOS-based high-density silicon microprobe arrays for electronic depth control in intracortical neural recording. *J. Microelectromech. Syst.* 20, 1439–1448. doi: 10.1109/JMEMS.2011.2167661
- Shahrokh, F., Abdelhalim, K., Serletis, D., Carlen, P. L., and Genov, R. (2010). The 128-channel fully differential digital integrated neural recording and stimulation interface. *IEEE Trans. Biomed. Circuits Syst.* 4, 149–161. doi: 10.1109/TBCAS.2010.2041350
- Simeone, T. A., Simeone, K. A., Samson, K. K., Kim, D. Y., and Rho, J. M. (2013). Loss of the Kv1.1 potassium channel promotes pathologic sharp waves and high frequency oscillations in *in vitro* hippocampal slices. *Neurobiol. Dis.* 54, 68–81. doi: 10.1016/j.nbd.2013.02.009
- Somogyvári, Z., Cserpán, D., Ulbert, I., and Erdi, P. (2012). Localization of single-cell current sources based on extracellular potential patterns: the spike CSD method. *Eur. J. Neurosci.* 36, 3299–3313. doi: 10.1111/j.1460-9568.2012.08249.x
- Somogyvári, Z., Zalányi, L., Ulbert, I., and Erdi, P. (2005). Model-based source localization of extracellular action potentials. *J. Neurosci. Methods* 147, 126–137. doi: 10.1016/j.jneumeth.2005.04.002
- Spira, M. E., and Hai, A. (2013). Multi-electrode array technologies for neuroscience and cardiology. *Nat. Nanotechnol.* 8, 83–94. doi: 10.1038/nano.2012.265
- Stett, A., Egert, U., Guenther, E., Hofmann, F., Meyer, T., Nisch, W., et al. (2003). Biological application of microelectrode arrays in drug discovery and basic research. *Anal. Bioanal. Chem.* 377, 486–495. doi: 10.1007/s00216-003-2149-x
- Stett, A., Müller, B., and Fromherz, P. (1997). Two-way silicon-neuron interface by electrical induction. *Phys. Rev. E* 55, 1779–1782. doi: 10.1103/PhysRevE.55.1779
- Steyaert, M. S. J., and Sansen, W. M. C. (1987). A micropower low-noise monolithic instrumentation amplifier for medical purposes. *IEEE J. Solid-State Circuits* 22, 1163–1168. doi: 10.1109/JSSC.1987.1052869
- Stratton, P., Cheung, A., Wiles, J., Kiyatkina, E., Sah, P., and Windels, F. (2012). Action potential waveform variability limits multi-unit separation in freely behaving rats. *PLoS ONE* 7:e38482. doi: 10.1371/journal.pone.0038482
- Stutzki, H., Leibig, C., Andreadaki, A., Fischer, D., and Zeck, G. (2014). Inflammatory stimulation preserves physiological properties of retinal ganglion cells after optic nerve injury. *Front. Cell. Neurosci.* 8:38. doi: 10.3389/fncel.2014.00038
- Sun, J.-J., Kilb, W., and Luhmann, H. J. (2010). Self-organization of repetitive spike patterns in developing neuronal networks *in vitro*. *Eur. J. Neurosci.* 32, 1289–1299. doi: 10.1111/j.1460-9568.2010.07383.x
- Takahashi, K., Kaizu, K., Hu, B., and Tomita, M. (2004). A multi-algorithm, multi-timescale method for cell simulation. *Bioinformatics* 20, 538–546. doi: 10.1093/bioinformatics/btg442
- Takekawa, T., Isomura, Y., and Fukai, T. (2010). Accurate spike sorting for multi-unit recordings. *Eur. J. Neurosci.* 31, 263–272. doi: 10.1111/j.1460-9568.2009.07068.x
- Takekawa, T., Isomura, Y., and Fukai, T. (2012). Spike sorting of heterogeneous neuron types by multimodality-weighted PCA and explicit robust variational Bayes. *Front. Neuroinform.* 6:5. doi: 10.3389/fninf.2012.00005
- Taketani, M., and Baudry, M. (2006). *Advances in Network Electrophysiology*. New York, NY: Springer.
- Tateno, T., and Nishikawa, J. (2014). A CMOS IC-based multisite measuring system for stimulation and recording in neural preparations *in vitro*. *Front. Neuroeng.* 7:39. doi: 10.3389/fneng.2014.00039
- Thakore, V., Molnar, P., and Hickman, J. J. (2012). An optimization-based study of equivalent circuit models for representing recordings at the neuron-electrode interface. *IEEE Trans. Biomed. Eng.* 59, 2338–2347. doi: 10.1109/TBME.2012.2203820
- Thomas, C. A., Springer, P. A., Loeb, G. E., Berwald-Netter, Y., and Okum, L. M. (1972). A miniature microelectrode array to monitor the bioelectric activity of cultured cells. *Exp. Cell Res.* 74, 61–66. doi: 10.1016/0014-4827(72)90481-8
- Tkačík, G., Marre, O., Amodei, D., Schneidman, E., Bialek, W., and Berry, M. J. (2014). Searching for collective behavior in a large network of sensory neurons. *PLoS Comput. Biol.* 10:e1003408. doi: 10.1371/journal.pcbi.1003408
- Tokuda, T., Yamamoto, A., Kagawa, K., Nunoshita, M., and Ohta, J. (2006). A CMOS image sensor with optical and potential dual imaging function for on-chip bioscientific applications. *Sens. Actuators A Phys.* 125, 273–280. doi: 10.1016/j.sna.2005.08.023
- Van Dijck, G., Seidl, K., Paul, O., Ruther, P., Van Hulle, M. M., and Maex, R. (2012). Enhancing the yield of high-density electrode arrays through automated electrode selection. *Int. J. Neural Syst.* 22, 1–19. doi: 10.1142/S012906571203055
- Velychko, D., Eickenscheidt, M., Thewes, R., and Zeck, G. (2014). “Simultaneous stimulation and recording of retinal action potentials using capacitively coupled high-density CMOS-based MEAs,” in *Proceedings of the 9th International Meeting on Substrate-Integrated Microelectrode Arrays* (Reutlingen), 78–79.
- Viswam, V., Jäckel, D., Ballini, M., Müller, J., Radivojevic, M., Frey, U., et al. (2014). “An automated method for characterizing electrode properties of high-density microelectrode arrays,” in *Proceedings of the 9th International Meeting on Substrate-Integrated Microelectrode Arrays* (Reutlingen), 302–303.
- Wagenaar, D. A., Pine, J., and Potter, S. M. (2004). Effective parameters for stimulation of dissociated cultures using multi-electrode arrays. *J. Neurosci. Methods* 138, 27–37. doi: 10.1016/j.jneumeth.2004.03.005
- Wagenaar, D. A., and Potter, S. M. (2002). Real-time multi-channel stimulus artifact suppression by local curve fitting. *J. Neurosci. Methods* 120, 113–120. doi: 10.1016/S0165-0270(02)00149-8
- Ward, M. P., Rajdev, P., Ellison, C., and Irazoqui, P. P. (2009). Toward a comparison of microelectrodes for acute and chronic recordings. *Brain Res.* 1282, 183–200. doi: 10.1016/j.brainres.2009.05.052
- Wässle, H. (2004). Parallel processing in the mammalian retina. *Nat. Rev. Neurosci.* 5, 747–757. doi: 10.1038/nrn1497
- Weale, R. A. (1951). A new micro-electrode for electro-physiological work. *Nature* 167, 529–530. doi: 10.1038/167529a0
- Weis, R., and Fromherz, P. (1997). Frequency dependent signal transfer in neuron transistors. *Phys. Rev. E* 55, 877–889. doi: 10.1103/PhysRevE.55.877
- Wils, S., and De Schutter, E. (2009). STEPS: modeling and simulating complex reaction-diffusion systems with python. *Front. Neuroinform.* 3:15. doi: 10.3389/neuro.11.015.2009
- Wilson, B. S., and Dorman, M. F. (2008). Interfacing sensors with the nervous system: lessons from the development and success of the cochlear implant. *IEEE Sens. J.* 8, 131–147. doi: 10.1109/JSEN.2007.912917
- Wise, K. D., Anderson, D. J., Hetke, J. F., Kipke, D. R., and Najafi, K. (2004). Wireless implantable Microsystems: high-density electronic interfaces to the nervous system. *Proc. IEEE* 92, 76–97. doi: 10.1109/JPROC.2003.820544
- Wise, K. D., Angell, J. B., and Starr, A. (1970). An integrated-circuit approach to extracellular microelectrodes. *IEEE Trans. Biomed. Eng.* BME-17, 238–247. doi: 10.1109/TBME.1970.4502738
- Wise, K. D., Sodagar, A. M., Gulari, M. N., Perlin, G. E., and Najafi, K. (2008). Microelectrodes, microelectronics, and implantable neural microsystems. *Proc. IEEE* 96, 1184–1202. doi: 10.1109/JPROC.2008.922564
- Wood, C., Williams, C., and Waldron, G. J. (2004). Patch clamping by numbers. *Drug Discov. Today* 9, 434–441. doi: 10.1016/S1359-6446(04)03064-8
- Yegin, U., Schindler, M., Ingebrandt, S., Eick, S., Kim, S. K., Hwang, C. S., et al. (2009). “CMOS sensor array for bi-directional communication with electrically

- active cells," in *2009 10th International Conference on Ultimate Integration of Silicon* (Aachen: IEEE), 237–240.
- Zeck, G., Lambacher, A., and Fromherz, P. (2011). Axonal transmission in the retina introduces a small dispersion of relative timing in the ganglion cell population response. *PLoS ONE* 6:e20810. doi: 10.1371/journal.pone.0020810
- Zrenner, E., Bartz-Schmidt, K. U., Benav, H., Besch, D., Bruckmann, A., Gabel, V.-P., et al. (2011). Subretinal electronic chips allow blind patients to read letters and combine them to words. *Proc. Biol. Sci.* 278, 1489–1497. doi: 10.1098/rspb.2010.1747

**Conflict of Interest Statement:** The authors declare that the research was conducted in the absence of any commercial or financial relationships that could be construed as a potential conflict of interest.

Received: 07 October 2014; accepted: 03 December 2014; published online: 06 January 2015.

Citation: Obien MEJ, Deligkaris K, Bullmann T, Balkum DJ and Frey U (2015) Revealing neuronal function through microelectrode array recordings. *Front. Neurosci.* 8:423. doi: 10.3389/fnins.2014.00423

This article was submitted to *Systems Biology*, a section of the journal *Frontiers in Neuroscience*.

Copyright © 2015 Obien, Deligkaris, Bullmann, Balkum and Frey. This is an open-access article distributed under the terms of the Creative Commons Attribution License (CC BY). The use, distribution or reproduction in other forums is permitted, provided the original author(s) or licensor are credited and that the original publication in this journal is cited, in accordance with accepted academic practice. No use, distribution or reproduction is permitted which does not comply with these terms.



# Quantifying periodicity in omics data

Cornelia Amariei, Masaru Tomita and Douglas B. Murray\*

Institute for Advanced Biosciences, Keio University, Tsuruoka, Japan

**Edited by:**

Noriko Hiroi, Keio University, Japan

**Reviewed by:**

Satyaprakash Nayak, Pfizer Inc., USA

Andy Hesketh, University of Cambridge, UK

Marcus Krantz,

Humboldt-Universität zu Berlin, Germany

**\*Correspondence:**

Douglas B. Murray, Institute for Advanced Biosciences, Keio University, Nipponkoku 403-1, Daihouji, Tsuruoka, Yamagata 997-0017, Japan

e-mail: dougie@ttck.keio.ac.jp

Oscillations play a significant role in biological systems, with many examples in the fast, ultradian, circadian, circalunar, and yearly time domains. However, determining periodicity in such data can be problematic. There are a number of computational methods to identify the periodic components in large datasets, such as signal-to-noise based Fourier decomposition, Fisher's *g*-test and autocorrelation. However, the available methods assume a sinusoidal model and do not attempt to quantify the waveform shape and the presence of multiple periodicities, which provide vital clues in determining the underlying dynamics. Here, we developed a Fourier based measure that generates a de-noised waveform from multiple significant frequencies. This waveform is then correlated with the raw data from the respiratory oscillation found in yeast, to provide oscillation statistics including waveform metrics and multi-periods. The method is compared and contrasted to commonly used statistics. Moreover, we show the utility of the program in the analysis of noisy datasets and other high-throughput analyses, such as metabolomics and flow cytometry, respectively.

**Keywords:** periodicity tests, waveform analysis, metabolic oscillation, metabolomics, flow cytometry

## INTRODUCTION

Cellular network dynamics are excitable and inherently non-linear, properties that stem from the multitude of feedback and feedforward loops involved in biological processes (Lloyd, 2008). These systems form an intimate feedback with the environment to generate the dynamic phenotype of the cell (e.g., oscillation/pulsing, bursting bistability) (Sobie, 2011; Levine et al., 2013). The feedback and feedforward systems have drastically different time scales that vary over several orders of magnitude (Aon et al., 2004), from the annual migration patterns found in monarch butterflies (Kyriacou, 2009), to the second oscillation of cardiomyocytes in one's heart (Aon et al., 2004). While our understanding of each time scale increases daily, the interaction between different dynamical processes remains poorly characterized. Understanding the dynamical interactions between time scales are key to understanding the complex phenotypes of embryogenesis (Kageyama et al., 2012), circadian biology in disease (Gibbison et al., 2013), and psychology (Salvatore et al., 2012; Salomon and Cowan, 2013).

Our studies using frequently sampled data from yeast and cardiomyocytes showed that the time-structure is highly organized (Aon et al., 2008) and had the properties of a fractal over five orders of magnitude, indicative of harmonic entrainment in cellular processes. Moreover, cellular energetics and especially mitochondrial activity play defining roles in rapidly shaping cellular dynamics. Thousands of data points are required to study these orders of magnitude (Sasidharan et al., 2012c). However, analysing multiperiodicity in less frequently sampled data (under 100 data points) remains difficult (de Lichtenberg et al., 2005), and these are the kind of datasets commonly used for time-series expression or metabolic studies. Perhaps one of the best characterized synchronous oscillatory systems in this regard is

the precisely controlled continuously cultured yeast. When environmental cues are removed, the resulting output in respiratory state (readily measured by residual dissolved oxygen measurements) is often a stable oscillatory or homeodynamic state (Lloyd et al., 2001; Lloyd and Murray, 2005, 2006, 2007; Johnson and Egli, 2014). This has been shown to be multi-oscillatory (Aon et al., 2008; Sasidharan et al., 2012c), to have period doubling events (Salgado et al., 2002; Klevecz and Li, 2007) caused by perturbation, and has multiple omic and high-throughput datasets available (Klevecz et al., 2004; Li and Klevecz, 2006; Murray et al., 2007; Sasidharan et al., 2012b,c). These properties make it an ideal model system for multi-scale dynamical studies.

Generally, analysis methods are restricted to the period of interest, such as the perturbation length or oscillation period, and the sampling frequency limits the use of many powerful time-series analysis tools (Dowse, 2007). Techniques such as autocorrelation (Yamada and Ueda, 2007) and Fourier transform (Yamada and Ueda, 2007; Lehmann et al., 2013) rely on targeting a particular frequency, and can be prone to generating false calls due to frequency changes and multi-oscillators. Singular Value Decomposition (SVD)/Principal Component Analysis (PCA) generally assumes that the largest variances are the most interesting (neglecting subtle effects), and also does not allow for the use of *a priori* dynamical knowledge to the analyses (Wang et al., 2012). Furthermore, it is difficult to assign meaning to the contributions of each time-series to the components (Raychaudhuri et al., 2000; Alter et al., 2003). Wavelets analyses are powerful, however the data density required makes it difficult to apply to the low-density time-series data generated from high-throughput experiments (Klevecz and Murray, 2001; Song et al., 2007; Prasad and Bruce, 2008; Sasidharan et al., 2012c).

Here, we introduce a tool that expands on the signal-noise (SN) ratio approach (Yamada and Ueda, 2007; Machné and Murray, 2012), by calculating the SN ratio of each frequency and then uses this to generate a model waveform whose goodness of fit to the original data is determined using coefficient of determination ( $R^2$ ). A user-specified significance or SN ratio cut-off determines the powers to use in constructing the model. We illustrate its utility using previously published data.

## MATERIALS AND METHODS

### FREQUENCY MODEL

Given a time-series of  $N$  points  $x_1, x_2, \dots, x_N$ , the corresponding discrete Fourier transform (DFT), as a series of complex numbers  $X_0, X_1, \dots, X_{N-1}$ , is given by the formula:

$$X_k = \sum_{n=0}^{N-1} x_n e^{-i2\pi k \frac{n}{N}}, k = 0, \dots, N-1,$$

where  $X_k$  represents the component of  $k$  cycles per time-series.

The component of frequency 0 ( $X_0$ ) is used to calculate the mean value of the time-series, referred to as the DC component:

$$DC = \frac{|X_0|}{N}$$

By the nature of the DFT, the remaining components  $X_1, X_2, \dots, X_{N-1}$  are mirrored:

$$X_k = X_{N-k}, k = 1, \dots, M, M = \lfloor (N-1)/2 \rfloor,$$

therefore, all further calculations are performed on the first half of these components.

The peak-to-peak amplitude  $A_k$  for each frequency  $X_k$  is given by the formula:

$$A_k = \frac{4}{N} * |X_k|, \quad k = 1, \dots, M$$

The SN ratio (Yamada and Ueda, 2007) represents the ratio between the amplitude of the target signal and the average amplitude of noise (i.e., the average amplitude of all other frequencies):

$$SN_k = \frac{(M-1) * A_k}{\left(\sum_{n=1}^M A_n\right) - A_k}, \quad k = 1, \dots, M$$

For the construction of the model, if no target frequency is specified (untargeted mode), the algorithm removes all frequencies that are considered noisy (i.e., that do not pass the arbitrary  $sn$  threshold). Thus, a filtered set of signals  $X_f$  is calculated by removing the frequencies with a SN ratio below the  $sn$  threshold, while preserving the DC component:

$$X_f = \begin{cases} X_k & \text{if } SN_k > sn \text{ or } k = 0 \\ 0 & \text{otherwise} \end{cases}, \quad k = 0, \dots, N-1$$

If a target frequency  $ta$  is specified (targeted mode), the intent of the algorithm is to preserve the harmonics of the specified

frequency that oscillate, including possible temporal drift into the frequency  $ta - 1$  and its harmonics, but to remove all frequencies that have an oscillation stronger than the target frequency, or are too noisy (below the  $sn$  threshold). Thus, only the frequencies  $ta - 1$  and higher are kept, only if they have a lower SN ratio than  $X_{ta}$  and only if they pass the  $sn$  threshold (also preserving component 0, i.e., the mean):

$$X_f = X_f = \begin{cases} X_k & \text{if } (SN_k > sn \text{ and } SN_k \leq SN_{ta}) \text{ and } k \geq (ta - 1) \text{ or } k = 0 \\ 0 & \text{otherwise} \end{cases}, \quad k = 0, \dots, M$$

If  $N$  is even, the middle component  $X_f_{M+1}$  is also set to 0.

As it can be seen, if the SN of the targeted frequency does not pass the  $sn$  threshold, all components are removed (resulting in a flat line). If the user-specified cut-off is given as a  $P$ -value, the  $sn$  cut-off is the corresponding SN ratio at the given  $P$ -value.

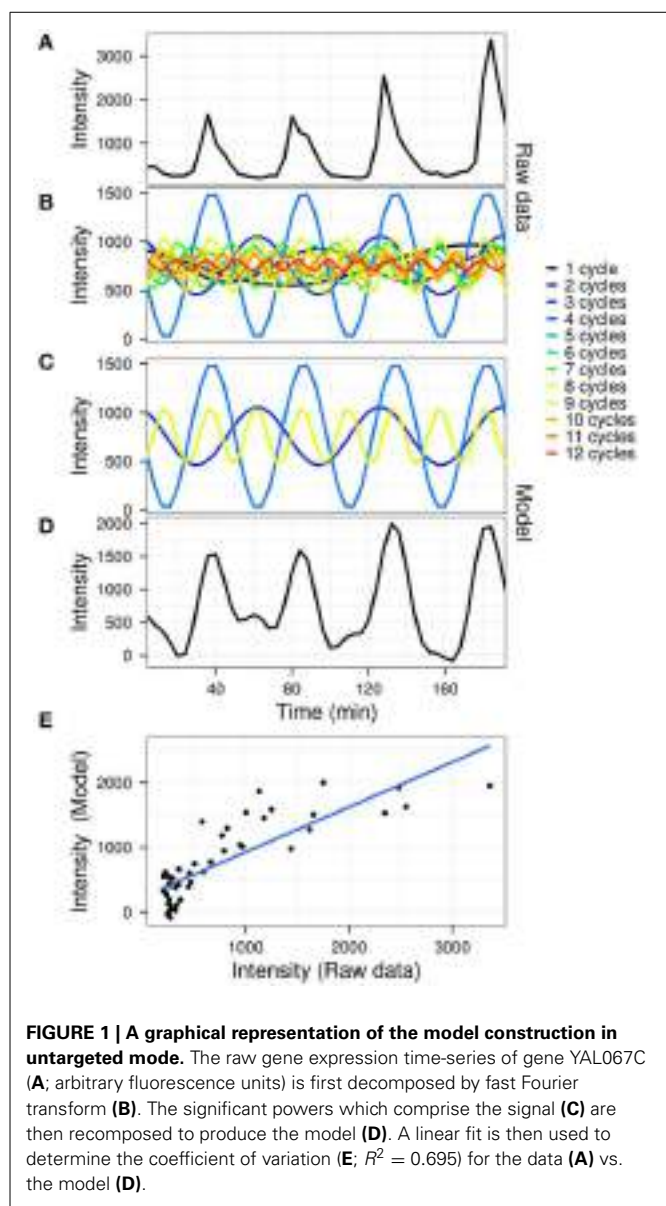
In all cases, the user can override these filters by manually specifying components to be omitted. The filtered waveform is reconstructed by the inverse DFT:

$$x_f = \frac{1}{N} \sum_{n=0}^{N-1} X_f n e^{i2\pi k \frac{n}{N}}, \quad k = 0, \dots, N-1$$

The goodness of fit between the model and the original data was calculated using  $R^2$  values. A graphical outline of the algorithm is presented in **Figure 1**, using the gene expression time-series (dataset described below) for yeast gene YAL067C (the first oscillator in the dataset).

The algorithm was developed in R (R Core Development Team, 2008) and is called waveform. The main parameters passed are the cut-off method (SN ratio or its  $P$ -value) and cut-off threshold (default to 2 and 0.05, respectively). The statistics necessary for full characterization of the Fourier components (DC, amplitude, and angle) are calculated by the underlying function `oscilGet`, which also generates statistics on autocorrelation (Venables and Ripley, 2002), Ljung-Box test (Ljung and Box, 1978), Oscillation Strength (Murray et al., 2007), and Fisher's exact g-test (Ahdesmäki et al., 2005).

The significance calculation method can also be specified, i.e., "model" for log normal distributions or a number of iterations for a permutation-based statistic (10,000 is the default). The model-based significance calculation first generates a normal probability distribution from 10,000 random samples, using the standard deviation of the analyzed dataset or a user-specified standard deviation. Next, the statistics for signal-noise ratio, oscillation strength, and/or autocorrelation on the model data are generated. The standard deviation and mean of the target statistics are used to generate a model distribution for each statistic, and the significance is then calculated from the experimental data and the model statistics' upper tail. For this approach to work, the distribution of the dataset should be checked carefully for the normality of the majority of the data. The distribution is sensitive to experimental noise (i.e., limits of experimental determination can result in skewed tails which alter the standard deviation of the dataset), and this can be accounted for prior to analysis by passing the standard deviation of the log-normal subset of the dataset



onto the algorithm (see supplemental package, data manuals for examples).

If the distribution deviates significantly from log normality, then the permutation approach can be used (with at least 10,000 iterations, to avoid high false discovery rates). The rows of the data matrix are permuted by the specified number of iterations, and  $P$ -values are defined as the ratio between the number of times the statistic of the permutation was greater than the statistic of the original data and the number of iterations. This is computationally intensive and one can specify the number of slaves (`nSlaves`) for multicore systems. Lower iteration numbers increase the false discovery rates; to address this, the optimal iteration number can be determined with existing R packages, such as `fdrtool` (Strimmer, 2008). For a  $P$ -value of 0.01 we found 10,000 iterations to give an acceptable false discovery rate (0.0043).

The supplemental R-package waveform contains full details, examples and the data used, and uses three main commands; `waveform`, `oscilGet`, and `DFT`. `DFT` is a wrapper for the default fast Fourier transform of R (`fft`), which uses a Mixed-Radix algorithm (Singleton, 1969). The package can be installed using the following command:

```
R CMD INSTALL waveform_1.0.1.tar.gz
```

The package requires the standard R packages: `GeneCycle`, `matrixStats`, `foreach`, `doSNOW`, `fdrtool`,  `iterators`, `snow`, and `e1071`. Updates will be available for download from <http://oscillat.iab.keio.ac.jp>.

## EXPERIMENTAL DATA

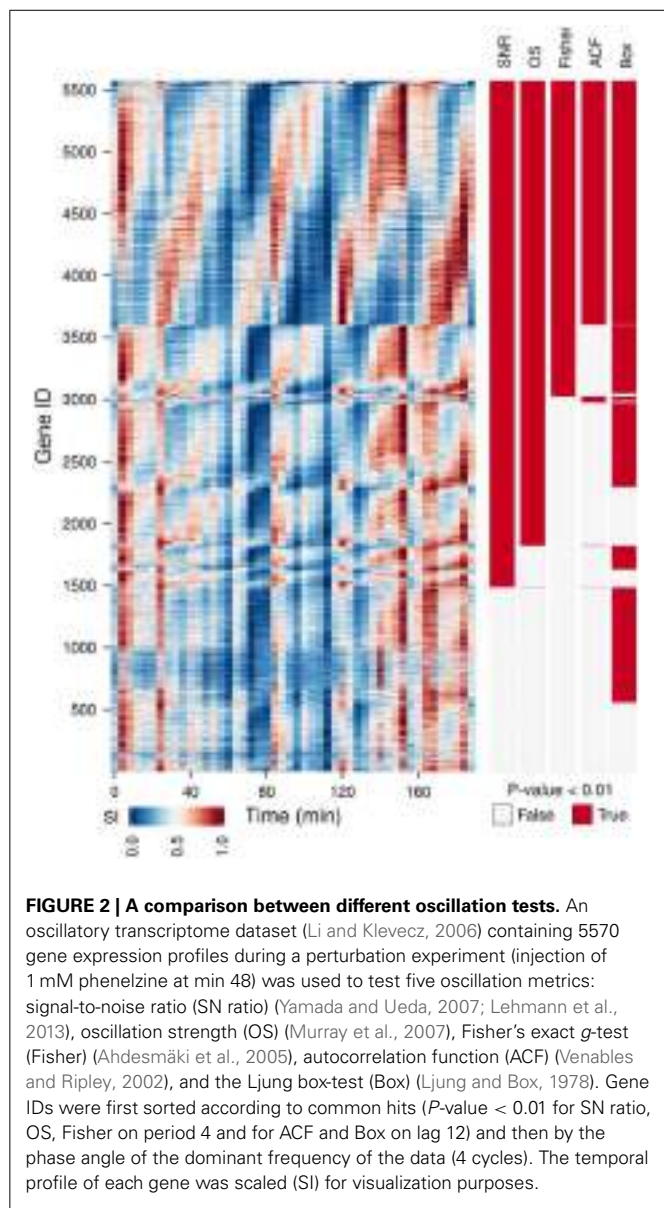
We used three published experimental datasets for this study. To illustrate the general uses of the algorithm, we used a highly oscillatory transcriptome (Affymetrix GeneChip®) experiment from metabolically synchronous continuous yeast cultures which were perturbed with the monoamine oxidase inhibitor, phenelzine (Li and Klevecz, 2006). This consisted of 4 oscillation cycles (48 samples, taken every 4 min) and was perturbed after 48 min (sample 12). As an example of a noisy dataset with unknown biological and technical peaks, we used a metabolome time-series, containing unidentified peaks, from similar metabolically synchronous cultures, comprising of 2 oscillation cycles (20 samples, taken every 4 min) that was not perturbed (Sasidharan et al., 2012b). Finally, we used a dataset with absolute quantified values, a set of propidium Iodide DNA stained flow cytometry yeast samples (Klevecz et al., 2004), which consisted of four unperturbed cycles (60 samples, taken every 2.5 min) and was aligned to the peaks observed at G<sub>1</sub> and G<sub>2</sub>. It is important to note that all the data shown here are raw and have not been normalized.

The distributions of these datasets (once zero and noisy low abundance measurements had been filtered) all approximated to a log normal distribution, thus we used the model-based approach for all analyses.

## RESULTS

### THE SN RATIO OUTPERFORMS OTHER TESTED OSCILLATION METRICS

We have tested the capabilities of 5 oscillation tests on a time-series microarray gene expression dataset (Li and Klevecz, 2006) containing 5570 gene expression profiles. A comparison between the oscillators with the main period of the dataset (4 cycles) detected (**Figure 2**, OS, SN ratio, Fisher's exact g-test, ACF, Box) shows a good agreement between methods for 35.8% of the genes, providing a gold standard for visualizing discrepancies between tests. As Fisher's exact g-test (the most conservative approach), SN and OS are based on similar methods, these provided the best agreement on the 4 cycle frequency. Fisher's exact g-test however only reports the dominant frequency in the dataset and was not useful for further characterization of multi-periodicity and period lengthening. OS and SN ratio detected major powers in profiles with strong multiperiodicities better. ACF failed to pick up clear oscillatory signals. Whereas, Ljung-Box analysis called many non-oscillatory time-series, probably due to the low amplitude, but significant 12 cycle frequency (**Figure 3**). Therefore, our algorithm was based on the SN ratio.



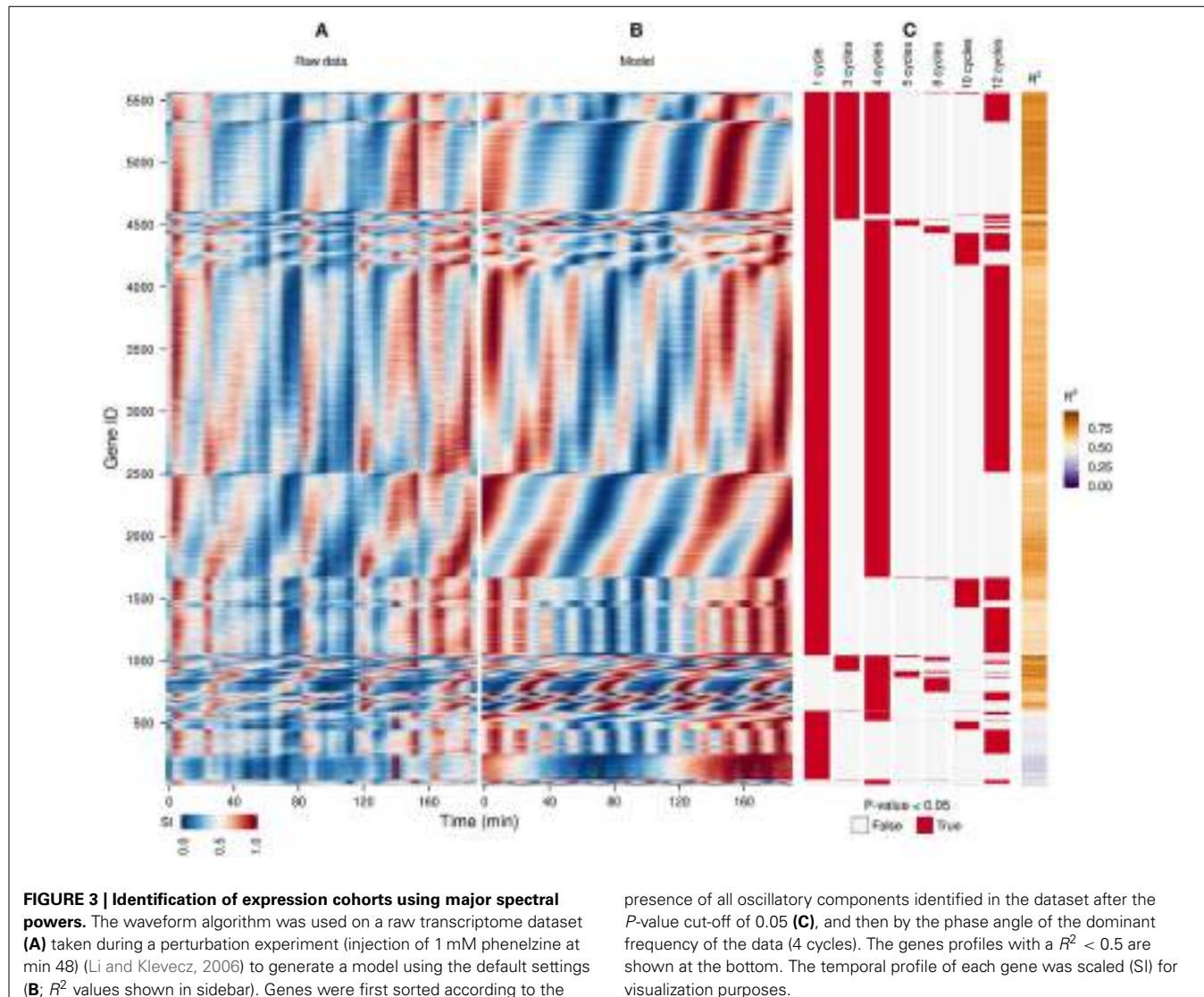
#### DETERMINATION OF FREQUENCIES AND PHASE RELATIONSHIPS DURING A PERTURBATION

A previous study of this gene expression dataset, which used the Fourier spectra for clustering (Machné and Murray, 2012) has successfully identified biologically-coherent clusters, but concentrated on characterizing the phase-relationship of gene expression with respect to the respiratory oscillation. However, the analysis of the dataset with the waveform algorithm, untargeted, with default parameters, indicated that several major frequencies occurred (1, 3, 4, 5, 8, 10 and 12 cycles, 91.3%, 21%, 79.4%, 2.2%, 4.5%, 10.2%, 54.3% genes, respectively). Visualization of cohorts obtained by grouping genes based on the presence of these periodicities in their filtered spectra and the  $R^2$  values pointed to components 1, 3–5 as sufficient to discriminate between the major expression patterns (Figure 3). To exemplify different responses to the perturbation, we selected 4 cohorts. The first one comprises

of genes who had no significant response to the drug (only significant frequency was 4 cycles; Figure 4A, 4.7% of genes), and was highly enriched in genes involved in cytosolic ribosomal assembly and sulfur amino acid processes (Table S1). Cohort 2 represents genes that had a significant response to the chemical perturbation, but did not show a strong increase or decrease in amplitude (significant 1 and 4 cycle, but not significant 3 and 5 cycle components; Figure 4B, 50% of genes). This cohort was enriched in translation (Table S1). Cohort 3 contained genes with significant 3 and 4 cycle components (Figure 4C; 20% of genes). The mRNA abundances of these genes were influenced by the period lengthening effects of the drug and show the intensities drop immediately after perturbation. However, they increase in intensity as the experiment progresses so that the final intensities on the perturbed long period cycles are higher than the initial cycle. Cohort 3 was highly enriched in mitochondrial and catabolic processes (Table S1). Cohort 4 comprised a combination of significant 4 and 5 cycles (Figure 4D; 2% of genes). The mRNA abundance of these genes showed a decrease in oscillation amplitude during the experiment's progression and the 5 cycle periodicity is due to the first 2 cycles which have higher amplitudes for these genes. Ontology enrichment showed that cohort 4 was primarily involved in anabolic processes, with the top 5 genes involved in the Arginine, Coenzyme A, and Histidine biosynthetic pathways. As 80% of the genes peak during the phase of high residual dissolved oxygen (Figure 4; gray dotted lines), the phase relationships between the cohorts was not evenly distributed. The maximum of cohort 1 was skewed toward the phase of low DO, cohort 2, representing the majority of the dataset (Li and Klevecz, 2006), peaked right after the transition between low and high DO, cohort 3 was almost exclusively expressed during the high DO phase and cohort 4 was skewed toward the end of the low DO phase. Further refinement of this classification based on the phase-angle of the main periodicity leads to similar results as the previous clustering-based approaches (Machné and Murray, 2012), exemplifying a way to significantly reduce the size of a dataset, in our case from 48 variables (time-points) to 5 (4 spectral components and the phase angle of the major component).

#### WAVEFORM ANALYSIS CAN EXTRACT INFORMATION FROM COMPLEX AND NOISY DATASETS

Hybridizations on microarrays produce data in which most of the signal should be biological in origin. However, mass spectrometry is much noisier, because many peaks are caused by environmental contamination, caused by column components or degradation. We analyzed a complex data matrix from a metabolomics study containing 2661 peaks (Sasidharan et al., 2012b) on which usual clustering could not easily discriminate between technical and biological signals (Figure 5A, left panel). We ran the waveform algorithm targeting the oscillation period (2 cycles,  $P$ -value cut-off 0.05), thus keeping only the peaks which had a significant 2-cycle component and removing all masking frequencies. The resulting waveforms, in which time-series with no significant 2-cycle components were reduced to flat signals, making the oscillators apparent throughout the dataset (Figure 5A, right panel), and after removing peaks with poor fit



( $P$ -value  $> 0.01$ ), 375 potential biological signals were identified (**Figure 5B**), demonstrating a quick and effective method for exploratory metabolomics.

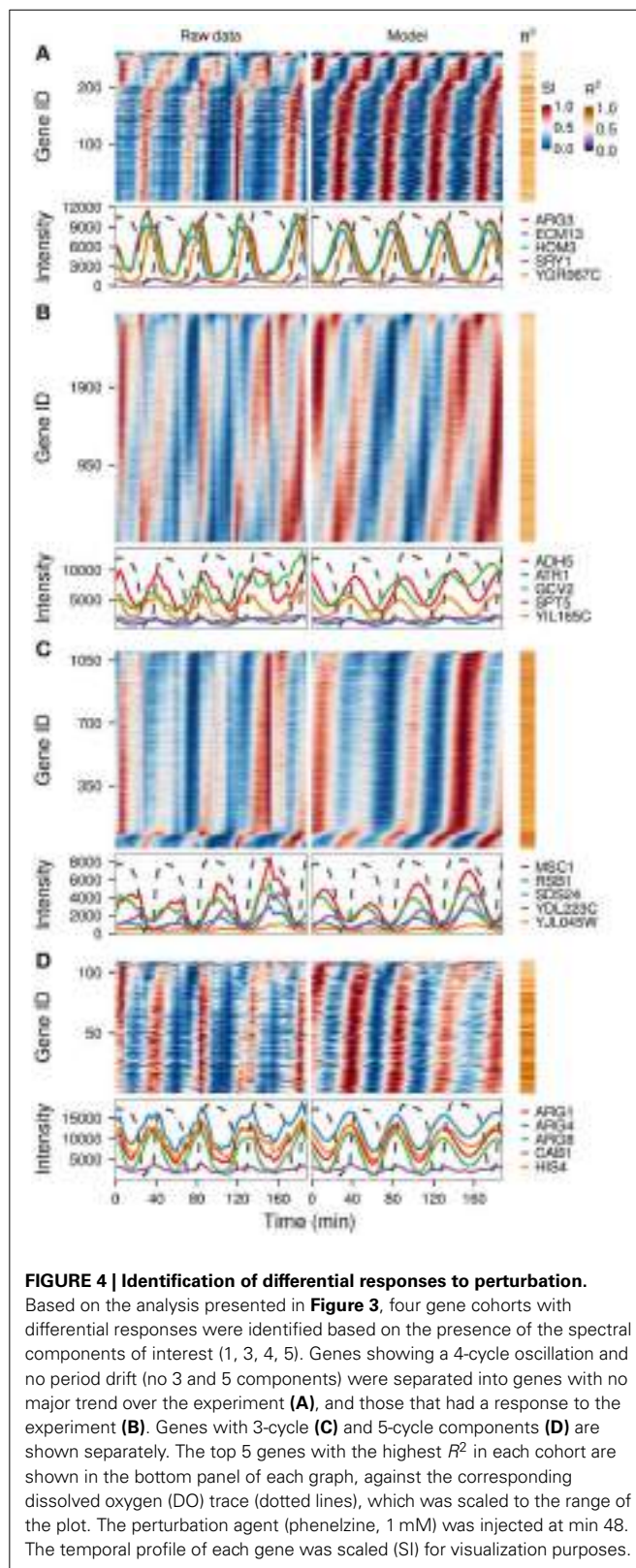
#### DATA PROCESSING WHILE PRESERVING PHASE ANGLES AND AMPLITUDES

The previous examples contained qualitative measurements, therefore amplitudes were relative values. To illustrate the use of Fourier decomposition in denoising data while preserving the temporal structure, we used a quantitative flow cytometry time-series dataset (**Figure 6A**) (Sasidharan et al., 2012a). The purpose of the analysis was to identify the phase-relationship, significance of oscillation and duration of the DNA division cycle. While subtracting the background (**Figure 6B**) already reveals the main patterns, information such as the precise timing of DNA replication with respect to the respiratory oscillation and the amplitude in the S-phase regions are not trivial to extract. The waveform model was used to accentuate the regions of interest by using an untargeted approach with the default parameters (**Figure 6C**).

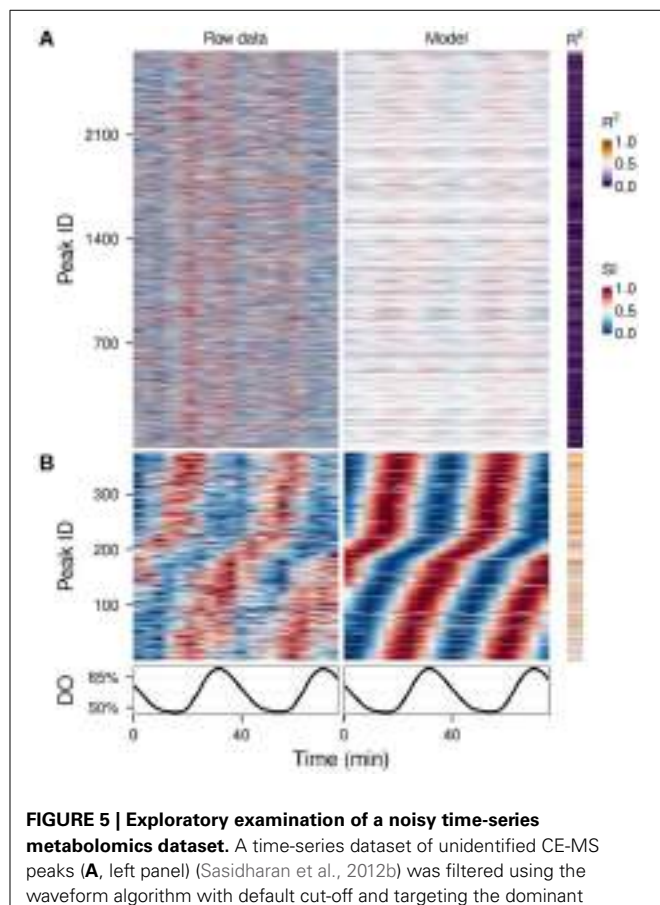
Interestingly, S-phase was shown to be a linear time series that continues throughout the respiratory cycle, starting during the phase where residual dissolved oxygen was lowest (**Figure 6E**), which was earlier than previously reported (Klevecz et al., 2004). This could only be observed when we filtered out the contaminating frequency components from the much larger G<sub>1</sub> and G<sub>2</sub> cell cycle phase peaks. This analysis may resolve observed differential timings of mid S-phase found for different oscillation periods (Slavov et al., 2011; Amarie et al., 2013).

#### DISCUSSION

We present a set of tools that can be used to dissect oscillatory data, with or without a perturbation. It can be used for any data matrix that is from an oscillatory system, such as transcriptomic, metabolomics, and proteomic, as well as other single or high-throughput measurements. We show its utility in highlighting biological processes such as S-phase (**Figure 6**), a separation of biologically relevant signals from noisy metabolomic data (**Figure 5**) and delineating perturbation effects



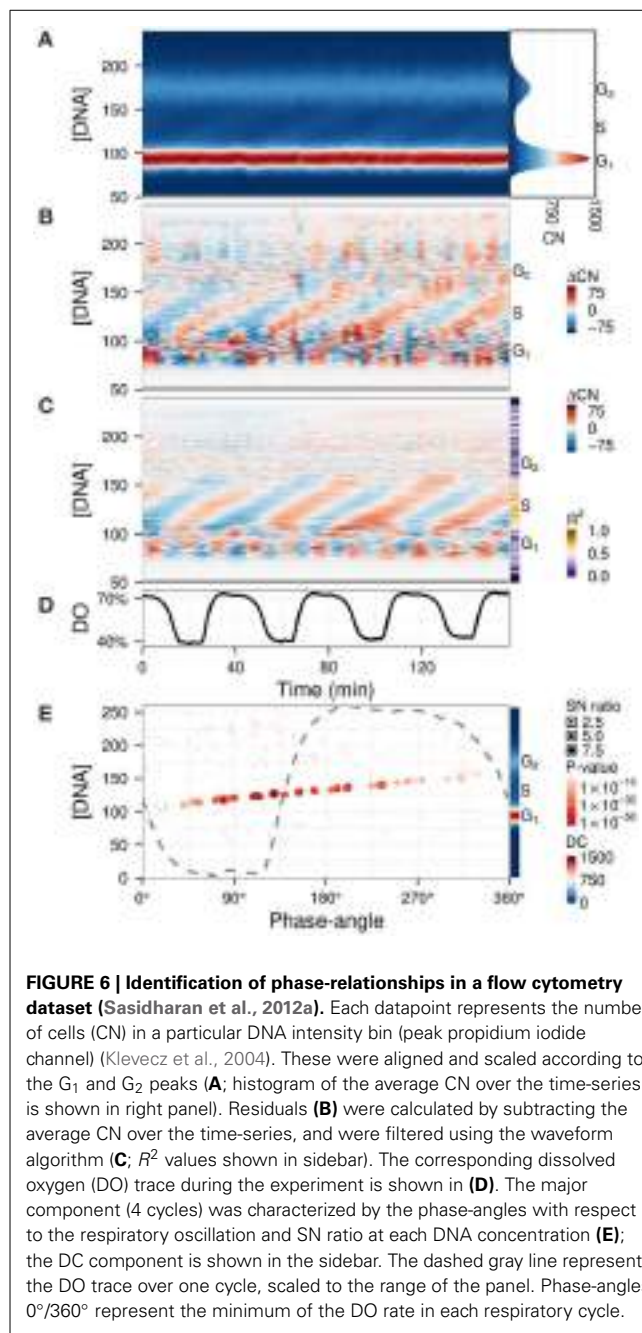
in a drug treatment experiment (**Figures 3, 4**). Additionally, analyses on this perturbation separated events spanning different time-scales, i.e., the long perturbation event (10 h) (Li and Klevecz, 2006), the oscillation (40 min) and sub-events that



may be related to changes in cofactor abundance (10–15 min) (Sasidharan et al., 2012c). For the yeast oscillatory system, it is relatively easy to cross-correlate time series taken in different laboratories, form different oscillation periods, using data taken months (or even years apart) by adjusting the phase angle with respect to a reference point on the residual dissolved oxygen data (Murray et al., 2003; Lloyd and Murray, 2007; Machné and Murray, 2012), thus opening up a wealth of data to the experimenter.

A common issue that arises when dealing with large datasets is the excessive requirements for computational power and memory for calculating distance matrices, which limits clustering methods. Filtering spectral components (**Figures 3, 4**) can be an effective way of reducing the complexity of the dataset before clustering. Indeed, the majority of the ontology enrichments previously observed by Machné and Murray (2012) were also reconstituted in the frequency analysis reported here.

Normalization of oscillatory time-series datasets is often a difficult task due to lack of an internal, biological set of non-oscillating references, and the steps taken can alter the data



structure significantly (Lehmann et al., 2013). If subjected to standard array-to-array normalization methods which include an alignment to the mean of individual arrays, the phase-angles of expression in **Figure 3** would be significantly skewed due to higher mRNA abundance in one phase of the respiratory oscillation. Even the seemingly noisy minor peaks that occur every 3–4 samples (the 12-cycle component which is found in over half of the transcripts) may be biological, as they coincide with the triphasic patterns of NAD(P)H fluorescence occurring during the yeast respiratory oscillation (Sasidharan et al., 2012c). Furthermore, attempting to normalize the metabolite dataset in **Figure 5** using internal standards deteriorated the 2-cycle

oscillatory signal, indicating that biological signals were less noisy than the external controls. Therefore, aggressive normalization of such periodic data should generally be avoided. However, when normalization is necessary, the presented algorithm can be used to identify a subset of least-oscillatory biological features on which normalization can be carried out, and the fitting parameters thus obtained can then be used to normalize the rest of the dataset, while preserving its temporal profile (Calza et al., 2008; Machné and Murray, 2012).

The methods presented here can readily be used to analyse short time-series data taken in triplicates, by concatenating the triplicate series to obtain a pseudo-waveform spanning 3 “pseudo-cycles.” However, one prerequisite and major limitation for general Fourier based approaches is that the analyzed dataset must be sampled at equal time intervals. If the time-series in question has uneven sample times (e.g., 0, 5, 15, 30, 60, 120, 480 min) it may still be possible to utilize the algorithm on the pseudo-waveform constructed from the triplicates, by applying the appropriate data window to adjust the monotonically increasing or decreasing profiles (such as Hamming or Hanning (Oppenheim et al., 1999); already implemented in the waveform package), as these are prone to spectral leakage (Lyon, 2009). The resulting data would then be readjusted to the original timing. Thus, future developments of the algorithm will be its application to certain non-oscillatory and non-equally sampled datasets.

## ACKNOWLEDGMENTS

We are grateful to Yamagata prefecture and Tsuruoka city for their financial support of the project. We are also indebted to Rainer Machné, Kalesh Sasidharan, Kazutaka Ikeda, Maki Sugawara, and Hiroko Ueda for their advice and technical assistance. Cornelia Amarie was funded in-part by the General Center of Excellence (GCOE), the Taikichiro Mori Memorial Research Grant and the Monbukagakusho Honors Scholarship. Douglas B. Murray was funded, in-part by a grant-in-aid from the Japan Society for the Promotion of Science and the Japan Science & Technology Agency.

## SUPPLEMENTARY MATERIAL

The Supplementary Material for this article can be found online at: <http://www.frontiersin.org/journal/10.3389/fcell.2014.00040/abstract>

**Supplementary R package:** waveform\_1.0.1.tar.gz.

**Table S1 | The gene ontology enrichment for Figure 4.** For GO ontology analysis, the genes in each cohort identified in **Figure 4** out of the 5570 genes contained by the dataset were checked for enrichment using the package GOSTats (Falcon and Gentleman, 2007).

## REFERENCES

- Ahdessmäki, M., Lähdesmäki, H., Pearson, R., Huttunen, H., and Yli-Harja, O. (2005). Robust detection of periodic time series measured from biological systems. *BMC Bioinformatics* 6:117. doi: 10.1186/1471-2105-6-117
- Alter, O., Brown, P. O., and Botstein, D. (2003). Generalized singular value decomposition for comparative analysis of genome-scale expression data sets of two different organisms. *Proc. Natl. Acad. Sci. U.S.A.* 100, 3351–3356. doi: 10.1073/pnas.0530258100

- Amarie, C., Machné, R., Sasidharan, K., Gottstein, W., Tomita, M., Soga, T., et al. (2013). The dynamics of cellular energetics during continuous yeast culture. *Conf. Proc. Annu. Int. Conf. IEEE Eng. Med. Biol. Soc.* 2013, 2708–2711. doi: 10.1109/EMBC.2013.610099
- Aon, M. A., Cortassa, S., and O'Rourke, B. (2004). Percolation and criticality in a mitochondrial network. *Proc. Natl. Acad. Sci. U.S.A.* 101, 4447–4452. doi: 10.1073/pnas.0307156101
- Aon, M. A., Roussel, M. R., Cortassa, S., O'Rourke, B., Murray, D. B., Beckmann, M., et al. (2008). The scale-free dynamics of eukaryotic cells. *PLoS ONE* 3:e3624. doi: 10.1371/journal.pone.0003624
- Calza, S., Valentini, D., and Pawitan, Y. (2008). Normalization of oligonucleotide arrays based on the least-variant set of genes. *BMC Bioinformatics* 9:140. doi: 10.1186/1471-2105-9-140
- de Lichtenberg, U., Jensen, L. J., Fausbøll, A., Jensen, T. S., Bork, P., and Brunak, S. (2005). Comparison of computational methods for the identification of cell cycle-regulated genes. *Bioinformatics* 21, 1164–1171. doi: 10.1093/bioinformatics/bti093
- Dowse, H. B. (2007). Statistical analysis of biological rhythm data. *Methods Mol. Biol.* 362, 29–45. doi: 10.1007/978-1-59745-257-1\_2
- Falcon, S., and Gentleman, R. (2007). Using GOSTats to test gene lists for GO term association. *Bioinformatics* 23, 257–258. doi: 10.1093/bioinformatics/btl567
- Gibbison, B., Angelini, G. D., and Lightman, S. L. (2013). Dynamic output and control of the hypothalamic-pituitary-adrenal axis in critical illness and major surgery. *Br. J. Anaesth.* 111, 347–360. doi: 10.1093/bja/aet077
- Johnson, C. H., and Egli, M. (2014). Metabolic compensation and circadian resilience in prokaryotic cyanobacteria. *Annu. Rev. Biochem.* 83, 221–247. doi: 10.1146/annurev-biochem-060713-035632
- Kageyama, R., Niwa, Y., Isomura, A., González, A., and Harima, Y. (2012). Oscillatory gene expression and somitogenesis. *Wiley Interdiscip. Rev. Dev. Biol.* 1, 629–641. doi: 10.1002/wdev.46
- Klevecz, R. R., Bolen, J., Forrest, G., and Murray, D. B. (2004). A genomewide oscillation in transcription gates DNA replication and cell cycle. *Proc. Natl. Acad. Sci. U.S.A.* 101, 1200–1205. doi: 10.1073/pnas.0306490101
- Klevecz, R. R., and Li, C. M. (2007). Evolution of the clock from yeast to man by period-doubling folds in the cellular oscillator. *Cold Spring Harb. Symp. Quant. Biol.* 72, 421–429. doi: 10.1101/sqb.2007.72.040
- Klevecz, R. R., and Murray, D. B. (2001). Genome wide oscillations in expression. Wavelet analysis of time series data from yeast expression arrays uncovers the dynamic architecture of phenotype. *Mol. Biol. Rep.* 28, 73–82. doi: 10.1023/A:1017909012215
- Kyriacou, C. P. (2009). Clocks, cryptochromes and Monarch migrations. *J. Biol.* 8, 55. doi: 10.1186/jbiol153
- Lehmann, R., Machné, R., Georg, J., Benary, M., Axmann, I., and Steuer, R. (2013). How cyanobacteria pose new problems to old methods: challenges in microarray time series analysis. *BMC Bioinformatics* 14:133. doi: 10.1186/1471-2105-14-133
- Levine, J. H., Lin, Y., and Elowitz, M. B. (2013). Functional roles of pulsing in genetic circuits. *Science* 342, 1193–1200. doi: 10.1126/science.123999
- Li, C. M., and Klevecz, R. R. (2006). A rapid genome-scale response of the transcriptional oscillator to perturbation reveals a period-doubling path to phenotypic change. *Proc. Natl. Acad. Sci. U.S.A.* 103, 16254–16259. doi: 10.1073/pnas.0604860103
- Ljung, G. M., and Box, G. E. P. (1978). On a measure of lack of fit in time series models. *Biometrika* 65, 297–303. doi: 10.1093/biomet/65.2.297
- Lloyd, D. (2008). “Intracellular time keeping: epigenetic oscillations reveal the functions of an ultradian clock,” in *Ultradian Rhythms from Molecules to Mind*, eds. D. Lloyd and E. L. Rossi (Dordrecht: Springer), 5–22.
- Lloyd, D., Aon, M. A., and Cortassa, S. (2001). Why homeodynamics, not homeostasis? *ScientificWorldJournal* 1, 133–145. doi: 10.1100/tsw.2001.20
- Lloyd, D., and Murray, D. B. (2005). Ultradian metronome: timekeeper for orchestration of cellular coherence. *Trends Biochem. Sci.* 30, 373–377. doi: 10.1016/j.tibs.2005.05.005
- Lloyd, D., and Murray, D. B. (2006). The temporal architecture of eukaryotic growth. *FEBS Lett.* 580, 2830–2835. doi: 10.1016/j.febslet.2006.02.066
- Lloyd, D., and Murray, D. B. (2007). Redox rhythmicity: clocks at the core of temporal coherence. *Bioessays* 29, 465–473. doi: 10.1002/bies.20575
- Lyon, D. A. (2009). The discrete fourier transform, part 4: spectral leakage. *J. Object Technol.* 8, 23–34. doi: 10.5381/jot.2009.8.7.c2
- Machné, R., and Murray, D. B. (2012). The yin and yang of yeast transcription: elements of a global feedback system between metabolism and chromatin. *PLoS ONE* 7:e37906. doi: 10.1371/journal.pone.0037906
- Murray, D. B., Beckmann, M., and Kitano, H. (2007). Regulation of yeast oscillatory dynamics. *Proc. Natl. Acad. Sci. U.S.A.* 104, 2241–2246. doi: 10.1073/pnas.0606677104
- Murray, D. B., Klevecz, R. R., and Lloyd, D. (2003). Generation and maintenance of synchrony in *Saccharomyces cerevisiae* continuous culture. *Exp. Cell Res.* 287, 10–15. doi: 10.1016/S0014-4827(03)00068-5
- Murtagh, F. (1985). *Multidimensional Clustering Algorithms*. COMPSTAT Lectures 4. Wuerzburg: Physica-Verlag.
- Oppenheim, A. V., Schafer, R. W., and Buck, J. R. (1999). *Discrete Time Signal Processing*. New Jersey: Prentice Hall.
- Prasad, S., and Bruce, L. M. (2008). Limitations of principal components analysis for hyperspectral target recognition. *IEEE Geosci. Remote Sens. Lett.* 5, 625–629. doi: 10.1109/LGRS.2008.2001282
- Raychaudhuri, S., Stuart, J. M., and Altman, R. B. (2000). Principal components analysis to summarize microarray experiments: application to sporulation time series. *Pac. Symp. Biocomput.* 455–66.
- Salgado, E., Murray, D. B., and Lloyd, D. (2002). Some antidepressant agents (Li+, monoamine oxidase type A inhibitors) perturb the ultradian clock in *Saccharomyces cerevisiae*. *Biol. Rhythm Res.* 33, 351–361. doi: 10.1076/brhm.33.3.351.8256
- Salomon, R. M., and Cowan, R. L. (2013). Oscillatory serotonin function in depression. *Synapse* 67, 801–820. doi: 10.1002/syn.21675
- Salvatore, P., Indic, P., Murray, G., and Baldessarini, R. J. (2012). Biological rhythms and mood disorders. *Dialogues Clin. Neurosci.* 14, 369–379.
- Sasidharan, K., Amarie, C., Tomita, M., and Murray, D. B. (2012a). Rapid DNA, RNA and protein extraction protocols optimized for slow continuously growing yeast cultures. *Yeast* 29, 311–322. doi: 10.1002/yea.2911
- Sasidharan, K., Soga, T., Tomita, M., and Murray, D. B. (2012b). A yeast metabolite extraction protocol optimised for time-series analyses. *PLoS ONE* 7:e44283. doi: 10.1371/journal.pone.0044283
- Sasidharan, K., Tomita, M., Aon, M., Lloyd, D., and Murray, D. B. (2012c). Time-structure of the yeast metabolism *in vivo*. *Adv. Exp. Med. Biol.* 736, 359–379. doi: 10.1007/978-1-4419-7210-1\_21
- Singleton, R. (1969). An algorithm for computing the mixed radix fast Fourier transform. *IEEE Trans. Audio Electroacoust.* 17, 93–103. doi: 10.1109/TAU.1969.1162042
- Slavov, N., Macinskis, J., Caudy, A., and Botstein, D. (2011). Metabolic cycling without cell division cycling in respiring yeast. *Proc. Natl. Acad. Sci. U.S.A.* 108, 19090–19095. doi: 10.1073/pnas.1116998108
- Sobie, E. A. (2011). Bistability in biochemical signaling models. *Sci. Signal.* 4, tr10. doi: 10.1126/scisignal.2001964
- Song, J. Z., Duan, K. M., Ware, T., and Surette, M. (2007). The wavelet-based cluster analysis for temporal gene expression data. *EURASIP J. Bioinform. Syst. Biol.* 2007, 39382. doi: 10.1155/2007/39382
- Strimmer, K. (2008). fdrttool: a versatile R package for estimating local and tail area-based false discovery rates. *Bioinformatics* 24, 1461–1462. doi: 10.1093/bioinformatics/btn209
- Team, R. D. C. (2008). *R: A Language and Environment for Statistical Computing*. Available at: <http://www.r-project.org>.
- Venables, W. N., and Ripley, B. D. (2002). *Modern Applied Statistics with S*, 4th Edn. New York, NY: Springer. doi: 10.1007/978-0-387-21706-2
- Wang, D., Arapostathis, A., Wilke, C. O., and Markey, M. K. (2012). Principal-oscillation-pattern analysis of gene expression. *PLoS ONE* 7:e28805. doi: 10.1371/journal.pone.0028805
- Ward, J. H. (1963). Hierarchical grouping to optimize an objective function. *J. Am. Stat. Assoc.* 58, 236–244. doi: 10.1080/01621459.1963.1050845

Yamada, R., and Ueda, H. R. (2007). Microarrays: statistical methods for circadian rhythms. *Methods Mol. Biol.* 362, 245–264. doi: 10.1007/978-1-59745-257-1\_17

**Conflict of Interest Statement:** The authors declare that the research was conducted in the absence of any commercial or financial relationships that could be construed as a potential conflict of interest.

Received: 13 June 2014; paper pending published: 13 July 2014; accepted: 31 July 2014; published online: 19 August 2014.

Citation: Amarie C, Tomita M and Murray DB (2014) Quantifying periodicity in omics data. *Front. Cell Dev. Biol.* 2:40. doi: 10.3389/fcell.2014.00040

This article was submitted to Systems Biology, a section of the journal *Frontiers in Cell and Developmental Biology*.

Copyright © 2014 Amarie, Tomita and Murray. This is an open-access article distributed under the terms of the Creative Commons Attribution License (CC BY). The use, distribution or reproduction in other forums is permitted, provided the original author(s) or licensor are credited and that the original publication in this journal is cited, in accordance with accepted academic practice. No use, distribution or reproduction is permitted which does not comply with these terms.



# Estimating cellular parameters through optimization procedures: elementary principles and applications

**Akatsuki Kimura<sup>1,2,3\*</sup>, Antonio Celani<sup>4</sup>, Hiromichi Nagao<sup>3,5,6</sup>, Timothy Stasevich<sup>7</sup> and Kazuyuki Nakamura<sup>8</sup>**

<sup>1</sup> Cell Architecture Laboratory, National Institute of Genetics, Mishima, Japan

<sup>2</sup> Department of Genetics, School of Life Science, SOKENDAI (The Graduate University for Advanced Studies), Mishima, Japan

<sup>3</sup> Transdisciplinary Research Integration Center and Data Centric Science Research Commons, Research Organization of Information and Systems, Tokyo, Japan

<sup>4</sup> Quantitative Life Sciences Unit, The Abdus Salam International Centre for Theoretical Physics, Trieste, Italy

<sup>5</sup> Research and Development Center for Data Assimilation, The Institute of Statistical Mathematics, Tokyo, Japan

<sup>6</sup> Research Center for Large-Scale Earthquake, Tsunami and Disaster, Earthquake Research Institute, The University of Tokyo, Tokyo, Japan

<sup>7</sup> Department of Biochemistry and Molecular Biology, Colorado State University, Fort Collins, CO, USA

<sup>8</sup> Department of Mathematical Sciences Based on Modeling and Analysis, School of Interdisciplinary Mathematical Sciences, Meiji University, Tokyo, Japan

**Edited by:**

Tetsuya J. Kobayashi, The University of Tokyo, Japan

**Reviewed by:**

Panagiota T. Fotinou, The Johns Hopkins University, USA

Yuki Tsukada, Nagoya University, Japan

Ryo Yoshida, The Institute of Statistical Mathematics, Japan

**\*Correspondence:**

Akatsuki Kimura, Cell Architecture Laboratory, Structural Biology Center, National Institute of Genetics, Yata 1111, Mishima 411-8540, Japan  
e-mail: akimura@nig.ac.jp

Construction of quantitative models is a primary goal of quantitative biology, which aims to understand cellular and organismal phenomena in a quantitative manner. In this article, we introduce optimization procedures to search for parameters in a quantitative model that can reproduce experimental data. The aim of optimization is to minimize the sum of squared errors (SSE) in a prediction or to maximize likelihood. A (local) maximum of likelihood or (local) minimum of the SSE can efficiently be identified using gradient approaches. Addition of a stochastic process enables us to identify the global maximum/minimum without becoming trapped in local maxima/minima. Sampling approaches take advantage of increasing computational power to test numerous sets of parameters in order to determine the optimum set. By combining Bayesian inference with gradient or sampling approaches, we can estimate both the optimum parameters and the form of the likelihood function related to the parameters. Finally, we introduce four examples of research that utilize parameter optimization to obtain biological insights from quantified data: transcriptional regulation, bacterial chemotaxis, morphogenesis, and cell cycle regulation. With practical knowledge of parameter optimization, cell and developmental biologists can develop realistic models that reproduce their observations and thus, obtain mechanistic insights into phenomena of interest.

**Keywords:** quantitative modeling, parameter optimization, model selection, likelihood, probability density function

## INTRODUCTION: REGRESSION ANALYSES FOR IDENTIFYING PARAMETER VALUES BY APPLYING EXPERIMENTAL DATA TO A QUANTITATIVE MODEL

The purpose of quantitative biology is to achieve biological discovery through quantitative data analyses and modeling. A quantitative model consists of a set of rules, often expressed by mathematical formulas, which involve a set of parameters governing variables for the rules and initial/boundary conditions. The simplest way to validate a given quantitative model is to test whether an appropriate set of rules and parameters reproduces experimental observations. If it does this successfully, it can be concluded that the model (i.e., the rules and parameter values) is “sufficient” to explain the observations. However, in many cases, we do not have information on the “appropriate parameters.” In such cases, we may want to identify a set of parameters that adequately explains the experimental observations under the stated rules. If the rules adequately represent the true mechanisms underlying the biological process, the identified parameters should reflect the quantitative properties of that process. In this way, we can argue that the model (i.e., the rules

and the “estimated” parameter values) is sufficient to explain the observations. The method for estimating parameters by fitting a given quantitative model to the observed data is called regression, and the overall workflow is comprehensively reviewed in Jaqaman and Danuser (2006). In this article, we focus on several practical procedures for identification of parameters and introduce recent applications of regression for characterization of cellular processes.

## SUM OF SQUARED ERRORS (SSE) OF PREDICTION AND LIKELIHOOD AS INDICES OF PARAMETER OPTIMIZATION

Minimization of the SSE and maximization of likelihood (abbreviated as “LS” and “ML,” respectively, in Jaqaman and Danuser, 2006) are the two most common regression schemes. We first review SSE and likelihood before explaining the methods for minimizing/maximizing these indices in Sections Minimization of SSE and Maximization of Likelihood. Minimization of SSE has been widely used as a simple and straightforward method to obtain an optimum parameter set. However, SSE does not provide further information, such as the uncertainty of the determined

parameter values. In contrast, likelihood, which is a powerful concept that covers the shortcomings of SSE, is capable of estimating both an optimum parameter set and a probability density function (PDF) related to the parameters, taking experimental error and the imperfections of the model into account. We sometimes encounter a problem in selecting an optimum model from among candidate models that contain different numbers of parameters. In Section Model selection Using Likelihood, we introduce information criteria, which enable us to solve this problem when used in combination with likelihood.

### MINIMIZATION OF SSE

Linear regression is the most familiar example of regression (Bremer and Doerge, 2010). When an obvious linear correlation is identified between two variables through a regression analysis (e.g.,  $X$  and  $Y$  in **Figure 1A**), we can assume a model, formulated as  $Y = a_0 + a_1 X$ , that describes the relationship between the variables. To identify the parameters of the model (i.e.,  $a_0$  and  $a_1$ ) that reproduce the experimental observations, a least-square method is frequently used (Bremer and Doerge, 2010). In this method, we define an evaluation function that sums the squared distance between the experimental data and the model with a given set of parameters. The SSE, which is defined as  $SSE = \sum_{i=1}^n [y_i - (a_0 + a_1 x_i)]^2$ , where  $n$  is the number of data points and  $(x_i, y_i)$  ( $i = 1, \dots, n$ ) are the data, is commonly used as an index for the least-squares method. Parameters that minimize the evaluation function are the optimum parameters, in the sense that they minimize the discrepancy between the model and the experimental results.

As a biological example of linear regression, we have demonstrated that there is a correlation between the cell size and the extent and speed of the elongation of the mitotic spindle in *Caenorhabditis elegans* embryos (Hara and Kimura, 2009). In this study, we further demonstrated that the elongation of the mitotic spindle depends on cell size by showing that the elongation of the mitotic spindle increased when we increased the cell size.

As another example, let us consider the motion of a particle inside a cell (**Figure 1B**). If the motion is driven by random Brownian forces, the mean square displacement (MSD) is linearly

proportional to the time lag ( $\tau$ ) (i.e.,  $MSD \propto \tau^1$ ) (Berg, 1993). The motion of a particle inside a cell is rarely random because it is confined to a crowded space. The MSD decreases, and such motion is called “sub-diffusion” (i.e.,  $MSD \propto \tau^\alpha, \alpha < 1$ ) (Saxton and Jacobson, 1997). In other cases, the particle may be moved by directional flow, and thus will be moved further than it would by random diffusion (i.e.,  $MSD \propto \tau^\alpha, \alpha > 1$ ). If we could estimate the value of  $\alpha$  in the  $MSD$ -vs.- $\tau$  plot, we would be able to determine whether the motion is better explained by random Brownian diffusion, sub-diffusion, or directed flow. To estimate  $\alpha$ , a log-log plot is useful (**Figure 1C**). In the log-log plot, i.e.,  $(\log MSD) = \alpha(\log \tau) + (\log C)$ ,  $\alpha$  is the slope and  $(\log C)$  is the intercept of the line. Therefore, using the above-mentioned linear regression analysis, we can identify the value of  $\alpha$  that minimizes SSE in the  $(\log MSD)$ -vs.- $(\log \tau)$  plot.

Such linear regression analysis of a double logarithmic plot is useful in characterizing how cellular parameters affect each other. We quantified the shape of mitotic spindles in *C. elegans* embryos and found a relationship described by  $SW = 1.5 \times P^{0.36} \times HL^{0.58}$ , where  $SW$  and  $HL$  are the width and hypotenuse length of the spindles and  $P$  is the ploidy of the embryos. Based on this formulation, we were able to propose a physical model that explains spindle shape (Hara and Kimura, 2013).

Minimization of SSE is applicable to both linear relationships and a variety of estimations. Because SSE is defined as the sum of the squared difference between the value estimated using the model and the actual observations, the value can be defined for any type of quantitative model. For example, in fluorescence recovery after photobleaching (FRAP) experiments, the recovery curve for the fluorescence intensity of the region where the fluorescent molecules were bleached can be modeled as an exponential curve, with its gradient reflecting the diffusion constant of the molecule (Axelrod et al., 1976). By identifying the parameter that minimizes the SSE between exponential curves and the experimental data for fluorescence intensity, one can estimate the diffusion constant of the molecule.

### MAXIMIZATION OF LIKELIHOOD

The simplicity of the SSE, which is a straightforward index for the discrepancy between a given model and the observations,

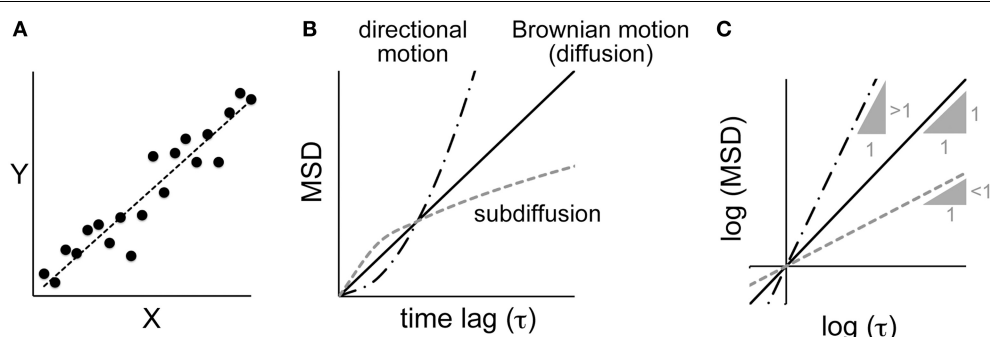


**FIGURE 1 | Correlation analyses between parameters.** (A) A linear correlation and linear regression.  $X$  and  $Y$  are two parameters of a dataset. Plotting the values of  $Y$  against  $X$  shows a correlation between the parameters, and the extent of that correlation can be calculated by regression analysis. (B) The relationship between the mean square displacement (MSD) and the time

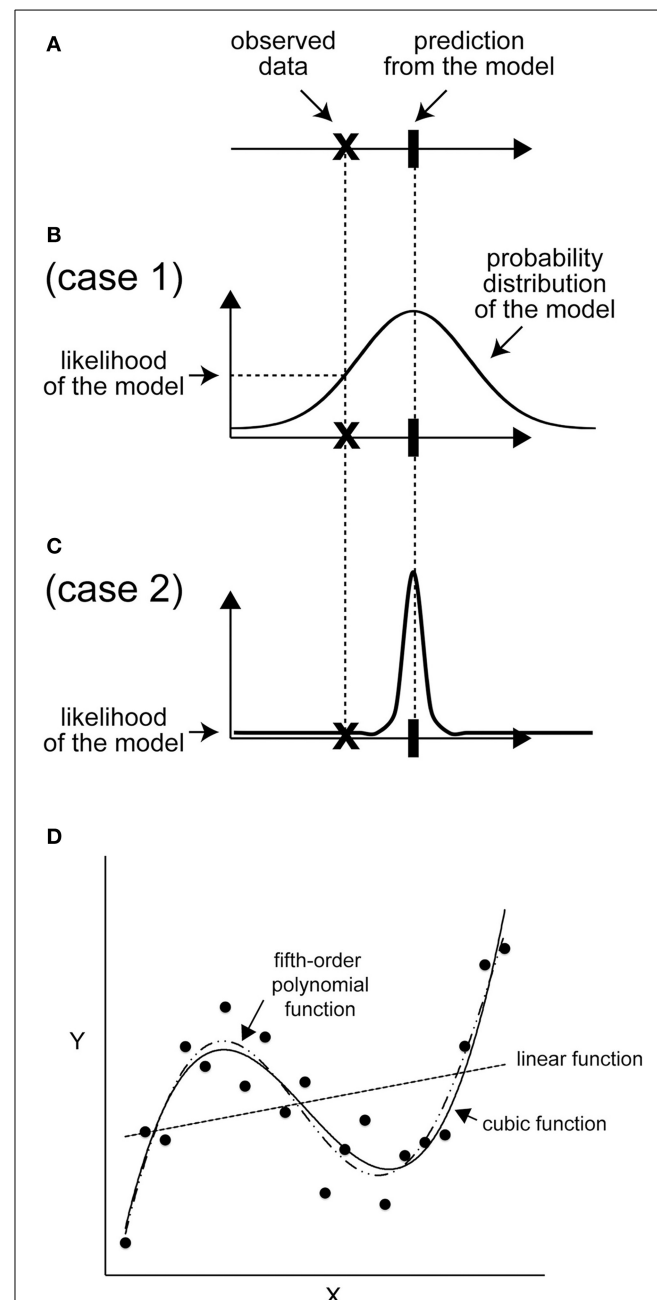
lag for various modes of motion (see text for details). (C) The same plot as shown in (B), except using logarithmic values. The three lines correspond to the different modes of motion in (B). For Brownian motion, the slope of the log-log plot is one. For directional motion and sub-diffusion, the log-log plots yield a linear relationship with a slope greater than one and less than one, respectively.

sometimes causes difficulties in real data analyses. Suppose that, for example, a phenomenon of interest is characterized by parameters having different physical dimensions (e.g., length and weight). How can we compute the sum of errors in different dimensions? In such a case, the observational data should be converted to dimensionless quantities through standardization of each type of data. Likelihood is another important index to evaluate how well a given model agrees with experimental results. Since the definition of likelihood naturally converts the observational data into dimensionless data, usage of likelihood can, unlike SSE, avoid the difficulty mentioned above. One of the major advantages of likelihood over SSE is that we can obtain both an optimum parameter set and a PDF related to the parameters. The obtained PDF provides valuable information not only of an optimum value for each parameter but also of its uncertainty due to errors contained in the observational data and the imperfections of the given model.

Let us consider a situation in which 1.1 is the experimental value ( $x$ ), while a given model predicts that  $x$  should be 1.0 (Figure 2A). How good is this model? (In other words, how “likely” is this model to describe the experimental result?) A conditional PDF related to an experimental value when results of the model are given is required to calculate the likelihood; a single value, such as a mean value, is insufficient. Suppose that we conduct simulations many times, and obtain results that follow a normal distribution with a mean ( $\mu$ ) of 1.0 ( $\sigma$ ) of 1.0. The likelihood ( $L$ ) indicates, roughly, the probability that the model yields the experimental value. For our current example, the likelihood is  $L = (2\pi\sigma^2)^{-1/2} \exp[-(x - \mu)^2/2\sigma^2] = 0.4$ , where the experimental value is 1.1 (Bishop, 2006; Kitagawa, 2010). If we had independently observed multiple experimental data points  $\{x_1, x_2, \dots, x_n\}$  for  $x$ , the likelihood of the dataset is given as a product of the likelihood of each data point, i.e.,  $L = \prod_{i=1}^n L_i$ . Often, we use log-likelihood,  $l = \ln L$ ; thus, the total log-likelihood of the model can be shown as  $l = \ln (\prod_{i=1}^n L_i) = \sum_{i=1}^n l_i$ . The likelihood  $L$ , or the log-likelihood  $l$ , is originally an indicator of how likely the obtained experimental data are, based on a model with a given parameter set. The larger the likelihood or log-likelihood, the better the model reproduces the observation. In the example shown in Figure 2, even when the distance between the observation and the mode of each likelihood function, i.e., the best observation that attains the likelihood function maximum, is equal for candidate models, we can reasonably select a model that has a broad likelihood function as the better model (Figures 2B,C). In turn, the parameter set that maximizes  $L$  or  $l$  is considered to be optimum to explain the experimental data. This method for estimating the optimum parameters is called the “maximum likelihood method.”

#### MODEL SELECTION USING LIKELIHOOD

When we wish to evaluate the validity of a model, a straightforward approach is to test whether the model can predict unknown data sets. Cross-validation and bootstrap methods are examples of such strategies (Hastie et al., 2009). As another strategy, we can select good models using likelihood as the index, just as we select good parameter values using likelihood. For example, suppose that the growth rate of a cell is found to increase when



	fitting with		
	linear	cubic	fifth-order polynomial
residual sum of squares	370	67	61
optimum variance	18	3.4	3.0
AIC	121	91	93

**FIGURE 2 | Likelihood: the distribution is important.** (A) An example of the mean of predicted values and observed data points. (B) If the distribution of the predicted values of the model is broad, the likelihood of the model is high because the probability of observing the data is high.

(Continued)

**FIGURE 2 | Continued**

**(C)** In contrast, if the distribution of the predicted value is narrow, the likelihood will be low. **(D)** An example of AIC calculation. Black dots represent an imaginary set of observed data. For  $x = 1, 2, 3, \dots, 20$ , the  $y$  value was calculated according to  $y = 0.025 \times (x - 3)(x - 10)(x - 17) + 10$ , and a Gaussian noise correction with a variance of four was added to each  $y$  value. Next, we calculated the best-fit linear, cubic, and fifth-order polynomial functions for the 20 data points.  $I_{\max} = -(n/2) \times \ln(2\pi\sigma^2) - (1/2\sigma^2) \times \sum_{i=1}^n [y_i - y_{\text{model}}(x_i)]^2$ , where  $n$  is the number of data points ( $n = 20$ ),  $\sigma^2$  is the variance of the model, and  $y_i$  and  $y_{\text{model}}(x_i)$  are observed and model values, respectively, at  $x = x_i$ . The sum of squared residuals is  $\sum_{i=1}^n [y_i - y_{\text{model}}(x_i)]^2$ . AIC is calculated as  $\text{AIC} = 2k - 2I_{\max}$ , where  $k$  is the number of free parameters in the model and is 3, 5, and 7 for linear, cubic, and fifth-order functions, respectively. Note that the variance of each model is also a free parameter to be optimized.

gene  $X$  is mutated, and that a theoretical framework that explains the growth rate of wild-type cells exists. The model selection procedure enables us to determine a better model among candidates: model 1, gene  $X$  affects one parameter (e.g., protein production rate); or model 2, gene  $X$  affects two parameters (e.g., protein production rate and RNA production rate).

We often have to consider selecting the best model among models that contain different numbers of parameters. In general, a model that contains more parameters tends to attain larger likelihood since it easily fits to observed data. However, the use of too many parameters leads to overfitting, in which the model loses predictability despite fitting well to observations.

To select a model that fits well to observed data and minimizes the number of parameters to avoid overfitting, the Akaike information criterion (AIC) is widely accepted in various fields of science (Akaike, 1974). The AIC is theoretically derived to be  $\text{AIC} = -2I_{\max} + 2k$ , where  $k$  is the number of free parameters in the model and  $I_{\max}$  is the maximum log-likelihood. The model with the smallest AIC is selected as the best one. The Bayesian information criterion (BIC) is another index used for model selection. BIC is slightly different from the AIC in the additional term, which penalizes the number of parameters more severely than the AIC (Jaqaman and Danuser, 2006). Example of the use of both AIC and BIC can be found in modeling of a FRAP experiment (Darzacq et al., 2007) and in identifying low-dimensional models to reproduce cell cycle regulations (Kondo et al., 2013).

**Figure 2D** shows an example of model selection using the AIC. The data are synthetically generated from a cubic function,  $y = 0.025 \times (x - 3)(x - 10)(x - 17) + 10 + \varepsilon$ , where  $\varepsilon$  is the observational noise, which follows a normal distribution with a mean of zero and a variance of four. We give candidate models for comparison with the observed data as a linear function ( $y = \theta_1 + \theta_2x + \varepsilon_1$ ), a cubic function ( $y = \theta_1 + \theta_2x + \theta_3x^2 + \theta_4x^3 + \varepsilon_2$ ), or a fifth-order polynomial function ( $y = \theta_1 + \theta_2x + \theta_3x^2 + \theta_4x^3 + \theta_5x^4 + \theta_6x^5 + \varepsilon_3$ ), where  $\varepsilon_1, \varepsilon_2$ , and  $\varepsilon_3$  are Gaussian noises. Under this assumption, the optimum parameter set ( $\theta_i$ ) determined based on the maximum likelihood method coincides with the solution of the least-squares method (Bishop, 2006). The sum of squared residuals is the smallest in the case of the fifth-order polynomial function, as expected, because the function contains more free parameters than the other models (**Figure 2D**). In contrast, the AIC is the smallest in the case of the

cubic function owing to the penalty term that inhibits a needless increase in the number of parameters (**Figure 2D**). Therefore, the AIC successfully selects the true cubic function as the best model avoiding the over- or under-parameterized models.

## PROCEDURES TO OPTIMIZE PARAMETERS

How can we optimize parameters, i.e., identify the set of parameters that maximizes the likelihood (or minimizes the SSE)? **Figure 3** shows a schematic of likelihood as a function of the parameter value. For simplicity, the parameter is assumed to change its value in one-dimensional space, although the parameter space is usually multi-dimensional in real cases. In the following sections, we introduce some procedures that can be used to identify the set of parameters that maximizes the likelihood. Minimization of SSE can be accomplished with similar procedures.

Optimization procedures can roughly be classified into two categories: gradient and sampling approaches. Gradient approaches search for the (local) maximum of a likelihood based on information from the local gradient, whereas sampling approaches examine numerous sets of parameters and select the sets that attain high likelihood. Gradient approaches can efficiently reach a (local) maximum with small computational cost, although they are inefficient for identifying the global maximum if there are multiple local maxima. In contrast, sampling approaches can detect multiple local maxima, if they exist, but require a massive computational cost.

## GRADIENT APPROACH

The gradient approach is based on a deterministic method of identifying maximum or minimum values of a given function. When the likelihood,  $L$ , is a continuous function of the parameters  $\Theta = \{\theta_1, \theta_2, \dots\}$ , the optimum parameters can be identified by analytical calculation. The solution of the system of partial differential equations  $\partial L / \partial \theta_i = 0 (i = 1, 2, \dots)$  is the set of parameters that yields the local maximum of the likelihood (**Figure 3A**). This procedure can also be used to minimize the SSE in linear regression analyses.

When it is difficult to solve the system of partial differential equations  $\partial L / \partial \theta_i = 0$  analytically, we must search for the solution numerically, based on the gradient approach, as follows: (1) set an appropriate initial parameter value  $\Theta = \Theta_0$ ; (2) compute the gradient of the likelihood for the initial value, i.e.,  $\partial L / \partial \Theta |_{\Theta=\Theta_0}$ ; (3) update  $\Theta$  in the direction of increase of the gradient to increase the likelihood  $L$ ; and (4) iterate (1) through (3) until the gradient converges with zero. We can directly reach one of the (local) maxima of  $L$  using this deterministic method (**Figure 3B**). This procedure is used in several areas of biological research, for estimation of values for bending elasticity during cytokinesis (Koyama et al., 2012), transcriptional parameters, and chemotaxis parameters (see later sections).

The gradient approach often leads not to the global maximum but to a local maximum when the likelihood is multimodal, i.e., multiple local maxima exist. To overcome this disadvantage, stochastic procedures are often adopted so that parameters can exit a local maximum by permitting the current searching point to move down the gradient with some probability

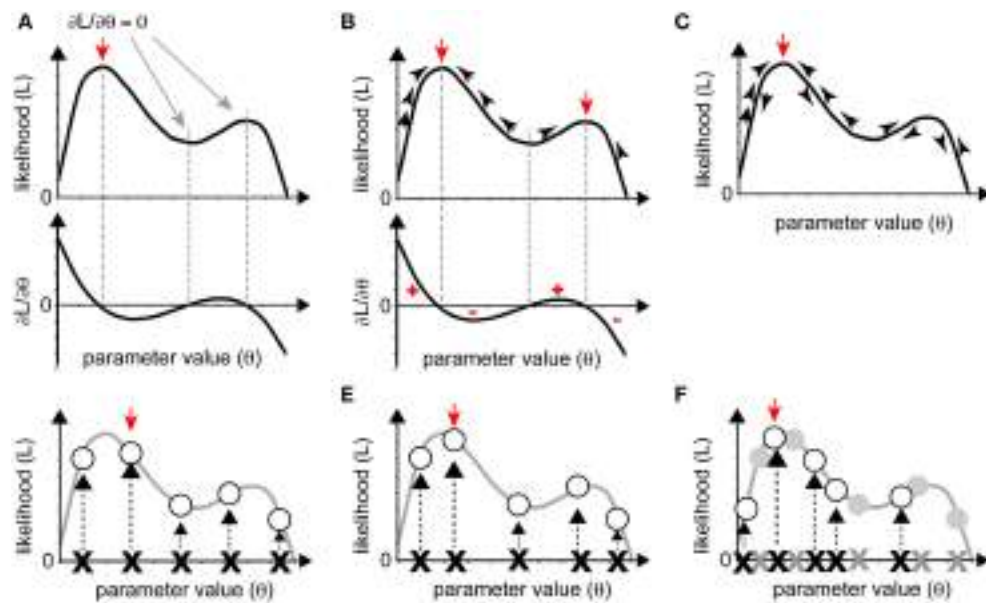


**FIGURE 3 | Various optimization strategies.** **(A–C)** Gradient approaches. **(A)** When the partial differential equations for likelihood can be solved as functions of parameters, the solutions yield local maxima or minima (red and gray arrows). The red arrow indicates maximum likelihood. **(B)** We can reach local maxima (red arrows) by iteratively following the gradient from a starting point. **(C)** If, in following the gradient, we add stochasticity, we may avoid being trapped in a local maximum and reach

the global maximum (red arrow). **(D–F)** Sampling approaches. The red arrow indicates the sampling point with the highest likelihood. **(D)** Grid sampling, in which sampling occurs at regular intervals. **(E)** Simple random sampling, where parameters are chosen at random. **(F)** Importance sampling was added to **(E)**. In the second round of sampling, more realizations were set near the realization with high likelihood from the initial round (gray crosses and circles).

(Figure 3C). As an example of a biological application of the gradient approach, one of the stochastic methods, the Metropolis algorithm, has been utilized in combination with a simulated annealing method to predict the positions of nucleosomes on the genome (NucPosSimulator, Schöpflin et al., 2013).

#### SAMPLING APPROACH

In principle, if we examined all sets of possible parameters, we could determine the entire form of a given likelihood and, thus, the parameters that yield the maximum likelihood. However, this strategy is not realistic in most cases. Instead, we sample a number of parameter sets and evaluate the likelihood for each set. As the number of samples increases, the parameter set that yields the largest likelihood approaches the optimum one. Roughly speaking, there are two ways to sample parameter sets; one is “grid sampling,” in which a sample is obtained at each parameter grid, at regular intervals (Farhadifar et al., 2007) (Figure 3D), and another is “random sampling,” in which samples are randomly obtained (Bergstra and Bengio, 2012) (Figure 3E). A typical sampling approach does not often work well due to “the curse of dimensionality,” which means that the enormous number of samples required for sufficient coverage of the high-dimensional space are impossible to process. The following two strategies can be used to overcome this problem. The first strategy is importance sampling (Section Importance Sampling), in which parameter space with higher likelihood will be searched recursively, to obtain as many samples as possible from a key area. The second strategy is to narrow the parameter space using prior information. We can statistically incorporate our prior guess using Bayes’ theorem

(Section Obtaining Posterior PDFs Using a Sampling Approach). In cell and developmental biology, we often have *a priori* information on the order of magnitude of parameter values.

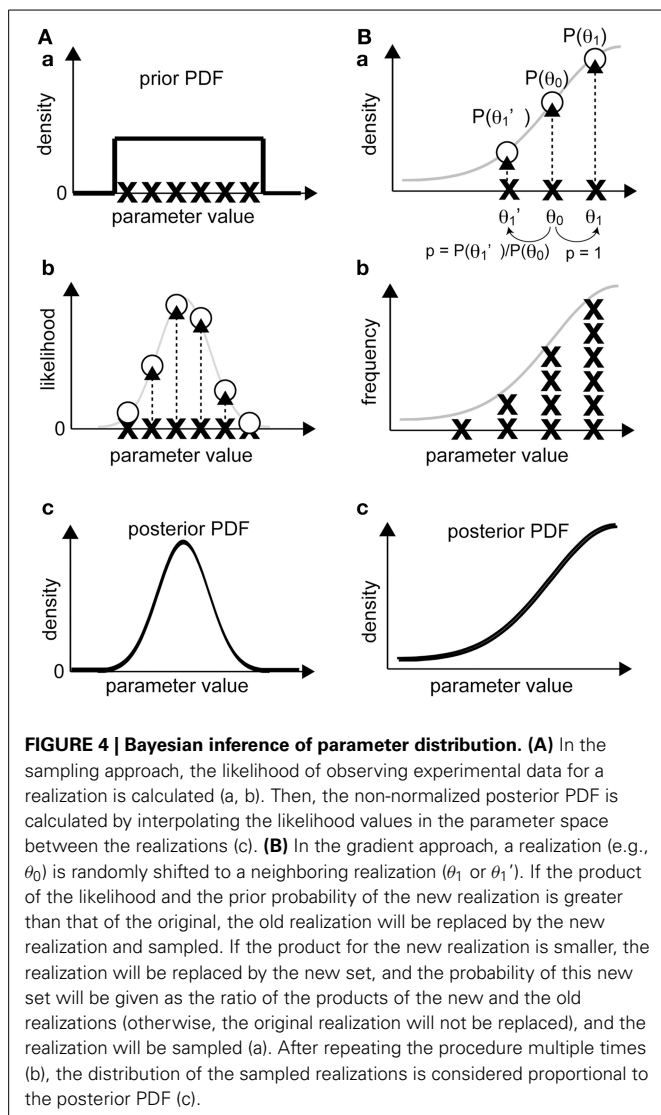
#### IMPORTANCE SAMPLING

Since parameters near the optimum parameters should have high likelihood, we can efficiently search the optimum parameters by focusing the investigation on parameter sets with high likelihood. In “importance sampling” (Figure 3F), after an initial round of grid or random sampling, we repeat the sampling, with greater intensity, near the samples with high likelihood.

An example that utilizes the importance sampling technique is the particle filter (PF), which is often applied to estimate a posterior distribution and/or parameters by means of a number of realizations called “particles.” Genetic algorithms (GAs) (Mitchell, 1998) are similar to PFs in that they both select important samples in accordance with likelihood (or other indices). However, GAs are not usually categorized as importance sampling methods because the outcomes are not guaranteed to converge to the target distribution function, due to stochastic events (“mutation” or “crossover”) unrelated to the likelihood.

#### BAYESIAN INFERENCE OF PARAMETER DISTRIBUTION

The above-mentioned sampling approaches enable us to determine not only the parameter set that yields the maximum likelihood but also the likelihood of all samples. Utilizing this information, we can estimate, in principle, the entire form of the likelihood function within the parameter space. Calculation of the likelihood function provides important information on the



inevitable measurement noise in biological experiments and the uncertainty of given stochastic models.

Unlike a straightforward approach to obtain the likelihood function using all possible sets of parameters, which would be unrealistic, a Bayesian approach provides a powerful and realistic methodology to estimate target PDFs as posterior distributions. In real data analyses or modeling, we often have prior information about parameters, e.g., a realistic range of parameters obtained through experimentation. Bayesian inference methods make use of prior information in order to limit the parameter space to be searched.

The outcome of the inference is a “posterior PDF,”  $p(\Theta|Y)$ , which indicates how probable a parameter set  $\Theta = \{\theta_1, \theta_2, \dots\}$  is when  $Y$ , usually an experimental observation, is given. In contrast, the prior PDF  $p(\Theta)$  indicates how probable  $\Theta$  is without knowing  $Y$ . The prior PDF reflects our initial guess of the parameter value. For example, if one supposes that a parameter must be within the range from 1 to 100 but has no additional information, a uniform distribution on the interval from 1 to 100

is the appropriate prior PDF. According to Bayes’ theorem, the posterior PDF is proportional to the product of the prior PDF and the likelihood, which is formulated as  $p(\Theta|Y) = p(Y|\Theta) \times p(\Theta)/p(Y)$  (Lee, 2012). Here,  $p(Y|\Theta)$  is the likelihood, which expresses how probable  $Y$  is when the parameter  $\Theta$  is given, and  $p(Y)$  is a PDF related to the observed data,  $Y$ , which is constant. It should be noted that the likelihood is not a probability distribution in the sense that its integral does not necessarily equal one (Bishop, 2006). Combining Bayesian inference with the sampling approach (Section Obtaining Posterior PDFs Using a Sampling Approach) or the gradient approach (Section Obtaining Posterior PDFs Using a Gradient Approach) enables us to obtain both likelihood and posterior PDFs.

### OBTAINING POSTERIOR PDFS USING A SAMPLING APPROACH

In this approach (Figure 4A), we sample a number of sets of parameter values, which are termed as “realizations,” according to the prior PDF [Figure 4A(a)]. Then, we calculate the likelihood of each realization by substituting it into our model [Figure 4A(b)]. According to Bayes’ theorem, the unnormalized posterior PDF, which is proportional to the normalized one, is obtained as a product of the likelihood and the prior PDF for each realization. Since we sampled from the prior PDF, the unnormalized posterior PDF is the likelihood at the sampling points whose deviation already reflects prior effects [Figure 4A(c)]. The normalized posterior PDF can be calculated by dividing the unnormalized posterior PDF by  $p(Y)$ , but this calculation requires a complex numerical integration. Without such normalization, the form of the function for the normalized and unnormalized posterior PDFs are identical, and thus the optimum parameter set can be obtained from the unnormalized one because  $p(Y)$  is constant. Therefore, calculation of an unnormalized posterior PDF is usually sufficient for our purposes. The parameter set at the mode of the unnormalized posterior PDF, i.e., the parameter set that attains the posterior PDF maximum, is called the maximum-a-posteriori (MAP) estimate.

PF, or sequential Monte Carlo, is a filtering method that is used to sequentially estimate, using importance sampling, posterior PDFs along with continuous input of observation data. Sets of parameters (“particles”) with a high likelihood will proliferate (or will be “resampled,” allowing duplication) (Figure 3F). Unlike GA, which focuses on finding the optimum set, PF enables us to estimate the likelihood and the posterior PDF. To avoid the problem of “degeneration,” which the plain PF often faces, some advanced PF methods, such as merging PF (Nakano et al., 2007), have been proposed. A real application of PF to estimation of parameters can be found in studies on transcriptional regulation of the circadian clock (Nakamura et al., 2009).

### OBTAINING POSTERIOR PDFS USING A GRADIENT APPROACH

In this subsection, we explain the procedure of the Metropolis algorithm (Figure 4B), which applies when the proposal density function that nominates the next candidate realization is symmetric (Gilks et al., 1995; Robert and Casella, 2010). Unlike the above-mentioned sampling approach, in which we calculate the likelihood of multiple and independent realizations, this method starts with a single realization. To obtain a posterior PDF

as the target distribution, the sampling procedure is as follows. First, we calculate the value of the posterior PDF related to the initial realization ( $P_{former}$ ), which is given by the product of the likelihood and the prior PDF. Next, the proposal density function randomly generates a new candidate realization, and we calculate the value of the posterior PDF ( $P_{latter}$ ). If  $P_{latter} > P_{former}$ , the candidate realization is accepted as a new realization of the posterior PDF. The key step in the Metropolis algorithm is that even if  $P_{former} > P_{latter}$ , the candidate realization is accepted with the probability of  $P_{latter}/P_{former}$  [Figure 4B(a)]. When a candidate is rejected, the former realization remains as the current realization. This sampling process is repeated until we obtain a sufficient number of realizations [Figure 4B(b)]. The process that allows a realization to move in the direction of decreasing posterior PDF provides a way to exit local maxima of posterior PDF. The distribution of the sampled realizations approximates the unnormalized posterior PDF [Figure 4B(c)], from which we can calculate the MAP, i.e., the optimum set of parameters that maximizes the posterior PDF.

The procedures for obtaining a posterior PDF using sampling methods based on the Markov process are generally referred to as Markov chain Monte Carlo methods. In this class, in addition to the Metropolis algorithm explained above, Gibbs sampling and Hamiltonian Monte Carlo algorithms are popular (Bishop, 2006). Approximate Bayesian computation (ABC) is another sampling approach that can be used to obtain a posterior PDF (Beaumont et al., 2002). The most remarkable feature of ABC is that instead of likelihood, any index in data space, such as SSE, can be used to determine acceptance/rejection of candidate realizations of parameters. Although it does not employ likelihood, ABC enables us to obtain samples from a target posterior PDF; the convergence speed strongly depends on the definition of the index in data space. This procedure has been used for estimation of the parameters for microtubule dynamics in a plant cell (Nakaoka et al., 2015). The estimated parameters were consistent with the values measured in independent experiments.

## EXAMPLES OF CELLULAR PARAMETER OPTIMIZATION

### TRANSCRIPTIONAL REGULATION

The initiation and elongation of gene transcription consist of multiple processes involving various regulatory proteins. Darzacq et al. constructed a simple model of transcriptional regulation consisting of three first-order ordinary differential equations describing promoter assembly, transcriptional initiation, and elongation (Darzacq et al., 2007). The six parameters in this model were optimized to fit the experimental results obtained through FRAP analyses of RNA polymerase II in cultured cells by minimizing the SSE. The optimization was conducted using the software SAAM II (The Epsilon Group, Charlottesville, USA).

More recently, Stasevich et al. quantified the accumulation of RNA polymerase II, discriminating between the initiation form (phosphorylated at Ser5 at its C-terminal domain, CTD) and the elongation form (phosphorylated at Ser2) using FabLEM (antibody fragment-based live endogenous modification labeling) technology (Stasevich et al., 2014). Combined with the results of the FRAP assays, the authors were able to narrow the optimum parameters for transcription kinetics.

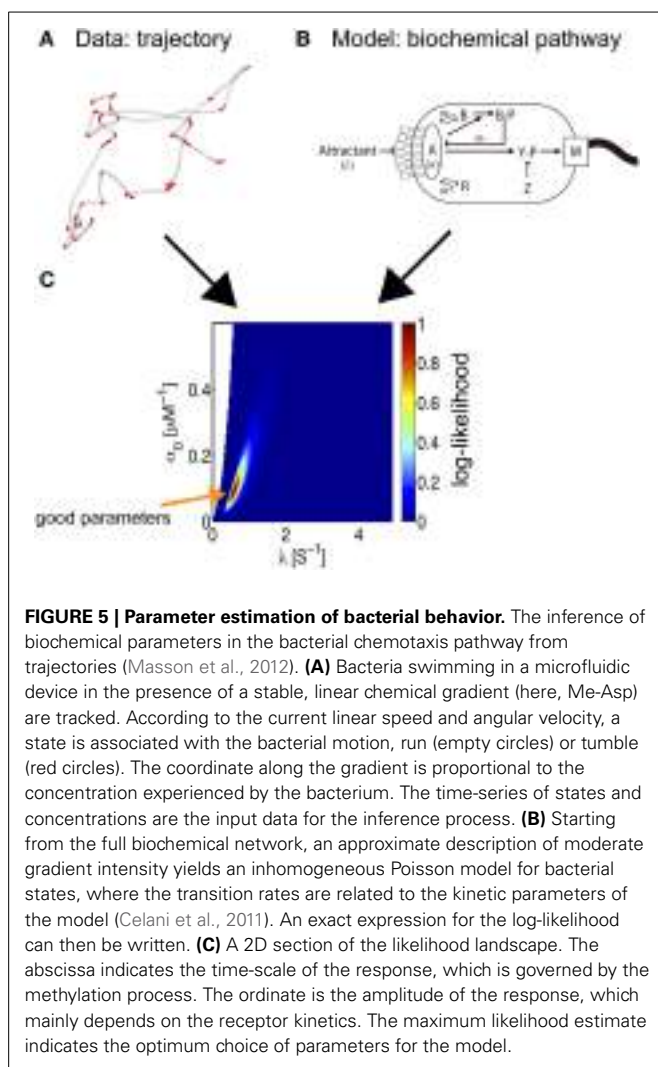
Minimization of the SSE was performed using the software Mathematica (Wolfram, Champaign, USA). Through these analyses, the authors succeeded in quantitatively and precisely characterizing the effect of histone acetylation on transcriptional regulation.

### BACTERIAL CHEMOTAXIS

The impulse response of bacteria has been estimated from bacterial chemotaxis trajectories, using inference methods (Masson et al., 2012). The model organism *Escherichia coli* senses the environmental concentration of chemicals and uses that information to regulate the rotation of flagellar motors and thus orient its trajectories of motion (Berg, 2004). Information on the chemical concentration sensed by the receptors is relayed via the kinase CheA, and the activity of this molecule is reduced by receptor binding. The second messenger in the chemotaxis pathway is the protein CheY. Its phosphorylated form, CheYp, binds to the flagellar motors and increases their rate of switching from counterclockwise rotation, corresponding to run phases, to clockwise rotation, thereby destabilizing the flagellar bundles that induce tumbling. Other important components of the pathway include the scaffold protein CheW, the phosphatase CheZ, the methyltransferase CheR, and the methylesterase CheB; the latter two are responsible for feedback from the receptors and the resulting adaptation (see Figure 5 and Vladimirov and Sourjik, 2009 for a recent review).

Is it possible to reconstruct the kinetics of biochemical interactions from an analysis of bacterial trajectories? In other words, can we infer the molecular pathways from paths in physical space? The task was greatly simplified by the fact that the model that describes the observations was known in advance, based on previous independent experimental assays and modeling efforts (reviewed in Celani et al., 2011). The goal was then reduced to the identification of the appropriate parameters. Furthermore, for the problem at hand, under physiological conditions, the response is linear. This convenient property allowed bacterial movement to be described as a two-state, inhomogeneous Poisson process, and closed-form expressions for the likelihood of a trajectory can be obtained. Additionally, in view of the compactness of the pathway, only three parameters are relevant: the intensity of the response ( $\alpha_0$ ), its duration ( $\alpha_1$ ), and the degree of adaptation ( $\lambda$ ), and the impulse response can be described as a function of time ( $t$ ) by  $K(t) = e^{-\lambda t} \times (\alpha_0 - \lambda \alpha_1 t)$ . These quantities are directly related to various molecular parameters, such as receptor affinities, protein copy numbers, and (de-)phosphorylation and (de-)methylation rates. The small number of parameters then allows for an exhaustive exploration of parameter space and a straightforward derivation of the best parameter set for the model.

Remarkably, when the trajectory of a single bacterium is tracked for a sufficiently long time, it is possible to infer the values of molecular parameters for that individual, allowing us to probe variations within a given isogenic population (Masson et al., 2012). To maximize the likelihood, optimization was performed using two types of gradient methods, a variable metric method and a simplex algorithm combined with a conjugate gradient method, and the MAP solution was calculated. Both methods yielded the same results, within acceptable statistical



uncertainty. Another notable advantage of this inference technique is its non-invasive nature; swimming bacteria are observed under the microscope and are not disturbed by the observation.

#### MORPHOGENESIS OF TISSUES AND ORGANS

Mechanical forces are critical for the morphogenesis of tissues and organs. However, such forces are difficult to measure. For example, if an object is not moving, we cannot tell whether a small force is acting on the object or strong forces are acting on the object but are balanced out. One way to estimate such forces is to ablate a part of a tissue/organ and measure the speed and direction in which the lesion spreads. This method is invasive and cannot be repeated for a given sample. Recent studies developed methods to infer a stress or deformation map during morphogenesis. To infer stress distribution in epithelial tissues (Chiou et al., 2012; Ishihara and Sugimura, 2012), the authors first constructed physical models assuming that the force balance involving tensions at cell contact surfaces and pressures of cells determines shapes of epithelial cells. The methods search for model parameters that reproduce the cell shapes in the tissues quantified from microscope images. In the method proposed by

Chiou et al. (2012), the tension and pressure of constituent cells were estimated analytically. In comparison, the method proposed by Ishihara and Sugimura (2012) reduces the number of parameters to be optimized to two, i.e., the variance of tension and the variance of observation/system errors. These parameters were optimized analytically or numerically through a gradient method. The authors were able to demonstrate the validity of the estimation by experimentally measuring the tension using laser ablation (Ishihara and Sugimura, 2012). The method was further utilized to demonstrate the importance of extrinsic anisotropy in mechanical forces for *Drosophila* wing development (Sugimura and Ishihara, 2013). A similar method was developed to create a deformation map of a whole organ during chick limb development (Morishita and Suzuki, 2014). This map precisely describes the type of deformation and its temporal regulation during organ morphogenesis.

#### CELL CYCLE REGULATION

The molecules that drive cell cycle progression and their relationships are well-studied. Detailed numerical models consisting of a number of molecules accurately reflect current experimental knowledge (Borisuk and Tyson, 1998; Tsai et al., 2008). Kondo et al. attempted to simplify the detailed models to identify “low-dimensional” models that sufficiently reproduce the observations of the detailed models (Kondo et al., 2013). The authors first constructed models with two dimensions (considering only active Cdc2 and cyclin) and various polynomial orders then optimized the parameters using a PF method. By calculating the AIC and BIC of the models, the authors concluded that the model with a third-order polynomial sufficiently reproduces characteristic behaviors of the cell cycle models.

#### PERSPECTIVE: FROM EXPLANATION TO PREDICTION

Data-driven science is gaining popularity in most scientific fields. With the rapid development of information technology, scientists can collect “big data” in their field and develop new methods for analysis. Use of such methodologies in other fields will provide clues regarding biological data analysis. For example, data assimilation (DA) is a fundamental computing technique used to predict future states by an integration of numerical simulation models and time-series data, using Bayesian statistics. DA has been used in weather forecasting and in predicting the status of the Earth’s interior that may trigger a large earthquake (Nagaoka et al., 2013). It has been applied to dynamic biological systems such as circadian rhythms (Nakamura et al., 2009). The method is also important in control theory for estimating the internal state of interest. Lillacci and Khammash applied an extended Kalman filter for parameter estimation in non-linear biological systems, including the heat shock response in *E. coli* (Lillacci and Khammash, 2010). An accurate prediction of the (unknown) future is not required in the field of experimental biology, which focuses on the explanation of experimental results. Importantly, the method enables us to conduct “on-line modeling,” in which a model is improved simultaneously with data acquisition. Such on-line modeling may be useful for the imaging of a moving object by controlling the field of view of the microscope with predictive information with respect to movement. In general, the

concepts and techniques used in cutting-edge statistics should be applicable to the field of experimental biology. With this in mind, we anticipate that a collaborative, trans-disciplinary approach will become more and more important in quantitative biology.

## ACKNOWLEDGMENTS

The authors thank Drs. Shuji Ishihara (Meiji Univ.) and Yohei Kondo (Kyoto Univ.) for valuable input. AK, HN, and KN are present or former members of the data assimilation project supported by Transdisciplinary Research Integration Center and Data Centric Science Research Commons in Research Organization of Information and Systems (Japan).

## REFERENCES

- Akaike, H. (1974). A new look at the statistical model identification. *IEEE Trans. Automat. Contr.* 19, 716–723. doi: 10.1109/TAC.1974.1100705
- Axelrod, D., Koppel, D. E., Schlessinger, J., Elson, E., and Webb, W. W. (1976). Mobility measurement by analysis of fluorescence photobleaching recovery kinetics. *Biophys. J.* 16, 1055–1069. doi: 10.1016/S0006-3495(76)85755-4
- Baumert, M. A., Zhang, W., and Balding, D. J. (2002). Approximate Bayesian computation in population genetics. *Genetics* 162, 2025–2035.
- Berg, H. C. (1993). *Random Walks in Biology*. Princeton, NJ: Princeton University Press.
- Berg, H. C. (2004). “*E. coli*,” in *Motion*, ed H. C. Berg (New York, NY: Springer Science and Business Media), 5–16.
- Bergstra, J., and Bengio, Y. (2012). Random search for hyper-parameter optimization. *J. Mac. Learn. Res.* 13, 281–305.
- Bishop, C. M. (2006). *Pattern Recognition and Machine Learning*. New York, NY: Springer Verlag.
- Borisuk, M., and Tyson, J. (1998). Bifurcation analysis of a model of mitotic control in frog eggs. *J. Theor. Biol.* 195, 69–85. doi: 10.1006/jtbi.1998.0781
- Bremer, M., and Doerge, R. W. (2010). *Statistics at the Bench: A Step-by-step Handbook for Biologists*. Cold Spring Harbor, NY: Cold Spring Harbor Laboratory Press.
- Celani, A., Shimizu, T. S., and Vergassola, M. (2011). Molecular and functional aspects of bacterial chemotaxis. *J. Stat. Phys.* 144, 219–240. doi: 10.1007/s10955-011-0251-6
- Chiou, K. K., Hufnagel, L., and Shraiman, B. I. (2012). Mechanical stress inference for two dimensional cell arrays. *PLoS Comp. Biol.* 8:e1002512. doi: 10.1371/journal.pcbi.1002512
- Darzacq, X., Shav-Tal, Y., de Turris, V., Brody, Y., Shenoy, S. M., Phair, R. D., et al. (2007). *In vivo* dynamics of RNA polymerase II transcription. *Nat. Struct. Mol. Biol.* 14, 796–806. doi: 10.1038/nsmb1280
- Farhadifar, R., Röper, J.-C., Aigouy, B., Eaton, S., and Jülicher, F. (2007). The influence of cell mechanics, cell-cell interactions, and proliferation on epithelial packing. *Curr. Biol.* 17, 2095–2104. doi: 10.1016/j.cub.2007.11.049
- Gilkis, W. R., Richardson, S., and Spiegelhalter, D. (1995). *Markov Chain Monte Carlo in Practice*. London: CRC Press.
- Hara, Y., and Kimura, A. (2009). Cell-size-dependent spindle elongation in the *Caenorhabditis elegans* early embryo. *Curr. Biol.* 19, 1549–1554. doi: 10.1016/j.cub.2009.07.050
- Hara, Y., and Kimura, A. (2013). An allometric relationship between mitotic spindle width, spindle length, and ploidy in *Caenorhabditis elegans* embryos. *Mol. Biol. Cell* 24, 1411–1419. doi: 10.1091/mbc.E12-07-0528
- Hastie, T., Tibshirani, R., and Friedman, J. (2009). *The Elements of Statistical Learning*. New York, NY: Springer Science and Business Media. doi: 10.1007/978-0-387-84858-7
- Ishihara, S., and Sugimura, K. (2012). Bayesian inference of force dynamics during morphogenesis. *J. Theor. Biol.* 313, 201–211. doi: 10.1016/j.jtbi.2012.08.017
- Jaqaman, K., and Danuser, G. (2006). Linking data to models: data regression. *Nat. Rev. Mol. Cell Biol.* 7, 813–819. doi: 10.1038/nrm2030
- Kitagawa, G. (2010). *Introduction to Time Series Modeling*. Boca Raton, FL: CRC Press. doi: 10.1201/9781584889229
- Kondo, Y., Kaneko, K., and Ishihara, S. (2013). Identifying dynamical systems with bifurcations from noisy partial observation. *Phys. Rev. E* 87:042716. doi: 10.1103/PhysRevE.87.042716
- Koyama, H., Umeda, T., Nakamura, K., Higuchi, T., and Kimura, A. (2012). A high-resolution shape fitting and simulation demonstrated equatorial cell surface softening during cytokinesis and its promotive role in cytokinesis. *PLoS ONE* 7:e31607. doi: 10.1371/journal.pone.0031607
- Lee, P. M. (2012). *Bayesian Statistics*. Chichester: John Wiley and Sons.
- Lillacci, G., and Khammash, M. (2010). Parameter estimation and model selection in computational biology. *PLoS Comp. Biol.* 6:e1000696. doi: 10.1371/journal.pcbi.1000696
- Masson, J.-B., Voisinne, G., Wong-Ng, J., Celani, A., and Vergassola, M. (2012). Noninvasive inference of the molecular chemotactic response using bacterial trajectories. *Proc. Natl. Acad. Sci. U.S.A.* 109, 1802–1807. doi: 10.1073/pnas.1116772109
- Mitchell, M. (1998). *An Introduction to Genetic Algorithms*. Cambridge: MIT Press.
- Morishita, Y., and Suzuki, T. (2014). Bayesian inference of whole-organ deformation dynamics from limited space-time point data. *J. Theor. Biol.* 357, 74–85. doi: 10.1016/j.jtbi.2014.04.027
- Nagao, H., Higuchi, T., Miura, S., and Inazu, D. (2013). Time-series modeling of tide gauge records for monitoring of the crustal activities related to oceanic trench earthquakes around Japan. *Comput. J.* 56, 355–364. doi: 10.1093/comjnl/bxs139
- Nakaoka, Y., Kimura, A., Tani, T., and Goshima, G. (2015). Cytoplasmic nucleation and atypical branching nucleation generate endoplasmic microtubules in *Physcomitrella patens*. *Plant Cell* 27, 228–242. doi: 10.1105/tpc.114.134817
- Nakamura, K., Yoshida, R., Nagasaki, M., Miyano, S., and Higuchi, T. (2009). Parameter estimation of *in silico* biological pathways with particle filtering towards a petascale computing. *Pac. Symp. Biocomput.* 14, 227–238. doi: 10.1142/9789812836939\_0022
- Nakano, S., Ueno, G., and Higuchi, T. (2007). Merging particle filter for sequential data assimilation. *Nonlin. Processes Geophys.* 14, 395–408. doi: 10.5194/npg-14-395-2007
- Robert, C., and Casella, G. (2010). *Monte Carlo Statistical Methods*. New York, NY: Springer.
- Saxton, M. J., and Jacobson, K. (1997). Single-particle tracking: applications to membrane dynamics. *Annu. Rev. Biophys. Biomol. Struct.* 26, 373–399. doi: 10.1146/annurev.biophys.26.1.373
- Schöpflin, R., Teif, V. B., Müller, O., Weinberg, C., Rippe, K., and Wedemann, G. G. (2013). Modeling nucleosome position distributions from experimental nucleosome positioning maps. *Bioinformatics* 29, 2380–2386. doi: 10.1093/bioinformatics/btt404
- Stasevich, T. J., Hayashi-Takanaka, Y., Sato, Y., Maehara, K., Ohkawa, Y., Sakata-Sogawa, K., et al. (2014). Regulation of RNA polymerase II activation by histone acetylation in single living cells. *Nature* 516, 272–275. doi: 10.1038/nature13714
- Sugimura, K., and Ishihara, S. (2013). The mechanical anisotropy in a tissue promotes ordering in hexagonal cell packing. *Development* 140, 4091–4101. doi: 10.1242/dev.094060
- Tsai, T. Y.-C., Choi, Y. S., Ma, W., Pomerening, J. R., Tang, C., and Ferrell, J. E. (2008). Robust, tunable biological oscillations from interlinked positive and negative feedback loops. *Science* 321, 126–129. doi: 10.1126/science.1156951
- Vladimirov, N., and Sourjik, V. (2009). Chemotaxis: how bacteria use memory. *Biol. Chem.* 390, 1097–1104. doi: 10.1515/BC.2009.130

**Conflict of Interest Statement:** The authors declare that the research was conducted in the absence of any commercial or financial relationships that could be construed as a potential conflict of interest.

**Received:** 17 October 2014; **accepted:** 14 February 2015; **published online:** 03 March 2015.

**Citation:** Kimura A, Celani A, Nagao H, Stasevich T and Nakamura K (2015) Estimating cellular parameters through optimization procedures: elementary principles and applications. *Front. Physiol.* 6:60. doi: 10.3389/fphys.2015.00060

This article was submitted to Systems Biology, a section of the journal *Frontiers in Physiology*.

Copyright © 2015 Kimura, Celani, Nagao, Stasevich and Nakamura. This is an open-access article distributed under the terms of the Creative Commons Attribution License (CC BY). The use, distribution or reproduction in other forums is permitted, provided the original author(s) or licensor are credited and that the original publication in this journal is cited, in accordance with accepted academic practice. No use, distribution or reproduction is permitted which does not comply with these terms.



# Acceleration of discrete stochastic biochemical simulation using GPGPU

Kei Sumiyoshi, Kazuki Hirata, Noriko Hiroi and Akira Funahashi\*

Systems Biology Laboratory, Department of Biosciences and Informatics, Keio University, Yokohama, Japan

**Edited by:**

Tetsuya J. Kobayashi, The University of Tokyo, Japan

**Reviewed by:**

Miguel Gonzalez, University of Extremadura, Spain

Yuichi Togashi, Hiroshima University, Japan

**\*Correspondence:**

Akira Funahashi, Systems Biology Laboratory, Department of Biosciences and Informatics, Keio University, 3-14-1 Hiyoshi Kouhoku-ku, Yokohama 223-8522, Kanagawa, Japan  
e-mail: funa@bio.keio.ac.jp

For systems made up of a small number of molecules, such as a biochemical network in a single cell, a simulation requires a stochastic approach, instead of a deterministic approach. The stochastic simulation algorithm (SSA) simulates the stochastic behavior of a spatially homogeneous system. Since stochastic approaches produce different results each time they are used, multiple runs are required in order to obtain statistical results; this results in a large computational cost. We have implemented a parallel method for using SSA to simulate a stochastic model; the method uses a graphics processing unit (GPU), which enables multiple realizations at the same time, and thus reduces the computational time and cost. During the simulation, for the purpose of analysis, each time course is recorded at each time step. A straightforward implementation of this method on a GPU is about 16 times faster than a sequential simulation on a CPU with hybrid parallelization; each of the multiple simulations is run simultaneously, and the computational tasks within each simulation are parallelized. We also implemented an improvement to the memory access and reduced the memory footprint, in order to optimize the computations on the GPU. We also implemented an asynchronous data transfer scheme to accelerate the time course recording function. To analyze the acceleration of our implementation on various sizes of model, we performed SSA simulations on different model sizes and compared these computation times to those for sequential simulations with a CPU. When used with the improved time course recording function, our method was shown to accelerate the SSA simulation by a factor of up to 130.

**Keywords:** GPGPU, stochastic simulation algorithm, direct method, parallel processing, CUDA, SBML

## 1. INTRODUCTION

Understanding biological phenomena as systems is one of the most crucial objectives in systems biology (Kitano, 2002). Mathematical modeling of biological systems and the simulation of such models will play an important role in helping us to understand unknown phenomena as systems. In systems biology, a deterministic approach, such as using ordinary differential equations (ODEs), is often used to understand the behavior of biochemical systems. A deterministic approach describes the system using molecular concentrations, and the results are the same for every realization. However, when we want to understand a system that contains a small number of molecules, such as a biochemical network in a single cell, a simulation must be executed using a stochastic approach, instead of a deterministic approach (McAdams and Arkin, 1997; Arkin et al., 1998).

The stochastic simulation algorithm (SSA) simulates the stochastic behavior of a spatially homogeneous system (Gillespie, 1977). Since stochastic approaches produce different results each time they are used, multiple runs are required in order to obtain statistical results, thus causing a large computational cost.

To reduce this large computational cost, we have focused on accelerating the SSA by using general-purpose computations on a graphics processing unit (GPGPU; Owens et al., 2007; Nvidia, 2014). GPGPU is a technology that uses a graphics processing

unit (GPU) to perform numerical calculations other than those for computer graphics, its original design purpose. GPUs contain a large number of arithmetic units in order to parallelize an enormous number of simple calculations. By efficiently parallelizing a problem and simultaneously performing the calculations on these arithmetic units, we can obtain significant improvement in the performance. GPUs are now widespread; they are included in personal computers (and even in laptop computers). Because of this, the ability to harness the computing power of GPUs has rapidly developed.

We have implemented a parallel method for using SSA to simulate a stochastic model; the method efficiently utilizes a GPU, and this enables multiple realizations on the same time sequence. Thus, multiple results are obtained simultaneously, and this reduces the computational time and cost. During the simulation, for the purpose of analysis, each time course is recorded at each time step. There are some existing studies of methods used to accelerate the SSA using the GPGPU; these include (Li and Petzold, 2010) on the direct method and (Komarov and D'Souza, 2012) on the optimized direct method. These proposed methods do not provide a functionality for storing the time course data, which is essential for understanding the dynamics of a model; our implementation achieves this, and thus aids analysis.

## 2. MATERIALS AND METHODS

### 2.1. THE SSA

The SSA was developed by Gillespie (1977), and it is an efficient and widely used algorithm for simulating the dynamics of chemically reacting systems including stochastic processes. The SSA has the following features:

- Each simulation step fires one reaction:

During the simulation, multiple reactions do not proceed simultaneously. A single reaction is selected from the model, considering the type of reaction and its required time, and each selected reaction is executed individually.

- The reactions are selected at random:

A reaction is selected by its propensity function. The propensity function represents its tendency to be selected; that is, a larger propensity function indicates a higher probability of being selected.

- The time required for each reaction is defined at random:

Each reaction time  $\tau$  is defined at random, but the calculated value of  $\tau$  depends on the sum of the propensity function.

- Each simulation step increases or decreases the number of molecules:

As a result of each reaction, changes are based on the number of molecules, not on their concentrations. A stoichiometry matrix is used to determine how many molecules are added or removed.

The original implementation of SSA is called the direct method. There are several additional implementations of the SSA (Gillespie, 1976; Gibson and Bruck, 2000; Cao et al., 2004; McCollum et al., 2006) that use various methods to speed up the computation time. In our implementation, we use the direct method, which is summarized as follows:

1. Initialization:

Initialize and define the number of molecules, the reactions, and the rate constants. The reactions are specified by a stoichiometry matrix.

2. Generate uniformly distributed random numbers:  $r_1, r_2$ , from  $(0 - 1]$ .

These numbers determine which reaction is fired in the next step  $\tau$ .

3. Calculate the propensity function  $a_i [i = 0 \dots (n - 1)]$  for each reaction, where  $n$  is the number of reactions:

The propensity function for each reaction will change, depending on the order of the reaction and the number of reactants. The order of each reaction should be in the range of 0th order to 2nd order; if the order of a reaction is greater than 2nd order, it should be rewritten as a combination of reactions of lower (0th–2nd) order.

4. Calculate the sum of the propensity function:

$$a_{total} = \sum_{i=0}^{n-1} a_i$$

5. Calculate the reaction time:  $\tau = (1/a_{total}) \log(1/r_1)$ .

6. Select the reaction: Select a reaction that satisfies

$$\sum_{i=0}^{m-1} a_i < r_2 \cdot a_{total} \leq \sum_{i=0}^m a_i.$$

7. Fire the selected ( $m$ th) reaction: Update the number of molecules, and add  $\tau$  to the cumulative simulation time.

8. Termination: If the cumulative time is less than a predetermined time, return to step 2.

### 2.2. RANDOM NUMBER GENERATION

SSA is an algorithm that uses random numbers to represent stochastic process in a model. As shown in the previous section, the direct method uses two random numbers ( $r_1$  and  $r_2$ ) for each step of a simulation: one to determine which reaction is to be fired and one to determine the reaction time. The generation of these random numbers is one of the most crucial steps in SSA; it is a time-consuming task and thus impacts the total simulation time. Another concern regarding the generation of random numbers is their distribution. In SSA, a great many random numbers are generated during each simulation, so it is essential to choose a generator that can produce uniformly distributed random numbers with high dimensionality and long periodicity. In our implementation, we used the Mersenne Twister (MT), a widely used pseudorandom number generator (Matsumoto and Nishimura, 1998). We implemented a parallelized MT algorithm on a GPU; it was based on the GPGPU implementation of MT included in CUDA SDK, NVIDIA's software development kit for their parallel computing platform (Podlozhnyuk, 2007). In this implementation, the generated random numbers are stored directly in the GPU memory; this requires less communication between the host computer and the GPU.

### 2.3. PARALLELIZATION OF THE DIRECT METHOD

To accelerate the execution of the direct method, we applied both coarse-grained and fine-grained parallelization. Coarse-grained parallelization of a stochastic simulation is straightforward. In principle, a stochastic simulation requires multiple simulations using the same model and the same set of parameters, because each result shows only one possibility. To understand the dynamics and characteristics of a model, it is necessary to obtain a results from multiple simulations. Coarse-grained parallelization executes multiple simulations simultaneously. The parallelization algorithm is quite simple, in that the model is located on the global memory of a GPU, and multiple arithmetic units are engaged to execute simulations with different sets of random numbers. The acceleration of the SSA by Li and Petzold (2010) was based on coarse-grained parallelization.

Fine-grained parallelization also parallelizes each component of each simulation. For example, in the direct method, the calculations of the propensities (step 3, Section 2.1) of the various reactions are parallelized. Similarly, updating the numbers of each molecular species (step 7, Section 2.1) is parallelized. The calculation time of step 3 is thus reduced by a factor equal to the number of reactions, and the time for step 7 is reduced by a factor equal to the number of molecular species affected. An overview

of fine-grained parallelization of the direct method is shown in **Figure 1**; the arrows indicate the execution times of each step. The blue arrow in the figure indicates calculation of the reaction time  $\tau$  and the selection of a reaction, and these cannot be parallelized. The orange and green arrows indicate calculation of the propensity and updating the number of molecules, respectively; these are independent processes and thus can be parallelized. As shown in **Figure 1**, the total execution time is reduced.

When implementing fine-grained parallelization with the CUDA programming language, we assigned a thread to the calculation of the propensity of each reaction. When updating the number of molecules, we assigned a thread to each molecular species.

#### 2.4. MEMORY ACCESS OPTIMIZATION ON A GPU

In the CUDA programming model, when a program is launched, data (e.g., matrices) are loaded from the host computer to the GPU's memory. The CPU on the host computer then sends a message to begin execution of the operation. Once the GPU has received this message, the arithmetic units begin to process in parallel as threads. Once all threads have been completed, the GPU returns the results to the host computer. Because multiple threads are executed simultaneously on a GPU, it is necessary to carefully design the access pattern of the threads in order to avoid collisions when they attempt to access the GPU memory to perform read or write operations.

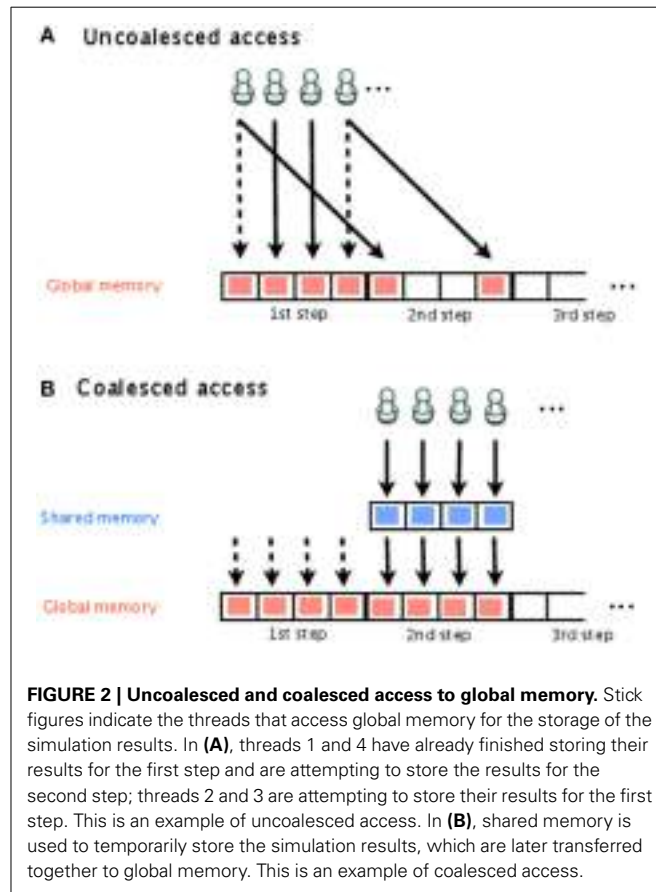
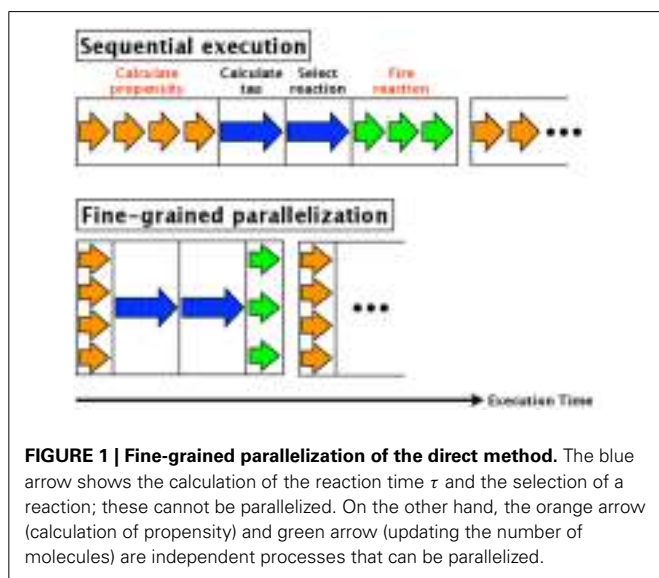
There are various types of memory available in CUDA, including global, constant, texture, and shared; these differ in capacity and speed of access. Global memory has the largest capacity but requires the longest access time. To avoid the high latency of global memory, access to global memory should be coalesced (Nvidia, 2014). This means that all threads should follow a specific access pattern.

On the other hand, shared memory has a short access time, but its capacity is very limited. A benefit of using shared memory is that it has low latency. Shared memory has small capacity,

so calculations must be partitioned (e.g., matrices and variables) and at any time, only the part being used is loaded to the shared memory. It is also important that access to shared memory be controlled in order to prevent collisions between threads. If there are 16 groups of physical addresses (banks), then the shared memory can give simultaneous access to 16 different threads. If multiple threads attempt to access the same bank, a “bank conflict” (Nvidia, 2014), this will result in sequential access, and thus result in high latency.

In our implementation, we stored the time course in the global memory and stored the number of molecules and propensities in shared memory. In this way, writing to the global memory was coalesced, and bank conflicts are avoided.

**Figure 2** shows storing of the time course, with both uncoalesced and coalesced access to global memory. Each thread is indicated by a stick figure. In this figure, it is assumed that there are four simulations executed simultaneously and that each one has its own thread for storing the results. Even though they are all simulating the same model, the execution time of each simulation will differ depending on one of the random numbers. In **Figure 2A**, threads 1 and 4 have already finished storing their results for the first step and are attempting to store their results for the second step, while threads 2 and 3 are attempting to store their results from the first step. This results in uncoalesced access. To avoid this problem, we temporarily store the results in shared memory, and then transfer the results from

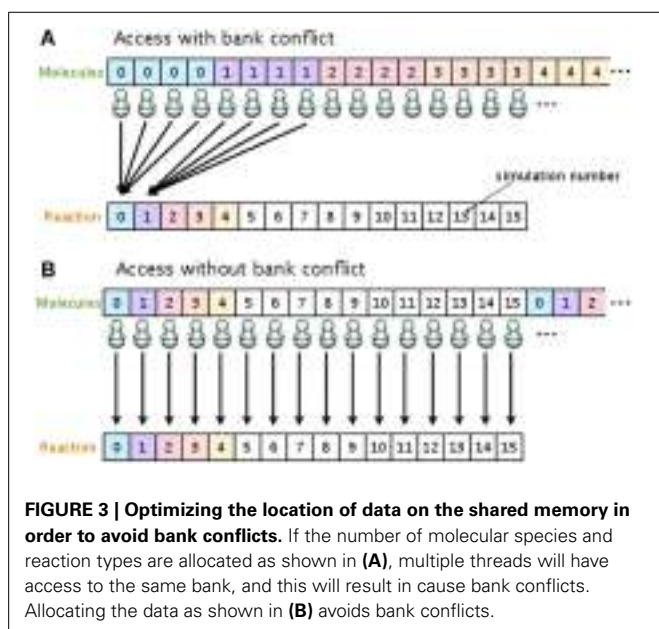


all threads to global memory at the same time, as shown in **Figure 2B**.

To eliminate the risk of a bank conflict, we optimized the location of the data on the shared memory. In our implementation, the shared memory is used to store the number of molecules and the propensity functions. **Figure 3** shows examples of access to shared memory with and without a bank conflict. In both **Figures 3A,B**, the upper arrays store the numbers of molecules in each species, and the lower arrays store the reaction type to be fired in the current simulation step. The number in each element of the array represents the simulation number (id). In this example, there are 16 simulations running simultaneously, and each simulation consists of four different molecular species. When it is time to update the number of molecules (step 7, Section 2.1), if the data are located as shown in **Figure 3A**, multiple threads will attempt to access the same bank (an element in the lower array), which will cause a bank conflict. To avoid this bank conflict, we have located the data as shown in **Figure 3B**. With this optimization, each element of the array is accessed by only a single thread, and thus bank conflicts are avoided.

## 2.5. REDUCTION OF THE TIME TO TRANSFER DATA BETWEEN THE GPU AND THE HOST COMPUTER

As described in Section 2.4, prior to executing a simulation, it is necessary to transfer data from the host computer to the GPU. Usually, the time required to do this is not negligible, and it adds to the total execution time. To estimate this overhead quantitatively, we have implemented a prototype of SSA on a GPU, and we profiled its execution time, as shown in **Table 1**. The most time-consuming task was found to be memory allocation, and this occupied almost 40% of the total execution time. The reason for this is that we store all of the time course results, which requires a large amount of memory. Data transfer is also time consuming, and it occupies 25% of the total execution time. When



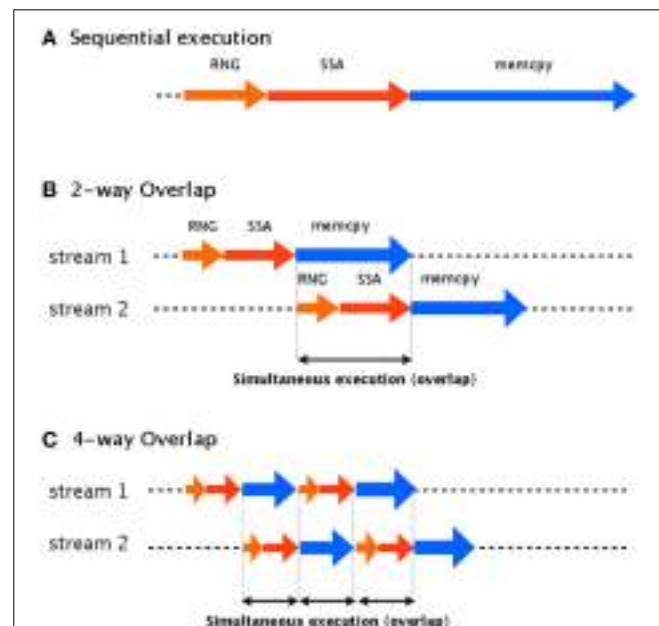
the time course results occupy a large amount of the GPU memory, the data transfer time from the GPU to the host computer will also increase. To overcome this problem, we implemented an asynchronous transfer scheme for moving data from the GPU to the host computer.

The idea of our asynchronous transfer scheme is to split the simulation into multiple streams and then execute these streams in parallel. Each stream contains random number generation (RNG), a stochastic simulation (SSA), and transfer of the data to the host computer (memcpy), as shown in **Figure 4**. If each stream runs independently, one thread can continue its computation on the GPU (kernel execution) while another stream is transferring the result to the host computer.

To implement this asynchronous data transfer scheme, we split the simulation tasks into two parts: kernel execution and data transfer. A schematic diagram of asynchronous transfer with two streams is shown in **Figure 4B**. While one stream (stream 1) is

**Table 1 | Execution time profile.**

Procedure	% of total execution time
Memory allocation (page lock)	38.0
Data transfer	25.0
Execution of kernel	23.3
Random number generation	13.3
Other	0.4



transferring its results to the host computer (`memcpy`), another (stream 2) begins to execute its kernel. This transfer scheme is called a two-way overlap. Note that in two-way overlapped data transfer, the data transfer time of stream 1 is suppressed by the kernel execution time of stream 2. Under ideal conditions, the data transfer time will be cut in half. In our implementation, we applied four-way overlapped data transfer. The difference between two-way and four-way overlap is the number of parts into which the stream is split. In four-way overlapped data transfer, the simulation is split into four parts, as shown in **Figure 4C**; this results in three areas of overlap, compared to only one for two-way overlap. Under ideal conditions, the data transfer time will be cut by a factor of four.

## 2.6. DATA COMPRESSION

Since CUDA requires that all of the data be loaded onto the GPU memory, the capacity of the GPU memory is a bottleneck. Unfortunately, it is impossible to extend the size of the memory of a GPU, although extending the memory is straightforward and cost effective on general-purpose computers. Moreover, the memory of a GPU is usually less than that of a personal computer. For example, the NVIDIA Tesla C1060, which we used for this study, has 4 GB of memory, while most desktop computers used for scientific calculations have more than 8 GB of memory, and, as mentioned, it is easy to increase the memory. Acceleration of processes on a GPU always encounters this problem; thus, effectively reducing the memory footprint is another important issue for such implementations.

In our implementation, we used the global memory to store the time course results and the constant memory to store the reaction rate constants and the stoichiometry matrix. The constant memory has low latency and small capacity (64 KB), compared with the global memory, and it is read-only access. Because the stoichiometry matrix and reaction rate constants do not change during the simulation, we located them in the constant memory. The structure that consumes the most memory is the stoichiometry matrix used in the SSA; however, this matrix is usually sparse, and so we implemented compressed row storage (CRS) to reduce its footprint.

**Figure 5** shows an example of a model, its stoichiometry matrix, and the compressed matrix. **Figure 5A** shows an example of a biochemical system (decay dimerization model). It consists of three molecular species ( $S_1$ – $S_3$ ) and four reactions ( $r_1$ – $r_4$ ). This biochemical system can be represented by a stoichiometry matrix, as shown in **Figure 5B**. Each row of the stoichiometry matrix represents a molecular species that is synthesized or degraded by one of the reactions. If the value is zero, then the corresponding molecular species is not included in the reaction for that column (in other words, the simulator does not have to consider this molecular species for this reaction). Most biochemical reaction networks are loosely coupled, and so the stoichiometry matrix is sparse Li and Petzold (2010). To compress this sparse matrix, we extracted the non-zero values and generated a new matrix that contains only these non-zero values and their original row and column indices, as shown in **Figure 5C**. This new matrix still has some redundant information, in that the row indices are repeated (e.g., 1, 1, 2, 2, 3, 3). We used CRS to avoid this redundancy

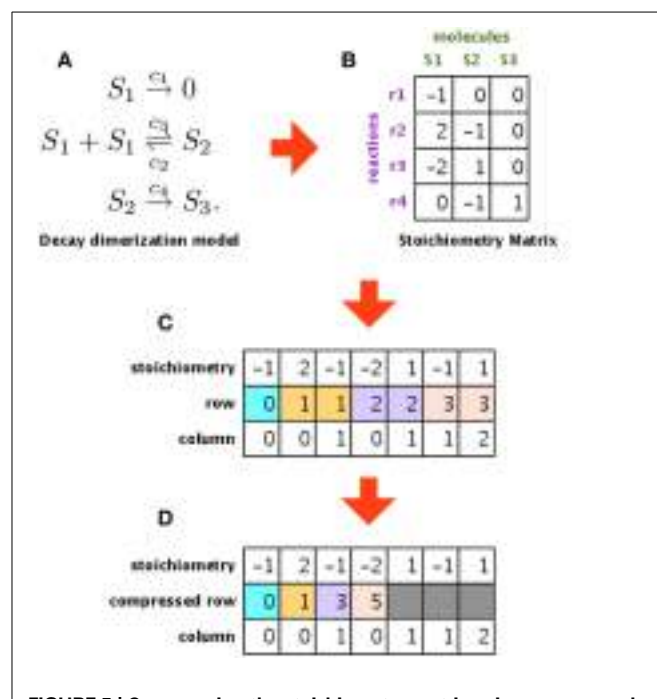


**FIGURE 5 | Compressing the stoichiometry matrix using compressed row storage.** **(A,B)** Show a decay dimerization model and its stoichiometry matrix, respectively. Each row of the stoichiometry matrix represents a molecular species that will be synthesized or destroyed by one of the reactions. **(C)** Shows a matrix that only stores the non-zero entries in the stoichiometry matrix, along with the original row and column indices. **(D)** Is a compressed matrix of **(C)**, obtained by eliminating duplicates of the same index in the second row.

and to store only the column indices in each compressed row, as shown in **Figure 5D**. By using CRS to convert the stoichiometry matrix, we succeeded in storing a decay dimerization model that had approximately 1400 reactions; for the same amount of memory, an unconverted matrix could only store approximately 120 reactions.

## 2.7. IMPORTING THE MODEL

Although not all studies of simulations on GPUs have mentioned or satisfied this requirement, it is crucial to separate the model from the implementation in order to provide a convenient software tool. If the model is hard-coded in the simulator, the program must be rewritten whenever the model is modified; the entire code must then be recompiled. This causes a problem for those end users who are not familiar with the necessary development tools. In particular, this can cause a high barrier for GPGPU, since most end users are not proficient in GPU programming.

To avoid this problem, we designed our simulator so that the model is imported; thus, our software package can be distributed in binary and does not need to be compiled by the end user. Our system uses the Systems Biology Markup Language (SBML), which is a tool-neutral computer-readable format for representing models of biochemical reaction networks; it is applicable to metabolic networks, cell signaling pathways, gene regulatory networks, and other modeling problems in systems biology (Hucka et al., 2003, 2004). To import SBML, we use LibSBML (Bornstein

et al., 2008) to easily access the SBML elements from the C programming language. The host computer converts the SBML elements (such as reactions, molecular species, and rate constants) to matrices, and then loads them into the GPU memory. Once the matrices have been successfully loaded, the simulator launches a kernel to start the simulation. All of the sample models that were used for evaluation of this procedure were described using SBML.

### 3. RESULTS

In this section, we will evaluate our implementation. For comparison, we implemented the direct method in the C programming language for sequential execution on a CPU. We compared the execution time of a stochastic simulation of the same model performed on both a CPU and a GPU. The GPU we used was an NVIDIA Tesla C1060, mounted on a host computer that had Core i7 2.80 GHz with 12 GB of memory. The CPU version of our simulator was executed on the host computer. The model we chose for the benchmark was a decay dimerization model, which consisted of four reactions and three molecular species, as follows:



This model is quite simple, but it is known to cause stochastic fluctuations, and a similar reaction system appears in previous research by McAdams and Arkin (1997). The decay dimerization model was also used as a benchmark model by Li and Petzold (2010), and we applied the same simulation conditions as used in that study; these conditions are shown in **Table 2**.

#### 3.1. HYBRID PARALLELIZATION

We evaluated the effect on SSA of hybrid parallelization, which is a combination of fine-grained and coarse-grained parallelization. Hybrid parallelization simultaneously executes multiple stochastic simulations as coarse-grained parallelization, and simultaneously calculates the propensity functions and updates the number of molecules for each stochastic simulation as a fine-grained parallelization. The execution time of the direct method with different numbers of realizations is shown in **Table 3**, and the ratio

**Table 2 | Simulation conditions for the decay dimerization model.**

REACTION RATE CONSTANTS	
$c_1$	1.0
$c_2$	0.002
$c_3$	0.5
$c_4$	0.04
INITIAL CONDITIONS	
$S_1$	10,000
$S_2$	0
$S_3$	0
Simulation steps	11,000

of the execution time on a CPU to that on a GPU is shown in **Figure 6**. From **Table 3** and **Figure 6**, we can see that there is no performance gain on a GPU when the number of realizations is small ( $<100$ ), but if the number of realizations is large ( $>1000$ ), the effect is apparent. We found that hybrid parallelization was up to 16 times faster than implementation on a CPU.

#### 3.2. MEMORY ACCESS OPTIMIZATION

Next, we evaluated the effect of optimizing the memory access. The ratios of execution times on a CPU and that on a GPU are shown in **Figure 7**; the blue line indicates the acceleration obtained by optimizing the memory access and using hybrid parallelization. Optimizing the memory access resulted in improving the time by a factor of 3.1; the overall result was 50 times faster than that on a CPU. In **Figure 6**, we see that there is less improvement when the number of realizations is small, because the parallelization has a smaller effect. On the other hand, optimizing the memory access on a GPU greatly improved performance

**Table 3 | Execution times with different numbers of realizations.**

Number of realizations	Execution time (s)		CPU/GPU
	CPU	GPU	
1	0.001	0.079	0.01
10	0.015	0.086	0.17
100	0.17	0.160	1.06
1000	1.91	0.276	6.92
5000	14.01	1.096	12.78
10,000	35.05	2.235	15.68
15,000	52.57	3.275	16.05
20,000	70.10	4.344	16.14
25,000	87.82	5.490	16.00
30,000	105.15	6.495	16.19

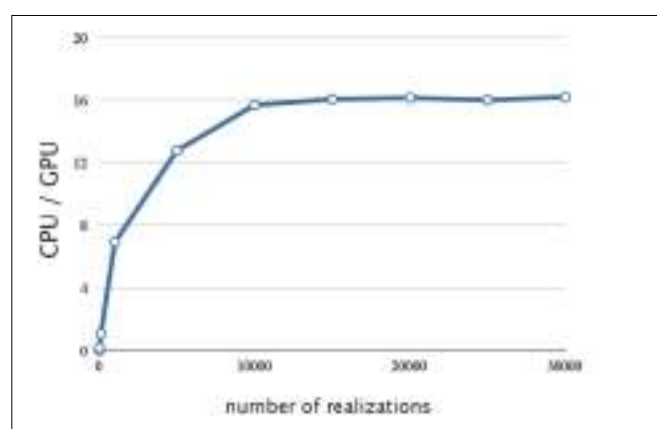


**FIGURE 6 | Performance analysis of hybrid parallelization w.r.t. the number of realizations.** This figure shows a plot of the ratios of the execution times for the decay dimerization model (**Table 2**) on a CPU(Core i7 2.80 GHz with 12 GB of memory) and on a GPU (NVIDIA Tesla C1060) as the vertical axis, and the number of realizations as the horizontal axis. With hybrid parallelization and for greater than 1000 realizations, the process is up to 16 times faster than on a CPU.

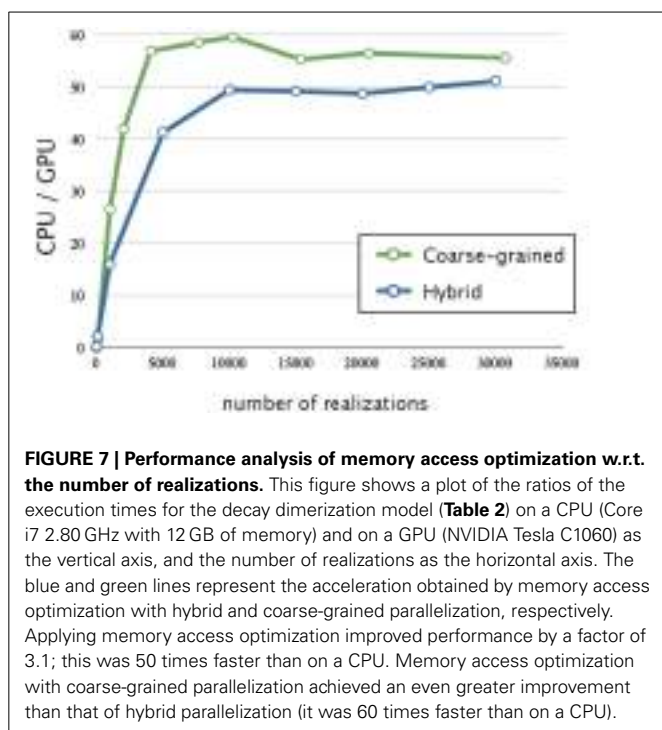


**FIGURE 7 | Performance analysis of memory access optimization w.r.t. the number of realizations.** This figure shows a plot of the ratios of the execution times for the decay dimerization model (**Table 2**) on a CPU (Core i7 2.80 GHz with 12 GB of memory) and on a GPU (NVIDIA Tesla C1060) as the vertical axis, and the number of realizations as the horizontal axis. The blue and green lines represent the acceleration obtained by memory access optimization with hybrid and coarse-grained parallelization, respectively. Applying memory access optimization improved performance by a factor of 3.1; this was 50 times faster than on a CPU. Memory access optimization with coarse-grained parallelization achieved an even greater improvement than that of hybrid parallelization (it was 60 times faster than on a CPU).

when there was a large number of realizations. This result suggests that the memory access on a GPU is a bottleneck; thus, it is essential to profile the access pattern of the code and optimize the data location and structure.

The green line in **Figure 7** indicates the acceleration obtained by optimizing the memory access and using coarse-grained parallelization. Interestingly, optimizing the memory access had a greater impact when using coarse-grained parallelization than when using hybrid parallelization; its execution was 60 times faster than on a CPU. This may be because coarse-grained parallelization requires less synchronization between the threads than does hybrid parallelization, and thus the threads may be executed more efficiently. We also note that coarse-grained parallelization requires relatively simple memory access compared to that required by hybrid parallelization, and this is advantageous. Although hybrid parallelization may have the greatest advantage for huge models with very large numbers of reactions, we decided to implement other acceleration methods for use with coarse-grained parallelization.

### 3.3. REDUCTION OF DATA TRANSFER TIME

In addition to parallelization and memory access optimization, we evaluated the improvement in performance achieved by the reduction of the time to transfer data. The execution times of 10,240 realizations with different methods of optimizing the data transfer ( $n$ -way overlap) is shown in **Table 4**, and **Figure 8** shows the ratio of the execution times on a CPU and a GPU, with four-way overlapped data transfer. Note that the total execution time when there was no overlap (0.67 s; **Table 4**) is about one third that for 10,000 realizations (2.235 s; **Table 3**). This is due to the optimization of memory access, as described in Section 3.2.

**Table 4 | Execution times for 10,240 realizations with different methods of optimizing data transfer.**

	Kernel (s)	Data transfer (s)	Total execution time (s)
No overlap	0.22	0.15	0.67
Two-way overlap	0.22	0.08	0.59
Four-way overlap	0.22	0.04	0.45

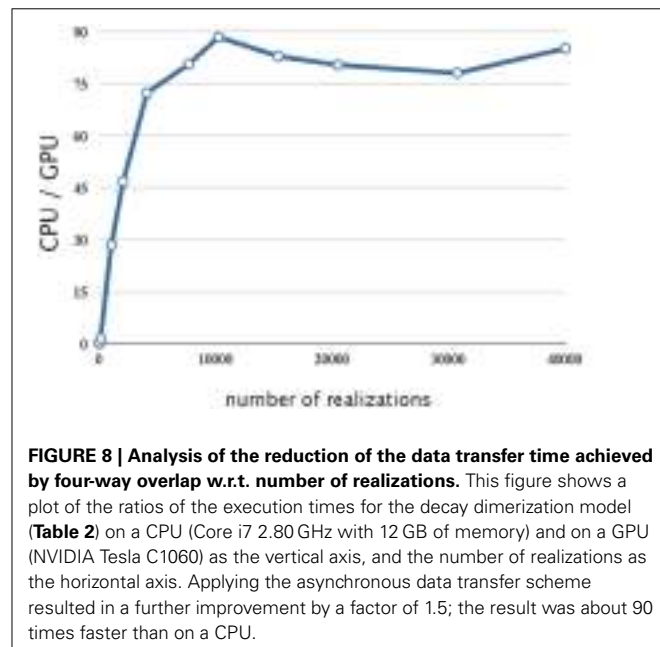


**FIGURE 8 | Analysis of the reduction of the data transfer time achieved by four-way overlap w.r.t. number of realizations.** This figure shows a plot of the ratios of the execution times for the decay dimerization model (**Table 2**) on a CPU (Core i7 2.80 GHz with 12 GB of memory) and on a GPU (NVIDIA Tesla C1060) as the vertical axis, and the number of realizations as the horizontal axis. Applying the asynchronous data transfer scheme resulted in a further improvement by a factor of 1.5; the result was about 90 times faster than on a CPU.

From **Figure 8**, we see that this implementation has a further improvement by a factor of 1.5 (this is about 90 times faster than on a CPU). The reduction in the data transfer time was motivated by noting that this consumed 25% of the execution time in our prototype implementation, as shown in **Table 1**. By implementing an asynchronous data transfer scheme, we reduced the data transfer time, to 50% and 25% of the original time for two-way and four-way overlap, respectively (see **Table 4**); this resulted in an improvement in performance by a factor of 1.5.

### 3.4. DATA COMPRESSION

As described in Section 2.6, using CRS to compress the stoichiometry matrix markedly reduced the memory footprint of the GPU implementation. To analyze the effect of this on the execution time, we created some sample models of various sizes. Each sample model consisted of several units of a single-gene production-reduction submodel. As an example, such a submodel consisting of two molecular species and two reactions is as follows:



For example, if a model consists of four independent single-gene production-reduction submodels, the model will contain eight molecular species and eight reactions. Because only one or two molecular species are involved in each reaction in each submodel, the stoichiometry matrix of the combined model will be sparse. Thus, we can expect that the use of CRS will have a notable effect. We created six models with different numbers of reactions (in the range of 8–256).

The execution times of 10,240 realizations with the different sizes of model are shown in **Table 5**, and the ratios of the execution times on a CPU and a GPU are shown in **Figure 9**. As a result of compressing the stoichiometry matrix, the stochastic simulation for a model with eight reactions is about 130 times faster on a GPU than on a CPU. This improvement was due to the implementation of CRS, and it was because of the sparseness of the data. In the previous implementation, it was necessary to perform a two-dimensional scan of the stoichiometry matrix in order to determine which molecules should be updated; with the

**Table 5 | Execution times of 10,240 realizations with various sizes of model.**

Number of reactions (model size)	Execution time (s)		CPU/GPU
	CPU	GPU	
8	58	0.45	128.89
16	70	0.59	118.64
32	98	0.85	115.29
64	142	1.54	92.21
128	237	2.88	82.29
256	406	5.52	73.55

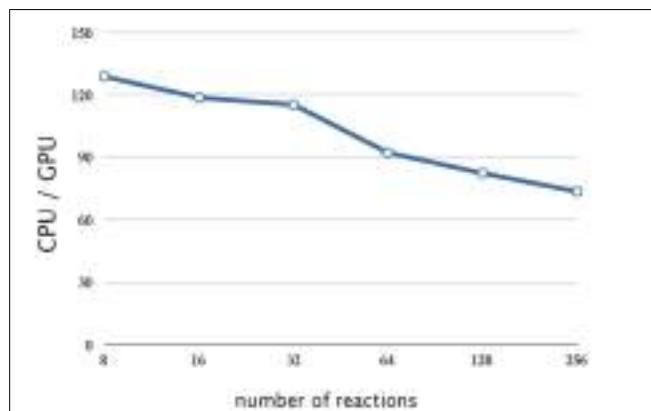


**FIGURE 9 | Performance analysis of data compression w.r.t. the number of reactions.** This figure shows a plot of the ratios of the execution times of 10,240 realization of a single-gene production-reduction model on a CPU (Core i7 2.80 GHz with 12 GB of memory) and on a GPU (NVIDIA Tesla C1060) as the vertical axis, and the number of reactions (model size) as the horizontal axis. Compression of the stoichiometry matrix resulted in a further improvement by a factor of 1.4 for a model with eight reactions; this was about 130 times faster than on a CPU. On the other hand, the execution time on a GPU was notably longer for larger models (>64 reactions).

CRS, the molecular information is stored as an index; thus, it is not necessary to scan the matrix, and the number of molecules can be updated with a minimal computational cost (**Figure 5**).

Although this implementation resulted in a drastic improvement in performance, the execution time on a GPU was notably longer for larger models (> 64 reactions), as shown in **Figure 9**. This is not caused by the firing of the reaction (step 7, Section 2.1), but by the calculation of the propensity function and the selection of the reaction (steps 3, 4, and 6 Section 2.1); this is because the execution time of these procedures increases with an increase in the number of reactions.

We now consider the effect of CRS on the memory footprint of the stoichiometry matrix. Assume that a model consists of  $r$  reactions and  $m$  molecular species; the size of the stoichiometry matrix  $S_{sm}$  will be

$$S_{sm} = m \times r \quad (6)$$

and after using CRS, the size of the new stoichiometry matrix  $S_{crs}$  will be

$$S_{crs} = r + 2\alpha \quad (7)$$

where  $\alpha$  is the total number of elements in the CRS. Assuming  $\bar{m}$  molecules are involved, on average, as reactants or products of each reaction,  $\alpha$  will satisfy  $\alpha = \bar{m} \cdot r$ ; thus the size of the modified matrix is as follows:

$$S_{crs} = (2\bar{m} + 1) \times r \quad (8)$$

From Equations (6, 8), the difference in the memory footprint depends on the values of  $m$  and  $\bar{m}$ . In the direct method (step 3, Section 2.1),  $\bar{m}$  will be a value between zero and two; CRS will result in a smaller memory footprint even with a small model.

## 4. DISCUSSION

In this section, we will summarize and discuss the results of our implementation.

**Table 6** summarizes the acceleration methods implemented in this work and the ratios of the execution times compared with the implementation of the direct method on a CPU (CPU/GPU). From **Table 6**, it can be seen that the memory access optimization resulted in the greatest improvement in the performance, followed by the asynchronous data transfer and data compression. Although a GPU has the potential to be used for high-performance computing, its computational power cannot be harnessed by simply parallelizing an algorithm; this is because the

**Table 6 | Summary of accelerated stochastic simulator and its various acceleration methods.**

Methods	Parallelization algorithm	Acceleration (CPU/GPU)
Parallelization of the direct method	Hybrid	16
Memory access optimization	Hybrid	50
	Coarse-grained	60
Asynchronous data transfer	Coarse-grained	90
Data compression	Coarse-grained	130

way in which data is accessed during execution is a critical factor in GPU computing. We demonstrated this with our results in Section 3.2.

The primary feature that differentiates a discrete stochastic simulation from a continuous simulation (such as numerical integration of a differential equation) is the use of random numbers. When numerically integrating a differential equation, it is obvious that, given identical initial conditions, each simulation will produce identical results. On the other hand, stochastic simulations require multiple realizations, the results of each one being determined by random numbers. Parallelization on a GPU is well-suited for this kind of simulation, because a simulator can share one model for multiple realizations, which reduces the memory footprint. Choosing the best parallelization algorithm from fine-grained, coarse-grained, and hybrid parallelization is another important need with GPU computing. In principle, coarse-grained parallelization is the most efficient method for multiple realizations, because it only requires infrequent synchronization between the threads. For the problem that we considered in this study, multiple realizations using one model was a requirement, so parallelizing one realization (fine-grained parallelization) was not as effective as parallelizing multiple realizations (coarse-grained parallelization), because of the need for frequent synchronization. This was also shown in Section 3.2. Fine-grained parallelization has the potential to accelerate a simulation when an objective model contains a large number of reactions and/or a large number of molecular species, which result in high computational cost for the calculation of the propensity functions. Although we did not consider fine-grained parallelization after Section 3.2, preliminary results were shown in Section 3.4. It was shown that the performance improvement obtained by coarse-grained parallelization will decrease logarithmically with the model size, as shown in Figure 9. This result suggests that it might be possible to solve this problem by calculating the propensity function using fine-grained parallelization. The efficiency of parallelization can be measured by the occupancy<sup>1</sup>, which is defined to be the number of active thread groups divided by the maximum number of thread groups. If there is a synchronization between threads during a simulation, some preceding threads will be required to wait until the remaining threads reach the synchronization point. The number of waiting threads will decrease the occupancy, because they will be included in the denominator. The occupancy depends on the particular problem and the parallelization method, but in principle, hybrid parallelization can lead to lower occupancy than that of coarse-grained parallelization. Applying hybrid parallelization is challenging, since high occupancy must be maintained.

Functionality for storing all of the time course data during a realization is an essential feature for understanding the dynamics of a model. We note that this functionality is found in most existing software tools that support stochastic simulation (Ramsey et al., 2005; Hoops et al., 2006; Mauch and Stalzer, 2011; Sanft et al., 2011). An existing proposal for the acceleration of the direct method using a GPU (Li and Petzold, 2010) performs faster than our method (speedups by a factor of about 200), but it lacks the functionality for storing all the time course data, which not only consumes memory but also increases execution time. Our

intent was to add functionality to store the time course data while improving performance. We used an asynchronous data transfer scheme so that the time course data would be transferred during the simulation and thus decrease the data transfer time (Figure 8). Overall, we achieved a speedup by a factor of 130 compared with a sequential realization on a CPU.

Our evaluation was performed on an NVIDIA Tesla C1060, which has 240 arithmetic units (cores) and 4 GB of memory. The peak performance of the C1060 is 933 Gflops in single-precision floating point format. Several GPUs have been released by NVIDIA for the purpose of GPGPU. For example, the NVIDIA Tesla K40, which is a high-end product with 2880 cores and 12 GB of memory, provides 4.29 Tflops at peak single-precision floating-point performance. By implementing our method on a high-end GPU, we would expect a greater improvement in performance. The performance is not affected only by the number of flops; current GPUs have a higher compute capability (3.5) compared with the C1060 (1.3). The difference in compute capability directly affects the memory access performance. In principle, higher compute capability will place a lower penalty on uncoalesced access and looser restrictions on coalesced access and bank conflicts. Benchmarking on a GPU with higher compute capability might show different results for improvements when using different acceleration methods.

In this study, we applied parallelization and several acceleration methods to the direct method, which is the most straightforward way to implement the SSA of Gillespie. As described in Section 2.1, there are several algorithms for the SSA, and the use of simulation algorithms can improve the total throughput. The next targets for improved implementation are the optimized direct method (Cao et al., 2004) and the sorting direct method (McCollum et al., 2006). The optimized direct method optimizes the order of  $\sum_{i=0}^{n-1} a_i$  (in step 6, Section 2.1) to reduce the calculation time. The sorting direct method is another improvement of the direct method. The difference between the optimized direct method and the sorting direct method is a pre-simulation step, in which the optimized direct method sorts the propensity functions. Since both algorithms are based on the direct method, extending our implementation to them is expected to have a notable effect on parallelization.

In this work, we have designed and implemented several parallelization algorithms and acceleration methods for the SSA. We have included a time course recording function while accelerating SSA simulations by a factor of up to 130. GPUs are known to be a cost-effective and power-saving solution for high-performance computing. With the added functionality for recording the time course and the ability to import a model that is described in SBML, we hope that our implementation will contribute to the field of systems biology, in which modeling and simulation play important roles in understanding complex biological systems.

## AUTHOR CONTRIBUTIONS

AF conceived of the study and coordinated the project. KS designed and implemented the majority of the source code; KH and AF participated in the design of the acceleration scheme. NH and AF supervised the project. KS, NH, and AF wrote the manuscript. All authors read and approved the final manuscript.

## FUNDING

This work was supported by JSPS KAKENHI Grant Numbers 23136513 and 24300112.

## ACKNOWLEDGMENTS

We are deeply grateful to Mr. Nobuyuki Ohta (Keio University), Mr. Kota Mashimo (Keio University) and Mr. Akito Tabira (Keio University) for our fruitful discussions.

## REFERENCES

- Arkin, A., Ross, J., and McAdams, H. (1998). Stochastic kinetic analysis of developmental pathway bifurcation in phage  $\lambda$ -infected *Escherichia coli* cells. *Genetics* 149, 1633–1648.
- Bornstein, B. J., Keating, S. M., Jouraku, A., and Hucka, M. (2008). LibSBML: an API library for SBML. *Bioinformatics* 24, 880–881. doi: 10.1093/bioinformatics/btn051
- Cao, Y., Li, H., and Petzold, L. (2004). Efficient formulation of the stochastic simulation algorithm for chemically reacting systems. *J. Chem. Phys.* 121, 4059–4067. doi: 10.1063/1.1778376
- Gibson, M., and Bruck, J. (2000). Efficient exact stochastic simulation of chemical systems with many species and many channels. *J. Phys. Chem. A* 104, 1876–1889. doi: 10.1021/jp993732q
- Gillespie, D. (1976). A general method for numerically simulating the stochastic time evolution of coupled chemical reactions. *J. Comput. Phys.* 22, 403–434. doi: 10.1016/0021-9991(76)90041-3
- Gillespie, D. (1977). Exact stochastic simulation of coupled chemical reactions. *J. Phys. Chem.* 81, 2340–2361. doi: 10.1021/j100540a008
- Hoops, S., Sahle, S., Gauges, R., Lee, C., Pahle, J., Simus, N., et al. (2006). COPASI—a COmplex PAthway SImlator. *Bioinformatics* 22, 3067–3074. doi: 10.1093/bioinformatics/btl485
- Hucka, M., Finney, A., Sauro, H. M., Bolouri, H., Doyle, J. C., Kitano, H., et al. (2003). The systems biology markup language (SBML): a medium for representation and exchange of biochemical network models. *Bioinformatics* 19, 524–531. doi: 10.1093/bioinformatics/btg015
- Hucka, M., Finney, A., Bornstein, B. J., Keating, S. M., Shapiro, B. E., Matthews, J., et al. (2004). Evolving a lingua franca and associated software infrastructure for computational systems biology: the Systems Biology Markup Language (SBML) project. *Syst. Biol.* 1, 41–53. doi: 10.1049/sb:20045008
- Kitano, H. (2002). Systems biology: a brief overview. *Science* 295, 1662–1664. doi: 10.1126/science.1069492
- Komarov, I., and D’Souza, R. M. (2012). Accelerating the gillespie exact stochastic simulation algorithm using hybrid parallel execution on graphics processing units. *PLoS ONE* 7:e46693. doi: 10.1371/journal.pone.0046693
- Li, H., and Petzold, L. (2010). Efficient parallelization of the stochastic simulation algorithm for chemically reacting systems on the graphics processing unit. *Int. J. High Perform. Comput. Appl.* 24, 107. doi: 10.1177/1094342009106066
- Matsumoto, M., and Nishimura, T. (1998). Mersenne twister: a 623-dimensionally equidistributed uniform pseudo-random number generator. *ACM Trans. Model. Comput. Simul.* 8, 3–30. doi: 10.1145/272991.272995
- Mauch, S., and Stalzer, M. (2011). Efficient formulations for exact stochastic simulation of chemical systems. *IEEE/ACM Trans. Comput. Biol. Bioinform.* 8, 27–35. doi: 10.1109/TCBB.2009.47
- McAdams, H. H., and Arkin, A. (1997). Stochastic mechanisms in gene expression. *Proc. Natl. Acad. Sci. U.S.A.* 94, 814–819. doi: 10.1073/pnas.94.3.814
- McCollum, J., Peterson, G., Cox, C., Simpson, M., and Samatova, N. (2006). The sorting direct method for stochastic simulation of biochemical systems with varying reaction execution behavior. *Comput. Biol. Chem.* 30, 39–49. doi: 10.1016/j.compbiochem.2005.10.007
- Nvidia. C. (2014). NVIDIA CUDA Programming Guide (version 6.5). Santa Clara, CA: NVIDIA Corporation. Available online at: <http://docs.nvidia.com/cuda/cuda-c-programming-guide/>
- Owens, J. D., Luebke, D., Govindaraju, N., Harris, M., Kruger, J., Lefohn, A. E., et al. (2007). A survey of general-purpose computation on graphics hardware. *Eurographics* 26, 80–113. doi: 10.1111/j.1467-8659.2007.01012.x
- Podlozhnyuk, V. (2007). Parallel Mersenne Twister. Santa Clara, CA: NVIDIA Corporation. Available online at: [http://developer.download.nvidia.com/compute/cuda/1.1-Beta/x86\\_website/projects/MersenneTwister/doc/MersenneTwister.pdf](http://developer.download.nvidia.com/compute/cuda/1.1-Beta/x86_website/projects/MersenneTwister/doc/MersenneTwister.pdf)
- Ramsey, S., Orrell, D., and Bolouri, H. (2005). Dizzy: stochastic simulation of large-scale genetic regulatory networks. *J. Bioinform. Comput. Biol.* 3, 415–436. doi: 10.1142/S0219720005001132
- Sanft, K. R., Wu, S., Roh, M., Fu, J., Lim, R. K., and Petzold, L. R. (2011). Stochkit2: software for discrete stochastic simulation of biochemical systems with events. *Bioinformatics* 27, 2457–2458. doi: 10.1093/bioinformatics/btr401

**Conflict of Interest Statement:** The authors declare that the research was conducted in the absence of any commercial or financial relationships that could be construed as a potential conflict of interest.

*Received: 16 October 2014; accepted: 29 January 2015; published online: 13 February 2015.*

*Citation: Sumiyoshi K, Hirata K, Hiroi N and Funahashi A (2015) Acceleration of discrete stochastic biochemical simulation using GPGPU. *Front. Physiol.* 6:42. doi: 10.3389/fphys.2015.00042*

*This article was submitted to Systems Biology, a section of the journal Frontiers in Physiology.*

*Copyright © 2015 Sumiyoshi, Hirata, Hiroi and Funahashi. This is an open-access article distributed under the terms of the Creative Commons Attribution License (CC BY). The use, distribution or reproduction in other forums is permitted, provided the original author(s) or licensor are credited and that the original publication in this journal is cited, in accordance with accepted academic practice. No use, distribution or reproduction is permitted which does not comply with these terms.*



# Function of metabolic and organelle networks in crowded and organized media

Miguel A. Aon \* and Sonia Cortassa

Department of Medicine, School of Medicine, Johns Hopkins University, Baltimore, MD, USA

**Edited by:**

Noriko Hiroi, Keio University, Japan

**Reviewed by:**

Julio Vera González, University Hospital Erlangen, Germany  
Akatsuki Kimura, National Institute of Genetics, Japan

**\*Correspondence:**

Miguel A. Aon, Department of Medicine, School of Medicine, Johns Hopkins University, 720 Rutland Avenue, Ross Bldg. 1059, Baltimore, MD 21205, USA  
e-mail: maon1@jhmi.edu

(Macro)molecular crowding and the ability of the ubiquitous cytoskeleton to dynamically polymerize–depolymerize are prevalent cytoplasmic conditions in prokaryotic and eukaryotic cells. Protein interactions, enzymatic or signaling reactions - single, sequential or in complexes - whole metabolic pathways and organelles can be affected by crowding, the type and polymeric status of cytoskeletal proteins (e.g., tubulin, actin), and their imparted organization. The self-organizing capability of the cytoskeleton can orchestrate metabolic fluxes through entire pathways while its fractal organization can frame the scaling of activities in several levels of organization. The intracellular environment dynamics (e.g., biochemical reactions) is dominated by the orderly cytoskeleton and the intrinsic randomness of molecular crowding. Existing evidence underscores the inherent capacity of intracellular organization to generate emergent global behavior. Yet unknown is the relative impact on cell function provided by organelle or functional compartmentation based on transient proteins association driven by weak interactions (quinary structures) under specific environmental challenges or functional conditions (e.g., hypoxia, division, differentiation). We propose a qualitative, integrated structural-functional model of cytoplasmic organization based on a modified version of the *Sierspinsky–Menger–Mandelbrot sponge*, a 3D representation of a percolation cluster, and examine its capacity to accommodate established experimental facts.

**Keywords:** enzyme kinetics, metabolism, quinary structures, cytoskeleton, molecular crowding, fractal, Sierpinsky sponge, percolation

*It seems to me that cells leave very little to random processes and that they have evolved the capacity to escape much of the chaos of solutions, (...). It appears unlikely that a messy alphabet soup would be used to spell out the elaborate prose of intermediary metabolism.*

James S. Clegg, 1984

## INTRODUCTION

Cells are very far from random mixtures of molecules. The classical experiments of Kempner and Miller (1968) showed that cells are not bags of freely floating enzymes. Using cells from the unicellular eukaryote Euglena as “centrifuge tubes” (Clegg, 1984a), these authors (Kempner and Miller, 1968) could distinguish several layers within cells (that remained viable) after centrifugation. No macromolecules could be detected in the “soluble phase” and many of the main enzymes considered to exist free in solution were instead associated with layers containing organelles (mitochondria, lysosomes, nucleus) and subcellular structures (ribosomes).

Ideas about cytoplasmic organization have a long history that can be traced back to the notion of protoplasm as the substratum of cellular activity (Welch and Clegg, 2010). Early microscopic techniques (reviewed in Aon and Cortassa, 1997, Chapter 6) and the more recent cryoelectron tomography (Medalia et al., 2002) unveiled the overall crowded nature of the cellular cytoplasm populated by complex macromolecular assemblies besides subcellular organelles (Luby-Phelps, 2000; Minton, 2001; Grunewald et al.,

2003; Ovádi and Norris, 2013) (see **Figure 2A**). Studies starting in the twentieth and well into the twenty-first centuries used advanced molecular-cellular biology methods including fluorescence recovery after photobleaching, in conjunction with confocal microscopy and time-resolved anisotropy methods, to establish a decrease in the diffusion coefficients of proteins in the cytoplasm and in the endoplasmic reticulum lumen compared with water (Luby-Phelps, 2000; Verkman, 2002; Rivas et al., 2004). The consequences of these results are very significant for cell function because diffusion of solutes and macromolecules in cellular compartments mediates many physiological processes, including metabolism and signaling events. On the other hand, active transport via motor proteins leads to a significantly higher mobility compared to diffusion processes (Fakhri et al., 2014).

Obtaining information about the molecular properties of proteins in the living cell is becoming an active field of research (Wirth and Gruebele, 2013). Existent and new molecular techniques and methodologies enable monitoring of native protein activity and folding in cells, offering information on concentration, dynamics, location, interactions and protein proximity (Diekmann and Hoischen, 2014; Fakhri et al., 2014).

## ENZYMATIC REACTIONS IN ORGANIZED CROWDED MEDIA

Supramolecular organization and crowding are two main traits of the intracellular milieu (Aon and Cortassa, 1997; Aon et al.,

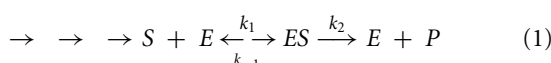
2001). The cellular cytoplasm contains (macro)molecules: a mixture of molecules of low (e.g., ATP, glutathione, NADH) and higher molecular weight (e.g., proteins, lipids, polysaccharides) and macromolecular arrays (e.g., tubulin and F-actin polymers, glycogen granules), at concentrations such that they occupy a large fraction of its total volume. Such media are “crowded” but no individual (macro)molecular species is present at a high concentration *per se* (Minton, 1997).

“Background” species concern (macro)molecules that do not interact specifically with either the reactants or products of a particular reaction. Proteins in the crowded cellular environment can stick to each other through non-specific interactions (e.g., electrostatic, hydrophobic). “Background” species can also contribute large steric repulsive forces in crowded environments (Minton, 2000) that may not be observed directly because they do not lead to the formation of complexes (Zhou et al., 2008). The excluded volume effect depends on the size and concentration of molecular crowders and refers to the volume between, e.g., a pair of interacting proteins, that cannot be occupied by a third protein (Wirth and Gruebele, 2013). If the size of a (macro)molecule is comparable to the size of background species, the available volume is considerably smaller (i.e., excluded volume higher) than in the case that the (macro)molecule is relatively tinier. Lower available volume increases the contribution of steric repulsion to reduce entropy and increase free energy (Rivas et al., 2004). If we consider that to maximize the available volume is a way to reduce free energy then (macro)molecular crowding facilitates a decrease in excluded (occupied) volume via, e.g., molecular compaction and association (Minton, 2000, 2001; Ellis, 2001). Another consequence of crowding is that, via decrease of excluded volume, the folded over the unfolded state of a protein or protein complex is favored (Wirth and Gruebele, 2013).

The reaction rate of an enzymatic reaction may be controlled at diffusional (substrate(s), *S*, access to the enzyme’s, *E*, active site) and/or kinetic (an intrinsic step in the reaction scheme limits the rate) levels. Broadly speaking, diffusional and kinetic control may be assessed through diffusion, percolation or transport of the species *S* and *E* involved, and  $k_2$ , the rate constant of the enzyme–substrate, *ES*, complex transformation into product according to the Henri–Michaelis–Menten (HMM) formalism (Segel, 1975).

For conceptual purpose, let us consider a simple reaction converting *S* into *P*, that involves one ligand, *S*, one catalytic site, *E*, and one enzyme–substrate complex, *ES* (Aon et al., 2004b):

*Diffusion, percolation, transport of S and/or E*



$k_2$ , also known as the catalytic rate constant,  $k_{cat}$ , and  $k_{-1}$  are monomolecular rate constants whereas  $k_1$  is a bimolecular rate constant. In the derivation of the HMM equation from a quasi-steady-state assumption, the dynamics of the *ES* complex association–dissociation is considered to be so fast that its concentration can be treated as if it were in steady state. Accordingly, the  $k_1$  step is considered not to be limiting the  $S \rightarrow P$  conversion. Importantly, from experiments performed over the past two decades, single-molecule enzymology has provided insights

into how specific enzymes—particularly molecular motors and nucleic acid enzymes—work at the molecular level. These studies confirmed that the HMM mechanism expressed in Equation (1) holds at the single molecule level (Xie, 2013).

In heterogeneous, organized, media the rate of encounter between *E* and *S* may be subjected to transport restrictions generated by anomalous diffusion. Protein stickiness will increase the apparent viscosity of the cytoplasm thus decreasing the diffusion coefficient, *D*, since both (viscosity vs. *D*) are inversely related (Dix and Verkman, 2008). Anomalous diffusion introduces a time dependence in *D*, essentially due to the medium heterogeneity (Wirth and Gruebele, 2013) (see below Section Fractal Kinetics in Organized Crowded Media). Both translational and rotational diffusion can be influenced by the excluded volume and the shape of the crowding protein more than other factors such as hydrodynamic or direct interactions (Balbo et al., 2013). Thus, molecular crowding can affect  $k_1$  decreasing enzymatic rates, essentially because as higher the excluded volume by (macro)molecules the higher the rate limitation of the *E*–*S* encounter (Homchaudhuri et al., 2006; Pastor et al., 2014). In support of this interpretation, enzymatic reactions occurring in the presence of increasing dextran concentrations exhibited lower  $V_{max}$  and higher  $K_M$ , the Michaelis–Menten constant (Pastor et al., 2014). The volume occupied by dextran, independent of its size, had an important role on the initial velocity of the hydrolysis of N-succinyl-L-phenyl-Ala-p-nitroanilide catalyzed by alpha-chymotrypsin (Pastor et al., 2011). The  $K_M$  increase could be attributed to a slower diffusion of the protein due to the presence of crowding, whereas the decrease in  $V_{max}$  could be explained by the effect of mixed inhibition by product, which is enhanced in crowded media (Pastor et al., 2014). These results also underscore the relevant role of enzyme size in the initial velocity of reactions occurring in dextran crowded media. When enzymes are small the reaction’s initial velocity mainly depends on the excluded volume. However, for large enzymes, the initial velocity of the reaction is also affected by the size of obstacles present in the environment.

Modeling and experimental work (Kim and Yethiraj, 2009; Pastor et al., 2014) also supports the idea that macromolecular crowding can contribute significantly to changes in enzymatic reactions (Vasilescu et al., 2013). To simulate rapid metabolite transfer between the enzymatic components of the phosphotransferase system (PTS), macromolecular crowding had to be assumed both to increase the association rate constants and to decrease the dissociation rate constants of the PTS complexes (Rohwer et al., 1998). However, crowding was not necessary to simulate yeast glycolysis suggesting that in this eukaryote it does not affect the glycolytic pathway (referred in Rivas et al., 2004). Cortassa and colleagues have also shown that, at least for two glycolytic enzyme couples, the effects of tubulin cytoskeleton proteins was specific and independent from crowding (Cortassa et al., 1994).

Very recent studies using carbon nanotubes for intracellular tracking of kinesin-1 motility highlight stirring dynamics as another important mode of active intracellular transport. Recorded kinesin-1 motility in COS-7 cells over five orders of magnitude in time (Fakhri et al., 2014) enabled the detection of different dynamic regimes ranging between the extremes of

random thermal diffusion and kinesin-driven directed transport propelled by stirring dynamics as a non-equilibrium regime between those extremes.

Weak interactions can mediate transient protein–protein interactions collectively known as “quinary structures,” a term introduced by McConkey (1982) to define a fifth level (beyond the quaternary) of inherently transient protein structural organization. Thermodynamically, the transience of a quinary structure is based on the low stability of the molecular interaction as well as the low energetic barrier between molecular states (Wirth and Gruebele, 2013). Quinary structure has been implicated in a number of cellular processes from metabolism [e.g., the metabolon (Srere, 1987), the protein synthesis pathway (Dang et al., 1985)] to cell signaling (Li et al., 2012). Its inherent transience facilitates dynamic spatial organization of macromolecules in the cytoplasm via loose groupings of, e.g., proteins, when they are working together, but not otherwise (Wirth and Gruebele, 2013).

Overall, (macro)molecular crowding can drive molecular associations in the cytoplasm, and via modulation of the available volume or transient quinary structures influence the kinetics of biochemical reactions.

## CYTOSKELETON ORGANIZATION AND METABOLIC FLUXES

The intracellular environment is not only highly crowded but exhibits a high degree of dynamic organization governed by the principles of self-organization, as they apply to thermodynamically open non-equilibrium systems such as cells (Nicolis and Prigogine, 1977; Aon and Cortassa, 1997; de la Fuente, 2013). By exchanging energy, matter or information with their environment cells or tissues can exhibit emergence that is they self-organize their internal structure and dynamics with novel and sometimes surprising macroscopic properties. For example, the ubiquitous cytoskeletal protein network (actin or tubulin) behaves as a non-linear dissipative system, i.e., it consumes adenine nucleotides to polymerize, with the ability to self-organize, e.g., oscillate (Mandelkow et al., 1989; Mandelkow and Mandelkow, 1992; Tabony and Job, 1992) or alternate in a bistable manner (Aon et al., 1996b; Aon and Cortassa, 1997) between polymerized and depolymerized states. Structurally, the cytoskeletal network exhibits fractal properties (Mandelbrot, 1982; Feder, 1988), i.e., spatially organized in a self-similar manner thus exhibiting an alike form when observed at different degrees of magnification (Rabouille et al., 1992; Aon and Cortassa, 1994; Losa and Nonnenmacher, 1996).

The highly dynamic polymer composite of the cellular cytoplasm is dominated by protein polymers, e.g., microtubules, F-actin and intermediate filaments. In axons in the spinal cord the interaction between neurofilaments and F-actin results in a gel with particular viscoelastic properties (Leterrier et al., 1996). The nucleotide triphosphate hydrolysis-driven polymerization–depolymerization dynamics of cytoskeletal proteins is reciprocally influencing and being influenced by the myriad of reactions involved in intracellular transport (e.g., motors), metabolism, cell locomotion, and muscle contraction among other functions. For example, microtubule tracks are embedded in the viscoelastic actin cytoskeleton, which in turn fluctuates as a result of stresses generated by cytoplasmic myosins; myosin locally

contracts the actin network with an attachment time of several seconds, followed by sudden release (Fakhri et al., 2014).

Cytoskeleton organization is also influenced by cytoplasmic molecular crowding because it favors protein interactions that may form modular complexes (Spirin and Mirny, 2003); some of these molecular complexes constitute stable or transient multienzyme associations (metabolon) (Srere, 1987) capable of metabolic channeling (Welch, 1977; Ovádi and Srere, 2000). In metabolic channels, reactions are facilitated by product–substrate transfer between closely associated enzymes (Ovádi and Srere, 2000).

Microtubules, actin microfilaments and intermediate filaments represent an enormous protein surface in the cell with an estimated area of  $3000 \mu\text{m}^2$  for a typical mammalian cell in culture (Luby-Phelps, 2000). Thus, the cytoskeleton provides an interface for binding a variety of proteins and enzymes. The binding affinity depends on several factors, including phosphorylation status (Luther and Lee, 1986; Roberts and Somero, 1987; Pedrotti et al., 1996), the presence of other proteins, e.g., Microtubule Associated Proteins (MAPs) (Cortassa et al., 1994; Aon and Cortassa, 1997), or enzymatic activity (Cortassa and Aon, 1994; Vertesey et al., 1997; Cassimeris et al., 2012). Protein binding also affects microtubule and enzyme dynamics (Aon et al., 2001; Ovádi and Norris, 2013; Olah et al., 2015). The enhancement of metabolic flux depends upon several factors: (i) the presence for some enzymatic reactions of MAPs apart from tubulin; (ii) the concentration of microtubular protein (MTP); and (iii) the polymeric status (Cortassa et al., 1994). For example, an increase in flux through pyruvate kinase coupled to lactate dehydrogenase was elicited by MTP in a particular concentration range (Cortassa et al., 1994; Aon et al., 1996a) (Figures 1A–C; see figure legend for details). Paclitaxel and nocodazole, two drugs affecting microtubule organization and dynamics in opposite ways, were able to alter the secretion of proteolytic enzymes associated with invasion and metastasis of tumor cells (Alonso et al., 1999). While paclitaxel promotes microtubules polymerization, nocodazole elicits de-polymerization and as such they enhanced or reduced, respectively, the secretion of the urokinase-type plasminogen activator and the matrix metalloproteinase 9 to the culture medium in F3II mammary-carcinoma cells (Alonso et al., 1999).

Ultrasensitivity is a more sensitive response than the one expected from the classical hyperbola of Michaelis–Menten kinetics (Goldbeter and Koshland, 1982; Koshland et al., 1982). The “normal” hyperbolic response requires an 81-fold change in ligand (e.g., substrate, effector) to increase the reaction rate from 10 to 90% of the maximal velocity. Thus, ultrasensitive systems are those that need less than 81-fold change whereas sub-sensitive ones demand more. Depending on their polymeric status, cytoskeletal protein dynamics (actin, MTP) can modulate the ultrasensitive response of enzymatic systems (Aon et al., 2001). This modulation can be mediated by the cytoskeleton in the cell stress response involving changes in volume due to osmotic regulation (Busch et al., 1994; Haussinger et al., 1994a,b; Aon et al., 2000b).

More recent studies show that the heterodimer tubulin composed of  $\alpha$  and  $\beta$  subunits can selectively modulate the mitochondrial outer membrane (MOM) permeability via the voltage-dependent anion channel (VDAC) (Rohwer et al., 1998; Rostovtseva and Bezrukova, 2012) thus having an impact

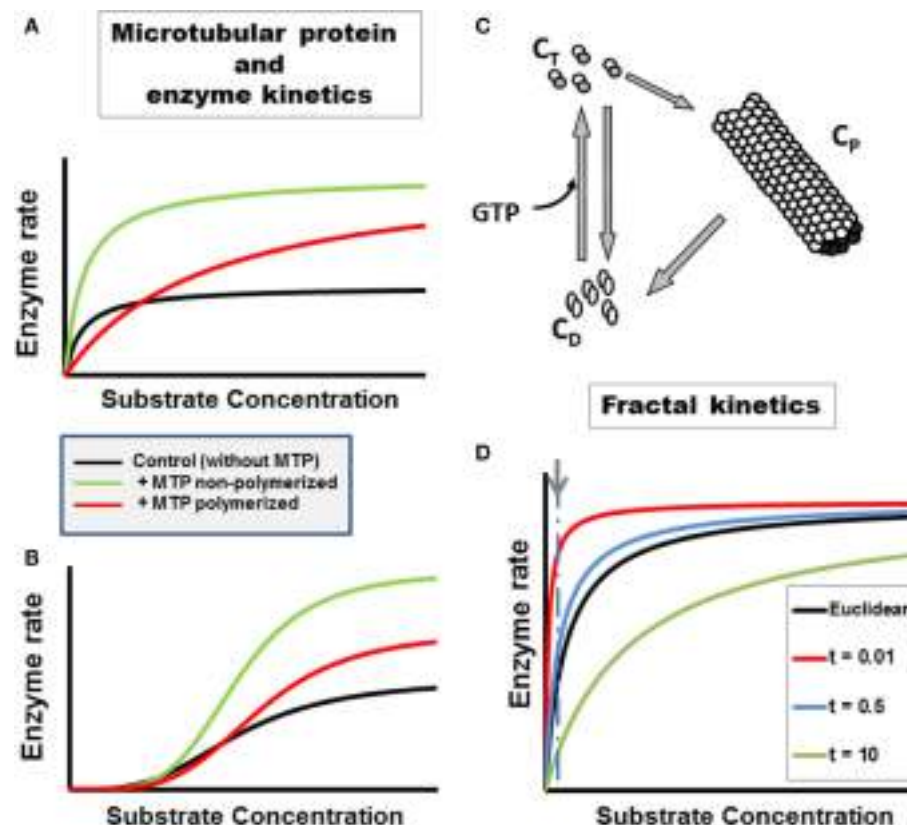
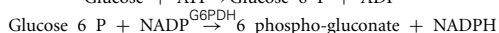
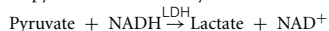
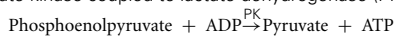


**FIGURE 1 | Enzyme kinetics in heterogeneous, organized fractal medium.** The concentration and polymeric status of the cytoskeleton components tubulin and microtubule associated proteins, i.e., microtubular protein (MTP), can modulate metabolic fluxes and the kinetics of enzymatic reactions through various mechanisms (Aon and Cortassa, 1997). Examples with two enzymatic couples, glucose 6 phosphate dehydrogenase coupled to hexokinase (G6PDH/HK, **A**):



or pyruvate kinase coupled to lactate dehydrogenase (PK/LDH, **B**):



Microtubular protein (MTP) in the flux-stimulatory range (1 mg/ml) (Cortassa et al., 1994) was added to the assay medium containing either G6PDH/HK (**A**) or PK/LDH (**B**). The substrate concentration of the limiting enzyme, NADP or phosphoenolpyruvate (PEP) for HK/GGPDH or PK/LDH couples, respectively, was varied. The presence of polymerized or non-polymerized brain MTP elicited changes in kinetic parameters: (**A**) In the presence of polymerized MTP, G6PDH exhibited an eight-fold increase in the  $K_m$  for NADP and a two-fold increase in  $V_{max}$  with respect to the control without MTP; non-polymerized MTP only induced a two-fold increase in  $V_{max}$  without changing the  $K_m$ . (**B**) In the presence of polymerized brain MTP,

PK exhibited an increase in cooperativity and in  $V_{max}$  with respect to controls as a function of PEP whereas non-polymerized MTP induced an even higher increase in cooperativity and  $V_{max}$ . (**C**) The cycle of assembly-disassembly of MTP. In this cartoon, the cycle of polymerization-depolymerization of MTP assumes that tubulin may exist in one of three forms: polymerized ( $C_p$ ), non-polymerized bound to GTP ( $C_T$ ) or bound to GDP ( $C_D$ ). A model of the MTP cycle and its effects on PK kinetics is presented in Aon and Cortassa (1997). (**D**) Michaelis-Menten kinetics in fractal medium. The dependence of the initial rate of a canonical enzymatically-catalyzed reaction as a function of its substrate is displayed. The  $h$  parameter, reflecting the characteristics of the medium, e.g., obstacle density, and the time-dependence of kinetic constants was calculated as described in Aon et al. (2004b) (see also Section Fractal Kinetics in Organized Crowded Media). The time points,  $t$ , at which the simulations were performed are those indicated in the symbol legend (in min). For simulating reactions occurring in Euclidean space, the parameter values were identical to those of fractal medium except that the rate constants were time-independent (see Aon et al., 2004b for calculation details). At short times the reaction rate becomes much larger, at low  $S$  levels, in fractal than in Euclidean space (indicated by arrow and dashed line). As time passes the reaction rate becomes, transiently, slower in fractal than in Euclidean space; the maximal rate being identical in both cases though achieved at larger  $S$  in fractal medium.

on cellular and mitochondrial energetics (Guzun et al., 2011; Gonzalez-Granillo et al., 2012; Rostovtseva and Bezrukov, 2012). Tubulin in the nM range can influence the voltage sensitivity of VDAC reconstituted into planar phospholipid membranes, and ADP availability to the adenine nucleotide translocator in isolated mitochondria (Rostovtseva et al., 2008). Indeed, VDAC (or porin) is the most abundant protein in the MOM

and is primarily involved in the ATP/ADP exchange between the cytoplasm and mitochondria (Rostovtseva and Colombini, 1997; Colombini, 2004).

## FRACTAL KINETICS IN ORGANIZED CROWDED MEDIA

The impact of self-organized cytoskeletal proteins in fractal forms upon the dynamics of cellular biochemistry started to be explored

more than 20 years ago. Studying chemical reactions in heterogeneous media, Kopelman (1988) made two crucial observations: (i) reactions proceed faster in disconnected (shredded) topologies than in connected ones, and (ii) the rate constants become time-dependent, scaling with time as  $t^{-h}$ ; the  $h$  parameter reflects the characteristics of the medium, e.g., obstacle density, through the fractal dimension, and provides a link with the kinetic rate constant (Kang and Redner, 1984; Dewey, 1995; Aon et al., 2004b). In a medium like the cellular cytoplasm, molecular diffusion becomes anomalous and diffusion coefficients time-dependent due to heterogeneity given not only by (macro)molecular crowding but also by rheological changes impinging on viscosity (Forgacs and Newman, 1994; Aon and Cortassa, 1997).

Aon and Cortassa (1994) and Forgacs (1995) proposed that the cellular cytoplasm is organized as a percolation cluster. It was further conjectured that as a highly shredded object, a percolation cluster may, in principle, bestow more catalytic power to cytoplasmic enzymes. Indeed, medium organization in percolation clusters may enhance reaction rates at short times (Aon et al., 2004b; Hiroi et al., 2011) (**Figure 1D**). The kinetics of biochemical reactions in the cytoplasm depend on (macro)molecular crowding given by the cytoskeleton organization. Hiroi et al. (2011) showed that changing the reaction rate may be possible when the degree of intracellular macromolecular crowding is modified by experimentally manipulating the structure of the cytoskeleton. Cytoskeleton disruption with cytochalasin B and colchicine changed the anomalous diffusion parameter exhibited by enzymes and substrates/products in the cellular cytoplasm. Since the total protein concentration was maintained this suggested that not merely the concentration of intracellular proteins, but also their physiological organization profoundly affects diffusion of free molecules in a cell (Hiroi et al., 2011).

In cellular biochemistry, the fractal approach has been directed to understanding the organization and behavior of (macro)molecules in cells (Rabouille et al., 1992; Savageau, 1995; Liebovitch and Todorov, 1996; Aon et al., 2004b; Schnell and Turner, 2004; Aon and Cortassa, 2009). The approach to fractal kinetics in cells differs between authors. The dependence of the rate constant upon  $h$  has been modeled according to a fractal (Zipf–Mandelbrot) distribution (Schnell and Turner, 2004); assuming HMM kinetics in 2D lattices using Monte Carlo simulations with time-dependent rate constant (Berry, 2002), or in terms of the dependence of the parameter  $h$  on the spectral dimension,  $D_s$ , for HMM or sigmoidal kinetics (Aon et al., 2004b; Hiroi et al., 2011). Main findings show that: (i) spatial segregation of substrate and products increase with the degree of obstruction in the medium making stronger the deviation of the rate constants at longer times and, consequently, the fractal kinetic description as compared with the classical approach (Berry, 2002; Schnell and Turner, 2004); (ii) at short times the reaction rate becomes much larger, at low substrate levels, in fractal than in Euclidean space (**Figure 1D**); this behavior depends on the time-dependence of the  $K_M$ , or an increase in cooperativity and reaction amplification in allosteric kinetics (Aon et al., 2004b). The quickly relaxing molecular mechanisms, when cells are challenged by sudden changes in environmental conditions, would provide fast and precise adaptation. Indeed, fast responses can

lead to slow exhaustion processes preventing lack of substrates, effectors for reactions locally, as found in fractal media organized like percolation clusters (Hiroi et al., 2011).

## COMPUTATIONAL MODELING OF CYTOPLASMIC STRUCTURE–FUNCTION

Interactivity in complex spatiotemporally organized systems like the cellular cytoplasm is fundamental to their counterintuitive behavior and one of the main reasons justifying the need of mathematical modeling for their study. What we seek to understand is how function is coordinated in a cell that exhibits spatially distributed heterogeneous and compartmentalized subsystems with simultaneously unfolding dynamics (Aon, 2013). Factually, (macro)molecular crowding and cytoskeleton organization (i.e., structural) are able to influence the dynamics of biochemical reactions (i.e., functional), yet how does the structural–functional coupling unfolds in physiologically meaningful spatiotemporal patterns is far from clear. One reason is that computational modeling has been mainly concerned with structural or biochemical networks but not with their integrated function. However, forced by computational burden, modeling of cytoplasmic structure–function faces some daunting challenges, beyond the complexity of the task, that demand choices between atomistic molecular-dynamic simulations (McGuffee and Elcock, 2010; Mereghetti and Wade, 2012) and lower resolution coarse-grained models (Moore et al., 2014). Mesoscale models represent a reasonable trade-off between higher simplicity (e.g., treating macromolecules as single interacting centers) while amenable to include finer biopolymer representations to address multiscale problems of diffusion and interaction, as recently reported for the *Escherichia coli* cytoplasm (Trovato and Tozzini, 2014). Modeling can help decide quantitative issues such as whether moderate attraction between proteins and crowding molecules, on the order of 1 kJ/mol, can counteract the excluded volume effect (Rosen et al., 2011) or which macromolecule sizes will experience the strongest attraction and anomalous diffusion (Trovato and Tozzini, 2014).

Some insight into how structural dynamics can affect biochemical function comes from computational modeling of MTP dynamics coupled to the glycolytic pathway and its branches to the Krebs cycle, ethanolic fermentation, and the pentose phosphate (PP) pathways. This study showed that MTP dynamics can coordinately increase or decrease the flux through glycolysis, and that depending on the degree of MTP polymerization a negative control may be exerted by the PP pathway on glycolysis (Aon and Cortassa, 2002). These results may be relevant for cancer therapy because the PP pathway is critical for tumor cells to generate intermediates for nucleic acid synthesis and provide NADPH required both for the synthesis of fatty acids and cell survival under oxidative stress (Patra and Hay, 2014).

A key for progress in this complicated research field will be to adopt an experimental–modeling synergy involving iteration of the loop: simulation–validation and prediction–experimentation (Cortassa and Aon, 2013).

## EMERGENCE IN SUBCELLULAR ORGANELLE NETWORKS

Cytoplasmic organization comprises not only biochemical reactions but also organelles representing membrane-bound

subcellular compartments. Depending on their specific function and situation, subcellular compartments such as mitochondria can play substantial roles in physiology as well as pathophysiology. In heart muscle, for example, mitochondria appear as a network in the form of a regular lattice, spanning the whole myocardial tissue like a power grid (Slodzinski et al., 2008; Aon et al., 2009). Certainly, other cytoplasmic organelles can be subject to the principles of self-organization such as the nucleus and the Golgi complex (Misteli, 2001) as well as the genome itself (Misteli, 2009), but this possibility needs experimental support.

Self-organized collective dynamics in cardiac myocytes arise from synergistically coupled subcellular networks of, e.g., mitochondria (Aon et al., 2006b) or  $\text{Ca}^{2+}$  release units, the latter constituted by four compartments (sarcoplasmic and junctional reticulum, myoplasmic and dyadic space) (Nivala et al., 2012). Emergence in these networks occurs through signaling via second messengers such as reactive oxygen species (ROS) or  $\text{Ca}^{2+}$ . In addition to the normal excitation–contraction–metabolism coupling, a rich dynamic spectrum results, including oscillations, electrical or chemical waves, action potential duration alternans, early or delayed after depolarizations among others (Aon et al., 2004a; Zhou et al., 2010; Nivala et al., 2012; Qu, 2013; Zorov et al., 2014).

In heart mitochondria it was found that the transition from physiological to pathophysiological behavior happens as an emergent phenomenon of the cardiac mitochondrial network, with all the characteristics of systems at critical state (Aon et al., 2006b). This transition occurs at the percolation threshold as determined by applying percolation theory (Aon et al., 2004a). Percolation describes how local neighbor–neighbor interactions among elements in a lattice can scale to produce a macroscopic response spanning from one to the other end of a mitochondrial array (Stauffer and Aharony, 1994). Such a “spanning cluster” forms when there is a critical density of elements close to the threshold for a transition (the percolation threshold). A mitochondrial percolation cluster attains criticality at a certain threshold level of ROS (Aon et al., 2004a). The transition is self-organized, occurs with all the traits of universality—that is, with similar critical exponents as predicted by percolation theory (Schroeder, 1991; Stauffer and Aharony, 1994; Sornette, 2000), and the mitochondrial cluster exhibits fractal organization (Aon et al., 2004b). The ensuing collective oscillations—which involve at least 60% of the mitochondrial network—are synchronized by ROS via ROS-induced ROS release (Zorov et al., 2000, 2014; Aon et al., 2003; Brady et al., 2006) through a diffusion-based mechanism (Zhou et al., 2010).

In yeast, spontaneous oscillations of *Saccharomyces cerevisiae* mitochondrial redox states and membrane potential occur within individual yeasts (Aon et al., 2007b), and synchrony of yeast population indicates the operation of an efficient system of cell–cell interaction to produce concerted metabolic multicellular behavior (Murray et al., 2003, 2013; Lloyd and Murray, 2006, 2007; Roussel and Lloyd, 2007).

## TOWARD AN INTEGRATED STRUCTURAL–FUNCTIONAL MODEL OF CYTOPLASMIC ORGANIZATION

A model compatible with the 3D visualization of the cellular cytoplasmic organization as a percolation cluster (Aon and

Cortassa, 1994; Forgacs, 1995) as suggested by its crowded-organized nature (Medalia et al., 2002) (**Figure 2A**) is the *Sierpinsky–Menger–Mandelbrot sponge* (Mandelbrot, 1982; Raicu and Popescu, 2008) (**Figure 2B**) or a modified version introduced by (Welch and Clegg, 2010) to account also for functional aspects given by “confined regions, ranging from organelles to protein complexes..., responsible for the execution of localized metabolic processes...” (**Figure 2C**).

The modified *Sierpinsky–Menger–Mandelbrot sponge* captures several structural–functional features discussed in this review: (1) the cytoplasmic structure represents a surface with the appearance of a 3D object, because the surface area increases as the volume shrinks. It is straightforward to imagine that the surface area will be modulated by the degree of polymerization of the cytoskeleton in turn influenced by (macro)molecular crowding. (2) It embodies the orderly cytoskeletal organization and the intrinsic randomness of (macro)molecular crowding. These two conditions can create zones of heterogeneity via exclusion (occupied) volume based on attracting (e.g., electrostatic, hydrophobic) or repulsing (e.g., steric) forces. Locally, these regions possess levels of free energy that modulate molecular association, compaction and folding/unfolding of proteins (Zhou et al., 2008; Wirth and Gruebele, 2013). (3) Is a good model for the percolation of fluids through the cytoplasm, including “confined regions” or locally separate clusters of biochemical activity that may extend to other cytoplasmic regions depending on the concentration and status of e.g., enzymatic or organelles’ physiology. These localized clusters determine a certain distance with respect to the percolation threshold where local activities become global thus providing a principle of coordinated functional organization (Aon et al., 2004a; Nivala et al., 2012). (4) Enzymes or enzymatic complexes through their binding to the cytoskeleton, and substrates/effectors/messengers percolating through the “sponge” would determine reaction rates (**Figure 1**) defining local clusters of activity that result in different product concentrations and gradients. (5) It accommodates the existence of “quinary” structures (McConkey, 1982) that drive transiently and loosely grouped ensemble of proteins working together in a dynamic and spatially organized way, e.g., a metabolon or supramolecularly organized enzymatic complex (Srere, 1987), thus explaining compartmentalization in cytoplasmic regions that are not bounded by membranes (Wirth and Gruebele, 2013) (**Figure 2C**). (6) The sponge-like model of the cytoplasm is sound from the status of intracellular water (Clegg, 1984a,b) and rheological standpoints. The ground plan of living cells has been pictured as a reversible, non-covalent gel network (Luby-Phelps et al., 1986; Rabouille et al., 1990) that can be subjected to sol–gel transitions. A colloidal sol state has liquid properties with well-defined viscosity whereas in a gel viscosity becomes practically infinite with the percolation threshold, given by the concentration of polymers in solution, as the critical parameter at which the sol–gel transitions happen (Forgacs and Newman, 1994).

With a model at hand, we can now put it to test and ask questions and/or verify certain predictions. For example, can confined cytoplasmic clusters of biochemical activity be experimentally demonstrated? Could the same enzyme(s), enzymatic complex or organelle behave differently according to local cytoplasmic conditions, e.g., higher presence of F-actin (G-actin) with respect

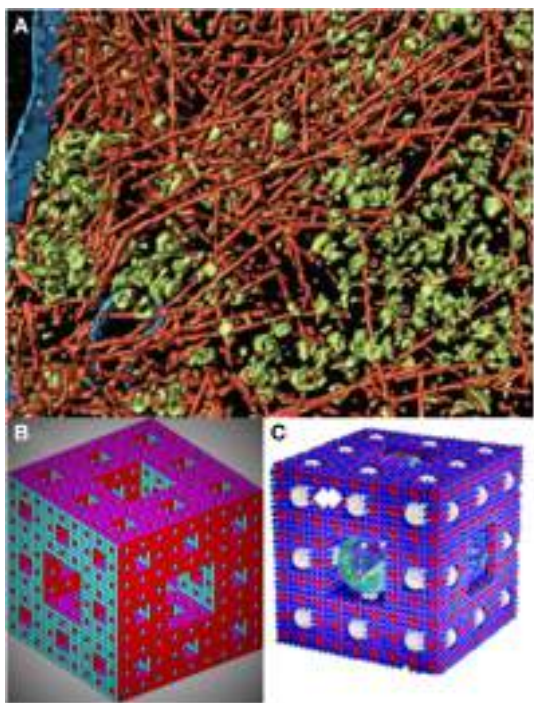


**FIGURE 2 | A fractal sponge-like model of cytoplasmic organization.**

**(A)** Visualization of actin network, membranes, and cytoplasmic macromolecular complexes from electron cryotomography. The pseudo color representation corresponds to actin filaments (red); other macromolecular complexes, mostly ribosomes (green), and membranes (blue) (modified from Medalia et al., 2002). **(B)** The *Sierpinsky carpet* (or gasket) arises from the recursive invariant procedure consisting in repeatedly removing an inverted equilateral triangle from the middle of an initial equilateral triangle (Mandelbrot, 1982). The *Sierpinski-Menger-Mandelbrot sponge* is an extension of the *Sierpinski's carpet* to the three-dimensional Euclidian space (Mandelbrot, 1982) (see also Raicu and Popescu, 2008). This fractal starts from a single cube with an iterative invariant pattern consisting in the removal of a middle cube. The fractal dimension of this structure is 2.727 and if the magnification and removal of the middle cubes continues for  $n \rightarrow \infty$ , it is found that the structure becomes a surface packed into a three dimensional Euclidian space (Raicu and Popescu, 2008), or as graphically put by Welch and Clegg (2010): “a fractal geometric form whose progressive ‘fractalfication’ results in the surface area increasing to (the theoretical limit of) infinity as the volume shrinks to zero” (Image created by Moses Boone; see <http://www.mathworks.com/matlabcentral/fileexchange/3524-sierpinski-sponge>). This is what we call the *Sierpinsky-Menger-Mandelbrot sponge*, or **(C)** the version including idealized spheres designated to account for localized metabolic microenvironments (indicated by a double white arrow on the top left), as first proposed by Welch and Clegg (2010) based on a copyrighted image created by Roman Maeder (see <http://www.mathconsult.ch/showroom/pubs/MathProg/htmls/p2-16.htm>) (modified from Welch and Clegg, 2010).

to microtubules (tubulin)? Can clusters of biochemical activity based on quinary structures be demonstrated, and are these clusters sensitive to the dynamic intracellular environment? Which intracellular conditions define percolation thresholds, and can we show local activity become globally spread? Do these conditions change with cellular stages of growth, division (e.g., G1, S phases) or differentiation? Is the status of cellular cytoplasmic

organization different in differentiated with respect to pluripotent stem cells? How, and to what extent, does the intracellular dynamic field of interrelating polymeric forces play out for the dynamics of metabolic and signaling pathways interacting or being influenced by those polymers, or forming supramolecular complexes themselves? All of these are fascinating and relevant questions that now can be addressed experimentally with emerging new methodologies and a unified structural-functional theoretical framework for cytoplasmic organization.

## REFERENCES

- Alonso, D. F., Farina, H. G., Arregui, C., Aon, M. A., and Gomez, D. E. (1999). Modulation of urokinase-type plasminogen activator and metalloproteinase activities in cultured mouse mammary-carcinoma cells: enhancement by paclitaxel and inhibition by nocodazole. *Int. J. Cancer* 83, 242–246.
- Aon, M. A. (2013). “Complex systems biology of networks: the riddle and the challenge,” in *Systems Biology of Metabolic and Signaling Networks. Energy, Mass and Information Transfer*, eds M.A. Aon, V. Saks, and U. Schlattner (Heidelberg; New York; Dordrecht; London: Springer-Verlag Berlin Heidelberg), 19–35.
- Aon, M. A., Caceres, A., and Cortassa, S. (1996a). Heterogeneous distribution and organization of cytoskeletal proteins drive differential modulation of metabolic fluxes. *J. Cell. Biochem.* 60, 271–278.
- Aon, M. A., and Cortassa, S. (1994). On the fractal nature of cytoplasm. *FEBS Lett.* 344, 1–4. doi: 10.1016/0014-5793(94)00321-1
- Aon, M. A., and Cortassa, S. (1997). *Dynamic Biological Organization. Fundamentals as Applied to Cellular Systems*. London: Chapman and Hall. doi: 10.1007/978-94-011-5828-2
- Aon, M. A., and Cortassa, S. (2002). Coherent and robust modulation of a metabolic network by cytoskeletal organization and dynamics. *Biophys. Chem.* 97, 213–231. doi: 10.1016/S0301-4622(02)00056-X
- Aon, M. A., and Cortassa, S. (2009). “Chaotic dynamics, noise and fractal space in biochemistry,” in *Encyclopedia of Complexity and Systems Science*, ed R. Meyers (New York, NY: Springer), 476–489.
- Aon, M. A., Cortassa, S., Akar, F. G., Brown, D. A., Zhou, L., and O'Rourke, B. (2009). From mitochondrial dynamics to arrhythmias. *Int. J. Biochem. Cell Biol.* 41, 1940–1948. doi: 10.1016/j.biocel.2009.02.016
- Aon, M. A., Cortassa, S., and Caceres, A. (1996b). “Models of cytoplasmic structure and function,” in *Computation in Cellular and Molecular Biological Systems*, eds R. Cuthbertson, R. Holcombe, and R. Paton (London: World Scientific), 195–207.
- Aon, M. A., Cortassa, S., Gomez Casati, D. F., and Iglesias, A. A. (2000b). Effects of stress on cellular infrastructure and metabolic organization in plant cells. *Int. Rev. Cytol.* 194, 239–273. doi: 10.1016/S0074-7696(08)62398-0
- Aon, M. A., Cortassa, S., Lemar, K. M., Hayes, A. J., and Lloyd, D. (2007b). Single and cell population respiratory oscillations in yeast: a 2-photon scanning laser microscopy study. *FEBS Lett.* 581, 8–14. doi: 10.1016/j.febslet.2006.11.068
- Aon, M. A., Cortassa, S., Marban, E., and O'Rourke, B. (2003). Synchronized whole cell oscillations in mitochondrial metabolism triggered by a local release of reactive oxygen species in cardiac myocytes. *J. Biol. Chem.* 278, 44735–44744. doi: 10.1074/jbc.M302673200
- Aon, M. A., Cortassa, S., and O'Rourke, B. (2004a). Percolation and criticality in a mitochondrial network. *Proc. Natl. Acad. Sci. U.S.A.* 101, 4447–4452. doi: 10.1073/pnas.0307156101
- Aon, M. A., Cortassa, S., and O'Rourke, B. (2006b). The fundamental organization of cardiac mitochondria as a network of coupled oscillators. *Biophys. J.* 91, 4317–4327. doi: 10.1529/biophysj.106.087817
- Aon, M. A., Gomez-Casati, D. F., Iglesias, A. A., and Cortassa, S. (2001). Ultrasensitivity in (supra)molecularly organized and crowded environments. *Cell Biol. Int.* 25, 1091–1099. doi: 10.1006/cbir.2001.0804
- Aon, M. A., O'Rourke, B., and Cortassa, S. (2004b). The fractal architecture of cytoplasmic organization: scaling, kinetics and emergence in metabolic networks. *Mol. Cell. Biochem.* 256–257, 169–184. doi: 10.1023/B:MCB.0000009867.54552.09
- Balbo, J., Mereghetti, P., Herten, D. P., and Wade, R. C. (2013). The shape of protein crowders is a major determinant of protein diffusion. *Biophys. J.* 104, 1576–1584. doi: 10.1016/j.bpj.2013.02.041

- Berry, H. (2002). Monte carlo simulations of enzyme reactions in two dimensions: fractal kinetics and spatial segregation. *Biophys. J.* 83, 1891–1901. doi: 10.1016/S0006-3495(02)73953-2
- Brady, N. R., Hamacher-Brady, A., Westerhoff, H. V., and Gottlieb, R. A. (2006). A wave of reactive oxygen species (ROS)-induced ROS release in a sea of excitable mitochondria. *Antioxid. Redox Signal.* 8, 1651–1665. doi: 10.1089/ars.2006.8.1651
- Busch, G. L., Schreiber, R., Dartsch, P. C., Volkl, H., Vom Dahl, S., Haussinger, D., et al. (1994). Involvement of microtubules in the link between cell volume and pH of acidic cellular compartments in rat and human hepatocytes. *Proc. Natl. Acad. Sci. U.S.A.* 91, 9165–9169. doi: 10.1073/pnas.91.19.9165
- Cassimeris, L., Silva, V. C., Miller, E., Ton, Q., Molnar, C., and Fong, J. (2012). Fueled by microtubules: does tubulin dimer/polymer partitioning regulate intracellular metabolism? *Cytoskeleton (Hoboken)*. 69, 133–143. doi: 10.1002/cm.21008
- Clegg, J. S. (1984a). Properties and metabolism of the aqueous cytoplasm and its boundaries. *Am. J. Physiol.* 246, R133–R151.
- Clegg, J. S. (1984b). Intracellular water and the cytomatrix: some methods of study and current views. *J. Cell Biol.* 99, 167s–171s. doi: 10.1083/jcb.99.1.167s
- Colombini, M. (2004). VDAC: the channel at the interface between mitochondria and the cytosol. *Mol. Cell. Biochem.* 256–257, 107–115. doi: 10.1023/B:MCBI.0000009862.17396.8d
- Cortassa, S., and Aon, M. A. (1994). Spatio-temporal regulation of glycolysis and oxidative phosphorylation *in vivo* in tumor and yeast cells. *Cell Biol. Int.* 18, 687–713. doi: 10.1006/cbir.1994.1099
- Cortassa, S., and Aon, M. A. (2013). “Dynamics of mitochondrial redox and energy networks: insights from an experimental-computational synergy,” in *Systems Biology of Metabolic and Signaling Networks. Energy, Mass and Information Transfer*, eds M.A. Aon, V. Saks, and U. Schlattner (Heidelberg; New York; Dordrecht; London: Springer-Verlag Berlin Heidelberg), 115–144.
- Cortassa, S., Caceres, A., and Aon, M. A. (1994). Microtubular protein in its polymerized or nonpolymerized states differentially modulates *in vitro* and intracellular fluxes catalyzed by enzymes of carbon metabolism. *J. Cell. Biochem.* 55, 120–132. doi: 10.1002/jcb.240550114
- Dang, C. V., Ferguson, B., Burke, D. J., Garcia, V., and Yang, D. C. (1985). Interactions of aminoacyl-tRNA synthetases in high-molecular-weight multienzyme complexes from rat liver. *Biochim. Biophys. Acta* 829, 319–326. doi: 10.1016/0167-4838(85)90239-0
- de la Fuente, I. M. (2013). “Metabolic dissipative structures,” in *Systems Biology of Metabolic and Signaling Networks. Energy, Mass and Information Transfer*, eds M.A. Aon, V. Saks, and U. Schlattner (Heidelberg; New York; Dordrecht; London: Springer-Verlag Berlin Heidelberg), 179–211.
- Dewey, T. G. (1995). Chemically-controlled reaction kinetics on fractals: application to hydrogen exchange in lysozyme. *Fractals* 3, 251–267. doi: 10.1142/S0218348X95000217
- Diekmann, S., and Hoischen, C. (2014). Biomolecular dynamics and binding studies in the living cell. *Phys. Life Rev.* 11, 1–30. doi: 10.1016/j.plrev.2013.11.011
- Dix, J. A., and Verkman, A. S. (2008). Crowding effects on diffusion in solutions and cells. *Annu. Rev. Biophys.* 37, 247–263. doi: 10.1146/annurev.biophys.37.032807.125824
- Ellis, R. J. (2001). Macromolecular crowding: an important but neglected aspect of the intracellular environment. *Curr. Opin. Struct. Biol.* 11, 114–119. doi: 10.1016/S0959-440X(00)00172-X
- Fakhri, N., Wessel, A. D., Willms, C., Pasquali, M., Klopfenstein, D. R., MacKintosh, F. C., et al. (2014). High-resolution mapping of intracellular fluctuations using carbon nanotubes. *Science* 344, 1031–1035. doi: 10.1126/science.1250170
- Feder, J. (1988). *Fractals*. New York, NY: Plenum Press. doi: 10.1007/978-1-4899-2124-6
- Forgacs, G. (1995). On the possible role of cytoskeletal filamentous networks in intracellular signaling: an approach based on percolation. *J. Cell Sci.* 108(Pt 6), 2131–2143.
- Forgacs, G., and Newman, S. A. (1994). Phase transitions, interfaces, and morphogenesis in a network of protein fibers. *Int. Rev. Cytol.* 150, 139–148. doi: 10.1016/S0074-7696(08)61540-5
- Goldbeter, A., and Koshland, D. E. Jr. (1982). Sensitivity amplification in biochemical systems. *Q. Rev. Biophys.* 15, 555–591. doi: 10.1017/S003583500003449
- Gonzalez-Granillo, M., Grichine, A., Guzun, R., Usson, Y., Tepp, K., Chekulayev, V., et al. (2012). Studies of the role of tubulin beta II isotype in regulation of mitochondrial respiration in intracellular energetic units in cardiac cells. *J. Mol. Cell. Cardiol.* 52, 437–447. doi: 10.1016/j.yjmcc.2011.07.027
- Grunewald, K., Medalia, O., Gross, A., Steven, A. C., and Baumeister, W. (2003). Prospects of electron cryotomography to visualize macromolecular complexes inside cellular compartments: implications of crowding. *Biophys. Chem.* 100, 577–591. doi: 10.1016/S0301-4622(02)00307-1
- Guzun, R., Karu-Varikmaa, M., Gonzalez-Granillo, M., Kuznetsov, A. V., Michel, L., Cottet-Rousselle, C., et al. (2011). Mitochondria-cytoskeleton interaction: distribution of beta-tubulins in cardiomyocytes and HL-1 cells. *Biochim. Biophys. Acta* 1807, 458–469. doi: 10.1016/j.bbabi.2011.01.010
- Haussinger, D., Lang, F., and Gerok, W. (1994a). Regulation of cell function by the cellular hydration state. *Am. J. Physiol.* 267, E343–E355.
- Haussinger, D., Stoll, B., vom Dahl, S., Theodoropoulos, P. A., Markogiannakis, E., Gravanis, A., et al. (1994b). Effect of hepatocyte swelling on microtubule stability and tubulin mRNA levels. *Biochem. Cell Biol.* 72, 12–19. doi: 10.1139/o94-003
- Hiroi, N., Lu, J., Iba, K., Tabira, A., Yamashita, S., Okada, Y., et al. (2011). Physiological environment induces quick response – slow exhaustion reactions. *Front. Physiol.* 2:50. doi: 10.3389/fphys.2011.00050
- Homchaudhuri, L., Sarma, N., and Swaminathan, R. (2006). Effect of crowding by dextrans and Ficolls on the rate of alkaline phosphatase-catalyzed hydrolysis: a size-dependent investigation. *Biopolymers* 83, 477–486. doi: 10.1002/bip.20578
- Kang, K., and Redner, S. (1984). Scaling approach for the kinetics of recombination processes. *Phys. Rev. Lett.* 52, 955–958. doi: 10.1103/PhysRevLett.52.955
- Kempner, E. S., and Miller, J. H. (1968). The molecular biology of *Euglena gracilis*. IV. Cellular stratification by centrifuging. *Exp. Cell Res.* 51, 141–149. doi: 10.1016/0014-4827(68)90164-X
- Kim, J. S., and Yethiraj, A. (2009). Effect of macromolecular crowding on reaction rates: a computational and theoretical study. *Biophys. J.* 96, 1333–1340. doi: 10.1016/j.bpj.2008.11.030
- Kopelman, R. (1988). Fractal reaction kinetics. *Science* 241, 1620–1626. doi: 10.1126/science.241.4873.1620
- Koshland, D. E. Jr., Goldbeter, A., and Stock, J. B. (1982). Amplification and adaptation in regulatory and sensory systems. *Science* 217, 220–225. doi: 10.1126/science.7089556
- Leterrier, J. F., Kas, J., Hartwig, J., Vegners, R., and Janmey, P. A. (1996). Mechanical effects of neurofilament cross-bridges. Modulation by phosphorylation, lipids, and interactions with F-actin. *J. Biol. Chem.* 271, 15687–15694. doi: 10.1074/jbc.271.26.15687
- Li, P., Banjade, S., Cheng, H. C., Kim, S., Chen, B., Guo, L., et al. (2012). Phase transitions in the assembly of multivalent signalling proteins. *Nature* 483, 336–340. doi: 10.1038/nature10879
- Liebovitch, L. S., and Todorov, A. T. (1996). Using fractals and nonlinear dynamics to determine the physical properties of ion channel proteins. *Crit. Rev. Neurobiol.* 10, 169–187. doi: 10.1615/CritRevNeurobiol.v10.i2.20
- Lloyd, D., and Murray, D. B. (2006). The temporal architecture of eukaryotic growth. *FEBS Lett.* 580, 2830–2835. doi: 10.1016/j.febslet.2006.02.066
- Lloyd, D., and Murray, D. B. (2007). Redox rhythmicity: clocks at the core of temporal coherence. *Bioessays* 29, 465–473. doi: 10.1002/bies.20575
- Losa, G. A., and Nonnenmacher, T. F. (1996). Self-similarity and fractal irregularity in pathologic tissues. *Mod. Pathol.* 9, 174–182.
- Luby-Phelps, K. (2000). Cytoarchitecture and physical properties of cytoplasm: volume, viscosity, diffusion, intracellular surface area. *Int. Rev. Cytol.* 192, 189–221. doi: 10.1016/S0074-7696(08)60527-6
- Luby-Phelps, K., Taylor, D. L., and Lanni, F. (1986). Probing the structure of cytoplasm. *J. Cell Biol.* 102, 2015–2022. doi: 10.1083/jcb.102.6.2015
- Luther, M. A., and Lee, J. C. (1986). The role of phosphorylation in the interaction of rabbit muscle phosphofructokinase with F-actin. *J. Biol. Chem.* 261, 1753–1759.
- Mandelbrot, B. B. (1982). *The Fractal Geometry of Nature*. New York, NY: W.H. Freeman.
- Mandelkow, E., Mandelkow, E. M., Hotani, H., Hess, B., and Muller, S. C. (1989). Spatial patterns from oscillating microtubules. *Science* 246, 1291–1293. doi: 10.1126/science.2588005
- Mandelkow, E. M., and Mandelkow, E. (1992). Microtubule oscillations. *Cell Motil. Cytoskeleton* 22, 235–244. doi: 10.1002/cm.970220403
- McConkey, E. H. (1982). Molecular evolution, intracellular organization, and the quinary structure of proteins. *Proc. Natl. Acad. Sci. U.S.A.* 79, 3236–3240. doi: 10.1073/pnas.79.10.3236

- McGuffee, S. R., and Elcock, A. H. (2010). Diffusion, crowding & protein stability in a dynamic molecular model of the bacterial cytoplasm. *PLoS Comput. Biol.* 6:e1000694. doi: 10.1371/journal.pcbi.1000694
- Medalia, O., Weber, I., Frangakis, A. S., Nicastro, D., Gerisch, G., and Baumeister, W. (2002). Macromolecular architecture in eukaryotic cells visualized by cryoelectron tomography. *Science* 298, 1209–1213. doi: 10.1126/science.1076184
- Mereghetti, P., and Wade, R. C. (2012). Atomic detail brownian dynamics simulations of concentrated protein solutions with a mean field treatment of hydrodynamic interactions. *J. Phys. Chem. B* 116, 8523–8533. doi: 10.1021/jp212532h
- Minton, A. P. (1997). Influence of excluded volume upon macromolecular structure and associations in “crowded” media. *Curr. Opin. Biotechnol.* 8, 65–69. doi: 10.1016/S0958-1669(97)80159-0
- Minton, A. P. (2000). Implications of macromolecular crowding for protein assembly. *Curr. Opin. Struct. Biol.* 10, 34–39. doi: 10.1016/S0959-440X(99)00045-7
- Minton, A. P. (2001). The influence of macromolecular crowding and macromolecular confinement on biochemical reactions in physiological media. *J. Biol. Chem.* 276, 10577–10580. doi: 10.1074/jbc.R100005200
- Misteli, T. (2001). The concept of self-organization in cellular architecture. *J. Cell Biol.* 155, 181–185. doi: 10.1083/jcb.200108110
- Misteli, T. (2009). Self-organization in the genome. *Proc. Natl. Acad. Sci. U.S.A.* 106, 6885–6886. doi: 10.1073/pnas.0902010106
- Moore, T., Wu, S. K., Michael, M., Yap, A. S., Gomez, G. A., and Neufeld, Z. (2014). Self-organizing actomyosin patterns on the cell cortex at epithelial cell-cell junctions. *Biophys. J.* 107, 2652–2661. doi: 10.1016/j.bpj.2014.10.045
- Murray, D. B., Amariel, C., Sasidharan, K., Machne, R., Aon, M. A., and Lloyd, D. (2013). “Temporal partitioning of the yeast cellular network,” in *Systems Biology of Metabolic and Signaling Networks. Energy, Mass and Information Transfer*, eds M.A. Aon, V. Saks, and U. Schlattner (Heidelberg; New York; Dordrecht; London: Springer-Verlag Berlin Heidelberg), 323–349.
- Murray, D. B., Klevecz, R. R., and Lloyd, D. (2003). Generation and maintenance of synchrony in *Saccharomyces cerevisiae* continuous culture. *Exp. Cell Res.* 287, 10–15. doi: 10.1016/S0014-4827(03)00068-5
- Nicolis, G., and Prigogine, I. (1977). *Self-organization in Nonequilibrium Systems: From Dissipative Structures to Order Through Fluctuations*. New York, NY: Wiley.
- Nivala, M., Ko, C. Y., Weiss, J. N., and Qu, Z. (2012). Criticality in intracellular calcium signaling in cardiac myocytes. *Biophys. J.* 102, 2433–2442. doi: 10.1016/j.bpj.2012.05.001
- Olah, J., Norris, V., and Ovádi, J. (2015). Modeling of sensing potency of cytoskeletal systems decorated with metabolic enzymes. *J. Theor. Biol.* 365, 190–196. doi: 10.1016/j.jtbi.2014.10.018
- Ovádi, J., and Norris, V. (2013). “Moonlighting function of the tubulin cytoskeleton: macromolecular architectures in the cytoplasm,” in *Systems Biology of Metabolic and Signaling Networks. Energy, Mass and Information Transfer*, eds M.A. Aon, V. Saks, and U. Schlattner (Heidelberg; New York; Dordrecht; London: Springer-Verlag Berlin Heidelberg), 165–178.
- Ovádi, J., and Srere, P. A. (2000). Macromolecular compartmentation and channeling. *Int. Rev. Cytol.* 192, 255–280. doi: 10.1016/S0074-7696(08)60529-X
- Pastor, I., Pitulice, L., Balcells, C., Vilaseca, E., Madurga, S., Isvoran, A., et al. (2014). Effect of crowding by Dextrans in enzymatic reactions. *Biophys. Chem.* 185, 8–13. doi: 10.1016/j.bpc.2013.10.006
- Pastor, I., Vilaseca, E., Madurga, S., Garces, J. L., Cascante, M., and Mas, F. (2011). Effect of crowding by dextrans on the hydrolysis of N-Succinyl-L-phenyl-Ala-p-nitroanilide catalyzed by alpha-chymotrypsin. *J. Phys. Chem. B* 115, 1115–1121. doi: 10.1021/jp105296c
- Patra, K. C., and Hay, N. (2014). The pentose phosphate pathway and cancer. *Trends Biochem. Sci.* 39, 347–354. doi: 10.1016/j.tibs.2014.06.005
- Pedrotti, B., Ulloa, L., Avila, J., and Islam, K. (1996). Characterization of microtubule-associated protein MAP1B: phosphorylation state, light chains, and binding to microtubules. *Biochemistry* 35, 3016–3023. doi: 10.1021/bi951314f
- Qu, Z. (2013). “Network dynamics in cardiac electrophysiology,” in *Systems Biology of Metabolic and Signaling Networks. Energy, Mass and Information Transfer*, eds M.A. Aon, V. Saks, and U. Schlattner (Heidelberg; New York; Dordrecht; London: Springer-Verlag Berlin Heidelberg), 243–260.
- Rabouille, C., Aon, M. A., Muller, G., Cartaud, J., and Thomas, D. (1990). The supramolecular organization of ovomucin. Biophysical and morphological studies. *Biochem. J.* 266, 697–706.
- Rabouille, C., Cortassa, S., and Aon, M. A. (1992). Fractal organisation in biological macromolecular lattices. *J. Biomol. Struct. Dyn.* 9, 1013–1024. doi: 10.1080/07391102.1992.10507973
- Raicu, V., and Popescu, A. (2008). *Integrated Molecular and Cellular Biophysics*. New York, NY: Springer. doi: 10.1007/978-1-4419-2826-9
- Rivas, G., Ferrone, F., and Herzfeld, J. (2004). Life in a crowded world. *EMBO Rep.* 5, 23–27. doi: 10.1038/sj.embor.7400056
- Roberts, S. J., and Somero, G. N. (1987). Binding of phosphofructokinase to filamentous actin. *Biochemistry* 26, 3437–3442. doi: 10.1021/bi00386a028
- Rohwer, J. M., Postma, P. W., Khodenko, B. N., and Westerhoff, H. V. (1998). Implications of macromolecular crowding for signal transduction and metabolite channeling. *Proc. Natl. Acad. Sci. U.S.A.* 95, 10547–10552. doi: 10.1073/pnas.95.18.10547
- Rosen, J., Kim, Y. C., and Mittal, J. (2011). Modest protein-crowder attractive interactions can counteract enhancement of protein association by intermolecular excluded volume interactions. *J. Phys. Chem. B* 115, 2683–2689. doi: 10.1021/jp200625k
- Rostovtseva, T., and Colombini, M. (1997). VDAC channels mediate and gate the flow of ATP: implications for the regulation of mitochondrial function. *Biophys. J.* 72, 1954–1962. doi: 10.1016/S0006-3495(97)78841-6
- Rostovtseva, T. K., and Bezrukova, S. M. (2012). VDAC inhibition by tubulin and its physiological implications. *Biochim. Biophys. Acta* 1818, 1526–1535. doi: 10.1016/j.bbamem.2011.11.004
- Rostovtseva, T. K., Sheldon, K. L., Hassanzadeh, E., Monge, C., Saks, V., Bezrukova, S. M., et al. (2008). Tubulin binding blocks mitochondrial voltage-dependent anion channel and regulates respiration. *Proc. Natl. Acad. Sci. U.S.A.* 105, 18746–18751. doi: 10.1073/pnas.0806303105
- Roussel, M. R., and Lloyd, D. (2007). Observation of a chaotic multioscillatory metabolic attractor by real-time monitoring of a yeast continuous culture. *FEBS J.* 274, 1011–1018. doi: 10.1111/j.1742-4658.2007.05651.x
- Savageau, M. A. (1995). Michaelis-Menten mechanism reconsidered: implications of fractal kinetics. *J. Theor. Biol.* 176, 115–124. doi: 10.1006/jtbi.1995.0181
- Schnell, S., and Turner, T. E. (2004). Reaction kinetics in intracellular environments with macromolecular crowding: simulations and rate laws. *Prog. Biophys. Mol. Biol.* 85, 235–260. doi: 10.1016/j.pbi.2004.01.012
- Schroeder, M. (1991). *Fractals, Chaos, Power Laws. Minutes from an Infinite Paradise*. New York, NY: W.H. Freeman and Company.
- Segel, I. H. (1975). *Enzyme Kinetics. Behavior and Analysis of Rapid Equilibrium and Steady State Enzyme Systems*. New York, NY: Wiley-Interscience Publications.
- Slodzinski, M. K., Aon, M. A., and O'Rourke, B. (2008). Glutathione oxidation as a trigger of mitochondrial depolarization and oscillation in intact hearts. *J. Mol. Cell. Cardiol.* 45, 650–660. doi: 10.1016/j.yjmcc.2008.07.017
- Sornette, D. (2000). *Critical Phenomena in Natural Sciences. Chaos, Fractals, Selforganization and Disorder: Concepts and Tools*. Berlin; Heidelberg: Springer-Verlag. doi: 10.1007/978-3-662-04174-1
- Spirin, V., and Mirny, L. A. (2003). Protein complexes and functional modules in molecular networks. *Proc. Natl. Acad. Sci. U.S.A.* 100, 12123–12128. doi: 10.1073/pnas.2032324100
- Srere, P. A. (1987). Complexes of sequential metabolic enzymes. *Annu. Rev. Biochem.* 56, 89–124. doi: 10.1146/annurev.bi.56.070187.000051
- Stauffer, D., and Aharony, A. (1994). *Introduction To Percolation Theory*. London: Taylor and Francis.
- Tabony, J., and Job, D. (1992). Gravitational symmetry breaking in microtubular dissipative structures. *Proc. Natl. Acad. Sci. U.S.A.* 89, 6948–6952. doi: 10.1073/pnas.89.15.6948
- Trovato, F., and Tozzini, V. (2014). Diffusion within the cytoplasm: a mesoscale model of interacting macromolecules. *Biophys. J.* 107, 2579–2591. doi: 10.1016/j.bpj.2014.09.043
- Vasilescu, C., Olteanu, M., Flondor, P., and Calin, G. A. (2013). Fractal-like kinetics of intracellular enzymatic reactions: a chemical framework of endotoxin tolerance and a possible non-specific contribution of macromolecular crowding to cross-tolerance. *Theor. Biol. Med. Model.* 10, 55. doi: 10.1186/1742-4682-10-55
- Verkman, A. S. (2002). Solute and macromolecule diffusion in cellular aqueous compartments. *Trends Biochem. Sci.* 27, 27–33. doi: 10.1016/S0968-0004(01)02003-5
- Vertessy, B. G., Orosz, F., Kovacs, J., and Ovádi, J. (1997). Alternative binding of two sequential glycolytic enzymes to microtubules. Molecular studies

- in the phosphofructokinase/aldolase/microtubule system. *J. Biol. Chem.* 272, 25542–25546. doi: 10.1074/jbc.272.41.25542
- Welch, G. R. (1977). On the role of organized multienzyme systems in cellular metabolism: a general synthesis. *Prog. Biophys. Mol. Biol.* 32, 103–191. doi: 10.1016/0079-6107(78)90019-6
- Welch, G. R., and Clegg, J. S. (2010). From protoplasmic theory to cellular systems biology: a 150-year reflection. *Am. J. Physiol. Cell Physiol.* 298, C1280–C1290. doi: 10.1152/ajpcell.00016.2010
- Wirth, A. J., and Gruebele, M. (2013). Quinary protein structure and the consequences of crowding in living cells: leaving the test-tube behind. *Bioessays* 35, 984–993. doi: 10.1002/bies.201300080
- Xie, X. S. (2013). Biochemistry. Enzyme kinetics, past and present. *Science* 342, 1457–1459. doi: 10.1126/science.1248859
- Zhou, H. X., Rivas, G., and Minton, A. P. (2008). Macromolecular crowding and confinement: biochemical, biophysical, and potential physiological consequences. *Annu. Rev. Biophys.* 37, 375–397. doi: 10.1146/annurev.biophys.37.032807.125817
- Zhou, L., Aon, M. A., Almas, T., Cortassa, S., Winslow, R. L., and O'Rourke, B. (2010). A reaction-diffusion model of ROS-induced ROS release in a mitochondrial network. *PLoS Comput. Biol.* 6:e1000657. doi: 10.1371/journal.pcbi.1000657
- Zorov, D. B., Filburn, C. R., Klotz, L. O., Zweier, J. L., and Sollott, S. J. (2000). Reactive oxygen species (ROS)-induced ROS release: a new phenomenon accompanying induction of the mitochondrial permeability transition in cardiac myocytes. *J. Exp. Med.* 192, 1001–1014. doi: 10.1084/jem.192.7.1001
- Zorov, D. B., Juhaszova, M., and Sollott, S. J. (2014). Mitochondrial reactive oxygen species (ROS) and ROS-induced ROS release. *Physiol. Rev.* 94, 909–950. doi: 10.1152/physrev.00026.2013

**Conflict of Interest Statement:** The authors declare that the research was conducted in the absence of any commercial or financial relationships that could be construed as a potential conflict of interest.

*Received: 15 October 2014; accepted: 19 December 2014; published online: 21 January 2015.*

*Citation: Aon MA and Cortassa S (2015) Function of metabolic and organelle networks in crowded and organized media. Front. Physiol. 5:523. doi: 10.3389/fphys.2014.00523*

*This article was submitted to Systems Biology, a section of the journal Frontiers in Physiology.*

*Copyright © 2015 Aon and Cortassa. This is an open-access article distributed under the terms of the Creative Commons Attribution License (CC BY). The use, distribution or reproduction in other forums is permitted, provided the original author(s) or licensor are credited and that the original publication in this journal is cited, in accordance with accepted academic practice. No use, distribution or reproduction is permitted which does not comply with these terms.*



# Surveying the floodgates: estimating protein flux into the endoplasmic reticulum lumen in *Saccharomyces cerevisiae*

Michael Vincent<sup>1,2</sup>, Mark Whidden<sup>1</sup> and Santiago Schnell<sup>1,3,4\*</sup>

<sup>1</sup> Department of Molecular & Integrative Physiology, University of Michigan Medical School, Ann Arbor, MI, USA

<sup>2</sup> Department of Molecular, Cellular, and Developmental Biology, University of Michigan, Ann Arbor, MI, USA

<sup>3</sup> Department of Computational Medicine & Bioinformatics, University of Michigan Medical School, Ann Arbor, MI, USA

<sup>4</sup> Brehm Center for Diabetes Research, University of Michigan Medical School, Ann Arbor, MI, USA

**Edited by:**

Noriko Hiroi, Keio University, Japan

**Reviewed by:**

Eduardo S. Zeron, Centro de Investigacion y de Estudios Avanzados del IPN, Mexico

David McMillen, University of Toronto Mississauga, Canada

**\*Correspondence:**

Santiago Schnell, University of Michigan Medical School, Brehm Center 5132, 1000 Wall Street, Ann Arbor, MI 48105-1915, USA  
e-mail: schnells@umich.edu

Endoplasmic reticulum resident proteins, along with all proteins traveling through the secretory pathway must enter endoplasmic reticulum lumen through membrane-embedded translocons. In *Saccharomyces cerevisiae* the heterotrimeric endoplasmic reticulum translocon is composed of the Sec61p, Sss1p, and Sbh1p core subunits. While the involvement of various molecules associated with the Sec61 complex has been thoroughly characterized, little attention has been given to the overall flux through these channels. In this work we carried out a meta-analysis to estimate the average and absolute flux of proteins into the endoplasmic reticulum lumen. We estimate an average of 460 proteins enter the endoplasmic reticulum every second, with an absolute minimum and maximum flux of 78 and 3700 molecules per second, respectively. With current technologies limiting the ability to obtain accurate measurements of these events, our estimates shed light on the flow of protein entering the endoplasmic reticulum lumen.

**Keywords:** endoplasmic reticulum, protein flux, translocon, protein import, Sec61, unfolded protein response

## INTRODUCTION

During the past few decades the research community has gathered an immense amount of information regarding the function and processes of the endoplasmic reticulum (ER). It is now well understood that this organelle marks the start of the secretory pathway, and orchestrates the folding, modification, and assembly of approximately one third of the eukaryotic proteome. Various physiological conditions, such as increases in protein folding demand or protein flux into the ER lumen, are capable of inducing the upregulation of ER protein folding machinery [for a detailed review, see (Schroder and Kaufman, 2005)]. Understanding the dynamic nature of ER proteostasis is particularly relevant to the investigation of protein misfolding diseases, many of which are characterized in part by the accumulation of misfolded protein in the ER lumen. Recent theoretical work modeling the ER as a continuous flow reactor has identified the inflow of unfolded proteins into the ER as a critical factor for determining threshold behavior of protein misfolding (Sandefur and Schnell, 2011), and support for this prediction has been obtained experimentally (Wright et al., 2013). Although the current of nascent unfolded polypeptides flowing into the ER lumen is recognized as important to understanding protein misfolding diseases, neither theoretical nor experimental attempts have been made to quantify the number of proteins entering the ER in a given unit of time.

High protein traffic is concomitant with high flux through membrane-embedded translocons that function as the proteinaceous gateway to the luminal space. Indeed, this traffic can vary greatly depending on both cellular demand and the protein

folding capacity of the ER itself. For instance, when the accumulation of unfolded and/or misfolded protein exceeds the capacity of the ER folding machinery, the ER exhibits a state of stress. To regain proteostasis, the ER activates the unfolded protein response (UPR), an evolutionarily conserved homeostatic mechanism. In yeast, the Inositol-requiring enzyme 1 exclusively mediates UPR activation, and consequently leads to the upregulation of UPR-target genes encoding protein-folding machinery (Lee, 1987; Kozutsumi et al., 1988; Shamu and Walter, 1996; Sidrauski et al., 1996; Sidrauski and Walter, 1997). However, although much is known regarding ER proteostasis and the circumstances capable of perturbing it, the basal current of protein flowing into the ER remains largely uncharacterized from a quantitative standpoint. Lacking this fundamental knowledge, it is difficult to truly evaluate the specific effect of state-altering perturbations on the ER. Furthermore, efforts to model processes of the ER have been hindered by the absence of this information as well. Current models utilizing unfolded protein source parameters have relied on parameter fitting techniques or assumptions based on biological intuition, but have not used values based on translocation measurements (Pincus et al., 2010; Chambers et al., 2012).

Motivated by the absence of objective measurements of protein import into the ER, we carried out a systematic meta-analysis of proteomic and kinetic data relevant to ER translocation in eukaryotes. We provide a novel estimate of the total import of nascent unfolded polypeptides into the lumen. Furthermore, our method enables others to estimate the flux of any yeast protein localizing to the ER (including both ER-resident and transient proteins). To our knowledge, this work serves as the first

quantitative data-driven estimate of protein flux into the ER in yeast.

## MATERIALS AND METHODS

### DEFINING THE POPULATION OF ER-RESIDENT AND TRANSIENT PROTEINS

By analyzing TAP-tagged strains with a quantitative western blotting approach, Ghaemmaghami et al. determined the single-cell abundances of a majority of the *Saccharomyces cerevisiae* proteome (Ghaemmaghami et al., 2003). The subcellular localization of the yeast proteome has also been determined as well. This was accomplished by analyzing protein localization in cells transfected with green fluorescent protein fusion constructs prepared for all open reading frames (ORFs) predicted in yeast (Huh et al., 2003). The latter study identified 296 ORFs encoding proteins localizing to the ER (Huh et al., 2003). The abundances of 23.6% (70/296) of these ORFs were unable to be quantified experimentally (Ghaemmaghami et al., 2003). Nevertheless, together the 226 quantifiable ORFs encode 3,972,824 ER-localized proteins, and we assume this value represents the total ER protein population. With the population of proteins in place, we next set out to define the population of ER translocons that serve as the entry points for all proteins traveling into the ER.

### ER TRANSLOCON ABUNDANCE ESTIMATES AND THEIR CORRESPONDING KINETIC PARAMETERS

Proteins destined for ER import traverse the membrane via either cotranslational translocation (signal-recognition particle-dependent; SRP-dependent) or posttranslational translocation (SRP-independent) (Katz et al., 1977; Glabe et al., 1980; Hann and Walter, 1991; Ng et al., 1996; Matlack et al., 1999). While differences in molecular machinery exist for each process, Sec61p, Sec62p, Sec63p, Sss1p, and Kar2p (the homolog of the mammalian chaperone BiP) have been identified as common translocon requirements for both processes (Deshaines and Schekman, 1987, 1989; Vogel et al., 1990; Esnault et al., 1993, 1994; Brodsky et al., 1995).

Much remains unknown regarding the specific stoichiometry of the ER translocon. The mammalian Sec61 complex is purified as a heterotrimer, leading many to believe this complex consists of equal numbers of Sec61 $\alpha$ , Sec61 $\beta$ , and Sec61 $\gamma$  subunits (Gorlich and Rapoport, 1993). In yeast, Sec61p-Sss1p-Sbh1p represents the corresponding heterotrimer. However, while Sec61 and Sss1 have been demonstrated as essential, this is not the case for Sbh1 as deletion mutants are viable with only minor protein transportation defects (Finke et al., 1996). Thus, we used the required components (core and auxiliary) encoded by essential genes to define the minimum number of ER translocons present. Fortunately, the cellular abundance has been determined for all but one of these components (Sss1p abundance is unknown). In yeast, Sec61p, Sec62p, and Sec63p are present at 24,800, 16,500, and 17,700 molecules per cell, respectively (Ghaemmaghami et al., 2003). Kar2p is highly abundant at 337,000 molecules per cell, and can be immediately ruled out as a limiting factor for translocon assembly (Ghaemmaghami et al., 2003). Thus, assuming one molecule of each subunit is present per translocon, we

arrive at an estimate of 16,500 ER translocons per cell, which matches the abundance of the limiting Sec62p subunit [inferred from proteomic information obtained from Ghaemmaghami et al. (2003)].

Kinetic parameters relevant to ER translocation are currently unavailable in yeast, however, the rate of translocation has been determined in COS-I cells (Goder et al., 2000). By monitoring the translocation of an N-terminal domain across the ER membrane, Goder et al. (2000) determined this process to occur at a rate of  $8.0 \pm 1.4$  amino acids per second. Assuming a normal distribution, the 95% confidence interval of the translocation rate is  $8.0 \pm 1.1$  amino acids per second. Note that the confidence interval of the average translocation rate falls within the experimentally determined range (Goder et al., 2000). Given the highly conserved nature of the translocation machinery in eukaryotes (Cao and Saier, 2003), it is reasonable to assume ER import proceeds at a similar rate in yeast, and thereby permits its use in our calculations. Having now defined both the general protein population and the gateways into the ER lumen, the stage has been set to estimate the flux of protein entering the ER.

## RESULTS

### ESTIMATING THE AVERAGE PROTEIN FLUX INTO THE ER LUMEN

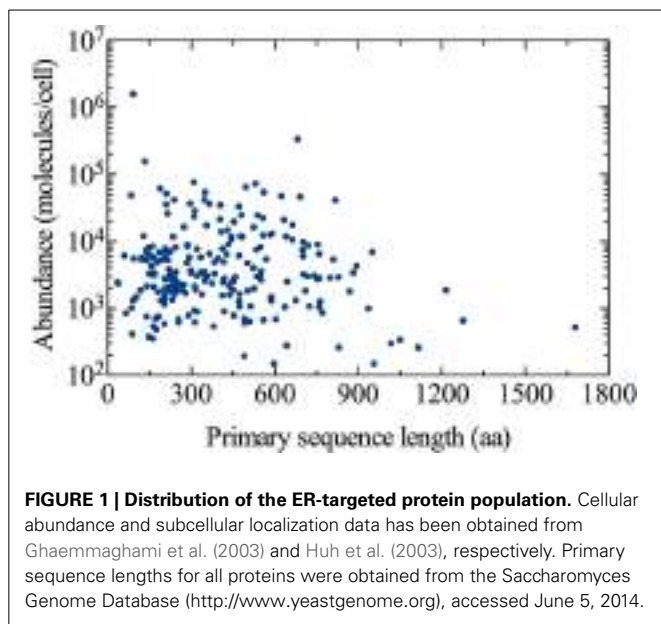
The time for a specific protein to traverse the ER-membrane depends, in part, on the length of its primary amino acid sequence. In reality, diverse populations of proteins with differing lengths flood the luminal space. We reason that the abundance-weighted average of amino acids could capture this overall flux. In the simplest case, a single peptide can be envisioned as a mere string consisting of a defined sequence of amino acids. Thus, the total number of amino acids entering the lumen during a given period of time can be captured by calculating the flow of an average length protein (weighted by abundance) into the ER.

We obtained the primary sequence length for each of the 226 ER-targeted proteins quantified by Ghaemmaghami et al. (2003) (Figure 1). Next, the average length of an ER-localized protein was determined by weighting the length of each by its corresponding abundance (number of molecules per cell of a specific protein divided by total number of ER-localized molecules per cell):

$$L = \frac{\sum_{i=1}^{226} (A_{X_i} \cdot L_{X_i})}{A_{ER}} \quad (1)$$

where  $L$  is the abundance-weighted average length of an ER-localized protein (in amino acids),  $A_{X_i}$  is the abundance of a specific ER localized protein (in molecules/cell),  $L_{X_i}$  is the length of protein  $A_{X_i}$ , and  $A_{ER}$  is the total population of protein localizing to the ER [3,972,824 molecules, determined by analyzing protein abundance data and subcellular localization data presented by Ghaemmaghami et al. (2003) and Huh et al. (2003), respectively].

Using Equation (1), we estimated  $\sim 292$  amino acids as the abundance-weighted average length of an ER-localized protein, with a minimum length of 36 amino acids corresponding to the OST4 subunit of the oligosaccharyltransferase complex



of the ER lumen (ORF: YDL232W), and the NTE1 serine esterase (ORF: YML059C) representing the maximum length of 1679 amino acids. Primary sequence lengths were obtained from the Saccharomyces Genome Database (<http://www.yeastgenome.org>), accessed June 5, 2014 (Cherry et al., 2012).

Having determined  $L$ , the average import time ( $I$ ) for a single protein entering the lumen can be calculated using the rate ( $R$ ) of 8.0 amino acids per second (Goder et al., 2000). Using Equation (2) provided below,

$$I = \frac{L}{R} \quad (2)$$

a value of 36 s is found for  $I$ . Assuming the number of proteins entering the cell at a given moment in time is proportional to the number of ER translocons present at the surface of the ER membrane, we obtain the following expression that describes the total flux of proteins into the ER:

$$F = \frac{A_T}{I} = \frac{A_T \cdot R}{L} \quad (3)$$

where  $F$  is the flux of proteins entering the ER lumen (in number of molecules per second),  $A_T$  is the number of ER translocons per cell (16,500),  $I$  is the import time (in seconds), and  $R$  is the translocation rate of 8.0 amino acids per second. A value of  $\sim 460$  proteins per second is found for  $F$  when calculated with an  $I$  of 36 s (see, Table 1).

#### ESTIMATES FOR THE MINIMUM AND MAXIMUM PROTEIN FLUX INTO THE ER

The demand for protein folding is highly dynamic, and involves increased flux of specific proteins into the ER that largely depends on the physiological state of the cell. Proteins imported into the ER are highly diverse in many aspects, including primary

**Table 1 | Summary of translocation estimates.**

	Average	Min	Max
$I$	36 s	4.5 s	210 s
$F$	460 molecules/s	78 molecules/s	3700 molecules/s

The estimated average protein import time ( $I$ ) and protein flux into the ER lumen ( $F$ ) have been calculated using Equations (2) and (3), respectively. The abundance-weighted average length of an ER-localized protein ( $L$ ) of 292 amino acids (aa) and a translocation rate ( $R$ ) of 8.0 aa/s were used to estimate the averages. In the second and third columns, minimum and maximum translocation estimates have been obtained using Equations (4) and (5), respectively (see, text for details). In the table, s denotes seconds.

sequence length (as observed in Figure 1). This implies the number of proteins entering the ER at a given moment in time can vary dramatically.

Accounting for these considerations, we next calculate the range of  $F$ . This range is fundamentally important because it illustrates the upper and lower theoretical bounds of protein current entering the ER lumen. The absolute minimum flux is defined here as the number of proteins, 1679 amino acids in length, entering the ER per unit time at a translocation rate of 8.0 amino acids per second. On the other hand, we define the absolute maximum flux as the number of 36 amino acid-long proteins entering the ER at a translocation rate of 8.0 amino acids per second. The minimum and maximum import times,  $I_{min}$  and  $I_{max}$ , can be calculated using modified forms of Equation (2):

$$F_{min} = \frac{A_T}{I_{max}}, I_{max} = \frac{L_{max}}{R} \quad (4)$$

$$F_{max} = \frac{A_T}{I_{min}}, I_{min} = \frac{L_{min}}{R} \quad (5)$$

After obtaining values of 210 s for  $I_{max}$  and 4.5 s for  $I_{min}$ , we are able to calculate  $F_{min}$  and  $F_{max}$  as 78 and 3700 molecules per second, respectively (Table 1). Interpreting these results in the context of the entire population of 3,972,824 ER-localized proteins [according to Ghaemmaghami et al. (2003), Huh et al. (2003)], this indicates that the ER imports a load of protein between  $\sim 0.1$  and 5% of its total steady state protein content every minute.

#### ESTIMATING THE IMPORT OF A SPECIFIC PROTEIN INTO THE ER

It is often of interest to many researchers modeling various ER processes to determine import rates of specific proteins. This is especially important to those modeling the UPR, as parameters of this nature define the basal inflow of unfolded proteins entering the system, or describe the flux of folding machinery that antagonize stress-elevating phenomena. The above expression for  $F$  can be extended to obtain such estimates, but must be modified to account for the abundance of the specific protein of interest with respect to the total ER population as a whole. Re-writing Equation (3) we obtain the following expression describing the steady-state flux of a specific protein, denoted  $F_X$ , into the ER

lumen (in molecules per second):

$$F_X = \frac{A_T \cdot A_X}{I_X \cdot A_{ER}} \quad (6)$$

In this expression,  $A_T$  is the number of ER translocons per cell (16,500),  $A_X$  is the abundance of a specific protein X (given in the number of molecules per cell),  $I_X$  is the import duration calculated for protein X and  $A_{ER}$  is total population of protein localizing to the ER (3,972,824 molecules).

To illustrate an application of Equation (6), we calculate the flux of the molecular chaperone Kar2p (BiP) into the ER lumen. Kar2p is highly abundant at 337,000 molecules per cell, and has a primary sequence length of 682 amino acids. Substituting its abundance for  $A_X$ , we calculate  $I_X$  as the product of the Kar2p sequence length and the inverse translocation rate ( $I_X = 85 \text{ s}^{-1}$  when calculated for Kar2p with an average translocation rate of 8.0 amino acids per second). Doing so, we determine the flux of Kar2p into the ER to be 16,466 molecules per second.

## DISCUSSION

We set out to provide data driven estimates for total protein flux into the ER. An illustration summarizing our estimations is presented in **Figure 2**. After first estimating the number of ER translocons present in a single cell, kinetic parameters determined in a eukaryotic system were used to define the rate of translocation of proteins entering the ER lumen. Subsequently, we estimated the ER to experience an average protein inflow of 460 proteins per second. With this value representing the import of an average length protein (weighted by abundance), it accounts for the

total amino acids entering the lumen and therefore respects the diversity of proteins associated with this organelle. Even in light of these considerations, we do not account for the time delay between protein import events, nor do we account for other physicochemical influences (aside from primary sequence length) that could impact this event as well.

Length variations likely hold tremendous influence over the number of distinct peptides entering the lumen in a given period of time. To characterize the effect that protein length has on total flux into the ER, we determined the absolute lower and upper bounds for protein import into the ER, based on the maximal and minimal lengths of all ER-targeted proteins, respectively. Provided this absolute range corresponds to between ~0.1 and 5% of protein content within the ER at steady state, our calculation implies that the combined effort of export and degradation machinery must dismiss roughly 3973–198,641 proteins every minute to maintain protein homeostasis in yeast.

We believe our estimates could be of great value to investigators constructing models of ER processes. The equations presented here can be used to estimate source terms for both specific proteins and larger protein populations entering the ER. Interestingly, it appears that our estimates regarding total protein flux in the ER lumen align well with a corresponding parameter value used in a recent model of the yeast unfolded protein response. Pincus et al. (2010) used parameter-fitting techniques to define the flux of unfolded protein into the ER as 310 proteins per second. This value lies within our absolute range of 78–3700 molecules per second (**Table 1**). While 310 molecules per second is in the lower end of our range, this value could be more appropriate for modeling the UPR as decreased protein translocation

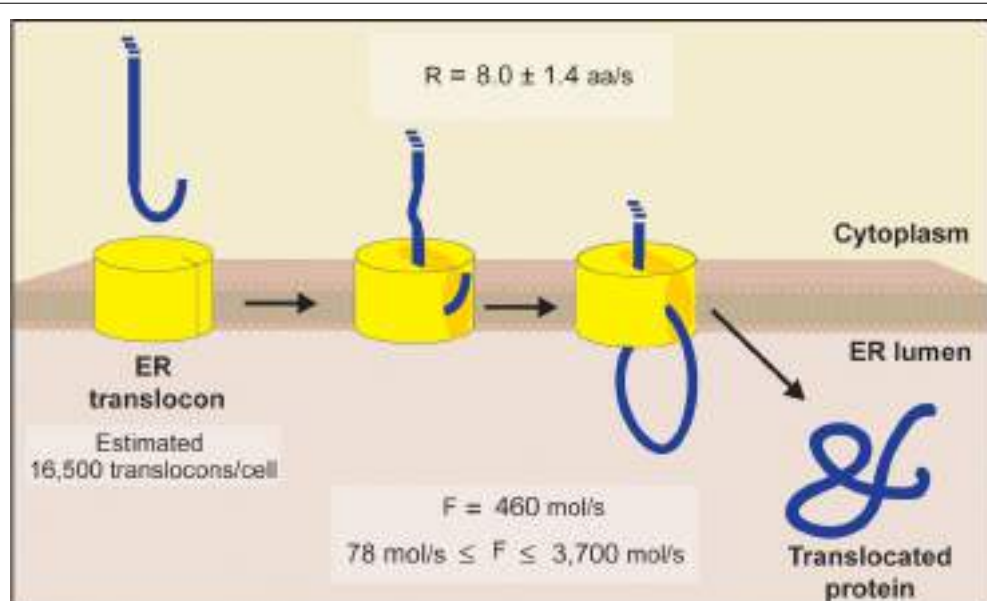


**FIGURE 2 | Schematic diagram of ER translocation summarizing our protein flux estimations.** An estimate of 16,500 translocons per cell was obtained by comparing the abundance of each essential subunit comprising the yeast ER translocon (Sec61p, Sec62p, Sec63p, Sss1p, and Kar2p). This value matches the abundance of Sec62p, the limiting subunit inferred from

proteomic information (Ghaemmaghami et al., 2003). Using translocation rates determined in a eukaryotic system (Goder et al., 2000), we next estimated the ER to experience an average flux of 460 molecules/s, with an absolute minimum and maximum flux of 78 molecules/s and 3700 molecules/s, respectively [see Equations (1–5) for details].

is thought to be one of the consequences of UPR activation (due to the challenge ER stress imposes on the chaperone population). Nevertheless, the estimates presented here may improve the biological accuracy of ER models in the near future.

To our knowledge, our estimate concerning the number of ER translocons per cell is the first that considers its composition in the context of the cellular abundance of each of its core subunits and auxiliary components. We used the abundance of molecules encoded by essential genes to define the translocon population. Interestingly, our estimate of 16,500 translocons per cell excludes the Sbh1p subunit, which is limited to 217 molecules per cell (Ghaemmaghami et al., 2003). Admittedly, yeast mutants lacking Sbh1p are viable, with intact, although impaired, protein translocation into the ER (Finke et al., 1996). This suggests a biologically important role for Sbh1p in the translocon assembly, which could involve aiding the import of a specific subset of proteins into the ER, or improving the overall efficiency of ER translocation.

We acknowledge our estimates were made possible by oversimplifying the process of translocation. For simplicity, we only considered unidirectional protein flow into the ER. Furthermore, we did not account for specific cotranslational and posttranslational translocation considerations, nor did we consider the cycling between ribosome-bound and ribosome-free states. The precise stoichiometry of targeting and auxiliary components distinguishing ER translocons operating in cotranslational vs. posttranslational processes is needed to further distribute our estimated 16,500 ER translocons between each. Also requiring further distribution is the overall population of protein localizing to the ER. If the overall translocon population were split into two subgroups, a consistent methodology would entail each distinct ER-localizing species to be divided among those imported cotranslationally vs. those imported after translation. Indeed, an additional layer of complexity would be provided if yet a third subpopulation were defined as well, composed of proteins that traverse the ER membrane via either mechanism as described by Ng et al. (1996).

Dividing flux estimates between co- and posttranslational translocation mechanisms is further hindered by process-specific details. This is especially true for the former process, which is dependent on the binding of an SRP to an SRP-receptor. The rate of translation carried out by ribosomes docked to the translocon also impacts this process. Kinetic rates for translation and SRP-targeting have been determined experimentally in mammalian systems (Hershey, 1991; Goder et al., 2000). We are unaware of corresponding parameters in yeast. Nevertheless, interactions between the pool of protein awaiting entry into the ER, SRP (and the SRP receptor), ribosomes, and the ER translocon are highly dynamic in nature. Stochastic models would be better suited for adequately addressing these considerations in the future.

Although our estimates are theoretical, we believe they offer valuable insight regarding the flow of protein entering the ER lumen. Taken together with existing proteomic information, we intend the equations contained herein to provide quantitative biologists investigating ER processes with a tool for estimating the import of any ER localizing protein in yeast. It is important that the modeling community continues to provide resources to aid in the identification of realistic parameters, as the use of inaccurate

or biologically irrelevant parameter values can jeopardize the reliability of model predictions. It should also be well understood that reliable parameter estimates are crucial for gaining insights from models in systems and computational biology, especially those involving non-linear phenomena. Nevertheless, this work merely represents an initial step toward quantifying the flow of protein entering the ER lumen. More accurate characterization of ER protein flux awaits further experimental investigation. With the ongoing development of critical biotechnologies, such as nanosensors and novel fluorescent markers, objective measurements of ER protein import may not be far away.

## ACKNOWLEDGMENTS

We thank Reviewer Eduardo S. Zeron for his suggestions and comments. This work is supported by the University of Michigan Protein Folding Diseases Initiative and the James S. McDonnell Foundation (Grant No. 220020223) under the 21st Century Science Initiative Studying Complex Systems. Mark Whidden is supported by an IRACDA Fellowship at the University of Michigan.

## REFERENCES

- Brodsky, J. L., Goeckeler, J., and Schekman, R. (1995). BiP and Sec63p are required for both co- and posttranslational protein translocation into the yeast endoplasmic reticulum. *Proc. Natl. Acad. Sci. U.S.A.* 92, 9643–9646. doi: 10.1073/pnas.92.21.9643
- Cao, T. B., and Saier, M. H. Jr. (2003). The general protein secretory pathway: phylogenetic analyses leading to evolutionary conclusions. *Biochim. Biophys. Acta* 1609, 115–125. doi: 10.1016/S0005-2736(02)00662-4
- Chambers, J. E., Petrova, K., Tomba, G., Vendruscolo, M., and Ron, D. (2012). ADP ribosylation adapts an ER chaperone response to short-term fluctuations in unfolded protein load. *J. Cell Biol.* 198, 371–385. doi: 10.1083/jcb.20120205
- Cherry, J. M., Hong, E. L., Amundsen, C., Balakrishnan, R., Binkley, G., Chan, E. T., et al. (2012). Saccharomyces Genome Database: the genomics resource of budding yeast. *Nucleic Acids Res.* 40, D700–D705. doi: 10.1093/nar/gkr1029
- Deshaias, R. J., and Schekman, R. (1987). A yeast mutant defective at an early stage in import of secretory protein precursors into the endoplasmic reticulum. *J. Cell Biol.* 105, 633–645. doi: 10.1083/jcb.105.2.633
- Deshaias, R. J., and Schekman, R. (1989). SEC62 encodes a putative membrane protein required for protein translocation into the yeast endoplasmic reticulum. *J. Cell Biol.* 109, 2653–2664. doi: 10.1083/jcb.109.6.2653
- Esnault, Y., Blondel, M. O., Deshaias, R. J., Schekman, R., and Kepes, F. (1993). The yeast SSS1 gene is essential for secretory protein translocation and encodes a conserved protein of the endoplasmic reticulum. *EMBO J.* 12, 4083–4093.
- Esnault, Y., Feldheim, D., Blondel, M. O., Schekman, R., and Kepes, F. (1994). SSS1 encodes a stabilizing component of the Sec61 subcomplex of the yeast protein translocation apparatus. *J. Biol. Chem.* 269, 27478–27485.
- Finke, K., Plath, K., Panzner, S., Prehn, S., Rapoport, T. A., Hartmann, E., et al. (1996). A second trimeric complex containing homologs of the Sec61p complex functions in protein transport across the ER membrane of *S. cerevisiae*. *EMBO J.* 15, 1482–1494.
- Ghaemmaghami, S., Huh, W. K., Bower, K., Howson, R. W., Belle, A., Dephoure, N., et al. (2003). Global analysis of protein expression in yeast. *Nature* 425, 737–741. doi: 10.1038/nature02046
- Glabe, C. G., Hanover, J. A., and Lennarz, W. J. (1980). Glycosylation of ovalbumin nascent chains. The spatial relationship between translation and glycosylation. *J. Biol. Chem.* 255, 9236–9242.
- Goder, V., Crottet, P., and Spiess, M. (2000). *In vivo* kinetics of protein targeting to the endoplasmic reticulum determined by site-specific phosphorylation. *EMBO J.* 19, 6704–6712. doi: 10.1093/emboj/19.24.6704
- Gorlich, D., and Rapoport, T. A. (1993). Protein translocation into proteoliposomes reconstituted from purified components of the endoplasmic reticulum membrane. *Cell* 75, 615–630. doi: 10.1016/0092-8674(93)90483-7

- Hann, B. C., and Walter, P. (1991). The signal recognition particle in *S. cerevisiae*. *Cell* 67, 131–144. doi: 10.1016/0092-8674(91)90577-L
- Hershey, J. W. (1991). Translational control in mammalian cells. *Annu. Rev. Biochem.* 60, 717–755. doi: 10.1146/annurev.bi.60.070191.003441
- Huh, W. K., Falvo, J. V., Gerke, L. C., Carroll, A. S., Howson, R. W., Weissman, J. S., et al. (2003). Global analysis of protein localization in budding yeast. *Nature* 425, 686–691. doi: 10.1038/nature02026
- Katz, F. N., Rothman, J. E., Lingappa, V. R., Blobel, G., and Lodish, H. F. (1977). Membrane assembly *in vitro*: synthesis, glycosylation, and asymmetric insertion of a transmembrane protein. *Proc. Natl. Acad. Sci. U.S.A.* 74, 3278–3282. doi: 10.1073/pnas.74.8.3278
- Kozutsumi, Y., Segal, M., Normington, K., Gething, M. J., and Sambrook, J. (1988). The presence of malfolded proteins in the endoplasmic reticulum signals the induction of glucose-regulated proteins. *Nature* 332, 462–464. doi: 10.1038/332462a0
- Lee, A. S. (1987). Coordinated regulation of a set of genes by glucose and calcium ionophores in mammalian cells. *Trends Biochem. Sci.* 12, 20–23. doi: 10.1016/0968-0004(87)90011-9
- Matlack, K. E., Misselwitz, B., Plath, K., and Rapoport, T. A. (1999). BiP acts as a molecular ratchet during posttranslational transport of prepro-alpha factor across the ER membrane. *Cell* 97, 553–564. doi: 10.1016/S0092-8674(00)80767-9
- Ng, D. T., Brown, J. D., and Walter, P. (1996). Signal sequences specify the targeting route to the endoplasmic reticulum membrane. *J. Cell Biol.* 134, 269–278. doi: 10.1083/jcb.134.2.269
- Pincus, D., Chevalier, M. W., Aragon, T., van Anken, E., Vidal, S. E., El-Samad, H., et al. (2010). BiP binding to the ER-stress sensor Ire1 tunes the homeostatic behavior of the unfolded protein response. *PLoS Biol.* 8:e1000415. doi: 10.1371/journal.pbio.1000415
- Sandefur, C. I., and Schnell, S. (2011). A model of threshold behavior reveals rescue mechanisms of bystander proteins in conformational diseases. *Biophys. J.* 100, 1864–1873. doi: 10.1016/j.bpj.2011.03.006
- Schroder, M., and Kaufman, R. J. (2005). ER stress and the unfolded protein response. *Mutat. Res.* 569, 29–63. doi: 10.1016/j.mrfmmm.2004.06.056
- Shamu, C. E., and Walter, P. (1996). Oligomerization and phosphorylation of the Ire1p kinase during intracellular signaling from the endoplasmic reticulum to the nucleus. *EMBO J.* 15, 3028–3039.
- Sidrauski, C., Cox, J. S., and Walter, P. (1996). tRNA ligase is required for regulated mRNA splicing in the unfolded protein response. *Cell* 87, 405–413. doi: 10.1016/S0092-8674(00)81361-6
- Sidrauski, C., and Walter, P. (1997). The transmembrane kinase Ire1p is a site-specific endonuclease that initiates mRNA splicing in the unfolded protein response. *Cell* 90, 1031–1039. doi: 10.1016/S0092-8674(00)80369-4
- Vogel, J. P., Misra, L. M., and Rose, M. D. (1990). Loss of BiP/GRP78 function blocks translocation of secretory proteins in yeast. *J. Cell Biol.* 110, 1885–1895. doi: 10.1083/jcb.110.6.1885
- Wright, J., Wang, X., Haataja, L., Kellogg, A. P., Lee, J., Liu, M., et al. (2013). Dominant protein interactions that influence the pathogenesis of conformational diseases. *J. Clin. Invest.* 123, 3124–3134. doi: 10.1172/JCI67260
- Conflict of Interest Statement:** The authors declare that the research was conducted in the absence of any commercial or financial relationships that could be construed as a potential conflict of interest.
- Received: 30 August 2014; accepted: 29 October 2014; published online: 13 November 2014.*
- Citation:* Vincent M, Whidden M and Schnell S (2014) Surveying the floodgates: estimating protein flux into the endoplasmic reticulum lumen in *Saccharomyces cerevisiae*. *Front. Physiol.* 5:444. doi: 10.3389/fphys.2014.00444
- This article was submitted to Systems Biology, a section of the journal Frontiers in Physiology.*
- Copyright © 2014 Vincent, Whidden and Schnell. This is an open-access article distributed under the terms of the Creative Commons Attribution License (CC BY). The use, distribution or reproduction in other forums is permitted, provided the original author(s) or licensor are credited and that the original publication in this journal is cited, in accordance with accepted academic practice. No use, distribution or reproduction is permitted which does not comply with these terms.*



# Spatial distributions at equilibrium under heterogeneous transient subdiffusion

Hugues Berry<sup>1,2\*</sup> and Hédi A. Soula<sup>1,3\*</sup>

<sup>1</sup> Beagle, Institut National de Recherche en Informatique et en Automatique, Villeurbanne, France

<sup>2</sup> Laboratoire d'InfoRmatique en Image et Systèmes d'information, UMR 5205 CNRS-INSA, Université de Lyon, Villeurbanne, France

<sup>3</sup> Institut Multidisciplinaire de Biochimie des Lipides, Inserm UMR1060, Université de Lyon, Villeurbanne, France

**Edited by:**

Noriko Hiroi, Keio University, Japan

**Reviewed by:**

Ralf Metzler, Technical University of Munich, Germany

Sergei Fedotov, The University of Manchester, UK

Yuichi Togashi, Hiroshima University, Japan

**\*Correspondence:**

Hugues Berry, Beagle, Institut National de Recherche en Informatique et en Automatique, 56 Blvd Niels Bohr, CS 52132, Villeurbanne Cedex 69603, France  
e-mail: hugues.berry@inria.fr;

Hédi A. Soula, Institut Multidisciplinaire de Biochimie des Lipides, Inserm UMR1060, Université de Lyon, 11 Avenue Jean Capelle, Villeurbanne 69621, France  
e-mail: hedi.soula@insa-lyon.fr

Experimental measurements of the mobility of macromolecules, especially proteins, in cells and their membranes consistently report transient subdiffusion with possibly position-dependent—non-homogeneous—properties. However, the spatiotemporal dynamics of protein mobility when transient subdiffusion is restricted to a subregion of space is still unclear. Here, we investigated the spatial distribution at equilibrium of proteins undergoing transient subdiffusion due to continuous-time random walks (CTRW) in a restricted subregion of a two-dimensional space. Our Monte-Carlo simulations suggest that this process leads to a non-homogeneous spatial distribution of the proteins at equilibrium, where proteins increasingly accumulate in the CTRW subregion as its anomalous properties are increasingly marked. In the case of transient CTRW, we show that this accumulation is dictated by the asymptotic Brownian regime and not by the initial anomalous transient dynamics. Moreover, our results also show that this dominance of the asymptotic Brownian regime cannot be simply generalized to other scenarios of transient subdiffusion. In particular, non-homogeneous transient subdiffusion due to hindrance by randomly-located immobile obstacles does not lead to such a strong local accumulation. These results suggest that, even though they exhibit the same time-dependence of the mean-squared displacement, the different scenarios proposed to account for subdiffusion in the cell lead to different protein distribution in space, even at equilibrium and without coupling with reaction.

**Keywords:** brownian diffusion, subdiffusion, spatial protein distribution, nonhomogeneous cellular media, continuous-time random walks

## 1. INTRODUCTION

Traditional biology and biochemistry approaches tend to view the inside of a cell and its constituent membranes as uniform, homogeneous and well-stirred media. However, under the light of the recent advances in experimental methodologies, they rather appear disordered and heterogeneous, with high levels of crowding typical of poorly-connected media (Dix and Verkman, 2008; Cambi and Lidke, 2012; Höfling and Franosch, 2013; Parry et al., 2014). For instance, cell membranes are heterogeneous collections of contiguous spatial micro- or nanodomains with various length and time scales (e.g., fences, lipid rafts, caveolae) (Jacobson et al., 2007; Cambi and Lidke, 2012), that restrict the lateral mobility of proteins in a position-dependent way (Kenworthy et al., 2004; Goodwin et al., 2005; Fujita et al., 2007; Day and Kenworthy, 2009; Kusumi et al., 2011).

In addition to the complexity brought about by the spatial heterogeneity of protein mobility, protein diffusion itself can deviate from the ideal case of Brownian motion. Measurements of the movement of proteins in living cells (in particular in membranes) has consistently been reported to exhibit subdiffusion (a variety of anomalous diffusion). In subdiffusion, the mean square displacement scales sub-linearly with time,  $\langle R^2(t) \rangle \propto t^\gamma$  with  $\gamma < 1$  (Schwille et al., 1999; Smith et al., 1999; Fujiwara

et al., 2002; Weigel et al., 2011; Höfling and Franosch, 2013), as opposed to  $\gamma = 1$  in Brownian motion. Currently, there exist three major theoretical scenarios to explain the observations of subdiffusion, all of which rest on the idea that the interior of cells and their membranes experience large molecular crowding due to their high densities of proteins, lipids, carbohydrates, filamentous networks and organelles, with widely-distributed sizes (Dix and Verkman, 2008; Höfling and Franosch, 2013). The arguably simplest scenario, referred to as “Fractional Brownian Motion,” is a generalization of the classical Brownian motion, where the random increments between two successive locations of the random walker are not independent (like in Brownian motion) but present long-range temporal correlations (Barkai et al., 2012). The second scenario is hindered diffusion in the presence of randomly-distributed immobile obstacles (Saxton, 1994; Berry, 2002; Höfling and Franosch, 2013). The third scenario, referred to as “Continuous-Time Random Walks” (CTRW) assumes that the complexity of the cellular media changes the statistics of the residence time  $\tau$  between two moves of the random walkers. Whereas Dirac—or exponentially—distributed residence times lead to the classical Brownian motion, power-law distributed residence time,  $\eta(\tau) \propto \tau^{-\alpha}$ , generates subdiffusive motion with  $\gamma = \alpha - 1$  provided  $1 < \alpha < 2$  (Bouchaud and Georges, 1990; Metzler and

Klafter, 2000; Höfling and Franosch, 2013). Those three scenarios all lead to sublinear scaling of the mean square displacement with time, i.e., subdiffusion. Other scenarios for subdiffusion have been explored (e.g., scaled Brownian motion, some heterogeneous Brownian processes or correlated CTRW) but are less well studied, see Metzler et al. (2014) for a review.

Whatever the underlying scenario considered, subdiffusion is usually studied in situations that are so simple that their applicability to biology can be questioned. Yet, several factors contribute to the complexity of the cellular media:

(i) *Subordination*: The three scenarios above need not be mutually exclusive but could combine in a subordinated process (Weigel et al., 2011; Tabei et al., 2013).

(ii) *Transience*: In several experimental reports (Platani et al., 2002; Murase et al., 2004; Saxton, 2007; Bronstein et al., 2009; Jeon et al., 2011), the anomalous regime is only transient: after the initial anomalous regime, the mean square displacement crossovers back to normal (Brownian) diffusion (with  $\gamma = 1$ ) but with a smaller apparent diffusion coefficient.

(iii) *Non-homogeneity*: The intensity of the molecular crowding, and/or the anomalous exponent  $\gamma$  may vary depending on the location inside the cell (Wachsmuth et al., 2000; Kühn et al., 2011), thus defining a position-dependent exponent  $\gamma(x)$ .

The spatiotemporal dynamics of protein mobility when any of those three factors is at play is still obscure. For instance, it is only recently that subdiffusion with space-dependent exponent has been explored. In a one-dimensional lattice-based space where the anomalous exponent is set to a much smaller value in one of the lattice sites, Fedotov and Falconer (2012) reported a striking accumulation phenomenon: after possibly a long transient,

all the mobile molecules locate at the lattice site with smallest exponent. Similar accumulation phenomena were reported by Korabel and Barkai for particle transport in binary systems, for which space is partitioned into two subdomains, where diffusion is Brownian or CTRW, respectively (Korabel and Barkai, 2010, 2011). Similarly, recent studies have shown that non-homogeneous Brownian motion (where the diffusion coefficient depends on space) can give rise to counterintuitive behaviors, including CTRW-like transport (Cherstvy et al., 2013, 2014).

In the present work, we focused on CTRW-based subdiffusion and studied the impact of transience and non-homogeneity on the spatial distribution of the proteins at equilibrium. In the framework of CTRW, transience is naturally introduced by the addition of an upper bound to the residence time  $\tau_C$  (cutoff time, see Materials and Methods). In such a transient CTRW,  $\langle R^2 \rangle$  indeed first scales as  $t^\gamma$  at short times, then crosses over to a Brownian motion (with  $\gamma = 1$ ) for  $t \gg \tau_C$ . This asymptotic Brownian regime can be considered a macroscopic view of the underlying microscopic subdiffusion, with a “macroscopic” diffusion coefficient (Figures 1A,B):

$$D_M = \frac{(\Delta x)^2}{4 \int_{\Delta t}^{\tau_C} \tau \eta(\tau) d\tau} \quad (1)$$

where  $\eta(\tau)$  is the distribution of the residence time,  $\Delta t$  the time step of the Monte-Carlo simulation and  $\int_{\Delta t}^{\tau_C} \tau \eta(\tau) d\tau$  is the mean residence time of the random walk. To introduce non-homogeneous diffusion, we considered a “patchy” two dimensional space domain (Figure 1C). In the center of the domain, we locate a square patch, of area fraction  $\phi$ , in which diffusion

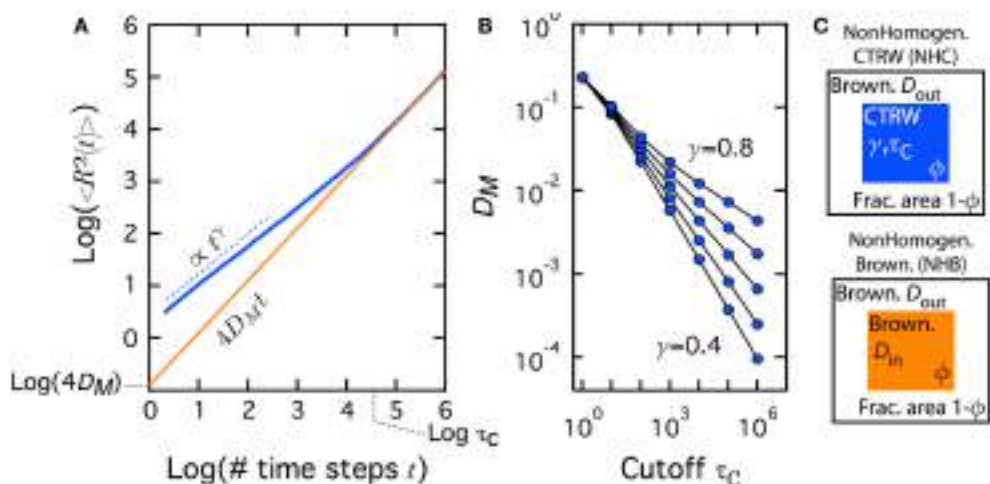


**FIGURE 1 | Transient subdiffusion (CTRW) turns Brownian at times longer than the cutoff  $\tau_C$ .** (A) The mean square displacement  $\langle R^2 \rangle$  in transient CTRW (blue curve) first scales as  $t^\gamma$  (where  $\gamma$  is the anomalous exponent), but at time scales larger than the cutoff  $\tau_C$ , transient CTRW converges to a Brownian motion with  $D_M$  as (macroscopic) diffusion coefficient, i.e.,  $\langle R^2 \rangle = 4D_M t$  (brown curve). The dashed line shows a scaling with exponent  $\gamma$ ,  $\langle R^2 \rangle \propto t^\gamma$ . (B) The microscopic diffusion coefficient  $D_M$  decreases rapidly with increasing cutoff times  $\tau_C$  and decreasing anomalous exponents.  $\gamma = 0.8, 0.7, 0.6, 0.5$ , and  $0.4$ , from top to bottom. (C) In the

following, we study the spatially non-homogeneous case where the diffusion conditions inside a central patch, of fraction area  $\phi$  differ from the diffusion conditions outside the patch. In the non-homogeneous CTRW (NHC) case, diffusion is Brownian with diffusion coefficient  $D_{out}$  outside the patch and a CTRW with parameters  $(\gamma, \tau_C)$  inside. In the non-homogeneous Brownian (NHB) case (used for comparison), diffusion is Brownian both outside the patch (diffusion coefficient  $D_{out}$ ) and inside the patch (with diffusion coefficient  $D_{in}$  set so as to match the macroscopic diffusion coefficient  $D_M$  obtained in transient CTRW with the same parameters  $\gamma$  and  $\tau_C$ ).

is due to a transient CTRW. Outside the patch, diffusion is Brownian. This setup therefore defines a non-homogeneous transient CTRW (NHC) process.

Our Monte-Carlo simulations show that the spatial distribution at equilibrium of proteins subject to such a transient NHC process is itself non-homogeneous: with increasingly strong subdiffusion (i.e., when  $\gamma$  decreases or  $\tau_C$  increases), the proteins progressively accumulate in the central patch. We show that this accumulation is totally controlled by the long-time (Brownian) regime of the transient CTRW and not the initial anomalous transient. However, we also show that the dominance of the long-time Brownian regime in transient subdiffusion cannot be extended to other scenarios. Indeed, non-homogeneous transient subdiffusion due to hindrance by randomly-located immobile obstacles also exhibit transient subdiffusion followed by a slowed-down Brownian regime. However, we show that this situation does not lead to such a strong local accumulation, but to depletion of the central patch or weak accumulation, depending on how concentrations are computed. Therefore, even in the simplest case of pure lateral mobility (i.e., no reaction), the knowledge of the time-dependence of the mean square displacement is not sufficient to predict the distribution of the proteins at equilibrium. This simulation work strongly suggests that the different scenarios proposed to account for transient subdiffusion in the cell could lead to different protein distribution in space, even at equilibrium and in the absence of any reaction (binding, post-translational modifications, internalization...).

## 2. MATERIALS AND METHODS

All simulations take place in a  $w \times w$  2D square lattice with reflective boundaries. At initialization, we position  $N_T$  proteins uniformly at random without excluded volume i.e., several proteins can occupy the same site. When a protein arrives at lattice site  $(i, j)$  at time  $t_{\text{arrival}}$ , its residence time  $\tau$  is sampled from a distribution  $\eta_{i,j}$ . The next jump time of the protein therefore is set as  $t_{\text{arrival}} + \tau$ .  $\eta_{i,j}$  depends on the nature of the arrival site  $(i, j)$ . If  $(i, j)$  belongs to an area of Brownian motion,  $\eta_{i,j}$  is an exponential distribution of parameter  $\tau_B \Delta t$  (where  $\Delta t$  is the simulation time step):  $\eta_{i,j}(\tau) = 1 / (\tau_B \Delta t) \exp(-\tau / (\tau_B \Delta t))$ .  $\tau_B \Delta t$  is the average residence time and sets the diffusion coefficient at site  $(i, j)$ :  $D(i, j) = \Delta x^2 / (4\tau_B \Delta t)$  where  $\Delta x$  is the lattice spacing (see Equation 1). If the site  $(i, j)$  belongs to an area of CTRW, the residence time is sampled from the power-law distribution  $\eta_{i,j}(\tau) = \gamma \tau^{-(1+\gamma)} / (\Delta t^{-\gamma} - \tau_C^{-\gamma})$ , for which  $\int_{\Delta t}^{\tau_c} \eta(\tau) d\tau = 1$ . Hence  $\Delta t$ , the simulation time step is the smallest residence time possible and  $\tau_c$ , the cut-off time, sets its maximal value. At each simulation time step  $t = n\Delta t$ , the algorithm finds all the proteins that have their jump time in  $[n-1, n]\Delta t$ . Each of those proteins independently jump to a destination site that is chosen uniformly at random from its 4 nearest neighbors ( $i \pm 1, j \pm 1$ ).

Note that in the literature, the cutoff of the residence time distribution is frequently introduced using a soft cutoff, instead of the hard cutoff used in this study. Such “tempered” (soft) cutoff is commonly obtained by adding an exponential cutoff to the distribution of residence times i.e.,  $\eta(\tau) = \gamma \Delta t^\gamma \tau^{-(1+\gamma)} \exp(-\tau/\tau_C)$ . In a subset of the simulations shown below, we have replaced our hard cutoff with a

tempered one and found that the results were identical to those obtained with our hard cutoff. We conclude that the exact implementation of the cutoff does not have significant impact on the results reported below.

For simulation of spatially non-homogeneous Brownian diffusion (NHB), we position the boundary of the slowed-down patch in the middle of neighbor lattice sites. Each lattice side  $(i, j)$  therefore belongs either to the slowed-down patch [we thus set its diffusion constant to  $D(i, j) = D_1$ ] or to the outer region (and we set  $D(i, j) = D_0 > D_1$ ). In the case of spatially non-homogeneous CTRW (NHC), we also position the boundary between the CTRW patch and the Brownian exterior in the middle of neighbor lattice sites. Therefore each lattice side  $(i, j)$  either belongs either to the CTRW patch or to the outer Brownian region.

To compare NHB and NHC, we simply computed the average residence time for the CTRW distribution according to the cut-off ( $\tau_c$ ) and  $\gamma$  parameters:  $\int_{\Delta t}^{\tau_c} \tau \eta(\tau) d\tau$  and use this value as the mean residence time for Brownian motion (see Equation 1).

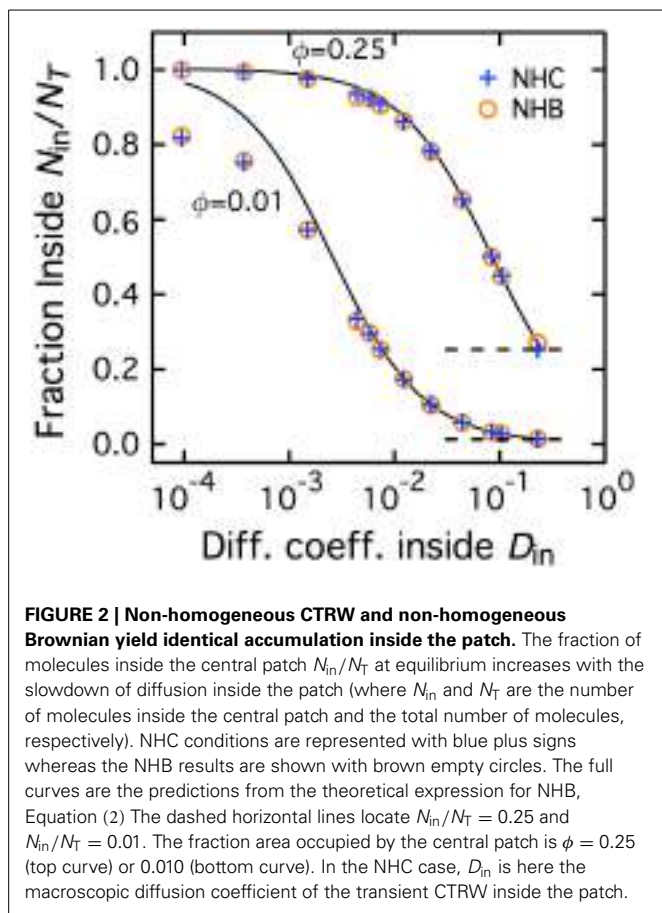
Subdiffusion due to obstacle hinderance was simulated by positioning obstacles at random locations (with uniform distribution) within the inner region at the beginning of the simulation. In this instance, obstacles behave a separate type of molecules that are kept unreactive and immobile. Moreover, they exclude the lattice site they occupy: whenever the chosen destination site of a moving protein contains an obstacle, the protein is reflected back to its origin site (the destination site becomes the origin position).

Standard parameter values were used throughout the article, unless otherwise specified: lattice size  $w = 800$ ,  $\Delta t = 1$ ,  $\Delta x = 1$  and diffusion coefficient  $D_{\text{out}} = 1/4$ . Every simulation was initiated with  $N_T = 10^4$  proteins and was run until the density of proteins reaches equilibrium. Depending on simulation conditions, equilibrium was typically reached after at most  $10^5$  (obstacles) to  $5 \times 10^5$  (slowed down Brownian diffusion or CTRW) time steps. The number of proteins present in the patch at equilibrium,  $N_{\text{in}}$ , was therefore computed as a time-average for  $t \in [9.5, 10.0] \times 10^5$ . Each simulation was repeated 20 times with different realizations of the pseudo-random numbers. The data presented below are averaged over those 20 runs.

## 3. RESULTS

**Figure 2** shows the average fraction of molecules present, at equilibrium, in patches of fraction area  $\phi = 0.25$  or  $0.01$ . The case of non-homogeneous CTRW (NHC), where diffusion is Brownian outside the patch and a transient CTRW inside, is plotted with blue plus (+) signs. Each data point corresponds to a value of the CTRW parameter pair  $(\gamma, \tau_C)$ . To facilitate visual presentation, we determined the macroscopic diffusion coefficient defined by each parameter pair (according to Equation 1) and plot the ratio of molecules inside the patch (at equilibrium)  $N_{\text{in}}/N_T$  against the corresponding value of  $D_M$  inside the patch ( $D_{\text{in}}$ ).

For large values of  $D_{\text{in}}$ , when diffusion is only weakly slowed down by the CTRW ( $\tau_C$  small and/or  $\gamma$  large),  $N_{\text{in}}/N_T$  tends to  $\phi$  (horizontal dashed lines), the fraction area of the patch. This is exactly the value expected when the densities of molecule inside and outside the patch are identical,  $N_{\text{in}}/\phi =$



$N_{out}/(1-\phi)$ . Therefore, when the CTRW inside the patch has a short or weakly anomalous transient, the spatial distribution remains uniform and homogeneous. When the transient anomalous regime becomes more marked ( $D_{in}$  decreases),  $N_{in}/N_T$  increases and becomes larger than  $\phi$ . This reveals that with increasingly marked anomalous regimes (longer lasting or more anomalous), the equilibrium spatial distribution becomes non-homogeneous: molecules progressively accumulate inside the patch [ $N_{in}/\phi > N_{out}/(1-\phi)$ ]. For the smaller  $D_{in}$  values, the fraction of molecules inside the patch even tends to unity. In other words, when the cutoff time  $\tau_C$  tends to very large values, accumulation reaches extreme levels since roughly all the diffusing molecules are found inside the slowed down patch.

Therefore, when the duration of the anomalous transient regime is large and/or the anomalous exponent small, non-homogeneous CTRW (NHC) leads to accumulation at equilibrium. To investigate the origin of this accumulation, we compared the results obtained with NHC to those with non-homogeneous Brownian motion (NHB), in which the motion remains Brownian inside the patch, but with a smaller diffusion coefficient  $D_{in}$ . In terms of mean-squared displacement  $\langle R^2 \rangle$ , NHB thus preserves the long-time behavior of NHC, but does not feature the initial anomalous transient. In a previous work (Soula et al., 2013), we showed that decreasing the ratio of diffusion coefficients  $D_{in}/D_{out}$  in NHB, leads to accumulation at

equilibrium inside the patch. We obtained a very good theoretical approximation of this accumulation with a simple expression:

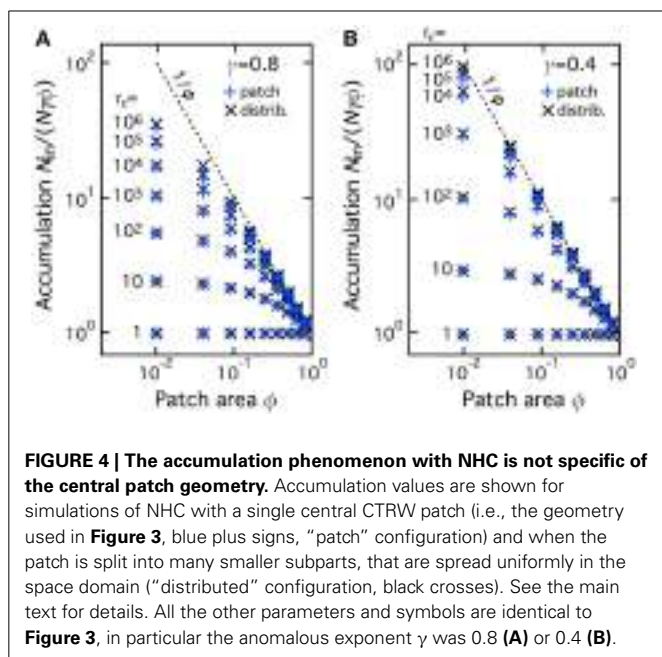
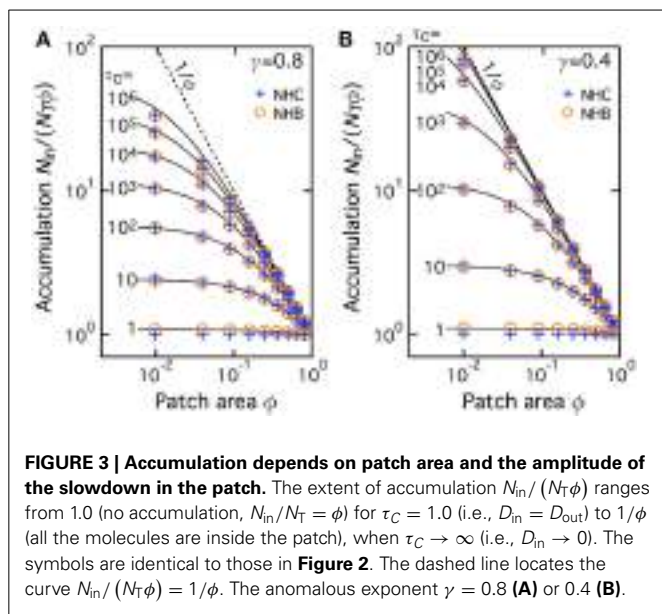
$$\frac{N_{in}}{N_T} = \frac{\phi}{\phi + (1-\phi) \frac{D_{in}}{D_{out}}} \quad (2)$$

Note in particular that in this expression,  $N_{in}/N_T \rightarrow \phi$  when  $D_{in} \rightarrow D_{out}$  (homogeneous distribution) while  $N_{in}/N_T \rightarrow 1$  when  $D_{in} \rightarrow 0$  (total accumulation in the patch).

The brown open circles in Figure 2 show the accumulation obtained with NHB, for various values of  $D_{in}$  (and constant  $D_{out}$ ). The accumulation values obtained in simulations of NHB match almost exactly those obtained with NHC. To confirm this result, we also plot in Figure 2 the theoretical predictions of Equation (2) (full black lines). The agreement between this theoretical prediction and the simulation results, either for NHB or NHC, is almost everywhere very good, confirming match between NHB and NHC values. A discrepancy between the theoretical prediction and the simulation results (both for NHB or NHC) appears for very small patch fraction area ( $\phi = 0.01$ ) and strong slowdown ( $D_{in} < 10^{-3}$ ). This discrepancy might be due to the fact that, with such extreme slowdown in the patch, our maximal simulation time may be too short to reach equilibrium. In any case, this discrepancy does not invalidate the very good match for most of the values.

We then extended this comparison to a larger set of values of the fraction area of the patch. To quantify the accumulation more directly, we plot on Figure 3 the values of  $N_{in}/(N_T\phi)$  for various values of the CTRW parameters in the patch: cutoff  $\tau_C$  and anomalous exponent ( $\gamma = 0.8$  in A and 0.4 in B). Using the same symbols as Figure 2 above, Figure 3 shows the results obtained with NHC and compare them to simulation and theoretical accumulation in a NHB with comparable  $D_{in}$ . In absence of accumulation (i.e., with homogeneous spatial distribution of the molecules), one expects  $N_{in}/(N_T\phi) \sim 1$  whereas  $N_{in}/(N_T\phi)$  should be close  $1/\phi$  (dashed line) when accumulation is close to complete in the patch. For both exponent values, the spatial distribution is found homogeneous (or close to homogeneous) for small cutoff times  $\tau_C$  and progressively converges to  $1/\phi$  when  $\tau_C \rightarrow \infty$ . The limit of almost-complete accumulation ( $1/\phi$ ) is reached for smaller  $\tau_C$  when  $\gamma$  is small (thus diffusion heavy anomalous) than when  $\gamma$  is large. This confirms that NHC progressively leads to complete accumulation when the cutoff time increases. Here again the match with the simulated and theoretical values of NHB is very good.

We next investigated whether this accumulation was specific to the geometry used in Figures 1–3. To this end we compared two geometries: (i) *Patch geometry*: CTRW takes place in a single patch of surface area  $\phi w^2$  (where  $w^2$  is the total domain surface area), located in the center of the domain. This is the geometry used in Figures 1–3 above; (ii) *Distributed geometry*: The patch is split into  $N_p$  squares of individual area  $S$  (we used unit area,  $S = 1$ ); the total patch area is preserved (i.e.,  $N_p S = \phi w^2$ ); the  $N_p$  patches are distributed uniformly at random in the domain (without overlapping). Figure 4 plots the values of  $N_{in}/(N_T\phi)$  for several CTRW parameter pairs ( $\gamma, \tau_C$ ) obtained from Monte-Carlo simulations of the two geometries. Clearly, the amounts



of accumulation observed for the two geometries, patch (blue “+” signs) or distributed (black “×” signs), are identical, for all the total patch areas and all the CTRW parameters we tested. Therefore, accumulation is also observed when the central patch is split into subpatches uniformly distributed in the domain. This indicates that the observed accumulation is a generic property of NHC that is not specific to the precise geometry configuration.

Those results therefore reveal that NHC leads to progressive accumulation of the molecules inside the central patch, whatever its area fraction. Since the amplitude of the accumulation due to NHC is almost identical to the amplitude of the accumulation due to NHB, one may conclude from those results

that, at least regarding the spatial distribution of the molecules at equilibrium, the transient anomalous regime has no significant impact. Accumulation would therefore be entirely controlled by the “macroscopic” Brownian regime that is exhibited at long times by transient CTRW.

A convenient way to test this hypothesis is to compare the results obtained with transient subdiffusion due to obstacle hindering. In this case, diffusion is still Brownian-like inside the patch, except for the presence of randomly-distributed immobile obstacles that hinder diffusion (see Materials and Methods) (Saxton, 1994; Berry, 2002; Höfling and Franosch, 2013). In this case (green curve in **Figure 5A**), the mean-squared displacement  $\langle R^2 \rangle$  is transiently anomalous with  $\gamma = 0.659$  in 2D (in continuum space) (Bouchaud and Georges, 1990; Kammerer et al., 2008). Just like in transient CTRW,  $\langle R^2 \rangle$  then converges to slowed-down Brownian motion with a “macroscopic” diffusion coefficient  $D_M$  (brown line in **Figure 5A**). When obstacle density  $\rho$  inside the patch increases, the crossover time from transient to Brownian regimes increases while  $D_M$  decays. Therefore, from the perspective of the mean-squared displacement, transient subdiffusion due to hindering by obstacles is very similar to transient CTRW. In particular, both exhibit a slowed-down Brownian behavior at long times.

**Figure 5B** shows the changes of  $N_{in}/(N_T\phi)$  when the obstacle density is changed, for a central patch with fraction area  $\phi = 0.25$ . Note that when immobile obstacles are added in the patch, some of the unobstructed sites of the patch find themselves isolated from the rest of the patch inside a cage made of obstacles. We found that in our simulations, those engagged sites were never present in a very significant amount (less than 9 % of the unobstructed patch sites, even at large obstacle densities). However, since they are not accessible for proteins located outside the cage, we included the fraction of such engagged isolated sites in the calculation of the obstacle density  $\rho$ . Without obstacles ( $\rho = 0$ ), one recovers the expected spatially homogeneous distribution of the molecules at equilibrium  $[N_{in}/(N_T\phi) = 1]$ . In a striking contrast with NHC or NHB, though, increasing the obstacle density in the patch (thus increasing  $\tau_C$  and decreasing  $D_{in}$ ) leads to a quick decay of the accumulated fraction below 1. This reveals that increasing the motion slowdown in the patch by obstacle hindering leads to a non-homogeneous equilibrium distribution of the molecules. But in opposition to the NHB or NHC case, this leads to a depletion of the molecule in the patch: the molecule density inside the patch becomes smaller than outside.

However, examination of **Figure 5B** shows that the values of  $N_{in}/(N_T\phi)$  decrease slightly slower than the available area fraction inside the patch  $(1 - \rho)$ , dashed line in the figure). This means that if one uses the accessible area in the patch  $[(1 - \rho)\phi]$  to compute concentration (and not the total patch area  $\phi$ ), hindering by immobile obstacles in fact leads to a slight accumulation. To quantify this further, we show on **Figure 5C** the results obtained when we compute accumulation using the effectively accessible volume  $(1 - \rho)\phi$ , i.e., we now compute accumulation as  $N_{in}/(N_T(1 - \rho)\phi)$ . In agreement with the above comment, this figure shows a slight accumulation, especially for large obstacle densities. Note however that this accumulation effect is small as it never get larger than 10%.

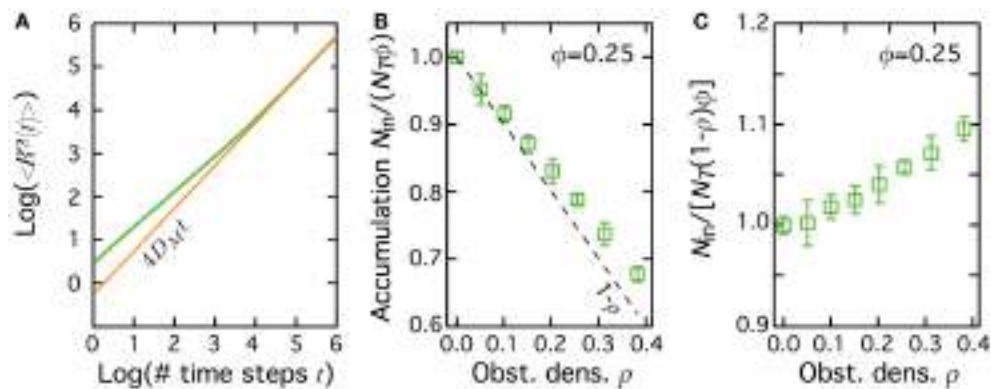


**FIGURE 5 | Diffusion hindering by obstacles leads to depletion of the molecules in the patch at equilibrium.** (A) The mean square displacement ( $\langle R^2 \rangle$ ) in transient subdiffusion due to hindrance by randomly-located immobile obstacles (green curve) first scales as  $t^\gamma$  (with  $\gamma < 1$ ), before converging to a Brownian motion with  $D_M$  a (macroscopic) diffusion coefficient, i.e.,  $\langle R^2 \rangle = 4D_M t$  (brown curve). Obstacle density  $\rho = 0.35$ , patch area fraction  $\phi = 1$ . (B) When the

obstacles are restricted to a central patch, the number of molecules inside the patch at equilibrium decreases below 1.0,  $N_{in}/(N_T\phi) \leq 1.0$  (depletion). The dashed line shows  $N_{in}/(N_T\phi) = 1 - \rho$ . (C) When accumulation is computed using the effectively accessible area in the patch  $(1 - \rho)\phi$ , and not the total patch area  $\phi$ , one gets instead a weak accumulation in the patch. In (B,C), bars indicate  $\pm 1$  s.d., and the fraction area of the patch  $\phi = 0.25$ .

Therefore, although they show very similar behaviors in terms of mean-square displacement, the impact on the equilibrium protein distribution in space of non-homogeneous transient subdiffusion due to obstacle hindrance or to CTRW are very different: while the latter leads to strong and robust accumulation in the patch, the former yields depletion or weak accumulation (depending on how concentrations are calculated).

#### 4. DISCUSSION

The lateral diffusion of proteins in membranes, and more generally, in the intracellular spaces is a complex process. First, many experimental reports evidence that their mobility does not agree with the classical Brownian motion but exhibit subdiffusion (Schwille et al., 1999; Smith et al., 1999; Fujiwara et al., 2002; Weigel et al., 2011; Höfling and Franosch, 2013). Moreover, the properties of their diffusion process can themselves vary from one location to another in the cell (or membrane) because of e.g., the non-homogeneous distribution of macromolecular crowding in space (Wachsmuth et al., 2000; Kühn et al., 2011; Parry et al., 2014) or the presence of nanodomains in the membranes that locally alter diffusion (Kenworthy et al., 2004; Goodwin et al., 2005; Fujita et al., 2007; Jacobson et al., 2007; Day and Kenworthy, 2009; Kusumi et al., 2011; Cambi and Lidke, 2012). Understanding protein mobility subject to such a complex process is still challenging. Here, we used Monte-Carlo simulations to study the spatial distribution (at equilibrium) of a protein that moves on a non-homogeneous two-dimensional domain with Brownian diffusion outside a central subregion (“patch”) and with transient CTRW inside (Figure 1C).

Our first finding is that in these conditions, proteins tend to accumulate inside the central patch (Figures 2, 3). When the anomalous regime becomes increasingly marked (i.e., the longer it lasts and the smaller its anomalous exponent), the density of proteins located at equilibrium inside the central patch is increasingly larger than the density of proteins outside.

At the limit where the CTRW becomes permanent (i.e., when the cutoff time diverges), this accumulation is complete, i.e., close to all the mobile proteins are found inside the central patch. This result agrees with the one-dimensional case studied by Korabel and Barkai (2010, 2011); Fedotov and Falconer (2012), extending them to two-dimensional spaces and generalizing it to variable fraction areas for the CTRW patch and to transient CTRW.

Our second contribution is that in the case of non-homogeneous transient CTRW, this accumulation phenomenon is entirely driven by the Brownian regime that is reached after the transient anomalous regime. The anomalous exponent impacts the accumulation phenomenon because it sets the effective macroscopic diffusion coefficient in the Brownian regime, not because it causes the initial sublinear scaling of the mean square displacement with time. Accordingly, when we suppressed the initial transient anomalous regime keeping the same asymptotic Brownian one (i.e., simulating non-homogeneous Brownian motion), our simulations show the same accumulation, quantitatively and qualitatively. However, we also show that this conclusion cannot be generalized to other mechanisms that cause transient subdiffusion. Indeed, the evolution with time of the mean square displacement when diffusion is hindered by randomly-located immobile obstacles exhibits the same changes with time as those of transient CTRW (compare Figure 5A with Figure 1A). Yet, when such a process is used to simulate non-homogeneous transient subdiffusion, our simulations did not evidence strong local accumulation of the proteins. Therefore, two mechanisms for subdiffusion, CTRW and obstacle hindrance, can present exactly the same regimes for the changes of the mean-squared displacement ( $\langle R^2 \rangle$ ) with time, but lead to very different results regarding the protein distribution at equilibrium.

Our simulations do not account for excluded volume between diffusing proteins as several proteins can share the same lattice

site at a given time. Including a hard limit on the maximal number of proteins that can share the same lattice site would lead to a significant decrease of the apparent diffusion coefficient (inside and outside the patch). This excluded volume interaction between proteins would arguably be more realistic but is also more demanding in terms of computation time. Moreover, we do not think it would change our main conclusions since excluded volume interaction between the proteins is not expected to modify their diffusion regime. However, it could of course have the trivial effect of limiting the amplitude of the reported accumulations inside the patch, since the bound on the number of proteins per lattice site implies a strict limitation of the number of proteins in the patch.

Taken together, our results provide a clear indication that the changes of  $\langle R^2(t) \rangle$  with time are not enough to explain the spatiotemporal dynamics of the proteins, even in the simple case, studied here, where the mobile protein does not interact via biochemical reactions or interactions. This realization has already started to emerge in the most recent experimental reports (see e.g., Parry et al., 2014). Other quantities that can be studied include quantifiers of the weak ergodicity breaking, specific to CTRWs (Burov et al., 2011; Weigel et al., 2011; Tabei et al., 2013) or quantifiers of how the distribution of the successive displacement deviates from a Gaussian distribution, that is expected for a Brownian motion (Parry et al., 2014). See e.g., Metzler et al. (2014) for a recent survey of those quantities. Moreover, CTRWs can give rise to spontaneous population splitting into mobile and immobile fractions (Schulz et al., 2013, 2014). This specificity of CTRWs could also be exploited to define more informative quantities.

Albeit the present work only concerns protein mobility, i.e., without coupling to a reaction, our results also shed new lights on the outcome of biochemical reactions when they occur among proteins with such non-homogeneous transient subdiffusion. In a recent article, we have studied the spatiotemporal dynamics of the ligand-binding equilibrium ( $L + R \rightleftharpoons C$ ) (Soula et al., 2013) in a similar space-dependent setup. We compared the apparent affinity of the reaction when diffusion in the central patch is restricted by transient subdiffusion either due to obstacle hindrance or NHC or NHB. We found that, while CTRW systematically decreases the apparent affinity of the reaction i.e., makes it less likely to occur, both non-homogeneous Brownian motion and local hinderance by obstacles increase it. The improvement of the affinity with non-homogeneous Brownian motion seems expected due to accumulation inside the patch. However, this explanation fails in the case of transient CTRW. It also fails in the case of transient subdiffusion due to obstacles. Indeed albeit obstacle hindrance yields depletion of the proteins inside the patch, it still gives rise to a slight improvement in apparent affinity of the ligand binding equilibrium. Therefore, our main conclusions is that both equilibrium concentrations or the asymptotic behavior of the mean square displacement are not the key control for the dynamics of the ligand-binding equilibrium. It seems that even at equilibrium the structure of the anomalous transient, and/or other quantifiers of the mobility have a deep impact. Future works will be needed to understand those impacts.

## AUTHOR CONTRIBUTIONS

Hugues Berry and Hédi A. Soula conceived and designed the work; acquired, analyzed and interpreted the simulation data and wrote the paper.

## REFERENCES

- Barkai, E., Garini, Y., and Metzler, R. (2012). Strange kinetics of single molecules in living cells. *Phys. Today* 65, 29+. doi: 10.1063/PT.3.1677
- Berry, H. (2002). Monte carlo simulations of enzyme reactions in two dimensions: fractal kinetics and spatial segregation. *Biophys. J.* 83, 1891–1901. doi: 10.1016/S0006-3495(02)73953-2
- Bouchaud, J.-P., and Georges, A. (1990). Anomalous diffusion in disordered media: statistical mechanisms, models and physical applications. *Phys. Rep.* 195, 127–293. doi: 10.1016/0370-1573(90)90099-N
- Bronstein, I., Israel, Y., Kepten, E., Mai, S., Shav-Tal, Y., Barkai, E., et al. (2009). Transient anomalous diffusion of telomeres in the nucleus of mammalian cells. *Phys. Rev. Lett.* 103, 018102. doi: 10.1103/PhysRevLett.103.018102
- Burov, S., Jeon, J.-H., Metzler, R., and Barkai, E. (2011). Single particle tracking in systems showing anomalous diffusion: the role of weak ergodicity breaking. *Phys. Chem. Chem. Phys.* 13, 1800–1812. doi: 10.1039/c0cp01879a
- Cambi, A., and Lidke, D. S. (2012). Nanoscale membrane organization: where biochemistry meets advanced microscopy. *ACS Chem. Biol.* 7, 139–149. doi: 10.1021/cb200326g
- Cherstvy, A. G., Chechkin, A. V., and Metzler, R. (2013). Anomalous diffusion and ergodicity breaking in heterogeneous diffusion processes. *New J. Phys.* 15, 083039. doi: 10.1088/1367-2630/15/8/083039
- Cherstvy, A. G., Chechkin, A. V., and Metzler, R. (2014). Particle invasion, survival, and non-ergodicity in 2d diffusion processes with space-dependent diffusivity. *Soft Matter* 10, 1591–1601. doi: 10.1039/c3sm52846d
- Day, C. A., and Kenworthy, A. K. (2009). Tracking microdomain dynamics in cell membranes. *Biochim. Biophys. Acta* 1788, 245–253. doi: 10.1016/j.bbamem.2008.10.024
- Dix, J. A., and Verkman, A. S. (2008). Crowding effects on diffusion in solutions and cells. *Annu. Rev. Biophys.* 37, 247–263. doi: 10.1146/annurev.biophys.37.032807.125824
- Fedotov, S., and Falconer, S. (2012). Subdiffusive master equation with space-dependent anomalous exponent and structural instability. *Phys. Rev. E* 85, 031132. doi: 10.1103/PhysRevE.85.031132
- Fujita, A., Cheng, J., Hirakawa, M., Furukawa, K., Kusunoki, S., and Fujimoto, T. (2007). Gangliosides gm1 and gm3 in the living cell membrane form clusters susceptible to cholesterol depletion and chilling. *Mol. Biol. Cell* 18, 2112–2122. doi: 10.1091/mbc.E07-01-0071
- Fujiwara, T., Ritchie, K., Murakoshi, H., Jacobson, K., and Kusumi, A. (2002). Phospholipids undergo hop diffusion in compartmentalized cell membrane. *J. Cell Biol.* 157, 1071–1081. doi: 10.1083/jcb.200202050
- Goodwin, J. S., Drake, K. R., Remmert, C. L., and Kenworthy, A. K. (2005). Ras diffusion is sensitive to plasma membrane viscosity. *Biophys. J.* 89, 1398–1410. doi: 10.1529/biophysj.104.055640
- Höfling, F., and Franosch, T. (2013). Anomalous transport in the crowded world of biological cells. *Rep. Prog. Phys.* 76, 046602. doi: 10.1088/0034-4885/76/4/046602
- Jacobson, K., Mouritsen, O. G., and Anderson, R. G. W. (2007). Lipid rafts: at a crossroad between cell biology and physics. *Nat. Cell Biol.* 9, 7–14. doi: 10.1038/ncb0107-7
- Jeon, J.-H., Tejedor, V., Burov, S., Barkai, E., Selhuber-Unkel, C., Berg-Sørensen, K., et al. (2011). In vivo anomalous diffusion and weak ergodicity breaking of lipid granules. *Phys. Rev. Lett.* 106, 048103. doi: 10.1103/PhysRevLett.106.048103
- Kammerer, A., Höfling, F., and Franosch, T. (2008). Cluster-resolved dynamic scaling theory and universal corrections for transport on percolating systems. *Europhys. Lett.* 84, 66002. doi: 10.1209/0295-5075/84/66002
- Kenworthy, A. K., Nichols, B. J., Remmert, C. L., Hendrix, G. M., Kumar, M., Zimmerberg, J., et al. (2004). Dynamics of putative raft-associated proteins at the cell surface. *J. Cell Biol.* 165, 735–746. doi: 10.1083/jcb.200312170
- Korabel, N., and Barkai, E. (2010). Paradoxes of subdiffusive infiltration in disordered systems. *Phys. Rev. Lett.* 104, 170603. doi: 10.1103/PhysRevLett.104.170603
- Korabel, N., and Barkai, E. (2011). Anomalous infiltration. *J. Stat. Mech. Theor. Exp.* 2011, P05022. doi: 10.1088/1742-5468/2011/05/P05022

- Kühn, T., Ihälainen, T. O., Hyväläoma, J., Dross, N., Willman, S. F., Langowski, J., et al. (2011). Protein diffusion in mammalian cell cytoplasm. *PLoS ONE* 6:e22962. doi: 10.1371/journal.pone.0022962
- Kusumi, A., Suzuki, K. G. N., Kasai, R. S., Ritchie, K., and Fujiwara, T. K. (2011). Hierarchical mesoscale domain organization of the plasma membrane. *Trends Biochem. Sci.* 36, 604–615. doi: 10.1016/j.tibs.2011.08.001
- Metzler, R., Jeon, J.-H., Cherstvy, A. G., and Barkai, E. (2014). Anomalous diffusion models and their properties: non-stationarity, non-ergodicity, and ageing at the centenary of single particle tracking. *Phys. Chem. Chem. Phys.* 16, 24128–24164. doi: 10.1039/C4CP03465A
- Metzler, R., and Klafter, J. (2000). The random walk's guide to anomalous diffusion: a fractional dynamics approach. *Phys. Rep.* 339, 1–77. doi: 10.1016/S0370-1573(00)00070-3
- Murase, K., Fujiwara, T., Umemura, Y., Suzuki, K., Iino, R., Yamashita, H., et al. (2004). Ultrafine membrane compartments for molecular diffusion as revealed by single molecule techniques. *Biophys. J.* 86, 4075–4093. doi: 10.1529/biophysj.103.035717
- Parry, B. R., Surovtsev, I. V., Cabeen, M. T., O'Hern, C. S., Dufresne, E. R., and Jacobs-Wagner, C. (2014). The bacterial cytoplasm has glass-like properties and is fluidized by metabolic activity. *Cell* 156, 183–194. doi: 10.1016/j.cell.2013.11.028
- Platani, M., Goldberg, I., Lamond, A. I., and Swedlow, J. R. (2002). Cajal body dynamics and association with chromatin are atp-dependent. *Nat. Cell Biol.* 4, 502–508. doi: 10.1038/ncb809
- Saxton, M. (2007). A biological interpretation of transient anomalous subdiffusion. i. qualitative model. *Biophys. J.* 92, 1178–1191. doi: 10.1529/biophysj.106.092619
- Saxton, M. J. (1994). Anomalous diffusion due to obstacles: a monte carlo study. *Biophys. J.* 66(Pt 1), 394–401. doi: 10.1016/S0006-3495(94)80789-1
- Schulz, J. H. P., Barkai, E., and Metzler, R. (2013). Aging effects and population splitting in single-particle trajectory averages. *Phys. Rev. Lett.* 110, 020602. doi: 10.1103/PhysRevLett.110.020602
- Schulz, J. H. P., Barkai, E., and Metzler, R. (2014). Aging renewal theory and application to random walks. *Phys. Rev. X* 4, 011028. doi: 10.1103/PhysRevX.4.011028
- Schwille, P., Korlach, J., and Webb, W. (1999). Fluorescence correlation spectroscopy with single-molecule sensitivity on cell and model membranes. *Cytometry* 36, 176–182. doi: 10.1002/(SICI)1097-0320(19990701)36:3<176::AID-CYTO5>3.0.CO;2-F
- Smith, P. R., Morrison, I. E., Wilson, K. M., Fernández, N., and Cherry, R. J. (1999). Anomalous diffusion of major histocompatibility complex class i molecules on hela cells determined by single particle tracking. *Biophys. J.* 76, 3331–3344. doi: 10.1016/S0006-3495(99)77486-2
- Soula, H., Caré, B., Beslon, G., and Berry, H. (2013). Anomalous versus slowed-down brownian diffusion in the ligand-binding equilibrium. *Biophys. J.* 105, 2064–2073. doi: 10.1016/j.bpj.2013.07.023
- Tabei, S. M. A., Burov, S., Kim, H. Y., Kuznetsov, A., Huynh, T., Jureller, J., et al. (2013). Intracellular transport of insulin granules is a subordinated random walk. *Proc. Natl. Acad. Sci. U.S.A.* 110, 4911–4916. doi: 10.1073/pnas.1221962110
- Wachsmuth, M., Waldeck, W., and Langowski, J. (2000). Anomalous diffusion of fluorescent probes inside living cell nuclei investigated by spatially-resolved fluorescence correlation spectroscopy. *J. Mol. Biol.* 298, 677–689. doi: 10.1006/jmbi.2000.3692
- Weigel, A. V., Simon, B., Tamkun, M. M., and Krapf, D. (2011). Ergodic and nonergodic processes coexist in the plasma membrane as observed by single-molecule tracking. *Proc. Natl. Acad. Sci. U.S.A.* 108, 6438–6443. doi: 10.1073/pnas.1016325108
- Conflict of Interest Statement:** The authors declare that the research was conducted in the absence of any commercial or financial relationships that could be construed as a potential conflict of interest.
- Received:** 25 September 2014; **accepted:** 27 October 2014; **published online:** 12 November 2014.
- Citation:** Berry H and Soula HA (2014) Spatial distributions at equilibrium under heterogeneous transient subdiffusion. *Front. Physiol.* 5:437. doi: 10.3389/fphys.2014.00437
- This article was submitted to Systems Biology, a section of the journal Frontiers in Physiology.*
- Copyright © 2014 Berry and Soula. This is an open-access article distributed under the terms of the Creative Commons Attribution License (CC BY). The use, distribution or reproduction in other forums is permitted, provided the original author(s) or licensor are credited and that the original publication in this journal is cited, in accordance with accepted academic practice. No use, distribution or reproduction is permitted which does not comply with these terms.



# Power law relationship between cell cycle duration and cell volume in the early embryonic development of *Caenorhabditis elegans*

Yukinobu Arata<sup>1,2\*</sup>, Hiroaki Takagi<sup>3</sup>, Yasushi Sako<sup>2</sup> and Hitoshi Sawa<sup>1,4</sup>

<sup>1</sup> Laboratory for Cell Fate Decision, Center for Developmental Biology, RIKEN, Hyogo, Japan

<sup>2</sup> Cellular Informatics Laboratory, RIKEN, Saitama, Japan

<sup>3</sup> Department of Physics, School of Medicine, Nara Medical University, Nara, Japan

<sup>4</sup> Multicellular Organization Laboratory, National Institute of Genetics, Shizuoka, Japan

**Edited by:**

Noriko Hiroi, Keio University, Japan

**Reviewed by:**

Mitsuyuki Nakao, Tohoku University, Japan

Santiago Schnell, University of Michigan Medical School, USA

**\*Correspondence:**

Yukinobu Arata, Cellular Informatics Laboratory, RIKEN, S356 Bioscience Bldg. 2-1 Hirosawa, Wako, 351-0198 Saitama, Japan  
e-mail: arata@riken.jp

Cell size is a critical factor for cell cycle regulation. In *Xenopus* embryos after midblastula transition (MBT), the cell cycle duration elongates in a power law relationship with the cell radius squared. This correlation has been explained by the model that cell surface area is a candidate to determine cell cycle duration. However, it remains unknown whether this second power law is conserved in other animal embryos. Here, we found that the relationship between cell cycle duration and cell size in *Caenorhabditis elegans* embryos exhibited a power law distribution. Interestingly, the powers of the time-size relationship could be grouped into at least three classes: highly size-correlated, moderately size-correlated, and potentially a size-non-correlated class according to *C. elegans* founder cell lineages (1.2, 0.81, and <0.39 in radius, respectively). Thus, the power law relationship is conserved in *Xenopus* and *C. elegans*, while the absolute powers in *C. elegans* were different from that in *Xenopus*. Furthermore, we found that the volume ratio between the nucleus and cell exhibited a power law relationship in the size-correlated classes. The power of the volume relationship was closest to that of the time-size relationship in the highly size-correlated class. This correlation raised the possibility that the time-size relationship, at least in the highly size-correlated class, is explained by the volume ratio of nuclear size and cell size. Thus, our quantitative measurements shed a light on the possibility that early embryonic *C. elegans* cell cycle duration is coordinated with cell size as a result of geometric constraints between intracellular structures.

**Keywords:** cell size, cell cycle duration, power law, nuclear-cytoplasmic volume ratio, *ima-3/Importin α*

## INTRODUCTION

Cell cycle is regulated in coordination with cell size in unicellular organisms and cells in animal embryos. In many invertebrate and vertebrate animals, the early embryonic stage after fertilization is characterized by rapid synchronous cleavage in all cells within the embryo. Later, this pattern of cell division abruptly changes to cycles of slow and asynchronous cleavage. This transition event was referred as the midblastula transition (MBT) originally in amphibian embryos (Gerhart, 1980; Newport and Kirschner, 1982). Experimental studies showed that the onset of events at or after MBT, such as asynchronous division, differentiation, and gastrulation, are affected by cell size as well as ploidy in *Drosophila* (Edgar et al., 1986) and *Xenopus* (Newport and Kirschner, 1982; Clute and Masui, 1995). These findings suggest that cell size and genome size are critical factors for determining the timing of MBT, which is the classic concept to explain the coordination between cellular events and cell size in early development of animal embryos.

Some variations of the classic concept have been reported based on quantitative measurements of cellular variables. Yoshio

Masui and Wang reported that the cell cycle duration after MBT is inversely proportional to the cell radius squared in *Xenopus* embryos (Masui and Wang, 1998; Wang et al., 2000). Their rationale for this second power law relationship was that mitosis-promoting factor (MPF) is produced in a quantity proportional to the cell surface area. This hypothesis implies that the cell cycle durations coordinate with cell size through cell surface area, rather than volume.

On the other hand, other researchers proposed that the volume ratio between the cell and nucleus, but not the ploidy, directs the timing of blastomere adhesiveness in starfish and sea urchin embryos (Masui and Kominami, 2001; Masui et al., 2001). In starfish embryos, cell adhesiveness begins to increase after the eighth cleavage to form a monolayered hollow blastula. In accordance with the classic concept, the timing of adhesiveness was accelerated in embryos with doubled ploidy, whereas the timing was delayed in large-sized embryos by the fusion of a non-nucleate egg fragment. In contrast to the classic concept, the timing of adhesiveness was not altered in half-sized embryos, and the timing was only delayed by one cell cycle in quarter-sized

embryos. They noticed that experimental manipulations changing cytoplasmic volume or changing ploidy altered the nuclear size, and they found that the cell adhesiveness appeared at a certain volume ratio of the nucleus to the cell (Masui et al., 2001). The same conclusion was derived from experimental observations of sea urchin embryos (Masui and Kominami, 2001). They concluded that the critical variable for determining the onset of blastomere adhesiveness in starfish and sea urchin embryos is the volume ratio between the nucleus and cell.

Thus, cellular events could be coordinated with cell size by the various ratios of cellular variables. However, quantitative measurements to reveal how cell cycle duration is coordinated with cell size have not been performed in embryos other than in the vertebrate, *Xenopus*. In the present work, we studied the time-size relationship in embryos of an invertebrate, *C. elegans*. In *C. elegans* embryo, the cell lineages and order of cell divisions are nearly invariant (Sulston et al., 1983; Schnabel et al., 1997). After fertilization, the P0 zygote divides into the large AB and smaller P1 daughters. Through several rounds of asymmetric cell division, the zygote eventually produces six founder cells: AB, MS, E, C, D, and P4.

Here, we report the time-size relationship—specifically, the cell cycle duration–cell volume (T–V) relationship—follows a power law relationship in *C. elegans*. Interestingly, the absolute powers differed among cell lineages in *C. elegans* and were less than the power in *Xenopus*. We discuss the possibility that cell cycle duration is coordinated with cell size through the volume ratio between nucleus and cell in *C. elegans* embryos. In addition, we discuss the difference and possible similarity of time-size relationships between *C. elegans* and *Xenopus* embryos.

## MATERIALS AND METHODS

### *C. ELEGANS* CULTURE CONDITIONS AND RECORDING OF EMBRYONIC CELL DIVISIONS

Wild-type *C. elegans* (N2) embryos were maintained at 22.5°C (Brenner, 1974). Embryos were isolated from gravid hermaphrodites. Cell divisions were recorded in a temperature-controlled room on an upright differential interference contrast (DIC) microscope with the Plan-Apochromat 63×/1.40 oil DIC objective lens (Carl Zeiss, Germany). Cell divisions were recorded at one-minute time intervals and 0.5-μm Z-axis intervals after the one-cell stage with Metamorph software (Molecular Devices, USA). Embryos were attached to a cover glass coated with polylysine (Sigma-Aldrich, USA). Cover glass was footed with petroleum jelly (Vaseline, Nacalai Tesque, Japan) on the slide glass. In this set-up, embryos that attached to the cover glass were separated from the slide glass, such that cell divisions proceed without the physical stress of compression between the cover glass and slide glass (Lee and Goldstein, 2003; Arata et al., 2010; Edgar and Goldstein, 2012). Polylysine attachment did not change the embryo shape (Figure S1). *C. elegans* embryos exhibited normal developmental progression and hatched in this setting.

### MEASUREMENTS OF CELL VOLUME

Cell volumes were measured by integrating 10 or more cylinder volumes (integral approach; IA). The volume of each cylinder was calculated from the cell area at each Z-plane and a constant

height, which was set as the Z-axis interval in the stage control system of the Metamorph software (Molecular Devices, USA). The cell area in a cylinder was determined as shown in Figure S1A. The length of one pixel in the DIC image was calibrated by an objective micrometer (Carl Zeiss, Germany). Measurement error was estimated by comparing the nuclear volume measured by the IA to the volume measured by the formula approach (FA). In the FA, the nucleus in each cell was assumed to be a perfect sphere and its volume was determined by  $4\pi r^3/3$ , by using the mean of four times measurements of the nuclear radius. The assumption is approximately correct, because the shape of the nucleus was close to a perfect circle in the X-Y and X-Z axes (Figure S1B). The measurement error in the IA was estimated to be 23.6% larger than the precise cell volume (Table 1). The error might be caused by integration error or slight elongation of the nucleus in the Z-axis (Figure S1B), probably due to the difference of refractive indices in the light path (Born and Wolf, 1999). Final cell volumes were determined by correcting measurement errors and averaging the volumes measured at three different time points during the cell cycle due to an absence of detectable cell growth in the embryonic cell cycle.

### STATISTICAL ANALYSES

To examine the power of the T–V relationship in cell lineages, the cell cycle duration and cell volume variables in the logarithmic or linear scale were fitted by the linear least-squares method or the Levenberg-Marquardt algorithm, respectively. To estimate the confidence interval (CI) of the estimated powers, a method combining regression analysis and a bootstrap method was used (Efron and Tibshirani, 1993). The values of power were resampled 10,000 times using residuals between experimental data and values derived from a model function. The 95% CIs were determined at the 2.5th and 97.5th percentiles in the appearance frequency of

**Table 1 | Volume correction measured by differential interference contrast (DIC) microscopy.**

Cell identity	Radius ± SD (μm)	Volume by FA ± SD (μm <sup>3</sup> )	Volume by IA, no error correction (μm <sup>3</sup> )	Error (%)
AB(1)	4.811 ± 0.150	467.4 ± 42.7	517.4	10.7
P(1)	4.436 ± 0.209	367.4 ± 52.1	433.7	18.0
AB(2)	4.321 ± 0.066	338.2 ± 15.7	433.0	28.0
AB(3)	3.845 ± 0.058	238.2 ± 10.7	312.4	31.2
AB(4)	3.132 ± 0.094	128.9 ± 11.3	164.7	27.7
AB(5)	2.871 ± 0.117	99.5 ± 12.2	116.2	16.8
AB(6)	2.352 ± 0.081	54.6 ± 5.7	72.7	33.0
Average ± SEM				23.6 ± 3.2

The measurement error of the integral approach (IA) for our DIC microscope settings was estimated by comparing the nuclear volumes measured by the IA and by the formula approach (FA). The numbers in parentheses indicate the cell generation in each founder cell lineage. For example, AB(1) indicates the AB cell, and AB(2) indicates the AB daughter cells. See details in the Materials and Methods. SD, standard deviation; SEM, standard error of the mean.

the values of power in linear scale data fitted by the Levenberg-Marquardt algorithm. The 95% CIs in the logarithmic scale fitted by the linear least-squares method were determined practically by the same method. The percentile method to estimate CIs can be applied to any symmetric statistical distribution.

## RESULTS

### QUANTITATIVE DETERMINATION OF THE T-V RELATIONSHIP IN *C. ELEGANS* EMBRYOS

We observed the timing of cell division in wild-type *C. elegans* embryos cultured at 25°C. The intervals of cell divisions between the generations in the same lineage appeared to increase gradually in all the founder cell lineages in an embryo (**Figure 1A**). The average and standard deviation of coefficient of variation (CV) of cell division timings in AB and MS lineages among different embryos were around several percent (1 to 4 ± 0.5 to 2.1) (**Figure 1B**), indicating that the cell divisions occurred synchronously in a highly reproducible manner among embryos. Thus, the *C. elegans* embryo is a good model system to study

a deterministic mechanism to regulate cell division timings in animal embryos.

Next, we examined the T-V relationship. Cell cycle duration was defined as the time from nuclear formation in a cell to nuclear formation in one of the daughter cells, in which the nucleus was formed earlier. Cell cycle duration correlated negatively with cell volume (**Figures 2A,B**). When we classified the T-V relationship data by cell lineage, cell cycle duration vs. cell volume appeared linear in double logarithmic plots (**Figures 2C–H**), suggesting a power law relationship. We fitted three different models (Gaussian, exponential, and power law) to the plots of cell cycle duration vs. cell volume in linear scale. The  $\chi^2$ -value in the model fitting was smallest (except for the E lineage) when the data were fitted by the power law model (**Figure S2**). Therefore, we concluded that the *C. elegans* T-V relationship in the AB, MS, C, and P lineages follows a power law relationship.

Absolute values of power in the T-V relationship (**Figure 2**) were similar between AB and MS lineages (0.27) and between C and P lineages (0.41). Bootstrapping statistical analyses showed

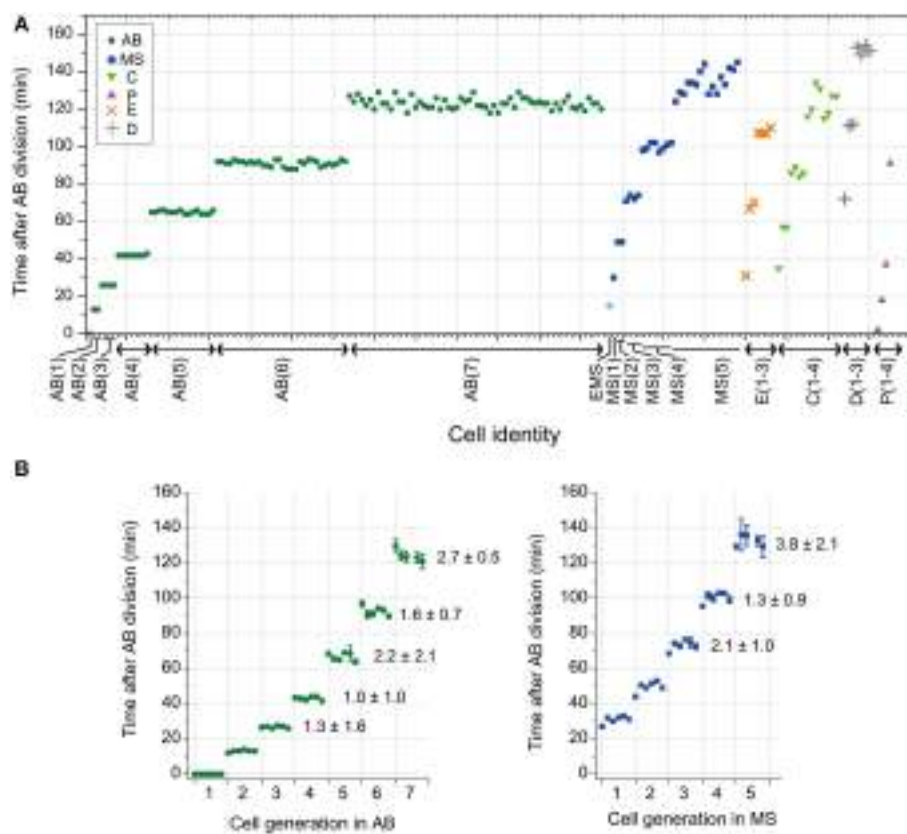
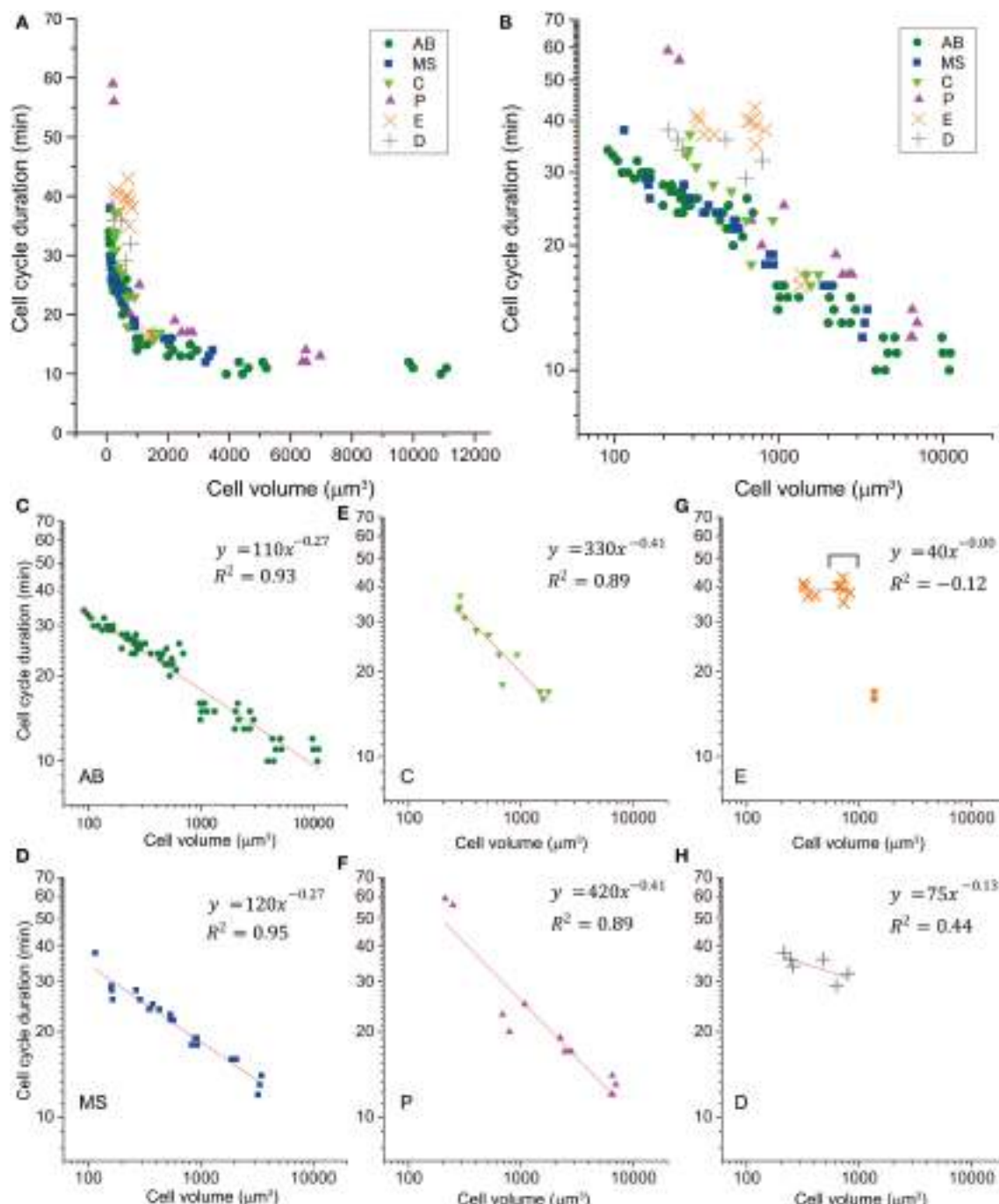


**FIGURE 1 | Cell division timing of *C. elegans* embryos. (A)** The cell division timings in an embryo cultured at 25°C. Cell identity is indicated on the horizontal axis. Cell division timing was determined by nuclear envelope breakdown (NEBD). The numbers in parentheses indicate the cell generation in each founder cell lineage. For example, AB(1) indicates the AB cell, and AB(2) indicates the AB daughter cells. **(B)** The average and standard deviation (SD) of cell division timings in the same generation in AB and MS lineages in an embryo were obtained; data obtained from six embryos were aligned on

the horizontal axis in order (the leftmost of AB and in the leftmost of MS were obtained from an embryo). The CV of cell division timings in the same generation in AB and MS lineages in an embryo were averaged among the six embryos and were shown with SD [the average CV ± SD (%)] in the right side of data in the graphs after the third generation. The NEBD of the AB cells was set as time 0. AB, MS, C, P, E, and D are indicated with a green dot, blue square, light green triangle, magenta triangle, orange x-mark, and gray cross, respectively. The EMS cell was indicated by a light blue square.



that the 95% CIs of the powers overlapped between AB and MS, C and P, and E and D lineages (Figures 3A,B). The larger absolute values of power in the C and P lineages indicated that the cell cycle duration elongates rapidly as the cell volume decreases (the

highly size-correlated class). In contrast, the smaller absolute values of power in the AB and MS lineages indicated that the cell cycle duration elongates slowly (the moderately size-correlated class). When the power is zero, the cell cycle duration is constant

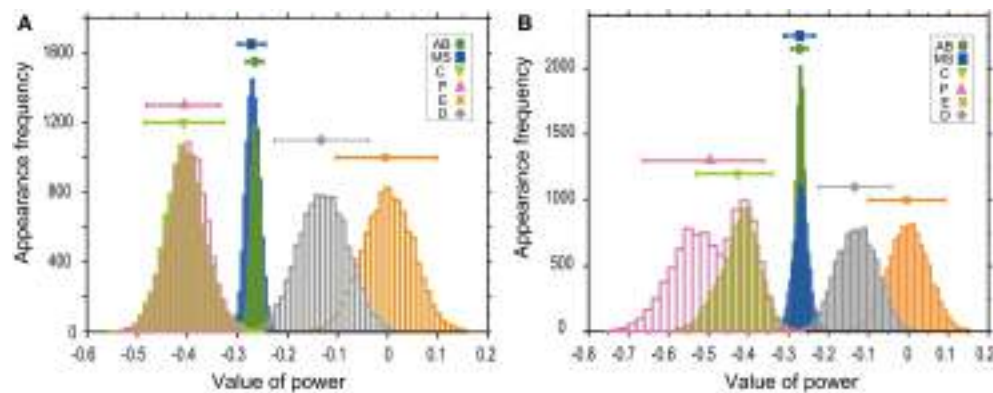


**FIGURE 3 | Powers of the T-V relationship could be classified into three classes.** T-V relationships in each lineage in the logarithmic (**A**) or linear (**B**) scale were fitted by a power law model. Statistical analysis combining regression analysis and a bootstrap method were performed 10,000 times, using the same data used in **Figure 2**. The estimated power is indicated in

the horizontal axis, while the appearance frequencies of the values of power is indicated in the vertical axis. The 95% CIs of the power of the T-V relationship were determined by the appearance frequency and are shown by long horizontal bars. Data for AB, MS, C, P, E, and D lineages are shown in green, blue, light green, magenta, orange, and gray, respectively.

or does not correlate with changes in cell size, indicating a size-non-correlated class. Cells in the E and D lineages exhibited lower values of power. Although it remains unclear due to small sample number, cells in the E and D lineages may be classified in another class with lower values of power, possibly the size-non-correlated class. These results suggest that the powers of the T-V relationship could be grouped into at least three classes.

In the bootstrap analysis performed to evaluate the T-V relationship in the logarithmic scale, the appearance frequencies of the values of power were symmetrically distributed (**Figure 3A**), which supports the validity of our estimation of the CIs. In the bootstrap analysis of the T-V relationship in the linear scale, the appearance frequencies of the AB, MS, E, and D lineages were symmetrically distributed, whereas the appearance frequencies of the C and P lineages showed monomodal and bimodal distributions with the shorter tail in the side of the larger values of power, respectively (**Figure 3B**). In these asymmetric distributions, the estimation of the CIs could be biased to the shorter tail side of the distributions. Because the similar skewness of the distributions was observed both in the C and P lineages, the asymmetry of the distributions does not affect our conclusion that the 95% CIs of the values of powers overlapped between the C and P lineages.

#### INTERMITOTIC PHASE DURATION ELONGATES EXPONENTIALLY AS CELL VOLUME DECREASES IN THE SIZE-CORRELATED CLASSES

To determine which cell cycle phase was responsible for elongation of the cell cycle duration, we measured the duration of the intermitotic and mitotic phases in cells in the size-correlated AB, MS, C, and P lineages. The duration of the intermitotic phase was elongated exponentially as the rounds of cell division increased, and became dominant in cell cycle duration in later generations (**Figure 4A**), whereas the duration of the mitotic phase was relatively constant among these lineages (**Figure 4B**). These observations indicated that cell cycle elongation was due to lengthening of the intermitotic phase but not the mitotic phase.

#### THE RELATIONSHIP BETWEEN THE NUCLEAR AND CELL VOLUMES IN THE SIZE-CORRELATED CLASSES

To explain the *C. elegans* power law T-V relationship, we focused on the relationship between the cell and nuclear volumes. We plotted the nuclear vs. cell volumes for cells in size-correlated AB, MS, C, and P lineages (**Figure 5A**). The relationship between the nuclear and cell volumes was non-linear in a linear plot, and showed a linear relationship in a double logarithmic plot (**Figure 5B**). The relationship was well-fitted by a power law model ( $R^2 = 0.94$ ; **Figure 5B**). Nuclear volume varied with cell volume, in a power law relationship with a slope of 0.63 (**Figure 5B**). If the volumes of the two spheres varied in a corresponding manner, then the power was unity; thus, the *C. elegans* relationship between the nuclear and cell volumes was allometric. Supposing that a factor critical for cell cycle regulation is transported between the nucleus and cytoplasm, we considered the ratio of the nuclear volume ( $V_n$ ) to the cell volume ( $V_c$ ). The power of the volume ratio was  $-0.37$  ( $V_n/V_c \propto V_c^{0.63}/V_c = V_c^{-0.37}$ ). We found that the absolute value of the power of the volume ratio (0.37) was closest to that of the T-V relationship in the highly size-correlated class (C and P lineages) (0.41), indicating a strong correlation with the volume ratio between the nucleus and cell.

#### GENETIC ANALYSIS OF THE T-V RELATIONSHIP IN *C. ELEGANS* EMBRYOS

We employed a genetic approach to assess the impact of altered cell volume and to examine the molecular mechanism of the T-V relationship. In *C. elegans*, genome-wide screening and classic genetics have identified genes related to egg size determination. Homozygous mutant embryos of *ptp-2*/SH2 domain-containing protein tyrosine phosphatase are larger than wild-type embryos, whereas *ima-3/importin α* RNAi embryos are smaller than wild-type embryos (**Figure 6A**) (Gutsch et al., 1998; Sonnichsen et al., 2005). We measured cell cycle duration and cell volume in the AB lineage of these two loss-of-function embryos. Volumes of

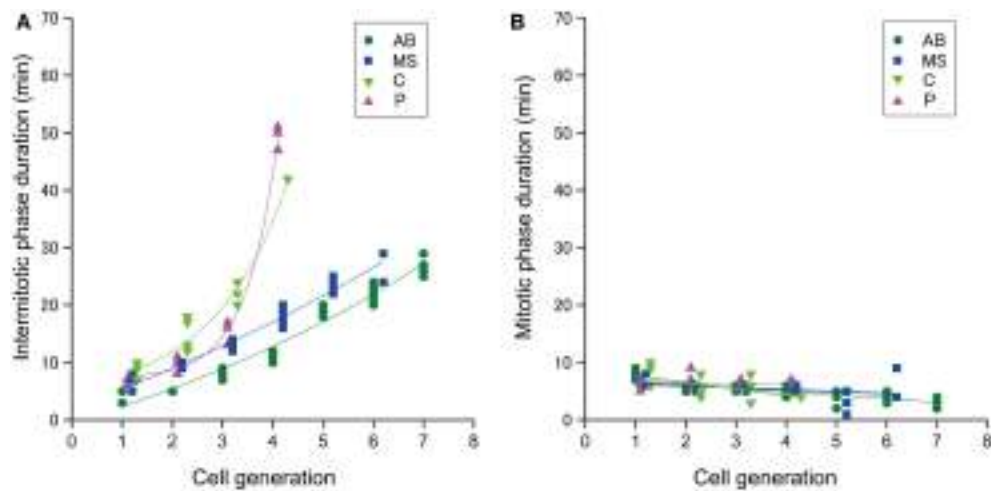


**FIGURE 4 | The duration of cell cycle phases in *C. elegans* embryos.** The duration of the (A) intermitotic phase or (B) mitotic phase in the size-correlated class; AB (green dot), MS (blue square), C (light green triangle), and P (magenta triangle) lineages are shown in linear plots in the

vertical axis. The cell generations in each founder cell lineage are shown in the horizontal axis. Data points are displaced along the horizontal axis to avoid overlap (A,B). This data displacement does not affect exponentiation of data. Duration data were obtained from three wild-type embryos.

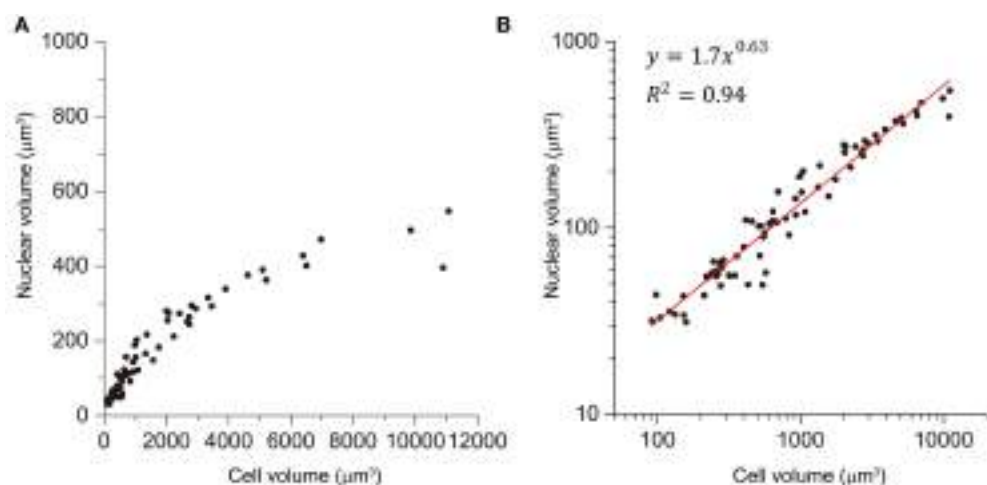


**FIGURE 5 | Power law relationship between the nuclear and cell volume.**

Relationship between nuclear and cell volume in size-correlated classes (AB, MS, C, and P) is shown in linear (A) and double logarithmic (B) plots. Cell volumes were determined by the integral approach with error correction,

whereas nuclear volumes were determined by the formula approach in three wild-type embryos. Data in logarithmic scale were fitted to the formula,  $y = a + bx$ , by the linear least-squares method. Degree of freedom in fitting was 75.

AB cells in the *ptp-2* mutant embryos and *ima-3* RNAi embryos were approximately twice and half the sizes, respectively, of AB cells from wild-type embryos (compare gray and black brackets in Figures 6B,C). The T-V relationship of the *ptp-2* AB lineage was well-fitted with a power law model with the absolute power, 0.25 ( $R^2 = 0.87$ ; Figure 6B), which was close to that of the wild-type AB lineage (0.27; Figure 2). Larger AB cells in *ptp-2* mutant embryos (black brackets) did not further shorten cell cycle durations compared to AB cells in wild-type embryos (gray brackets; Figure 6B). Thus, the cell cycle duration may have a minimum limit, and eventually appeared to have the minimum limit in the T-V relationship.

The power law relationship was maintained in the *ima-3* AB lineage, but the absolute value of the power of the *ima-3* RNAi embryos was increased (0.39,  $R^2 = 0.94$ ; Figure 6C) close to the absolute value of the power of the highly size-correlated class (C and P lineages) in wild-type embryos (0.41; Figure 2). Thus, *ima-3* is required to determine the proper cell cycle elongation, and eventually appeared to determine the proper power of the T-V relationship. The order of cell divisions in the *ima-3* RNAi embryos was the same as in the wild-type embryos, at least until the 16-cell stage (data not shown). Thus, it is unlikely that the rapid elongation of cell cycle in *ima-3* RNAi embryos was caused by defects in cell fate determination of the founder cells.

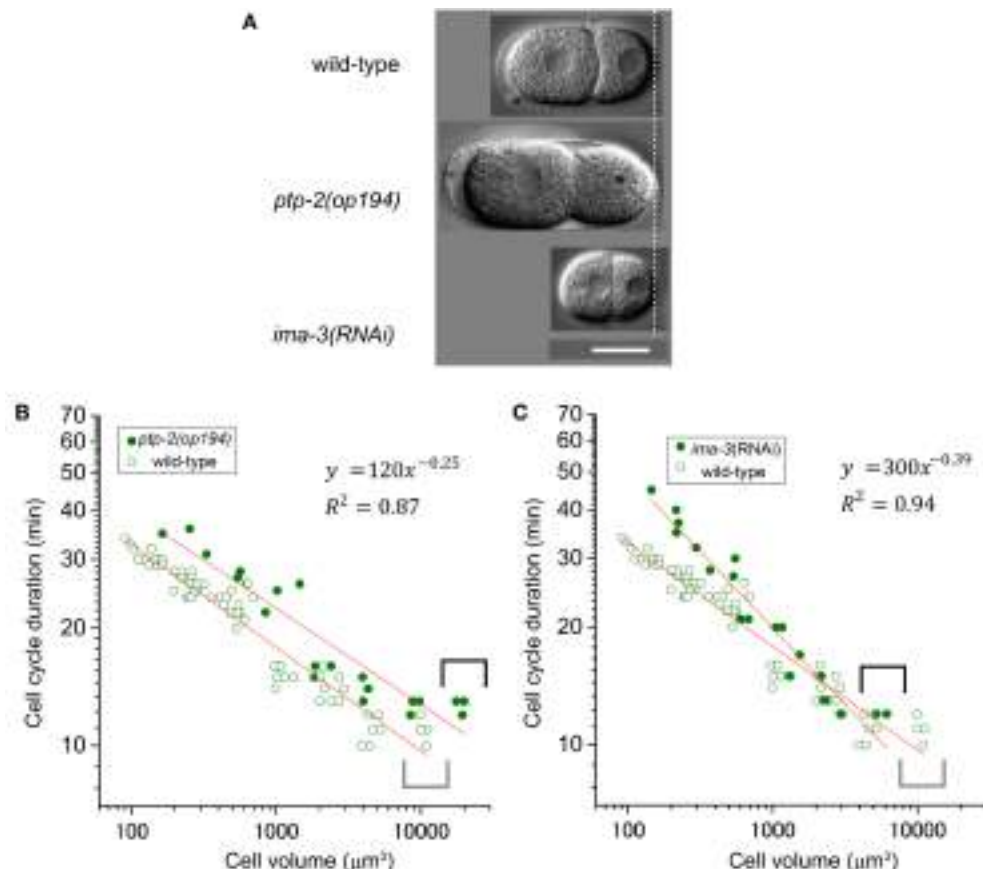


**FIGURE 6 | Relationship between cell cycle duration and cell volume in loss-of-function embryos. (A)** Images of embryos at the two-cell stage for wild-type, *ptp-2(op194)*, and *ima-3* RNAi embryos were obtained by differential interference contrast (DIC) microscopy. Scale bar = 20  $\mu\text{m}$ . Relationship between cell cycle duration and cell volume in AB lineage in *ptp-2(op194)* [filled circles in (B)] and *ima-3*(RNAi) [filled circles in (C)]

embryos are shown with that in wild-type embryos [open circles in (B,C)] in double logarithmic plots. Cell volume and cell cycle duration data in loss-of-function embryos were obtained from each of three embryos. Data in the logarithmic scale were fitted to the formula,  $y = a + bx$ , by the linear least-squares method. Degrees of freedom in fitting (B,C) were 19 and 19, respectively.

## DISCUSSION

Cell cycle duration is coordinated with cell size in cultured mammalian cells and unicellular organisms. For example, *Amoeba proteus* cells did not enter the mitotic phase when the cell volume was reduced by cytoplasmic amputation (Prescott, 1955). By changing cell size with genetic or culture manipulations, cell cycle progression has been shown to be affected in budding yeast (Johnston et al., 1977), fission yeast (Nurse, 1975; Sveiczer et al., 1996), ciliates (Berger, 1984), and mammalian cultured cells (Dolznig et al., 2004). A quantitative relationship between cell cycle duration and cell size was reported in embryos of the vertebrate, *Xenopus* (Masui and Wang, 1998; Wang et al., 2000). In this work, we studied the quantitative relationship in embryos of an invertebrate, *C. elegans*.

### POWERS OF THE T-V RELATIONSHIP AMONG CELL LINEAGES IN *C. ELEGANS*

We found that the relationship between cell volume and cell cycle duration followed a power law relationship. In *C. elegans*, AB and P1 cells divide asynchronously, with the larger

AB cells dividing before the smaller P1 cells (Sulston et al., 1983; Brauchle et al., 2003). The zygotes that are depleted of subunits of the heterotrimeric G-proteins, GOA-1/GPA-16, or GoLoco-containing proteins, GPR-1/GPR-2, exhibit normal anterior-posterior polarity, but divide into equally sized AB and P1 cells (Gotta and Ahringer, 2001; Colombo et al., 2003; Gotta et al., 2003; Srinivasan et al., 2003). The equally sized AB and P1 cells divide in a more synchronized manner compared to the differently sized AB and P1 cells in wild-type embryos. Thus, the cell cycle duration in AB and P1 cells is strongly correlated with cell size. Brauchle et al. proposed that unequal cell size of AB and P1 cells contributes to asynchrony of cell division, although it is still possible that G protein signaling is specifically required for differential checkpoint activation at the two-cell stage or for another cellular process modulating cell cycle progression (Brauchle et al., 2003). The power law relationship between cell cycle duration and cell size in later embryonic development may be regulated by a mechanism similar to the asynchrony of AB and P1 divisions.

Our statistical analyses suggest that there are at least three different classes of the T-V relationship according to the founder

cell lineages in *C. elegans*: highly size-correlated, moderately size-correlated, and probably size-non-correlated classes (absolute powers of 0.41, 0.27, and <0.13 for volume, respectively). *C. elegans* founder cells give rise to different types of differentiated cells: cells in AB and MS lineages primarily produce ectodermal and mesodermal cells, C and P lineages produce mesodermal and germline cells, and E and D lineages produce endodermal and mesodermal cells, respectively (Sulston et al., 1983). Thus, the cell fates do not correlate with the classes according to the power of the T-V relationship. Instead, the classification might correlate with a mode of cell divisions. Cells in AB and MS lineages of the moderately size-correlated class share prominently synchronous and symmetric cell divisions (**Figure 1**) (Sulston et al., 1983), while cells in the P lineage undergo asymmetric cell divisions, in which the two daughter cells clearly differ in size from each other (Sulston et al., 1983). Similarly, many cells in the C lineage undergo asymmetric cell division, which has a clear size asymmetry (**Figure S3**). Thus, cells in P and C lineages in the highly size-correlated class share size-asymmetric cell division. It remains unclear what cell feature the E and D lineages share. Daughter cells of each E cell exhibited an abrupt deviation from the T-V relationship that the mother E cell followed, and subsequently, the descendants appeared to exhibit a lower power in the T-V relationship (**Figures 2B,G**). The E daughters are the first cells that have the Gap phase (G2 phase) in *C. elegans* embryos (Edgar and McGhee, 1988). Therefore, the deviation may be caused by the introduction of the Gap phase. This cell cycle dynamics in E lineage may be shared with D lineage.

Overall, our quantitative measurements revealed the diversity of powers in the T-V relationship among *C. elegans* cell lineages. Cells may sense their own size through distinct mechanisms among cell lineages in *C. elegans* embryos.

#### POWERS OF THE T-V RELATIONSHIP IN *C. ELEGANS* AND *XENOPUS*

We found that any of the absolute powers of the *C. elegans* lineages (<0.39, 0.81, and 1.2 in radius; <0.13, 0.27, and 0.41 in volume, respectively) were smaller than that in *Xenopus* embryos (2.0 in radius; 0.67 in volume). The cell cycle duration of *C. elegans* embryos elongates more slowly than that in *Xenopus* after MBT. Thus, the T-V relationship in *C. elegans* may be determined by mechanisms different from those used by *Xenopus* embryos. Alternatively, there remains a possibility that a same mechanism functions for the time-size relationship in *C. elegans* and *Xenopus* embryos. In *Xenopus* embryos, the time-size relationship has only been examined in cells near the animal cap. It is possible that the diversity according to cell lineages is also observed in the *Xenopus* embryo. Recently, it has been reported that nuclear size correlates non-linearly with cell size in *Xenopus* embryos (Jevtic and Levy, 2015), similarly to *C. elegans* (**Figure 5A**). In budding and fission yeasts, the relationship between the nuclear and cell volumes was reported to be linear (Jorgensen et al., 2007; Neumann and Nurse, 2007). In addition, nuclear size has been strongly correlated with cell size (Jorgensen et al., 2007; Neumann and Nurse, 2007), even when cell size was changed 35-fold or nuclear DNA content was changed 16-fold in fission yeast (Neumann and Nurse, 2007). The volume ratio of the nucleus to the cell was rapidly corrected by the growth of the cell or nucleus, when the nuclear or cell size

was changed by manipulating the genetic or culture conditions (Neumann and Nurse, 2007). Thus, there is a mechanism that links the sizes of the nucleus and cell in yeasts. Although the mechanism to link the sizes of the nucleus and cell in yeasts is different from animal embryos, the interesting correlation of volume ratio between the nucleus and cell in yeasts and animal embryos raise a possibility that the volume ratio can be a general mean by which cells “sense” their size. The power of the time-size relationship was different between *C. elegans* and *Xenopus* embryos, while the time-size relationship may strongly correlate with the volume ratio between the nucleus and cell in *Xenopus* embryos, like *C. elegans* embryos (See Section The Relationship Between the Nuclear and Cell Volumes in the Size-Correlated Classes). As a future issue, it is interesting to test this possibility to seek a general mechanism that coordinates cell size and cell cycle duration in animal embryos.

In *C. elegans*, cell cycle elongation was due to lengthening of the intermitotic, but not the mitotic, phase in size-correlated AB, MS, C, and P lineages. The *C. elegans* embryonic cell cycle is occupied with S phase at least until the 16-cell stage (Edgar and McGhee, 1988). The gradual elongation of cell cycle duration in the size-correlated AB, MS, C, and P lineages was not due to introduction of the Gap phase, rather due to the elongation of the S phase at least before the 16-cell stage. On the other hand, the Gap phase introduction, which first occurs in the daughters of the E cell (Edgar and McGhee, 1988) was accompanied with abrupt deviation from the T-V relationship that followed by cells in the AB and MS lineages (**Figures 2B,G**). In *Xenopus*, the transition to size-correlated elongation of cell cycle duration is accompanied, in order, by elongation of the S phase just after MBT, introduction of G1 and G2 phases, and elongation of S and G1 phases (Iwao et al., 2005). Durations of the G2 phase are not correlated with cell cycle elongation. Therefore, size-correlated elongation of the cell cycle duration in *C. elegans* embryos is caused by a cell cycle control mechanism different from *Xenopus*.

#### POSSIBLE MODEL TO EXPLAIN THE POWER LAW RELATIONSHIP BETWEEN CELL CYCLE DURATION AND CELL VOLUME IN THE HIGHLY SIZE-CORRELATED CLASS

The *C. elegans* cell cycle duration is likely elongated by S phase elongation at least before the 16-cell stage (Edgar and McGhee, 1988). DNA replication is initiated from specific sites in the chromosomes in eukaryotic cells, called replication origins (Costa et al., 2013). The initiation step of DNA replication, or origin firing, is tightly controlled by the interaction of the replication origin with the initiation factors for DNA replication (IFs) to ensure that the entire genome is replicated precisely once in each cell cycle (Pospiech et al., 2010; Costa et al., 2013). It has been reported that IFs were involved in the asynchrony of division timing of AB and P1 cells (Benkemoun et al., 2014). The asynchrony was explained by the different frequency of the origin firing, such that the length of DNA replication responsible for a single origin may be different between AB and P1 cells (Benkemoun et al., 2014). In this explanation, more origin firing in AB, with DNA replication proceeding from more origins, a shorter time is needed to completely replicate the whole genome DNA than less origin firing in P1.

In *C. elegans* embryos depleted of the ataxia telangiectasia mutated (ATM)-like kinase, *atl-1*, and the checkpoint kinase, *chk-1*, the AB and P1 cell divisions are more synchronous than in wild-type embryos (Brauchle et al., 2003). In *Xenopus* egg extract, ATM-related (ATR)/Chk1 signaling regulates the initiation and progression of DNA synthesis in S phase, even in the absence of DNA damage (Marheineke and Hyrien, 2004; Shechter et al., 2004), probably through modulating the activity of S phase-promoting kinases (Cdk2 and Cdc7) (Marheineke and Hyrien, 2004; Shechter et al., 2004). Therefore, through the regulation of S phase-promoting kinases, ATR/Chk1 signaling may eventually regulate the rate of replication origin firing. Although it remains unknown whether IFs and ATR/Chk1 signaling affect cell cycle duration in *C. elegans* embryos after the two-cell stage, the elongation of cell cycle duration observed in this work may be regulated by the differential regulation of origin firing rate.

We found that the cell cycle was rapidly elongated in *ima-3* RNAi embryos. It has been reported that loss-of-function embryos of *ima-3* exhibit an embryonic lethal phenotype (Geles and Adam, 2001). The rapid elongation of cell cycle in *ima-3* RNAi embryos may be caused by pleiotropic effects of the embryonic lethal phenotype in the late embryonic stage. However, the cell cycle elongation in *ima-3* RNAi embryos was gradual, but not stepwise, such that the slope can be fitted by a power law function. One interesting possibility is that *ima-3* is directly involved in a mechanism regulating the cell cycle progression in *C. elegans* embryos, especially under the control of cell size. The importin family encodes proteins that mediate nuclear import and various molecular processes, including transcription by RNA polymerase III, spindle formation, chromosome segregation, and nuclear envelope assembly (Adam, 2009). Further analyses are necessary to study which of IMA-3 functions causes the rapid elongation of cell cycle in *ima-3* RNAi embryos. Importin  $\alpha$  was found to be involved in nuclear size determination (Levy and Heald, 2010; Edens et al., 2013). Recently, it has been shown that by manipulating expression or function of factors to regulate nuclear size, including Importin  $\alpha$ , it has been shown nuclear size contributes to the regulation of MBT timing in *Xenopus* embryos (Jevtic and Levy, 2015). The same mechanism could function in the T-V relationship in *C. elegans* embryos. Although it remains an open question whether loss of function of *ima-3* leads to altering of nuclear volume in *C. elegans*, there are two intriguing possibilities that IMA-3 mediates the T-V relationship; (1) by regulating nuclear import rate of IFs and/or (2) by regulating nuclear size. Both of the mechanisms affect the T-V relationship through determining their nucleoplasmic concentration of IFs. It will be necessary to test whether one or both of these possibilities were true for evaluating our hypothesis. A theoretical formalization was discussed based on the results of quantitative measurements in this work (Appendix).

## ACKNOWLEDGMENTS

We thank Masashi Tachikawa, Hirofumi Wada, Yoshimi Tanaka, and Noriko Hiroi for valuable discussions, Tomomi Takano for technical assistance, and the *Caenorhabditis* Genetics Center for strains. This work was supported by Special Postdoctoral

Researchers Program, RIKEN (Yukinobu Arata) and by a grant from the Japanese Ministry of Education, Culture, Sports, Science and Technology (Yukinobu Arata and Hitoshi Sawa).

## SUPPLEMENTARY MATERIAL

The Supplementary Material for this article can be found online at: <http://www.frontiersin.org/journal/10.3389/fphys.2014.00529/abstract>

**Figure S1 | Integral approach for measuring cell volume.** **(A)** Serial images of an embryo at the four-cell stage along the Z-axis at 3- $\mu\text{m}$  intervals. The image at 0  $\mu\text{m}$  was at the closest side of the embryo to the objective lens. The focus position moved to the farther side of the embryo in an upright microscope. Cell contours were shown as blue circles, which were traced by following the cell periphery and granules in focus located around the cell boundary. **(B)** Three-dimensional reconstruction of an embryo in the two-cell stage from serial images obtained along the Z-axis at 0.5- $\mu\text{m}$  intervals using Image J. In the reconstructed image in the X-Z axis, nuclear peripheries are indicated by black dots.

**Figure S2 | Statistical analyses to select a model to explain the T-V relationships in *C. elegans*.** Relationship between cell cycle duration and cell volume in AB **(A)**, MS **(B)**, C **(C)**, P **(D)**, E **(E)**, and D **(F)** lineages in the linear scale was fitted by three different models: Gaussian, exponential, or power law function by the Levenberg-Marquardt algorithm, using the same data used in **Figure 2**. Fitted functions and  $\chi^2$ -values are shown in the boxes.

**Figure S3 | Size asymmetry between daughter cells in *C. elegans* C lineage.** Diagram shows the cell division pattern in C lineage. Anterior and posterior daughters are indicated as "a" and "p," respectively. The cell sizes were observed in serial images along the Z-axis, and are shown at the Z axis plane, where the nuclei are located in focus with blue circles. Cell division of Ca, Caa, Cp, and Cpa was asymmetric in the daughter cell sizes, in which the anterior daughter was larger than the posterior daughter. Cpa and Cpp were located in different Z-planes in an embryo. Scale bar = 10  $\mu\text{m}$ .

## REFERENCES

- Adam, S. A. (2009). The nuclear transport machinery in *Caenorhabditis elegans*: a central role in morphogenesis. *Semin. Cell Dev. Biol.* 20, 576–581. doi: 10.1016/j.semcd.2009.03.013
- Arata, Y., Lee, J. Y., Goldstein, B., and Sawa, H. (2010). Extracellular control of PAR protein localization during asymmetric cell division in the *C. elegans* embryo. *Development* 137, 3337–3345. doi: 10.1242/dev.054742
- Benkemoun, L., Descoteaux, C., Chartier, N. T., Pintard, L., and Labbe, J. C. (2014). PAR-4/LKB1 regulates DNA replication during asynchronous division of the early *C. elegans* embryo. *J. Cell Biol.* 205, 447–455. doi: 10.1083/jcb.201312029
- Berger, J. D. (1984). "The ciliate cell cycle," in *The Microbial Cell Cycle*, eds P. Nurse and E. Streiblová (Boca Raton, FL: CRC Press), 191.
- Born, M., and Wolf, E. (1999). *Principles of Optics : Electromagnetic Theory of Propagation, Interference and Diffraction of Light*. Cambridge; New York: Cambridge University Press.
- Brauchle, M., Baumer, K., and Gonczy, P. (2003). Differential activation of the DNA replication checkpoint contributes to asynchrony of cell division in *C. elegans* embryos. *Curr. Biol.* 13, 819–827. doi: 10.1016/S0960-9822(03)00295-1
- Brenner, S. (1974). The genetics of *Caenorhabditis elegans*. *Genetics* 77, 71–94.
- Clute, P., and Masui, Y. (1995). Regulation of the appearance of division asynchrony and microtubule-dependent chromosome cycles in *Xenopus laevis* embryos. *Dev. Biol.* 171, 273–285. doi: 10.1006/dbio.1995.1280
- Colombo, K., Grill, S. W., Kimple, R. J., Willard, F. S., Siderovski, D. P., and Gonczy, P. (2003). Translation of polarity cues into asymmetric spindle positioning

- in *Caenorhabditis elegans* embryos. *Science* 300, 1957–1961. doi: 10.1126/science.1084146
- Costa, A., Hood, I. V., and Berger, J. M. (2013). Mechanisms for initiating cellular DNA replication. *Annu. Rev. Biochem.* 82, 25–54. doi: 10.1146/annurev-biochem-052610-094414
- Dolznig, H., Grebien, F., Sauer, T., Beug, H., and Mullner, E. W. (2004). Evidence for a size-sensing mechanism in animal cells. *Nat. Cell Biol.* 6, 899–905. doi: 10.1038/ncb1166
- Edens, L. J., White, K. H., Jevtic, P., Li, X., and Levy, D. L. (2013). Nuclear size regulation: from single cells to development and disease. *Trends Cell Biol.* 23, 151–159. doi: 10.1016/j.tcb.2012.11.004
- Edgar, B. A., Kiehle, C. P., and Schubiger, G. (1986). Cell cycle control by the nucleo-cytoplasmic ratio in early *Drosophila* development. *Cell* 44, 365–372. doi: 10.1016/0092-8674(86)90771-3
- Edgar, L. G., and Goldstein, B. (2012). Culture and manipulation of embryonic cells. *Methods Cell Biol.* 107, 151–175. doi: 10.1016/B978-0-12-394620-1.00005-9
- Edgar, L. G., and McGhee, J. D. (1988). DNA synthesis and the control of embryonic gene expression in *C. elegans*. *Cell* 53, 589–599. doi: 10.1016/0092-8674(88)90575-2
- Efron, B., and Tibshirani, R. (1993). *An Introduction to the Bootstrap*. New York, NY: Chapman and Hall. doi: 10.1007/978-1-4899-4541-9
- Geles, K. G., and Adam, S. A. (2001). Germline and developmental roles of the nuclear transport factor importin alpha3 in *C. elegans*. *Development* 128, 1817–1830.
- Gerhart, J. C. (1980). “Mechanisms regulating pattern formation in the amphibian egg and early embryo,” in *Biological Regulation and Development*, ed R. F. Goldberger (New York, NY: Springer), 133–316.
- Gotta, M., and Ahringer, J. (2001). Distinct roles for Galpha and Gbetagamma in regulating spindle position and orientation in *Caenorhabditis elegans* embryos. *Nat. Cell Biol.* 3, 297–300. doi: 10.1038/35060092
- Gotta, M., Dong, Y., Peterson, Y. K., Lanier, S. M., and Ahringer, J. (2003). Asymmetrically distributed *C. elegans* homologs of AGS3/PINS control spindle position in the early embryo. *Curr. Biol.* 13, 1029–1037. doi: 10.1016/S0960-9822(03)00371-3
- Gutch, M. J., Flint, A. J., Keller, J., Tonks, N. K., and Hengartner, M. O. (1998). The *Caenorhabditis elegans* SH2 domain-containing protein tyrosine phosphatase PTP-2 participates in signal transduction during oogenesis and vulval development. *Genes Dev.* 12, 571–585. doi: 10.1101/gad.12.4.571
- Iwao, Y., Uchida, Y., Ueno, S., Yoshizaki, N., and Masui, Y. (2005). Midblastula transition (MBT) of the cell cycles in the yolk and pigment granule-free translucent blastomeres obtained from centrifuged *Xenopus* embryos. *Dev. Growth Differ.* 47, 283–294. doi: 10.1111/j.1440-169X.2005.00802.x
- Jevtic, P., and Levy, D. L. (2015). Nuclear Size Scaling during *Xenopus* early development contributes to midblastula transition timing. *Curr. Biol.* 25, 45–52. doi: 10.1016/j.cub.2014.10.051
- Johnston, G. C., Pringle, J. R., and Hartwell, L. H. (1977). Coordination of growth with cell division in the yeast *Saccharomyces cerevisiae*. *Exp. Cell Res.* 105, 79–98. doi: 10.1016/0014-4827(77)90154-9
- Jorgensen, P., Edgington, N. P., Schneider, B. L., Rupes, I., Tyers, M., and Futcher, B. (2007). The size of the nucleus increases as yeast cells grow. *Mol. Biol. Cell* 18, 3523–3532. doi: 10.1091/mbc.E06-10-0973
- Lee, J. Y., and Goldstein, B. (2003). Mechanisms of cell positioning during *C. elegans* gastrulation. *Development* 130, 307–320. doi: 10.1242/dev.00211
- Levy, D. L., and Heald, R. (2010). Nuclear size is regulated by importin alpha and Ntf2 in *Xenopus*. *Cell* 143, 288–298. doi: 10.1016/j.cell.2010.09.012
- Marheineke, K., and Hyrien, O. (2004). Control of replication origin density and firing time in *Xenopus* egg extracts: role of a caffeine-sensitive, ATR-dependent checkpoint. *J. Biol. Chem.* 279, 28071–28081. doi: 10.1074/jbc.M401574200
- Masui, M., and Kominami, T. (2001). Change in the adhesive properties of blastomeres during early cleavage stages in sea urchin embryo. *Dev. Growth Differ.* 43, 43–53. doi: 10.1046/j.1440-169X.2001.00555.x
- Masui, M., Yoneda, M., and Kominami, T. (2001). Nucleus: cell volume ratio directs the timing of the increase in blastomere adhesiveness in starfish embryos. *Dev. Growth Differ.* 43, 295–304. doi: 10.1046/j.1440-169X.2001.00573.x
- Masui, Y., and Wang, P. (1998). Cell cycle transition in early embryonic development of *Xenopus laevis*. *Biol. Cell* 90, 537–548. doi: 10.1111/j.1765-322X.1998.tb01062.x
- Neumann, F. R., and Nurse, P. (2007). Nuclear size control in fission yeast. *J. Cell Biol.* 179, 593–600. doi: 10.1083/jcb.200708054
- Newport, J., and Kirschner, M. (1982). A major developmental transition in early *Xenopus* embryos: I. characterization and timing of cellular changes at the midblastula stage. *Cell* 30, 675–686. doi: 10.1016/0092-8674(82)90272-0
- Nurse, P. (1975). Genetic control of cell size at cell division in yeast. *Nature* 256, 547–551. doi: 10.1038/256547a0
- Pospiech, H., Grosse, F., and Pisani, F. M. (2010). The initiation step of eukaryotic DNA replication. *Subcell Biochem.* 50, 79–104. doi: 10.1007/978-90-481-3471-7\_5
- Prescott, D. M. (1955). Relations between cell growth and cell division. I. Reduced weight, cell volume, protein content, and nuclear volume of *Amoeba proteus* from division to division. *Exp. Cell Res.* 9, 328–337. doi: 10.1016/0014-4827(55)90106-3
- Schnabel, R., Hutter, H., Moerman, D., and Schnabel, H. (1997). Assessing normal embryogenesis in *Caenorhabditis elegans* using a 4D microscope: variability of development and regional specification. *Dev. Biol.* 184, 234–265. doi: 10.1006/dbio.1997.8509
- Shechter, D., Costanzo, V., and Gautier, J. (2004). ATR and ATM regulate the timing of DNA replication origin firing. *Nat. Cell Biol.* 6, 648–655. doi: 10.1038/ncb1145
- Sonnichsen, B., Koski, L. B., Walsh, A., Marschall, P., Neumann, B., Brehm, M., et al. (2005). Full-genome RNAi profiling of early embryogenesis in *Caenorhabditis elegans*. *Nature* 434, 462–469. doi: 10.1038/nature03353
- Srinivasan, D. G., Fisk, R. M., Xu, H., and van den Heuvel, S. (2003). A complex of LIN-5 and GPR proteins regulates G protein signaling and spindle function in *C. elegans*. *Genes Dev.* 17, 1225–1239. doi: 10.1101/gad.1081203
- Sulston, J. E., Schierenberg, E., White, J. G., and Thomson, J. N. (1983). The embryonic cell lineage of the nematode *Caenorhabditis elegans*. *Dev. Biol.* 100, 64–119. doi: 10.1016/0012-1606(83)90201-4
- Sveiczer, A., Novak, B., and Mitchison, J. M. (1996). The size control of fission yeast revisited. *J. Cell Sci.* 109(pt 12), 2947–2957.
- Wang, P., Hayden, S., and Masui, Y. (2000). Transition of the blastomere cell cycle from cell size-independent to size-dependent control at the midblastula stage in *Xenopus laevis*. *J. Exp. Zool.* 287, 128–144. doi: 10.1002/1097-010X(20000701)287:2<128::AID-JEZ3>3.0.CO;2-G
- Conflict of Interest Statement:** The authors declare that the research was conducted in the absence of any commercial or financial relationships that could be construed as a potential conflict of interest.
- Received:** 30 September 2014; **accepted:** 27 December 2014; **published online:** 28 January 2015.
- Citation:** Arata Y, Takagi H, Sako Y and Sawa H (2015) Power law relationship between cell cycle duration and cell volume in the early embryonic development of *Caenorhabditis elegans*. *Front. Physiol.* 5:529. doi: 10.3389/fphys.2014.00529
- This article was submitted to Systems Biology, a section of the journal *Frontiers in Physiology*.
- Copyright © 2015 Arata, Takagi, Sako and Sawa. This is an open-access article distributed under the terms of the Creative Commons Attribution License (CC BY). The use, distribution or reproduction in other forums is permitted, provided the original author(s) or licensor are credited and that the original publication in this journal is cited, in accordance with accepted academic practice. No use, distribution or reproduction is permitted which does not comply with these terms.

## APPENDIX

### NUMERICAL FORMULARIZATION OF OUR MODEL

We showed that the *C. elegans* T–V relationship in the highly size-correlated class correlated with the volume ratio between the nucleus and cell (Section The Relationship Between the Nuclear and Cell Volumes in the Size-Correlated Classes). Here, we discuss a possible molecular mechanism to regulate the T–V relationship (Section Possible Model to Explain the Power Law Relationship Between Cell Cycle Duration and Cell Volume in the Highly Size-Correlated Class), based on a theoretical numerical formulation of our model. The causal relationship between the cell cycle duration and cell volume has not previously been shown in *C. elegans* embryos, and knowledge of molecular mechanisms regulating cell cycle duration are insufficient. Thus, this model does not exclude alternative numerical models.

We presume that the cell cycle duration in the highly size-correlated class ( $T$ ), which is occupied with S phase, is determined by the whole genome size ( $L$ ; [n.a.]), the replication velocity ( $k$ , [n.a./s]) which is assumed to be constant in embryonic cells, and the number of replication origins that are fired during S phase ( $N$  [–]), where, n.a. indicates the number of nucleic acids:

$$T = \frac{L}{N \cdot k} \quad (\text{A1})$$

In addition, we presumed that the number of fired origins during S phase is in proportion to the concentration of the IFs in the nucleoplasm ([ $nucIF$ ]):

$$N \propto [nucIF] \quad (\text{A2})$$

We also presumed that the total amount of IFs is constant in embryos. The amount of IFs in each cell ( $cytoIF$ ) is determined following the segregation of daughter cells from the mother cell according to the daughter cell volume. The nucleoplasmic IF concentration is presumed to be determined by active transport via the Importin system (Section Possible Model to Explain the

Power Law Relationship Between Cell Cycle Duration and Cell Volume in the Highly Size-Correlated Class), so that the nucleoplasmic concentration of the IFs is reduced according to embryonic cell cleavage events that follow the power law of the volume ratio between the nucleus and cell (Figure 5B). Consequently, the T–V relationship in the highly size-correlated class elongated according to the volume ratio between the nucleus and cell.

$$[nucIF] \propto \frac{cytoIF}{V_n} \propto \frac{V_c}{V_n} \quad (\text{A3})$$

From Equations (A2, A3):

$$N \propto V_c/V_n \quad (\text{A4})$$

From Equations (A1, A4):

$$T \propto \frac{L}{V_c/V_n \cdot k} \propto \frac{V_n}{V_c} \quad (\text{A5})$$

From our experimental measurements of nuclear and cell volume (Section The Relationship Between the Nuclear and Cell Volumes in the Size-Correlated Classes),

$$\frac{V_n}{V_c} \propto V_c^{-0.37} \quad (\text{A6})$$

Therefore, from Equations (A5, A6):

$$T \propto V_c^{-0.37}.$$

Thus, the cell cycle duration in the highly size-correlated class can be determined by the amount of IFs that are inherited in proportion to cell size and function in proportion to nuclear size. Eventually, cell cycle duration is elongated in proportion to cell volume with the power –0.37.



# Need for multi-scale systems to identify spindle orientation regulators relevant to tissue disorganization in solid cancers

Hui Men Selina Chin<sup>†</sup>, Karandeep Nandra<sup>†</sup>, Joanna Clark and Viji M. Draviam \*

Department of Genetics, Cancer Cell Biology, University of Cambridge, Cambridge, UK

\*Correspondence: viji.draviam@gen.cam.ac.uk

<sup>†</sup>These authors have contributed equally to this work.

## Edited by:

Akatsuki Kimura, National Institute of Genetics, Japan

## Reviewed by:

Akatsuki Kimura, National Institute of Genetics, Japan

Fumiko Toyoshima, Kyoto University, Japan

**Keywords:** cell division, cancer initiation, cancer progression, spindle orientation, Hippo pathway, microtubules, Wnt pathway, PTEN regulation

## INTRODUCTION

During cell division, the mitotic spindle captures chromosomes and segregates them into two equal sets. The orientation and position of the mitotic spindle is important because the spindle equator becomes the plane of cell division. For instance, in a columnar cell with apical and basal polarity, if the spindle pole-to-pole axis orients along the cell's long axis, the cell will divide along its short-axis; however, if the spindle axis orients along the cell's short axis, the cell will divide along its long-axis (**Figure 1A**). Similarly when the spindle is off-centered (mis-positioned), it results in asymmetric cell sizes in the two daughter cells, which is often used to control tissue organization (**Figure 1B**). Thus, errors in the orientation and positioning of the mitotic spindle can cause incorrect plane of cell division leading to incorrect cell size, content and neighborhood of daughter cells (**Figures 1A,B**).

A human body experiences over a trillion divisions and through age errors in cell division can accumulate; errors in spindle orientation can contribute to tissue disorganization, a hallmark of several age-related conditions and also, carcinogenesis. However, mutations in classical cortical force generators that rotate the spindle to the correct orientation have not been shown to promote carcinogenesis. In contrast, several proteins known to play a role in cancer initiation and progression are being newly identified as regulators of spindle positioning and orientation. In this opinion article, we

briefly discuss the surprising lack of direct evidence for classical spindle rotation regulators in oncogenesis and present examples of oncogenic pathway components that influence spindle orientation. We conclude with the need for new strategies to uncover the contribution of spindle orientation defects to tissue disorganization commonly found in cancers and also ageing disorders.

## A WEAK CASE FOR CORTICAL FORCE GENERATORS IN CANCER INITIATION

For a detailed review on the mechanisms of spindle positioning and orientation, we recommend a recent review from Kulukian and Fuchs (2013). Astral microtubules of the spindle (**Figure 1C**) are pulled at and this rotates the entire spindle to a pre-defined position. Forces to pull the astral microtubules can arise from the cortex or within the cytoplasm, although classical evolutionarily conserved players have been reported at the cell cortex (reviewed McNally, 2013). Cortical pulling forces are essential for mitotic spindle positioning and orientation in human cells (see next para). Although it is very likely that compromising cortical pulling forces would lead to tissue disorganization and carcinogenesis, cortical force generator mutations are not prevalent in tumors and their genetic loss-of-function in mice do not present tumors (reviewed in Noatynska et al., 2012).

Dynein is the key player in cortical force generation and its localization is controlled by the cortical platform

consisting of  $\text{G}\alpha_i$ , LGN, and NuMA (**Figure 1C**) (Kiyomitsu and Cheeseman, 2012; Kotak et al., 2012; Corrigan et al., 2013). Considering that LGN is the primary platform for cortical dynein recruitment and absolutely essential in epithelial cells for biased rotation of the spindle (Corrigan et al., 2013), one would expect a more severe phenotype than the reported epidermal stratification defects in LGN depleted mouse skin (Williams et al., 2011). An explanation for this paradox can be gleaned from proliferation and cell death studies: First, LGN mutant mice lacking LGN's C-terminus are viable, but compromised for planar spindle orientation in the brain (Konno et al., 2008). This shows that the control of spindle orientation is essential for maintaining a population of neuroepithelial cells, but is dispensable for proliferative or differentiative decisions. In support of this idea, loss of Par3, a polarity protein that forms a complex with Par6/aPKC and controls spindle orientation (Hao et al., 2010), promotes breast tumorigenesis and metastasis, only in combination with oncogenic Notch or Ras (61L) expression (McCaffrey et al., 2012). Second, combining defects in cell death and spindle alignment disrupts epithelial integrity and causes tumor-like masses (Nakajima et al., 2013). Thus, spindle orientation defects and resulting cell fate defects could be resolved by other cell number control pathways (for example, cell proliferation and cell death), which indicates a cooperative role for orientation defects in tissue disorganization and

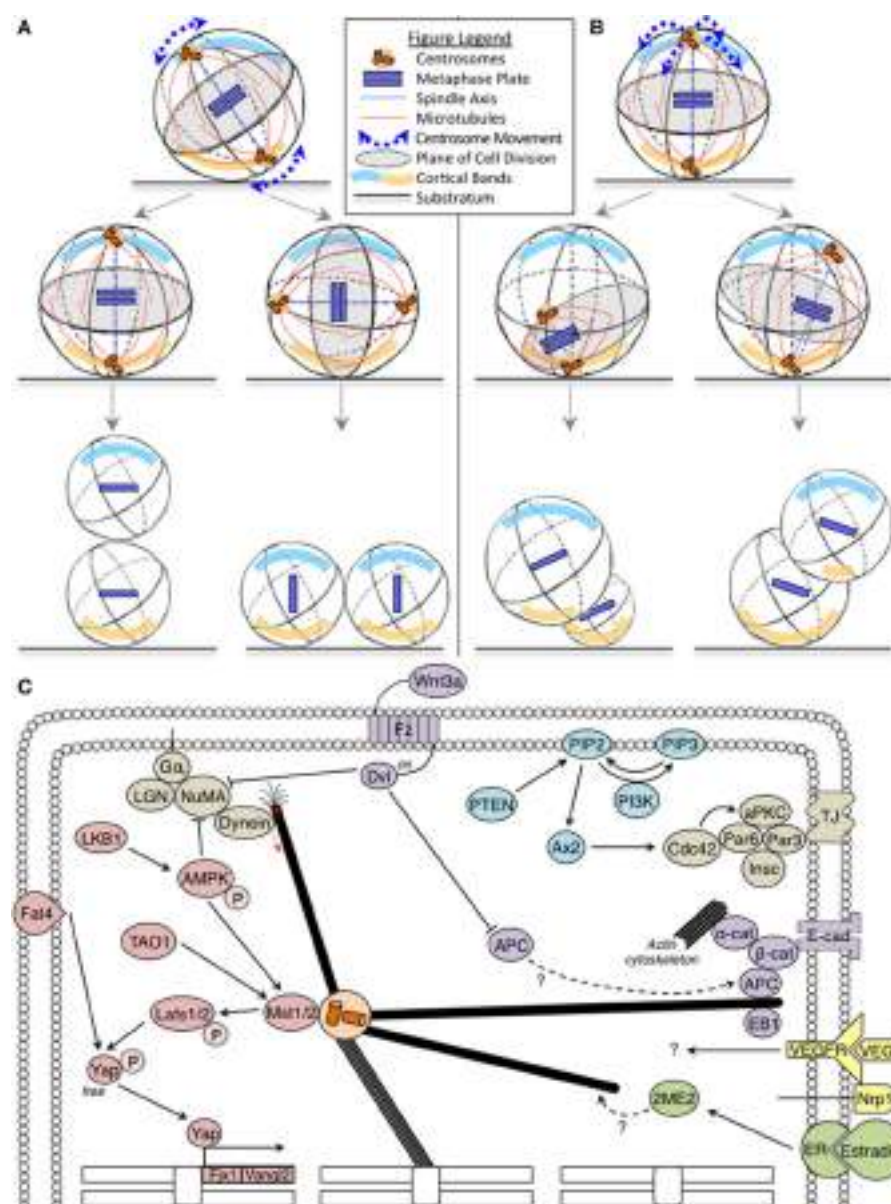


**FIGURE 1 | (A,B)** Fates of incorrect spindle orientation and positioning: Cartoons show mitotic spindle movements relative to the substratum leading to spindle mis-orientation (**A**) and mis-positioning (**B**) with cortical bands highlighting polarity differences. In (**A**), misorientation alters the relative positions and contents of daughter cells, without affecting progenitor cell sizes. In (**B**), mispositioning affects daughter cell size, relative positions and their contents. Legend describing cell substratum, spindle microtubules, metaphase plate, and spindle

movements included. **(C)** Oncogenic pathways implicated in spindle orientation: The Hippo, PTEN-PI3K, and Wnt tumor suppressor pathway components are marked in pink, blue, and purple, respectively. The oncogenic estrogen receptor (ER) pathway is marked in green. Together, these pathways regulate astral microtubule (marked in bold) function. Red arrows indicate force generation events. The Hippo pathway also influences transcriptional regulation of several genes involved in orientation (marked on chromosomes).

cancer progression, rather than cancer initiation *per se*.

### KEY ONCOGENIC PATHWAYS IMPLICATED IN SPINDLE ORIENTATION

While mutations in cortical force generators present a weak case for orientation defects leading to carcinogenesis, emerging evidence show a role for

oncogenic and tumor suppressor pathways in ensuring spindle orientation. Three key examples are:

#### 1. Hippo tumor suppressor pathway

The Hippo pathway is disrupted in a variety of cancers (reviewed in Harvey et al., 2013). Fat4, a member of the Hippo

pathway in vertebrates (Skouloudaki et al., 2009) orients the plane of cell division to maintain the planar cell polarity (PCP) of elongating tubules during kidney development and prevents cyst formation common to ageing kidneys (Saburi et al., 2008; Mao et al., 2011). Fat4 regulates the expression of Vangl2 and Fjx1 (Saburi et al., 2008), which

are asymmetrically localized Wnt-Fz PCP components (Montcouquiol et al., 2006). Recent additions to the Hippo pathway, LKB1 tumor suppressor (Mohseni et al., 2014), AMPK (Thaiparambil et al., 2012) and TAO1 kinase (Poon et al., 2011) are also YAP regulators that act on Lats1 and MST2, and are important for mitosis and spindle orientation (Wojtala et al., 2011; Wei et al., 2012; Shrestha et al., 2014). It is currently unclear how Fat4, TAO1, LKB1 and the Hippo pathway link spindle orientation and tissue maintenance (**Figure 1C**), which is an important topic to be addressed.

## 2. PTEN-PI3K signaling pathway

The Phosphatase and tensin homolog deleted on chromosome 10 (PTEN) that regulates the PI3K-Akt-mTOR pathway are among the most frequently inactivated tumor suppressor genes in sporadic cancers (reviewed in Chalhoub and Baker, 2009). PI3K influences spindle orientation in non-polarized cells (Toyoshima et al., 2007). PTEN deficiency impairs glandular morphogenesis, through Ax2 and Cdc42, leading to abnormal multi-luminal phenotypes (Martin-Belmonte et al., 2007; Jagan et al., 2013). Thus, loss of PTEN-PI3K signaling can result in incorrectly oriented daughter cells, which may be of relevance to PTEN-associated tissue disorganization common to geriatric conditions and carcinogenesis.

## 3. Wnt signaling pathway

Multiple components of Wnt pathway are known to control spindle orientation. First, spatial restriction of Wnt3a is sufficient to align the spindle parallel to the axis of cell polarity and induce asymmetrical cell division leading to asymmetrical inheritance of Wnt signaling components. This provides a mechanism for extrinsic control of cell fate and differentiation (Habib et al., 2013), but its specific role in cancer is unclear. Second, APC, a Wnt pathway member, is a tumor suppressor and regulator of microtubule stability and cell polarity (Zumbrunn et al., 2001; Etienne-Manneville and Hall, 2003). APC and its interactors, EB1 (a microtubule-end binding protein) and  $\beta$ -catenin are all needed for stable spindle positioning

(Draviam et al., 2006; Wu et al., 2010 and reviewed in Tamura and Draviam, 2012). While inactivation of both APC alleles is required for carcinogenesis (reviewed in Reya and Clevers, 2005), loss of a single allele is sufficient for spindle misorientation (Fleming et al., 2009). It is unclear if APC's role in spindle orientation and Wnt signaling converge in preventing carcinogenesis (**Figure 1C**). However, APC is known to bind  $\beta$ -catenin, which together with E-cadherin and  $\alpha$ -catenin, are actin regulators with a role in spindle orientation (reviewed in Allan and Nähk, 2001). Third, Dvl is another component of the Wnt-PCP pathway which influences spindle orientation (Ségalen et al., 2010), and its role in linking spindle orientation with carcinogenesis is also not known.

In summary, studies of PTEN, Hippo and Wnt tumor suppressor pathways show evidence for more than one protein of any single pathway being involved in spindle orientation (**Figure 1C**). Whether their role in spindle orientation is important for their tumor suppressor function is not known and is an important question to address.

## EXCITING FUTURE DIRECTIONS FOR ELUCIDATING HOW DEFECTIVE SPINDLE ORIENTATION IS LINKED TO TISSUE DISORGANIZATION IN AGEING DISORDERS AND CANCERS

Multiple lines of evidence show the co-existence of spindle orientation failure and growth dysregulation. Is this a mere coincidence? Alternatively, does this co-existence play any role in tissue disorganization seen in cancers or ageing disorders? To help address these questions, two approaches are going to be pivotal:

### 1. Multi-scale imaging (Single-cell and tissue-level studies: two sides of a coin)

Multi-scale systems that capture single-cell and tissue level information are crucial to track the emergence of tissue-level defects (growth dysregulation) from single-cell errors (spindle orientation failure). For instance, in cancer stem cells of skin papilloma, the inhibition of VEGF alters the ratio of symmetric:asymmetric cell divisions causing tumor regression (Beck

et al., 2011). How VEGF and its co-receptor Nrp1 influence the plane of cell division is unclear (**Figure 1C**); and establishing this may very well require single-cell studies of the perivascular niche Cancer Stem Cells exposed to tumor-cell derived VEGF. In some cases, tissue-specific organotypic models (such as the 3D cyst model; Durgan et al., 2011) amenable to single-cell tracking may be sufficient. For example, chronic estrogen application is linked to hyperplasia and cancer: estrogen increases symmetric cell division (Gunin et al., 2001), and an estrogen metabolite, 2-methoxy estradiol (2ME), alters microtubule dynamics and disrupts spindle orientation (Corrigan et al., 2013). Determining how sub-cellular microtubule perturbation ultimately manifests into changes in symmetric vs. asymmetric cell division rates in tissues could be addressed using organotypic models that can recapitulate estradiol-dependent morphogenesis.

## 2. A quantitative way to define intermediary dynamic steps of spindle orientation

In cell cultures that have lost polarity and resemble those that have gone through Epithelial-Mesenchymal transition, even a small directional bias in moving the spindle toward the final destination is sufficient to achieve the correct orientation of the spindle (Corrigan et al., 2013)—what is the molecular basis of this robustness? Is this dependent on the microtubule -wall or -end interaction at the cell-cortex, similar to microtubule interaction geometries at chromosomes (Shrestha and Draviam, 2013)? Is this dependent exclusively on cortical pulling forces that act on microtubules or also on pushing forces of microtubules against the actin mesh-work, or forces generated by intracellular transport (reviewed in McNally, 2013). Addressing these in human cells will require us to consider the temporal evolution of various spindle movements and not simply the binary end-outcome of spindle orientation “failure” vs. “success.” Examples of similar approach have been already fruitful in *C.elegans* (Pecreaux et al., 2006; Kimura and Onami, 2010). Finally, understanding the evolution of spindle movements is important because even a simple delay

in spindle movements can increase the probability of spindle orientation defects, as human cells have not been reported to have a spindle orientation checkpoint so far.

## CONCLUSIONS

Knowing the intermediary steps of the spindle orientation process can help reveal how growth regulatory pathways like the Hippo or mTOR pathway that receive various signals from developmental and stress cues, jointly regulate spindle movements. This along with multi-scale systems will be important for determining molecular lesions in spindle orientation and positioning which are frequently associated with tissue disorganization observed in ageing disorders and solid cancers.

## ACKNOWLEDGMENTS

Viji M. Draviam is a Cancer Research UK career development fellow. We thank Prof. Frederick Campbell, Queens University, Belfast, UK and Dr. Noriko Hiroi, Keio University, Japan for insightful comments. We thank members of the Draviam laboratory, particularly Mr. Roshan Shrestha and Mr. Duccio Conti for help with proofreading the article.

## REFERENCES

- Allan, V., and Nähthke, I. S. (2001). Catch and pull a microtubule: getting a grasp on the cortex. *Nat. Cell Biol.* 3, E226–E228. doi: 10.1038/ncb1001-e226
- Beck, B., Driessens, G., Goossens, S., Youssef, K. K., Kuchnio, A., Caauew, A., et al. (2011). A vascular niche and a VEG-Nrp1 loop regulate the initiation and stemness of skin tumours. *Nature* 478, 399–403. doi: 10.1038/nature10525
- Boggiano, J., Vanderzalm, P., and Fehon, R. (2011). Tao-1 phosphorylates hippo/MST kinases to regulate the hippo-salvador-warts tumour suppressor pathway. *Dev. Cell* 21, 888–895. doi: 10.1016/j.devcel.2011.08.028
- Chalhoub, N., and Baker, S. J. (2009). PTEN and the PI3-kinase pathway in cancer. *Annu. Rev. Pathol.* 4, 127–150. doi: 10.1146/annurev.pathol.4.110807.092311
- Corrigan, A. M., Shrestha, R. L., Zulkilpi, I., Hiroi, N., Liu, Y., Tamura, N., et al. (2013). Automated tracking of mitotic spindle pole positions shows that LGN is required for spindle rotation but not orientation maintenance. *Cell Cycle* 12, 2643–2655. doi: 10.4161/cc.25671
- Draviam, V. M., Shapiro, I., Aldridge, B., and Sorger, P. K. (2006). Misorientation and reduced stretching of aligned sister kinetochores promote chromosome missegregation in EB1– or APC–depleted cells. *EMBO J.* 25, 2814–2827. doi: 10.1038/sj.emboj.7601168
- Durgan, J., Kaji, N., Jin, D., and Hall, A. (2011). Par6B and atypical PKC regulate mitotic spindle orientation during epithelial morphogenesis. *J. Biol. Chem.* 286, 12461–12474. doi: 10.1074/jbc.M110.174235
- Etienne-Manneville, S., and Hall, A. (2003). Cdc42 regulates GSK-3β and adenomatous polyposis coli to control cell polarity. *Nature* 421, 753–756. doi: 10.1038/nature01423
- Fleming, E. S., Temchin, M., Wu, Q., Maggio-Price, L., and Tirnauer, J. S. (2009). Spindle misorientation in tumors from APCmin/+ mice. *Mol. Carcinog.* 48, 592–598. doi: 10.1002/mc.20506
- Gunin, A. G., Mashin, I. N., and Zakharov, D. A. (2001). Proliferation, mitosis orientation and morphogenetic changes in the uterus of mice following chronic treatment with both estrogen and glucocorticoid hormones. *J. Endocrinol.* 169, 23–31. doi: 10.1677/joe.0.1690023
- Habib, S. J., Chen, B., Tsai, F., Anastassiadis, K., Meyer, T., Betzig, E., et al. (2013). A localized wnt signal orients asymmetric stem cell division in vitro. *Science* 339, 1445–1448. doi: 10.1126/science.1231077
- Hao, Y., Du, Q., Chen, X., Zheng, Z., Balsbaugh, J. L., Maitra, S., et al. (2010). Par3 controls epithelial spindle orientation by aPKC-Mediated phosphorylation of apical pins. *Curr. Biol.* 20, 1809–1818. doi: 10.1016/j.cub.2010.09.032
- Harvey, K. F., Zhang, X., and Thomas, D. M. (2013). The Hippo pathway and human cancer. *Nat. Rev. Cancer* 13, 246–257. doi: 10.1038/nrc3458
- Jagan, I. C., Deevi, R. K., Fatehullah, A., Topley, R., Eves, J., Stevenson, M., et al. (2013). PTEN phosphatase-independent maintenance of glandular morphology in a predictive colorectal cancer model system. *Neoplasia* 15, 1218–1230. doi: 10.1593/neo.121516
- Kimura, A., and Onami, S. (2010). Modelling microtubule-mediated forces and centrosome positioning in *caenorhabditis elegans* embryos. *Methods Cell Biol.* 97, 437–453. doi: 10.1016/S0091-679X(10)97023-4
- Kiyomitsu, T., and Cheeseman, I. M. (2012). Chromosome- and spindle-pole-derived signals generate an intrinsic code for spindle position and orientation. *Nat. Cell Biol.* 14, 311–317. doi: 10.1038/ncb2440
- Konno, D., Shioi, G., Shitamukai, A., Mori, A., Kiyonari, H., Miyata, T., et al. (2008). Neuroepithelial progenitors undergo LGN-dependent planar divisions to maintain self-renewability during mammalian neurogenesis. *Nat. Cell Biol.* 10, 93–101. doi: 10.1038/ncb1673
- Kotak, S., Busso, C., and Gönczy, P. (2012). Cortical dynein is critical for proper spindle positioning in human cells. *J. Cell Biol.* 199, 97–110. doi: 10.1083/jcb.20120316
- Kulukian, A., and Fuchs, E. (2013). Spindle orientation and epidermal morphogenesis. *Philos. Trans. R. Soc. Lond. B* 368, 20130016. doi: 10.1098/rstb.2013.0016
- Mao, Y., Mulvaney, J., Zakaria, S., Yu, T., Morgan, K. M., Allen, S., Irvine, K. D., et al. (2011). Characterization of a Dchs1 mutant mouse reveals requirements for Dchs1-Fat4 signaling during mammalian development. *Development* 138, 947–957. doi: 10.1242/dev.057166
- Martin-Belmonte, F., Gassama, A., Datta, A., Yu, W., Rescher, U., Gerke, V., et al. (2007). PTEN-mediated apical segregation of phosphoinositides controls epithelial morphogenesis through Cdc42. *Cell* 128, 383–397. doi: 10.1016/j.cell.2006.11.051
- McCaffrey, L. M., Montalbano, J., Mihai, C., and Macara, I. G. (2012). Loss of the Par3 polarity protein promotes breast tumorigenesis and metastasis. *Cancer Cell* 22, 601–614. doi: 10.1016/j.ccr.2012.10.003
- McNally, F. (2013). Mechanisms of spindle positioning. *J. Cell Biol.* 200, 131–140. doi: 10.1083/jcb.201210007
- Mohseni, M., Sun, J., Lau, A., Curtis, S., Goldsmith, J., Fox, V. L., et al. (2014). A genetic screen identifies an LKB1-MARK signalling axis controlling the hippo-YAP pathway. *Nat. Cell Biol.* 16, 108–117. doi: 10.1038/ncb2884
- Montcouquiol, M., Sans, N., Huss, D., Kach, J., Dickman, J. D., Forge, A., et al. (2006). Asymmetric localization of Vangl2 and Fz3 indicate novel mechanisms for planar cell polarity in mammals. *J. Neurosci.* 26, 5265–5275. doi: 10.1523/JNEUROSCI.4680-05.2006
- Nakajima, Y., Meyer, E. J., Kroesen, A., McKinney, S. A., and Gibson, M. C. (2013). Epithelial junctions maintain tissue architecture by directing planar spindle orientation. *Nature* 500, 359–362. doi: 10.1038/nature12335
- Noatynska, A., Gotta, M., and Meraldi, P. (2012). Mitotic spindle (DIS)orientation and DISease: cause or consequence? *J. Cell Biol.* 199, 1025–1035. doi: 10.1083/jcb.201209015
- Pecreaux, J., Roper, J., Kruse, K., Julicher, F., Hyman, A., Grill, S., et al. (2006). Spindle oscillations during asymmetric cell division require a threshold number of active cortical force generators. *Curr. Biol.* 16, 2111–2122. doi: 10.1016/j.cub.2006.09.030
- Poon, C., Lin, J., Zhang, X., and Harvey, K. (2011). The sterile 20-like kinase tao-1 controls tissue growth by regulating the salvador-warts-hippo pathway. *Dev. Cell* 21, 896–906. doi: 10.1016/j.devcel.2011.09.012
- Reya, T., and Clevers, H. (2005). Wnt signalling in stem cells and cancer. *Nature* 434, 843–850. doi: 10.1038/nature03319
- Saburi, S., Hester, I., Fischer, E., Pontoglio, M., Eremina, V., Gessler, M., et al. (2008). Loss of Fat4 disrupts PCP signaling and oriented cell division and leads to cystic kidney disease. *Nat. Genet.* 40, 1010–1015. doi: 10.1038/ng.179
- Ségalen, M., Johnston, C. A., Martin, C. A., Dumortier, J. G., Prehoda, K. E., David, N. B., et al. (2010). The Fz-Dsh planar cell polarity pathway induces oriented cell division via Mud/NuMA in drosophila and zebrafish. *Dev. Cell* 19, 740–752. doi: 10.1016/j.devcel.2010.10.004
- Shrestha, R. L., and Draviam, V. M. (2013). Lateral to end-on conversion of chromosome-microtubule attachment requires kinesins CENP-E and MCAK. *Curr. Biol.* 23, 1514–1526. doi: 10.1016/j.cub.2013.06.040
- Shrestha, R. L., Tamura, N., Fries, A., Levin, N., Clark, J., and Draviam, V. M. (2014). TAO1 kinase maintains chromosomal stability by facilitating proper congression of chromosomes. *Open Biol.* 4:130108. doi: 10.1098/rsob.130108

- Skouloudaki, K., Puetz, M., Simons, M., Courbard, J., Boehlke, C., Hartleben, B., et al. (2009). Scribble participates in hippo signaling and is required for normal zebrafish pronephros development. *Proc. Natl. Acad. Sci. U.S.A.* 106, 8579–8584. doi: 10.1073/pnas.0811691106
- Tamura, N., and Draviam, V. M. (2012). Microtubule plus-ends within a mitotic cell are ‘moving platforms’ with anchoring, signalling and force-coupling roles. *Open Biol.* 2:120132. doi: 10.1098/rsob.120132
- Thaiparambil, J. T., Eggers, C. M., and Marcus, A. I. (2012). AMPK regulates mitotic spindle orientation through phosphorylation of myosin regulatory light chain. *Mol. Cell. Biol.* 32, 3203–3217. doi: 10.1128/MCB.00418-12
- Toyoshima, F., Matsumura, S., Morimoto, H., Mitsushima, M., and Nishida, E. (2007). PtdIns(3,4,5)P<sub>3</sub> regulates spindle orientation in adherent cells. *Dev. Cell* 13, 796–811. doi: 10.1016/j.devcel.2007.10.014
- Wei, C., Bhattaram, V. K., Igwe, J. C., Fleming, E., and Tirnauer, J. S. (2012). The LKB1 tumor suppressor controls spindle orientation and localization of activated AMPK in mitotic epithelial cells. *PLoS ONE* 7:e41118. doi: 10.1371/journal.pone.0041118
- Williams, S. E., Beronja, S., Pasolli, H. A., and Fuchs, E. (2011). Asymmetric cell divisions promote notch-dependent epidermal differentiation. *Nature* 470, 353–358. doi: 10.1038/nature09793
- Wojtala, R. L., Tavares, I. A., Morton, P. E., Valderrama, F., Thomas, N. S. B., and Morris, J. D. H. (2011). Prostate-derived Sterile 20-like kinases (PSKs/TAOKs) Are activated in mitosis and contribute to mitotic cell rounding and spindle positioning. *J. Biol. Chem.* 286, 30161–30170. doi: 10.1074/jbc.M111.228320
- Wu, M., Smith, C. L., Hall, J. A., Lee, I., Luby-Phelps, K., and Tallquist, M. D. (2010). Epicardial spindle orientation controls cell entry into the myocardium. *Dev. Cell* 19, 114–125. doi: 10.1016/j.devcel.2010.06.011
- Zumbrunn, J., Kinoshita, K., Hyman, A. A., and Nathke, I. S. (2001). Binding of the adenomatous polyposis coli protein to microtubules increases microtubule stability and is regulated by GSK3β phosphorylation. *Curr. Biol.* 11, 44–49. doi: 10.1016/S0960-9822(01)00002-1
- Conflict of Interest Statement:** The authors declare that the research was conducted in the absence of any commercial or financial relationships that could be construed as a potential conflict of interest.
- Received: 16 May 2014; paper pending published: 20 June 2014; accepted: 08 July 2014; published online: 25 July 2014.*
- Citation: Chin HMS, Nandra K, Clark J and Draviam VM (2014) Need for multi-scale systems to identify spindle orientation regulators relevant to tissue disorganization in solid cancers. *Front. Physiol.* 5:278. doi: 10.3389/fphys.2014.00278*
- This article was submitted to Systems Biology, a section of the journal Frontiers in Physiology.*
- Copyright © 2014 Chin, Nandra, Clark and Draviam. This is an open-access article distributed under the terms of the Creative Commons Attribution License (CC BY). The use, distribution or reproduction in other forums is permitted, provided the original author(s) or licensor are credited and that the original publication in this journal is cited, in accordance with accepted academic practice. No use, distribution or reproduction is permitted which does not comply with these terms.*



# The dynamics of signal amplification by macromolecular assemblies for the control of chromosome segregation

Semin Lee<sup>1</sup> and Victor M. Bolanos-Garcia<sup>2\*</sup>

<sup>1</sup> Center for Biomedical Informatics, Harvard Medical School, Harvard University, Boston, MA, USA

<sup>2</sup> Department of Biological and Medical Sciences, Faculty of Health and Life Sciences, Oxford Brookes University, Oxford, UK

**Edited by:**

Viji M. Draviam, University of Cambridge, UK

**Reviewed by:**

Hassan Bousbaa, Cooperativa de Ensino Superior Politécnico e Universitário, Portugal  
Arockia Jeyaprakash Arulanandam, University of Edinburgh, UK

**\*Correspondence:**

Victor M. Bolanos-Garcia,  
Department of Biological and Medical Sciences, Faculty of Health and Life Sciences, Oxford Brookes University, Gipsy Lane, Headington, Oxford OX3 0BP, UK  
e-mail: vbolanos-garcia@brookes.ac.uk

The control of chromosome segregation relies on the spindle assembly checkpoint (SAC), a complex regulatory system that ensures the high fidelity of chromosome segregation in higher organisms by delaying the onset of anaphase until each chromosome is properly bi-oriented on the mitotic spindle. Central to this process is the establishment of multiple yet specific protein-protein interactions in a narrow time-space window. Here we discuss the highly dynamic nature of multi-protein complexes that control chromosome segregation in which an intricate network of weak but cooperative interactions modulate signal amplification to ensure a proper SAC response. We also discuss the current structural understanding of the communication between the SAC and the kinetochore; how transient interactions can regulate the assembly and disassembly of the SAC as well as the challenges and opportunities for the definition and the manipulation of the flow of information in SAC signaling.

**Keywords:** spindle assembly checkpoint (SAC), genome instability, chromosome segregation, signal amplification, cell cycle regulation, kinetochore-microtubules network, cancer, protein-protein interactions

## THE SPINDLE ASSEMBLY CHECKPOINT (SAC)

The regulation of chromosome division in time and space requires amplification of specific signals across an intricate network of protein-protein interactions. Central to this process is the spindle assembly checkpoint (SAC), the essential and evolutionarily conserved self-regulatory system of the eukaryotic cell cycle that ensures accurate chromosome segregation by controlling cell cycle progression in response to microtubule-kinetochore attachment defects (Hardwick et al., 2000; Warren et al., 2002; Morrow et al., 2005; Yao and Dai, 2012; Foley and Kapoor, 2013; Jia et al., 2013). SAC function requires its communication with the kinetochore, the multiprotein network that assembles on mitotic or meiotic centromeres to link centromeric DNA with microtubules.

Three serine/threonine protein kinases, Bub1, BubR1, and Mps1 play essential roles in the mitotic checkpoint. Bub1 is required for the recruitment to the kinetochore, the site for attachment of chromosomes to microtubule polymers that pull sister chromatids apart during cell division, of several checkpoint components in cells that have the checkpoint unsatisfied. Bub1 is also important for the assembly of the inner centromere. BubR1 is required for the establishment of proper kinetochore-microtubule attachment and chromosome alignment and together with the proteins Bub3, Mad2, and Cdc20 forms part of the mitotic checkpoint complex (MCC) that inhibits the E3 ubiquitin ligase activity of the anaphase-promoting complex (also known as the cyclosome, APC/C) toward its substrates Securin and Cyclin B1 (Tang et al., 2004; Vanoostruysse and Hardwick, 2005; Boyarchuk et al., 2007; Bolanos-Garcia and Blundell, 2011; Elowe, 2011; Chao et al., 2012). Mps1 is a dual-specificity kinase that localizes to kinetochores during mitosis and that through phosphorylation of

kinetochore targets prevents aneuploidy by promoting both productive chromosome attachment and SAC function. Loss of Mps1 function in organisms from yeasts to humans overrides mitotic checkpoint signaling (Weiss and Winey, 1996; Abrieu et al., 2001; Maciejowski et al., 2010; Tipton et al., 2013). Mps1 has been identified in the signature of the top 25 genes overexpressed in tumors of different origins including bladder, anaplastic thyroid, breast, lung, esophagus, and prostate (Carter et al., 2006; Janssen et al., 2009). Recruitment of Bub1, BubR1, Mps1, Bub3, Cdc20, Mad1, and Mad2 to the kinetochore is essential for the full activity and optimal function of the mitotic checkpoint (revised in Musacchio, 2011; Hauf, 2013). APC/C inhibition is released after proper bipolar attachment and alignment of all chromosomes at the center of the cell, thus allowing chromosome separation and mitotic progression (revised in Jia et al., 2013).

Here we discuss the nature of protein-protein interactions underpinning mitotic checkpoint function, in which weak but cooperative association of individual protein components of the SAC to form larger, dynamic macromolecular assemblies has arisen as successful strategy to ensure the amplification of specific signals that control chromosome segregation in the crowded environment of the cell. We also discuss how emerging technologies and multidisciplinary strategies enable us to gain insights into SAC signaling with an unprecedented level of detail.

## STRUCTURAL FEATURES OF SAC PROTEIN COMPONENTS

Important clues into the inner working of the SAC have been derived from the structural understanding of central SAC components. For instance, the three protein kinases Bub1, BubR1 and Mps1, which share a common multidomain organization and play roles that are essential for the SAC, contain an N-terminal

region that is organized as a tandem arrangement of the tetratrico peptide repeat (TPR) motif and a C-terminal kinase domain. In addition to Bub1, BubR1, and Mps1 kinases, the proteins Bub3, Mad1, Mad2, and Cdc20 also mediate key functions in SAC signaling. The crystal structure of Bub3 has shown that this protein is globular and contains a single domain (Larsen and Harrison, 2004; Wilson et al., 2005) that adopts the WD40-repeat fold. Despite its small size and presence of a single domain, Bub3 is known to physically interact with Bub1, BubR1, and Knl1. Another key molecule is Cdc20, a co-activator of the APC/C, the macromolecular assembly that is responsible for targeting proteins for ubiquitin-mediated degradation during mitosis (Nilsson et al., 2008; Izawa and Pines, 2012; Sedgwick et al., 2013), thus leading to the arrest of cells in mitosis (Musacchio and Salmon, 2007; Chao et al., 2012). Similar to Bub3, Cdc20 adopts the WD40-repeat fold (**Figures 1A,B**, respectively). However, in mammals Cdc20 also contains two independent degradation

signals: the KEN box (Pfleger and Kirschner, 2000) and the CRY box (Reis et al., 2006). The former box is required for the APC/C dependent degradation of Cdc20 (Huang et al., 2001) whereas the CRY box (consensus amino acid sequence CRYxPS) functions as a second degradation signal in Cdc20 (Reis et al., 2006).

Mad1 is a predominantly coiled-coil protein that in humans encompasses 718 amino acid residues (Hardwick and Murray, 1995; Schuyler et al., 2012). Depletion of Mad1 in human cells results in genome instability and chromosome segregation defects (Luo et al., 2000; Maciejowski et al., 2010; Meyer et al., 2013) thus evidencing its essential role in the SAC (Luo et al., 2002). Mad2 adopts the HORMA (for Hop1, Rev7, and Mad2) domain (Luo et al., 2000) (**Figure 1C**). Mad2 binds to Mad1 to form a stable heterocomplex *in vitro* (Luo et al., 2002) that regulates the progression of mitosis by controlling the flow of Cdc20 into the SAC. In one hand, the Mad2-Mad1 heterocomplex binds to improperly attached kinetochores, inducing the hyper-phosphorylation and activation of Mad1 by Mps1 (Winey and Huneycutt, 2002; Hewitt et al., 2010). On the other hand, kinetochore bound Mad1-Mad2 catalyzes the assembly of a Mad2-Cdc20 complex (**Figure 1D**) (Sironi et al., 2001, 2002; Chung and Chen, 2002; De Antoni et al., 2005; Nezi et al., 2006; Mapelli et al., 2007; Yang et al., 2008; Kulukian et al., 2009; Lad et al., 2009; Fava et al., 2011) in a process that involves the conversion of Mad2 from an “open” into a “closed” Cdc20-bound conformation (Luo et al., 2000, 2004). How the above interactions lead to conformational transitions that contribute to regulate the segregation of chromosomes in space and time? This fascinating aspect of the SAC is addressed in the section below.

## DYNAMICS OF MACROMOLECULAR ASSEMBLY/DISASSEMBLY

Earlier clues of the dynamic nature of the network of interactions underpinning SAC signaling were provided by the crystal and NMR structures of members of the Mad protein family. For instance, Sironi and collaborators reported the structure of a Mad1-Mad2 complex that revealed a loop around the Cdc20 binding site of Mad2 (**Figure 1D**) and suggested a “safety-belt” mechanism underlying the regulation of the interactions between Mad2-Mad1 and Mad2-Cdc20 (**Figure 1E**) (Sironi et al., 2002). Further structural details of Mad2 transitions between an “open” and a “closed” conformational state have been established by X-ray protein crystallography and NMR (Luo and Yu, 2008; Kim et al., 2010; Li et al., 2014). The 3D structures show that the transition of Mad2 from the “open” to the “closed” conformation involves a large conformational rearrangement of the polypeptide chain. This dramatic conformational switch is regarded as the rate-limiting step in cells mounting a SAC response (De Antoni et al., 2005; Vink et al., 2006; Hewitt et al., 2010; Maldonado and Kapoor, 2011; Lau and Murray, 2012).

SAC signaling is antagonized by the protein p31<sup>comet</sup> (Habu et al., 2002; Xia et al., 2004). The crystal structure of the closed conformation of Mad2 in complex with p31<sup>comet</sup> showed that the latter protein interacts extensively with the Mad2 dimerization interface in such a way it inhibits the conformational transition to the Mad2 open state (Yang et al., 2007). The binding of Mad3 (the yeast BubR1 homolog that lacks the catalytic kinase

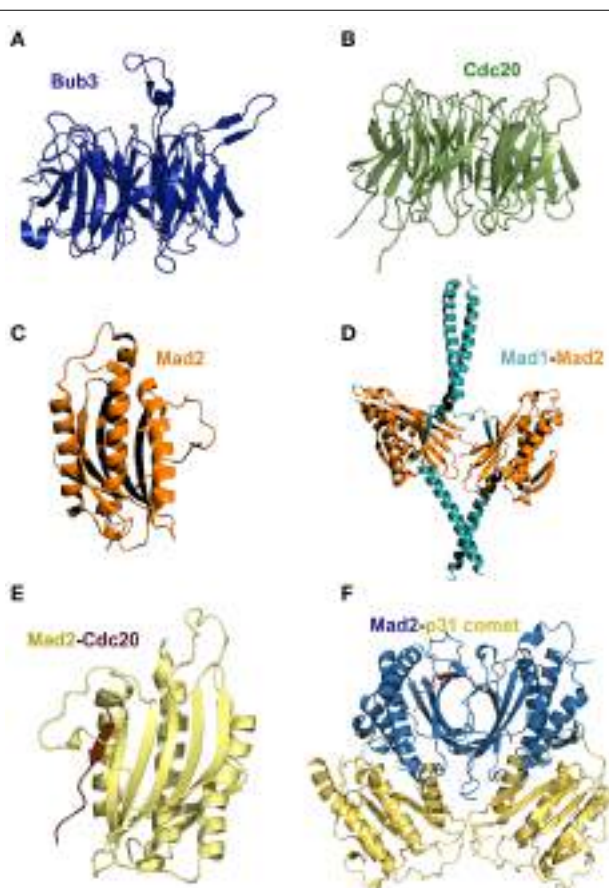


**FIGURE 1 | (A)** Bub3 and **(B)** Cdc20 both adopt a seven-blades, WD 40 fold (pdb 1UAC and 4GGA, respectively). **(C)** The architecture of Mad2 defines a characteristic HORMA domain (pdb 1DUJ). **(D)** The structure of the Mad1-Mad2 complex shows that the two chains of Mad1 interact with Mad2 through the N-terminal coiled-coil region (pdb 1GO4). **(E)** Structure of a Cdc20 fragment bound to Mad2 (pdb 1KLQ). **(F)** Crystal structure of the Mad2/p31<sup>comet</sup> complex (pdb 2QYF). A comparison of the latter two structures shows that p31<sup>comet</sup> inhibits Mad2 activation through structural mimicry. Figures generated with PyMOL (DeLano, 2002).

domain) and p31<sup>comet</sup> to the same Mad2 interface implies a competition between p31<sup>comet</sup> and Mad3 to bind Mad2 (**Figure 1E**). The structure of the p31<sup>comet</sup>-Mad2 complex (**Figure 1F**) thus provides structural insights into the regulation of MCC assembly and disassembly. Furthermore, the crystal structure of the mitotic checkpoint complex (MCC, **Figure 2A**) from fission yeasts revealed the mode in which Mad2 and Mad3 cooperate to inhibit Cdc20 (Chao et al., 2012). The MCC structure shows that Mad2 and Mad3 complex formation facilitates the presentation of the KEN box motif of Mad3 to the KEN-box motif of Cdc20 (**Figure 2A**). Interestingly, an unexpected D-box mimic located at the C-terminal end of Mad3 revealed the D-box-binding site on Cdc20, which provided the first structural insight into the mechanism of degron recognition by co-activators (an aspect of SAC signaling that has been nicely revised by Zhang et al., 2014). The structure of the MCC shows that APC/C ubiquitin ligase activity is modulated by steric hindrance that impedes substrate recognition and also through conformational changes that disrupt the architecture of the substrate-binding site. Such mode of regulation closely resembles the molecular mechanisms underlying the control of protein kinases (Chao et al., 2012). This mode of regulation is in sharp contrast with the mechanism of regulation of other signaling systems such as the SCF (SKP1-Cullin1-F-box-Rbx1) complex. In the latter case, the E3

ubiquitin ligase activity of SCF is regulated at the level of substrate recognition in a process that involves phosphorylation of a degradation signal (degron) consensus motif, IL-I/L/PpT-P, that is present on substrates targeted for proteasomal degradation (Welcker and Clurman, 2008; Zhou et al., 2013).

## SAC COMMUNICATION WITH THE KMN NETWORK

SAC function requires its communication with the kinetochore, the multiprotein complex that is assembled on mitotic or meiotic centromeres to connect centromeric DNA with microtubules (Funabiki and Wynne, 2013; Westhorpe and Straight, 2013). Although the assembly of the kinetochore is a crucial event in cell division, the precise sequence of events underlying the process remains obscure. As discussed below, recent structural insights show that the establishment of kinetochore complexes often involves dramatic conformational changes, including disorder-to-order transitions. Although the amino acid sequence in most kinetochore proteins is clearly divergent, the overall architecture of the kinetochore remains highly conserved across species (Przewloka and Glover, 2009; Tanaka, 2013; Westhorpe and Straight, 2013). The structural core of the kinetochore is the KMN network, which constitutes a docking platform for the kinetochore recruitment of SAC components. The KMN network is composed by the single protein Knl1 (a protein also known as CASC5, Blinkin, and AF15Q14 in humans; Spc105 in budding yeast and flies and Spc7 in fission yeast) (Kiyomitsu et al., 2007, 2011; Bolanos-Garcia et al., 2009) and the protein complexes Mis12/Mtw1/MIND and Ndc80/HEC1. The latter two assemblies are commonly referred to as the Mis12 and Ndc80 complexes.

Knl1 is a large, predominantly disordered protein of the KMN network that acts as molecular platform for the recruitment of several proteins to the kinetochore (Kiyomitsu et al., 2007; Przewloka and Glover, 2009; Santaguida and Musacchio, 2009; Ghongane et al., 2014). In mammals, depletion and/or suppression of the expression of Knl1 lead to extensive chromosome missegregation with phenotypes that closely resemble those caused by depletion of Bub1 and BubR1 kinases (Cheeseman et al., 2006, 2008; Kiyomitsu et al., 2007). Knl1 plays a central role in the dynamics of the assembly/disassembly of the KMN network and directly interacts with a range of proteins that are essential for proper chromosome segregation, including Protein phosphatase 1 (Pp1), Bub1, BubR1, Bub3, Zwint, and Nsl1, a component of the Mis12 complex. Such complex choreography of interactions confers exquisite regulation to the SAC. For example, the very N-terminal end region of Knl1 recruits Pp1 to the kinetochore; another N-terminal segment binds to the TPR motifs of Bub1 and BubR1 (**Figure 2B**) (Bolanos-Garcia et al., 2011; Rosenberg et al., 2011; Krenn et al., 2012; London et al., 2012; Sheppard et al., 2012; Funabiki and Wynne, 2013) whereas C-terminal Knl1 binds directly to Nsl1 (Primorac et al., 2013; Petrovic et al., 2014) and possibly also to Dsn1, another protein component of the Mis12 complex (Cheeseman et al., 2006; Kiyomitsu et al., 2007). The majority of Knl1 homologs contain an arrangement of motif repeat units, the MELT motif, that thus far seem to be a unique feature of this kinetochore docking platform. The specific amino acid sequence and the number of MELT repeat units is widely variable across species thus suggesting that the differences

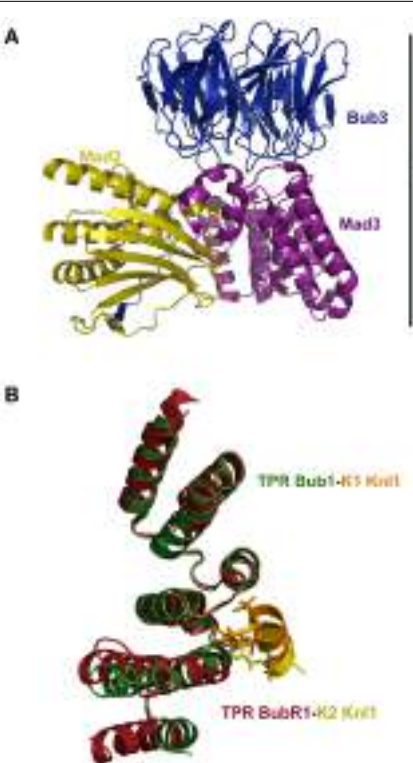


**FIGURE 2 | (A)** Crystal structure of the Mitotic Checkpoint Complex (MCC) from *Schizosaccharomyces pombe* (pdb 4AEZ). **(B)** The N-terminal regions of Bub1 and BubR1 are organized as a triple tandem of the TPR motif. Superposition of the structures of TPR Bub1 and TPR BubR1 in complex with the K1 motifs of Knl1 (pdb 4AIG and 3SI5, respectively) revealed a similar mode of binding underlying disorder-to-order transitions.

contribute to the species-specific recognition of different Knl1 partners. A comparison of the buried area upon complex formation between SAC proteins and between SAC-KMN components show a relatively small buried area, ranging from approx. 500 to 1700 Å<sup>2</sup> (**Table 1**), values that are similar to those calculated for non-obligate complexes (Jones and Thornton, 1996). It has been shown that the binding of Spc105, the fly homolog of Knl1, to Nnf1a, Nnf1b, Nsl1, and Mis12 is interdependent as the proteins need of each other for their recruitment to the kinetochore (Venkei et al., 2012). Although such feature suggests a cooperative mode of interaction between these proteins, it would be important to define more precisely the dynamics and stoichiometry of the interactions and to establish if a similar interdependence for their recruitment to the kinetochore occurs in other species.

### THE IMPORTANCE OF LOW STRUCTURAL COMPLEXITY IN THE SAC

The organization of a polypeptide chain in regions that exhibit low structural complexity is a recurrent feature of protein molecules (Dunker et al., 1998; Dyson and Wright, 2002, 2005; Gsponer and Babu, 2009; Babu et al., 2012). A bioinformatics study helps to illustrate this as it shows that 35–51% of eukaryotic proteins have at least one disordered region that span fifty or more amino acid residues (Dunker et al., 2002). The Protein Disorder Database DisProt (<http://www.disprot.org>; Sickmeier et al., 2007) provides additional support this view. Up to date (last release date 05/24/2013) the database has annotated 1539 disorder regions in a total of 694 proteins. Importantly, diverse bioinformatics studies have demonstrated that large polypeptide segments of low structural complexity are abundant in proteins that act as docking platforms for the binding of multiple partners (Dunker et al., 2005; Dosztanyi et al., 2006; Haynes et al., 2006; Kim et al., 2006a). The highly flexible surfaces of regions of low structural complexity can be critical for the formation of productive macromolecular complexes (Dyson and Wright, 2005; Kim et al., 2006a; Schlessinger et al., 2007; Dunker et al., 2008). Indeed,

it has been established that disordered binding regions play a critical role in diverse biological processes (Dyson and Wright, 2002) and that the association of individual proteins to form macromolecular assemblies can have a profound effect on the stability; transport properties; subcellular localization of the complexes and affect further interactions with additional molecules and/or assemblies (Sasahara et al., 2003; Banks and Fradin, 2005; McGuffee and Elcock, 2010; Wang et al., 2010, 2012; Cino et al., 2012; Miermont et al., 2013). In principle, large polypeptide segments of low structural complexity in hub proteins including Knl1 and other components of the KMN network can allow different conformers of the same polypeptide chain to bind with different affinity to interacting partners. An interesting suggestion is that interactions mediated by certain protein families involve the binding to specific linear motifs that capture key residues responsible for the interactions. Such linear motifs have been categorized and used to complement the prediction of binding sites in regions of low structural complexity with specific motif searches (Puntervoll et al., 2003). One interesting property of regions of low structural complexity is the transition from a disorder to a more ordered state upon ligand binding (a feature also known as coupled folding and binding). Examples of this class of transitions in SAC signaling occur upon binding of N-terminal Bub1 and BubR1 to KI motifs of Knl1; the interaction of Mad2 with Mad1 and Cdc20 and Bub3 binding to the MELT motifs of Knl1, to name a few. A more detailed discussion of the importance of this mode of binding in the SAC is show below, in the section entitled disorder-to-order transitions. Intrinsic disorder proteins seem prone to initiate promiscuous molecular interactions when over expressed and that for this reason they can contribute to toxicity/pathology (Vavouri et al., 2009). Interestingly, the structural properties of intrinsic disorder proteins seem to correlate strongly with the observed dosage sensitive (i.e., give place to a pathological condition when the expression is increased) of oncogenes, suggesting that mass action driven molecular interactions may be an important cause of cancer (Vavouri et al., 2009). Because dosage-sensitive genes seem to be slightly enriched in those mediating cell cycle regulation (Sopko et al., 2006), it would be important to define the dosage sensitive of genes associated with SAC signaling and its contribution (if any) to the onset of chromosome segregation defects and/or aneuploidy.

**Table 1 | Analysis of interface area in Å<sup>2</sup>, calculated as difference in total accessible surface areas of isolated and interfacing structures divided by two, according to ePISA (Protein Interfaces, Surfaces and Assemblies) tool (EMBL-EBI, UK).**

Protein complex	Protein-protein interface area (Å <sup>2</sup> )	PDB code	Reference
Bub1-GLEBS motif of Bub3	1664	2I3S	Larsen and Harrison, 2007
Mad3-GLEBS motif of Bub3	1681	2I3T	Larsen and Harrison, 2007
Bub1-Bub3 in ternary complex	1655	4BL0	Primorac et al., 2013
Bub3-MELT motif of Knl1 in ternary complex	654	4BL0	Primorac et al., 2013
Bub1-KI-1motif of Knl1	527	4A1G	Krenn et al., 2012
BubR1-KI-2 motif of Knl1	464	3S15	Bolanos-Garcia et al., 2011
Nsl1-RWD domain of Knl1	565	4NF9	Petrovic et al., 2014

### DNA COMPACTION AND CROWDING EFFECTS

As discussed by Burgess and collaborators in their excellent mini-review, the repair of DNA damage during mitosis is generally difficult due to the suppression of gene transcription and translation caused by the level of DNA compaction (Burgess et al., 2014). For example, little is known about the effect of centromeric DNA compaction on the assembly of the kinetochore. What is known is that DNA binding to the kinetochore does not depend on a specific DNA sequence (with a few exceptions) and that the deposition of Cenp-A-containing nucleosomes at the centromeric chromatin is likely to rely on epigenetic mechanisms. However, definition in greater detail of the extent in which centromere identity is specified by epigenetic mechanisms remains a central question in the study of chromosome inheritance and genome stability.

It has been established that a constitutive complex, the centromere-associated network (CCAN), is assembled onto centromeric Cenp-A chromatin. The CCAN consists of 16 proteins: Cenp-C, Cenp-H/Cenp-I/Cenp-K, Cenp-L/Cenp-M/Cenp-N, Cenp-O/Cenp-P/Cenp-Q/Cenp-R/Cenp-U, Cenp-T/Cenp-W, and Cenp-S/Cenp-X (revised by Perpelescu and Fukagawa, 2011). CCAN recruits the outer kinetochore components of the KMN network Kn1, the Mis12 complex, and the Ndc80 complex thus linking structural and regulatory kinetochore proteins which spindle microtubules. Cenp-A, a conserved centromere-specific variant of the protein histone H3 (Palmer et al., 1991; Stoler et al., 1995; Perpelescu and Fukagawa, 2011), plays a role in the propagation of centromere identity and the formation of the kinetochore (Barnhart et al., 2011; Mendiburo et al., 2011; Fachinetti et al., 2013). This manner, the centromere-kinetochore assembly guides the movement of chromosomes and the progression of the cell cycle throughout mitosis (Wan et al., 2009). Cenp-C and Cenp-T, two components of the CCAN, are required for spindle attachment. Structural insights of the human centromeric nucleosome containing Cenp-A in complex with its cognate  $\alpha$ -satellite DNA derivative revealed that in the human Cenp-A nucleosome, the DNA wraps around a histone octamer comprising two molecules of histones H2A, H2B, H4, and Cenp-A (Tachiwana et al., 2011). The crystal structure of the Cenp-A nucleosome (pdb ID 3AN2) supports the octasome model (Figure 3A). However, the existence of a Cenp-A nucleosome complex comprising one of each core histone (a complex referred to as the hemisome) has been suggested (Tachiwana et al., 2011). The two different complexes may not be mutually exclusive as there is a possibility both the octasome and the hemisome can be assembled *in vivo*. This is an aspect that should be clarified if we are to understand the precise role of Cenp-A in the control of chromatin assembly and its influence in the formation of the kinetochore.

Interestingly, among all the protein that are known to associate constitutively with human Cenp-A chromatin, only Cenp-C has been identified in all model organisms (Stoler et al., 1995). Human Cenp-C consists of four functional regions (Figure 3B). The N-terminal region binds to the Mis12 complex (Barnhart et al., 2011). The central region of Cenp-C is required for the targeting of the protein to the centromere (Fachinetti et al., 2013) in a process that involves the recognition of the carboxyl tail of Cenp-A in the centromeric nucleosome (Mendiburo et al., 2011). The C-terminal region of Cenp-C is responsible for homo dimerization of the protein (Hori et al., 2013). The specific recognition of the histone variant Cenp-A in the centromeric nucleosome by Cenp-C is critical for the assembly of the kinetochore. The crystal structure of Cenp-C in complex with the nucleosome core particle (pdb 4INM) has revealed the determinants of the recognition mechanism. The structure shows that Cenp-C binds a hydrophobic region in the Cenp-A tail and docks onto the acidic patch of histone H2A/H2B. The Cenp-C-nucleosome core particle complex thus revealed a conserved mechanism for recruitment of proteins to centromeres. It also provides insights into the molecular mechanism of histone recognition in which a disordered peptide binds the histone tail. Such mode of nucleosome docking is facilitated by extensive hydrophobic interactions, a structural feature also observed in diverse SAC and kinetochore

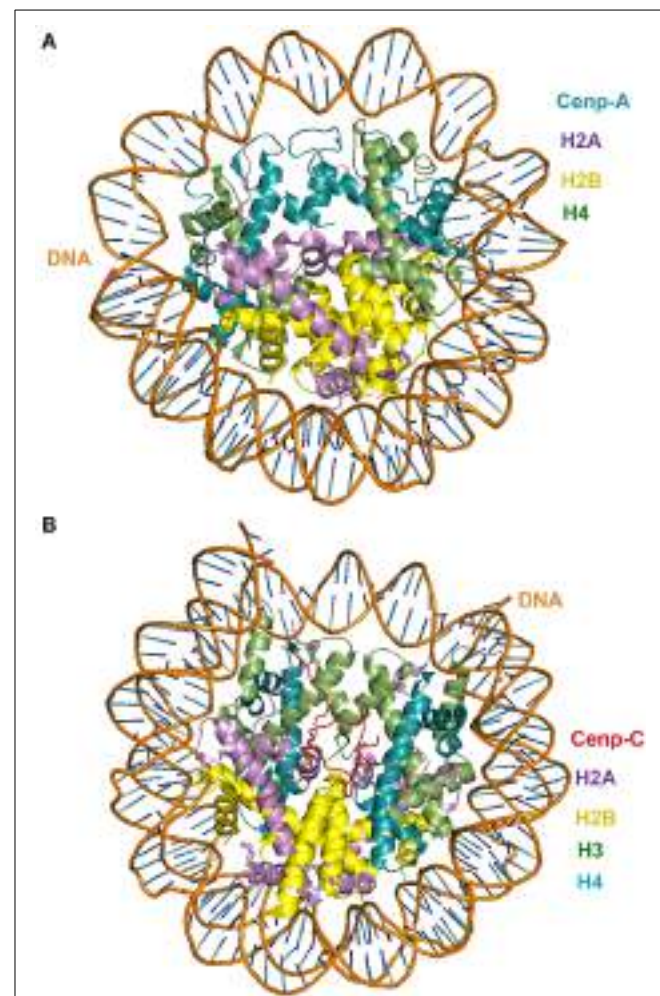


**FIGURE 3 | (A)** Crystal structure of Cenp-A in complex with centromeric nucleosome; **(B)** crystal structure of Cenp-C in complex with centromeric nucleosome. In both cases the view is in the axis of the DNA supercoil.

assemblies that involve disorder-to-order transitions, an aspect that is discussed in more detail in the next section.

Cenp-E is a member of the Cenp protein family (Perpelescu and Fukagawa, 2011; Przewloka et al., 2011) that, similar to Cenp-C and Kn1, contains large segments of low structural complexity throughout the polypeptide chain. Cenp-E functions as a plus-end directed molecular kinesin-like motor protein that is localized specifically to kinetochores during mitosis and that is required for efficient capture and attachment of kinetochores to the spindle microtubules (McEwen et al., 2001; Putkey et al., 2002; Kapoor et al., 2006). In human cells, Cenp-E depletion by RNA interference (Tanudji et al., 2004) or antisense oligonucleotides (Yao et al., 2000) and inhibition of its recruitment to kinetochores by antibody microinjection (Schaar et al., 1997; McEwen et al., 2001) result in chromosome congression aberrations. The intrinsic structural flexibility of Kn1, Cenp-C, Cenp-E and other kinetochore proteins should facilitate the establishment of productive and specific interactions with diverse interacting partners (Mao et al., 2003). In a broader sense, the recurrence of regions

of low structural complexity in SAC and KMN protein components is likely to play a critical roles in the control of chromosome segregation none less because greater selectivity can be achieved through interactions that involve multiple components.

Macromolecular crowding refers to the confinement in the cellular space of macromolecules at high concentration (Elcock, 2010; Hancock, 2012). Studies carried out in mice showed that abnormal higher Mad2 levels lead to aberrant SAC function and induced tumorigenesis (Sotillo et al., 2007, 2010; Schwartzman et al., 2011). It would be important to establish to what extent Mad2 crowding contributes to the above-mentioned abnormal processes.

Some proteins can process distinct molecular signals under the crowding conditions of the cell. An example of this phenomenon is transport kinesins (such as kinesin-1), which seems to have evolved molecular properties that prevent it from forming traffic jams in the crowded conditions of the cells (Leduc et al., 2012) and the kinesin motor protein kinase ERK, which can be phosphorylated in a processive manner in HeLa cells (Aoki et al., 2011). Interestingly, under conditions that recreate physiological molecular crowding, the mode of ERK phosphorylation shifts from distributive to processive (Aoki et al., 2011), in which case ERK does not form a stable substrate-enzyme complex, a behavior that is the opposite to that observed in the processive phosphorylation model. It would be important to establish if phosphorylation shifts from distributive to processive or vice versa occurs in components of the KMN network such as Knl1, Cenp-C, and Cenp-E.

## DISORDER-TO-ORDER TRANSITIONS

Comparison of the structures of diverse SAC and kinetochore complexes reveals a recurrent mode of binding that is characterized by disorder-to-order transitions. Examples of this class of transitions occur in the interaction of Mad2 with Mad1 and Cdc20; the binding of TPR domains of Bub1 and BubR1 to KI motifs of Knl1 (Figure 2B); the binding of Bub3 to the MELT motifs of Knl1 (Figure 4A) and the binding of the RWD domain of Knl1 to a synthetic peptide that mimics Nsl1 (Figure 4B) (Bolanos-Garcia et al., 2011; Kiyomitsu et al., 2011; Krenn et al., 2012; Primorac et al., 2013; Petrovic et al., 2014; revised in Ghongane et al., 2014). In all these complexes the binding of an otherwise predominantly disordered protein fragment to the globular partner involves dramatic conformational transitions that lead to the formation of an  $\alpha$ -helix upon complex formation. The predominance of cooperative, stabilizing hydrophobic interactions is another structural feature that emerges from the analysis of the aforementioned complexes, where only little conformational changes are observed in the BUBs after complex formation.

The interaction of SAC kinases Bub1 and BubR1 with the protein Knl1 physically links SAC signaling with the kinetochore (Kiyomitsu et al., 2007, 2011; Bolanos-Garcia et al., 2011). The crystal structure of N-terminal Knl1 with TPR BubR1 defines an extensive hydrophobic interface in which a mechanistic zipper mode of binding has been suggested. In this model, several Knl1 residues (I213, F215, F218, and I219) sequentially dock into BubR1 pockets, thus ensuring high specificity and sensitive

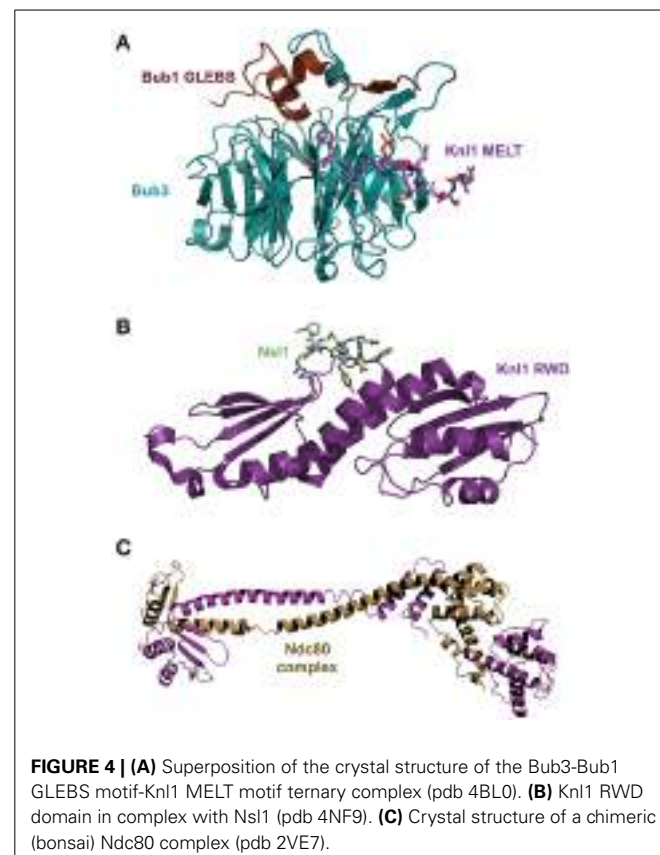


**FIGURE 4 | (A)** Superposition of the crystal structure of the Bub3-Bub1 GLEBS motif-Knl1 MELT motif ternary complex (Pdb 4BL0). **(B)** Knl1 RWD domain in complex with Nsl1 (Pdb 4NF9). **(C)** Crystal structure of a chimeric (bonsai) Ndc80 complex (Pdb 2VE7).

regulation. Furthermore, comparison of the crystal structure of the TPR BubR1-Knl1 binary complex with free Knl1 peptides titrations using 2,2,2-trifluoroethanol and monitored by far-UV circular dichroism revealed a disorder-to-order transition of N-terminal Knl1 upon binding BubR1. This is possible because a hydrophobic environment can be mimic experimentally with 2,2,2-trifluoroethanol, a solvent of low dielectric constant,  $\epsilon$ , ( $\epsilon = 8.55$ ). The observed disorder-to-order transition of N-terminal Knl1 when binding to BubR1 can be expected for the interaction of Knl1 with Bub1, given the similar mode of binding (Figure 2B). Importantly, the local conformational changes triggered by disorder-to-order transitions upon BUBs binding should influence the interaction of Knl1 with other interacting partners such as specific kinases and/or phosphatases thus contributing to the regulation of the SAC (Liu et al., 2010; Rosenberg et al., 2011).

Bub1 and BubR1 (Mad3 in yeast) have a conserved stretch of about 40 amino acid residues downstream the N-terminal TPR domain that is predicted to be of low structural complexity and that harbor a Bub3 binding region commonly referred to as the GLE2p-binding sequence (GLEBS) motif. The crystal structures of two independent complexes formed between the GLEBS motifs of Mad3 and yeast Bub1 with Bub3 show the establishment of an extensive interface along the top surface of Bub3 upon complex formation (Larsen and Harrison, 2007) (Figure 4A). Such mode of binding implies a large conformational shift of the GLEBS motifs from a disorder to an ordered state. In a similar

fashion, the crystal structure of a Mad1 fragment (residues 485–584) in complex with Mad2 revealed that the Mad1 fragment adopts a predominantly  $\alpha$ -helix conformation upon complex formation (Luo et al., 2000) (**Figure 1D**). Furthermore, binding studies *in vitro* suggest an important conformational transition in which Mad1 primes the Mad2 binding site for the interaction with Cdc20 (Luo et al., 2002). *In vivo*, such concerted conformational rearrangements should ensure the tight regulation of the APC/C's ubiquitin-ligase activity (Tang et al., 2001; Jia et al., 2013).

### SAC-KMN SIGNAL AMPLIFICATION BY THE MEANS OF WEAK, COOPERATIVE INTERACTIONS

Because multiprotein complexes that form cooperatively would less likely to be formed fortuitously (Blundell et al., 2002; Bolanos-Garcia et al., 2012), the cooperative association of higher order SAC signaling complexes resulting from binary interactions that are both specific and of low-affinity should favor the amplification of specific signals to mount an effective SAC response. The cooperative assembly of the KMN subcomplexes Mis12 and Ndc80 illustrates how the establishment of higher order signaling complexes can regulate the SAC. The Ndc80 subcomplex is composed of four subunits: Ndc80 (the subunit that gives its name to the entire subcomplex), Nuf2, Spc24, and Spc25 (Ciferri et al., 2005, 2008; Wei et al., 2005, 2007; Wan et al., 2009). The Ndc80 subcomplex adopts a dumbbell shape molecule with Spc24-Spc25 and Nuf2-Ndc80 located in opposite ends of the molecule (**Figure 4C**) (Ciferri et al., 2005; Wei et al., 2005). The association of Nuf2-Ndc80 is required for the binding of the Ndc80 complex to microtubules while the formation of the Spc24-Spc25 heterodimer is required for binding Knl1 and the Mis12 complex (Cheeseman et al., 2006; Kiyomitsu et al., 2007; Wei et al., 2007; Ciferri et al., 2008; Joglekar and DeLuca, 2009; Wan et al., 2009).

The exquisite regulation of the SAC is a fine example of how the remodeling of macromolecular assemblies in time and space has evolved as a successful strategy that increases selectivity of signals with a minimal margin for errors. At the same time, the highly versatile and dynamic remodeling of macromolecular assemblies constitutes a great challenge for their functional, biochemical and structural characterisation in space and time. Furthermore, a wide range of post-translational modifications such as acetylation, phosphorylation, ubiquitylation and sumoylation can have a significant impact on protein stability, turnover, reversibility, sub-cellular localisation and the hierarchical order of assembly/disassembly of protein complexes thus constituting and additional layer of control of cell signaling (Pawson and Nash, 2003; Kim et al., 2006b; Seet et al., 2006; Simorellis and Flynn, 2006; Mao et al., 2011; Wan et al., 2012; Jia et al., 2013).

### NEW APPROACHES TO THE STUDY OF SAC MACROMOLECULAR ASSEMBLIES

Our discussion of the interactions underpinning SAC signaling is typical of many cell regulation systems, where a large number of macromolecules tend to associate, thus requiring the ability to describe the dynamics of transient complex formation and

dissociation in both space and time. One strategy to achieve this is to combine a range of biophysical and biochemical methods with spatial techniques for structural biology. For example, time-resolved Raman scattering and X-ray scattering can be very powerful to study the dynamics of macromolecular interactions when they are combined with X-ray protein crystallography, Nuclear Magnetic Resonance (NMR), Small Angle X-ray Scattering (SAXS), and Electron Microscopy (EM). A useful approach to the study of the dynamic of macromolecular complexes underpinning the SAC-kinetochore-microtubule interactome is the stabilization and fixation of the complexes which can be achieved by incorporation of phospho-mimicking mutations; truncation or extension of the polypeptide chain; the addition of post-translational modifications, such as phosphorylation, acetylation, methylation and the use of crosslinking agents, to name just a few. The stabilization and fixation of complexes can be combined with Förster resonance energy transfer (FRET) to define temporal aspects of the interactions but also local conformational changes associated with SAC signaling. Importantly, exiting new experimental strategies for the study of dynamic systems are currently in fast development. For example, free-electron lasers (FEL) a technique that relies on the generation of X-ray pulses of very high intensity and short duration, has facilitated the structural determination of macromolecular complexes even from very small crystals of relatively low quality. The ultrashort X-ray flashes ensure that the molecules hardly change during the exposure and enable the study of functional processes through the monitoring of the motion of molecules from instant to instant. This is particularly attractive to the study of the interactions underpinning the SAC where is important to closely follow the dynamics of the association and dissociation of macromolecular assemblies. Current free-electron lasers facilities are the European X-ray free-electron laser, the Linac Coherent Light Source (LCLS) at the SLAC National Accelerator Laboratory, the Free electron LASer in Hamburg (FLASH), the SPring-8 Compact SASE Source (SCSS), and the PSI SwissFEL. Another exciting new development is transmission electron microscopy (TEM). A TEM variant that uses cryo-technology (Cryo-TEM) permits a full range of semi-automated applications, including 2D electron crystallography, single particle analysis, cryo electron microscopy, and dual-axis cellular tomography of frozen hydrated cell organelles and cells. Cryo-TEM, when combined with protein X-ray crystallography, NMR and molecular modeling studies, facilitates the generation of complete atomic models. Additional advantages of cryo-TEM are: (1) it is suitable to study complexes that are 250 kDa or larger; (2) it can be applied to the study of heterogeneous samples and (3) it can provide structural details of dynamic complexes, such as those defining the architectures of the kinetochore and the nucleosome, that are difficult to examine with other structural biology techniques.

A major challenge will be to extend the analysis of structure and dynamics of isolated SAC and kinetochore assemblies to the understanding of the organization of signal generation and amplification in the cell in space and time. Because large multi-protein complexes play critical roles in cell regulation, interfering with the dynamics of their assembly and/or dissociation rises as an attractive strategy for the treatment of diseases.

## CLOSING REMARKS

The function and regulation of the SAC depends upon a hierarchical organization of macromolecular assemblies in time and space to ensure the accurate and timely transmission of the genetic material to descendants. A common theme emerging from the structural analysis of SAC complexes is the adoption of a regular structure by one of the interaction partners upon complex formation.

SAC components that are intrinsically disordered in the unbound form often associate to binding partners with low affinity but high specificity thus mounting an effective SAC response. Interaction with one or more ligands through multiple linear motifs is an effective strategy to control the flow of information and to modulate the signal. Therefore, the greater selectivity that communication of the SAC with the KMN network demands is gained by the involvement of multiple components that assemble in a cooperative fashion. Undoubtedly, the structural characterisation of larger SAC protein assemblies will reveal novel molecular details of how signal amplification is achieved to control chromosome segregation in higher organisms.

Therefore, the timely assembly of protein subcomplexes in which at least one of the components shows low structural complexity appears a reiterate structural feature in SAC signalling.

Importantly, regulation of this critical cellular process relies on the establishment of transient interactions in space and time. This manner, multi-protein assemblies can associate cooperatively to confer high selectivity and sensitivity to the interactions.

Undoubtedly, the detailed knowledge of the architecture of large SAC and kinetochore complexes will provide the structural basis for the rational targeting of specific protein-protein interfaces with drugs, being these small size molecules, peptides, nucleic acids or carbohydrates.

## REFERENCES

- Abrieu, A., Magnaghi-Jaulin, L., Kahana, J. A., Peter, M., Castro, A., Vigneron, S., et al. (2001). Mps1 is a kinetochore-associated kinase essential for the vertebrate mitotic checkpoint. *Cell* 106, 83–93. doi: 10.1016/S0092-8674(01)00410-X
- Aoki, K., Yamada, M., Kunida, K., Yasuda, S., and Matsuda, M. (2011). Processive phosphorylation of ERK MAP kinase in mammalian cells. *Proc. Natl. Acad. Sci. U.S.A.* 108, 12675–12680. doi: 10.1073/pnas.1104030108
- Babu, M. M., Kriwacki, R. W., and Pappu, R. V. (2012). Structural biology. Versatility from protein disorder. *Science* 337, 1460–1461. doi: 10.1126/science.1228775
- Banks, D. S., and Fradin, C. (2005). Anomalous diffusion of proteins due to molecular crowding. *Biophys. J.* 89, 2960–2971. doi: 10.1529/biophysj.104.051078
- Barnhart, M. C., Kuich, P. H., Stellfox, M. E., Ward, J. A., Bassett, E. A., Black, B. E., et al. (2011). HJURP is a CENP-A chromatin assembly factor sufficient to form a functional de novo kinetochore. *J. Cell Biol.* 194, 229–243. doi: 10.1083/jcb.201012017
- Blundell, T. L., Bolanos-Garcia, V., Chirgadze, D. Y., Harmer, N. J., Lo, T., Pellegrini, L., et al. (2002). Asymmetry in the multiprotein systems of molecular biology. *Struct. Chem.* 13, 405–412. doi: 10.1023/A:1015888617329
- Bolanos-Garcia, V. M., and Blundell, T. L. (2011). BUB1 and BUBR1: multifaceted kinases of the cell cycle. *Trends Biochem. Sci.* 36, 141–150. doi: 10.1016/j.tibs.2010.08.004
- Bolanos-Garcia, V. M., Kiyomitsu, T., D'Arcy, S., Chirgadze, D. Y., Grossmann, J. G., Matak-Vinkovic, D., et al. (2009). The crystal structure of the N-terminal region of BUB1 provides insight into the mechanism of BUB1 recruitment to kinetochores. *Structure* 17, 105–116. doi: 10.1016/j.str.2008.10.015
- Bolanos-Garcia, V. M., Lischetti, T., Matak-Vinkovic, D., Cota, E., Simpson, P. J., Chirgadze, D. Y., et al. (2011). Structure of a Blinkin-BUBR1 complex reveals an interaction crucial for kinetochore-mitotic checkpoint regulation via an unanticipated binding site. *Structure* 19, 1691–1700. doi: 10.1016/j.str.2011.09.017
- Bolanos-Garcia, V. M., Wu, Q., Ochi, T., Chirgadze, D. Y., Sibanda, B. L., and Blundell, T. L. (2012). Spatial and temporal organisation of multiprotein assemblies: achieving sensitive control in information-rich cell regulatory systems. *Philos. Transact. A Math. Phys. Eng. Sci.* 370, 3023–3039. doi: 10.1098/rsta.2011.0268
- Boyarchuk, Y., Salic, A., Dasso, M., and Arnaoutov, A. (2007). Bub1 is essential for assembly of the functional inner centromere. *J. Cell Biol.* 176, 919–928. doi: 10.1083/jcb.200609044
- Burgess, A., Rasouli, M., and Rogers, S. (2014). Stressing mitosis to death. *Front. Oncol.* 4:140. doi: 10.3389/fonc.2014.00140
- Carter, S. L., Eklund, A. C., Kohane, I. S., Harris, L. N., and Szallasi, Z. (2006). A signature of chromosomal instability inferred from gene expression profiles predicts clinical outcome in multiple human cancers. *Nat. Genet.* 38, 1043–1048. doi: 10.1038/ng1861
- Chao, W. C., Kulkarni, K., Zhang, Z., Kong, E. H., and Barford, D. (2012). Structure of the mitotic checkpoint complex. *Nature* 484, 208–213. doi: 10.1038/nature10896
- Cheeseman, I. M., Chappie, J. S., Wilson-Kubalek, E. M., and Desai, A. (2006). The conserved KMN network constitutes the core microtubule-binding site of the kinetochore. *Cell* 127, 983–997. doi: 10.1016/j.cell.2006.09.039
- Cheeseman, I. M., Hori, T., Fukagawa, T., and Desai, A. (2008). KNL1 and the CENP-H/I/K complex coordinately direct kinetochore assembly in vertebrates. *Mol. Biol. Cell* 19, 587–594. doi: 10.1091/mbc.E07-10-1051
- Chung, E., and Chen, R. H. (2002). Spindle checkpoint requires Mad1-bound and Mad1-free Mad2. *Mol. Biol. Cell* 13, 1501–1511. doi: 10.1091/mbc.02-01-0003
- Ciferri, C., De Luca, J., Monzani, S., Ferrari, K. J., Ristic, D., Wyman, C., et al. (2005). Architecture of the human Ndc80-Hec1 complex, a critical constituent of the outer kinetochore. *J. Biol. Chem.* 280, 29088–29095. doi: 10.1074/jbc.M504070200
- Ciferri, C., Pasqualato, S., Scrpanti, E., Varetti, G., Santaguida, S., Dos Reis, G., et al. (2008). Implications for kinetochore-microtubule attachment from the structure of an engineered Ndc80 complex. *Cell* 133, 427–439. doi: 10.1016/j.cell.2008.03.020
- Cino, E. A., Karttunen, M., and Choy, W.-Y. (2012). Effects of molecular crowding on the dynamics of intrinsically disordered proteins. *PLoS ONE* 7:e49876. doi: 10.1371/journal.pone.0049876
- De Antoni, A., Pearson, C. G., Cimini, D., Canman, J. C., Sala, V., Nezi, L., et al. (2005). The Mad1/Mad2 complex as a template for Mad2 activation in the spindle assembly checkpoint. *Curr. Biol.* 15, 214–225. doi: 10.1016/j.cub.2005.01.038
- DeLano, W. L. (2002). *The PyMOL Molecular Graphics System*. San Carlos, CA: DeLano Scientific.
- Dosztanyi, Z., Chen, J., Dunker, A. K., Simon, I., and Tompa, P. (2006). Disorder and sequence repeats in hub proteins and their implications for network evolution. *J. Proteome Res.* 5, 2985–2995. doi: 10.1021/pr0601710
- Dunker, A. K., Brown, C. J., Lawson, J. D., Iakoucheva, L. M., and Obradović, Z. (2002). Intrinsic disorder and protein function. *Biochemistry* 41, 6573–6582. doi: 10.1021/bi012159+
- Dunker, A. K., Cortese, M. S., Romero, P., Iakoucheva, L. M., and Uversky, V. N. (2005). Flexible nets: the roles of intrinsic disorder in protein interaction networks. *FEBS J.* 272, 5129–5148. doi: 10.1111/j.1742-4658.2005.04948.x
- Dunker, A. K., Garner, E., Guillot, S., Romero, P., Albrecht, K., Hart, J., et al. (1998). Protein disorder and the evolution of molecular recognition: theory, predictions and observations. *Pac. Symp. Biocomput.* 473–484.
- Dunker, A. K., Oldfield, C. J., Meng, J., Romero, P., Yang, J. Y., Chen, J. W., et al. (2008). The unfoldomics decade: an update on intrinsically disordered proteins. *BMC Genomics* 9:S1. doi: 10.1186/1471-2164-9-S2-S1
- Dyson, H. J., and Wright, P. E. (2002). Coupling of folding and binding for unstructured proteins. *Curr. Opin. Struct. Biol.* 12, 54–60. doi: 10.1016/S0959-440X(02)00289-0
- Dyson, H. J., and Wright, P. E. (2005). Intrinsically unstructured proteins and their functions. *Nat. Rev. Mol. Cell Biol.* 6, 197–208. doi: 10.1038/nrm1589
- Elcock, A. H. (2010). Models of macromolecular crowding effects and the need for quantitative comparisons with experiment. *Curr. Opin. Struct. Biol.* 20, 196–206. doi: 10.1016/j.sbi.2010.01.008

- Elowe, S. (2011). Bub1 and BubR1: at the interface between chromosome attachment and the spindle checkpoint. *Mol. Cell. Biol.* 31, 3085–3093. doi: 10.1128/MCB.05326-11
- Fachinetti, D., Folco, H. D., Nechemia-Arbely, Y., Valente, L. P., Nguyen, K., Wong, A. J., et al. (2013). A two-step mechanism for epigenetic specification of centromere identity and function. *Nat. Cell Biol.* 15, 1056–1066. doi: 10.1038/ncb2805
- Fava, L. L., Kaulich, M., Nigg, E. A., and Santamaría, A. (2011). Probing the *in vivo* function of Mad1:C-Mad2 in the spindle assembly checkpoint. *EMBO J.* 30, 3322–3336. doi: 10.1038/emboj.2011.239
- Foley, E. A., and Kapoor, T. M. (2013). Microtubule attachment and spindle assembly checkpoint signalling at the kinetochore. *Nat. Rev. Mol. Cell Biol.* 14, 25–37. doi: 10.1038/nrm3494
- Funabiki, H., and Wynne, D. J. (2013). Making an effective switch at the kinetochore by phosphorylation and dephosphorylation. *Chromosoma* 122, 135–158. doi: 10.1007/s00412-013-0401-5
- Ghongane, P., Kapanidou, M., Asghar, A., Elowe, S., and Bolanos-Garcia, V. M. (2014). The dynamic protein KNL1: a kinetochore rendezvous. *J. Cell Sci.* 127, 3415–3423. doi: 10.1242/jcs.149922
- Gsponer, J., and Babu, M. M. (2009). The rules of disorder or why disorder rules. *Prog. Biophys. Mol. Biol.* 99, 94–103. doi: 10.1016/j.pbiomolbio.2009.03.001
- Habu, T., Kim, S. H., Weinstein, J., and Matsumoto, T. (2002). Identification of a MAD2-binding protein, CMT2, and its role in mitosis. *EMBO J.* 21, 6419–6428. doi: 10.1093/emboj/cdf659
- Hancock, R. (2012). Structure of metaphase chromosomes: a role for effects of macromolecular crowding. *PLoS ONE* 7:e36045. doi: 10.1371/journal.pone.0036045
- Hardwick, K. G., Johnston, R. C., Smith, D. L., and Murray, A. W. (2000). MAD3 encodes a novel component of the spindle checkpoint which interacts with Bub3p, CDC20p, and MAD2p. *J. Cell Biol.* 148, 871–882. doi: 10.1083/jcb.148.5.871
- Hardwick, K. G., and Murray, A. W. (1995). Mad1p, a phosphoprotein component of the spindle assembly checkpoint in budding yeast. *J. Cell Biol.* 131, 709–720. doi: 10.1083/jcb.131.3.709
- Hauf, S. (2013). The spindle assembly checkpoint: progress and persistent puzzles. *Biochem. Soc. Trans.* 41, 1755–1760. doi: 10.1042/BST20130240
- Haynes, C., Oldfield, C. J., Ji, F., Klitgord, N., Cusick, M. E., Radivojac, P., et al. (2006). Intrinsic disorder is a common feature of hub proteins from four eukaryotic interactomes. *PLoS Comput. Biol.* 2:e100. doi: 10.1371/journal.pcbi.0020100
- Hewitt, L., Tighe, A., Santaguida, S., White, A. M., Jones, C. D., Musacchio, A., et al. (2010). Sustained Mps1 activity is required in mitosis to recruit O-Mad2 to the Mad1-C-Mad2 core complex. *J. Cell Biol.* 190, 25–34. doi: 10.1083/jcb.201002133
- Hori, T., Shang, W. H., Takeuchi, K., and Fukagawa, T. (2013). The CCAN recruits CENP-A to the centromere and forms the structural core for kinetochore assembly. *J. Cell Biol.* 200, 45–60. doi: 10.1083/jcb.201210106
- Huang, J. N., Park, I., Ellington, E., Littlepage, L. E., and Pellman, D. (2001). Activity of the APC(Cdh1) form of the anaphase-promoting complex persists until S phase and prevents the premature expression of Cdc20p. *J. Cell Biol.* 154, 85–94. doi: 10.1083/jcb.200102007
- Izawa, D., and Pines, J. (2012). Mad2 and the APC/C compete for the same site on Cdc20 to ensure proper chromosome segregation. *J. Cell Biol.* 199, 27–37. doi: 10.1083/jcb.201205170
- Janssen, A., Kops, G. J., and Medema, R. H. (2009). Elevating the frequency of chromosome missegregation as a strategy to kill tumor cells. *Proc. Natl. Acad. Sci. U. S. A.* 106, 19108–19113. doi: 10.1073/pnas.0904343106
- Jia, L., Kim, S., and Yu, H. (2013). Tracking spindle checkpoint signals from kinetochores to APC/C. *Trends Biochem. Sci.* 38, 302–311. doi: 10.1016/j.tibs.2013.03.004
- Joglekar, A. P., and DeLuca, J. G. (2009). Chromosome segregation: Ndc80 can carry the load. *Curr. Biol.* 19, R404–R407. doi: 10.1016/j.cub.2009.04.014
- Jones, S., and Thornton, J. M. (1996). Principles of protein-protein interactions. *Proc. Natl. Acad. Sci. U.S.A.* 93, 13–20. doi: 10.1073/pnas.93.1.13
- Kapoor, T. M., Lampson, M. A., Hergert, P., Cameron, L., Cimini, D., Salmon, E. D., et al. (2006). Chromosomes can congress to the metaphase plate before biorientation. *Science* 311, 388–391. doi: 10.1126/science.1122142
- Kim, P. M., Lu, L. J., Xia, Y., and Gerstein, M. B. (2006a). Relating three-dimensional structures to protein networks provides evolutionary insights. *Science* 314, 1938–1941. doi: 10.1126/science.1136174
- Kim, S., Sun, H., Ball, H. L., Wassmann, K., Luo, X., and Yu, H. (2010). Phosphorylation of the spindle checkpoint protein Mad2 regulates its conformational transition. *Proc. Natl. Acad. Sci. U.S.A.* 107, 19772–19777. doi: 10.1073/pnas.100900107
- Kim, S. C., Sprung, R., Chen, Y., Xu, Y., Ball, H., Pei, J., et al. (2006b). Substrate and functional diversity of lysine acetylation revealed by a proteomics survey. *Mol. Cell* 23, 607–618. doi: 10.1016/j.molcel.2006.06.026
- Kiyomitsu, T., Murakami, H., and Yanagida, M. (2011). Protein interaction domain mapping of human kinetochore protein Blinkin reveals a consensus motif for binding of spindle assembly checkpoint proteins Bub1 and BubR1. *Mol. Cell. Biol.* 31, 998–1011. doi: 10.1128/MCB.00815-10
- Kiyomitsu, T., Obuse, C., and Yanagida, M. (2007). Human Blinkin/AF15q14 is required for chromosome alignment and the mitotic checkpoint through direct interaction with Bub1 and BubR1. *Dev. Cell* 13, 663–676. doi: 10.1016/j.devcel.2007.09.005
- Krenn, V., Wehenkel, A., Li, X., Santaguida, S., and Musacchio, A. (2012). Structural analysis reveals features of the spindle checkpoint kinase Bub1-kinetochore subunit Kn1 interaction. *J. Cell Biol.* 196, 451–467. doi: 10.1083/jcb.201110013
- Kulukian, A., Han, J. S., and Cleveland, D. W. (2009). Unattached kinetochores catalyze production of an anaphase inhibitor that requires a Mad2 template to prime Cdc20 for BubR1 binding. *Dev. Cell* 16, 105–117. doi: 10.1016/j.devcel.2008.11.005
- Lad, L., Lichtsteiner, S., Hartman, J. J., Wood, K. W., and Sakowicz, R. (2009). Kinetic analysis of Mad2-Cdc20 formation: conformational changes in Mad2 are catalyzed by a C-Mad2-ligand complex. *Biochemistry* 48, 9503–9515. doi: 10.1021/bi900718e
- Larsen, N. A., and Harrison, S. C. (2004). Crystal structure of the spindle assembly checkpoint protein Bub3. *J. Mol. Biol.* 344, 885–892. doi: 10.1016/j.jmb.2004.09.094
- Larsen, N. A., and Harrison, S. C. (2007). Structural analysis of Bub3 interactions in the mitotic spindle checkpoint. *Proc. Natl. Acad. Sci. U.S.A.* 104, 1201–1206. doi: 10.1073/pnas.0610358104
- Lau, D. T., and Murray, A. W. (2012). Mad2 and Mad3 cooperate to arrest budding yeast in mitosis. *Curr. Biol.* 22, 180–190. doi: 10.1016/j.cub.2011.12.029
- Leduc, C., Padberg-Gehle, K., Varga, V., Helbing, D., Diez, S., and Howard, J. (2012). Molecular crowding creates traffic jams of kinesin motors on microtubules. *Proc. Natl. Acad. Sci. U.S.A.* 109, 6100–6105. doi: 10.1073/pnas.1107281109
- Li, C., Zhu, Y., Wang, Y., and Chen, G. (2014). Molecular dynamics simulation on the conformational transition of the mad2 protein from the open to the closed state. *Int. J. Mol. Sci.* 15, 5553–5569. doi: 10.3390/ijms15045553
- Liu, D., Vleugel, M., Backer, C. B., Hori, T., Fukagawa, T., Cheeseman, I. M., et al. (2010). Regulated targeting of protein phosphatase 1 to the outer kinetochore by KNL1 opposes Aurora B kinase. *J. Cell Biol.* 188, 809–920. doi: 10.1083/jcb.201001006
- London, N., Ceto, S., Ranish, J. A., and Biggins, S. (2012). Phosphoregulation of Spc105 by Mps1 and PP1 regulates Bub1 localization to kinetochores. *Curr. Biol.* 22, 900–906. doi: 10.1016/j.cub.2012.03.052
- Luo, X., Fang, G., Coldiron, M., Lin, Y., Yu, H., Kirschner, M. W., et al. (2000). Structure of the MAD2 spindle assembly checkpoint protein and its interaction with CDC20. *Nat. Struct. Biol.* 7, 224–229. doi: 10.1038/73338
- Luo, X., Tang, Z., Rizo, J., and Yu, H. (2002). The MAD2 spindle checkpoint protein undergoes similar major conformational changes upon binding to either MAD1 or CDC20. *Mol. Cell* 9, 59–71. doi: 10.1016/S1097-2765(01)00435-X
- Luo, X., Tang, Z., Xia, G., Wassmann, K., Matsumoto, T., Rizo, J., et al. (2004). The Mad2 spindle checkpoint protein has two distinct natively folded states. *Nat. Struct. Mol. Biol.* 11, 338–345. doi: 10.1038/nsmb748
- Luo, X., and Yu, H. (2008). Protein metamorphosis: the two-state behavior of Mad2. *Structure* 16, 1616–1625. doi: 10.1016/j.str.2008.10.002
- Maciejowski, J., George, K. A., Terret, M. E., Zhang, C., Shokat, K. M., and Jallepalli, P. V. (2010). Mps1 directs the assembly of Cdc20 inhibitory complexes during interphase and mitosis to control M phase timing and spindle checkpoint signaling. *J. Cell Biol.* 190, 89–100. doi: 10.1083/jcb.201001050
- Maldonado, M., and Kapoor, T. M. (2011). Constitutive Mad1 targeting to kinetochores uncouples checkpoint signalling from chromosome biorientation.

- Nat. Cell Biol.* 13, 475–482. Erratum in: *Nat. Cell Biol.* (2011) 13, 633. doi: 10.1038/ncb2223
- Mao, Y., Abrieu, A., and Cleveland, D. W. (2003). Activating and silencing the mitotic checkpoint through CENP-E-dependent activation/inactivation of BubR1. *Cell* 114, 87–98. doi: 10.1016/S0092-8674(03)00475-6
- Mao, Y. S., Zhang, B., and Spector, D. L. (2011). Biogenesis and function of nuclear bodies. *Trends Genet.* 27, 295–306. doi: 10.1016/j.tig.2011.05.006
- Mapelli, M., Massimiliano, L., Santaguida, S., and Musacchio, A. (2007). The Mad2 conformational dimer: structure and implications for the spindle assembly checkpoint. *Cell* 131, 730–743. doi: 10.1016/j.cell.2007.08.049
- McEwen, B. F., Chan, G. K., Zubrowski, B., Savoian, M. S., Sauer, M. T., and Yen, T. J. (2001). CENP-E is essential for reliable bioriented spindle attachment, but chromosome alignment can be achieved via redundant mechanisms in mammalian cells. *Mol. Biol. Cell* 12, 2776–2789. doi: 10.1091/mbc.12.9.2776
- McGuffee, S. R., and Elcock, A. H. (2010). Diffusion, crowding and protein stability in a dynamic molecular model of the bacterial cytoplasm. *PLoS Comput. Biol.* 6:e1000694. doi: 10.1371/journal.pcbi.1000694
- Mendiburo, M. J., Padeken, J., Fulop, S., Schepers, A., and Heun, P. (2011). Drosophila CENH3 is sufficient for centromere formation. *Science* 334, 686–690. doi: 10.1126/science.1206880
- Meyer, R. E., Kim, S., Obeso, D., Straight, P. D., Winey, M., and Dawson, D. S. (2013). Mps1 and Ipl1/Aurora B act sequentially to correctly orient chromosomes on the meiotic spindle of budding yeast. *Science* 339, 1071–1074. doi: 10.1126/science.1232518
- Miermont, A., Waharte, F., Hu, S., McClean, M. N., Bottani, S., Léon, S., et al. (2013). Severe osmotic compression triggers a slowdown of intracellular signaling, which can be explained by molecular crowding. *Proc. Natl. Acad. Sci. U.S.A.* 110, 5725–5730. doi: 10.1073/pnas.1215367110
- Morrow, C. J., Tighe, A., Johnson, V. L., Scott, M. I., Ditchfield, C., and Taylor, S. S. (2005). BUB1 and aurora B cooperate to maintain BubR1-mediated inhibition of APC/CCDC20. *J. Cell Sci.* 118, 3639–3652. doi: 10.1242/jcs.02487
- Musacchio, A. (2011). Spindle assembly checkpoint: the third decade. *Philos. Trans. R. Soc. Lond. B Biol. Sci.* 366, 3595–3604. doi: 10.1098/rstb.2011.0072
- Musacchio, A., and Salmon, E. D. (2007). The spindle-assembly checkpoint in space and time. *Nat. Rev. Mol. Cell Biol.* 8, 379–393. doi: 10.1038/nrm2163
- Nezi, L., Rancati, G., De Antoni, A., Pasqualato, S., Piatti, S., and Musacchio, A. (2006). Accumulation of Mad2-Cdc20 complex during spindle checkpoint activation requires binding of open and closed conformers of Mad2 in *Saccharomyces cerevisiae*. *J. Cell. Biol.* 174, 39–51. doi: 10.1083/jcb.200602109
- Nilsson, J., Yekezare, M., Minshull, J., and Pines, J. (2008). The APC/C maintains the spindle assembly checkpoint by targeting Cdc20 for destruction. *Nat. Cell Biol.* 10, 1411–1420. doi: 10.1038/ncb1799
- Palmer, D. K., O'Day, K., Trong, H. L., Charbonneau, H., and Margolis, R. L. (1991). Purification of the centromerespecific protein CENP-A and demonstration that it is a distinctive histone. *Proc. Natl. Acad. Sci. U.S.A.* 88, 3734–3738.
- Pawson, T., and Nash, P. (2003). Assembly of cell regulatory systems through protein interaction domains. *Science* 300, 445–452. doi: 10.1126/science.1083653
- Perpelescu, M., and Fukagawa, T. (2011). The ABCs of CENPs. *Chromosoma* 120, 425–446. doi: 10.1007/s00412-011-0330-0
- Petrovic, A., Mosalaganti, S., Keller, J., Mattiuzzo, M., Overlack, K., Krenn, V., et al. (2014). Modular assembly of RWD domains on the Mis12 complex underlies outer kinetochore organization. *Mol. Cell* 53, 591–605. doi: 10.1016/j.molcel.2014.01.019
- Pfleger, C. M., and Kirschner, M. W. (2000). The KEN box: an APC recognition signal distinct from the D box targeted by Cdh1. *Genes Dev.* 14, 655–665.
- Primorac, I., Weir, J. R., Chiroli, E., Gross, F., Hoffmann, I., van Gerwen, S., et al. (2013). Bub3 reads phosphorylated MELT repeats to promote spindle assembly checkpoint signaling. *eLife* 2:e01030. doi: 10.7554/eLife.01030
- Przewloka, M. R., and Glover, D. M. (2009). The kinetochore and the centromere: a working long distance relationship. *Annu. Rev. Genet.* 43, 439–465. doi: 10.1146/annurev-genet-102108-134310
- Przewloka, M. R., Venkei, Z., Bolanos-Garcia, V. M., Debski, J., Dadlez, M., and Glover, D. M. (2011). CENP-C is a structural platform for kinetochore assembly. *Curr. Biol.* 21, 399–405. doi: 10.1016/j.cub.2011.02.005
- Punttovall, P., Linding, R., Gemünd, C., Chabanis-Davidson, S., Mattingdal, M., Cameron, S., et al. (2003). ELM server: a new resource for investigating short functional sites in modular eukaryotic proteins. *Nucleic Acids Res.* 31, 3625–3630. doi: 10.1093/nar/gkg545
- Putkey, F. R., Cramer, T., Morphew, M. K., Silk, A. D., Johnson, R. S., McIntosh, J. R., et al. (2002). Unstable kinetochore-microtubule capture and chromosomal instability following deletion of CENP-E. *Dev. Cell* 3, 351–365. doi: 10.1016/S1534-5807(02)00255-1
- Reis, A., Levesque, M., Chang, H. Y., Elliott, D. J., and Jones, K. T. (2006). The CRY box: a second APCcdh1-dependent degron in mammalian cdc20. *EMBO Rep.* 7, 1040–1045. doi: 10.1038/sj.emboj.7400772
- Rosenberg, J. S., Cross, F. R., and Funabiki, H. (2011). KNL1/Spc105 recruits PP1 to silence the spindle assembly checkpoint. *Curr. Biol.* 21, 942–947. doi: 10.1016/j.cub.2011.04.011
- Santaguida, S., and Musacchio, A. (2009). The life and miracles of kinetochores. *EMBO J.* 28, 2511–2531. doi: 10.1038/embj.2009.173
- Sasahara, K., McPhie, P., and Minton, A. P. (2003). Effect of dextran on protein stability and conformation attributed to macromolecular crowding. *J. Mol. Biol.* 326, 1227–1237. doi: 10.1016/S0022-2836(02)01443-2
- Schaar, B. T., Chan, G. K., Maddox, P., Salmon, E. D., and Yen, T. J. (1997). CENP-E function at kinetochores is essential for chromosome alignment. *J. Cell Biol.* 139, 1373–1382. doi: 10.1083/jcb.139.6.1373
- Schlessinger, A., Liu, J., and Rost, B. (2007). Natively unstructured loops differ from other loops. *PLoS Comput. Biol.* 3:e140. doi: 10.1371/journal.pcbi.0030140
- Schuylar, S. C., Wu, Y. F., and Kuan, V. J. (2012). The Mad1-Mad2 balancing act—a damaged spindle checkpoint in chromosome instability and cancer. *J. Cell Sci.* 125, 4197–4206. doi: 10.1242/jcs.107037
- Schwartzman, J. M., Duijf, P. H., Sotillo, R., Coker, C., and Benezra, R. (2011). Mad2 is a critical mediator of the chromosome instability observed upon Rb and p53 pathway inhibition. *Cancer Cell* 19, 701–714. doi: 10.1016/j.ccr.2011.04.017
- Sedgwick, G. G., Hayward, D. G., Di Fiore, B., Pardo, M., Yu, L., Pines, J., et al. (2013). Mechanisms controlling the temporal degradation of Nek2A and Kif18A by the APC/C-Cdc20 complex. *EMBO J.* 32, 303–314. doi: 10.1038/embj.2012.335
- Seet, B. T., Dikic, I., Zhou, M. M., and Pawson, T. (2006). Reading protein modifications with interaction domains. *Nat. Rev. Mol. Cell Biol.* 7, 473–483. doi: 10.1038/nrm1960
- Shepperd, L. A., Meadows, J. C., Sochaj, A. M., Lancaster, T. C., Zou, J., Buttrick, G. J., et al. (2012). Phosphodependent recruitment of Bub1 and Bub3 to Spc7/KNL1 by Mph1 kinase maintains the spindle checkpoint. *Curr. Biol.* 22, 891–899. doi: 10.1016/j.cub.2012.03.051
- Sickmeier, M., Hamilton, J. A., LeGall, T., Vacic, V., Cortese, M. S., Tantos, A., et al. (2007). DisProt: the database of disordered proteins. *Nucleic Acids Res.* 35, D786–D793. doi: 10.1093/nar/gkl893
- Simorellis, A. K., and Flynn, P. F. (2006). Fast local backbone dynamics of encapsulated ubiquitin. *J. Am. Chem. Soc.* 128, 9580–9581. doi: 10.1021/ja061705p
- Sironi, L., Mapelli, M., Knapp, S., De Antoni, A., Jeang, K. T., and Musacchio, A. (2002). Crystal structure of the tetrameric Mad1-Mad2 core complex: implications of a ‘safety belt’ binding mechanism for the spindle checkpoint. *EMBO J.* 21, 2496–2506. doi: 10.1093/embj/21.10.2496
- Sironi, L., Melixetian, M., Faretta, M., Prosperini, E., Helin, K., and Musacchio, A. (2001). Mad2 binding to Mad1 and Cdc20, rather than oligomerization, is required for the spindle checkpoint. *EMBO J.* 20, 6371–6382. doi: 10.1093/embj/20.22.6371
- Sopko, R., Huang, D., Preston, N., Chua, G., Papp, B., Kafadar, K., et al. (2006). Mapping pathways and phenotypes by systematic gene overexpression. *Mol. Cell* 21, 319–330. doi: 10.1016/j.molcel.2005.12.011
- Sotillo, R., Hernando, E., Diaz-Rodriguez, E., Teruya-Feldstein, J., Cordón-Cardo, C., Lowe, S. W., et al. (2007). Mad2 overexpression promotes aneuploidy and tumorigenesis in mice. *Cancer Cell* 11, 9–23. doi: 10.1016/j.ccr.2006.10.019
- Sotillo, R., Schwartzman, J. M., Soccia, N. D., and Benezra, R. (2010). Mad2-induced chromosome instability leads to lung tumour relapse after oncogene withdrawal. *Nature* 464, 436–440. doi: 10.1038/nature08803
- Stoler, S., Keith, K. C., Curnick, K. E., and Fitzgerald-Hayes, M. (1995). A mutation in CSE4, an essential gene encoding a novel chromatin-associated protein in yeast, causes chromosome nondisjunction and cell cycle arrest at mitosis. *Genes Dev.* 9, 573–586. doi: 10.1101/gad.9.5.573
- Tachiwana, H., Kagawa, W., Shiga, T., Osakabe, A., Miya, Y., Saito, K., et al. (2011). Crystal structure of the human centromeric nucleosome containing CENP-A. *Nature* 476, 232–235. doi: 10.1038/nature10258
- Tanaka, K. (2013). Regulatory mechanisms of kinetochore-microtubule interaction in mitosis. *Cell Mol. Life Sci.* 70, 559–579. doi: 10.1007/s00018-012-1057-7

- Tang, Z., Bharadwaj, R., Li, B., and Yu, H. (2001). Mad2-independent inhibition of APC<sup>Cdc20</sup> by the mitotic checkpoint protein BubR1. *Dev. Cell* 1, 227–237. doi: 10.1016/S1534-5807(01)00019-3
- Tang, Z., Shu, H., Oncel, D., Chen, S., and Yu, H. (2004). Phosphorylation of CDC20 by Bub1 provides a catalytic mechanism for APC/C inhibition by the spindle checkpoint. *Mol. Cell* 16, 387–397. doi: 10.1016/j.molcel.2004.09.031
- Tanudji, M., Shoemaker, J., L'Italien, L., Russell, L., Chin, G., and Schebye, X. M. (2004). Gene silencing of CENP-E by small interfering RNA in HeLa cells leads to missegregation of chromosomes after a mitotic delay. *Mol. Biol. Cell* 15, 3771–3781. doi: 10.1091/mbc.E03-07-0482
- Tipton, A. R., Ji, W., Sturt-Gillespie, B., Bekier, M. E. 2nd., Wang, K., Taylor, W. R., et al. (2013). Monopolar spindle 1 (MPS1) kinase promotes production of closed MAD2 (C-MAD2) conformer and assembly of the mitotic checkpoint complex. *J. Biol. Chem.* 288, 35149–35158. doi: 10.1074/jbc.M113.522375
- Vanoosthuysse, V., and Hardwick, K. G. (2005). Bub1 and the multilayered inhibition of CDC20-APC/C in mitosis. *Trends Cell Biol.* 15, 231–233. doi: 10.1016/j.tcb.2005.03.003
- Vavouri, T., Semple, J. I., Garcia-Verdugo, R., and Lehner, B. (2009). Intrinsic protein disorder and interaction promiscuity are widely associated with dosage sensitivity. *Cell* 138, 198–208. doi: 10.1016/j.cell.2009.04.029
- Venkei, Z., Przewloka, M. R., Ladak, Y., Albadri, S., Sossick, A., Juhasz, G., et al. (2012). Spatiotemporal dynamics of Spc105 regulates the assembly of the Drosophila kinetochore. *Open Biol.* 2, 110032. doi: 10.1098/rsob.110032
- Vink, M., Simonetta, M., Transidico, P., Ferrari, K., Mapelli, M., De Antoni, A., et al. (2006). *In vitro* FRAP identifies the minimal requirements for Mad2 kinetochore dynamics. *Curr. Biol.* 16, 755–766. doi: 10.1016/j.cub.2006.03.057
- Wan, J., Subramonian, D., and Zhang, X. D. (2012). SUMOylation in control of accurate chromosome segregation during mitosis. *Curr. Protein Pept. Sci.* 13, 467–481. doi: 10.2174/138920312802430563
- Wan, X., O'Quinn, R. P., Pierce, H. L., Joglekar, A. P., Gall, W. E., DeLuca, J. G., et al. (2009). Protein architecture of the human kinetochore microtubule attachment site. *Cell* 137, 672–684. doi: 10.1016/j.cell.2009.03.035
- Wang, Y., Li, C., and Pielak, G. J. (2010). Effects of proteins on protein diffusion. *J. Am. Chem. Soc.* 132, 9392–9397. doi: 10.1021/ja102296k
- Wang, Y., Sarkar, M., Smith, A. E., Krois, A. S., and Pielak, G. J. (2012). Macromolecular crowding and protein stability. *J. Am. Chem. Soc.* 134, 16614–16618. doi: 10.1021/ja305300m
- Warren, C. D., Brady, D. M., Johnston, R. C., Hanna, J. S., Hardwick, K. G., and Spencer, F. A. (2002). Distinct chromosome segregation roles for spindle checkpoint proteins. *Mol. Biol. Cell* 13, 3029–3041. doi: 10.1091/mbc.E02-04-0203
- Wei, R. R., Al-Bassam, J., and Harrison, S. C. (2007). The Ndc80/HEC1 complex is a contact point for kinetochore-microtubule attachment. *Nat. Struct. Mol. Biol.* 14, 54–55. doi: 10.1038/nsmb1186
- Wei, R. R., Sorger, P. K., and Harrison, S. C. (2005). Molecular organization of the Ndc80 complex, an essential kinetochore component. *Proc. Natl. Acad. Sci. U.S.A.* 102, 5363–5367. doi: 10.1073/pnas.0501168102
- Weiss, E., and Winey, M. (1996). The *Saccharomyces cerevisiae* spindle pole body duplication gene *MPS1* is part of a mitotic checkpoint. *J. Cell Biol.* 132, 111–123. doi: 10.1083/jcb.132.1.111
- Welcker, M., and Clurman, B. E. (2008). FBW7 ubiquitin ligase: a tumour suppressor at the crossroads of cell division, growth and differentiation. *Nat. Rev. Cancer* 8, 83–93. doi: 10.1038/nrc2290
- Westhorpe, F. G., and Straight, A. F. (2013). Functions of the centromere and kinetochores in chromosome segregation. *Curr. Opin. Cell Biol.* 25, 334–340. doi: 10.1016/j.ceb.2013.02.001
- Wilson, D. K., Cerna, D., and Chew, E. (2005). The 1.1-angstrom structure of the spindle checkpoint protein Bub3p reveals functional regions. *J. Biol. Chem.* 280, 13944–13951. doi: 10.1074/jbc.M412919200
- Winey, M., and Huneycutt, B. J. (2002). Centrosomes and checkpoints: the MPS1 family of kinases. *Oncogene* 21, 6161–6169. doi: 10.1038/sj.onc.1205712
- Xia, G., Luo, X., Habu, T., Rizo, J., Matsumoto, T., and Yu, H. (2004). Conformation-specific binding of p31(comet) antagonizes the function of Mad2 in the spindle checkpoint. *EMBO J.* 23, 3133–3143. doi: 10.1038/sj.emboj.7600322
- Yang, M., Li, B., Liu, C. J., Tomchick, D. R., Machius, M., Rizo, J., et al. (2008). Insights into mad2 regulation in the spindle checkpoint revealed by the crystal structure of the symmetric mad2 dimer. *PLoS Biol.* 6:e50. doi: 10.1371/journal.pbio.0060050
- Yang, M., Li, B., Tomchick, D. R., Machius, M., Rizo, J., Yu, H., et al. (2007). p31comet blocks Mad2 activation through structural mimicry. *Cell* 131, 744–755. doi: 10.1016/j.cell.2007.08.048
- Yao, X., Abrieu, A., Zheng, Y., Sullivan, K. F., and Cleveland, D. W. (2000). CENP-E forms a link between attachment of spindle microtubules to kinetochores and the mitotic checkpoint. *Nat. Cell Biol.* 2, 484–491. doi: 10.1038/35019518
- Yao, Y., and Dai, W. (2012). Mitotic checkpoint control and chromatin remodeling. *Front. Biosci.* 17, 976–983. doi: 10.2741/3968
- Zhang, J., Wan, L., Dai, X., Sun, Y., and Wei, W. (2014). Functional characterization of Anaphase Promoting Complex/Cyclosome (APC/C) E3 ubiquitin ligases in tumorigenesis. *Biochim. Biophys. Acta.* 1845, 277–293. doi: 10.1016/j.bbcan.2014.02.001
- Zhou, W., Wei, W., and Sun, Y. (2013). Genetically engineered mouse models for functional studies of SKP1-CUL1-F-box-protein (SCF) E3 ubiquitin ligases. *Cell Res.* 23, 599–619. doi: 10.1038/cr.2013.44

**Conflict of Interest Statement:** The authors declare that the research was conducted in the absence of any commercial or financial relationships that could be construed as a potential conflict of interest.

*Received: 30 June 2014; accepted: 07 September 2014; published online: 29 September 2014.*

*Citation: Lee S and Bolanos-Garcia VM (2014) The dynamics of signal amplification by macromolecular assemblies for the control of chromosome segregation. *Front. Physiol.* 5:368. doi: 10.3389/fphys.2014.00368*

*This article was submitted to Systems Biology, a section of the journal Frontiers in Physiology.*

*Copyright © 2014 Lee and Bolanos-Garcia. This is an open-access article distributed under the terms of the Creative Commons Attribution License (CC BY). The use, distribution or reproduction in other forums is permitted, provided the original author(s) or licensor are credited and that the original publication in this journal is cited, in accordance with accepted academic practice. No use, distribution or reproduction is permitted which does not comply with these terms.*

# Advantages of publishing in Frontiers



## OPEN ACCESS

Articles are free to read,  
for greatest visibility



## COLLABORATIVE PEER-REVIEW

Designed to be rigorous  
– yet also collaborative,  
fair and constructive



## FAST PUBLICATION

Average 85 days from  
submission to publication  
(across all journals)



## COPYRIGHT TO AUTHORS

No limit to article  
distribution and re-use



## TRANSPARENT

Editors and reviewers  
acknowledged by name  
on published articles



## SUPPORT

By our Swiss-based  
editorial team



## IMPACT METRICS

Advanced metrics  
track your article's impact



## GLOBAL SPREAD

5'100'000+ monthly  
article views  
and downloads



## LOOP RESEARCH NETWORK

Our network  
increases readership  
for your article

## Frontiers

EPFL Innovation Park, Building I • 1015 Lausanne • Switzerland  
Tel +41 21 510 17 00 • Fax +41 21 510 17 01 • info@frontiersin.org  
[www.frontiersin.org](http://www.frontiersin.org)

## Find us on

